

All eyes north

The Arctic — particularly Greenland — needs to become a major focus of research for years to come.

Halfway through the International Polar Year (IPY), which actually stretches from March 2007 to March 2009, it is clear that polar research has received exactly the kind of boost that its planners were seeking. As of last month, more than 160 projects were under way with full or partial funding. Some 60 countries are involved, including such unexpected ones as Portugal and Iran.

Public outreach has been particularly successful, with children and students getting involved in polar celebrations, video links to researchers in the field and websites. The ranks of polar artists are swelling with painters, sculptors and even a puppeteer. There are IPY stamps and IPY coins, and Sweden has made toilet paper with the IPY logo on it.

More seriously, several multidisciplinary, multinational projects have now begun. Europe is deep in the throes of planning its icebreaker-cum-drillship, the *Aurora Borealis*, for launch in 2014. Denmark has started its next Greenland ice-core drilling project. In Antarctica, teams have drilled through the ice shelf to the sediment below, and others are planning an assault on the buried Gamburtsev Mountains.

Yet for all this apparent vigour, major problems remain for polar research — chief among them funding. A number of IPY-approved projects struggled to get off the ground last year, as money for them was slow to come from national governments. This includes the US National Science Foundation (NSF), the powerhouse of polar research, which was hamstrung by, among other things, the late approval by Congress of its 2008 budget.

Some money is now flowing. According to IPY managers, around \$400 million in new funds is being distributed across the entire IPY; added to the \$800 million that would normally be spent worldwide on polar research during that time, they argue it's like getting three years' funding in two years.

But that doesn't solve the tougher issue of how resources should be allocated. With its long tradition as the scientific continent, Antarctica has historically drawn the lion's share of funding. The NSF, for instance, spends about \$325 million on the continent annually, largely to maintain its massive research infrastructure there. Arctic sciences, in contrast, get about \$100 million.

Attention needs to shift northwards, and fast. The precise north-south

balance can certainly be debated. But consider how surprised researchers have been by the sudden and dramatic shrinking of the Arctic sea ice in recent summers. That fact alone signals that more monitoring and modelling is needed to understand what might happen next.

The most pressing Arctic question concerns the future of the Greenland ice sheet (see page 798). Too little attention is paid to monitoring its ice loss each summer and modelling what that might mean for the future. In total, Greenland's ice could raise the sea level by 7 metres — far less than the 21 metres locked in Antarctica, but far closer to complete meltdown. Yet Greenland gets just \$10.5 million annually of NSF money — \$9 million of which goes on logistics. Denmark pours twice that amount in, but it is still not enough.

Currently, a handful of individually motivated researchers heroically rush to the island each summer to set up monitoring stations. They capture the jerky motions of the massive outlet glaciers that are dumping Greenland's ice into the sea, and videotape the huge meltwater lakes that form on the ice sheet each summer and then drain away into oblivion. They patch together data from a motley collection of remote-sensing satellites, trying to capture the changes in Greenland's ice as they happen.

But they can only do so much. The entire polar-research community needs to come together to monitor Greenland's meltdown on a comprehensive scale. In the best of worlds, the IPY would open the eyes of those who control the purse strings to the need for more Arctic monitoring. Members of the US Congress, for one, have been happily signing up for trips to the South Pole and to Summit Station atop Greenland. It remains to be seen whether those visits will make any difference when it comes to Congress voting on money for the NSF — or whether the NSF would even choose to give more money to its Office of Polar Programs given the competing demands on its resources. But it is time to spend more on Greenland, and to think more about Greenland, and to make sure this continues for years to come. ■

"The entire polar-research community needs to come together to monitor Greenland's meltdown on a comprehensive scale."

A ghost of battles past

The US veterans' administration should go ahead with a much-delayed study of Agent Orange.

Even by government standards, a near 30-year delay in getting a study approved is extreme. But that is essentially what has happened with a proposed large-scale epidemiological study of the possible effects of the defoliant Agent Orange and other combat factors on US veterans of the Vietnam War. This US administration,

or the next, would do well to heed the advice issued last month by the National Academy of Sciences that such a study should now proceed.

The academy argues that new data, and advances in geographical information systems (J. M. Stellman *et al.* *Nature* **422**, 681–687; 2003), could plug a significant gap in earlier epidemiological studies (see page 786). Today, a study should be able to provide key information about when and where troops were exposed to the defoliant, which contained highly toxic compounds called dioxins. And advances in computing and databases mean that the study would cost a fraction of earlier estimates.

The question is whether the US Department of Veterans Affairs (VA) will cooperate. In the 1980s, pilot studies by the VA and several other government agencies found little evidence for a link between Agent Orange and veterans' health problems. They concluded that poor data made doing the large-scale study requested by Congress in 1979 impossible. The VA has been sceptical of the health claims ever since. But critics questioned the independence of those studies. So in 1991, Congress asked the National Academies to assess both the evidence for the health links and the feasibility of full-blown epidemiological studies. It disagreed with the previous analysis, saying that a large-scale study was indeed feasible. But there matters have stood ever since. An independent study cannot happen until the VA provides the funding — which has not been forthcoming.

It is time to stop stalling. It is true that veterans would not be the first choice for a study on the toxicity of herbicides and dioxins — better-documented accidental exposures would be preferable. But that misses the point. The proposed study is both a legitimate research opportunity and a moral imperative. There are privacy issues with medical and other records, but these are not insurmountable. And even if the data and science are not perfect, the new models and techniques can be refined. A lot of data on some 3 million veterans

are already sitting in the government's databases — or in some cases are gathering dust, undigitized, on its shelves. Cleaning up and tying those data together would itself be valuable archival housekeeping, and would aid research.

The process would also benefit the VA. More eyes on the data would stimulate creativity, and a greater involvement of outside researchers would bolster credibility and public acceptance of the study's results. This is particularly crucial following the debate over 'Gulf War syndrome', in which government studies lasting more than a decade failed to properly identify or exclude debilitating war-related illnesses in veterans from the first Gulf War. With an increasing number of soldiers from the current war reporting symptoms of post-traumatic stress disorder, it is essential that the VA includes external scientific input as early as possible in the process of helping to treat them.

And there is a bigger picture. US veterans are not the only ones suffering as a result of the Vietnam War. So scientists and the US and Vietnamese governments need to revive stalled bilateral collaborations (see *Nature* **434**, 687; 2005) on the health effects of Agent Orange on the Vietnamese population itself. The responsibilities of warfare do not end on the battlefield, nor can they be limited by the battle lines that once divided friend from foe. ■

Broken promises

Efforts to boost science in the Islamic world need financial commitment from the nations themselves.

As part of the biggest shake-up of science and technology governance in two decades, the 57-member Organisation of the Islamic Conference (OIC) last month designated COMSTECH — its committee of science ministers — as its official agency for overseeing science. As a result, COMSTECH will now play an active part in the OIC's ten-year plan for modernization.

The OIC's member states are among the world's lowest producers of patents and research papers. According to the organization's own data, scientists from Islamic-majority countries contributed just 2.5% of articles in peer-reviewed journals between 1995 and 2005.

The OIC's long-term goal is to turn this situation around completely. It wants to see at least 20 OIC universities joining the world's top 500 — there are currently none. It is also planning a new centre for science and innovation policy, and a new network of centres of research excellence. As well as improving access to capital for technology start-ups, the OIC's plans aim to boost the capacity of industry to produce more vaccines, affordable cars and planes, and to increase collaborations with scientists and organizations outside the OIC world.

COMSTECH will share the responsibility for implementing these changes with the OIC secretariat's newly revived science and technology office in Jeddah, and with the Islamic Development Bank, which has allocated 10% of its grants and loans for science and technology. Strategic guidance and oversight will come from a task force that includes the OIC secretary-general, Ekmeleddin Ihsanoglu, a science historian from Turkey, and the chemist Atta-ur-Rahman from Pakistan, who heads the COMSTECH secretariat.

The plans are ambitious and impressive, and deserve the whole-hearted support of the OIC's member states. But the big test now is whether that support will be forthcoming. In principle, money should not be a problem: OIC member states include some of the wealthiest nations in the world. Unlike other wealthy states, however, they allocate less than 0.5% of their gross domestic product to research and development.

Related to this is the fact that the member states have a reputation inside the OIC for not delivering on their promises. Witness the controversy over COMSTECH's existing budget. For the fiscal year 2006–7, ministers approved a budget of US\$18 million for COMSTECH's work. But only \$7 million came through, including \$2.3 million from the Islamic Development Bank and \$2.6 million from member states. Of this, COMSTECH's host country, Pakistan, contributed \$2 million. Twelve of the other 56 countries contributed a mere \$600,000 between them. The rest promised much, but gave nothing.

One of the reasons for these broken promises is that, until now, a decision made by a science minister at a COMSTECH meeting has carried little or no weight in that minister's national parliament, or with his or her finance minister. COMSTECH's new status as an official body of the OIC should begin to change this. Jordan, Iran, Pakistan and Saudi Arabia have promised new money, and, for the first time, COMSTECH ministers will be able to stand before heads of state and call to account those who do not deliver.

Of course, it will still be possible for any member state to make a commitment and then completely ignore it. But such states need to understand that plans to upgrade universities or build affordable cars need a massive injection of new money. And they must appreciate that OIC institutions created to deliver those promises must be adequately funded. The OIC is right to engage the private sector and development banks in efforts to reform science and technology, but public institutions must also play their part. ■

RESEARCH HIGHLIGHTS

EVOLUTION

The meek shall...

Proc. Natl Acad. Sci. USA doi: 10.1073/pnas.0709763105 (2008)

An elephant can expect to see sixty summers, a mouse perhaps two or three. But in evolutionary terms, it seems that large mammals are more ephemeral than their smaller brethren.

Mining a database of Eurasian fossil mammals, Nils Stenseth of the University of Oslo, Norway, and his colleagues found that small-bodied groups such as rodents last longer than those in large-bodied families, such as carnivores. Large mammals had both higher origination and extinction rates.

The team suggests that small mammals tend to last longer because they can escape hard times by burrowing or hibernating. The longest-surviving groups — such as moles and dormice — burrow, hibernate, or both. Most large mammals, meanwhile, must weather whatever the environment throws at them, and their slow reproductive rates and small populations make them more vulnerable to extinction.

IMMUNOLOGY

Phantom germs

Proc. Natl Acad. Sci. USA **105**, 5549–5554 (2008)

Are nanobacteria real or merely lumps of abiotic matter? The latter, according to a pair of researchers who show that gradually precipitating calcium carbonate looks and behaves just like the purported microorganisms.

Nanometre-sized blobs that grow in liquid cell culture media have been shown to provoke immune responses and been linked to kidney-stone formation and cancer. But John Ding-E Young of Rockefeller University in New York and Jan Martel of Chang Gung University in Taiwan were able to produce many of these particles' characteristic properties with calcium carbonate lumps. The precipitates were membrane-delineated, vesicle-like particles of uniform size that aggregated in colonies, and exhibited cell-like division. Tellingly, nanobacteria-like

Vestigial finery

Anim. Behav. **75**, 1209–1219 (2008)

The elaborate train of the Indian peacock (*Pavo cristatus*) is the textbook example of a trait that is driven by female mate choice — or so everybody believed.

Mariko Takahashi at the University of Tokyo and her colleagues ran a seven-year study examining interactions between feral peahens and peacocks. They found no evidence that peahens preferred peacocks with trains that were longer, more marked or more symmetrical. They also noticed that peacocks usually actively shook their train after peahens initiated courtship, suggesting that train display is not luring females.

The train may once have been driven by sexual selection, but today it seems that the hens have grown weary of the ornament.

particles the researchers obtained from human blood withstood massive doses of ionizing radiation. Furthermore, monoclonal antibodies supposedly specific for nanobacteria react with serum albumin, the most abundant protein in plasma.

PHYSICS

Tiny twisters

Phys. Rev. Lett. **100**, 144501 (2008)

Hurricanes span hundreds of kilometres across the globe, but a centimetre-scale version can be made on the surface of a soap bubble.

Fanny Seychelles of the University of Bordeaux in France and her colleagues blew a hemispheric soap bubble on top of a soapy solution. As they heated the solution, they sometimes saw isolated vortices form on the bubble's surface (pictured left).

They found that the vortices' random motion resembled that of real-world hurricanes.

The authors say that bubble twisters are a useful lab model for studying turbulent fluids.

ACOUSTICS

Undersea rain sounds

J. Acoust. Soc. Am. **123**, 1952–1962 (2008)

Measuring rainfall over the oceans is tough — there are few rain gauges and satellite radar resolution is poor. Jeffrey Nystuen at the University of Washington in Seattle and his colleagues have found a way around this: listening to the rain from underwater.

The researchers dropped a string of hydrophones to various depths in an area of the Ionian sea, near Greece, that is well covered by land-based radar. They separated the sounds of raindrops from noise due to drizzle, wind, ships and the clicks of diving beaked whales. The acoustic rainfall rates matched those deduced from radar. The results suggest that a hydrophone dropped to a depth of 2 kilometres could monitor rainfall over an area of 30–50 square kilometres.

EVOLUTION

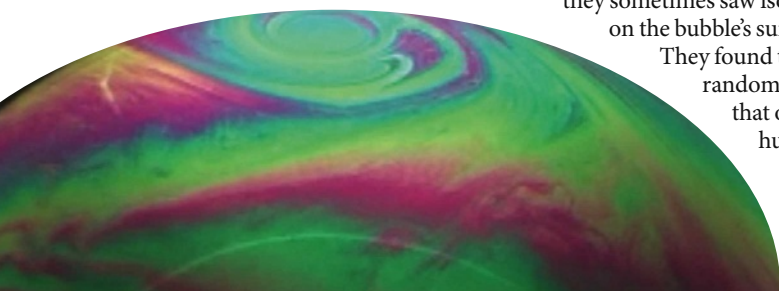
Lungless life

Curr. Biol. **10.1016/j.cub.2008.03.010** (2008)

All hail the first lungless frog: *Barbourula kalimantanensis* of Borneo, a small, flat creature that lives in fast-flowing streams. Djoko Iskandar at the Bandung Institute of



B. SACHA/CORBIS



F. SEYCHELLES/H. KELLY

Technology in Indonesia first described the frog 30 years ago. Now he, David Bickford of the National University of Singapore and Anggraini Barlian, also at the Bandung Institute, have determined by dissection that it is entirely without lungs. Instead, it breathes through its skin.

Lunglessness among the four-limbed vertebrates is rare; only two families of salamander and one species of caecilian — a limbless amphibian — are known to have evolved this trait. Unfortunately, the frog is endangered by habitat loss and gold mining, which warms, pollutes and muddies its formerly cool and clear home streams.

CLIMATOLOGY

Low cloud cover

Science **320**, 195 (2008)

The presence of fewer clouds could help to explain how global temperatures rose so markedly in 'supergreenhouse' events of the past.

The key, say Lee Kump and David Pollard of Pennsylvania State University, is the number of tiny particles in the atmosphere that serve as nuclei for clouds to condense around. In the unpolluted atmosphere, these are mostly aerosols produced by organisms such as ocean algae. The researchers used a global climate model to simulate the climate 100 million years ago. They found that if rising temperatures cause algae to be less productive, and thus provide fewer aerosol seeds for clouds to form around, clouds would be thinner and less reflective.

This would have cut the amount of solar energy reflected back into space, leading to even more drastic warming.



PALAEONTOLOGY

Unpunctuated

Evolution **62–63**, 511–520 (2008)

Palaeontologists have re-evaluated one of the first pieces of evidence to support 'punctuated equilibrium' — the theory that evolution can proceed in fits and starts — and found it lacking.

In the late 1970s and early 1980s, fossil molluscs (pictured above) from the Turkana Basin, Kenya, were interpreted as showing three bursts of rapid evolutionary change during a 3.3-million-year period. Now, Bert Van Bocxlaer of Ghent University in Belgium and his colleagues say that changes in the mollusc species can be explained more prosaically: environmental change in wet periods caused new species from outside the basin to colonize the area.

QUANTUM PHYSICS

Missing holes add up

Phys. Rev. Lett. **100**, 136804 (2008)

Quantum computing might be done on a gossamer-thin sheet of carbon, suggest Thomas Pedersen of Aalborg University in

Denmark and his co-workers. Their calculations show that a single sheet of graphene — a graphite-like material comprising a monolayer of hexagonal carbon rings joined edge to edge — could supply an array of 'quantum bits' (qubits) when perforated with a regularly spaced lattice of nanometre-scale holes.

Omitting holes in the lattice creates localized defects in the sea of electrons spread across the sheet, which act like particles with quantum-mechanical spin.

Different spin states can be used to encode bits of binary information, and adjacent spins can interact with each other for data processing. In addition, the lattice produces a controllable energy gap that could pave the way for graphene-based semiconductor devices.

BIOMEDICINE

Resisting radiation

Science **320**, 226–230 (2008)

High doses of ionizing radiation, such as those used in radiotherapy for cancer, can cause many of the body's normal cells to self-destruct. But a tool pinched from cancer's own arsenal might keep those cells alive.

Elena Feinstein of Cleveland BioLabs in Buffalo, New York, and Andrei Gudkov of the Roswell Park Cancer Institute, also in Buffalo, developed a drug from a bacterial protein, flagellin, that activates a cell-survival pathway, known as the NF- κ B pathway, that is constantly active in the majority of tumours.

Mice given 0.2 milligrams per kilogram of body weight of this protein — flagellin — survived usually lethal doses of radiation, up to 13 joules per kilogram of tissue.

JOURNAL CLUB

Bob O'Hara

University of Helsinki, Finland

A statistician wonders about the influence of additive variance.

Where complex problems are concerned, it makes things simpler if some factors can be safely ignored. In quantitative genetics, one such assumption is that the bulk of genetic variation is additive. That is, the effect of an allele — a particular version of a gene — can be adequately described by its average effect in

a population. But we know that genes often do not act additively; alleles interact, both with others of the same gene (a phenomenon known as dominance) and those of different genes (epistasis). All this contributes to the total genetic variation. But does this matter?

This question is tackled by Hill *et al.* (*PLoS Genet.* **4**, e1000008; 2008). Reviewing the literature, they show that additive genetic variance is often close to total genetic variance. The authors then look at some mathematical models with strong non-additive genetic effects, and average over

reasonable distributions of allele frequencies to show that the genetic variance is mainly additive. So non-additive genetic variation is usually of minor significance and we can continue to concentrate on additive genetic variance.

This is probably true on average, but may not always be so. Any trait is affected by only a finite, and in some cases small, number of genes. So averaging over all possible allele frequencies may say little about a particular case. There is also a much subtler problem. The authors conclude that additive genetic variance

swamps other types of variation largely because most alleles common to a population occur with close to 100% frequency. But these extreme frequencies also reduce the total genetic variance. So, in practice, a lot of traits with strong additive effects might be classified as having no detectable genetic variation, and overall the importance of additive genetic effects would be diminished. Is this a genuine problem? Ah, more research is obviously needed.

Discuss this paper at <http://blogs.nature.com/nature/journalclub>

NEWS

Further delays to full Agent Orange study

A study to investigate the health effects of Agent Orange on Vietnam War veterans is being obstructed by the US Department of Veterans Affairs (VA), claim scientists and veterans' organizations.

The department compensates veterans exposed to Agent Orange who have since gone on to develop conditions known to be linked to dioxins in the herbicide, such as non-Hodgkin's lymphoma and soft-tissue cancer. But for many other diseases, the department says there is not enough evidence to establish a link. The list of diseases that are accepted for compensation purposes comes from better-documented studies on industrial and other accidental exposures to dioxins.

In 2003, the US Institute of Medicine (IOM) recommended that the VA should commission a large-scale, independent epidemiological study on how the herbicide affected the health of veterans. The recommendation received strong bipartisan backing by both congressional and Senate veterans committees. But five years later, the VA has yet to act, and instead has pursued its own \$700,000 internal study to 'validate' the models endorsed by the IOM. The VA also asked a different panel of experts at the IOM — not involved in Agent Orange research — to look again at whether such a study was needed. It reached much the same conclusions as the first panel.

"The whole thing makes me very sad, as we have lost five years," says Jeanne Stellman, an Agent Orange expert now at SUNY Downstate Medical Center in New York, who doubts that the department will ever support the study.

It was a paper by Stellman and her colleagues (J. M. Stellman *et al.* *Nature* 422, 681–687; 2003) that prompted the IOM's initial recommendations. Her team analysed data from flight records of US military aircraft and provided the most detailed computerized maps — or geographical information systems — of where, when and how much herbicide was sprayed in Vietnam. The US Air Force sprayed Agent Orange from 1961 to 1971 to wipe out the jungle vegetation concealing their Viet Cong opposition. Stellman's team calculated that four times more dioxin was sprayed than had previously been estimated.

Her system could allow researchers to combine

data on the positions of individual troops and databases of the health of veterans and so make a study feasible, the IOM decided. In November 2003, a bipartisan group from the veterans committees of both the Congress and Senate requested the VA to "immediately contract with IOM to establish an \$8 million epidemiology research programme for independent investigators". But in a reply the following month, the then VA head Anthony Principi snubbed the request, declining to contract with the IOM, arguing that it was better placed to contract out that research itself. It has yet to do so.

The IOM's latest report says that the in-house research the VA has launched cannot meet its stated goal of validating the model, is "insufficient" and "falls short of the complete array of work that the committee believes would be appropriate".

In testimony to the IOM panel last year, Mark Brown, director of the environmental agents section of the VA, said that he still considered an epidemiological study to be "a little naive ... due to the lack of usable exposure and troop location data". Brown said that the department's existing approach to veteran compensation was adequate.

"Not to follow up on the Stellman work would be missing an opportunity," says David Savitz, chair of the IOM panel and an epidemiologist at Mount Sinai School of Medicine in New York. It would go some way to redressing the dearth of studies on herbicide exposure in veterans, Savitz

says. It is not so much about dioxin science per se, for which much better data are available elsewhere, he says, but about learning more about the exposure and health of Vietnam veterans. There is an element of "social justice", he says, but ultimately, whether the study is pursued is also a political question.

Congress first mandated such a large-scale epidemiological study in 1979. But the US Centers for Disease Control and Prevention in Atlanta, Georgia, cancelled it, handing back much of the \$70-million funding, arguing that a pilot study showed that it was impossible to disentangle the effects of Agent Orange from other causes. Many politicians and scientists argued at the time that

"There is an element of social justice, but ultimately, whether the study is pursued is a political question."



the study was politically rigged to fail.

In the latest twist, a paper published on 12 March in the *Journal of Exposure Science and Environmental Epidemiology* reports that the Stellman system overestimated the drift of herbicide from flight paths when compared with other crop-spraying aerial-dispersion models. The paper concludes that the system therefore "cannot be used to provide individual exposure estimates for the purpose of conducting epidemiologic studies". The work was sponsored by Monsanto and Dow Chemical Company, firms that manufactured Agent Orange and remain embroiled in lawsuits involving veterans.

The authors, from the consultancies M. E. Ginevan & Associates in Silver Spring, Maryland, and Infoscientific.com in Carmichael, California, presented a draft of the paper to the IOM panel, which concluded that it did not seem to fundamentally detract from the model. Richard Clapp, an epidemiologist at Boston University in Massachusetts, says that he "is not impressed" by the new paper. "It strikes me as manufacturing uncertainty, and primarily

BETTMANN/CORBIS



Agent Orange was used to defoliate jungle vegetation during the Vietnam War.

aimed at undermining the Stelman exposure index, which the US National Academy of Sciences committee also evaluated and ultimately endorsed," he says. "The Stelman model is not perfect," he concedes, "but it is a substantial, significant improvement over existing methods." The new paper's authors were unavailable for comment before *Nature* went to press.

Almost all research on veterans is funded by the VA. Several researchers interviewed by *Nature* complain that non-VA scientists face enormous difficulties in gaining access to the department's data. One of the key IOM recommendations, says Savitz, is that government agencies should create a clearing-house to streamline and ease access to military data. This could "set a model for future conflicts," he says. John Sommer, executive director of the Washington bureau of the American Legion, a veterans body, says he intends to renew discussions with Congress and the VA. "We will push to have the study done." ■

Declan Butler

See Editorial, page 781.

Deal for Holy Land artefacts

A draft agreement on how archaeological sites and artefacts should be allocated in the event of an Israel-Palestine peace deal was received positively last week by Israeli archaeologists in Jerusalem.

There are nearly 7,000 archaeological sites in the West Bank and East Jerusalem, of which about 1,000 have been excavated, according to a database compiled as part of the work on the agreement. Finds include artefacts such as the Dead Sea scrolls. But the future disposition of these sites has not been discussed in the framework of talks between Israelis and Palestinians, even though such excavations are closely tied to both national identities and to historical and political claims to the territory.

Under the draft agreement, control of sites and artefacts would be determined by territorial sovereignty, and artefacts removed since Israel gained control of the West Bank in 1967 would be handed over to the new state. It also recommends that the designated world-heritage site containing the Old City of Jerusalem be enlarged to include important sites nearby. Archaeology here would be governed by a special regime in which both Israelis and Palestinians would participate. However, Israeli scholars would be allowed five years to complete study and publication of finds in such areas before their repatriation.

In the case of specific items of

archaeological heritage that have unique symbolic value — such as the Dead Sea scrolls — the agreement recommends that both sides consider loan and exchange pacts.

Debby Hershman, a curator at the Israel Museum in Jerusalem, welcomes the draft but says that it does not guarantee cooperation. "Countries Israel has signed peace agreements with — Jordan and Egypt — and to which artefacts have been repatriated, have consistently refused to loan these objects to Israeli museums," she says.

The scrolls are a particularly emotive issue. Uzi Dahari, deputy director of the Israel Antiquities Authority in Jerusalem, likes the agreement, but says that the scrolls must remain in Israeli hands. Nazmi al-Jubeih, one of the Palestinian members of the working group, disagrees. "We do not accept the argument that the scrolls are part of Israeli heritage. Jewish heritage is part of our heritage and our history as well." International treaties, al-Jubeih notes, usually make territorial sovereignty and not cultural affiliation the determining factor in deciding who controls sites and artefacts.

Al-Jubeih will present the draft to Palestinian scholars and officials at a public meeting similar to the one held in Israel, and he says it has been well-received by those who have already seen it in the Palestinian community. ■

Haim Watzman

Costa Rican biotech centre in peril

Costa Rica is on the verge of losing a multimillion-euro donation from the European Union (EU) to build a state-of-the-art biotech facility, because of government procrastination.

The EU put forward €10.9 million (US\$17.3 million) for the National Centre for Biotechnological Innovation (CENIBiot) in 2005, but is threatening to withdraw it because the Costa Rican government has so far failed to produce the necessary contracts to purchase equipment and begin construction at the facility. The government, which is to contribute €4 million, is finally expected to issue its first tenders this week. But these will have to be answered, reviewed and approved by the end of this year if the money is to be kept. "The project is at a critical stage," says Roelf Smit, the first councillor at the European Commission's

delegation in San José, Costa Rica.

CENIBiot was conceived as a technology-transfer laboratory to meet the needs of the Costa Rican economy, mainly in agriculture. Planners hope the centre will aid Costa Rica's coffee, pineapple and banana trade and lead to the development of locally grown biofuels. But two years after its inception, equipment has not been purchased and renovations have yet to begin at the site in a San José suburb. Marta Valdez, CENIBiot's director, declined to comment on the exact cause of the delay, and the government's Ministry of Science and Technology did not respond to *Nature's* enquiries.

Smit says the decision to recall the money is standard procedure for the EU. "We don't want to have money sitting around for more than three years," he says. ■

Geoff Brumfiel

SCORECARD

**Fake thunderstorms**

European researchers have become the first to deliberately trigger electrical discharges in thunderclouds using lasers.

**Fragrant spring breezes**

The fragrance of flowers travels only around one-quarter as far in today's polluted city air as it did two centuries ago, according to a University of Virginia study. Perhaps this is one cause of sharply declining bee populations.



NUMBER CRUNCH

960 is the number of significant 'natural hazard losses' — events often more colourfully described as 'acts of God' — in 2007, according to figures compiled by German insurance firm Munich Re.

US\$82 billion is the total financial cost of these events, of which the insurance industry repaid around \$30 billion.

49 fatalities occurred in the most financially costly event, Europe's Winter Storm Kyrill. The deadliest event, Cyclone Sidr in Bangladesh, cost only one-third as much, but claimed more than 3,000 lives.

ROBOT NEWS

Gender watch

Japanese company Omron has developed a system that allows security cameras to tell the difference between male and female faces automatically. It could lead to even more targeted snooping into shoppers' habits.

Sources: Opt. Soc. Am., Atmos. Environ., Munich Re, Omron Corp.

James Watson's genome sequenced at high speed

The first full genome to be sequenced using next-generation rapid-sequencing technology is published today (see page 872)¹, marking another milestone in the extraordinarily fast-moving field of human genome sequencing.

It took just four months, a handful of scientists and less than US\$1.5 million to sequence the 6 billion base pairs of DNA pioneer James Watson. The achievement is first proof of principle that these rapid-sequencing machines can decipher large, complex genomes (see page 819)². Made in this case by Connecticut-based 454 Life Sciences — a division of Roche Diagnostics — they allow many more sequencing reactions to proceed at the same time, on the same surface, than the previous generation of machines that produced the inaugural human genomes^{3,4}. That change has had big pay-offs in speed, efficiency and, ultimately, cost (see table).

James Watson's is not the first full genome to be published; that distinction goes to genomics entrepreneur J. Craig Venter, whose genome was sequenced using previous-generation machines⁵ at a cost of \$100 million. "Venter's genome was at the end of the last generation," says 454 founder Jonathan Rothberg of the Rothberg Institute for Childhood Diseases in Guilford, Connecticut, who is the Watson paper's lead author. "We did this work in January 2007, with last January's technology," he points out; the raw data were released in May 2007. "It just keeps on getting better and cheaper." Rothberg calls Watson "the first of the rest of us", but the low cost the team managed is still a far cry from the '\$1,000 genome' challenge set by the X Prize Foundation.

Not everyone agrees the method is better. "It's a new standard of sequencing technology," says Venter. "But I don't think it's a new standard of genome coverage and independent assembly."

One concern is that rapid-sequencing methods cut DNA into much shorter snippets (in this case, 250 bases) for decoding than the old method used by the international Human Genome Project (HGP) and Venter's former

company Celera for their 2001 sequences. These used 500–1,000-base snippets. Shorter snippets make reassembly more technically challenging and mean it is harder to probe areas of the genome that have large, repeating sequences.

Evan Eichler, a geneticist at the University of Washington in Seattle, notes that 5–10% of the genome consists of these complex areas, which contain disease-causing genes and vary widely among individuals. "My concern specifically is whether short-sequence technology will give us any information in those areas," Eichler says. "How much do we understand about these particular regions in Jim Watson's genome?"

Others point out that the authors on the Watson paper relied heavily on the HGP reference sequence, which they used as a guide to help them reassemble the snippets. "This paper certainly seems to be proof that they can do a good job with the 454 sequencing when they have a reference genome," says Jonathan Eisen, an evolutionary biologist at the University of California, Davis, who wants to use the machines to sequence other species. "Their next task will be to show that they can do a good job when they have no reference genome."

Despite all the sequencing advances, very little is known about how to read the book of life that is opening before us, says Michael Egholm, vice-president of research and development at 454. Egholm was part of a counselling session advising Watson on the meaning of the 20 mutations in his sequence that are reported to be associated with increased disease risk. "It was so profound, how little we were actually able to say [to him] about that," he says. "To me, it really proved that this is the beginning, not the end."

Meredith Wadman

1. Wheeler, D. A. *et al.* *Nature* **452**, 872–876 (2008).
2. Olson, M. V. *Nature* **452**, 819–820 (2008).
3. The International Human Genome Mapping Consortium *Nature* **409**, 934–941 (2001).
4. Venter, J. C. *et al.* *Science* **291**, 1304–1351 (2001).
5. Levy, S. *et al.* *PLoS Biol.* **5**, e254–e286 (2007).

QUICKER, SMALLER, CHEAPER

Genome sequenced (publication year)	HGP (2003)	Venter (2007)	Watson (2008)
Time taken (start to finish)	13 years	4 years	4.5 months
Number of scientists listed as authors	> 2,800	31	27
Cost of sequencing (start to finish)	\$2.7 billion	\$100 million	< \$1.5 million
Coverage	8–10 ×	7.5 ×	7.4 ×
Number of institutes involved	16	5	2
Number of countries involved	6	3	1

Novel analysis identifies highly biodiverse hotspots

E. E. LOUIS JR.

Biologists in Madagascar have come up with a highly detailed conservation plan using a new tool for identifying biodiversity hotspots, which analyses an unprecedented range of species in small geographical areas.

Where the world's major biodiversity hotspots lie on the world map may be well known, but planning protected areas within these sizable patches requires working out the hotspots' hottest parts — a controversial task. Most conservation strategies focus on saving individual species, but Claire Kremen and Alison Cameron of the University of California,

Berkeley, and their colleagues have considered the Madagascan ecosystem as a complex web of co-habiting species (C. Kremen *et al. Science* **320**, 222–226; 2008). The method, they say, could be rolled out for use anywhere around the globe.

Madagascar has an especially rich biodiversity with a large proportion of species found nowhere else in the world, including lemurs and many orchids. But only a small fraction of original habitat remains, and how to conserve this remainder has become a contested issue. Kremen's group has come up with a plan of unprecedented detail, putting their cards on the table before October, when a ban on mining in the country's most biodiverse areas comes up for review.

In 2003, the island state's President Marc Ravalomanana proclaimed that protected areas would be tripled in size to cover 6 million hectares — one-tenth of the country — by 2008. That deadline has held for the initial stages of identifying conservation areas, although legal protection covering the full expansion will wait until 2012. So far, the 1.7 million hectares that were gazetted five years ago have swelled to 4.3 million hectares, leaving a further 1.7 million hectares to be assigned. "We're at a critical point," says James MacKinnon, Conservation International's technical director for the region. "We have to make some really hard decisions about the last 1.7 million hectares and this study will be very helpful for that."

The new research suggests ways to expand



Safety in numbers: woolly lemurs, only found on Madagascar.

the existing protected areas and how reserve land added to the total since 2003 might be refined. Unlike previous models that set priorities, this one handled data for 2,315 species across six major taxonomic groups (including often-ignored insects and plants). And it used spatial resolutions of those species' ranges of less than one square kilometre. It took Kremen and Cameron several years, just to gather the information together and considerable computing horsepower to ponder the problem.

With their colleagues they drew proposed extensions to the existing network of reserves so that protected land and sea covered as much of all the species' ranges as possible. And the researchers weighted the species according to how endangered they were and corrected for the tendency of distributional models to overestimate the geographical range of each species.

They were under pressure to come up with results. In October 2004, Madagascar's ministries of mines and environment agreed a two-year moratorium on mining and large-scale logging in regions that might make the reserve quota. This was extended in 2006, says Mandimby 'Dimby' Razafimpahanana, the chief analyst for SAPM, an organisation that represents the national system of protected areas. "But the mining guys don't want to renew it again," he says. Kremen and her colleagues' results, along with the recommendations of two earlier analyses, will provide the scientific basis for the horse-trading to come. ■

Anna Petherick

Q&A

Kerry Sieh

Earthquake geologist **Kerry Sieh** of the California Institute of Technology in Pasadena is moving to Singapore in July to head the new S\$300 million (US\$220 million) Earth Observatory of Singapore. He talks to David Cyranoski.



investigators and about 50 graduate students and 20 postdocs. Eventually I hope to have an undergraduate programme as well.

How is Singapore's Earth science scene?

There currently isn't one. Between 25° N at Taipei and 35° S at the Australian National University in Canberra, there are no well-funded Earth research centres. We will have to create it, just as Berkeley and Stanford had to back at the end of the nineteenth century. But there are Earth scientists in other countries in the region. They just aren't very well funded. We are already talking to our Japanese and Taiwanese colleagues, for example.

Did former prime minister Lee Kuan Yew's statement: "no public purpose is served by interfering in [gay people's] private lives" influence your decision to go?

Yes, Yew weighed in on the issue while I was there last year. It was quite reassuring. There is a ban on homosexual sex. I'm not a political type, but I'm also not a sycophant. I decided to leave my acceptance speech for the gay scientist of the year award on my homepage, although I knew that Singapore might have issues with it. I don't want to be a poster boy for the Singapore gay community, but I wouldn't have gone if I couldn't bring my partner. ■

Why did you decide to move to Asia?

There are many, many interesting questions regarding Earth processes related to natural hazards in the region — the biggest ones are tsunamis, earthquakes, volcanism, sea-level rise and climate change. Most of these questions are not being addressed there, because of sparse funding regionally and thin ranks of academic researchers. The longer I have worked in the region, the more I have enjoyed it and the more aware I have become of the need for doing basic Earth science aimed at improving civilization's chances for survival. Singapore's government was very receptive to this big idea.

Singapore is not known for volcanoes, tsunamis or earthquakes, though.

Many of Singapore's neighbours are exposed to these natural processes, and its economic and political health is very much influenced

by the state of its neighbours. Singapore could get covered in 20 centimetres of ash from an Indonesian volcanic eruption. And Singapore will certainly be exposed to the effects of climate change.

What are your plans for the institute?

I am in my mid-50s now, and I have developed some grand visions about science — I have always wanted to see the impact of science on people's lives. We're proposing to do basic science to assess danger. If you want to know the risk facing an area on a fault, you need to know whether there might be a magnitude 9 earthquake or whether it's more likely to be a flurry of 8s.

Who have you recruited so far?

Paul Tapponnier will lead the tectonics group and Chris Newhall will lead the volcanology group. There will be 20 principal

Merck accused of disguising its role in research

International drug giant Merck stands accused this week of manipulating research papers on one of its products published in medical journals.

Thousands of documents relating to Merck's withdrawn painkiller rofecoxib (Vioxx) were made available as part of a legal action. They were reviewed by medical researchers paid by the litigants in the trial, which ended in 2006, and seem to show Merck's extensive involvement in ghost-writing and 'guest authorship' of research and review papers. The results of the analysis are published this week in the *Journal of the American Medical Association* (JAMA).

By omitting the names — or downgrading the involvement — of drug-industry writers, and adding the names of academics who were not substantially involved in a paper, the industry's

role in research may be concealed. And doctors may be misled over the independence of the work.

"The idea of a company conducting a clinical trial, having its employees design the trial, analyse the data, write the paper, and then towards the very end recruit academic authors to put their name on the paper to give it that seal of supposed authenticity is very wrong," says Joseph Ross, a doctor at Mount Sinai School of Medicine, New York, and one of those behind the analysis (J. S. Ross *et al.* *JAMA* **299**, 1800–1812; 2008).

Ross and his colleagues closely scrutinized 250 documents released by Merck during the case relating to rofecoxib and say there are some strong suggestions of ghost-writing. For example, one of the Merck-held documents lists a number of clinical trials in which a Merck employee is

to be author of the first draft of a manuscript. However, when these trials were published, in 16 of 20 of the articles an external academic is listed as first author.

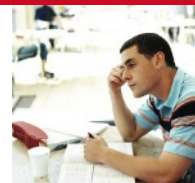
Where Ross's team was able to identify manuscript drafts before and after leaving Merck, they found "scant documentary evidence" that authors subsequently named on studies were actually involved. A pattern of "inappropriately attributing authorship to academic authors and a failure to disclose relevant financial relations" emerges from the Merck documents, they say.

Another article based on documents from a separate court case reports "striking" disparities between mortality results for the drug in published papers and those contained in Merck's internal analyses (B. M. Psaty and R. A. Kronmal *JAMA* **299**, 1813–1817; 2008).

Taken together, say two of JAMA's editors, these papers show that Merck "apparently manipulated dozens of publications to promote one of its products".

Merck rejects the allegations of manipulation and misrepresentation and denies that the documents show any wrongdoing. Jim Fitzpatrick, a partner at Merck's external counsel Hughes Hubbard & Reed in New York, says, "These are allegations that were made by these particular authors who acted as experts for the plaintiffs in the Vioxx litigation, and during the course of that litigation Merck responded to all those allegations. Quite frankly, we think that a lot of the conclusions and statements in the articles are either outright incorrect or really misleading because they lack any context surrounding them." ■

Daniel Cressey



DECISION TIME

Your brain knows what you will do before you do.

www.nature.com/news

PUNCHSTOCK

Glacial melt thaws South Asian rivalry

More than 70 international climate scientists met in Kathmandu earlier this month to begin the tricky scientific — and diplomatic — task of mapping glacial retreat in the world's highest mountains.

The massive glaciers of the Hindu Kush–Himalaya ranges supply some 1.3 billion people in the surrounding countries with water, and their retreat will have an impact on wetlands, agriculture and rangeland. Glacial lakes left by the melt are brimming, threatening to destroy homes and power stations (see *Nature* 438, 275–276; 2005). Yet there is little information about how the glaciers are changing as Earth warms. A comprehensive report released last year by the Intergovernmental Panel on Climate Change detailed the impact of global warming over much of the cryosphere — areas covered in snow, ice or permafrost — but the Himalayas were barely mentioned.

"This has been a blind spot, a big scientific question mark," says geographer Mats Eriksson, programme manager for water and hazard management at the International Centre for Integrated Mountain Development (ICIMOD) based in Kathmandu, which helped organize the three-day workshop.

The aim is to combine data from all over the region on atmospheric temperature, precipitation, wind speed, river discharge, topography and elevation to assemble models of water availability that might be useful for making policies on, for example, agriculture. There are



Increased monitoring is needed for Earth's highest glaciers.

too few remote-sensing stations, meaning that some models have been based on "very faulty information," says Michael Bishop, a physical geographer at the University of Nebraska in Omaha, who helped organize the workshop. And different countries use different algorithms to process remote-sensing data. "We need protocols so the data can be prepared," Bishop says.

The dearth of data makes it hard to assess danger and take measures to head off disaster. Studies outlining the impact of the retreating glaciers on people's lives, such as a 2005 report on glaciers in India, Nepal and China by the conservation group WWF, mostly depended on data five or ten years old, says WWF's Lifeng Li. ICIMOD, an independent centre funded by

its eight member countries — Afghanistan, Bangladesh, Bhutan, China, India, Myanmar, Nepal and Pakistan — held the workshop to address these problems. It's been a long time coming, says Bishop, who spent four years trying to coordinate research activities among the region's scientists. Political friction always prevented members from attending.

Political sensitivities also make member countries hesitant to share data. Pakistan considers all aerial photos to be state secrets, and India is wary of sharing oceanographic and land-survey data. Both are reluctant to reveal locations of observatories, Bishop says. After more than two decades working in Pakistan with data from low-altitude

climate stations, he was surprised to find out that the country also has high-altitude stations.

At the end of the workshop, the scientists called for each member state to have at least "one focal glacier under close long-term study, preferably including mass balance and velocity studies" and to "create basin-wide water scenarios for all major basins in the region".

It is not yet clear to what extent the countries will increase investment in data collection. And the workshop's call to make data sharing "politically correct" will probably face resistance. But Bishop is hopeful: "For the first time I see Pakistanis and Indians really talking, really excited, and recognizing the scientific successes of the other country."

David Cyranoski

G. DIXON/LONELY PLANET/GETTY

\$50 million cyberchallenge for plant scientists

Plant biologists were offered a dream ticket last week: US\$50 million to address the biggest challenges in their field. But the money comes with a catch. It can't be used to generate new data, only to create user-friendly computational tools. And, perhaps hardest of all, researchers have to persuade others in the field to collaborate on how to spend the funds.

The offer was presented at the inaugural meeting of the iPlant Collaborative, a project funded by the US National Science Foundation to address 'grand challenges' in

plant biology. During the coming months, researchers will form grand-challenge teams to hammer out proposals. The hope, says iPlant director Richard Jorgensen of Arizona State University in Tempe, is that the project will generate new interdisciplinary collaborations and deliver useful computational tools to the community.

Many at last week's meeting, held at the Cold Spring Harbor Laboratory, New York, were sceptical. Some thought it premature to shift the focus away from data collection when many databases are contaminated with poorly described

experiments and low-quality data. Others wondered if iPlant would meet the same fate as several previous cyberprojects that were abandoned once funding ran dry.

iPlant plans to adopt an open-source model, in which users are encouraged to develop the programs to suit their needs. That could extend the life of iPlant computational tools beyond the day that the project ends, but only if a wide community is motivated to develop them. For Jorgensen, one of the earliest challenges has been encouraging participation from ecologists and evolutionary

biologists and not just molecular biologists.

Early suggestions for grand challenges include understanding the effects of climate change to modelling how a single cell becomes a multicellular plant. Because the iPlant organizers want ideas to come from the community, they offer little guidance on what a grand challenge ought to be. As a result, preliminary brainstorming sessions were meandering and unfocused. "It's a creative chaos," says Jorgensen. "As long as we don't let it drive us completely off the cliff, we're fine." ■ Heidi Ledford

SNAPSHOT

Shuttle at cruise speed

Cold war-era Russian space shuttle Buran II is seen chugging down the River Rhine on its last, but surely most remarkable, mission. Its route, lined with hundreds of thousands of spectators, winds from Rotterdam in the Netherlands through Germany to Speyer, where the shuttle will arrive on 12 April and will eventually be installed in the Speyer Technik Museum.

The Soviet space-shuttle programme Buran (meaning 'blizzard') was conceived in 1973 and stopped in 1989. The first Buran shuttle completed one unmanned orbital flight in 1988, but was destroyed when a hangar collapsed on it in 2002. Buran II undertook 25 unmanned atmospheric test flights, but was never launched into orbit.

The shuttle was previously on show at the 2000 Olympic Games in Sydney, and in Bahrain. ■
Quirin Schiermeier



W. RATTAY/REUTERS

Germany eases ban on embryonic stem-cell lines

German researchers will be able to use hundreds more human embryonic stem-cell lines following a vote in parliament to amend the country's controversial stem-cell law.

This law had restricted researchers to working on lines created before 1 January 2002. The amendment advances the cut-off date to 1 May 2007. It will also no longer be a criminal offence for German scientists to use even newer cell lines in countries where such research is allowed.

Around 500 cell lines were created

between 2002 and 2007. "There are enough cell lines here of good quality that we can now use," says Oliver Brüstle, a stem-cell researcher at the University of Bonn.

Most scientists had been campaigning for a complete abandonment of the cut-off date, but the amendment explicitly states that it is a 'one-off' extension. This means Germans won't be able to work on cell lines that are now being developed for use in patients — but it is an acceptable compromise, says Brüstle.

Further reports announced by climate-change panel

The fifth Intergovernmental Panel on Climate Change (IPCC) report will be out by 2014, IPCC chair Rajendra Pachauri announced last week in Budapest. The report from the first working group will come out in 2013, however, so that its findings can be incorporated more fully into the reports from the second and third working groups.

At its planning meeting, the IPCC also released a smaller report on the effects of climate change on water supplies worldwide. In addition, the agency plans to produce a special report on renewable energy, which is expected to be released in 2010.

Evolution supporters unhappy with Florida bill

A bill to protect teachers who present "the full range of views" on evolution is gaining ground in the Florida legislature. Critics say that if the bill is passed administrators will not be able to discipline teachers who deviate from the recently approved state education standards supporting the teaching of evolution.

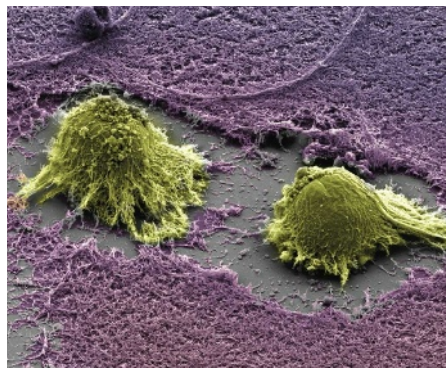
"It's a really, really bad bill," says Joe Wolf, president of Florida Citizens for Science. "Any teacher who wants to can slip in a religious idea, intelligent design or the flying spaghetti monster, and they can't be fired."

The 'academic freedom' bill borrows language from a template put together by the Discovery Institute, a Seattle-based think-tank known for its work on intelligent design.

Last week, the bill cleared committees in both chambers of the Florida legislature. Final votes are expected by early May.

Drug-safety agency names its first chief scientist

The 102-year-old US Food and Drug Administration (FDA) appointed its first chief scientist last week, acting at the behest



German researchers will have greater access to human embryonic stem cells after law change.

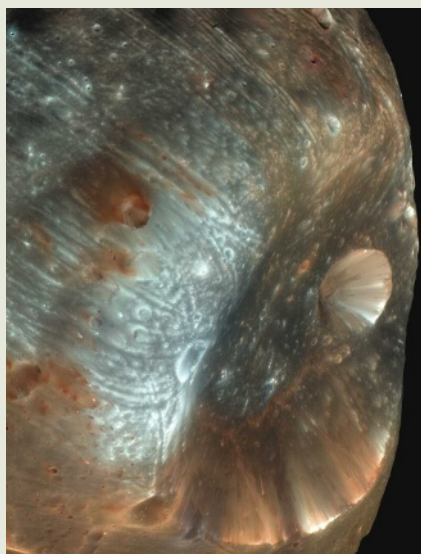
A. LEONARD/SPL

Mars moon in high resolution

The crater Stickney, on Mars's moon Phobos, is shown beautifully in this new picture acquired by the HiRISE high-resolution imaging instrument aboard the Mars Reconnaissance Orbiter.

The bluish (false) colour in this image could represent material younger than the rest of the moon's surface. Stickney, named after the wife of Phobos's discoverer, was probably formed in a giant impact that nearly shattered the moon. The crater is 9 kilometres across, the moon itself just 22 kilometres.

The long grooves that radiate out from Stickney may be left over from the impact that created it, or could have been formed by debris from the impact of another body on Mars itself, which is less than 6,000 kilometres from the moon.



Indian journals push for clinical-trial registration

Eleven of India's leading medical journals will now consider publishing the results of clinical trials only if the trial in question has been registered with the Indian Council of Medical Research (ICMR) in New Delhi or any primary clinical-trial register.

The move follows the 2005 decision by the International Committee of Medical Journal Editors to publish only the results of registered trials. According to Kanikaram Satyanarayana, deputy chief of the ICMR, the delay was partly due to reluctance by the journal editors and pressure from industry. In addition, the ICMR had hoped that a bill it drafted in 2006 to regulate human trials would become law.

Trials that start in or after June of this year must be registered before enrolling their first participant; those beginning before this must register retrospectively. The ICMR says mandatory registration will ensure transparency and honesty, and discourage unethical trials.

An estimated 250 drug trials are under way in India, with applications for 30 more received on average each month.

of Congress, which mandated the position last September.

Frank Torti, a clinician and molecular oncologist who chairs the department of cancer biology at Wake Forest University in Winston-Salem, North Carolina, will begin the job next month. He will also serve as principal deputy commissioner, effectively the agency's second-in-command.

An expert on prostate and bladder cancer

who has run many clinical trials, Torti will be charged with ensuring the quality of the agency's intramural research in response to a recent dire assessment of its scientific capabilities (see *Nature* 450, 1143; 2007).

He will also launch a high-profile, two-year FDA fellowship programme aimed at recruiting, training and retaining scientists and administrators in an effort to combat attrition at the agency.

When people talk about catastrophic climate change, there's a fair chance that Greenland is on their mind. If they use the term 'tipping point', then it is pretty much a sure thing. One-twentieth of the world's ice is locked up atop that island, and if it were to melt completely, global sea levels would rise by seven metres. The collapse of the Greenland ice sheet is in the front rank of potential climate catastrophes.

Melting is already undoubtedly and dramatically underway. Glaciers are spitting icebergs into the ocean and scurrying back up their narrow fjords like rats up drainpipes. Giant lakes are forming on the frozen surface, sending torrents of water plunging through fissures in the ice sheet and thus, perhaps, accelerating its slipping and sliding seawards. Over the past four summers, Greenland has shed an average of between 380 billion tonnes and 490 billion tonnes of ice each year — on average 150 billion tonnes more than it gains in snow in winter.

That's a lot of water. It is not, as yet, a lot of Greenland's ice, which totals 2.9 million cubic kilometres. Such size brings with it an inherent sense of stability. We do not expect things bigger than mountain ranges just to go away. But there's a disturbing sense in which Greenland shouldn't be here in the first place. It is a holdover of the most recent ice age, a creature of conditions that no longer apply. No ice sheet would grow in Greenland if the current one were to vanish — even without human-induced warming, the climate would not allow it. The ice is a relic, stranded out of time. And relics are fragile.

The question is, how fragile? Has the warming the sheet has experienced so far and the further warming already in the pipeline enough to push the ice sheet past a point of no return? If that is not yet the case, how far from that threshold are we? And if the sheet does start to go, how fast will it do so? The sheet will not vanish tomorrow, nor in a century — but assumptions that such processes take millennia are being reexamined on the basis of the changes already seen. The most recent synthesis report from the Intergovernmental Panel on Climate Change notes that the changes seen in Greenland today are not fully factored into the estimates of sea-level rise given in earlier science reports from the panel — a note that those who see Greenland as a potential poster child for catastrophe have made much of.

As yet, these pressing questions simply cannot be answered. They require models and theories not yet fully developed. And that lack of development is in part a lack of data — good data that show clear trends. Even

LOSING GREENLAND

Is the Arctic's biggest ice sheet in irreversible meltdown? And would we know if it were?

Alexandra Witze reports.

though researchers scatter themselves around the island every summer to try to capture the meltdown's extent and processes, there is no systematic, long-term, broadly based monitoring of the sort needed to produce a truly comprehensive account of what is happening with the ice sheet. "Do we have the data we need to understand what's driving these changes?" asks Ian Howat, a glaciologist at Ohio State University in Columbus. "The answer is definitely no."

The gravity of the situation

To get the best overview of the great Greenland meltdown, you need to go to space and look for gravity. The Gravity Recovery and Climate Experiment (GRACE) is a pair of US-German satellites that orbit Earth 500

kilometres up, one close behind the other. Through constant interchange of microwaves the satellites measure the distance between them very precisely, and that distance changes as massive objects below tug at the leader and the follower in slightly different ways at any given instant. The small discrepancies so produced can be used to calculate a gravity map for the planet. As masses move around, that map will change.

Data from GRACE have revealed how the water flow in the Amazon basin changes with the seasons, and which Asian aquifers are replenished by the monsoons. The mission has also provided new information about the flow of water off the massive ice sheets in Greenland and Antarctica. "When you look at a lot of the insight we have" about Greenland, says



Konrad Steffen, a glaciologist at the University of Colorado at Boulder, “it’s GRACE”.

The estimates vary as to how much mass is lost through melting each summer. Isabella Velicogna of the University of California, Irvine, leads a group that takes a large-scale approach², averaging the global gravity numbers provided by GRACE for each 30-day period. Her latest estimate suggests that 211 billion tonnes of ice are being lost each year, mainly from southern Greenland. “There is no doubt that things are changing faster than we expected,” she says. Meanwhile, Scott Luthcke of NASA’s Goddard Space Flight Center in Greenbelt, Maryland, takes a different tack, using the changing distance between the satellites to calculate the pull of smaller mass concentrations on the ground over time³.

Including the 2007 melt season, he gets preliminary estimates of 154 billion tonnes of ice lost per year. The numbers sound different, but both groups emphasize how close they are, and over time there seems to be some convergence. “These are two vastly different ways of processing data, and they’re almost within the error bars,” says Luthcke. “Greenland is losing a lot of mass.”

GRACE is also providing clues as to how the situation varies from year to year — particularly for the last melt season, when surface temperatures were 4–6 °C higher than average and during which 500 billion tonnes of ice vanished. That’s 30% more than the previous year, and 4% more than the previous record, set in 2005. “2007 was a shocking year,” says Luthcke. And GRACE’s findings are bolstered by observations of dramatic ice losses by other satellites. Radar measurements, for instance, have shown⁴ that glaciers in southern Greenland are dumping ice into the ocean ever more quickly. At the American Geophysical Union meeting in San Francisco in December, Velicogna presented results showing that the GRACE estimates are supported by data taken from the Ice, Cloud and Land Elevation Satellite (ICESat), which uses a laser altimeter to measure elevation changes on the ice sheet.

An island rising

One reason why extra information is needed to supplement the data from GRACE is the problem of ‘post-glacial rebound’. As big as Greenland’s ice sheet is today, in the ice age it was just a part of something far bigger, ice that reached as far south as the Ohio Valley and as far east as the Urals. That vast mass pressed the crust beneath it down into the denser mantle below. Although most of the ice has long since disappeared, large parts of the high-latitude crust have yet to recover from this repressed position. Scandinavia, for instance, rises 9 millimetres higher every year as the denser mantle pushes the lighter crust back up. This ongoing bounceback makes analysing the GRACE data harder.

Help may soon come from a system of global-positioning receivers that have just been installed around Greenland to measure how the bedrock is rising over time. Last summer, a team of researchers from the United States, Denmark and Luxembourg put 24 stations around the rocky, ice-free edges of the island — tripling Greenland’s global positioning system (GPS) infrastructure in one field season, according to Michael Bevis, the project leader at Ohio State University. The Greenland GPS Network (GNET) is one of the northern com-

ponents of a two-pole effort called POLENET to measure post-glacial rebound and other phenomena; there will eventually be around 50 GNET stations in Greenland. “We need much improved models of post-glacial rebound, otherwise GRACE measurements will have very limited value in Greenland and Antarctica,” says Bevis. “If we can pull this off, GRACE will become the most powerful system ever devised for measuring ice mass change.”

The GNET stations are strung along the rocky margin of Greenland, mainly in remote areas (see map, page 800). They require a lot of battery capacity to continue operating throughout the winter months, and links to five of the stations installed last summer have already gone down. The team is planning to retrieve the data manually and fix the stations this summer.

All this makes GNET a fairly expensive proposition. The last field season consumed about

US\$1 million, and flat budgets, rising fuel costs and the weak dollar are making things even tighter this year. The rest of the GNET stations will have to go in over the next two summers instead of all in 2008, as originally planned.

The GNET receivers are expensive, highly precise, heavy and, in principle, durable. Another monitoring strategy takes the opposite tack; it uses GPS equipment cheap enough to lose, embedded at the calving fronts of some of Greenland’s most active ‘outlet glaciers’. These are the thick streams of ice that flow through narrow fjords into the oceans surrounding Greenland. A decade ago, researchers thought that these outlet glaciers moved slowly, creeping downward from the high centre of the ice sheet. In recent years, though, the glaciers have been doing a veritable hokey-cokey on their approach to the ocean, first advancing rapidly, then pulling back.

It started more than a decade ago with the biggest outlet glacier of all, Jakobshavn Isbræ on the west coast, which among its claims to fame is the most likely source of the iceberg that sank the *Titanic*. Between 1992 and 2003, Jakobshavn Isbræ accelerated from 5.7 kilometres per year to 12.6 kilometres per year⁵. “That was incredibly dramatic,” says Ian Joughin, a glaciologist at the University of Washington’s Applied Physics Laboratory in Seattle. “A decade ago, nobody would have anticipated one of Greenland’s biggest outlet glaciers doubling its speed.” Faster glacier movement means more ice dumped into the ocean, and a thinning of the central ice sheet from which the glaciers feed.

Over on the east coast, the island’s other two big outlet glaciers also started speeding up⁶: Helheim in 2002, and Kangerdlugssuaq in 2005. The process didn’t go smoothly.

“2007 was a shocking year.”
— Scott Luthcke

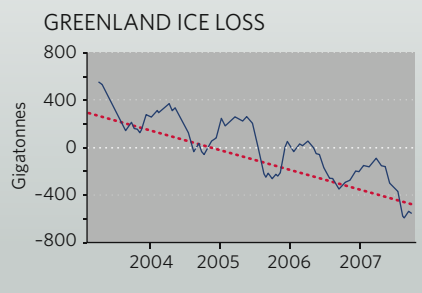
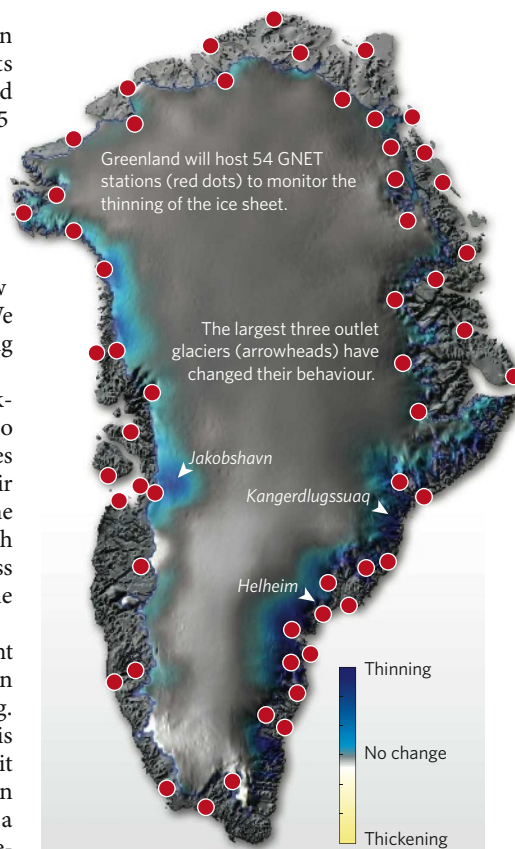


Helheim, for instance, retreated more than 3 kilometres between 2001 and 2003 as its front melted away faster than new ice flowed down to make up the difference. Then in 2005 it began advancing again as flow took over. This back-and-forth is captured most dramatically in remote-sensing images from satellites such as NASA's Terra and Aqua. "There is a lot of variability, and the important thing to remember is we only have a few good years of observations," says Joughin. "We don't know if we are looking at the beginning of a longer-term trend."

Joughin and others suspect that the back-and-forth of the outlet glaciers has a lot to do with the geometry of the fjords the ice squeezes through. The glaciers inch forward until their ends finally break off, calving icebergs into the ocean. This relieves stress on the glacier, which begins to surge, much as removing a buttress holding up a rickety old house will cause the house to collapse.

But the scenario is not as clear-cut as it might seem. In the past, glaciers advanced and then calved off icebergs when they got too long. Now, the calving happens while the glacier is advancing. What this means is unclear, but it does suggest that the glaciers are behaving in a fundamentally different manner than just a few years earlier. "This is what we cannot predict," says Steffen.

But the unpredictable is not necessarily unprecedented. During the 1920s, Greenland experienced a rapid warm-up; average annual temperatures rose more than 2 °C over the decade. At Ohio State, meteorologist Jason Box and student Adam Herrington have been looking for records of what happened to the Big Three outlet glaciers back then, to see whether there are lessons about what to expect in the future. Among their finds



was a series of maps showing the snout of the Kangerdlugssuaq glacier. Over just a few years in the early 1930s, the glacier retreated some 10 kilometres upstream — having lost an area up to 70 square kilometres in what may have been a single large calving event. The break-up, says Box, was "exceptional" in that the ice would have taken years to grow back to its previous state. And it suggests that the sort of rapid response to warming seen in recent years is the glaciers' expected response to warming.

One emerging area of research is the effect that ocean temperatures — as opposed to air temperatures — have on the outlet glaciers. Howat says, for instance, that warm ocean temperatures in the summer of 2003 coincided with a time when several of the outlet glaciers feeding into that warmer sea began speeding up dramatically. But little work has been done to correlate ocean temperatures with the glacier retreats. The ocean has been "a total blank spot on the map," Howat says. "You have a big ice sheet with a lot of it sitting in the water — you'd think you'd want to know what's happening in the water." Some researchers are starting to target this as their next area of interest.

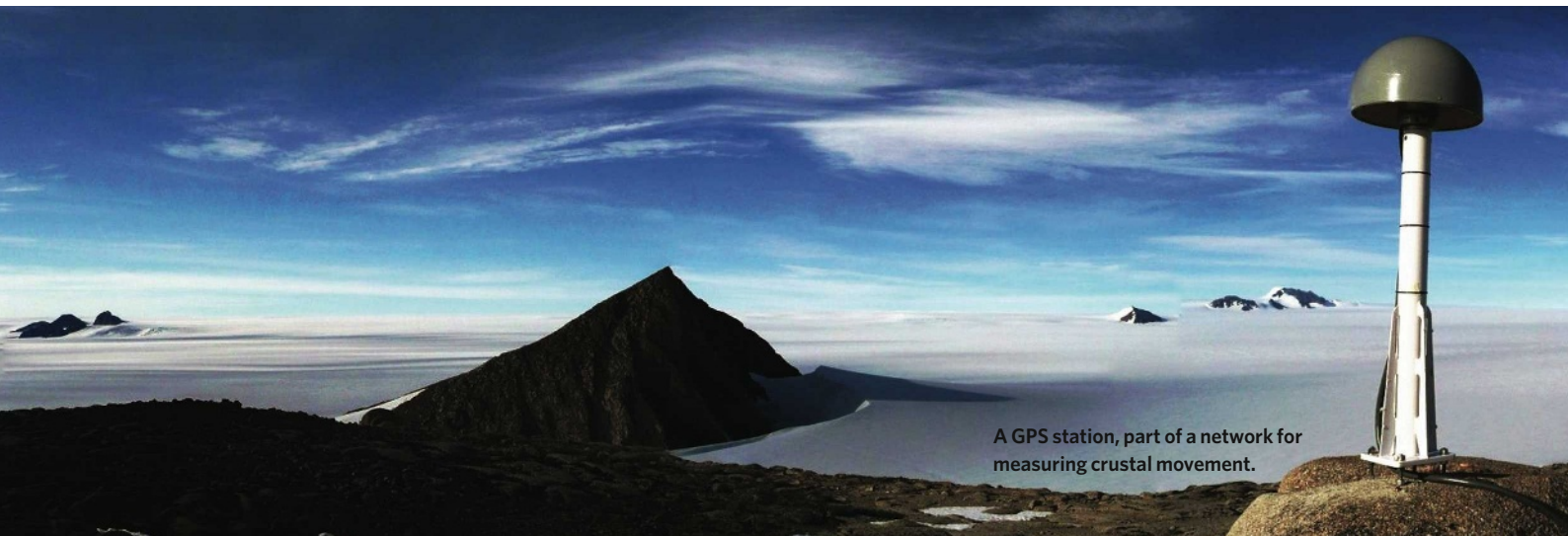
Lakes on ice

The water that surrounds Greenland has been there forever. More novel is the increasing amount of water which, in summer, sits on top of it. What starts out in the winter as cold white snow ends up in the summer as a landscape of blue water, as more than 1,000 shallow melt lakes up to 5 kilometres across form on the ice. It is like Minnesota — but white.

2007 was a particularly good year to study this surface melting, because there was a great deal of it. High-pressure weather systems

NASA/GSFC VISUALISATION STUDIO

SOURCE: S. LUTHCHE



A GPS station, part of a network for measuring crustal movement.

throughout much of the summer kept storms away, allowed the Sun to beat down on the ice almost without cease. The melt season lasted 25–30 days longer than average, and 19,000 square kilometres turned from ice to water, says Marco Tedesco of Goddard — that is roughly the area of Wales. The effect was particularly noticeable at higher elevations; as warm air swept ever higher, the area that melted at 2,000 metres or greater was 150% larger than normal.

Even in a normal May to August field season, researchers have to make sure that their instruments stay anchored on the ice sheet, planting their poles 2–3 metres deep to make sure they can withstand the melt. It's not just the water that makes things difficult — it's the unpredictability. Melt lakes have been known to drain away tens of millions of cubic metres of water in the space of a day, swirling down some unknown drain channel in the ice. Huge waterfalls appear and then disappear overnight. How exactly the water gets from the top of the ice to its bowels isn't known, but understanding the plumbing could help illuminate a crucial question — does the water that reaches the bottom of the ice sheet lubricate it in a way that encourages movement and collapse? This has become a commonplace speculation among Greenland catastrophists, but the degree to which it is actually happening, how well it explains the ice loss measured by GRACE and to what extent it may change the shorelines of the world is not yet clear.

Back to the Eemian

The suddenly apparent pace of change has led some to question previous, rather staid models of ice-sheet dynamics, which suggest that even fast changes take several centuries. "It has only been in the past five years that we have

realized that hey, the ice sheet is falling apart, these changes are happening, our models are way off," says Howat. But predicting how far off they actually are — and some believe they may not be as soon as catastrophists predict — is not easy. Anecdotes of this or that particular, however momentous, are no match for thorough, consistent monitoring. If you want models of the future you can rely on, you have to monitor the process you model. "The modelling has not happened because there are just not enough data," says Philippe Huybrechts, an ice-sheet modeller at the Free University in Brussels. Researchers on the ice might see moulins forming, or outlet glaciers calving, but "it is just in one place and for one season, or for a few weeks", he says. "To generalize from that over a whole ice sheet in a way that you can predict things, it's just not possible."

At the moment, the best Greenland modellers are stretched by trying to explain what has already happened, without even thinking about what is to come. They are responsive, not predictive. But some are trying to change that. At the University of Kansas, Cornelis Van der Veen is helping to lead an effort to improve ice-sheet models; he and others are planning a major conference to be held in July in St Petersburg, Russia. The idea is to identify the big unknowns and figure out how to tackle them, one by one. "One outlet glacier speeding up isn't really the end of the world," he notes. "But if they are doing that all over the place then that is an indication that something is going on that we really do not understand. It is not something that can be solved within a couple of months."

"It's very difficult to model a new process, such as why glaciers accelerate, before you have an understanding of why it is happening," says Dorthe Dahl-Jensen of the University of Copenhagen. "One thing is to observe it. The next step is to understand it. The third is to put it into the model and predict the future. We are at step two, struggling to understand the process."

One route to understanding may be through palaeoclimate studies. Dahl-Jensen is leading a team that aims to drill a core 2,500 metres

into the ice of northwestern Greenland over the next couple of summers. This core — the North Greenland Eemian Ice Drilling — would complement the pioneering climate records cored out of Greenland's ice over the past couple of decades. None of the earlier cores was able to extract an unbroken record of the Eemian stage, some 120,000 years ago and the last time that Earth was

"You have a big ice sheet with a lot of it sitting in the water — you'd think you'd want to know what's happening in the water." — Jason Box

in a warm 'interglacial' period. Understanding what Greenland was like then could help scientists understand how the ice sheet might respond in a warmed future, says Dahl-Jensen. Temperatures in Greenland were roughly 5 °C higher during the Eemian than they are today. Yet sea level was only one or two metres higher, and every ice core that has ever been drilled deep enough on the island has included some ice from the Eemian. "A major part of the Greenland ice sheet survived," says Dahl-Jensen — and argues that more sampling of this period might help to pinpoint the factors that could allow ice to stick around when temperatures are higher than today.

But this is not necessarily the encouraging

M. BEVIS

J. BALOG/AURORA PHOTOS



The calving rate of some Greenland glaciers has increased.

news it might seem. Because global warming is amplified near the poles, 5 °C of warming in Greenland might be achieved with just 2.5 °C of average global warming — which is quite plausible. And an important regional factor here might be the dramatic recent reductions seen in the sea ice to the island's north. The extent to which the cold, reflective ice on the sea keeps Greenland cool is simply not known.

The long view needed

More sampling of the past, together with that of the present, may help us to unravel the future of the Greenland ice sheet. For now, though, things seem to be getting more unravelled, not less. Every year brings a new set of data, a new insight into the behaviour of Greenland's interlocking ice-sheet dynamics, stream flows and glacial surges. "We are just learning so much," says Leigh Stearns, a glaciologist at the University of Maine at Orono. "Every summer brings something totally different."

But if the learning is copious, it is not systematic. Despite the real risk of a meltdown — and the real benefits to be gained from being

able to say something reliable about how long there is to go, and how high the seas might rise — the investigation of the ice's every nook and cranny is far from over. One idea is to use unmanned aerial vehicles (UAVs) to fly across the ice sheet gathering data such as the depths of melt lakes. But this is easier said than done; John Adler, a PhD student at the University of Colorado at Boulder, ran some tests last August in which he took three types of commercially available UAVs to Kangerlussuaq airport and ran flights over the melt lakes for a week. He is still getting the kinks out of the system, but says that UAVs could provide a cheaper and more repeatable way to get local measurements than relying on expensive helicopter flights, as is done today. Even so, the UAVs are labour-intensive and cannot be operated all year round.

Over the long term, satellites should provide the most coherent record of change. The Terra and Aqua satellites, along with Europe's Envisat and other surface-monitoring satellites,

are workhorses that regularly photograph the advance and retreat of outlet glaciers. Despite its glitches, the ICESat altimeter sends back elevation changes that track the thinning of the ice sheet; a successor, ICESat-II, is already in the works. And the European Space Agency is working to launch a successor to the ice-thickness-measuring CryoSat, the first incarnation of which failed after launch in 2005.

Yet major problems remain in acquiring and using Earth-observation data (see *Nature* **450**, 782–785; 2007). Access to data from Canada's Radarsat-1 and Radarsat-2 for instance, is ensnared in a potential takeover by a US company, a sale

that was blocked last week by the Canadian government.

Even with the right satellites, not everything can be done from space. Yet very few researchers have Greenland as the main focus of their scientific work. Decades from now, this could turn out to be one of the most short-sighted allocations of resources that began the twenty-first century. Climate change elsewhere in the Arctic has been swifter than anticipated. The remarkable shrinkage of the sea is "the largest change in Earth's surface that humans have probably ever observed," Howat points out. Trying to get any and every handle on how that affects the poised mass of ice next door must surely be a priority, he says. "This should be a critical thing to study."

Alexandra Witze is *Nature's* chief of correspondents for America.

"Every summer brings something totally different."
— Leigh Stearns

I. JOUGHIN



Melt water draining into moulins could accelerate the movement of the ice sheet.

1. Gregory, J. M., Huybrechts, P. & Raper, S. C. B. *Nature* **428**, 616 (2004).
2. Velicogna, I. & Wahr, J. *Nature* **443**, 329–331 (2006).
3. Luthcke, S. B. et al. *Science* **314**, 1286–1289 (2006).
4. Rignot, E. & Kanagaratnam, P. *Science* **311**, 986–990 (2006).
5. Joughin, I., Abdalati, W. & Fahnestock, M. *Nature* **432**, 608–610 (2004).
6. Joughin, I. et al. *J. Geophys. Res.* **113**, F01004 (2008).
7. Zwally, J. et al. *Science* **297**, 218–222 (2002).

See Editorial, page 781. For a video of a camera being dropped down a moulin on the Greenland ice sheet, see <http://tinyurl.com/5dua42>.

THE DREAMWEAVER'S ABACUS

Some experts think that a quantum computation could be plaited like a skein of string. And now they may have found the sorts of string they need, finds **Liesbeth Venema**.

How much absurdity can you take? If you are a mathematician or a quantum physicist, the answer is probably quite a lot. Topologists, for example, regard a coffee mug and a doughnut as essentially one and the same: two different variations on a basic shape-with-a-hole-in-it theme. Quantum-computer enthusiasts are happy to deal with the idea of 'qubits' that can be ones and zeroes at the same time. Condensed-matter physicists have no problem with the idea that electrons can break up into 'quasiparticles' with fractional charges — a third that of one of the original electrons, say. And theorists are happy to accept that there are particles called anyons that live only in two dimensions and are part electric charge, part magnetic flux.

But there are limits. And when in 1997 Alexei Kitaev, now at the California Institute of Technology in Pasadena, published a preprint suggesting that the topological properties of quasiparticles, moving around each other and behaving as anyons, could be used as the basis for a new form of error-proof quantum computing¹, it seemed that he had gone beyond them.

"I laughed when I first read it," recalls Nick Bonesteel, a theoretical physicist at Florida State University in Tallahassee. And there may still be some people laughing today — but at least a few of them are doing so with excited anticipation. "Intellectually, the idea might seem far-out," admits mathematician Michael Freedman, currently based at the Microsoft research group called 'Station Q'. Station Q was founded in 2005 at the University of California, Santa Barbara, specifically to tackle this sort of topological quantum computing. "To understand it requires knowledge of the maths as well as condensed-matter physics, which may be off-putting at first." But gradually, the far-out came in.

The attraction of the proposal is that the quasiparticles singled out by Kitaev happen to turn up in one of the most intensively studied condensed-matter systems of the past few decades — a quantum Hall device. These are systems in which, under the right conditions, charge carriers are forced into 'current channels'



C. DARTIN

governed by the rules of quantum mechanics.

In the early 2000s several theorists, including Bonesteel, began thinking seriously about ways to create qubits, the building blocks of quantum computing, in a quantum Hall device. Sankar Das Sarma, a theoretical physicist at the University of Maryland in College Park, teamed up with Freedman. "First we developed this crazy idea about manipulating quasiparticles with a microscope tip. Then we realized that the current paths in a quantum Hall device already move quasiparticles around," says Das Sarma. Their blueprint for a topological qubit, together with related proposals from other groups, was presented at a meeting on 'Emergent phenomena in quantum Hall systems' in Taos, New Mexico, in 2005. Moty Heiblum, an experimental physicist at the Weizmann Institute of Science in Rehovot, Israel, says that the meeting made him and his colleagues return to

the lab. "Most of us had been feeling that the topic was already exhausted, but the meeting revived the field. For the first time, it was driven by theorists," he says.

Neither boson nor fermion

A very clear task was set out for the experimentalists; construct a quantum Hall device in which the right type of quasiparticle shows up. Quantum Hall devices are made from stacks of semiconductor put together using well-known microelectronics fabrication techniques so as to create a two-dimensional electron gas, or 2DEG, at the interface between two of the layers in the stack. When a magnetic field is applied perpendicularly to one of these electronic flatlands, current channels form along the edges of the sample in which a specific number of electrons can travel — this is the quantum Hall effect. Chill the 2DEG down

further, and crank up the magnetic field, and the electrons' behaviour becomes stranger; they start to interact strongly with each other and, as a result, appear to break up into smaller pieces: these are the quasiparticles. They have no independent existence — you couldn't lift one out of a 2DEG and set it on its way — but within the 2DEG they really do act in a particle-like manner.

Still, they have peculiarities. Because they move in just two dimensions they do not follow the same quantum mechanical rules as real particles out in the three-dimensional world. Those particles come in two types: bosons, like the photon, and fermions, like the electron. These particles are something fundamentally different: anyons (see 'Braiding anyons').

Non-abelian abilities

Not any old anyon can work as a qubit, though. A qubit has to be able to exist in several states at once. That is what, in computational terms, lets them represent '0' and '1' at the same time, which is what gives a quantum computer its power; where classical computer bits are either '0' or '1', qubits can be various degrees of both — and thus, in effect, can carry out different versions of a computation in parallel. This powerful capability, also called 'superposition' can be exploited to design quantum computers that can tackle challenging tasks such as factoring large prime numbers to break codes, searching databases much larger than any yet built, and simulating complex processes in interesting materials such as high-temperature superconductors.

Superposition has already been demonstrated for some physical systems. Qubits with 'superposition' states can be based on trapped atoms and electrons; the sorts of quantum-logic operation that could lead to ultrafast factoring have been demonstrated on them. But this has happened only in very small circuits of four or fewer qubits. And it has become frustratingly clear how difficult it is to protect the fragile states of a qubit based on a trapped particle from the outside world. Even minute interactions with nearby surroundings can destroy them. And for each additional qubit in a circuit, many more calculation errors are introduced. "In theory it is possible, but the engineering problem to build a scalable quantum computer may be too big" says Das Sarma.

The topological nature of anyon-computing would get round the sensitivity problems, as long as the anyons were of the right sort. The key attribute is that the order in which a given set of interactions between anyons happens has to matter. That allows a given state to be a superposition of different histories — different ways of braiding the particles together. This 'order



"To understand this requires knowing the maths and the condensed-matter physics."
—Michael Freedman

matters' criterion is expressed, mathematically, in terms of the structure of the group, which describes the interactions as being "non-abelian". If order didn't matter, they'd be abelian.

Whether a quasiparticle will behave as a non-abelian anyon or not depends on the details of the way that the fractional quantum Hall effect gets electrons in the 2DEG to interact. By slowly turning up the magnetic field, experimentalists can 'tune' a quantum Hall device into different regimes. The regime seen as the most likely breeding ground for the quasiparticles that can act as non-abelian anyons has been described before², but it is a delicate one, and has been hard to characterize or investigate.

One of the most salient features, and one of those that was hardest to discern, is that the quasiparticles appearing in this regime should have a quarter of the charge of an electron. The evenness of the fraction is in itself a curiosity: so far, mainly odd fractions, such as a third,

or a fifth of an electron, have been seen. But not any round number would do. Half-charge quasiparticles would not be non-abelian, and this has been a real worry to the field, as there seemed to be a possibility that quarter-charge particles would clump into half-charge ones, thus losing their non-abelian mojo.

Now such worries can be put to rest. In this issue of *Nature*, Moty Heiblum and his co-workers report³ measuring fractional charges in quantum Hall devices by forming a narrow constriction of controllable width, called a point contact, in the middle of the 2DEG, making it look something like a flattened hour-glass (see inset picture opposite). Current injected at one end is carried in the form of quasiparticles along one edge of the 2DEG and through the central constriction. But if the constriction is thin enough, not all the quasiparticles can make it from one lobe to the other: some fail to get through the point contact and jump to the other edge of the lobe in which they started. The discrete movements of quasiparticles that are diverted in this way at the point contact cause fluctuations in the currents on both sides of the contact. Analysis of this reverberating 'shot' noise reveals the precise value of the quasiparticles' charge.

Because there are many other sources of noise that can mask the fluctuations, this kind of experiment demands an extremely clean and carefully constructed device. Merav Dolev, the graduate student on the project at the Weizmann Institute, had to balance many

Braiding anyons

In classical mechanics, if two identical particles are swapped around, the end state is identical to the initial state. In quantum mechanics things are more complex. When two electrons exchange places, the quantum mechanical wavefunction that describes them is shifted so that what used to be peaks in the function become troughs and vice versa. Exchanging a pair of photons also shifts the wavefunction, but by exactly one period so that the peaks and troughs stay in the same place. All other everyday particles behave either like electrons, if they are fermions, or like photons if they are bosons.

Anyons make things more complicated; it's a result of the fact that, being

defined from the start as two dimensional, they are described by different statistical rules. When two anyons are swapped, the wavefunction that describes them shifts phases not by a whole period or half a period, but by some other fraction of a period. If a number of anyons swap places repeatedly, weaving around each other, the wavefunction undergoes a distinct series of phase shifts, depending on which was where, and when. It captures the braided trajectories of the anyons moving to and fro.

If anyons are swapped according to specific rules, the braided histories recorded in the wavefunction can be seen as steps in a computation. If the anyons

are 'non abelian' (see main text) then one set of particles can have a whole range of different braids recorded in their combined wavefunction. And so the arrangement of the anyons — the topology of the system — becomes a quantum computation.

The attraction of this approach is that it is the overall shape — the topology of the braid — that matters, not the precise details of every movement that went into it. Topology is a robust quality; a doughnut is doughnut shaped even if it gets a bit squashed — or distorted into the shape of a mug. This insensitivity to detail makes a topological approach to quantum computing very attractive, and largely immune to error. **L. V.**

parameters during fabrication of the device which is about a millimetre in width and is made from a number of layers of gallium arsenide and aluminium gallium arsenide. The density of electrons in the 2DEG has to be very high — about three billion in a square millimetre — while the structure has to be so clean that electrons can move through the 2DEG for up to half a millimetre without hitting any sort of defect. And the 2DEG will inevitably be damaged in the process of putting down metallic wires to form the point contact, which means it has to start off even better than is needed.

2DEG or not 2DEG

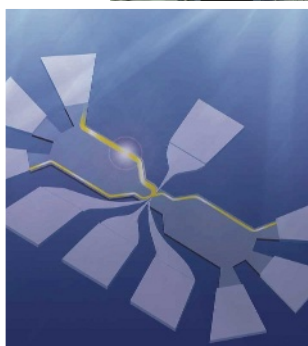
But the effort has paid off. An enormous amount of shot noise recorded while the device was cooled down to 10 milliKelvin has provided solid evidence in favour of quarter-charge quasiparticles. Independent confirmation of the existence of quarter-charge particles in such a set-up comes from a team at Harvard, the Massachusetts Institute of Technology in Cambridge and Bell Laboratories in Murray Hill, New Jersey. These researchers used a similar device, but measured the conductance between the two current channels at the point contact, rather than the shot noise⁴.

This is the news the field has been waiting for. “In all my talks on topological quantum computation I’ve said this is the one experiment that needed to be done first. And frankly I didn’t expect it this soon,” says Das Sarma. However, although experts regard the experiments as important and necessary, many also see them as insufficient in themselves. To really validate the idea of making a computer this way you need to show that the quarter-charge quasiparticles really do behave in a non-abelian way. This can be done by making the quasiparticles encircle an island of anyons, as a rudimentary anyon braid. To do this, at least two point contacts need to be constructed that can be shut tightly so that all quasiparticles can be made to jump from one side of the 2DEG to the other. The quantum properties of the braid that is formed by this weaving around of quasiparticles will show up in the measured current-voltage characteristics.

Building such a ‘quasiparticle interferometer’ is a challenge, given that making just one point contact in the required quantum Hall regime has proved difficult enough, but it is not a far-fetched ambition. Can we expect it this year? Dolev is cautious. “This field is just starting. In the next few months we will find out what the experimental difficulties are,” she says. For example, the interferometer needs much more



Merav Dolev (above left), Moty Heiblum and an artists impression of the quantum Hall device (left) in which they measured even fractional charges.



stable point contacts than were used in the system that first demonstrated the existence of quarter-charges.

However, having identified a particular side-effect of the 2DEG fabrication process that produces instabilities in the point contacts, the group is already getting stabler devices. And if they don’t succeed, competitors inspired by their work may. “Proving the non-abelian properties of [quarter charge] quasiparticles would be a hard experiment, but the work by Dolev *et al.* will certainly motivate people to try it,” says Bonesteel.

“One of the most exciting aspects of this demonstration is that it shows the quality of devices is steadily improving,” says Kirill Shtengel, a theoretical physicist at the University at California, Riverside. “With luck, we might see a non-abelian interferometer within a year.”

There are many experimental challenges

to be met before a topological qubit sees the light. But everyone agrees that the concept of topological quantum computation is so attractive that it is worth a try. Ady Stern, a theorist with the Weizmann group, explains; “Other quantum computing approaches have a head start, but the concept is amazingly beautiful and the one advantage — topological protection of quantum states — is huge.” Shtengel agrees: “Other approaches have serious problems with scalability. Right now we are behind, but once we have a non-abelian quasiparticle interferometer, a topological qubit should soon follow.” Getting those qubits to knit together as computations will require geometries a lot more complex than a flattened hour-glass. In the long run, it is possible that some more suitable system will be found for topological quantum computing — something perhaps a little more user, or developer, friendly than an ultra-clean and precisely designed quantum Hall device that needs to be cooled down to near-zero temperatures. Whether it will sound any less absurd to begin with, though, we will have to wait and see.

Liesbeth Venema is a senior physical sciences editor at *Nature*.



“Proving these non-abelian properties would be hard, but this will certainly motivate people to try.”

— Nick Bonesteel

1. Kitaev, A. Y. *Ann. Phys. (NY)* **303**, 2–30 (2003).
2. Willett, R. *et al. Phys. Rev. Lett.* **59**, 1776–1779 (1987).
3. Dolev, M., Heiblum, M., Umansky, V., Stern, A. & Mahalu, D. *Nature* **452**, 829–834 (2008).
4. Radu, I. P. *et al.* preprint at <http://arxiv.org/abs/0803.3530> (2008).

See News & Views, page 823.

BONES, ISLES AND VIDEOTAPE

Old human remains found on the Pacific islands of Palau are caught in the crossfire between entertainment and science. **Rex Dalton** reports.

Circled by a protective coral reef, the 300-island archipelago of Palau is one of the Pacific Ocean's most biodiverse ecosystems. The first intrepid voyagers who arrived here, more than 3,000 years ago, would have found lush plants and waters teeming with fish and crustaceans. By 2,500 years ago the Palauans were even practising sophisticated agriculture, creating terraces on the archipelago's largest island on which to grow crops.

Given this evidence, many archaeologists were stunned by a report last month that a tribe of small-bodied humans had purportedly lived on some of the islands 1,000–3,000 years ago and possibly suffered dwarfing because of limited resources.

The article¹, by palaeoanthropologist Lee Berger of the University of Witwatersrand in South Africa and his colleagues, suggested that the tiny Palauans might help inform the debate over the controversial 'hobbits'. These remains, found on the Indonesian island of Flores, 2,000 kilometres to the south of Palau, are believed by many researchers to represent a distinct dwarf species called *Homo floresiensis*, which died out 12,000 years ago^{2–4}. Berger and his team argue that their Palau find suggests that the hobbits may not be a separate species, as dwarfing can occur in island environments.

But veteran Pacific anthropologists quickly began dissecting the new article. Many of them now hold that the report offers little support

for the assertions of a dwarfed tribe. In fact, they say the bones are likely to be from normal-sized island dwellers, possibly juveniles.

"The more I read their paper, the more I am convinced it is complete nonsense and cannot be accepted as serious science," says Michael Pietrusewsky, an anthropologist at the University of Hawaii at Manoa, who is considered

to be the primary authority on Pacific island skeletons. The use of these bones to make assertions about *H. floresiensis* or other *Homo* species, he says, "is totally inappropriate".

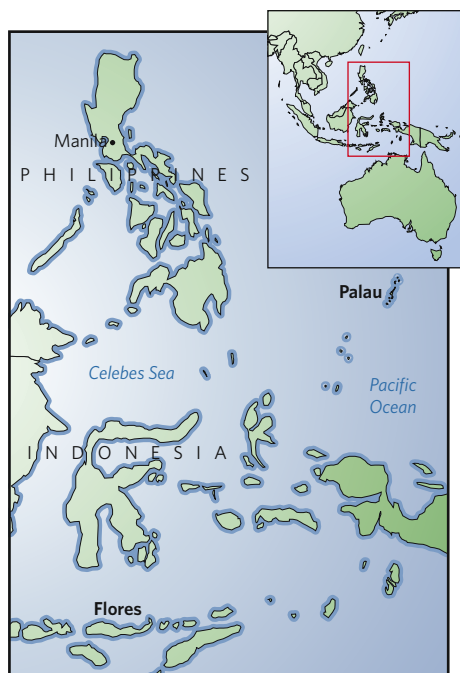
Berger responds that such criticism is ill-founded. "Might it be that such critics have not read our manuscript as carefully as is required of a sophisticated debate on human variation before commenting?", he told *Nature* in an e-mailed response to questions.

The drama of discovery

To some, the Palau story illustrates how science can get caught up in the entertainment process. Like many palaeoanthropologists, Berger has long worked with film crews to document discoveries. But sometimes the demands to catch a significant finding on tape can clash with the slow, rigorous nature of the scientific process. The question anthropologists are asking now is: did entertainment needs in Palau overwhelm the evidence from field research?

In other areas of his research, Berger has worked on a planned television series featuring him called *Fossil Hunter*, which uses the slogan "entertainment first, science second". For the Palau work, he teamed up with a London-based production company, Parthenon Entertainment, to create a film later distributed by the National Geographic Society of Washington DC.

The National Geographic Society awards



some \$5 million in grants annually to researchers from a number of disciplines — including the popular ones involving human ancestors, dinosaurs or animal stories. For scientists in these fields, small seed grants to pay for field trips are hard to secure, so the society's grants are valued highly and often produce quality research.

But National Geographic is also a non-profit media empire, netting \$100 million on revenues of \$500 million in 2006. Its editors work to get featured discoveries by its funded researchers into both its flagship magazine and peer-reviewed journals at the same time. This arrangement can sometimes backfire, such as in 2000 when the magazine featured a report on a flying dinosaur fossil that later turned out to be a cleverly faked composite^{5,6}.

Berger's project in Palau provides a behind-the-scenes view of when entertainment and science meet. It is a process that can sometimes leave scientists disgruntled (see 'Caught out on camera', overleaf), and can lead to accusations from some communities in developing nations that they have been exploited. For some, what happened in Palau offers examples of some of the pitfalls. "There is something unseemly about how this evolved and was orchestrated," says William Jungers, a palaeoanthropologist at Stony Brook University in New York.

Paradise place

The tale of the Palau project began in April 2006, when Berger, an American by birth, was on holiday with his family from Johannesburg. With countless channels of placid shallows, coral reefs and more fish than Hawaii, Palau is known worldwide to divers and kayakers. Its jungle has also been used to film the reality television programme *Survivor*.

On the last day of his trip, Berger says, a guide took him on a kayak trip to a cave called Ucheliungs, which a brochure noted held bones. Venturing inside, Berger nosed around and spotted some remains, including a skull with a prominent brow over the eye sockets — a sure sign of primitive traits.

The island containing the high-domed cave is off-limits to visitors, officials say. Berger later acknowledged that he didn't know the rules at the time. But other researchers, such as Timothy Rieth, an archaeologist at the International Archaeological Research Institute in Honolulu, Hawaii, questioned those steps ashore. A decade ago, Rieth worked on an archaeological assessment of an unrelated Palau project. On a boat trip one day, Rieth viewed the mouth of the other cave studied by Berger, called Omedokel, but didn't venture inside even though bone piles could be seen. "I don't just go inside burial caves on vacation because it's fun," says Rieth, who

was with a Palau cultural official at the time.

Berger has made waves with his research before. In 1995, early in his career in South Africa, he and his Witwatersrand colleague Ron Clarke gained attention for their proposal that the 'Taung child', a 2.5-million-year-old fossil from South Africa, had been damaged by an eagle or other large bird of prey⁷. Berger still strongly supports this hypothesis: in 2006, he published a paper arguing that the bird had actually preyed on the Taung child⁸.

After returning to South Africa from Palau, Berger flew to Washington DC, seeking research funds from National Geographic to



Fossil hunter: Lee Berger has appeared in several science-related television films.

explore the caves. By June 2006, he was back in Palau's largest city, Koror, with an emergency grant to seek permission from authorities to commence a full research project.

Formerly a US protectorate, Palau became independent in 1994. Today, the nation is still learning how to balance traditional customs with US-like laws. Quickly, Berger's proposal became caught in a political power struggle between the Koror government and the state Council of Chiefs, whose members represent various traditional groups.

Culturally, Palauans like to be accommodating. In the end, they supported Berger, who received the necessary permits from the Palau Bureau of Arts and Culture. In summer 2006, accompanied by a film crew, he began exploring both Ucheliungs and Omedokel.

Team member Steven Churchill, a palaeo-anthropologist at Duke University in Durham, North Carolina, recalls how excited they all were at finding so many bones of what they thought were small-bodied and ancient people; they suspected that they might have found a cave of dwarfed humans that predated any other Palauans. If so, the people might have been related to the Indonesian 'hobbits', or might offer insight into how *H. floresiensis* shrank in size over time. This was a selling point of the National Geographic grant application, says a member of the society's research committee, palaeontologist Philip Gingerich of the University of Michigan in Ann Arbor.

Short shrift

To archaeologists who have long studied the archipelago, bones in Palauan caves are nothing new. An archaeological survey that started in the 1950s reported Omedokel as a burial cave for the young, including the child of an ancient chief⁹. In the late 1970s, Pietrusewsky began studying another collection of western Pacific skulls, including 13 gathered on Palau by Germans in the late nineteenth century. He also studied other Palau skeletal remains in different museums. "I found no evidence of people of short stature," says Pietrusewsky.

And starting in 2000, archaeologist Scott Fitzpatrick of North Carolina State University in Raleigh began excavations in a burial cemetery on the island of Orrak, about 4 kilometres north of Ucheliungs. In 2003, he reported the oldest human burials in the western Pacific, dating to 3,000 years ago¹⁰. These included the remains of many youths and children.

Fitzpatrick says he has also found explicit evidence undermining Berger's theory that the island residents were small-bodied individuals. The Berger paper describes heads of femur bones that suggest the people there were small. But the shafts of these leg bones are missing from the specimens, limiting the ability to compute body height. Fitzpatrick, however, found femoral heads of similar size at Orrak, but with the shaft. Analysing the shaft indicates that the people at Orrak were of normal height, he says. Berger, charges Fitzpatrick, "hasn't made adequate comparisons to other skeletal material from Palau. And I don't think he understands variance in human populations."


Berger notes that the techniques for estimating body size can have large error bars, but says that more than 61 skeletal elements from the caves suggest the people were at the extreme low end of the range. He also says that the bones described in the team's paper all show indications of coming from adults. "We published the entire inventory," adds Churchill. "A number are adults. I'm willing to accept there are some juveniles,

but they don't change our conclusions."

John Hawks, an anthropologist at the University of Wisconsin in Madison who served as editor for the article's peer review, says "it is quite evident" that the skeletons represent humans "in the normal range" of being small.

Another area of dispute is how exactly the people, if adults, got so small. The original founding population of the caves, says Berger, may have been naturally small. Or the tribe may have dwarfed over time, perhaps because of a lack of large mammals or reptiles to hunt or because of environmental stresses. But other experts disagree — including Stephen Athens of the Honolulu research institute, who has drilled repeated cores in Palau wetlands capturing pollen records dating back 5,000 years¹¹. There is nothing in the environmental record to indicate resource depletion, he says. Pollen shows taro root and coconut. Along with the marine resources, "that is a pretty darn good diet", Athens says.

In fact, the pollen record shows a sharp rise in grasses and ferns about 4,000 years ago — which could mean humans were clearing forest for agriculture then. And work by Jolie Liston, an American archaeologist studying Palau, describes elaborate agricultural terraces by 2,500 years ago on Palau's largest island, Babeldaob¹². "These terraces run five to six kilometres," says Liston. "Land is sculpted,



Into the unknown: Chief Santos Ikluk, 60, ventures into the Omedokel cave for the first time despite having boated past many times before.

dirt removed, gullies formed — all to create about a dozen distinct districts."

In late 2006, when the first skull bones from Berger's excavations were prepared in the Palau National Museum in Koror, Berger's team learned it didn't have, as hoped, a group that dated to 10,000 years or more. The heavy brow over the eyes that suggested primitiveness turned out to be calcite, which came off as

the bones were being prepared. "The idea they were pre-Palauans went out the window then," says Churchill. Instead, the team decided to focus on describing the bones; the small nature of the remains could provide context for other finds such as *H. floresiensis*.

Meanwhile, resource managers in Koror hope the attention will bring funds from National Geographic to help protect the caves. Increased attention, they say, will bring more people wanting access to the caves, which need to be preserved. Koror governor Yositaka Adachi says the state hopes to get about \$500,000, including a new patrol boat. Barbara Moffet, a spokeswoman for the society, says that the society hasn't had any such requests yet, but that "we are willing to consider helping them in some way if such assistance is appropriate".

But for other researchers, the affair has tainted the entire field. "Ultimately," says Fitzpatrick, "I worry this will put a strain on all archaeologists doing research in Palau."

Rex Dalton is a US West Coast correspondent for Nature.

- Berger, L. R., Churchill, S. E., De Klerk, B. & Quinn, R. L. *PLoS One* **3**, e1780 (2008).
- Morwood, M. J. *et al. Nature* **437**, 1012–1017 (2005).
- Brown, P. *et al. Nature* **431**, 1055–1061 (2004).
- Morwood, M. J. *et al. Nature* **431**, 1087–1091 (2004).
- Dalton, R. *Nature* **403**, 689–690 (2000).
- Rowe, T. *et al. Nature* **410**, 539–540 (2001).
- Berger, L. R. & Clarke, R. J. *J. Hum. Evol.* **29**, 275–299 (1995).
- Berger, L. R. *Am. J. Phys. Anthropol.* **131**, 166–168 (2006).
- Osborne, D. *Archaeology of the Palau Islands: An Intensive Survey* (Bishop Museum Press, Honolulu, 1966).
- Fitzpatrick, S. M. *Antiquity* **77**, 719–731 (2003).
- Dickinson, W. R. & Athens, J. S. *J. Island & Coastal Arch.* **2**, 175–196 (2007).
- Liston, J. & Tuggle, H. D. in *Archaeology of Warfare* (eds Arkush, E. N. & Allen, M. W.) 148–183 (Univ. Florida Press, Gainesville, 2006).
- Good, K. & Chanoff, D. *Into the Heart* (Simon & Schuster, New York, 1991).

Caught out on camera

Looking back at the filming last autumn, William Jungers can't believe he was that naive. The anthropologist at Stony Brook University, New York, allowed himself to be videotaped for a documentary without knowing what it was actually about.

The film described a purported small-bodied tribe in Palau, and was broadcast last month as an article was published on the theory¹. He has now dissociated himself from both the film and the research it described. "I would never do this again," he says.

Jungers was one of at least four anthropologists filmed by London-based Parthenon Entertainment. The film crew asked the scientists about an unnamed and undescribed research project examining a rapidly dwarfing group of humans, along with what that

might mean for the 'hobbit' fossils, *Homo floresiensis*.

Dean Falk, an anthropologist at Florida State University in Tallahassee who also was taped, says she was very suspicious and qualified her remarks extensively. She declined to speak freely for fear her research might not be funded again by the National Geographic Society, which distributed the film.

"We have not heard from any of the scientists interviewed for the film but would urge them to contact us with any concerns," says a spokesperson for National Geographic. "In general, the filmmakers were careful not to discuss any details of the film's content because it was the subject of an embargoed scientific paper."

Other researchers have had similar run-ins. New Jersey

anthropologist Kenneth Good fell out with the society in 1993, after signing a contract on his studies and life with the Yanomami tribe in Venezuela¹³. Good says the society sent him a new contract, which he signed without noting that it prohibited him from working on other film projects. "Things spun out of control," says the now-retired Robert Pool, who was the society's editor on the project.

Others note it's important to pay attention when signing documents. "Scientists have to be very careful when working with varying organizations, but my experience has been very positive," says Luis Chiappe, the palaeontology curator at the Natural History Museum of Los Angeles County in California.

R.D.

Malaria programmes need informed advocacy

SIR — Your Editorial ‘Time to take control’ (*Nature* 451, 1030; 2008) seems to downplay the current importance of advocacy for maintaining funds in the fight against malaria. But funding for all elements of malaria programmes — from research and development, design, implementation and commodities, to monitoring and evaluation — is essential to success.

Results don’t happen without dedicated and predictable financial resources and, although commitments have increased, we still have a long way to go. A recent study by McKinsey (see <http://tinyurl.com/52aoda>) estimates that an investment of some US\$2.2 billion a year for five years is needed to achieve full coverage of prevention and treatment measures in just 30 of the hardest-hit African countries where malaria is endemic, addressing 90% of current malaria deaths. Without continued pressure on donors to keep up their commitments, there is no guarantee that additional funding will ever materialize.

Also, advocacy is critical for ensuring that malaria efforts reach the communities most in need. On-the-ground efforts to engage national health leaders, navigate bureaucracies and encourage effective implementation of sound public-health policies are crucial. Without them, life-saving drugs, bed nets and insecticides will sit and spoil in warehouses. Generating and supporting participation and commitment on the spot is essential to the success of any programme.

The Editorial highlights one of the most extreme situations where informed advocacy is needed. In the Democratic Republic of the Congo, the first step in addressing the extremely high burden of malaria is fervent advocacy to increase investment in malaria programmes in challenging regions. Without that advocacy, government and donors will continue to avoid investment, and there will be no progress to measure.

Matthew Lynch

Global Program on Malaria,
Center for Communication Programs,
Johns Hopkins University, 111 Market Place,
Suite 310, Baltimore, Maryland 21202, USA

Malaria: efforts starting to show widespread results

SIR — Your Editorial ‘Time to take control’ misrepresents the role and work of the Roll Back Malaria (RBM) Partnership, and is apparently at odds with the successes described in the News Features and Commentary in the same issue (*Nature* 451, 1030, 1042–1049 and 1051–1052; 2008).

The RBM Partnership, a coalition of hundreds of organizations, is an independent

global public-health partnership that is governed by an international board. The board’s members include the governments of countries where malaria is endemic, donor governments, bilateral and multilateral organizations, academia, civil society, the private sector and various foundations.

We agree that disease surveillance is essential for effective malaria control. Many RBM partners advocate more funding for this purpose. Indeed, RBM has provided the technical leadership and coordination to develop the approach and tools for national malaria indicator surveys that have provided valuable data to assess progress on coverage and impact.

We continue to advocate rapidly improving access to the bed nets and treatments that, every day, prevent unnecessary deaths. Strong advocacy is vital for surveillance to strengthen as prevention and treatment coverage expands.

Malaria control was severely under-resourced until the first grants from the Global Fund to Fight AIDS, Tuberculosis and Malaria began to reach country programmes in 2004. New support — from the Bill and Melinda Gates Foundation, the US President’s Malaria Initiative and the World Bank booster programme — further increased global resources, and nationwide scale-up of malaria control is now possible. However, much more funding is still needed.

Although many countries are still far from reaching RBM’s target of 80% coverage, a growing number — including Benin, Cameroon, Eritrea, Ethiopia, Kenya, Madagascar, Mali, Niger and Rwanda — have recently achieved significant progress in increasing access to long-lasting nets as a result of large-scale distribution campaigns carried out in the past four years.

Many countries have not yet conducted

household surveys to record these higher coverage rates, but the improvements have been well documented (see, for example, <http://tinyurl.com/3foako> and <http://tinyurl.com/3oj3ey>).

Results-oriented country support is a major feature of the partnership’s work plan. It builds on 2007’s successes, when the RBM Partnership led a strong campaign to help countries improve the quality of their proposals to the Global Fund. The success rate of proposals in Round 7 doubled from that of 2006, adding US\$471 million to fight malaria. Both Nigeria and

the Democratic Republic of the Congo were prioritized at the last RBM board meeting in 2007 to receive additional implementation support from partners in 2008.

We believe that your Editorial does a disservice to our global efforts to turn back this preventable and treatable disease, at a time when we are seeing positive results.

Awa Marie Coll-Seck, Tedros Adhanom

Ghebreyesus, Alan Court

RBM Partnership, Secretariat hosted by the
World Health Organization, 20 Avenue Appia,
CH-1211 Geneva 27, Switzerland

Tibetan wildlife is getting used to the railway

SIR — Your News story ‘Acclaimed photo was faked’ (*Nature* 451, 1034–1035; 2008)

indirectly calls into question the impact of China’s Qinghai–Tibet railway on the migration of Tibetan antelopes. As zoologists officially responsible for evaluating the impact of the railway on plateau wildlife, we have been monitoring the situation annually from the time construction began in 2003, through its completion in 2006 and on to the present.

During the railway’s main construction period, the antelopes were very much disturbed. But they soon adjusted their migration routes, westward in spring and eastward in August, to avoid most human activity. The railway has many underpasses, including 143 that are more than 100 metres wide; these wide underpasses have a total width of 46 kilometres. Adding in the many smaller ones, underpasses encompass 259 kilometres of the antelopes’ main range.

Contrary to any impression that might have been conveyed by the faking of the acclaimed photograph, the animals have readily adapted

to these underpasses, at present concentrating on



Building bridges? Migrating antelopes are not put off by the new railway.

only a few of them. In 2006 we counted 2,952 antelopes migrating east, of which 98.17% crossed by using the wildlife underpasses.

A highway built in the 1950s runs parallel to the railway, at about 500–1,500 metres away in our research area. (Outside our research area, the distance between road and railway ranges from 200 metres to 35 kilometres.)

The antelopes usually wait for a lull in the heavy flow of daytime traffic before hurrying across the road. Some animals even forage along the highway, seemingly ignoring the cars and trucks.

It seems, then, that the Tibetan antelopes have largely adapted to the presence of the Qinghai–Tibet railway. As the area develops further, care must be taken to ensure that these animals can continue their ancient pattern of migration.

Qisen Yang, Lin Xia

Institute of Zoology, Chinese Academy of Sciences, Beijing 100101, China

Vaccine trial provided valuable information

SIR — Your Editorials ‘Broken promises’ and ‘Mismanaged measures’ (*Nature* 452, 503 and 504; 2008) seem to be contradictory. In the former, you excoriate the research community for running human efficacy trials for AIDS vaccines, whereas in the latter you complain about the use of surrogate end points.

You were right in the second Editorial. Without human efficacy trials on AIDS vaccines, we have had to rely on surrogate — mainly preclinical — end points.

Until the Merck trial, we were searching in a wilderness of preclinical data. The Merck trial, although it unfortunately did not show efficacy, taught us more than all the surrogate experiments.

Without efficacy data in humans, particularly when we are dealing with a human viral disease that lacks a good animal model, we are always guessing. To have experimental correlates of human efficacy would be wonderful, but we are still a long way from that situation. Meanwhile, you should be supporting more human experimentation, not less.

David Baltimore

California Institute of Technology,
1200 East California Boulevard, Pasadena,
California 91125, USA

NIH funds support more than a researcher's own lab

SIR — According to your News story ‘222 NIH grants: 22 researchers’ (*Nature* 452, 258–259; 2008), I receive a large number of dollars from the US National Institutes of

Health (NIH) for ‘cancer research’. As any knowledgeable reader will guess, more than 90% of that supports institutional activities, such as our Comprehensive Cancer Center at Memorial Sloan-Kettering, and not my own research laboratory. The story’s bar chart may provide a source of (misleading) gossip, but it does not usefully serve readers looking for insight into the current crisis of funding at the NIH.

Harold Varmus

Memorial Sloan-Kettering Cancer Center,
1275 York Avenue, New York 10021, USA

NIH: grants revamp needs grounding in evidence

SIR — Further to your News story ‘Revamp for NIH grants’ (*Nature* 451, 1035; 2008), the final draft of the US National Institutes of Health (NIH) 2007–08 peer-review self-study report tackles a critical set of issues for us grantees and reviewers. We all want an efficient and stable system; we all particularly care about junior investigators. But the solutions need to be grounded in evidence.

As you point out, a back-of-the-envelope calculation shows that eliminating more than two grants per investigator would allow a 5% increase in the number of grants. But is this better? Another casual calculation shows that requiring all grants to be shared by two investigators would more than double the number of grantees. So?

How do we know that eliminating amended applications will help? Amended applications are what keeps everyone honest. Without the back-and-forth of peer review, efforts by the NIH will degenerate into the dismal and ad hoc review process that characterizes many other agencies. And I would be reluctant to review the expanded load of always-new proposals.

Would a shorter application really enhance the quality of research or the efficiency of the review process? I don’t want to spend extra time looking for lost key information. Is this a good idea? Why don’t we study it?

Likewise, it is unclear whether using more than four reviewers would enhance the system or bring it to a screeching halt owing to the huge burden of review.

Also, what is the evidence that giving more R01 grants (individual grants that are the mainstay of extramural funding through the NIH) for early-career investigators will work in attracting the best and brightest to the life sciences and biomedical research? The issue is complex. I am not sure whether attaining that first R01 is the solution: it is the ability to stay there in a healthy and productive career.

Some suggestions are ‘pilots’, which

should be applauded, but again there is little discussion of what is being measured and how.

It is high time for the NIH to conduct research on the review process itself. With hundreds of study sections meeting and thousands of applications reviewed every year, the material is there for retrospective analysis and for prospective studies that test specific hypotheses and interventions.

Perhaps the peer-review self-study should have submitted an R01 application on the proposed changes.

Yusuf A. Hannun

Department of Biochemistry and Molecular Biology, Medical University of South Carolina, Charleston, South Carolina 29425, USA

NIH: researchers lose out to war, not to each other

SIR — In your News story ‘222 NIH grants: 22 researchers’ (*Nature* 452, 258–259; 2008), you contrast the concerns of junior investigators in the face of the flat budget of the US National Institutes of Health (NIH) with the comparative prosperity of a handful of their senior colleagues. Against this, I would argue that your review of grant numbers is flawed. It is absurd to consider supplements to parent grants, such as centre-support grants or training add-ons, as separate grants. Training grants should not be seen as counter to the self-interest of junior investigators. Also, you should have explained that junior investigators are supported by large centres or networks (in which hundreds of junior investigators may be engaged), although the NIH demands a single administrative leader — therefore a large grant is attributed to one person, often with many centres or supplements.

The end of the rise in funding for the NIH corresponded to the start of the war in Iraq, with its no-bid multibillion-dollar contracts and support of 150,000 Americans overseas. Half-a-trillion dollars (a very conservative estimate) has been spent there during the past five years, nearly four times the annual NIH budget in each of those years. The costs show no signs of abating — and all this in the context of tax cuts and economic recession.

So *Nature* should keep asking the tough questions about NIH funding decisions and effort-reporting policies. But please consider alternatives to your simplistic thesis.

Sten H. Vermund

Institute for Global Health, Vanderbilt University School of Medicine, 319 Light Hall, 2215 Garland Avenue, Nashville, Tennessee 37323-0242, USA

Contributions to Correspondence may be submitted to correspondence@nature.com. Please see <http://tinyurl.com/373jsv>.

BOOKS & ARTS



D. SHEEHAN/CORBIS

Farms, fields and roads
in the United States were
transformed by the Civilian
Conservation Corps.

Blazing a new trail for nature

Could the army of green workers who transformed the US landscape inspire today's ecological revolution?

Nature's New Deal: The Civilian Conservation Corps and the Roots of the American Environmental Movement

by Neil M. Maher

Oxford University Press: 2007. 328 pp. \$35

Jon Christensen

Imagine a government agency that transforms people's relationship with nature, creates millions of jobs and helps pull a nation out of an economic nadir. While political pundits on the left and right nit-pick, citizens embrace the agency's programme and forge a new constituency and political consensus that lasts for generations. The agency's work profoundly changes the physical landscape — parks, forests, farm fields, trails and roads — in ways that continue to remind people of the benefits of caring for nature within their communities. Such an agency existed, 70 years ago during the Great Depression in the United States. It lasted for less than a decade.

That agency was the Civilian Conservation Corps (CCC). It put three million unemployed men to work repairing the land, helping communities and themselves. The story of the CCC is recounted in *Nature's New Deal*.

In the midst of current economic and environmental crises, one may muse: "If only we could uncork this dream today!" Historian Neil M. Maher never makes the argument that the CCC should be reinvented in the present. But with jittery financial markets around the world

evoking nervous comparisons to the Depression, we might look to the New Deal — President Franklin D. Roosevelt's response to the 1930s crisis — for historical lessons.

On the financial front, those lessons seem clear. The Glass–Steagall Act was a New Deal law that separated consumer banking from speculative investment banking. Its repeal in the late 1990s was one of the laissez-faire reforms that enabled the current troubles to develop and spread so widely. Now, we are again contemplating the recalibration of government oversight of financial markets on a scale first set by the New Deal.

Would we today mint a New Deal for nature too? The time is right. Global climate change demands policies at a global scale. And nations too must act. So far the United States has not, but with Republican and Democratic presidential candidates advocating a change from the Bush administration's do-nothing approach, a new policy on climate change is expected to emerge in the next administration. Aspects of that policy might look a lot like the CCC. Maher's history of the corps illuminates the possibilities, and limitations, of such an approach.

One can hear echoes of the CCC in a growing US campaign calling for the creation of 'green jobs' that will give 'energy independence' and so slow global warming. The Apollo Alliance — a coalition of labour unions and environmental groups — is even calling for the

same number of jobs: three million workers to install solar panels, insulate homes and build wind turbines. The number is, perhaps, just a curious coincidence. But it does highlight a problem. That problem is scale.

The CCC did a lot with 3 million jobs. It planted more than 2 billion trees, slowed erosion on 16 million hectares of farmland and developed 800 new state parks, while constructing more than 10,000 small reservoirs, 46,000 vehicular bridges, 13,000 miles of hiking trails and nearly 1 million miles of fencing. Maher writes: "All told, conservative estimates indicate that corps projects across the United States altered more than 118 million acres, an area approximately 3 times the size of Connecticut." Actually, that is more than 30 times the size of Connecticut. An area larger than California, yet smaller than Texas, this is still only about 5% of the total land area of the United States.

Most CCC projects were concentrated along the rivers and tributaries of the Mississippi watershed, where erosion and floods were rife. The corps deployed idle manpower in a massive 'green jobs' programme, giving unemployed, single young men work outdoors, plus room and board. The men sent their salaries home, providing relief for their families.

It was also good politics. The CCC was a friendly local face for the New Deal programme. Roosevelt readily hitched his wagon to an agency that enjoyed approval ratings of

better than 80%, even while the rest of the New Deal came under increasing attack. He talked of “a plan of cooperation with nature instead of what we have been doing in the past — trying to buck nature”. This was an appeal for cooperation among the people too.

Maher uses the CCC to make a sophisticated argument within the field of environmental history in the United States. He argues, in effect, that it is the missing link between the simple conservation of the Theodore Roosevelt era (1901–09) and the environmentalism that emerged after the Second World War. The link was forged by Franklin D. Roosevelt’s ‘broader conservation’, which went beyond concern for efficiently managing natural resources to include people and communities in a more ecological form of national planning.

Just as important for Maher’s argument were the grassroots reactions to the CCC. Planting trees seemed to be all for the good until early conservation biologists began to worry about how wildlife habitats were being changed. Meanwhile, the CCC’s mania for blazing trails and building roads inspired a movement to preserve roadless wilderness areas. Maher argues for a bottom-up view of this new deal for nature, effectively turning the significance of the original New Deal (an undeniably top-down enterprise) on its head.

If the New Deal is going to be a touchstone for our economy and environment today, our inspiration should go further than the CCC. Maher leans too heavily on this one agency to explain the enormous changes that took place during the Depression and in its aftermath. One fundamental problem here is making a virtue of necessity. The CCC, like the rest of the New Deal, was tightly constrained by American politics, which was (still is) enamoured with the idea of bottom-up change, and thus wary of economic and environmental planning on a national scale.

Maher briefly opens up a view on this larger context in a chapter on the CCC’s work with the Tennessee Valley Authority, a massive regional development programme undertaken by the national government. He does not follow the story into the authority’s hydroelectric dams and energy. It is there, in the nexus of energy and environment, that we might find the real lessons of the New Deal for our troubled times. Unfortunately, it was not so much the New Deal as the Second World War that ultimately transformed the economy of the United States. Arguably, the war also transformed the country’s relationship with the environment more than the CCC did. But that is another story. One can only hope that particular history does not have to be repeated for the United States to resolve another new deal for nature in this current era of global change. ■

Jon Christensen is associate director of the Spatial History Project in the Bill Lane Center for the Study of the North American West at Stanford University, California 94305-4225, USA.

Bedtime reading

Insomniac

by Gayle Green

University of California Press: 2008.

520 pp. \$29.95

Jim Horne

Californian professor Gayle Green has been an insomniac for 50 years. For her, insomnia has been an ordeal of suffering and anger, directed largely at medical professionals, sleep clinics and the providers of various potions, pills and other sleep aids. In spite of this, her informed insider’s account of insomnia is a testament to how well we can apparently survive on far less than eight hours of sleep per night.

Although her inability to function is a message Green may want to convey, being a professor of literature we must allow her some poetic licence. After pouring out her woes, and pointing out that rats die without sleep and that insomnia may lead to all manner of ills, the book settles down to an interesting read. Green gives a fair reflection of how difficult life can be for insomniacs. Focusing on the United States, she interviews insomnia experts, tries out every conceivable sleep treatment and attends learned conferences on sleep disorders. Albeit from a personal viewpoint, she provides home truths and insights that many sleep researchers and doctors have lost track of; they would benefit from reading this book.

Claiming not to be depressed, obsessive or hypochondriacal, Green believes she has a genetic form of insomnia that leads to

‘physiological hyperarousal’ with additional hormonal underpinnings. For her, it is a physical condition and not ‘all in the mind’. In my mind lingers the thought that “the lady doth protest too much”. Make of the author what you will, *Insomniac* is among the best books of its kind. Besides, there are millions of people just like her, seemingly beyond the bounds of modern medicine.

Insomnia is one of the few disorders that a general practitioner will allow a patient to self-diagnose. The patient may be rewarded with a short course of hypnotic drugs; but even the best of these medicines is unlikely to lengthen night sleep by more than 20 minutes, usually by quickening sleep onset by the same amount. This is not enough to improve daytime alertness, mainly because many sufferers are hyperaroused and constantly ‘on the go’ — that’s why they can’t sleep. Others, such as Green, report being tired all the time, which is different from sleepiness and the propensity to fall asleep.

This tiredness can be linked to insomnia, but both are usually symptoms of something more deep-seated. Treating the insomnia alone (by hypnotic drugs, for example) makes little difference and can be an expensive, frustrating and fruitless course of action, especially in the United States, where sleep induction is a billion-dollar industry. Many, like Green, then seek the solace and sympathies of alternative therapies.

Insomnia comes in many forms: difficulty in falling asleep, too many fitful awakenings or waking up too early. Although there



Insomnia is one of the few disorders that a general practitioner will allow a patient to self-diagnose.

PRIVATE COLLECTION/JAMES GOODMAN GALLERY, NEW YORK/BRIDGEMAN ART LIBRARY

may be obvious physical causes, such as pain and physical illness, for most other sufferers (especially Green) insomnia is more a problem of wakefulness intruding into sleep, rather than just bad sleep. To be more explicit, it is a 24-hour disorder in which persistent anxiety, anger or miserable notions, sitting constantly at the back of a person's mind, ruin the expectations of their next sleep. Clearly, the eventual cure must address this state of waking mind. It is pointless going to bed with these stresses.

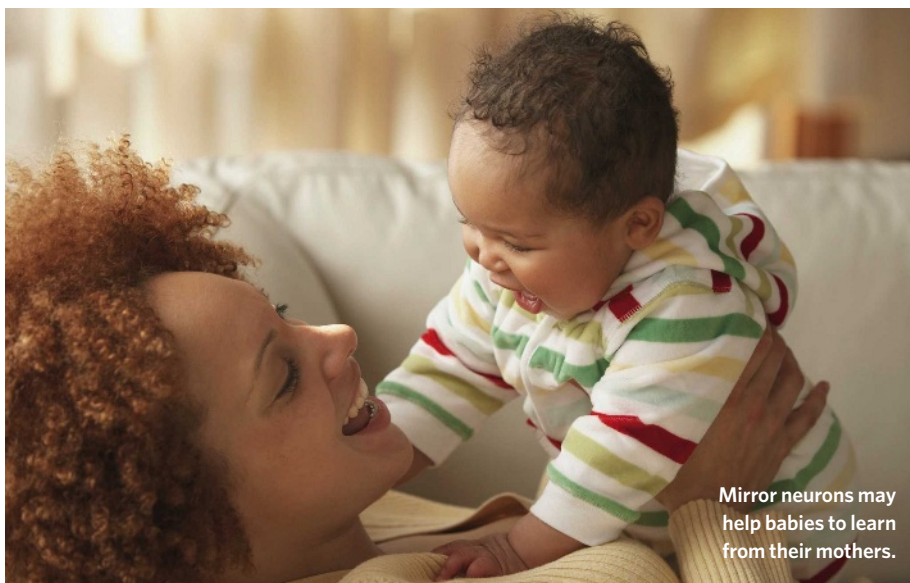
Despite the author's fears, insomnia by itself in an otherwise healthy person is unlikely to cause depression or mental illness, unless these are quietly developing for other reasons. Most sufferers also sleep for longer than they realize, and sleep-restriction therapy can actually be useful in treating severe depression.

Worsening Green's plight are the questionable exhortations that we live in a sleepless society riven with 'sleep debt'. Deprived sleepers supposedly run the risk of obesity, developing metabolic syndrome (a combination of risk factors associated with increased cardiovascular disease, liver disease and type 2 diabetes) or worse. This idea is based on old and often misquoted arguments that our grandparents got, on average, nine hours of sleep every night, so we should do the same. This number is flawed. The original research was carried out 100 years ago and focused on school children, not adults. Since the 1960s, findings from the United Kingdom have shown that the average daily sleep has remained consistent at around seven-and-a-quarter hours.

Recent claims that inadequate sleep causes obesity mostly come from over-generalized laboratory and epidemiological findings. Acute sleep restriction — for example, four hours daily over six days — may produce metabolic changes, but few people can cope with so little sleep and the profound sleepiness that results. Even enduring less than five hours sleep a night for many years would result in only modest weight gain, on average about 1 kilogram per year. Insomniacs usually sleep more than this. Proving the possible corollary that one might lose weight by extending sleep would probably take years to accomplish; contrast this with the rapid effectiveness of exercise and diet.

Maybe Green should pause to be thankful about her life, her writing ability and even her sleep in her no doubt comfortable bedroom. The typical worker living a century ago would have toiled long hours and gone home to an impoverished, cold, damp and noisy abode, sharing a lumpy bed with the rest of the family, bed-bugs and fleas. Yet he probably slept quite well. ■

Jim Horne is professor of psychophysiology at Loughborough University, Leicestershire LE11 3TU, UK, and author of *Sleepfaring: A Journey Through the Science of Sleep*.



Mirror neurons may help babies to learn from their mothers.

Reflecting on the mind

Mirrors in the Brain

by Giacomo Rizzolatti and Corrado Sinigaglia. Translated by Frances Anderson

Oxford University Press: 2007. 256 pp. \$49.95

Vilayanur S. Ramachandran

When a paradigm-shattering discovery is made in science, it goes through three stages before gaining acceptance. First, people don't believe it; second, they claim it is of no interest; and third, they say that they have always known it. The discovery of mirror neurons in the early 1990s by Giacomo Rizzolatti, Vittorio Gallese, Marco Iacoboni and others, has been through all three stages. Happily, the idea seems to have emerged unscathed, judging from *Mirrors in the Brain*.

In their readable new book, Rizzolatti and philosopher of science Corrado Sinigaglia survey the growing field that the research has spawned, setting it in historical context. They begin with an overview of the neural circuits in the brain that are involved in simple goal-directed movements. When a monkey reaches for a fruit or puts something in its mouth, motor-command neurons in area F5 in the frontal lobes fire. Different neurons fire for different actions.

Rizzolatti discovered that some of these motor-command neurons fire even when a monkey just watches another monkey performing the same action. He called these cells mirror neurons. They allow one monkey to simulate or imagine another monkey's impending action. Mirror neurons have also been found that fire when a monkey watches another monkey being touched. Another class, canonical neurons, fire both when orchestrating the precise hand and finger movements required to grab a specific object and when

one simply looks at that object. It is as if mere readiness to engage in a cylindrical grasp is synonymous — in terms of neural activity — with the perception of a cylinder.

Monitoring mirror-neuron activity might allow us to decipher the computations that lie at the elusive interface between perception and action, providing a key to understanding human cognition. If you extend the definition of action to include more abstract behavioural propensities, you could speak of the cells as representing 'meaning'. For example, an apple can conjure many ideas that neural activity may represent differently: it can be reached for and eaten, be used to tempt Eve, can keep the doctor away, go into a pie and so on.

Mirror neurons may be involved in seemingly unrelated mental abilities, such as pretend play in children, imitating skilled actions, emotional empathy and constructing a useful model of another's actions to predict his or her intentions. Because these abilities are lost in autism, it has been suggested that the condition may result partly from mirror-neuron deficiency.

If a mirror neuron fires when someone touches you and when you watch someone being touched, how do you know the difference? One possibility is that when you watch someone else being touched, tactile receptors in your skin inform the regular, non-mirror neuron cells in your brain that they are not being touched, which inhibits the output of your mirror neurons. This would explain our observation that people who have had a hand amputated experience touch sensations in their phantom hand when watching another person's intact hand being touched. The absence of signals from the missing hand removes the inhibition, causing the patient to literally experience another person's sensations, dissolving the barrier between self and others. I have dubbed the cells involved here 'Gandhi neurons'. But the

inhibition of mirror-neuron output by non-mirror neurons isn't perfect even in people with no amputation, as first noted by Charles Darwin. He observed that we tend to unconsciously tense our calf muscles when watching someone getting ready to throw a javelin, for example.

We may have evolved mirror neurons or acquired them by associative learning. To explain the latter, every time the network that a neuron is part of sends a command, you see your hand moving; eventually, as a result of conditioning, the mere appearance of a moving hand (even someone else's) triggers the same neuron. This hypothesis cannot explain why regular, non-mirror, sensory neurons do not also develop such properties through associative conditioning. To explain this, one has to invoke a pre-existing, genetically specified scaffolding that imposes constraints on what is learned.

Infants imitate their mother smiling or sticking out her tongue, implying a mirror-neuron-like computation for translating the visual appearance into the sequence of muscle twitches. Learning cannot be involved because the infant has never seen its own face. It is possible that the infant's smile is just a reflex that doesn't require elaborate translation. This can be ruled out if the newborn can also mimic an

asymmetrical smile or a peculiar expression, which demands a sophisticated interfacing between visual appearance and motor output.

Mirror neurons may also have clinical relevance for phantom pain and stroke rehabilitation. If a mirror is propped up vertically on a table in front of a patient with, for example, a paralysed left hand (so that one edge of the mirror is against his chest), the patient gets the illusion that the left hand is moving when he moves his right hand. We and others have found that this causes recovery from paralysis, perhaps by visually reviving dormant mirror neurons.

Mirrors in the Brain documents how this new science has been received. Some psychologists have criticized the idea of mirror neurons as being reductionist. Others think it is a mere metaphor for what psychologists have long called the 'theory of mind module' — the ability of our brains to construct internal models of other people's minds to predict their behaviour. This criticism reveals a fear that neuroscience might displace psychology ('neuron envy'), and a misunderstanding of reductionism. It is a bit like saying that the complementarity of the two strands of DNA is a metaphor for the complementarity of offspring and parent.

Psychological and neural explanations are complementary, not mutually exclusive.

In their book, the authors present a long-awaited review of many empirical findings, and discuss the deeper implications of these observations for psychology, cognitive science and psycholinguistics, including language origins. Moreover, they write in a jargon-free style that should be intelligible to all.

There has been a lot of media hype surrounding mirror neurons. The real danger is that too much is explained, not too little. This is inevitable with any new discovery but does not, in itself, vitiate the discovery's intrinsic importance. Nearly a decade ago, I wrote that "mirror neurons will do for psychology what DNA did for biology". It remains to be seen whether they will turn out to be anything as important as that, but as Sherlock Holmes said to Watson: "The game is afoot."

Vilayanur S. Ramachandran is professor and director of the Center for Brain and Cognition, University of California, San Diego, La Jolla, California 92093-0109, USA. He is author of *The Emerging Mind: The BBC Reith Lectures*.

Correction

Joel Shurkin's review of *Internet Alley* by Paul E. Ceruzzi (*Nature* 452, 533; 2008) wrongly asserted that the book lacks an index; in fact, it does have one.

EXHIBITION

Design crystallized in the 1950s

Colin Martin

In the 1950s, the booming science of X-ray crystallography inspired designers as well as scientists to ponder the structures of nature. The exhibition *From Atoms to Patterns: Crystal Structure Designs from the 1951 Festival of Britain* at the Wellcome Collection in London explores how these two groups collaborated to bring molecular patterns into our homes.

Crystallographer Helen Megaw saw artistic possibilities for using the patterns generated by X-ray crystallography in wallpapers and fabrics. As a wedding gift for biochemist Dorothy Hodgkin in 1937, she embroidered a design based on the structure of aluminium hydroxide onto a cushion. Megaw thought that "the combination of really attractive pattern with the assurance of scientific accuracy would win a lot of attention".

While planning for the Festival of Britain — a morale-raising national exhibition in London after the Second World War — in the summer of 1951, Mark Hartland Thomas at the Council of Industrial

Design welcomed Megaw's idea. He persuaded 28 British manufacturers, including Dunlop, Wedgwood and the chemical company ICI to join the Festival Pattern Group (FPG) that produced 80 new designs for textiles, wallpapers, ceramics, glass, metal and plastic.

As the FPG's adviser on crystal structure diagrams, Megaw played a pivotal role. She persuaded eminent crystallographers to participate, including Lawrence Bragg, Max Perutz and John Kendrew as well

as Hodgkin. The diagrams on which the designs were based were selected by Megaw, who also advised manufacturers on their interpretation. Atomic structures of minerals (such as awillite and apophyllite), biological molecules (insulin, haemoglobin) and synthetic polymers were incorporated.

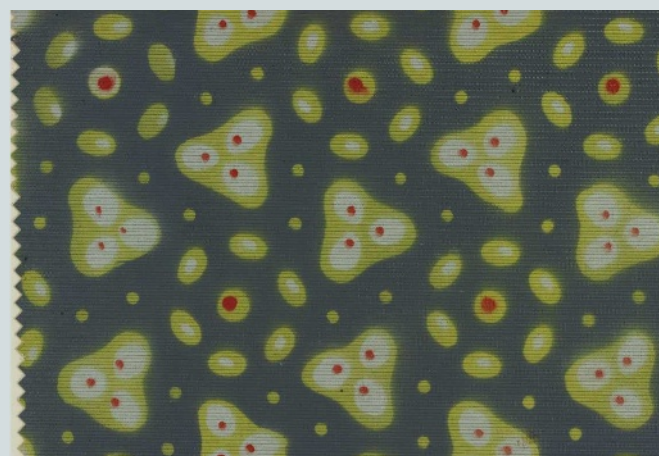
At the Festival of Britain, the science of X-ray crystallography featured in displays at the Dome of Discovery on London's South Bank and the Exhibition of Science at the Science Museum. The museum used FPG furnishings — its cinema foyer walls were covered with insulin wallpaper (pictured) and

the benches were upholstered in myoglobin leathercloth.

More FPG furnishings decorated the Regatta Restaurant on the South Bank. Diners walked on carpets patterned with resorcinol, gazed at awillite curtains and haemoglobin laminates, and were served by waitresses whose uniforms had hydrargillite-patterned lace collars. They stubbed out their cigarettes in pentaerythritol glass ashtrays, and used lavatories fitted with apophyllite glass screens.

Writing of the FPG's success, Hartland Thomas observed that the fresh and original designs "were essentially modern because the technique that constructed them was quite recent, and yet, like all successful decoration of the past, they derived from nature — although it was nature at a sub-microscopic scale not previously revealed."

Colin Martin is a writer based in London.



From Atoms to Patterns: Crystal Structure Designs From the 1951 Festival of Britain runs at the Wellcome Collection, London, from 24 April to 10 August (www.wellcomecollection.org).

Triumph of the medieval mind

Modern science began several hundred years earlier than we have come to imagine. It got going in the twelfth century — and with it, the long-standing rift between reason and faith.

Philip Ball

The popular caricature locates the origins of modern science in the natural philosophies of ancient Greece and the rediscovery of their spirit during the Renaissance and the Enlightenment. It passes decorously over the intervening period, deemed to be a hotbed of superstition. In fact, the notion of a Universe governed by laws accessible to human reason — the precondition for science — emerged in Western Europe largely during the twelfth century, several hundred years earlier than we have come to imagine.

“The eleventh-century Christians,” says historian Georges Duby, “still felt utterly crushed by mystery, overwhelmed by the unknown world their eyes could not see.”¹ By 1300, the foundations of a scientific world view were in place. The architects of this new philosophy attempted to reconcile their perspective with the pervasive religious sentiment of the Middle Ages. But in so doing they opened the schism between faith and reason that has since widened to a chasm.

From around 1120, an influx of classical texts revitalized European thought. These had been translated previously into Arabic within the Islamic world, and were now

rendered in Latin by energetic scholars working at the volatile boundaries of Christendom and Islam. Most of these books were scientific texts by writers such as Euclid, Aristotle, Archimedes and Ptolemy.

There was more to the ‘twelfth-century renaissance’² than the recycling of ancient learning. Islamic scholars such as Averroës, Al-Khwarizmi and Avicenna made original contributions of their own in subjects ranging from mathematics to medicine. So too did some of the medieval Europeans often depicted now as mere translators. Strangely, although Christian Europe showed little prejudice against learning from Muslims, it was reluctant to accept new ideas from its own people. The very antiquity of old knowledge was thought to make it more reliable.

One of the most active translators, the Englishman Adelard of Bath, was a startlingly original and perceptive thinker. Rueing how difficult it was to get his ideas accepted, he wrote: “Our generation ... refuses to accept anything that seems to come from the moderns. Thus when I have a new idea, if I wish to publish it I attribute it to someone else.”³ This is why so many of the works of natural philosophy from antiquity to the Renaissance have apocryphal attribution: a book apparently by Pliny or Aristotle

was more likely to be read. The progressive thinkers of the early Middle Ages hid their new wine in old flasks, so that others would take them seriously.

The translations guided scholars towards a mode of inquiry governed by scepticism and reason rather than by the search for validation in the Bible or St Augustine. In his book *Sic et Non*, the combative Frenchman Peter Abelard pointed out that the writings of the Church Fathers were not always consistent. These inconsistencies, he urged, should be reconciled using logic. *Sic et Non* is something of a sceptic’s manual: “We seek through doubt,” Abelard wrote, “and by seeking we perceive the truth.”⁴

Natural questions

A rationalist position was also nurtured at the cathedral school of Chartres (see ‘Rationality in stone’, page 818). From around the 1120s, this school acquired several chancellors with a deep interest in natural philosophy. These included Bernard of Chartres and his brother (or possibly pupil) Thierry, arguably one of the true founders of Western science. The Chartres scholars were platonists: they believed that the mundane world is underpinned by a transcendental realm governed by order and geometry. Thierry attempted to show how platonic ‘physics’ could be used to comprehend the world systematically, and even to interpret the biblical creation in Genesis.

Another Chartres scholar and teacher, William of Conches, got into trouble for pushing the rational agenda even harder. His *Philosophia Mundi* provided twelfth-century Europe with its first comprehensive treatise on the physical world. He argued that natural phenomena arise from forces that, although created by God, act under their own agency. William insisted, echoing Plato, that the divine system of nature is coherent and consistent, and therefore comprehensible: if we ask questions of nature, we can expect to get answers, and to be able to understand them.

That is a necessary belief for one even to imagine conducting science. If everything is subject to the whim of God, there is no guarantee that a phenomenon will happen tomorrow as it does today, therefore there is then no point in seeking any consistency in nature. But William of Conches could not countenance a Creator who was constantly intervening in the world. He saw the Universe as a divinely wrought mechanism: God simply set the wheels in motion. It is in the twelfth century that the



Empirical skills combined with the new philosophy to create the high Gothic style.

A. ROWBOTHAM/AGFOTO



With God as ultimate architect, the workings of the Universe were now open to rational study.

first references to the Universe as *machina* begin to appear.

Some conservative theologians denounced this attempt to develop a Christian platonic natural philosophy. They felt that taking too strong an interest in nature as a physical entity was tantamount to second-guessing God's plans. As everything was surely determined moment to moment by the will of God, it was futile and impious, they believed, to seek anything akin to what we now regard as physical law. The quest for laws of nature was also condemned because it seemed to limit God's omnipotence. As the eleventh-century Italian cleric Peter Damian insisted, one could not know anything for certain, as God could alter it all in an instant.

William of Conches didn't try to deny God's absolute power; he argued that it wasn't the issue. "Certainly God could make a calf out of the trunk of a tree, as country bumpkins might say, but did he ever do so? Therefore show some reason why a thing is so, or cease to hold that it is so."³ Adelard of Bath, another Chartres student, agreed: "I

do not detract from God. Everything that is, is from him, and because of him. But [nature] is not confused and without system, and so far as human knowledge has progressed it should be given a hearing. Only when it fails utterly should there be recourse to God."

Adelard's book *Quaestiones Naturales* reveals a mind full of curiosity about the world. Why do some animals see better at night? Why don't babies walk as soon as they are born? Why can sound pass through walls? In addressing these questions, he offers perhaps the most elegant and dignified defence of science ever written: "If we turned our backs on the amazing rational beauty of the universe we live in, we should indeed deserve to be driven therefrom, like a guest unappreciative of the house into which he has been received."⁴

These things were said by deeply devout men in an age that could not contemplate a world without God. How narrow and theologically immature they make the dogmas of contemporary religious

fundamentalists seem by comparison.

The twelfth-century trust in reason and interest in nature for its own sake flourished in the following century. This was particularly so in the aristotelianism of Thomas Aquinas, Robert Grosseteste and Roger Bacon. Their emphasis on attention to detail and careful observation signals the beginnings of an experimental approach — something that was unlikely to emerge from the abstract platonism of Chartres. Crudely speaking, Plato focused on the generalities, Aristotle on the particulars.

The backlash begins

But the golden age of rationalism in the early thirteenth century instigated a theological backlash, a kind of medieval Counter-Reformation. This culminated in the papal declaration of 1277 condemning many propositions in Aristotle's works. It was a metaphysical power struggle: was the world ruled by God's whims or Aristotle's laws? Could God contradict Aristotle? The battle was also more prosaic: did the universities' theology faculties have more authority than the arts faculties?

The Condemnation of 1277 forced some scholars to compromise on the elegant 'dual truth' we are still struggling to expunge. 'Scientific truth' was right about the world, but they had to concede that theological truth, with its mysteries and miracles, could overrule it. Nevertheless, the efforts of scholars such as Aquinas eventually legitimized logic and natural philosophy on religious grounds almost to a counterproductive extent. Indeed, by the Renaissance it became almost a heresy to challenge Aristotle.

Opposition to medieval rationalism was motivated in part by valid concerns about the dangers of bringing science into scripture. When, for example, William of Conches was denounced for seeking physical explanations for the creation of Eve from one of Adam's ribs, conservatives were right to voice dismay at this apparent transformation of the Bible into a work of science. Read as a kind of moral mythology, holy books may have some social value. Deeming them sources of natural facts must lead to the absurdities of today's creationism.

By making God a natural phenomenon, the medieval rationalists turned Him into an explicatory contingency for which there has since seemed ever less need. By degrees, such secular learning was found to have so much explanatory power that it rivalled, rather than rationalized, theology itself. The consequent rift between faith and reason has now left traditional religions so compromised they are susceptible to displacement by more naive and dogmatic varieties.

The emergence of Western science as

Rationality in stone

The twelfth-century renaissance gave rise to the artistic style now known as Gothic. In architecture this is characterized by hierarchical, orderly structures based on symmetry and proportion. Vaults and spires soar to unprecedented heights, yet the masonry, linked into a web of delicately balanced forces, seems almost weightless, flooded with light from immense coloured windows.

Some historians — most influentially Erwin Panofsky in the 1940s⁴ — have suspected a link between this style and the emerging belief in cosmic order. If a medieval church was in some sense a representation of heaven on Earth, they argue, then changes in church design must have something to tell us about how the Middle Ages conceptualized the cosmos. If the world was “God’s discourse to man”, in Umberto Eco’s words, then cathedrals “actualized a synthetic vision of man, of his history, of his relation to the universe”.

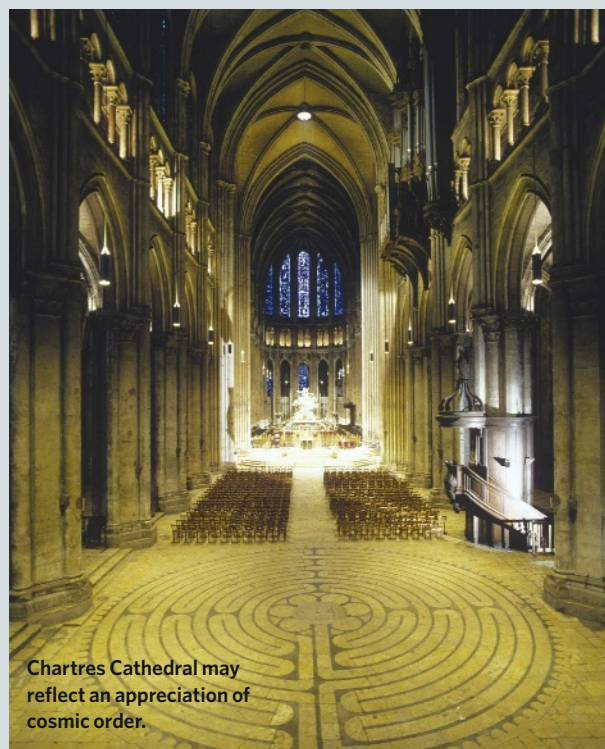
Panofsky proposed that the nascent French universities and academies in and around Paris influenced the Gothic architecture that originated here. Both architects and scholars, he said, used division and subdivision “to make the orderliness and logic of their thought palpably explicit”⁴. In the 1950s, historian Otto von Simson gave Panofsky’s argument greater force when he

scrutinized the role of geometry in the relationship between the intellectual and architectural worlds.

Von Simson argues that the first Gothic “marks and reflects an epoch in the history of Christian thought, the change from the mystical to the rational approach to truth”⁵. Historian of technology Lynn White agrees: “The transition from Romanesque to Gothic charts the passage from an age indifferent to the investigation of nature to one deeply concerned with it.”

Today many historians consider Panofsky’s argument to have been overstated, even misplaced. Some identify socioeconomic conditions as the principal force behind Gothic church building. Others say that geometry in architecture amounted to little more than convenient rules of thumb, lacking mathematical foundation. The truth probably lies somewhere in between.

A link between building and theology was sometimes explicit. To the scholars of Chartres, God was the great *architectus*, who used geometrical schemes to construct the Universe. Some medieval writers distinguished between the ‘theoretical’ geometry of the cathedral schools and universities, governed by mathematical proof, and the ‘practical’ geometry that could be used mechanically for constructing



Chartres Cathedral may reflect an appreciation of cosmic order.

pillars and vaults. Builders probably had little need of mathematical understanding: they could draw and interpret plans encoded in sequences of operations that could be learnt by rote and passed on orally.

A fifteenth-century builders’ handbook gives prescriptions for how to construct regular polygons, or to find the centre of a circle from an arc, with compass and ruler, with no indication that the writer knew of, or felt the need for, Euclid’s proofs.

Yet classical geometry and pythagorean symbolism do sometimes emerge in masonry. For example, medieval sculptors

often used a lens-shaped figure called the *vesica piscis* to frame Christ seated in majesty. The shape is found in *Ars geometriae et arithmeticae* by the early sixth-century Roman writer Boethius as the overlap between two equal circles whose circumferences pass through one another’s centres. Boethius explains that this construction, which can be made with a pair of compasses, may be used to make the most ‘perfect’ of triangles, the equilateral. So the shape would have been used to frame the figure of Christ not simply because it was pleasing and convenient but for its symbolic connotations. P.B.



Classical philosopher Pythagoras is honoured in stone on Chartres Cathedral.

a branch of humanism should thus be properly located in the high Middle Ages, not, as is traditional, in the Renaissance. It was in the twelfth and thirteenth centuries that the Universe ceased to be a forest of symbols designed by God for humankind’s spiritual edification, and became instead a source of intrinsic intellectual value and fascination, governed by logic. One can see this even in the shifting religious imagery of the time, such as the transformation of the sculpted flora of the Gothic churches from stylized forms to identifiable plant species. Art, theology, philosophy, social structures — all felt the influence of this altered perspective as we began to find our true place in the world. ■

Philip Ball is a consultant editor for Nature. His new book *Universe of Stone: Chartres Cathedral and the Triumph of the Medieval Mind* is published next month by Bodley Head.

1. Duby, G. *The Age of Cathedrals: Art and Society* (Univ. Chicago Press, 1981).
2. Haskins, C. H. *The Renaissance of the Twelfth Century* (Harvard Univ. Press, Cambridge, MA, 1927).
3. Le Goff, J. *Intellectuals in the Middle Ages* (Blackwell, Oxford, 1993).
4. Panofsky, E. *Gothic Architecture and Scholasticism* (New American Library, New York, 1957).
5. von Simson, O. G. *The Gothic Cathedral* 2nd edn (Harper & Row, New York, 1964).

For further reading visit <http://tinyurl.com/3gfjte>

A. ROWBOTHAM/AGRFOTO

HUMAN GENETICS

Dr Watson's base pairs

Maynard V. Olson

The application of new technology to sequence the genome of an individual yields few biological insights. Nonetheless, the feat heralds an era of 'personal genomics' based on cheap sequencing.

This issue of *Nature* contains a paper that is, in a curious way, a sequel to one published 55 years ago — the description by James Watson and Francis Crick¹ of the double-helical structure of DNA. At the information-carrying core of this beautiful structure, with its far-reaching implications for biology and medicine, are the base pairs that Watson discovered by fitting together cardboard cut-outs of the bases adenine, thymine, guanine and cytosine. Now, on page 872, Wheeler *et al.*² describe the use of massively parallel DNA sequencing to determine the order of the base pairs in Watson's own genome. This achievement is a technical *tour de force* that points towards routine use of whole-genome sequencing as a research tool in human genetics. Given the choice of James Watson as an identified research subject, the paper is also a conspicuous effort to publicize the arrival of the era of personal genomics and the willingness of a famous geneticist to put his genome sequence in the public domain.

Technically, the paper's interest stems from its reliance on a DNA-sequencing platform that differs greatly from the one used during the first great era of genome sequencing, which culminated in the Human Genome Project (HGP). In the HGP platform, each kilobase-pair fragment of genomic DNA was captured as a bacterial 'clone' using recombinant-DNA techniques and processed in its own microtitre-scale well in a microtitre plate. Following a series of biochemical steps, each sample was analysed electrophoretically in a dedicated, metre-long glass capillary. To achieve the required redundancy in sequence coverage, investigators in the HGP processed tens of millions of individual samples en route to determining the order of the 3 billion base pairs present in a single, composite instance of the human genome. This achievement required the development of industrial-scale genome

TGCTTACGGCATCGAGCTGCTCGACAGCTTCGTACGCTGCTGCTGCGCATATTATATTAGCTGAT
AGCTGTTGTGAATTTAGTATGGGCCCTCGTTACGGCATCGAGCTGCTGCGAGAGCTTCGTACGCTG
TTAGCTGATCGTGATTTCTGAATGCTAGCTGTTGTGAATTTAGTATGGGCCCTCGTTACGGCATC
CGTACCTCGTACGCTGCTGCTGCGCATATTATATTAGCTGATCGTGATTTCTGAATGCTAGCTGCT
CCCTCGTTACGGCATCGAGCTGCTGCGAGAGCTTCGTACGCTGCTGCTGCGCATATTATATTAGCT
GCTAGCTGTTGTGAATTTAGTATGGGCCCTCGTTACGGCATCGAGCTGCTGCGAGAGCTTCGTACG
ATATTAGCTGATCGTGATTTCTGAATGCTAGCTGTTGTGAATTTAGTATGGGCCCTCGTTACGGC
CTTCGTACGCTGCTGCTGCGCATATTATATTAGCTGATCGTGATTTCTGAATGCTAGCTGTTGTG
CGTTACGGCATCGAGCTGCTGCGAGAGCTTCGTACGCTGCTGCTGCGCATATTATATTAGCTGATC
CGAGCTGCTGCGAGAGCTTCGTACGCTGCTGCTGCGCATATTATATTAGCTGATCGTGATTTCTGA
TTTATGATGGGCCCTCGTTACGGCATCGAGCTGCTGCGAGAGCTTCGTACGCTGCTGCTGCGCAT
GATTTCTGAATGCTAGCTGTTGTGAATTTAGTATGGGCCCTCGTTACGATTTCTGAATGCTAGCT
GGCCCTCGTTACGGCATCGAGCTGCTGCGAGAGCTTCGTACGCTGCTGCTGCGCATATTATATTAG
ATGCTAGCTGTTGTGAATTTAGTATGGGCCCTCGTTACGGCATCGAGCTGCTGCGAGAGCTTCGT
TTATATTAGCTGATCGTGATTTCTGAATGCTAGCTGTTGTGAATTTAGTATGGGCCCTCGTTACG
AGCTTCGTAGCTGCTGCTGCGCATATTATATTAGCTGATCGTGATTTCTGAATGCTAGCTGTTGTG
CTGTTACGGCATCGAGCTGCTGCGAGAGCTTCGTACGCTGCTGCTGCGCATATTATATTAGCTGATC
TGTGTGAATTTAGTATGGGCCCTCGTTACGGCATCGAGCTGCTGCGAGAGCTTCGTACGCTGCTG
GCTGTCGTGATTTCTGAATGCTAGCTGTTGTGAATTTAGTATGGGCCCTCGTTACGGCATCGAG
TTAGTATGGGCCCTCGTTACGGCATCGAGCTGCTGCGAGAGCTTCGTACGCTGCTGCTGCGCAT
TGAATTTAGTATGGGCCCTCGTTACGGCATCGAGCTGCTGCGAGAGCTTCGTACGCTGCTGCTGCG
TCGTGATTTCTGAATGCTAGCTGTTGTGAATTTAGTATGGGCCCTCGTTACGGCATCGAGCTGCT
CTGATTCGTGATTTATATTAGCTGATCGTGATTTCTGAATGCTAGCTGTTGTGAATTTAGTATGG
CGAGCTGCTGCGAGAGCTTCGTACGCTGCTGCTGCGCATATTATATTAGCTGATCGTGATTTCTGA
TTTATGATGGGCCCTCGTTACGGCATCGAGCTGCTGCGAGAGCTTCGTACGCTGCTGCTGCGCAT
GATTTCTGAATGCTAGCTGTTGTGAATTTAGTATGGGCCCTCGTTACGGCATCGAGCTGCTGCGAG
CTGCGCATATTATATTAGCTGATCGTGATTTCTGAATGCTAGCTGTTGTGAATTTAGTATGGGCC
AATGCTAGCTGTTGTGAATTTAGTATGGGCCCTCGTTACGGCATCGAGCTGCTGCGAGAGCTTCGT
ATTATATTAGCTGATCGTGATTTCTGAATGCTAGCTGTTGTGAATTTAGTATGGGCCCTCGTTAC
GAGCTTCGTGATCGTGATTTCTGAATGCTAGCTGTTGTGAATTTAGTATGGGCCCTCGTTACGG
CCTCGTTACGGCATCGAGCTGCTGCGAGAGCTTCGTACGCTGCTGCTGCGCATATTATATTAGCT
CTAGCTGTTGTGAATTTAGTATGGGCCCTCGTTACGGCATCGAGCTGCTGCGAGAGCTTCGTAC
TATTAGCTGATCGTGATTTCTGAATGCTAGCTGTTGTGAATTTAGTATGGGCCCTCGTTACGG
TTTACGGCATCGAGCTGCTGCGAGAGCTTCGTACGCTGCTGCTGCGCATATTATATTAGCTGATC
CTGTTGTGAATTTAGTATGGGCCCTCGTTACGGCATCGAGCTGCTGCGAGAGCTTCGTACGCTG
AGCTGATCGTGATTTCTGAATGCTAGCTGTTGTGAATTTAGTATGGGCCCTCGTTACGGCATCGA
TACGCTGCTGCTGCGCATATTATATTAGCTGATCGTGATTTCTGAATGCTAGCTGTTGTGAATTT
CGGCATCGAGCTGCTGCGAGAGCTTCGTACGCTGCTGCTGCGCATATTATATTAGCTGATCGTG
TGTGAATTTAGTATGGGCCCTCGTTACGGCATCGAGCTGCTGCGAGAGCTTCGTACGCTGCTG
GTGAATTTAGTATGGGCCCTCGTTACGGCATCGAGCTGCTGCGAGAGCTTCGTACGCTGCTG
ATCGTGAATTTCTGAATGCTAGCTGTTGTGAATTTAGTATGGGCCCTCGTTACGGCATCGAGCT
GTGAGCTGCGCATATTATATTAGCTGATCGTGATTTCTGAATGCTAGCTGTTGTGAATTTAGTAT
TCGAGCTGCTGCGAGAGCTTCGTACGCTGCTGCTGCGCATATTATATTAGCTGATCGTGATTTCT
CTAGCTGTTGTGAATTTAGTATGGGCCCTCGTTACGGCATCGAGCTGCTGCGAGAGCTTCGTAC
TATTAGCTGATCGTGATTTCTGAATGCTAGCTGTTGTGAATTTAGTATGGGCCCTCGTTACGG
GATTTCTGAATGCTAGCTGTTGTGAATTTAGTATGGGCCCTCGTTACGGCATCGAGCTGCTGCGA
CTGCGCATATTATATTAGCTGATCGTGATTTCTGAATGCTAGCTGTTGTGAATTTAGTATGGGCC
CTGCTGCGAGAGCTTCGTACGCTGCTGCTGCGCATATTATATTAGCTGATCGTGATTTCTGAAT
GTATGGGCCCTCGTTACGGCATCGAGCTGCTGCGAGAGCTTCGTACGCTGCTGCTGCGCAT
TCTGAATGCTAGCTGTTGTGAATTTAGTATGGGCCCTCGTTACGGCATCGAGCTGCTGCGAG
CGGCATCGAGCTGCTGCGAGAGCTTCGTACGCTGCTGCTGCGCATATTATATTAGCTGATCGTG

James Watson decoded.

centres that looked more like manufacturing plants than laboratories. The data-production costs alone were hundreds of millions of dollars.

Wheeler *et al.*² used one of several new DNA-sequencing platforms that can achieve much the same result at perhaps 1% of the cost^{3,4}. Note, however, that at their present stage of development none of these methods would allow a simple, bargain-basement replay of the HGP: analysis of the data remains heavily dependent on the high-quality reference sequence produced by that project. The key to the increased

efficiency of the new methods lies in massive parallelization of the biochemical and measurement steps. The instruments used by Wheeler *et al.* are marketed by 454 Life Sciences, a component of Roche Diagnostics, which joined forces with the Human Genome Sequencing Center at Baylor College of Medicine in Houston, Texas, to sequence Watson's genome.

The 454 instruments achieve massive parallelization in two different ways⁵. In an initial step, single DNA molecules are attached to synthetic beads and then amplified enzymatically. During amplification, the beads are trapped in tiny water droplets within a water-oil emulsion; hence, more than 100,000 samples can be processed in parallel in a single test tube. In a later step, during which optical measurements are used to collect the actual sequencing data, each bead is confined to a picolitre-scale well etched into the end of a glass fibre within a fibre-optic bundle. Although costs have not yet dropped to the much-ballyhooed target of US\$1,000 per genome⁶, they are now low enough to make the era of personal genomics a reality rather than a distant dream.

What can we expect to learn from the sequences of individual genomes? The main lesson from the analyses by Wheeler *et al.* is that it will be extremely difficult to extract medically, or even biologically, reliable inferences from individual sequences. Consider the challenge of interpreting Watson's single nucleotide polymorphisms (SNPs — simple substitutions of one base for another at a particular site in the genome). Wheeler *et al.* report about 3,300,000 SNPs in Watson's genome relative to the HGP reference sequence. Of these SNPs, 82% had already been described in other individuals, a result suggesting that public databases are starting to have a good representation of common SNPs. Most of these variants are presumed neutral (that is, of no evolutionary or functional significance).

However, some 11,000 of Watson's SNPs (85% previously known, 15% novel) are predicted to change the amino-acid sequence — and so, perhaps, the function — of a protein. An unknown number of additional SNPs undoubtedly affect the regulation of protein levels. Because there are only around 20,000 protein-coding genes in humans, it seems that if the proteins of any two individuals were compared in detail, a significant fraction would be found to differ. In only a few cases do we have any knowledge of possible biological effects of these differences.

The level and overall pattern of variation in Watson's genome seem to be typical of the variation present in other individuals of predominantly European ancestry. In part, this conclusion rests on the existence of one other example of a personal-genome sequence, that of J. Craig Venter, who was head of Celera Genomics when it competed with the HGP to produce the first human genome sequence. The publication of Venter's sequence last year⁷ attracted relatively little attention because the project used HGP-era methods and much of the data had already been reported. Nonetheless, the similarity of the bulk statistics for these two personal-genome sequences helps validate the new methods used by Wheeler and colleagues.

If Watson took his sequence to a genetic counsellor, there would be little to discuss. The sequence seems to show that he is a carrier for a handful of mutations that might catch a counsellor's interest. But these mutations have no known effects on Watson himself, and would confer risk on offspring only in the highly unlikely event of a marriage between two carriers. None of these mutations is ever likely to be considered an appropriate candidate for screening in the general population — of which, for these purposes, Watson is a representative member.

Recognition of the thin clinical value of this sequence may cause some investors in the new sequencing methods to take pause, given that the major capital investments required to commercialize these technologies have been motivated more by their perceived medical potential than by research applications.

Basic scientists are likely to greet the work of Wheeler *et al.*², and the era it inaugurates, with more enthusiasm. The central challenge in human genetics now is to learn how to correlate genotype with phenotype (the observable characteristics of an organism), with special attention to disease predisposition and response to therapy. Whole-genome sequencing of case-control populations is an attractive alternative to the surrogates for this procedure on which human geneticists have relied for the past 25 years. These surrogates frequently depend on educated guesses about which genes to sequence in subjects with particular phenotypes. They also rely on efforts to detect co-inheritance of a phenotype — in families or even among individuals who are only evolutionarily related — with 'genetic

markers' (neutral DNA variants that can reveal the common ancestry of local segments of the genome). In these indirect 'linkage' or 'association' methods, the observed genetic markers can indicate the approximate genomic position of the unknown functional variants that influence the phenotype. In the era of whole-genome resequencing, all variants, including the functionally important ones, will be observed directly.

The actual practice of personalized medicine based on genome sequences will have to wait until we can make reliable predictions from the data. At present, we have little ability to do so. To take one seemingly simple example of a highly heritable trait, we could not even make a rough prediction of Watson's height from his genome sequence: the most informative known SNPs that influence height account for only a few millimetres of variation in a trait whose standard deviation is 7 centimetres (ref. 8).

In short, the symbolic significance of Wheeler and colleagues' paper² is greater than its immediate contributions to human biology. But it is irresistible to speculate on how biologically revealing the data will ultimately prove to be. James Watson is a brilliant scientist with a remarkable life story. He both laid the deep scientific foundations for genomic

biology and devoted much of his life — through his teaching, his leadership and the sheer force of his personality — to building this science to its current productive state. Along the way, he stepped on more than one landmine. Future historians will find him a rich and elusive subject. Perhaps, informed by the advanced genetics of their day, they will scrutinize the data left behind by Wheeler *et al.* for clues to why he was the way he was. However, I suspect that they will have to rely instead, as historians do today, on what Watson wrote, said and did during his lifetime rather than on the order of the base pairs in his genome. ■

Maynard V. Olson is in the Division of Medical Genetics, Department of Medicine, University of Washington School of Medicine, Seattle, Washington 98195-7720, USA.
e-mail: mvo@u.washington.edu

1. Watson, J. D. & Crick, F. H. C. *Nature* **171**, 737–738 (1953).
2. Wheeler, D. A. *et al.* *Nature* **452**, 872–876 (2008).
3. Bentley, D. R. *Curr. Opin. Genet. Dev.* **16**, 545–552 (2006).
4. Shendure, J., Mitra, R. D., Varma, C. & Church, G. M. *Nature Rev. Genet.* **5**, 335–344 (2004).
5. Margulies, M. *et al.* *Nature* **437**, 376–380 (2005).
6. Collins, F. S., Green, E. D., Guttmacher, A. E. & Guyer, M. S. *Nature* **422**, 835–847 (2003).
7. Levy, S. *et al.* *PLoS Biol.* **5**, e254 (2007).
8. Weedon, M. N. *et al.* *Nature Genet.* **39**, 1245–1250 (2007).

PLANETARY SCIENCE

Message from Mercury

H. Jay Melosh

After a 30-year gap, all eyes are back on Mercury as the MESSENGER probe gives us our second glance at the Sun's nearest neighbour. Hints of intriguing results to come are already at hand.

On 10 March, scientists from MESSENGER, NASA's mission to the planet Mercury, reported their first observations of the planet at the annual conference of the Lunar and Planetary Institute*. The probe — its name stands for 'Mercury Surface, Space Environment, Geochemistry, and Ranging' — was launched from Cape Canaveral on 3 August 2004. Its goal is to orbit the Solar System's innermost planet, and thus answer 30-year-old questions raised when the Mariner 10 spacecraft flew past the planet three times during 1974 and 1975.

Mercury sits deep inside the Sun's gravity well, making it more difficult to reach from Earth than even Pluto. No chemically fuelled spacecraft can achieve the velocity necessary to cancel out the motion of Earth's orbit and thus rendezvous directly with Mercury under its own steam. MESSENGER instead flew a tortuous path, using the gravity of Earth once and that of Venus twice to shed angular momentum and so to spiral down into the

* 39th Lunar and Planetary Science Conference, 10–14 March 2008, League City, Texas.

inner Solar System. Mission destination was finally reached on 14 January of this year, when the probe completed the first of three planned fly-bys at just 200 kilometres above Mercury's surface (S. Solomon, Carnegie Inst.).

Mariner 10 had already revealed the Moon-like nature of this surface, and returned images of a vast impact crater, the Caloris Basin, as well as evidence of a distinctly un-Moon-like uniformity of colour: Mercury's lavas seem to be almost as bright as the rest of its surface, and so do not produce the Man-in-the-Moon contrasts familiar from our satellite. Widespread lobe-shaped scarps, seemingly the result of compressive thrust faulting as the planet cooled in its early history, diversify the planet's surface.

Mariner 10 was never able to image Mercury's entire surface, and its camera systems provided only 1-km resolution over the 45% of the planet imaged, with a few images at a higher resolution of about 300 metres. MESSENGER's more sophisticated instruments have already confirmed and added

detail to Mariner 10's findings with 1,200-odd images from the January fly-by, some covering previously unimaged terrain (L. Proctor, Johns Hopkins Univ.). The Caloris Basin, for example, about a third of which was covered by Mariner 10, has now been imaged in its entirety, and found to be about 1,540 km in diameter, somewhat larger than previously thought (S. Murchie, Johns Hopkins Univ.).

Tectonic relics

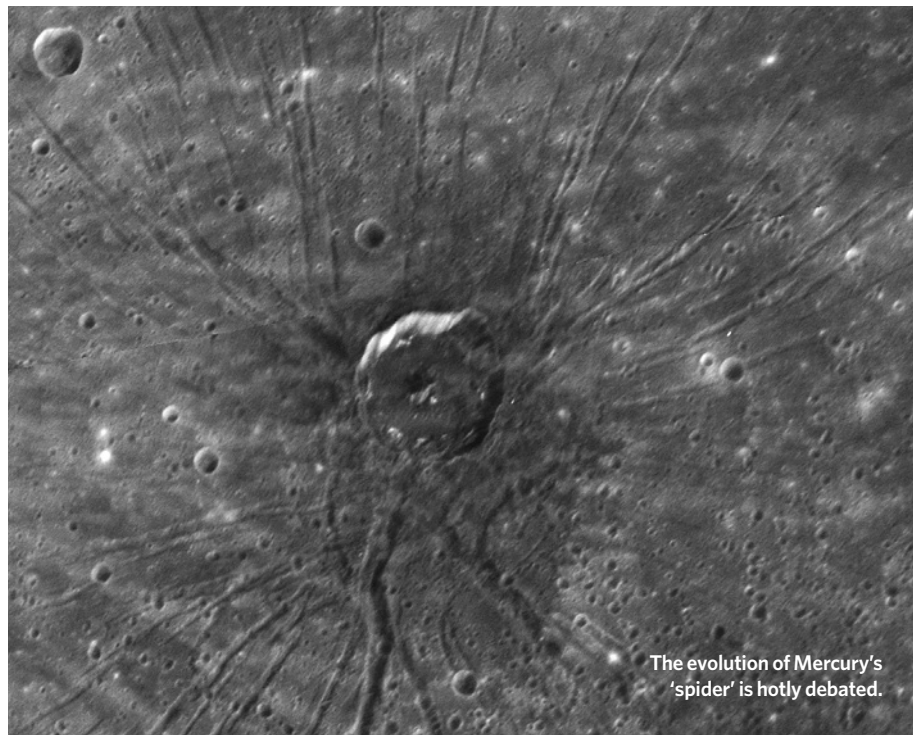
Much of MESSENGER's improvement on Mariner is the product of 30 years' development in high-resolution imaging technology. But the new probe is also equipped with instruments that had not even been dreamed of in Mariner's time: its laser altimeter, for instance, will eventually provide a detailed topographic map of the planet's northern hemisphere. During the first fly-by, this instrument revealed that Mercury's impact basins are shallower than those on the Moon (M. Zuber, MIT). This might reflect either a thinner crust on Mercury or a smaller density contrast between the crust and mantle.

Mariner 10 had revealed broad volcanic plains on Mercury, but close analysis of MESSENGER images of the Caloris Basin reveal for the first time what seem to be volcanic vents in its southwestern quadrant, from which material could have erupted (J. Head, Brown Univ.). Areas of high surface reflectivity near those vents suggest pyroclastic deposits, further evidence for former volcanic activity.

Perhaps MESSENGER's most surprising discovery was a 42-km-diameter impact crater (pictured) located almost dead in the centre of the Caloris Basin, from which radial spokes, each marking a topographic trough, extend out hundreds of kilometres (T. Watters, Smithsonian National Air and Space Mus.). The origin of this striking landform, dubbed 'the spider', has been eagerly debated, with possibilities discussed ranging from a network of lava-filled fissures that almost reached the surface, similar to the Novae seen on Venus (J. Head), to fault-bounded trenches (graben) formed as the basin floor rose up and expanded, perhaps under pressure from the surrounding volcanic plains (T. Watters). Another plausible explanation presented is that the central crater of the spider simply concentrated tectonic stresses in the basin, leading to graben formation (A. Freed, Purdue Univ.).

Which of these alternatives is right hinges on whether the central crater is younger or older than the surrounding troughs. No consensus has been reached on this point, although preliminary crater counts do indicate that the plains exterior to Caloris are younger than those inside (R. Strom, Univ. Arizona), a result that accords nicely with tectonic models of uplift of the interior crater floor.

Preliminary mapping indicates that, although Mercury's impact craters seem



The evolution of Mercury's 'spider' is hotly debated.

generally similar in size to those on the Moon or Mars, the surrounding secondary impact craters may be considerably larger than those seen on the Moon (C. Chapman, Southwest Research Inst.). This is puzzling. Larger secondary fragments correlate with, if anything, lower shock pressures and impact speeds; but the average impact velocity on Mercury is thought to be about 50 km s^{-1} , compared with about 20 km s^{-1} on the Moon and 7 km s^{-1} on Mars. At present, there is no plausible explanation for this observation: it seems simply as if Mercury's crust is much stronger than that of the Moon or Mars under the shock of impact ejection.

Iron findings

Spectroscopic study of Mercury's surface is still very preliminary: although MESSENGER's X-ray, γ -ray and neutron spectrometers promise a detailed chemical analysis of Mercury's surface, an unexpectedly quiet Sun that yielded few X- and γ -rays, coupled with the short duration of the January fly-by, meant that little was detected other than an X-ray line from silicon (L. Nittler, Carnegie Inst.). The imaging spectrometer revealed that ferrous iron seems to be strangely absent from Mercury's crust (W. McClintock, Univ. Colorado). Despite their outward similarity, Mercury's surface thus seems to be very different from the Moon's, which has abundant iron. There are, however, some indications of the presence of opaque minerals in Mercury's crust, one of which could be the iron titanium oxide ilmenite (M. Robinson, Arizona State Univ.).

One of the most startling discoveries made by Mariner 10 was that, despite its small size and slow rotation, Mercury has

a small magnetic field. MESSENGER's magnetometer confirmed this, and showed that the field's strength has not changed substantially in the past 30 years. The field is stronger in the northern hemisphere than in the southern, and so is not consistent with a pure dipole located at the planet's centre, as is (approximately) the case on Earth, but requires a substantial quadrupole contribution (B. Anderson, Johns Hopkins Univ.). At present, there is also no evidence for Earth-like Van Allen belts of particles trapped in Mercury's external magnetic field: sodium and hydrogen were observed in the planet's exosphere, but were accompanied by few of the energetic charged particles that characterize Earth's engirdling belts. This might be due to the lack of particle injection from the solar wind under the current quiet Sun conditions (R. McNutt, Johns Hopkins Univ.).

MESSENGER's January encounter is only the preliminary to a much greater scientific show ahead. More complete imaging of Mercury's surface will come with the probe's second and third fly-bys in October 2008 and September 2009, and after its eventual insertion into an elliptical orbit around Mercury in March 2011. Only then will the spacecraft's neutron spectrometer test the suggestion that craters in Mercury's northern polar region harbour deposits of ice, and will we be able to map out the global distributions of mass anomalies, topographic elevations and chemical elements. After a 30-year hiatus, the study of the Solar System's innermost planet is again moving to centre stage.

H. Jay Melosh is in the Lunar and Planetary Laboratory, University of Arizona, Tucson, Arizona 85721, USA.
e-mail: jmelosh@lpl.arizona.edu

BIOPHYSICS

The sweetest candy for the virus

Andreas O. Frank and Horst Kessler

For some viruses, the first step in infecting cells is to latch onto sugars on the cell membrane. The chemical basis of this virus–host recognition process has been identified using an NMR spectroscopic technique.

A few weeks ago, many of our friends suffered from ‘winter vomiting disease’, a form of gastroenteritis that swept epidemically across Germany. This unpleasant disease is caused by the highly contagious norovirus, a member of the Caliciviridae family of RNA viruses. Caliciviruses are unusual because they dock to sugar residues on the surfaces of cells to be invaded, rather than to proteins. The chemical details of this process were unknown, but reporting in the *Journal of the American Chemical Society*, Rademacher *et al.*¹ present a nuclear magnetic resonance (NMR) study that determines which sugar residues are involved in the binding of another calicivirus, rabbit haemorrhagic disease virus (RHDV), to cells. Their technique could be used to develop drugs that block the entry of viruses into cells.

In adult rabbits, RHDV infection leads to severe hepatitis, usually causing death within 48 hours^{2,3}. The crucial step of RHDV infection is attachment of the virus to certain host antigens (known as histo-blood group antigens)

that form branched ‘tails’ on the surfaces of cells lining the respiratory and digestive tracts⁴. The same kind of antigens are also found on human red blood cells, and form the basis of the ‘ABO’ classification system for blood groups.

Histo-blood group antigens consist of combinations of different sugar molecules. Furthermore, some of these antigens can adopt two kinds of structure (type I and type II), depending on the linkage between the first two sugars. The exact combination of sugars varies both between individuals and between species. Different caliciviruses infect only those organisms that display the specific antigens targeted by the virus. For example, RHDV docks exclusively to ‘H antigens’ that have type II structures⁴, whereas most noroviruses attack humans by attaching to type I H-antigens⁵.

Thus, the only way to explain the different susceptibilities of organisms to particular caliciviruses is to identify the chemical basis of virus–host recognition. Rademacher *et al.*¹ addressed this issue by determining which parts

of different histo-blood group antigens are involved, directly or indirectly, in binding to the protein surface of virus-like particles (VLPs). These particles were made from the structural proteins of RHDV, and had the same shape, size and antigens as natural virus particles, but contained no nucleic acid⁶. The authors weren’t able to use actual RHDVs in their study, as the viruses cannot be cultivated.

Because VLPs are large protein assemblies, whereas the sugars to which they attach are relatively small, Rademacher *et al.*¹ were able to use a technique known as saturation-transfer difference (STD) NMR^{7,8}, which exploits the different sizes of the molecules under investigation. The authors placed a solution of synthetic antigens (or their fragments) and VLPs in a strong homogeneous magnetic field, and then irradiated the sample with radiofrequency pulses in such a way that only the virus particles absorbed energy from the pulses. Because of the large size of the particles, the energy received — known as saturation — is rapidly distributed over the whole VLP. The saturation is also transmitted to those antigens that can bind to the surface of the VLPs, so that the VLP-binding pocket leaves its structural imprint on these fragments. When the bound sugar molecules dissociate from the particle, the saturation is carried with them into the surrounding solution, where it can be detected as small changes of intensity in the NMR spectrum.

The efficiency with which saturation is transmitted between VLPs and antigens is distance-dependent, so that antigen atoms that interact directly with a binding pocket gain more energy than atoms that interact only indirectly. Furthermore, strong binders receive more energy than weak ones; non-binding antigens receive no saturation at all. By subtracting the NMR spectrum of the irradiated sample from that of a non-irradiated sample, the small changes in intensity caused by saturation transfer can be measured, and so the antigen fragments that bind to the VLPs can be identified.

By systematically screening several antigen fragments, the authors¹ found that only those containing the sugar L-fucose were recognized by the VLPs (Fig. 1). None of the structures that lacked fucose showed any binding affinity, except for one fragment that gave a moderate STD response. In each of the VLP-binding fragments, the L-fucose part of the molecule showed the strongest STD effect.

The authors did find one example of an L-fucose-containing antigen that didn’t bind to the VLPs. The unusual behaviour of this compound can be attributed to its type I structure — the other antigens had type II structures that presumably fit better into the binding site on the VLPs. Taking everything into consideration, the authors conclude that L-fucose is the essential motif to which RHDVs bind in type II antigens. This crucial information opens the door to the rational design of compounds that block the entry of RHDVs into cells.

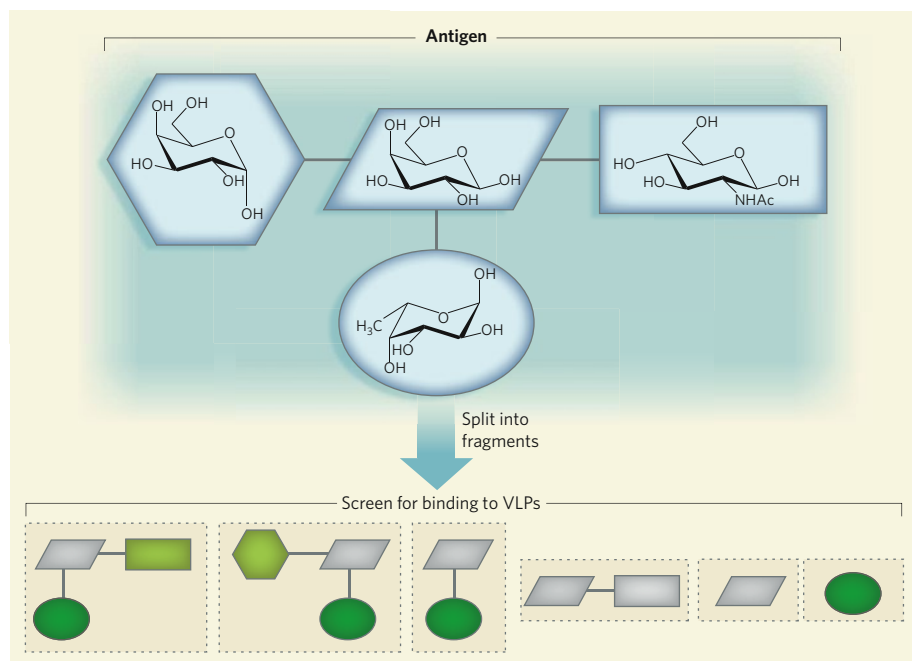


Figure 1 | Viral recognition of an antigen. The first step in the infection of cells by rabbit haemorrhagic disease virus (RHDV) is binding of the virus to antigens on the cells’ membranes. The antigens investigated consist of four different connected sugars (structures indicated; Ac is an acetyl group). Rademacher *et al.*¹ use a technique called saturation-transfer difference NMR spectroscopy to study the binding of the antigens and their fragments to virus-like particles (VLPs), which closely model RHDV. For each fragment that binds to the particles, the sugar that contributes most to binding is shown in dark green; sugars that bind less strongly are paler green; and sugars that contribute nothing to virus–host interactions are grey. The authors conclude that the sugar L-fucose (oval) is essential for RHDV binding to the antigen.

Rademacher and colleagues' results demonstrate the potential of STD NMR for the rapid, unequivocal identification of small molecules that bind to proteins. The technique offers several benefits — for example, no structural information about the protein is required, and the mode of binding of the molecules is also revealed. It has already been shown that, of all the current NMR screening techniques^{9–11}, STD NMR is the most efficient at identifying false-positive hits from high-throughput biological assays. Rademacher *et al.*¹ have provided further compelling arguments for the routine use of this technique in drug development. ■

Andreas O. Frank and Horst Kessler are in the Center of Integrated Protein Science, Technische Universität München, Lichtenbergstrasse 4, D-85747 Garching, Germany.

e-mails: andreas.frank@ch.tum.de;
horst.kessler@ch.tum.de

1. Rademacher, C., Krishna, N. R., Palcic, M., Parra, F. & Peters, T. J. *Am. Chem. Soc.* **130**, 3669–3675 (2008).
2. Thiel, H. J. & König, M. *Vet. Microbiol.* **69**, 55–62 (1999).
3. Parra, F. & Prieto, M. J. *Viol.* **64**, 4013–4015 (1990).
4. Ruvoën-Clouet, N., Ganière, J. P., André-Fontaine, G., Blanchard, D. & Le Pendu, J. J. *Viol.* **74**, 11950–11954 (2000).
5. Harrington, P. R., Vinjé, J., Moe, C. L. & Baric, R. S. J. *Viol.* **78**, 3035–3045 (2004).
6. Laurent, S., Vautherot, J. F., Madelaine, M. F., Le Gall, G. & Rasschaert, D. J. *Viol.* **68**, 6794–6798 (1994).
7. Mayer, M. & Meyer, B. *Angew. Chem. Int. Edn* **38**, 1784–1788 (1999).
8. Meyer, B. & Peters, T. *Angew. Chem. Int. Edn* **42**, 864–890 (2003).
9. Klages, J., Coles, M. & Kessler, H. *Analyst* **132**, 692–705 (2007).
10. Manzenrieder, F., Frank, A. O. & Kessler, H. *Angew. Chem. Int. Edn* **47**, 2608–2611 (2008).
11. Pellecchia, M. *et al.* *Nature Rev. Drug Disc.* (in the press).

QUANTUM PHYSICS

Debut of the quarter electron

Eduardo Fradkin

A particle-like object with a quarter of an electron's charge is the latest find in a hotbed of quantum-physical experimentation, the fractional quantum Hall fluid. Its significance is more than esoteric.

On page 829 of this issue, Dolev *et al.*¹ report the detection of vortices in a fluid of electrons confined to two dimensions within a semiconductor structure that carry just 1/4 of the electron's charge. These 'quasiparticles' are an exciting find: according to theoretical predictions, their collective behaviour should be described by an unusual type of particle statistics known as non-abelian statistics. Above all, that could make them useful in an exotic, but highly promising, brand of quantum computer — the topological quantum computer (see News Feature on page 803)².

It is an established fact that, if a large magnetic field is applied perpendicular to the plane confining a soup of mobile electrons in a gallium arsenide semiconductor structure, the confined electrons can be made to enter correlated states with very unusual properties. When an electric field is applied in the plane, and at certain values of the 'filling fraction' ν (defined as the ratio of the number of electrons in the fluid to the number of magnetic field quanta penetrating through the sample), the electrons will flow without encountering any resistance. In such states, the conductivity transverse to the electric field, the Hall conductivity, takes on the universal value ve^2/h , where e is the electron charge, h is Planck's constant and $\nu = 1/m$; m is an odd integer.

This 'fractional quantum Hall effect' was discovered³ in 1982, and explained theoretically⁴ a year later — achievements that were rewarded with a Nobel prize in 1998. In the theoretical treatment, a quantum Hall state at

filling fraction $1/m$ will involve quasiparticles of fractional electric charge e/m . Such quasiparticles were first detected in 1997 through measurements of the statistical fluctuations of electrical current ('shot noise') on a single point contact in a quantum Hall device^{5,6}.

As well as having a charge somewhere between 0 and 1, these quasiparticles obey an intermediate form of quantum statistics that lies somewhere between the two established forms, Fermi–Dirac statistics and Bose–Einstein statistics. Fermi–Dirac statistics applies to systems of spin-1/2 'fermions', which obey the Pauli exclusion principle; particles covered include electrons, protons, neutrons, quarks, neutrinos and atoms with an odd number of constituent particles. Bose–Einstein statistics governs the behaviour of collections of integer-spin 'bosons': atoms with an even number of constituents such as photons, gluons and the yet-to-be-found Higgs particle.

A crucial difference between fermions and bosons is that a wavefunction describing two bosons is symmetrical when the two particles are swapped around in space: it does not change sign, and the wavefunctions before and after the particle exchange are said to have a phase factor of 0. The wavefunction describing two fermions, on the other hand, is antisymmetrical, flipping sign when particles are exchanged (phase factor π). But the phase of the wavefunction representing two quasiparticles in a two-dimensional system such as a quantum Hall fluid can change by an arbitrary phase factor, not just 0 or π . The precise value of this phase



50 YEARS AGO

'Recent discoveries at Olduvai Gorge, Tanganyika' By Dr. L. S. B. Leakey — Work has, in the main, been concentrated upon two sites: BK II at the lowest level of Bed II Olduvai, where it rests uncomfortably upon the eroded top of Bed I, and at SHK II at a level about 10 ft. above the base of Bed II ... At each of these two sites, living floors of Chellean man have been found, with big accumulations of stone tools, waste flakes and the fossilized remains of the animals upon which Chellean man lived ... In addition [were found] ... two hominid teeth. It was hoped that this important discovery, made at the close of the 1955 season, was the precursor of further finds of hominid material, but the hope has not been fulfilled and, therefore, a preliminary description of these teeth is given here.

From *Nature* 19 April 1958.

100 YEARS AGO

'The condensation of helium' — In *NATURE* of March 12 I have found a note referring to my experiments on the expansion of helium, made in consequence of my determinations on the isothermals of helium, at -252°C . and -259°C ., which yielded nearly -5°K . for the critical temperature of helium. The prosecution of the experiments has shown that what I observed in expanding the gas was not the evaporation of solid helium, but solution phenomena of solid hydrogen in gaseous helium. I have communicated to the Amsterdam Academy a note on my experiments, which at the moment leave the condensation of helium a yet undecided question. Of course, I have written the details to Sir James Dewar, and I hoped to do so to you to-day, but by pressing duties I cannot do it before to-night, and you will probably go to press before that letter reaches you. So I beg to be allowed to send you this first short notice.

H. Kamerlingh Onnes

From *Nature* 16 April 1908.

50 & 100 YEARS AGO

depends on both the nature of the two quasiparticles and how their paths through space-time intertwine or 'braid' — a latitude that led to these quasiparticles being dubbed 'anyons' (see also 'Braiding anyons'² on page 804). Anyons in a fractional quantum Hall fluid with filling factor $1/m$ are predicted to have fractional statistical phase π/m .

And indeed, the fractional quantum Hall states observed so far do largely follow that prediction. But remember that m is supposed to be an odd number; thus, the discovery some 20 years ago⁷ of a no-resistance quantum Hall state with an even denominator, at a filling factor of $5/2$, was initially puzzling. This state was soon realized to have very special properties^{8,9}: the associated quasiparticles would also have fractional charge, but would obey non-abelian statistics.

The definition of non-abelian statistics is complex, but one facet is that the state of a system of many quasiparticles obeying non-abelian statistics cannot be completely determined by knowing the quasiparticles' spatial coordinates. Several linearly independent wavefunctions are possible: a system with four quasiparticles, for instance, can have two different states. In this situation, the final state of an exchange interaction is a linear combination of the two initial states, and the braiding process as particles interact and their trajectories intertwine is encoded in a two-by-two matrix. More generally, for a system with $2n$ quasiparticles, there are 2^{n-1} states. In general, because any pair of quasiparticles in the quantum fluid can become intertwined, these states do not commute with each other — in other words, the order in which the exchange interactions between quasiparticles occur will determine the system's final state. This order-dependence of the state is crucial to the proposed use of non-abelian quasiparticles as the basic 'qubits' of information in a topological quantum computer^{2,10,11}.

Dolev and colleagues' detection¹ of a quasiparticle of charge $e/4$ is a first step in that direction. The discovery was made in a shot-noise experiment similar to those in which the original quasiparticle states were found^{5,6}. But the new measurement was much harder to make than those pioneering experiments: the $5/2$ state is so delicate that to study it requires a sample quality such that the mean free path of electrons before they collide with impurities in the semiconductor structure is very long (about 0.5 millimetres). It also requires low temperatures so that thermal fluctuations do not obscure the state.

Naively, one would have expected that the quasiparticle in the $5/2$ state, with its denominator of 2, would have a charge of $e/2$ (the multiplier of 5 in the numerator is not relevant to these considerations). But through a series of non-trivial consistency checks, Dolev *et al.* show that the charge at filling fraction $5/2$ is consistent with $e/4$, but not with $e/2$ (at integer filling fraction, the measured charge is just e and at a filling fraction $1/3$ it is $e/3$). For that reason, this

quasiparticle is also called a 'half-vortex' state.

Measuring the charge to be $e/4$ is a necessary, but not sufficient proof of a non-abelian state: there is a conceivable (but very unlikely) possible 'strongly paired' abelian state with the same filling fraction and charge. But an independent (and as-yet unpublished)¹² direct-current transport measurement at a point contact has not only measured the same value of the fractional charge, but also a tunnelling probability consistent with the predictions for a non-abelian state.

Further tests of the statistics of these intriguing quasiparticles at single point contacts will be the next step. They will be the key to the development of well-controlled, multi-contact quantum interferometers that are needed to test the properties of these intriguing quasiparticles, and thus to construct the qubits of a topological computer. ■

Eduardo Fradkin is in the Department of Physics, University of Illinois at Urbana-Champaign, 1110 West Green Street, Urbana, Illinois 61801-3080, USA.

e-mail: efradkin@uiuc.edu

1. Dolev, M., Heiblum, M., Umansky, V., Stern, A. & Mahalu, D. *Nature* **452**, 829–834 (2008).
2. *Nature* **452**, 803–805 (2008).
3. Tsui, D. C., Stormer, H. L. & Gossard, A. C. *Phys. Rev. Lett.* **48**, 1559–1562 (1982).
4. Laughlin, R. B. *Phys. Rev. Lett.* **50**, 1395–1398 (1983).
5. de-Picciotto, R. *et al.* *Nature* **389**, 162–164 (1997).
6. Saminadayar, L., Glattli, D. C., Jin, Y. & Etienne, B. *Phys. Rev. Lett.* **79**, 2526–2529 (1997).
7. Willett, R. *et al.* *Phys. Rev. Lett.* **59**, 1776–1779 (1987).
8. Moore, G. & Read, N. *Nucl. Phys. B* **360**, 362–396 (1991).
9. Wen, X. G. *Phys. Rev. Lett.* **66**, 802–805 (1991).
10. Kitaev, A. Yu. *Ann. Phys.* **303**, 2–30 (2003).
11. Nayak, C., Simon, S. H., Stern, A., Freedman, M. & Das Sarma, S. *Rev. Mod. Phys.* (in the press); preprint at <http://arxiv.org/abs/0707.1889> (2007).
12. Radu, I. P. *et al.* preprint at <http://arxiv.org/abs/0803.3530> (2008).

SYSTEMS BIOLOGY

Genome rewired

Matthew R. Bennett and Jeff Hasty

Within a genome, genes are connected to each other through a complex network of interactions. One way to assess how robust and evolvable such genomic networks are is to introduce new links between unrelated genes.

Change in the genetic code is the driving force of classical evolution. Typically, it is thought that mutations in single nucleotides within the DNA sequence ensure such change, but other random alterations such as deletion, duplication and recombination of gene sequences can also occur. The robustness of organisms to such changes, which are necessary for evolution, is of fundamental interest, and so previous studies have investigated the sturdiness of gene-regulatory networks by either deleting¹ or overexpressing² individual genes. On page 840 of this issue, Isalan *et al.*³ describe a different

approach. They used high-throughput assay techniques to systemically rewire the architecture of the genetic network of the bacterium *Escherichia coli*. Their findings provide insight into not only the robustness but also the evolvability of this network.

The DNA sequence of a given gene generally consists of two parts: a regulatory promoter and an open reading frame (ORF). The promoter interacts with gene transcription factors to either increase or decrease the level of the gene's expression. Once transcription is initiated, the gene's ORF is transcribed into

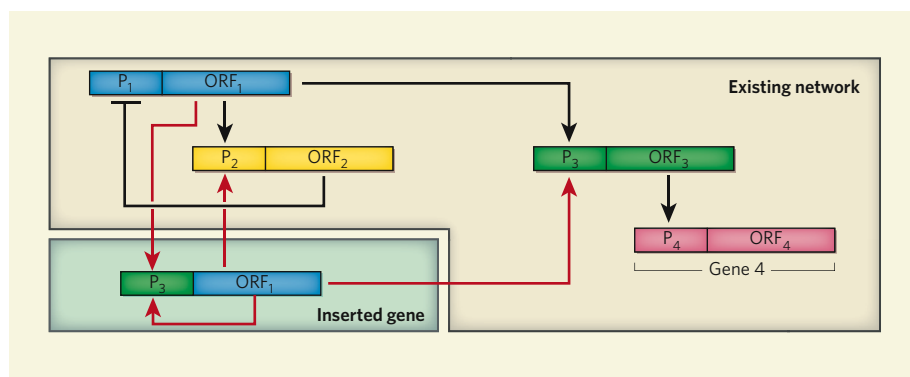


Figure 1 | Intra-network communication. A simplified example of Isalan and colleagues' experiment³, in which they rewired the network of genes for *E. coli* transcription factors to create new network connections, is shown. Here, the existing network consists of four genes. The promoter of gene 3 (P₃) can be fused to the ORF of gene 1 (ORF₁) to create a new gene. On insertion of this 'hybrid' gene into the normal cell, the new gene creates new regulatory links (shown in red) that could alter the functionality of the network.

messenger RNA. Isalan *et al.* recombined the promoters and ORFs of unrelated genes, encoding many of the 300 transcription factors in the *E. coli* genome, to create about 600 new promoter–ORF connections, or genes. They then placed each of these genes, one at a time, into *E. coli* cells and measured their viability.

This type of genetic rewiring is akin to randomly placing wires between nodes within a computer's central processing unit, where the new wires would reroute signals from one section of the processor to another — perhaps unrelated — section. The introduction of new network connections will almost certainly preclude a central processing unit from operating properly, if at all. Surprisingly, Isalan and colleagues³ find that the genetic network of *E. coli* is much more robust to rewiring than its electronic counterpart. Of the roughly 600 new connections the authors introduced into the network, almost all were well tolerated by the cells. Furthermore, the vast majority of connections showed no apparent deleterious effects, and some strains even grew better than the original.

These observations indicate that small-scale rewiring events probe the network landscape for fitness of the associated changes, without causing great detriment to the organism. From an evolutionary standpoint, therefore, they indicate that organisms can evolve by changing the architecture of their genetic network. This certainly makes sense, otherwise new network functionality could evolve only by large-scale rewiring events, which are probably extremely rare.

This conclusion also flies in the face of the popular misconception among opponents of the evolutionary theory, who believe that the genetic code is irreducibly complex. For instance, advocates of 'intelligent design' compare the genome to modern engineered machines such as integrated circuits and clocks, which will cease to function if their internal design is altered. Although sometimes it is instructive to point to similarities between the design principles behind modern technology and those behind genetics, the analogy can only go so far. Engineered devices are generally designed to work just above the point of failure, so that any tampering with their construction will result in catastrophe. In the event of failure, new clocks can be purchased or central processing units replaced. But nature does not have that option. To survive — and so evolve — organisms must be able to tolerate random mutations, deletions and recombination events. And Isalan and colleagues' work provides an important step forward in quantifying just how robust the genetic code can be.

In addition to screening the new strains for fitness, the authors measured the activity levels of genes that were most directly affected by network rewiring. They predicted that, if a new gene introduces a feedback loop into the network, the protein levels of its 'parent' gene should be altered accordingly. For instance, the

synthetic gene inserted into the simple gene-regulatory network depicted in Figure 1 introduces a positive feedback loop into the creation of the protein encoded by ORF₁. Therefore, levels of that protein should be higher in the mutant than in the normal strain. But this is not what Isalan *et al.* find. Instead, introduction of direct feedback loops (either positive or negative) led to no significant differences in the levels of the proteins concerned.

There could be two explanations for why new feedback loops have almost no effect on protein levels. For one, the dynamics of large-scale, transcriptionally regulated genetic networks are probably more complicated than thought. In other words, analysing large networks by decomposing them into simpler sub-networks, as Isalan *et al.* have done, may lead to faulty conclusions about how the subsystems work within the whole. Alternatively, it may be that transcriptional regulation is less important than expected. Perhaps post-transcriptional regulatory mechanisms^{4,5} that affect mRNA translation regulate the network to a larger extent. But considerable effort has gone into

the creation of synthetic gene networks^{6,7} that are controlled at the transcriptional level, and many of these studies have had great success^{8,9}. So the findings of Isalan *et al.*³ should be seen both as a cautionary tale and as encouragement for research into the regulatory mechanisms of large-scale networks.

Matthew R. Bennett and Jeff Hasty are in the Department of Bioengineering and Institute for Nonlinear Science, University of California, San Diego, La Jolla, California 92093-0412, USA. e-mail: hasty@bioeng.ucsd.edu

1. Baba, T. *et al.* *Mol. Syst. Biol.* doi:10.1038/msb4100050 (2006).
2. Sopko, R. *et al.* *Mol. Cell* **21**, 319–330 (2006).
3. Isalan, M. *et al.* *Nature* **452**, 840–845 (2008).
4. Filipowicz, W., Bhattacharyya, S. N. & Sonenberg, N. *Nature Rev. Genet.* **9**, 102–114 (2008).
5. Isaacs, F. J., Dwyer, D. J. & Collins, J. J. *Nature Biotechnol.* **24**, 545–554 (2006).
6. Wall, M. E., Hlavacek, W. S. & Savageau, M. A. *Nature Rev. Genet.* **5**, 34–42 (2004).
7. Hasty, J., Isaacs, F., Dolnik, M., McMillen, D. & Collins, J. J. *Chaos* **11**, 207–220 (2001).
8. McDaniel, R. & Weiss, R. *Curr. Opin. Biotechnol.* **16**, 476–483 (2005).
9. Elowitz, M. B. & Leibler, S. *Nature* **403**, 335–338 (2000).

ECOLOGY

Destabilized fish stocks

Nils Chr. Stenseth and Tristan Rouyer

Fishing of natural populations increases the variability of fish abundance. A unique data set from the southern California Current has allowed an evaluation of three hypotheses for why that should be so.

Understanding variation in the abundances of plants and animals has long been a central topic in population ecology¹. It is one of particular significance when it comes to exploited populations, such as those of many fish stocks, and is revisited by Anderson *et al.* on page 835 of this issue².

Extensive fluctuations of harvested fish stocks are clearly undesirable economically — too much uncertainty in expected income will adversely affect fishing communities. Such fluctuations are also harmful from a conservation perspective, as high variability may increase the (local) probability of extinctions. It has long been suggested³ by fisheries ecologists that fishing might itself increase the temporal variability of exploited populations. But long-term data on unexploited populations are needed for comparative (control) purposes, and the lack of such data has made it difficult to separate the effects of fishing from the effects of variations in environmental conditions.

In 2006, such a long-term data set — the California Cooperative Oceanic Fisheries Investigations (CalCOFI) record of larval fish abundance — was subject to comparative analysis by Hsieh *et al.*⁴, from which they concluded that, as their title put it, 'Fishing elevates

variability in the abundance of exploited species'. But this study, pioneering as it was, did not look into the nature of the underlying mechanisms. Anderson *et al.*², a group that includes many of the same authors, now report an extended analysis of the 50-year CalCOFI data set under the title 'Why fishing magnifies fluctuations in fish abundance'. In doing so they provide valuable, empirically based insights into the fluctuations of exploited populations. Their analysis convincingly shows that the observed increased variation of harvested fish stocks is caused by the selective removal of the larger (and older) individuals, leading to a decreasing average size and age of the fish that destabilizes the population dynamics.

Anderson *et al.*² looked at three hypotheses. They found no support for the first one, that the observed variability of exploited fish stocks is a direct effect of variable fishing intensity. Then there is the selective removal of larger and so older individuals by fishing, known as the age-truncation effect. This 'juvenescence' of the population can affect the dynamics in two ways, leading to the second and third hypotheses.

The second hypothesis is that younger, smaller individuals may be more susceptible

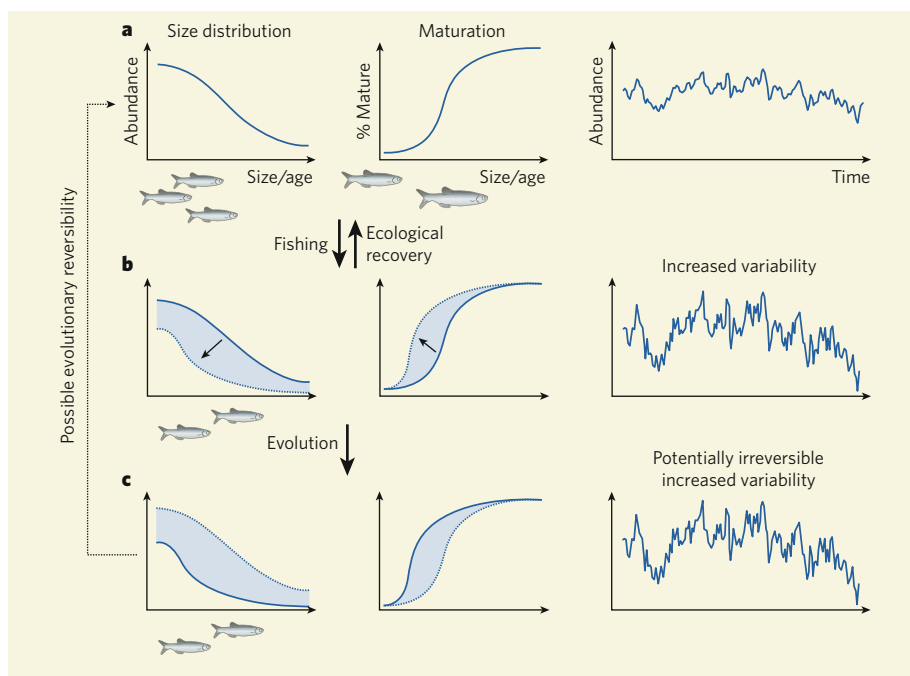


Figure 1 | The ecological and evolutionary effects of fishing on fish-stock dynamics². **a**, The size distribution and maturation profile of an unexploited population, which shows a certain level of variability in abundance over time. **b**, The age-truncation — juvenescence — effect caused by fishing leads to a population with a lower average age, and is often associated with individuals attaining maturity at younger ages. The result is increased variability in abundance. If the change is phenotypic (ecological) only, recovery is possible. **c**, A more permanent (evolutionary) change in the demographics leads to potentially irreversible increased variability in abundance, unless there is a high degree of genetic variability left in the population to return it to the unexploited state.

to environmental change than older, larger individuals that, as the authors put it, can survive hard times better. The third is that the changed age structure may affect demographic parameters, such as the age of maturation, and intensify the nonlinear nature of the processes involved in population dynamics (for example, through an increased population growth rate, or by increasing the nonlinear coupling of demographic parameters to environmental changes). Anderson and co-workers find some support for the former effect and strong support for the latter — that is, the observed increase in population variability seems to be caused by an increased nonlinearity of the underlying population dynamics of exploited fish stocks as compared with unexploited populations.

The higher mortality experienced by older and bigger fish, directly caused by size-selective harvesting, can induce earlier maturation of fish within the stock, and can do so in two ways that are not mutually exclusive. One is 'phenotypic plasticity', the ability of the fish to change its characteristics, or phenotype, in response to changes in its environment. This is a reversible response that is primarily an ecological effect⁵. The other is a potentially irreversible evolutionary response due to harvesting^{5–8}. Many recent studies have provided evidence for this second effect, and show that the ecological–evolutionary consequences of harvesting can occur at a much faster rate than previously thought. Through the evolutionary effect, for which there is growing

support^{7,9}, age truncation can make the abundance of exploited fish stocks permanently more variable (Fig. 1).

Taken together with Anderson and colleagues' findings², the implication is that fisheries management needs to give priority to precautionary measures. Juvenescence may be irreversible⁹. When the ecological effects of fishing a particular population are observed, the evolutionary consequences may have already set in, and may be irreversible, or

at least only slowly reversible, depending on whether sufficient genetic variability remains in the stocks¹⁰. In other words, it will often be quicker to create a demographic change in a fish stock than to reverse that change and the increased variability in population abundance that stems from it.

The combined ecological and evolutionary juvenescence of exploited populations prompts various thoughts. Ecologists need to give more consideration to the ecological effects of life-history changes such as earlier maturation, and evolutionary biologists need to take more account of the ecological effects of evolutionary changes. Indeed, we would like to see many more combined ecological and evolutionary studies on the effect of exploitation. Such a research agenda is not easy to implement, given the scarcity of long-term data on unexploited fish stocks, and we require more data sets like the CalCOFI record. Otherwise, investigation of the heritability of the demographic parameters that Anderson *et al.* conclude amplify the nonlinear population behaviour would help us understand the evolutionary effect of the observed changes — and also help in assessing to what degree such an effect could be reversed through management policies.

Nils Chr. Stenseth and Tristan Rouyer are at the Centre for Ecological and Evolutionary Synthesis, Department of Biology, University of Oslo, PO Box 1066 Blindern, N-0316 Oslo, Norway. e-mail: n.c.stenseth@bio.uio.no

1. May, R. *Theoretical Ecology: Principles and Applications* (Blackwell, Oxford, 1976).
2. Anderson, C. N. K. *et al. Nature* **452**, 835–839 (2008).
3. Beddington, J. R. & May, R. M. *Science* **197**, 463–465 (1977).
4. Hsieh, C. *et al. Nature* **443**, 859–862 (2006).
5. Ernande, B., Dieckmann, U. & Heino, M. *Proc. R. Soc. Lond. B* **271**, 415–423 (2003).
6. Olsen, E. M. *et al. Nature* **428**, 932–935 (2004).
7. Jørgensen, C. *et al. Science* **378**, 1247–1248 (2007).
8. Hilborn, R. *Fisheries* **31**, 554–555 (2006).
9. Law, R. & Grey, D. R. *Evol. Ecol.* **3**, 343–359 (1989).
10. Futuyma, D. J. *Evolutionary Biology* 3rd edn (Sinauer, Sunderland, MA, 1998).

ASTROPHYSICS

Blown away by cosmic rays

Dieter Breitschwerdt

X-ray data reveal that our Galaxy is shedding part of its gas, a phenomenon previously associated only with much more active star-forming galaxies. So what is driving the process in the Milky Way?

It has long been known that 'starburst' galaxies, which have extremely high rates of star formation, extravagantly blow away some of their star-forming gas. Writing in *The Astrophysical Journal*, Everett *et al.*¹ produce convincing evidence that, although it forms stars at a more moderate rate, our own Milky Way also belongs to this profligate club. In a new twist, it seems that the high-energy particles known as

cosmic rays are among the agents of the Milky Way's wind.

That galaxies should so casually discard some of their substance might seem surprising, for the process by which they come into being is long and arduous. Galaxies began to be assembled from primordial gas pulled together by the gravity of mysterious, unseen 'dark matter' during the infancy of our Universe,

when it was less than a billion years old² (it is currently some 13.6 billion years old). As these protogalaxies condensed into thin disks, local gravitational instabilities caused the formation of the first stars.

This was the beginning of a cyclical process. As this first generation of stars started to age, its more massive members began to explode in the cosmic cataclysms known as supernovae. In doing so, they shed a tremendous amount of energy, as well as chemical elements heavier than helium (elements up to iron in the periodic table are almost exclusively created in stellar burning), into the interstellar gas. These small traces of 'metals' make up less than 1% of the total gas mass. But they are crucial to cooling the gas down, allowing it to condense into molecular clouds, and so to form the next generation of stars through gravitational collapse.

This boom-and-bust process keeps the galactic engine running. But it is inherently wasteful: in certain particularly active galaxies in both the local and the distant Universe, the energy released in many supernova explosions is sufficient to heat up a large amount of gas to temperatures of between 10^6 and 10^8 kelvin. At such temperatures, the gas is energetic enough to escape the gravitational potential of the galaxy and blow away into the intergalactic medium (Fig. 1).

Middle-of-the-road galaxies such as our Milky Way have a star-formation rate that is lower than that of these most active galaxies by a factor of anything up to ten or more. Do they also lose gas in a wind? Until recently, there was no direct observational evidence to support this possibility. There was admittedly some hint that in the halo of the galaxy NGC 891, which is sometimes labelled a twin of the Milky Way, electrons originally travelling at speeds comparable to the speed of light lose some of their energy in a characteristic way. This might indicate that they are being carried along with escaping hot gas while transferring some of their energy to it³; but the escaping gas has not itself been seen directly.

Now Everett *et al.*¹ show that the distribution of X-ray emission across a region towards the centre of our Galaxy can be fitted better to a model assuming that the disk's atmosphere is windy, rather than static. The data were obtained with the ROSAT satellite⁴, a joint venture between Germany, the United States and Britain. The observations are at energies that include prominent emission lines from the polyvalent oxygen ions O^{5+} , O^{6+} and O^{7+} that crucially can be used to establish the equilibrium temperature of the interstellar gas.

There is a catch: the data and the model seem to fit well only if some unknown extra mechanism is helping to activate the wind. The authors suggest that the elusive high-energy particles known as cosmic rays are the culprit. The average energy density of cosmic rays in the interstellar medium is about 1 electronvolt

per cubic centimetre. Although cosmic rays were neglected in most earlier galactic-wind models, this density is in fact comparable to the respective energy densities of thermal gas, magnetic fields and turbulent motions. This energy is concentrated in a few individual particles: 99% protons and heavy nuclei, and 1% electrons. These charged particles travel initially at almost the speed of light, and have energies of up to 10^{21} electronvolts — as much energy as a tennis ball being served, despite their tiny size. Because they are charged, they also interact strongly with the magnetic field that permeates our Galaxy, which reduces their drift speed by a factor of a thousand, so that they take much longer to reach us than would light.

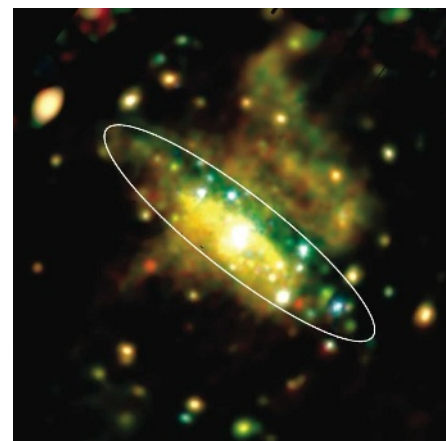
By scattering off particular fluctuations of the magnetic field called magnetohydrodynamical waves, cosmic rays are known to couple to the interstellar gas^{5,6}, and so exert a pressure on it. Cosmic rays can also generate their own waves on which they may 'surf', a process called gyroresonance or streaming instability⁷. Compared with thermal gas, cosmic rays have the advantage that they do not 'cool' (that is, lose energy through atomic excitations). In addition, the heavier particles that largely make up cosmic rays and that are responsible for driving the wind do not lose large amounts of synchrotron radiation when accelerated in a magnetic field.

Earlier models^{8,9} had shown that a steady-state wind driven by cosmic rays pervading the entire Milky Way could blow away about a solar-mass-worth of gas per year. Everett *et al.*³ find a similar gas loss of 2.1 solar masses per year from the best fit to their X-ray data. In their picture, the cosmic-ray pressure is crucial to the existence of a large-scale wind in the Milky Way.

The calculated mass loss would add up to more than 50% of the gas in the Galaxy's disk within 10 billion years. So, do we face the prospect that the Milky Way will be devoid of gas in the distant future? Probably not: first, our Galaxy is still accreting matter at a similar rate to that at which it is losing it; second, the Galactic matter cycle is self-regulating, in that gas loss lowers the average gas density. If the density drops, the star-formation rate will drop, and mass loss through a Galactic wind will be quenched.

Modelling low-energy X-ray data, as Everett *et al.* have done, is the best and most direct way of tracking down a galactic wind in the Milky Way (and in other galaxies), because hot winds are most likely to radiate at X-ray wavelengths. Modelling other regions of the Galaxy in a similar way would be desirable. A future survey of the entire sky at X-ray wavelengths, as envisaged by the approved German–Russian–UK mission eROSITA¹⁰, will significantly improve on the ROSAT data using instrumentation of higher sensitivity and larger spatial and spectral resolution.

In the meantime, astronomers will be



M. BAUER/MPE

Figure 1 | Blown away? Galaxies with high rates of star formation generate a large amount of gas that is hot enough to escape the galaxy's gravitational potential well — a galactic wind. This image from the XMM-Newton X-ray observatory, run jointly by the European Space Agency and NASA, shows diffuse soft X-ray emission of hot gas in three energy bands (red, 200–500 eV; green, 500–1,000 eV; blue, 1,000–2,000 eV) from the starburst galaxy NGC 253, which lies 8.4 million light years away. The galaxy is seen edge-on; the white ellipse outlines the disk of the galaxy. The yellow-green areas above and below the disk show X-ray-emitting gas escaping as a galactic wind. Everett *et al.*¹ now propose that our own Milky Way may host a galactic wind. (Image reproduced with permission from ref. 13.)

impatiently waiting for the first γ -ray data from NASA's GLAST satellite¹¹, to be launched later this year. Measurements from the Compton Gamma Ray Observatory satellite have already indicated that the emission of diffuse γ -rays drops less steeply as we move outwards from the centre of our Galaxy than does the distribution of supernova remnants (the supposed source of cosmic rays). If GLAST confirms this, it will provide further, albeit indirect, evidence for the existence of a large-scale galactic wind in the Milky Way that carries away cosmic rays before they can generate many γ -rays in the Galactic disk^{3,12}.

Dieter Breitschwerdt is at the Institute of Astronomy, University of Vienna, Türkenschanzstraße 17, 1180 Vienna, Austria. e-mail: dieter.breitschwerdt@univie.ac.at

1. Everett, J. E. *et al.* *Astrophys. J.* **674**, 258–270 (2008).
2. Iye, M. *et al.* *Nature* **443**, 186–188 (2006).
3. Dahlem, M., Dettmar, R.-J. & Hummel, E. *Astron. Astrophys.* **290**, 384–392 (1994).
4. Snowden, S. L. *et al.* *Astrophys. J.* **485**, 125–135 (1997).
5. Skilling, J. *Mon. Not. R. Astron. Soc.* **172**, 557–566 (1975).
6. Drury, L. O'C. & Völk, H. J. *Astrophys. J.* **248**, 344–351 (1981).
7. Kuhsrud, R. M. & Pearce, W. P. *Astrophys. J.* **156**, 445–469 (1969).
8. Breitschwerdt, D., McKenzie, J. F. & Völk, H. J. *Astron. Astrophys.* **245**, 79–98 (1991).
9. Breitschwerdt, D., McKenzie, J. F. & Völk, H. J. *Astron. Astrophys.* **269**, 54–66 (1993).
10. www.mpe-garching.mpg.de/projects.html#erosita
11. www.nasa.gov/mission_pages/GLAST/main/index.html
12. Breitschwerdt, D., Dogiel, V. A. & Völk, H. J. *Astron. Astrophys.* **385**, 216–238 (2002).
13. Bauer, M. *et al.* preprint available at <http://arxiv.org/abs/0711.3182> (2007).

Observation of a quarter of an electron charge at the $\nu = 5/2$ quantum Hall state

M. Dolev¹, M. Heiblum¹, V. Umansky¹, Ady Stern¹ & D. Mahalu¹

The fractional quantum Hall effect, where plateaus in the Hall resistance at values of $h/\nu e^2$ coexist with zeros in the longitudinal resistance, results from electron correlations in two dimensions under a strong magnetic field. (Here h is Planck's constant, ν the filling factor and e the electron charge.) Current flows along the sample edges and is carried by charged excitations (quasiparticles) whose charge is a fraction of the electron charge. Although earlier research concentrated on odd denominator fractional values of ν , the observation of the even denominator $\nu = 5/2$ state sparked much interest. This state is conjectured to be characterized by quasiparticles of charge $e/4$, whose statistics are 'non-abelian'—in other words, interchanging two quasiparticles may modify the state of the system into a different one, rather than just adding a phase as is the case for fermions or bosons. As such, these quasiparticles may be useful for the construction of a topological quantum computer. Here we report data on shot noise generated by partitioning edge currents in the $\nu = 5/2$ state, consistent with the charge of the quasiparticle being $e/4$, and inconsistent with other possible values, such as $e/2$ and e . Although this finding does not prove the non-abelian nature of the $\nu = 5/2$ state, it is the first step towards a full understanding of these new fractional charges.

Theoretical predictions regarding the nature of the even denominator $\nu = 5/2$ quantum Hall state rekindled strong interest in the fractional quantum Hall effect (FQHE)^{1–3}. Primarily, this interest emanates from the unique properties of quasiparticles in this state, predicted by Moore and Read^{4,5}: a fractional charge of a quarter of the electron charge ($e/4$) and non-abelian quantum statistics. The quantum statistics are reflected in the evolution of the ground state wavefunction when two $e/4$ quasiparticles are adiabatically interchanged. For conventional FQHE states, where the statistics are abelian, such an interchange merely multiplies the wavefunction by a phase. For non-abelian states, the presence of quasiparticles makes the ground state degenerate and an adiabatic interchange of two quasiparticles leads to a topological unitary transformation—where the topology of the path determines the transformation—that takes the system from one ground state to another. Unitary transformations that correspond to different interchanges do not generally commute with each other; hence the name non-abelian.

The topological nature of these transformations makes the $\nu = 5/2$ state a test ground of the basic ideas of topological quantum computation, as it introduces remarkable immunity against decoherence and errors due to local uncontrollable perturbations^{6–8}. Ideas proposed in these directions are based on interference experiments where inter-edge tunnelling of $e/4$ quasiparticles takes place. For these experiments to succeed, two requirements should be satisfied: the first is that the $\nu = 5/2$ state must be of the Moore–Read type, and the second is that the tunnelling quasiparticles must have charge $e/4$. These characteristics are predicted but not yet experimentally confirmed. The Moore–Read theory is based on a trial wavefunction inspired by considerations of conformal field theory⁴. It may be rederived⁹ by considering weak Cooper pairing of composite fermions, which, under a magnetic field corresponding to the $\nu = 5/2$ state, are fermions carrying an electron charge and two fictitious flux quanta. It is also supported by numerical exact diagonalization¹⁰. As for the second requirement, if electron or $e/2$ quasiparticle tunnelling dominates over that of the $e/4$ quasiparticles, inter-edge tunnelling

would not be a useful tool for examining the non-abelian statistics of the latter.

In this work we present shot noise measurements^{11,12}, which result from partitioning of a stream of quasiparticles that tunnel between edge channels of a $\nu = 5/2$ state. Measurements were performed on a patterned high-purity two-dimensional electron gas (2DEG) with a built-in constriction that allowed controlled tunnelling from one edge to another. From the dependence of the shot noise on the current, we deduced the charge of the quasiparticles, which was found to be consistent with charge $e/4$, and inconsistent with charge $e/2$ or an electron charge e . In order to further validate the measurements, the charge of quasiparticles in other FQHE states in the vicinity of the $\nu = 5/2$ state, such as at $\nu = 5/3$, 2 , $8/3$ and 3 , was also measured by partitioning their current carrying states. Although these measurements do not directly probe non-abelian statistics, they do pave the way for such a measurement, which is likely to be based on interference effects^{13–16}.

The $5/2$ fractional quantum Hall state

The $\nu = 5/2$ state is characterized by a zero longitudinal conductance and a Hall conductance plateau $g_{5/2} = 5e^2/2h$. At $\nu = 5/2$, the highly interacting electronic system can be mapped onto a system of weakly interacting, spin polarized, composite fermions at zero average magnetic field. The theory that predicts the $\nu = 5/2$ state to be non-abelian starts with the Moore–Read wavefunction⁴. Within this theory, the composite fermions form a superconductor of Cooper pairs, with $p_x + ip_y$ symmetry⁹, where the non-abelian quasiparticles are vortices, carrying half of a quantum flux, $\phi_0/2 = h/2e$. Because inserting these vortices costs a finite amount of energy (the Meissner effect in the condensate), the system is in an incompressible quantum Hall state with an energy gap for these excitations. With the flux carried by a vortex being $h/2e$ and the uppermost Landau level half-filled, the charge that is associated with the quasiparticles was theoretically predicted⁴ to be $e^* = e/4$. However, recent numerical

¹Braun Center for Submicron Research, Department of Condensed Matter Physics, Weizmann Institute of Science, Rehovot 76100, Israel.

calculations raise the possibility that these quasiparticles may tend to form bound pairs of charge $e/2$ (ref. 17). Only a small number of studies have thus far tested the predictions of Moore–Read theory⁴. The observed energy gap was measured to be significantly smaller than predicted¹⁸; the survival of the state in a small constriction was studied¹⁹; and the spin polarization of the state is thus far supported only by a numerical exact diagonalization method¹⁰. What makes measurements at the $\nu = 5/2$ state rather scarce is the extreme fragility of that state. Only an extremely high-quality 2DEG and a rather low electron temperature support such states.

Set-up and the basics of the measurements

The most important ingredient in our measurements is the GaAs–AlGaAs heterostructure that supports the 2DEG. The 2DEG has an electron density of $\sim 3.2 \times 10^{11} \text{ cm}^{-2}$, and a low-temperature mobility of $30.5 \times 10^6 \text{ cm}^2 \text{ V}^{-1} \text{ s}^{-1}$, measured in the dark (see Methods for more details). The Hall effect data, measured at 10 mK in a Hall bar 1 mm wide, revealed five significant fractions in the second Landau level, $\nu = 11/5, 7/3, 5/2, 8/3$ and $14/5$, with a nearly zero longitudinal resistance at $\nu = 5/2$ (Fig. 1a). These data indicate transport via edge channels with negligible current flowing in the bulk.

The samples were patterned in a shape of a Hall bar, with a single quantum point contact (QPC) in its centre and multiple ohmic contacts (Fig. 1b). The QPC partitioned the incoming current by bringing the forward propagating edge channel, with a chemical potential determined by the applied voltage V , into close proximity with the backward propagating edge channel returning from the grounded

contact (cold grounds²⁰, see Methods for more details), hence inducing backscattering, partitioning and shot noise. A DC current I_{imp} was driven from the source contact (S), with the QPC partitioning it to the transmitted and backscattered currents. Shot noise, at 910 kHz, was amplified by a home-made preamplifier cooled to 4.2 K, with its output fed into a room temperature amplifier followed by a spectrum analyser (see Methods for more details). As long as the longitudinal resistance was zero, the resistance between terminals D and 2 was always the Hall resistance²¹ (see Methods for more details).

We measured the two-terminal conductance and the current noise as a function of the source–drain voltage, at different partitioning values set by the QPC. Performing the noise measurements turned out to be challenging. A severe difficulty during the measurements was the instability and irreproducibility of the gates. Consequently, the desired partitioning by the QPC, which was determined by the filling factor within the QPC, was achieved by controlling the gate voltage (which controls the density within the QPC) simultaneously with tuning the magnetic field along a conductance Hall plateau in the bulk. This difficulty was compounded by the fact that the shot noise signal at the $\nu = 5/2$ state is very weak. The spectral density of shot noise current fluctuations S^i is proportional to the effective charge e^* and to the impinging current in the partitioned edge channel. At $\nu = 5/2$ the relevant partitioned current, which generates the noise, is only a small fraction of the total impinging current, depending on the next-lower channel within the QPC (for example, if the lower channel is $\nu = 2$, only $1/5$ of the impinging current generates the noise). Furthermore, as our ‘cold preamplifier’ amplifies voltage fluctuations S^v , and $S^v = S^i / (g_{5/2})^2$, the large conductance at $\nu = 5/2$ leads to a rather weak voltage signal.

The analysis of shot noise

For the extraction of the quasiparticles’ charge, we use a rather simplified picture that was successful in analysing the shot noise of quasiparticles with charge $e/3$ at $\nu = 1/3$, $e/5$ at $\nu = 2/5$ and $e/7$ at $\nu = 3/7$ (refs 11, 20, 22). In this picture, we assume that in a conductance Hall plateau the current is being carried by quasiparticles in chiral edge channels with no bulk currents. When the bulk is in a certain conductance plateau and the QPC is wide open, the edge currents, which are noiseless (at zero temperature), traverse the QPC unaltered. As the QPC starts to close, the innermost forward propagating edge channel is coupled to the innermost backward propagating edge channel via tunnelling, leading to statistically independent backscattering events. Pinching the QPC further leads eventually to a full reflection of this partitioned edge channel with the conductance through the QPC reaching a lower conductance plateau.

When the conductance-dependent current through the QPC $g(I_{\text{imp}})$ is in a transition between two plateaus, one corresponding to a lower lying state ν_{i-1} (with conductance $g_{i-1} = \nu_{i-1} e^2/h$) and another to the state above ν_i (with conductance $g_i = \nu_i e^2/h$), the current that impinges on the innermost channel is $I_{\text{imp}}(i) = V \Delta g_i$ with $\Delta g_i = g_i - g_{i-1}$, where V is the applied DC voltage at the source. This current, which is in general smaller than the total impinging current I_{imp} , is being partitioned, hence generating shot noise. Similarly, the transmission of this channel’s current is defined as $t_{\nu_i - \nu_{i-1}} = \frac{g(I_{\text{imp}}) - g_{i-1}}{\Delta g_i}$. At zero temperature ($T = 0$), the low frequency spectral density of the current fluctuations $S^i(0)$ is related to the quasiparticle’s effective charge e^* through^{23,24}:

$$S^i(0)_{T=0} = 2e^* V \Delta g_i t_{\nu_i - \nu_{i-1}} (1 - t_{\nu_i - \nu_{i-1}}) \quad (1)$$

At finite temperatures, the thermal contribution adds in and the shot noise is modified to the so-called ‘excess noise’²⁵. The expression in equation (1) is then modified²⁵:

$$S^i(0)_T = 2e^* V \Delta g_i t_{\nu_i - \nu_{i-1}} (1 - t_{\nu_i - \nu_{i-1}}) \left[\coth\left(\frac{e^* V}{2k_B T}\right) - \frac{2k_B T}{e^* V} \right] + 4k_B T g \quad (2)$$

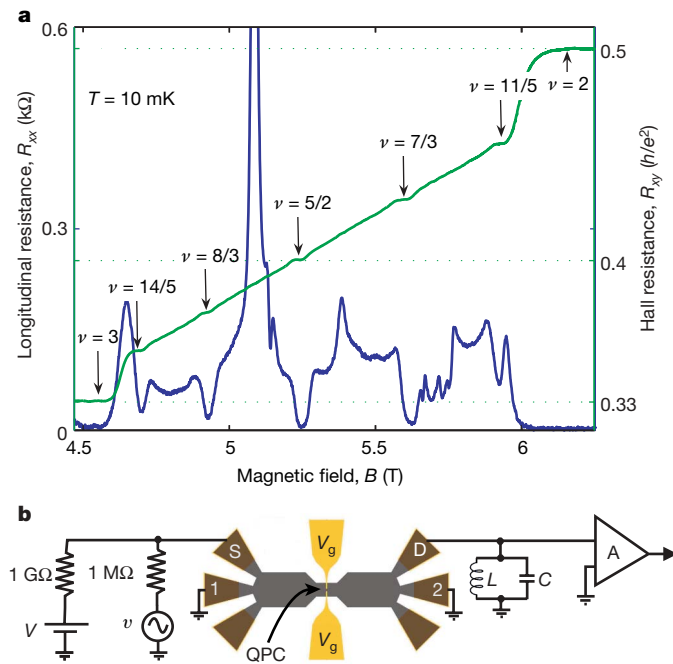


Figure 1 | Quantum Hall effect in the second Landau level. **a**, Hall resistance (green curve, right axis) and longitudinal resistance (blue curve, left axis) measured on an ungated Hall bar, 1 mm \times 2.5 mm, with carrier density $3.15 \times 10^{11} \text{ cm}^{-2}$ (determined at high magnetic field). The five main fractions, $14/5, 8/3, 5/2, 7/3$ and $11/5$ measured in a four-terminal configuration on the Hall bar, are highlighted. **b**, Diagram of the patterned sample and associated circuitry. Carrier density in this sample was $3.27 \times 10^{11} \text{ cm}^{-2}$. The two grounds, at 1 and 2, are ‘cold grounds’, cooling the electrons to ~ 10 mK. DC current is driven to the sample through the source (S), provided by a DC voltage V and a large resistor in series. The AC voltage v is used to measure the conductance. Drain voltage (at D) is filtered with an LC resonant circuit, tuned to 910 kHz, and amplified by a preamplifier (A) cooled to 4.2 K, adjacent to the sample. The quantum point contact (QPC), controlled by V_g , is tuned for the desired transmission of the impinging current.

with k_B the Boltzmann constant. The assumption of statistical independence of the backscattered quasiparticles is expected to hold when $t_{v_i-v_{i-1}}$ is close to zero (with rarely transmitted quasiparticles) or close to unity (with rarely reflected quasiparticles), but may be less reliable in intermediate values of $t_{v_i-v_{i-1}}$. Yet, previous works on Laughlin's quasiparticles have proved that if the nonlinear transmission is taken into account, then the prediction of the quasiparticles' charge from equations (1) and (2) agrees with the expected one. This might be attributed to the fact that equation (2) does have the correct limits at low and high temperatures, as well as the correct scale for the transition between the two.

Identification of the structure of edge channels in the QPC

Deducing the charge from the measured shot noise (via equation (2)) requires a measurement of the relevant transmission $t_{v_i-v_{i-1}}$ (defined above) and the corresponding impinging current $I_{\text{imp}}(i)$, which in turn requires the identification of the next-lower quantized Hall conductance g_{i-1} (the next to innermost edge channel) within the QPC. Our procedure for identifying the occupied channels in the QPC is demonstrated in Fig. 2. At low temperature, the transmission of the QPC depends strongly on the impinging DC current. This dependence does not generally agree with the prediction of the chiral Luttinger liquid (CLL) theory. As had been already observed before, in the integer and fractional quantum Hall regime^{19,26,27}, under weak backscattering conditions of the i th state (the QPC is tuned to just below the i th plateau in the bulk, such that the i th edge channel is weakly backscattered), the transmission decreases with increasing DC current, exhibiting 'mound-like' behaviour. Alternatively, for strong backscattering conditions (the QPC is tuned to almost completely pinch off the i th state and the transmission is just above the lower lying ($i-1$)th plateau, such that the i th channel is almost fully backscattered), the transmission increases with DC current, exhibiting 'valley-like' behaviour. We attribute the 'mound-like' and 'valley-like' behaviours to a combination of several factors. Generally speaking, a larger applied voltage on the QPC barrier is expected to enhance the bare tunnelling probability for independent particles. 'Mound-like' behaviour appears in the limit of $t_{v_i-v_{i-1}}$ close to unity, where tunnelling is between the forward and backward propagating channels. Then, tunnelling is responsible for the weak backscattering and thus applying larger voltage across the QPC increases backscattering and decreases the transmission. In contrast, 'valley-like' behaviour appears in the limit of $t_{v_i-v_{i-1}}$ close to zero, where the high barrier is for forward tunnelling over the QPC; hence, tunnelling is responsible for the small transmission, which increases with the impinging current. The renormalization of the tunnelling rates predicted by the CLL presumably coexists with this mechanism. However, CLL alone cannot explain this reproducible 'mound-valley' behaviour, as it predicts enhancement of the tunnelling probability due to a decrease in the applied voltage. Altogether, as the QPC closes and the conductance crosses a quantized plateau, the transmission dependence on the impinging current switches from 'valley-like', to 'flat', and finally to 'mound-like' behaviour, offering us a way to identify the plateau that is being crossed.

We demonstrate this evolution in Fig. 2a, where we plot the dependence of the transmission on the total impinging DC current I_{imp} at bulk filling factor $\nu_B = 3$. The filling factor within the QPC, ν_{QPC} , was varied either by the applied gate voltage V_g or by varying slightly the magnetic field within the bulk plateau of $\nu_B = 3$. One can follow the evolution from $\nu_{\text{QPC}} = 3$ to $\nu_{\text{QPC}} = 7/3$, with a dependence on the impinging current as mentioned above. In Fig. 2b, we plot the dependence of the linear transmission (at zero DC current) on the filling factor in the QPC (the measurement was taken at two different gate voltages with a varying magnetic field at each gate voltage). Clear plateaus were observed within the QPC at $\nu_{\text{QPC}} = 5/2$ and $\nu_{\text{QPC}} = 7/3$, and a weaker one at $\nu_{\text{QPC}} = 8/3$, in agreement with the values in Fig. 2a at which a transition was observed. Moreover,

at these plateaus no shot noise had been measured at a finite DC current.

The identification of a plateau that corresponds to a certain filling factor in the QPC under a certain gate voltage and magnetic field almost guarantees that this filling factor exists, as a lower lying state or as an outer edge channel, at higher values of QPC conductance. This is because at a less negative gate voltage (or a lower magnetic field) the QPC is more open, thus resembling the bulk and allowing the existence of incompressible regions within the QPC. However, the absence of such a plateau near an expected filling factor cannot rule out the existence of this lower lying state when the QPC is more open.

In some cases, at the lowest temperature of 10 mK the transmission of the QPC strongly depended on the impinging DC current, making data interpretation difficult. Hence, measurements were also performed at 40 mK and at 90 mK, where the transmission dependence on the current weakens and the excess noise agrees with equation (2)

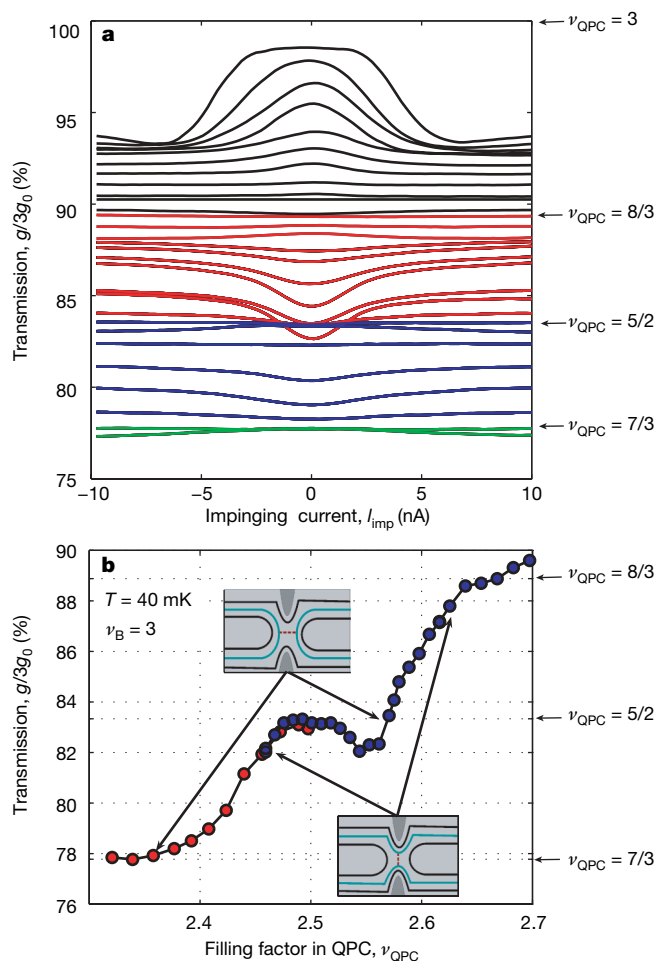


Figure 2 | The procedure used to identify lower lying states within the QPC.

a, Differential transmission of the QPC as a function of impinging current at different filling factors in the QPC, ν_{QPC} , which are adjusted by the gate voltage and the magnetic field (while staying on the $\nu_B = 3$ plateau). Each fraction formed within the QPC is identified by a flat dependence of the conductance as function of current, surrounded by a 'mound-like' dependence for a slightly lower filling factor and a 'valley-like' dependence for a slightly higher filling factor. Three underlying states were found using this method: lines are shown black for the partitioned state, red for 8/3, blue for 5/2, and green for 7/3. The valley crossing near $\nu_{\text{QPC}} = 5/2$ is due to the integer quantum Hall re-entrant behaviour near that fraction. **b**, Linear transmission (at zero DC current) of the QPC as a function of ν_{QPC} . The two colours designate two different gate voltages; at each gate voltage the filling factor was tuned with the magnetic field (on the $\nu_B = 3$ plateau). The two insets show schematically regions of weak backscattering (under a plateau; bottom inset), and regions of strong backscattering (just above the lower lying plateau; top inset).

(see Supplementary Information for more details), suggesting an almost single particle-like behaviour (see also refs 11, 21, 22, 26). The nonlinear transmission was taken into account using two different models for the effective transmission $t_{v_i-v_{i-1}}$: a differential model, where for each value of the total impinging current, I_{imp} , we take $t_{v_i-v_{i-1}} \equiv t_{\text{diff}}(I_{\text{imp}}) = \frac{g(I_{\text{imp}}) - g_{i-1}}{\Delta g_i}$; and an average model, $t_{v_i-v_{i-1}} = t_{\text{aver}}(I_{\text{imp}})$, where the transmission is obtained by an average of the differential transmissions in the current range $0 - I_{\text{imp}}$. Whereas in the differential model the underlying assumption is that the potential barrier in the QPC is affected by the applied voltage, in the average model we assume implicitly that the potential barrier in the QPC is independent of the applied voltage. Although each model is not accurate, they represent a lower and an upper limit of the transmission of the QPC.

Measurements of shot noise were performed in a wide range of filling factors in the QPC ($\nu_{\text{QPC}} = 5/3 \dots 3$), while in the bulk the filling factor was kept at $\nu_B = 2$, $\nu_B = 5/2$ or at $\nu_B = 3$. The corresponding charge of the quasiparticles in state v_i is best measured at the weak backscattering limit of that state, as one expects then rare and independent backscattering events, and moreover, a weaker dependence of the effective transmission on the correct identification of the next lower lying channel, v_{i-1} . Note that although equation (2) should also be valid at small transmission, the charge of the quasiparticles may change in this limit, reflecting already the nature of the

next lower lying state, v_{i-1} (ref. 28). In our set-up, a weak and persistent reflection by the QPC, even at an applied zero gate voltage, prevented a sufficiently small backscattering coefficient being reached at $\nu_B = 5/2$, so we also conducted measurements at bulk filling $\nu_B = 3$ with the QPC tuned to filling factors in the range $\nu_{\text{QPC}} = 7/3 \dots 5/2$, as we describe below.

Shot noise measurements and charge determination

Conductance and shot noise measurements were conducted at different bulk filling factors and were analysed on the basis of our method of identifying the lower lying states in the QPC described above. As will be shown below, we also tested, when in question, the consequence of a different choice of the next lower lying channel (see Supplementary Information for more details).

We started with measurements of a partitioned $5/2$ state within the QPC while the bulk filling factor was $\nu_B = 3$. The conductance and shot noise are plotted as function of the total impinging DC current $I_{\text{imp}} = 3Ve^2/h$ at a temperature of 40 mK (Fig. 3). The impinging current and the differential transmission were calculated under the assumption that the lower channel is $\nu_{\text{QPC}} = 7/3$ (see measurement results in Fig. 2), namely, $I_{\text{imp}}(i) = V\Delta g_{5/2} = V\frac{e^2}{6h}$ and $t_{5/2-7/3} = \frac{g(I_{\text{imp}}) - g_{7/3}}{\Delta g_{5/2}} = 0.55\text{--}0.72$ (as the impinging current increases). The two models for the effective transmission (t_{diff} and t_{aver}) led to similar predictions for the expected noise, with that for charge $e^* = e/4$ plotted in Fig. 3 (black line). Although the scattering of the data was relatively large (even after 48 h of measurement time), the agreement with $e^* = e/4$, excluding thus $e^* = e/2$ (also plotted for comparison), is evident. We note that assuming a next lower lying channel $\nu_{\text{QPC}} = 2$ does not significantly change our conclusion. In the latter case, the effective transmission varies in the range 0.86–0.90 and the analysis of the shot noise agrees with a quasiparticle charge $e^* = e/5\text{--}e/4$; this definitely excludes a charge $e^* = e/2$ (see Supplementary Information).

In order to further study the quasiparticles' charge, we also performed measurements at bulk filling factor $\nu_B = 5/2$ and different QPC transmissions. Measurements of the nonlinear conductance (similar to Fig. 2) were performed in order to verify the next lower lying channel. They revealed that for these parameters the next lower lying state in the QPC was $\nu_{\text{QPC}} = 2$. Moreover, the absence of the $\nu_{\text{QPC}} = 7/3$ lower channel was also verified: first, by not observing a flat transmission as a function of impinging current, and second, by the absence of noise suppression when the conductance corresponded to $\nu_{\text{QPC}} = 7/3$. Figure 4 displays three measurements of shot noise as a function of the total impinging current I_{imp} : Fig. 4a, b, with measurements at 10 mK and at a reasonably weak backscattering; Fig. 4c, d, with measurements at 10 mK and transmission $t_{5/2-2} \approx 0.5$; and Fig. 4e, f, with measurements at 40 mK and very strong backscattering. For weak backscattering (Fig. 4b), both models for the effective transmission coincide, leading to quasiparticle charge $e^* = e/4$ (the curve for $e^* = e/2$ is also shown for comparison). Figure 4d presents data where the reliability of equation (2) is questionable (as the transmission is intermediate, the scattering events may not be independent), and the two models for transmission clearly deviated from each other (shown in the figure). Here, the apparent charge is again close to $e^* = e/4$ although the data fit better to a charge $e^* \approx 0.2e$. When the $5/2$ channel is almost completely pinched at zero impinging current, and the transmission is highly nonlinear and changes from 2% to 20% as function of the current (Fig. 4e), again both models for the transmission provide an upper and lower limit for the shot noise, yet corresponding nicely to a quasiparticle charge $e^* = e/4$ (Fig. 4f). This is somewhat surprising, because one might have expected that (in this strong backscattering regime, with the next lower lying channel $\nu_{\text{QPC}} = 2$) the tunnelling particle would be an electron.

It is obviously desirable to measure the effective charge at different quantum Hall states in the same device in the vicinity of $\nu_{\text{QPC}} = 5/2$. Figure 5 summarizes some of the measurements that we did in the

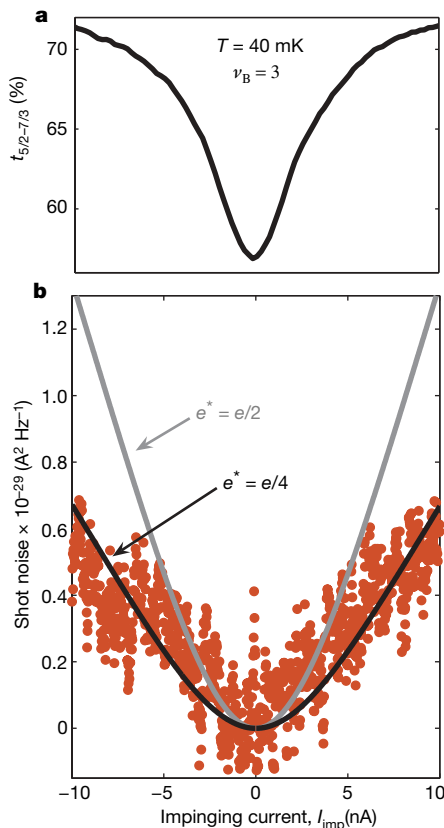


Figure 3 | Conductance and shot noise measurements of partitioned particles at the $5/2$ state. **a, b,** For a filling factor in the bulk $\nu_B = 3$ and that in the QPC tuned to weak backscattering of the $5/2$ state, transmission **(a)** and shot noise **(b)** were measured as function of the impinging current $I_{\text{imp}} = Vg_i$, with $g_i = 3e^2/h$. The effective transmission of the partitioned channel was calculated assuming that the lower state below the $5/2$ is the $7/3$ state (see Fig. 2). Measurement points (1,000) were taken over 40 s, as the impinging current changed from -10 nA to 10 nA . This measurement was repeated a few hundred times, and then averaged. The amplification system, calibrated with a calibrated noise signal at 4.2 K, had a voltage gain of 2,000. In **b**, the predicted shot noise (equation (2)) for charge $e^* = e/4$ (black line) and for $e^* = e/2$ (grey line) is plotted on the data. The data exclude the contribution of charge $e^* = e/2$ to the noise.

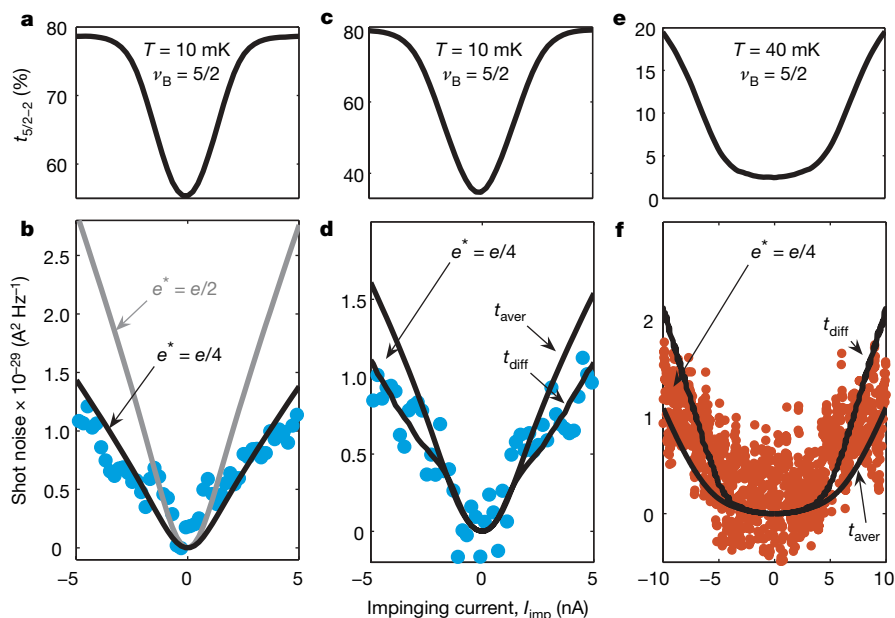


Figure 4 | Conductance and shot noise measurements of partitioned particles at the 5/2 state, with a filling factor in the bulk of $\nu_B = 5/2$. Transmission and shot noise were measured as function of the impinging current $I_{\text{imp}} = Vg_i$, with $g_i = 2.5e^2/h$. The effective transmission of the partitioned channel was calculated assuming that the lower state below the $\nu = 5/2$ is the $\nu = 2$ state, determined by a similar method to that described in Fig. 2. Measurements were done in a similar fashion to that described in Fig. 3, but some of the data are represented by fewer points, which were

obtained after averaging. **a, b**, Measurements at 10 mK, at weak backscattering, where both models of the transmission coincide (see text). **c, d**, Measurements at 10 mK, transmission ~ 0.5 , where the two models for the transmission provide the two limits of the expected noise. **e, f**, Measurements at 40 mK, strong backscattering, where the two models for the transmission provide the two limits of the expected noise. Surprisingly, the charge remains $e^* = e/4$, with no evident ‘bunching’ to e when the QPC is nearly pinched.

range $\nu_{\text{QPC}} = 5/3, \dots, 3$, identified on the two-terminal Hall conductance of the actual sample on which the measurements were made. In the top row, we show the effective transmission of the state under study with the identification of the next lower lying state, which was identified by the method shown in Fig. 2 (in some of the cases we did not plot the conductance and shot noise due to lack of space, but

present them in Supplementary Information). The panel at top left in Fig. 5 was measured at $\nu_B = 3$, with relatively weak backscattering induced by the QPC. The transmission drops with increasing current in a ‘mound-like’ fashion and saturates around 5 nA. The saturation at higher currents (or voltage) is typical (see, for example, ref. 26), and is accompanied by a saturation of the shot noise. It could be

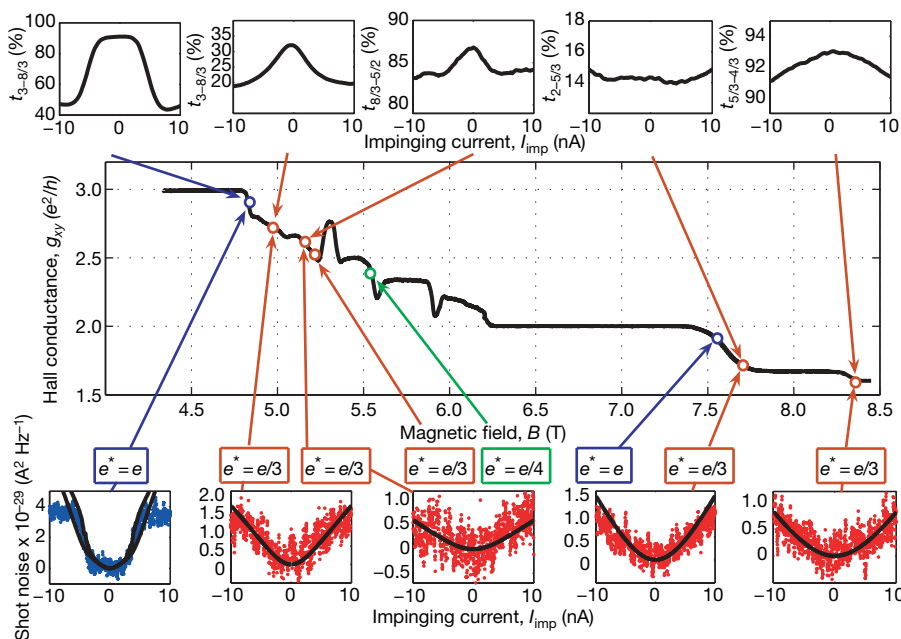


Figure 5 | Conductance and shot noise at different filling factors in the QPC. The main plot shows the two-terminal Hall conductance of the sample as a function of magnetic field; measurement points are indicated on this curve. For each measurement point, the top row shows the transmission as a function of impinging current, and the bottom row shows the shot noise as a function of impinging current. Measured charge is shown boxed below the

main plot. Except for the 5/2 state, measurements in the range $\nu_{\text{QPC}} = 3 \dots 2$ were performed at $\nu_B = 3$ and at $T = 40$ mK, and measurements in the range $\nu_{\text{QPC}} = 2 \dots 5/3$ were performed at $\nu_B = 2$ and at $T = 90$ mK. Near integer fillings (2 and 3) the measured charge was e , whereas near (above and below) the fractional fillings (8/3 and 5/3) the measured charge was $e/3$.

related to the deforming shape of the barrier or interactions (charging) induced by the increased current. Here, near $\nu_{\text{QPC}} = 3$, we observed a nice agreement with charge e , as expected (bottom left panel in Fig. 5). Pinching the QPC further, as in the second panel, the conductance approaches the one corresponding to $\nu_{\text{QPC}} = 8/3$, and the charge fractionalizes with a clear quasiparticle charge $e^* = e/3$ (second panel, bottom row). A very similar behaviour is observed when the filling factor in the QPC is slightly lower than $\nu_{\text{QPC}} = 2$ (measured at $\nu_B = 2$ and at a temperature of 90 mK), agreeing with a charge e , as expected. This charge fractionalized to $e^* = e/3$ as the filling factor lowered to just above $\nu_{\text{QPC}} = 5/3$. Such fractionalization of the charge as the effective barrier for electrons increases was surprising at first. We attribute it to the formation of a FQHE region of $\nu_{\text{QPC}} = 5/3$ within the QPC, separating the two regions on both sides of the QPC. Then, the observed fractional charge may be viewed as the charge of the quasi-holes with charge $e^* = e/3$ tunnelling across the $\nu_{\text{QPC}} = 5/3$ region. When the filling factor in the QPC drops further to slightly below $\nu = 5/3$, and similarly also below $\nu = 8/3$, we also measured $e^* = e/3$, as was expected¹¹ (see panels in Fig. 5).

Discussion

We have presented direct evidence of a quasiparticle charge of $e^* = e/4$ at an even denominator fractional filling of $5/2$ in the second Landau level of the quantum Hall effect. The affirmation of the predicted charge of the quasiparticles is a strong indication that the $\nu = 5/2$ is a paired state, where pairs of composite fermions condense into a gapped state. It is consistent with the Moore–Read⁴ theory, and indicates that if this theory is indeed correct, the quasiparticles that tunnel across a point contact are non-abelian quasiparticles with charge $e/4$. Our experiment does not probe the non-abelian statistics: in order to do this, a direct measurement (say, via interference^{7,13–16,29}) should be conducted. Finally, we also measured the charge of quasiparticles in adjacent filling factors.

METHODS SUMMARY

The 2DEG and the sample. Our structure consisted of a 29-nm-wide GaAs- $\text{Al}_{0.25}\text{Ga}_{0.75}\text{As}$ quantum well, doped on both sides with Si ‘delta-doping’ (a deposited fraction of a Si monolayer). The two ‘delta-doping’ layers were placed in narrow quantum wells, being part of a short period superlattice, separated from the 2DEG by an undoped $\text{Al}_{0.25}\text{Ga}_{0.75}\text{As}$ layer with thickness 80 nm. The 2DEG was located 160 nm below the surface, with the AlAs mole fraction rising to 35% near the surface.

The sample was patterned by optical lithography and electron beam lithography. Measurements were done on an unilluminated sample. The conductance of the QPC was found to be irreproducible as a function of gate voltage, and tended to vary as function of time after the gate voltage was changed.

Note that the 2DEG mobility and the quantum scattering time were found to be poor indicators for the ‘quality of FQHE features’. Some lower-mobility samples (around $15 \times 10^6 \text{ cm}^2 \text{ V}^{-1} \text{ s}^{-1}$) showed nice fractional states, while higher-mobility samples (as high as $36 \times 10^6 \text{ cm}^2 \text{ V}^{-1} \text{ s}^{-1}$) sometimes showed poorer behaviour.

Measuring shot noise. Using a multi-terminal configuration ensured that the sample conductance in a quantum Hall plateau was at a constant $\nu e^2/h$ value and independent of the QPC transmission. To avoid the large $1/f$ noise at low frequencies, a resonant circuit was connected between the drain (D) and ground, made of a copper coil (L) and a capacitor (C), tuned to a resonance frequency of 910 kHz. This was followed by a home-made preamplifier cooled to 4.2 K, a room temperature amplifier (NF SA-220F5), and a spectrum analyser (bandwidth 30 kHz or 100 kHz).

Comparing the expected spectral density of the voltage noise S_v at $\nu = 1/3$ and at $\nu = 5/2$, we find $S_{1/3}/S_{5/2} = 50$. As the signal (the shot noise) to noise (the uncorrelated system noise) ratio is proportional to $(\Delta f \times \tau)^{-1/2}$, with Δf the bandwidth, an unreasonable 2,500 times longer measurement time τ is required for the same signal to noise ratio. Hence, a larger voltage was applied ($V = 10$ – $100 \mu\text{V}$, with the associated energy e^*V being some 10–100 times larger than the thermal energy $k_B T$); combined with a wider bandwidth of the LC circuit at the $\nu = 5/2$ state (due to the higher conductance), it enabled a more reasonable measurement time.

Full Methods and any associated references are available in the online version of the paper at www.nature.com/nature.

Received 9 November 2007; accepted 14 February 2008.

1. Tsui, D. C., Stormer, H. L. & Gossard, A. C. Two-dimensional magnetotransport in the extreme quantum limit. *Phys. Rev. Lett.* **48**, 1559–1562 (1982).
2. Prange, R. E. & Girvin, S. M. (eds) *The Quantum Hall Effect* (Springer, New York, 1987).
3. Willett, R. et al. Observation of an even-denominator quantum number in the fractional quantum Hall effect. *Phys. Rev. Lett.* **59**, 1776–1779 (1987).
4. Moore, G. & Read, N. Nonabelions in the fractional quantum Hall effect. *Nucl. Phys. B* **360**, 362–396 (1991).
5. Read, N. Paired fractional quantum Hall states and the $\nu=5/2$ puzzle. Preprint at (<http://arxiv.org/abs/cond-mat/0011338>) (2000).
6. Kitaev, A. Fault tolerant quantum computation by anyons. *Ann. Phys. (NY)* **303**, 2–30 (2003).
7. Das Sarma, S., Freedman, M., Nayak, C., Simon, S. & Stern, A. Non-abelian anyons and topological quantum computation. Preprint at (<http://arxiv.org/abs/0707.1889>) (2007).
8. Das Sarma, S., Freedman, M. & Nayak, C. Topologically protected qubits from a possible non-abelian fractional quantum Hall state. *Phys. Rev. Lett.* **94**, 166802 (2005).
9. Read, N. & Green, D. Paired states of fermions in two dimensions with breaking of parity and time-reversal symmetries and the fractional quantum Hall effect. *Phys. Rev. B* **61**, 10267–10297 (2000).
10. Morf, R. H. Transition from quantum Hall to compressible states in the second Landau level: New light on the $5/2$ enigma. *Phys. Rev. Lett.* **80**, 1505–1508 (1998).
11. de Picciotto, R. et al. Direct observation of a fractional charge. *Nature* **389**, 162–164 (1997).
12. Saminadayar, L., Glattli, D. C., Jin, Y. & Etienne, B. Observation of the $e/3$ fractionally charged Laughlin quasiparticles. *Phys. Rev. Lett.* **79**, 2526–2529 (1997).
13. Stern, A. & Halperin, B. I. Proposed experiments to probe the non-abelian $\nu=5/2$ quantum Hall state. *Phys. Rev. Lett.* **96**, 016802 (2006).
14. Fradkin, E. et al. A Chern-Simons effective field theory for the Pfaffian quantum Hall state. *Nucl. Phys. B* **516**, 704–718 (1998).
15. Bonderson, P., Kitaev, A. & Shtengel, K. Detecting non-abelian statistics in the $\nu=5/2$ fractional quantum Hall state. *Phys. Rev. Lett.* **96**, 016803 (2006).
16. Feldman, D. E., Gefen, Y., Kitaev, A., Law, K. T. & Stern, A. Shot noise in anyonic Mach-Zehnder interferometer. *Phys. Rev. B* **76**, 085333 (2007).
17. Toke, C. & Jain, J. K. Understanding the $5/2$ fractional quantum Hall effect without the Pfaffian wave function. *Phys. Rev. Lett.* **96**, 246805 (2006).
18. Pan, W. et al. The other even-denominator fractions. *Physica E* **9**, 9–16 (2001).
19. Miller, J. B. et al. Fractional quantum Hall effect in a quantum point contact at filling fraction $5/2$. *Nature Phys.* **3**, 561–565 (2007).
20. Chung, Y. C., Heiblum, M. & Umansky, V. Scattering of bunched fractionally charged quasiparticles. *Phys. Rev. Lett.* **91**, 216804 (2003).
21. Griffiths, T. G., Comfari, E., Heiblum, M., Stern, A. & Umansky, V. Evolution of the quasiparticle charge in the fractional quantum Hall regime. *Phys. Rev. Lett.* **85**, 3918–3921 (2000).
22. Reznikov, M. et al. Observation of quasiparticles with one-fifth of an electron's charge. *Nature* **389**, 238–241 (1999).
23. Lesovik, G. B. Excess quantum shot noise in 2D ballistic point contacts. *JETP Lett.* **49**, 592–594 (1989).
24. Bena, C. & Nayak, C. Effects of non-Abelian statistics on two-terminal shot noise in a quantum Hall liquid in the Pfaffian state. *Phys. Rev. B* **73**, 155335 (2006).
25. Martin, T. & Landauer, R. Wave packet approach to noise in multi-channel mesoscopic systems. *Phys. Rev. B* **45**, 1742–1755 (1992).
26. Chung, Y. C. et al. Anomalous chiral Luttinger liquid behavior of diluted fractionally charged quasiparticles. *Phys. Rev. B* **67**, 201104 (2003).
27. Roddaro, S., Pellegrini, V. & Beltram, F. Particle-hole Luttinger liquids in a quantum Hall circuit. *Phys. Rev. Lett.* **95**, 156804 (2005).
28. Kane, C. L. & Fisher, M. P. A. Nonequilibrium noise and fractional charge in the quantum Hall effect. *Phys. Rev. Lett.* **72**, 724–727 (1994).
29. Stevn, A. Anyons and the quantum Hall effect—A pedagogical review. *Ann. Phys.* **1**, 204–249 (2008).

Supplementary Information is linked to the online version of the paper at www.nature.com/nature.

Acknowledgements We thank A. Ra'anan for laying the foundations for these experiments; A. Schreier, I. Neder, N. Ofek, Y. Gross, E. Grosfeld, Y. Gefen, B. I. Halperin, Y. Levinson, B. Rosenow and S. Das Sarma for their suggestions and assistance; J. Miller and C. Marcus for sharing with us their experience of the fabrication process; and L. Pfeiffer for providing us with a sample for initial experimentation. M.H. acknowledges partial support from the Israeli Science Foundation (ISF), the German Israeli Foundation (GIF), and the Minerva Foundation. A.S. acknowledges support from the US-Israel Bi-national Science Foundation, the Minerva foundation, and the ISF.

Author Information Reprints and permissions information is available at www.nature.com/reprints. Correspondence and requests for materials should be addressed to M.D. (merav.dolev@weizmann.ac.il).

METHODS

The 2DEG. The enabling ingredient for the experiment is the quality of the 2DEG. Only extremely high-mobility structures showed the fragile even denominator $5/2$ fraction. The electron density of our 2DEG was $\sim 3.2 \times 10^{11} \text{ cm}^{-2}$, with a low-temperature mobility of $30.5 \times 10^6 \text{ cm}^2 \text{ V}^{-1} \text{ s}^{-1}$, measured in the dark. The quantum scattering time of the electrons was estimated from Shubnikov de Haas oscillations to be around 12 ps. Our heterostructure consisted of a 29-nm-wide GaAs- $\text{Al}_{0.25}\text{Ga}_{0.75}\text{As}$ quantum well containing the 2DEG, doped on both sides with Si 'delta-doping', which serve as donors. The two 'delta-doping' layers were also placed in narrow quantum wells, being part of a short period superlattice, separated from the 2DEG by an undoped $\text{Al}_{0.25}\text{Ga}_{0.75}\text{As}$ layer (spacer) with thickness 80 nm. Uniform doping, some 60 nm below the surface, compensated the surface states and thus terminated the depletion layer. The 2DEG was located 160 nm below the surface, with the AlAs mole fraction rising from 25% at the uniform doping to 35% near the surface. A thin GaAs cap terminated the structure in order to prevent oxidation and facilitate better ohmic contacts.

The mobility of the 2DEG. Note that the mobility of 2DEG and the quantum scattering time were found to be rather poor indicators for the 'quality of FQHE features'. Indeed, high-mobility 2DEGs are needed to observe the fragile fractional states, however, in this high range some lower-mobility samples (around $15 \times 10^6 \text{ cm}^2 \text{ V}^{-1} \text{ s}^{-1}$) showed nice fractional states while higher-mobility samples (as high as $36 \times 10^6 \text{ cm}^2 \text{ V}^{-1} \text{ s}^{-1}$) showed sometimes poorer behaviour. This behaviour is poorly understood, however, as the mobility and quantum times represent only the second order correlator of the potential fluctuations, and it is likely that higher order correlators (namely, the detailed shape of the potential landscape) are responsible for the localization in high magnetic field.

The sample. The samples were patterned in a shape of a Hall bar, with a single QPC in its centre and multiple ohmic contacts. The QPC partitioned the incoming current by bringing the forward propagating edge channel, with a chemical potential determined by the applied voltage V , into close proximity with the backward propagating edge channel returning from the grounded contact, hence inducing backscattering, partitioning and shot noise. Two contacts, 1 and 2, were grounded directly to the cold finger ('cold grounds'), which was attached directly to the mixing chamber, in order to cool the electrons to $\sim 10 \text{ mK}$. When needed, a heater was used to heat the mixing chamber, and hence the sample, above base temperature. The sample was patterned by optical lithography and electron beam lithography. Metallic gates were formed by deposition of 15 nm of PdAu and 15 nm of Au. Measurements were done on unilluminated samples. The conductance of the QPC was found to be irreproducible as a function of the gate voltage, and tended to vary as function of time after the gate voltage was changed. Hence, the desired conductance was achieved by tuning the gate voltage and the magnetic field along the quantum Hall plateau.

Measuring shot noise. A DC current I_{imp} was driven from the source contact (S), with the QPC partitioning it to the transmitted and backscattered currents. To avoid the large $1/f$ noise at low frequencies, a resonant circuit was connected between the drain (D) and ground, made of a copper coil (L) and a capacitor (C , formed mostly by the capacitance of the coaxial cable), tuned to a resonance frequency of 910 kHz. This was followed by a home-made preamplifier cooled to 4.2 K, a room temperature amplifier (NF SA-220F5), and a spectrum analyser (bandwidth 30 kHz or 100 kHz). The multi-terminal configuration of the sample ensured a constant input resistance to the preamplifier when the quantum Hall effect was tuned to a conductance plateau, independent of the transmission of the QPC (as long as the longitudinal resistance was zero, the resistance between terminals D and 2 was always the Hall resistance). This allowed the 'resistance dependent' noise components, namely, the 'current noise' of the preamplifier (backward injected current by the preamplifier into the sample) and the thermal noise of the sample (together being some 50 times larger than the desired shot noise signal), to be subtracted from the measured total signal (their summed value was measured by setting the impinging current to zero).

Comparing the expected spectral density of the voltage noise S^v at $\nu = 1/3$ and at $\nu = 5/2$, we find $S^v_{1/3}/S^v_{5/2} = 50$. As the signal-to-noise ratio (the shot noise to the uncorrelated system noise ratio) is proportional to $(\Delta f \times \tau)^{-1/2}$, with Δf the bandwidth and τ the measurement time, an unreasonable measurement time (2,500 times longer) was required for the same signal to noise ratio. Hence, a larger voltage (and current) was applied (10–100 μV , being some 10–100 times larger than the electron temperature), which combined with a wider bandwidth of the LC circuit at the $\nu = 5/2$ state (due to the relatively high conductance) enabled a more reasonable measurement time.

Why fishing magnifies fluctuations in fish abundance

Christian N. K. Anderson¹, Chih-hao Hsieh^{1,2,3,4}, Stuart A. Sandin¹, Roger Hewitt⁵, Anne Hollowed⁶, John Beddington⁷, Robert M. May⁸ & George Sugihara¹

It is now clear that fished populations can fluctuate more than unharvested stocks. However, it is not clear why. Here we distinguish among three major competing mechanisms for this phenomenon, by using the 50-year California Cooperative Oceanic Fisheries Investigations (CalCOFI) larval fish record. First, variable fishing pressure directly increases variability in exploited populations. Second, commercial fishing can decrease the average body size and age of a stock, causing the truncated population to track environmental fluctuations directly. Third, age-truncated or juvenescent populations have increasingly unstable population dynamics because of changing demographic parameters such as intrinsic growth rates. We find no evidence for the first hypothesis, limited evidence for the second and strong evidence for the third. Therefore, in California Current fisheries, increased temporal variability in the population does not arise from variable exploitation, nor does it reflect direct environmental tracking. More fundamentally, it arises from increased instability in dynamics. This finding has implications for resource management as an empirical example of how selective harvesting can alter the basic dynamics of exploited populations, and lead to unstable booms and busts that can precede systematic declines in stock levels.

Ecologists have long suspected that harvesting a species has the unintended consequence of destabilizing the abundance of that species^{1,2}. This would be undesirable, because boom-and-bust cycles can increase the likelihood of local extinctions³ and can harm the economic market for the species. However, this connection has been remarkably difficult to prove. A historic example is the collapse of the California sardine fishery in the late 1940s, which some argued was caused primarily by fishing^{4,5}, but which others attributed to cooling sea surface temperatures or to shifting wind patterns^{6–8}. Because landings records contain no information about unexploited species, there is no control group to disentangle environmental effects from fishing effects. Partly to address this conundrum, CalCOFI was initiated to collect data both on fished and unfished species living in the same environment. CalCOFI overcame the reliance on landings data by sampling the ichthyoplankton assemblage, a well-known proxy for current adult (spawning) biomass^{9–11}. Fifty years into the study, Hsieh *et al.*⁹ used the CalCOFI ichthyoplankton database¹² to separate the effects of fishing from other variables, and demonstrated that fishing significantly increases temporal variability of populations in the southern sector of the California Current ecosystem (Fig. 1). Increased variability is thought to be related to the truncated age/size structure^{3,4,9,13–17} of commercially fished species, a phenomenon caused by selective removals of larger, older individuals that previously provided stability to the population.

Here we examine three competing hypotheses for the link between fishing and stock variability^{1,2,9,16,18}. First, fishing itself can vary year to year and this can translate directly into increased population variability¹⁹. Second, fished populations that become dominated by relatively small-bodied and young individuals are less able to smooth out environmental fluctuations, and are thus more likely than unfished stocks to track directly those fluctuations^{4,9,13}. Finally,

fished populations that become dominated by small-bodied and young individuals are more prone to exhibit unstable dynamics due to changing demographic parameters^{20,21}. These are not mutually

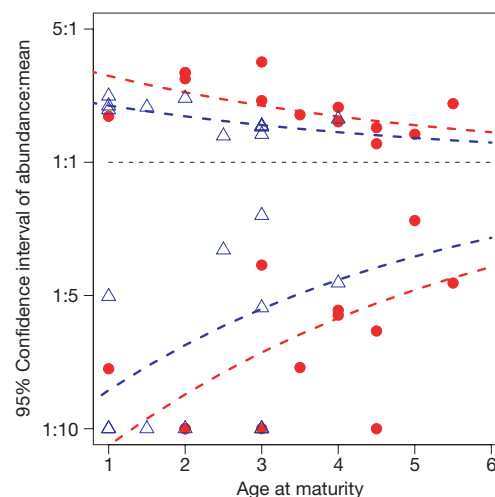


Figure 1 | In addition to an increased coefficient of variation⁹, exploited species (red dots) exhibit larger booms and busts than unexploited species (blue triangles) of a similar age. The 95th and the 5th percentiles of abundance are shown for each species, with exponential fits (dashed lines) for the exploited and unexploited species. Note that for all species, the busts (lower range) are more pronounced than the booms ($P < 0.0001$). Populations less than one-tenth mean size probably fell below detection levels and were conservatively fixed at one-tenth mean size; thus, the effect may be more pronounced than depicted here.

¹Scripps Institution of Oceanography, University of California, San Diego, La Jolla, California 92093, USA. ²Center for Ecological Research, Kyoto University, Hirano, 2-509-3, Otsu, 520-2113, Japan. ³Institute of Oceanography, National Taiwan University, No. 1, Section 4, Roosevelt Road, Taipei, 10617, Taiwan. ⁴Institute of Marine Environmental Chemistry and Ecology, National Taiwan Ocean University, 2, Pei-Ning Road, Keelung, 20224, Taiwan. ⁵Southwest Fisheries Science Center, National Marine Fisheries Service, 8604 La Jolla Shores Drive, La Jolla, California 92037, USA. ⁶Alaska Fisheries Science Center, National Marine Fisheries Service, 7600 Sand Point Way NE, Seattle, Washington 98115, USA. ⁷Division of Biology, Faculty of Natural Sciences, Imperial College London, RSM Building, South Kensington Campus, London SW7 2AZ, UK. ⁸Department of Zoology, University of Oxford, South Parks Road, Oxford OX1 3PS, UK.

exclusive hypotheses; all three could act together to increase variability. Here we analyse the relative importance of each hypothesis as a cause of the increase in population variability of fished stocks observed in the southern California Current ecosystem.

Hypothesis 1 (variable fishing)

According to hypothesis 1, a fish stock is expected to vary more if exploited heavily some years and lightly in others. Jonzén *et al.*²² discovered a positive correlation between the variance in fishing mortality and the variance in the standing stock biomass of Baltic cod populations. We use their method on the CalCOFI database, to test this hypothesis for the seven exploited species whose fishing mortality is available from National Marine Fisheries Service stock assessment reports (Supplementary Table 1) and find no evidence that variability in fishing mortality is associated with variability in either larval density (Fig. 2) or estimated spawning biomass (Supplementary Fig. 2). Therefore, although it is reasonable to expect the variability of these populations to be somewhat influenced by year-to-year differences in fishing effort, hypothesis 1 alone does not explain the observed increase in variability of these data.

Hypotheses 2 and 3 (age-truncation effects)

The other two hypotheses are closely related. Because fishing typically targets the larger individuals of a species, the average size—and thus age—of target populations is often found to decrease^{14–16,18,23}. Age truncation leading to increased population variability has been documented in several populations⁹, and is here referred to as the ‘age truncation effect’ (ATE)¹³. Such juvenescence can affect population variance in two separable ways.

Hypothesis 2 suggests that when new recruits compose most of the stock, the juvenescent population is more likely to track variable environmental processes directly^{4,5}. Although younger and smaller fish are more susceptible to changes in the environment, older and larger fish tend to integrate over environmental fluctuations and survive hard times better through ‘bet-hedging’ strategies^{18,24–27} including fat storage, the ability to migrate and avoid poor areas, having flexibility in spawning times and locations, and production of high-quality offspring that survive in a broader suite of environmental conditions¹⁸. Bet-hedging strategies are well documented in

association with long-tailed age distributions^{18,24–27}. Loss of hedging capacity through age truncation should produce a time-series signal that more closely exhibits the linear (statistically noisy) characteristics found in physical oceanographic data for that region²¹.

By contrast, under hypothesis 3, the increased variability of exploited fish stocks comes from changes in demographic parameters that amplify nonlinear behaviour^{20,21}. There are many ways that the ATE can change demographic parameters, for example by increasing intrinsic population growth rates or by increasing nonlinear coupling of demographic parameters to environmental noise^{20,28}. The resulting population dynamics will produce a more variable time series with more nonlinear behaviour than seen in unexploited fish stocks.

Separating environment and demography

Because hypothesis 2 implies increased tracking of linear environmental variation, whereas hypothesis 3 describes an enhanced nonlinear response, we can distinguish these subtle alternatives by comparing the nonlinearity in the time series of exploited species relative to unexploited species. Here, nonlinearity is quantified using S-maps²⁹, a model validation criterion that uses out-of-sample predictions from equivalent linear versus nonlinear models to identify the dynamics behind time-series observations. The model either weights all data equally ($\theta = 0$) to make linear forecasts, or gives more weight to data points with similar recent histories ($\theta > 0$), a hallmark of nonlinear behaviour^{29,30}. The nonlinearity of a time series is determined by how much the correlation (ρ) between forecasts and observations increases as models are tuned towards nonlinear solutions; that is, how much forecast skill increases ($\Delta\rho$) when $\theta > 0$ ($\Delta\rho = \rho_{\theta > 0} - \rho_{\theta = 0}$; see Methods).

When CalCOFI ichthyoplankton time series are modelled using linear autoregression (S-maps with $\theta = 0$), fished species are slightly more predictable than unfished species ($\rho = 0.514$ and 0.504 , respectively; Fisher's test $P = 0.64$; Supplementary Fig. 3). However, this possible evidence for hypothesis 2 is marginal (Supplementary Table 2). Indeed, nonlinear models describe the CalCOFI ichthyoplankton time series better ($\theta = 0.3$ for both), and more importantly, fished species exhibit significantly more nonlinearity than the unfished group (Fig. 3a; unfished $\Delta\rho = 0.037$, $P = 0.25$; fished $\Delta\rho = 0.083$, $P < 0.01$; Fisher's test, $P < 0.003$). If the increase in variance is due to vulnerable, young fish simply tracking the linear environment more closely, then the nonlinearity ($\Delta\rho$) of fished species should decrease. This prediction is contradicted by the data.

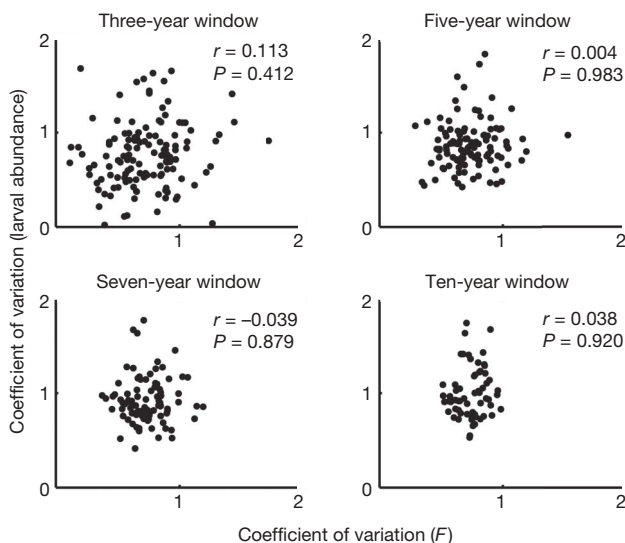


Figure 2 | Hypothesis 1: does variable fishing cause variability in fish stocks? There is no positive relation between the variability in the coefficient of variation of fishing mortality (F) and population variability coefficient of variation (larval abundance) using a three-, five-, seven-, and ten-year moving window. Thus variability in fishing mortality (removing more fish some years than others) does not account for variability in fished stocks in the CalCOFI domain.

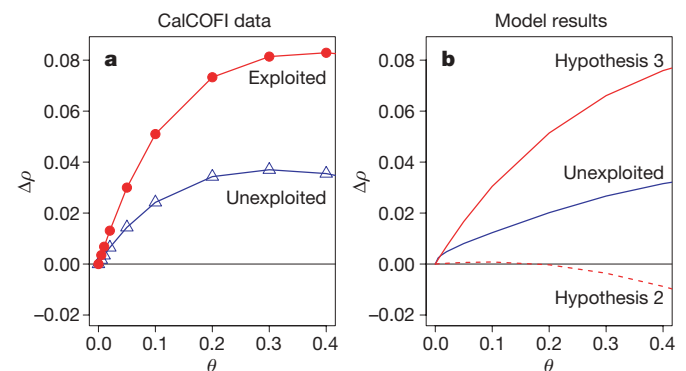


Figure 3 | Discriminating between hypotheses 2 and 3. A larger $\Delta\rho$ as θ is tuned from linear ($\theta = 0$) towards nonlinear solutions ($\theta > 0$) indicates a stronger nonlinear signal ($\Delta\rho = \rho_{\theta > 0} - \rho_{\theta = 0}$). **a**, S-map analysis shows that fished populations (red) are significantly more nonlinear than unexploited populations (blue) ($P = 0.0027$), supporting hypothesis 3 (demographic change), not hypothesis 2 (tracking), as the agent behind amplified variability with fishing. **b**, Corroborative model results. Equation (1) was fitted to data for unexploited species (blue line). Increased environmental sensitivity makes time series appear more linear (dashed red line). However, increasing growth rate r produces an enhanced nonlinear signature (solid red line) as observed for exploited species in **a**.

Rather, fishing pressure has enhanced the nonlinear behaviour of the fished populations. Therefore, the data suggest that altered dynamics resulting from a truncated age structure overwhelm the propensity of young fish to track the environment passively and that dynamic instability is the agent behind the observed increase in variance. Increased nonlinearity has explained higher variance in other contexts^{29,31}.

Identifying sources of nonlinearity

We illustrate the distinction between hypotheses 2 and 3 with a population growth model having the familiar Ricker-form^{29,32}

$$N_{t+1} = N_t \exp[r(1 - N_t)] + c\varepsilon \quad (1)$$

where N is population size (in units of number or biomass), r is the intrinsic population growth rate, ε is environmental variability with unit standard deviation, and c is environmental susceptibility (see Methods, Supplementary Fig. 4 and Supplementary Discussion). Hypothesis 2 corresponds to an increase in environmental susceptibility c ; hypothesis 3 corresponds to alteration of a demographic parameter: for this example we increase r . Forecast skill does not improve with nonlinear tuning ($\theta > 0$) as environmental noise ($c\varepsilon$) is increased, but declines with θ , as would be expected if the time series were dominated by linear statistical effects (Fig. 3b, dashed line; see Methods). We find this result is maintained whether ε is 'white' noise, autocorrelated 'red' noise, $1/f$ 'pink' noise or the actual values of the Pacific Decadal Oscillation^{33–35}. However, under hypothesis 3 (Fig. 3b, solid red line), exploited model populations present an enhanced nonlinear signature as r is increased.

At first glance, it seems counterintuitive that age truncation would increase intrinsic population growth rates (because fishing removes the largest individuals that produce the most and best quality eggs^{18,24–27}); yet this trend is observed empirically in the California Current ecosystem. Because individual body size decreased and total biomass remained statistically constant (26 of 29 stocks⁹), the number of young fish has increased. A larger population of shorter-lived fish requires a higher intrinsic rate of growth (r); the population must produce more surviving offspring per capita per year to compensate for the shortened life span. The ultimate mechanism behind this ATE-induced increase could be competitive release and/or decreased cannibalism or possibly evolution^{23,36,37}, leading to increased somatic growth or increased per-capita fecundity. Although other factors are probably operating, the evidence from CalCOFI points to increased growth rates as a dominant factor supporting the increase in nonlinearity observed in Fig. 3a.

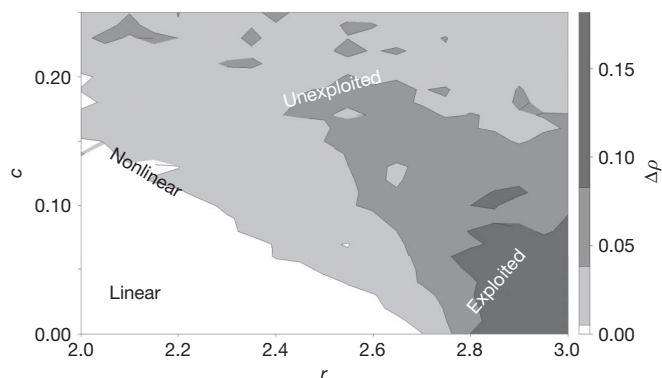


Figure 4 | Nonlinear behaviour can emerge at modest growth rates (r) with process noise ($\varepsilon_{\text{process}}$). Models that are underspecified (missing important components) are said to contain process noise. In this example, we evaluate the nonlinearity of $Z_{t+1} = G(Z_t + \varepsilon_{\text{process}})$, where G is equation (1) and $\varepsilon_{\text{process}}$ is normally distributed with mean 0 and standard deviation c . Process noise can amplify a nonlinear signature in the simple model for values of r that would be linear alone.

Although it is well known that increasing growth rates in simple discrete growth models can lead to unstable dynamics³⁸, values of r required to evoke such behaviour in single species models are often unrealistically high. However, models with multiple species³⁹, multiple stable states²⁸ or models having demographic parameters that vary in complex ways with the environment^{20,21} produce nonlinear behaviour even at modest growth rates. More generally, process noise (error from incompletely specified models) can induce instability in otherwise stable models when the error multiplies in specific ways; that is, when an essential detail is added that has a nonlinear effect. Using the commonly studied²⁹ form of process noise $Z_{t+1} = G(Z_t + \varepsilon_{\text{process}})$ where equation (1) is an example of G , Fig. 4 shows that generic process noise evokes nonlinear behaviour at lower growth rates. This toy representation portrays nonlinear or biologically amplified process errors.

Thus, increasing either process noise or growth rates can amplify nonlinearity. And fishing may affect both. For example, incorporating variable fishing F_t into equation (1) so that variability in F is an expression of process noise,

$$N_{t+1} = N_t \exp[r(1 - N_t/K_t - F_t)] \quad (2)$$

leads to amplified nonlinearity (Fig. 5). (However, the lack of a relation in Fig. 2 eliminates this as a cause for increased variability in these data.) Similarly, modelling process errors more explicitly by adding variability directly to the demographic parameters r or K in equation (2) will provoke a nonlinear signature, regardless of the particular form of the noise (see Methods and Supplementary Fig. 5). It is reasonable to speculate that the baseline nonlinearity seen in the unexploited state is an expression of nonlinear process errors related to variable demographic parameters, such as those tied to ecosystem shifts and climate events for example^{8,9,20}. So, although neither variability in fishing nor in the environment correlates with variability in abundance, these two sources of process error may be implicated in complex ways with the instability that accompanies fishing. Notwithstanding their potential destabilizing effects, by themselves these processes have little direct effect on the overall stock variability we observed in CalCOFI (Fig. 2, Supplementary Fig. 2, and Supplementary Tables 2 and 3).

Life-history traits and nonlinearity

Are there characteristics that make some fish stocks more susceptible to the nonlinear effects of fishing than others? To answer this question we compared the nonlinearity of exploited and unexploited stocks for various life-history traits (Table 1 and Supplementary Table 4). Table 1 identifies a qualitative tendency for the following characteristics to be associated with vulnerability to fishing: larger size at sexual maturity (≥ 25 cm), greater age at sexual maturity (≥ 3 years), longer spawning duration (> 7 months), higher fecundity ($\geq 200,000$ eggs per female per year), lower trophic level and

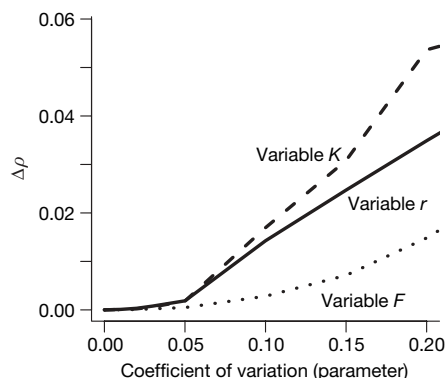


Figure 5 | Variable fishing F (dotted line), growth r (solid line), or carrying capacity K (dashed line), can induce nonlinearity.

Table 1 | Vulnerability of species with different life histories to destabilization by fishing

Life-history trait	Cut-off value	Below cut-off			Above cut-off			Difference in fishing effect
		Unfished $\Delta\rho$ (n)	Fished $\Delta\rho$ (n)	Fishing effect	Unfished $\Delta\rho$ (n)	Fished $\Delta\rho$ (n)	Fishing effect	
Maximum size (cm)	50	0.062 (14)	0.171 (3)	0.109 ($P = 0.06$)	0.067 (2)	0.113 (10)	0.047 ($P < 0.01$)	-0.062 ($P = 0.19$)
Size at maturity (cm)	25	0.071 (13)	0.078 (4)	0.007 ($P = 0.04$)	0.040 (3)	0.143 (9)	0.103 ($P < 0.01$)	0.096 ($P < 0.01$)
Age at maturity (years)	3	0.065 (9)	0.055 (4)	-0.010 ($P = 0.92$)	0.055 (7)	0.064 (9)	0.009 ($P = 0.03$)	0.019 ($P = 0.11$)
Fecundity (eggs per female per year)	200,000	0.071 (13)	0.082 (5)	0.011 ($P = 0.03$)	0.040 (3)	0.072 (8)	0.032 ($P = 0.03$)	0.021 ($P = 0.21$)
Spawning duration (months per year)	7	0.023 (6)	0.093 (7)	0.070 ($P < 0.01$)	0.091 (10)	0.205 (6)	0.114 ($P < 0.01$)	0.044 ($P = 0.03$)
Trophic level	3.5	0.066 (11)	0.092 (6)	0.026 ($P < 0.01$)	0.063 (5)	0.056 (7)	-0.006 ($P = 0.84$)	-0.032 ($P = 0.04$)
Coefficient of variation	0.9	0.055 (11)	0.081 (4)	0.026 ($P = 0.02$)	0.054 (5)	0.100 (9)	0.047 ($P < 0.01$)	0.020 ($P = 0.11$)

Species are separated into groups on the basis of having life-history traits above or below a cut-off value, and the nonlinearity ($\Delta\rho$) of exploited and unexploited species within these groups is compared. Significance is calculated by jack-knifing the data set, S-mapping and then comparing $\Delta\rho$ distributions of the fished and unfished data (one-tailed P values). Fishing significantly increased the nonlinearity of 12 of the 14 groups investigated. To evaluate which life-history traits are most impacted by fishing, the differences in $\Delta\rho$ values were compared (two-tailed P values in the right-hand column). Qualitatively, susceptibility to fishing is greater in late-maturing, fecund, low-trophic-level species with year-round spawning and high variability.

more variability in abundance (coefficient of variation ≥ 0.9). Thus, acknowledging the uncertainty arising from the small number of species involved in some groups, one may speculate that to a first approximation, large-maturing lower-trophic-level species that are also fecund, may be most susceptible to further destabilization by fishing, and regardless of life history the evidence suggests that increasing growth rates are driving this effect.

Management implications

In summary, fishing for big individuals without consideration of the impact on the age distribution can lead to unstable nonlinear population dynamics, and this enhanced nonlinearity helps to explain much of the volatility seen in fish stocks today (Fig. 1). Our study shows that when unconstrained, an observed demographic consequence of the ATE, that is, the effective increase of r , makes dramatic population change more likely—and paradoxically, in this case, can make those changes slightly more predictable in the short run. Thus target species are in double jeopardy from both fishing removals and the ATE, as stocks with higher mortality also suffer increasing fluctuations. Reduced size and age distributions have been documented in many common fisheries species, for example in Pacific salmon⁴⁰, Pacific rockfish⁴¹, and North Sea ground fish^{42,43}, suggesting the potential relevance of the ATE for many commercially important species. In terms of stock recovery, it can be premature therefore to resume fishing activities solely on the basis of recovery of biomass but before restoration of historical age distributions, even though short-term industry pressures may make this difficult to realize (for example, Atlantic swordfish⁴⁴).

It is encouraging, however, that some managers are adopting precautionary harvest policies that protect against stock depletion and the ATE^{45,46}. For example, in Alaska, where fishing is managed through a complex system of harvest controls, there has been relatively minor impact on the mean age of the population^{47,48}. Nonetheless, in other areas, current policies and industry pressures that encourage lifting bans on fishing when biomass is rehabilitated, but where maximum age is not, contain risk^{18,44,49}. Unless fishing is conducted with informed harvest controls and with market mechanisms to align incentives and manage financial risks associated with volatile supplies, we can expect a future of instability in fish populations and suboptimal performance of the industries built on them.

METHODS SUMMARY

Hypothesis 1 was tested by examining the relation between the coefficient of variation in fishing mortality and the coefficient of variation of spawning biomass (larval indicators and fishery-based estimates) for Southern Region California Current fisheries (Fig. 2 and Supplementary Fig. 2). Variability was calculated for windows 3–10 years long.

Hypotheses 2 and 3 were tested with S-maps on composite CalCOFI ichthyoplankton time series, using methods described in detail elsewhere^{21,50}. Briefly, larval time series were composited end-to-end, and nonlinearity of fished versus unfished species was assessed by computing $\Delta\rho$ with an embedding dimension $E = 3$ (Supplementary Materials).

Hypotheses 2 and 3 are illustrated with a simple model (equation (1)) whose behaviour is generic to a large class of fisheries models (Supplementary Discussion). First, a baseline is established by fitting parameters to the observed variance (Supplementary Fig. 6) and nonlinearity of unexploited CalCOFI populations (Fig. 3b, blue line). Next, to model hypothesis 2, environmental susceptibility (c) is increased to simulate direct environmental tracking with the ATE (Fig. 3b, dashed line). Alternative types of environmental noise were simulated for hypothesis 2 (red, 1/f, white, low-pass filtered and the actual Pacific Decadal Oscillation values^{33–35}), and did not affect the qualitative outcome. Finally, hypothesis 3 is here simulated by increasing species-specific growth rates (r) (Fig. 3b, solid red line). Various forms of process noise were also simulated. All standard statistical analyses were performed with R software version 2.3.0.

Received 12 November 2007; accepted 22 February 2008.

- Beddington, J. R. & May, R. M. Harvesting natural populations in a randomly fluctuating environment. *Science* **197**, 463–465 (1977).
- May, R. M., Beddington, J. R., Horwood, J. W. & Shepherd, J. G. Exploiting natural populations in an uncertain world. *Math. Biosci.* **42**, 219–252 (1978).
- Lande, R., Engen, S. & Saether, B. *Stochastic Population Dynamics in Ecology and Conservation* (Oxford Univ. Press, New York, 2003).
- Murphy, G. I. Vital statistics of the Pacific sardine (*Sardinops caerulea*) and the population consequences. *Ecology* **48**, 731–736 (1967).
- Murphy, G. I. Population biology of the Pacific sardine (*Sardine caerulea*). *Proc. Calif. Acad. Sci.* 4th ser. **34**, 1–84 (1966).
- Marr, J. C. in *Proc. World Sci. Meeting Biol. Sardines Related Species* (eds Rosa, H. & Murphy, G.) 667–791 (FAO, Rome, 1960).
- Clark, F. N. & Marr, J. C. Population dynamics of the Pacific sardine. *CalCOFI Prog. Rep.* **4**, 11–48 (1955).
- Rykaczewski, R. R. & Checkley, D. M. Jr. Influence of ocean winds on the pelagic ecosystem in upwelling regions. *Proc. Natl Acad. Sci. USA* **105**, 1965–1970 (2008).
- Hsieh, C. H. et al. Fishing elevates variability in the abundance of exploited species. *Nature* **443**, 859–862 (2006).
- Hunter, J. R. & Lo, N. C. H. Ichthyoplankton methods for estimating fish biomass introduction and terminology. *Bull. Mar. Sci.* **53**, 723–727 (1993).
- Gunderson, D. R. *Surveys of Fisheries Resources* (John Wiley, New York, 1993).
- Hsieh, C. H. et al. A comparison of long-term trends and variability in populations of larvae of exploited and unexploited fishes in the southern California region: a community approach. *Prog. Oceanogr.* **67**, 160–185 (2005).
- Murphy, G. I. Pattern in life history and the environment. *Am. Nat.* **102**, 391–403 (1968).
- Hutchings, J. A. & Reynolds, J. D. Marine fish population collapses: consequences for recovery and extinction risk. *BioScience* **13**, 297–309 (2004).
- Hutchings, J. & Baum, J. Measuring marine fishes biodiversity: temporal changes in abundance, life history and demography. *Phil. Trans. R. Soc. B* **360**, 315–338 (2005).
- Longhurst, A. The sustainability myth. *Fish. Res.* **81**, 107–112 (2006).
- Hsieh, C. H., Reiss, S. C., Hewitt, R. P. & Sugihara, G. Spatial analysis shows fishing enhances the climatic sensitivity of marine fishes. *Can. J. Fish. Aquat. Sci.* (in the press).

18. Berkeley, S. A., Hixon, M. A., Larson, R. J. & Love, M. S. Fisheries sustainability via protection of age structure and spatial distribution of fish populations. *Fisheries* **29**, 23–32 (2004).
19. Jonzen, N., Ripa, J. & Lundberg, P. A theory of stochastic harvesting in stochastic environments. *Am. Nat.* **159**, 427–437 (2002).
20. Dixon, P. A., Milicich, M. J. & Sugihara, G. Episodic fluctuations in larval supply. *Science* **283**, 1528–1530 (1999).
21. Hsieh, C. H., Glaser, S. M., Lucas, A. J. & Sugihara, G. Distinguishing random environmental fluctuations from ecological catastrophes for the North Pacific Ocean. *Nature* **435**, 336–340 (2005).
22. Jonzen, N., Lundberg, P., Cardinale, M. & Arrhenius, F. Variable fishing mortality and the possible commercial extinction of the eastern Baltic cod. *Mar. Ecol. Prog. Ser.* **210**, 291–296 (2001).
23. Jorgensen, C. *et al.* Managing evolving fish stocks. *Science* **318**, 1247–1248 (2007).
24. Lambert, T. C. Duration and intensity of spawning in herring *Clupea harengus* as related to the age structure of the population. *Mar. Ecol. Prog. Ser.* **39**, 209–220 (1987).
25. Marteinsdottir, G. & Steinarsson, A. Maternal influence on the size and viability of Iceland cod (*Gadus morhua*) eggs and larvae. *J. Fish Biol.* **52**, 1241–1258 (1998).
26. Hutchings, J. A. & Myers, R. A. Effect of age on the seasonality of maturation and spawning of Atlantic cod, *Gadus morhua*, in the northwest Atlantic. *Can. J. Fish. Aquat. Sci.* **50**, 2468–2474 (1993).
27. Bobko, S. J. & Berkeley, S. A. Maturity, ovarian cycle, fecundity, and age-specific parturition of black rockfish (*Sebastes melanops*). *Fish. Bull.* **102**, 418–429 (2004).
28. Steele, J. H. & Henderson, E. W. Modeling long-term fluctuations in fish stocks. *Science* **224**, 985–987 (1984).
29. Sugihara, G. Nonlinear forecasting for the classification of natural time series. *Phil. Trans. R. Soc. Lond. A* **348**, 477–495 (1994).
30. Sugihara, G., Grenfell, B. & May, R. M. Distinguishing error from chaos in ecological time series. *Phil. Trans. R. Soc. Lond. B* **330**, 235–250 (1990).
31. Sugihara, G. *et al.* Residual delay maps unveil global patterns of atmospheric nonlinearity and produce improved local forecasts. *Proc. Natl Acad. Sci. USA* **96**, 14210–14215 (1999).
32. Hilborn, R. & Walters, C. J. *Quantitative Fisheries Stock Assessment: Choice, Dynamics and Uncertainty* (Chapman and Hall, New York, 1992).
33. Halley, J. M. Ecology, evolution and 1/f-noise. *Trends Ecol. Evol.* **11**, 33–37 (1996).
34. Steele, J. H. A comparison of terrestrial and marine ecological systems. *Nature* **313**, 355–358 (1985).
35. Vasseur, D. A. & Yodzis, P. The color of environmental noise. *Ecology* **85**, 1146–1152 (2004).
36. Conover, D. O. & Munch, S. B. Sustaining fisheries yields over evolutionary time scales. *Science* **297**, 94–96 (2002).
37. Kuparinen, A. & Merila, J. Detecting and managing fisheries-induced evolution. *Trends Ecol. Evol.* **22**, 652–659 (2007).
38. May, R. M. Biological populations with nonoverlapping generations: stable points, stable cycles, and chaos. *Science* **186**, 645–647 (1974).
39. Hastings, A. & Powell, T. Chaos in a three-species food chain. *Ecology* **72**, 869–903 (1991).
40. Ricker, W. E. Changes in the average size and average age of Pacific salmon. *Can. J. Fish. Aquat. Sci.* **38**, 1636–1656 (1981).
41. Harvey, C. J., Tolimieri, N. & Levin, P. S. Changes in body size, abundance, and energy allocation in rockfish assemblages of the northeast Pacific. *Ecol. Appl.* **16**, 1502–1515 (2006).
42. Armstrong, M., Dann, J. & Sullivan, K. *Programme 1: North East Cod*. Fisheries Science Partnership 2006/07 Final Report (Cefas, Lowestoft, 2006).
43. Poulsen, R. T., Cooper, A. B., Holm, P. & MacKenzie, B. R. An abundance estimate of ling (*Molva molva*) and cod (*Gadus morhua*) in the Skagerrak and the northeastern North Sea, 1872. *Fish. Res.* **87**, 196–207 (2007).
44. ICCAT. Standing Committee on Research and Statistics (ICCAT-SCRS) *Stock Status Report – Swordfish – North Atlantic* 2006 (FAO, Rome, 2006).
45. Murawski, S. A., Rago, P. J. & Trippel, E. A. Impacts of demographic variation in spawning characteristics on reference points for fishery management. *ICES J. Mar. Sci.* **58**, 1002–1014 (2001).
46. Stefansson, G. & Rosenberg, A. A. Combining control measures for more effective management of fisheries under uncertainty: quotas, effort limitation and protected areas. *Phil. Trans. R. Soc. B* **360**, 133–146 (2005).
47. Spencer, P. D., Hanselman, D. & Dorn, M. in *Biology, Assessment, and Management of North Pacific Rockfishes*. Univ. Alaska Sea Grant Program Report No. AK-SG-07-01 (eds Heifetz, J. *et al.*) 513–533 (Univ. Alaska Fairbanks, Fairbanks, Alaska, 2007).
48. Anonymous. *Alaska Groundfish Fisheries Final Programmatic Supplemental Environmental Impact Statement* (US Department of Commerce, National Oceanic and Atmospheric Administration, National Marine Fisheries Service, Alaska Region, Juneau, Alaska, 2004).
49. Sibert, J., Hampton, J., Kleiber, P. & Maunder, M. Biomass, size, and trophic status of top predators in the Pacific Ocean. *Science* **314**, 1773–1776 (2006).
50. Hsieh, C. H., Anderson, C. & Sugihara, G. Extending nonlinear analysis to short ecological time series. *Am. Nat.* **171**, 71–80 (2008).

Supplementary Information is linked to the online version of the paper at www.nature.com/nature.

Acknowledgements We acknowledge support from National Oceanic and Atmospheric Administration Fisheries and the Environment, the McQuown Chair Endowment in Natural Science, the Deutsche Bank – Jameson Complexity Studies Fund, the Sugihara Family Trust, National Science Council-Long-term Observation Research of the East China Sea, the Center for Marine Bioscience and Biotechnology, and a grant for Biodiversity Research of the 21st Century Center of Excellence at Kyoto University. M. Maunder, P. Hull, V. Dakos, S. Carpenter, J. Bascompte, M. Scheffer, C. Folke, E. H. van Nes, B. Brock, J. Murray, N. Yamamura and H.-H. Lee provided comments.

Author Contributions G.S., C.N.K.A., C.-h.H., R.M.M. and J.B. helped to frame the original research to investigate hypothesis 3. C.-h.H. and G.S. performed the initial S-map analysis on the CalCOFI data that verified hypothesis 3. C.N.K.A., with assistance from C.-h.H. and G.S., did the model analyses, statistical tests and the documentation of life-history results. All co-authors assisted with the evolution of the research plan and the refinement and final exposition of ideas.

Author Information Reprints and permissions information is available at www.nature.com/reprints. Correspondence and requests for materials should be addressed to G.S. (gsugihara@ucsd.edu).

ARTICLES

Evolvability and hierarchy in rewired bacterial gene networks

Mark Isalan¹, Caroline Lemerle², Konstantinos Michalodimitrakis¹, Carsten Horn², Pedro Beltrao², Emanuele Raineri¹, Mireia Garriga-Canut¹ & Luis Serrano¹

Sequencing DNA from several organisms has revealed that duplication and drift of existing genes have primarily moulded the contents of a given genome. Though the effect of knocking out or overexpressing a particular gene has been studied in many organisms, no study has systematically explored the effect of adding new links in a biological network. To explore network evolvability, we constructed 598 recombinations of promoters (including regulatory regions) with different transcription or σ -factor genes in *Escherichia coli*, added over a wild-type genetic background. Here we show that ~95% of new networks are tolerated by the bacteria, that very few alter growth, and that expression level correlates with factor position in the wild-type network hierarchy. Most importantly, we find that certain networks consistently survive over the wild type under various selection pressures. Therefore new links in the network are rarely a barrier for evolution and can even confer a fitness advantage.

The *E. coli* genome codes for ~300 transcription factors (TFs)^{1,2}, organized hierarchically, with few master regulators^{3–5} (Fig. 1). Only nine regulatory proteins (CRP, FNR, IHF, Fis, ArcA, NarL, H-NS, Fur and Lrp) control over half of all genes, through direct and indirect interactions^{6,7}. Lower-tier nodes are more sparsely connected and the network structure has a scale-free power-law degree distribution^{8,9}. It has been argued that such networks are particularly robust to random errors as only a few nodes are highly connected hubs, whose perturbation would affect the network drastically¹⁰. This conclusion is based on the effects of deleting or overexpressing individual nodes. However, the addition of new interactions is thought to be an equally important process for evolution, and the network responses to such changes remain to be systematically explored.

Genomes are moulded by gene duplication, transfer, mutation and loss. Duplication occurs rapidly in all species^{11,12} and through mutation serves as material for innovation. This drives cellular network evolution^{13,14}, even though relatively few duplications become fixed in populations^{11,12}. We therefore chose to reconstruct events where an open reading frame (ORF) or gene is duplicated and subsequently becomes linked to a new regulatory input. Thus, promoter region–ORF fusions were constructed on high copy number plasmids and a subset were stably integrated in the *E. coli* chromosome. Although evolution is unlikely to take such a direct approach, except in rare cases such as gene fusions in chromosomal rearrangements, our approach provides a systematic way to sample the viability of new connectivity. By adding new connections to the existing framework across different levels in the network hierarchy, including hub genes, we created a map of the network's robustness to change.

Rewired constructs and network robustness

Reconnected gene networks (598) were constructed using the genes for seven master TFs, seven σ -factors and eight downstream TFs⁵ (Fig. 1). Each construct creates network paths which inherit the inputs to the regulatory region and connect these to the downstream outputs of the ORF. As new connections are added to the wild-type network, they can generate new network motifs⁵, such as simple feedback loops. For example, if node A activates node B then a

promoter-B:ORF-A fusion gives a direct positive feedback loop (for example, *fliA–flhD*; Fig. 1). Highly complex reconnections are also possible (for example, *csgD–crp*, where four *csgD* promoter inputs—CRP, RpoS, OmpR and CsgD—are connected to CRP output, creating more than four multi-layer feedback loops).

All 598 rewired high-copy plasmids were cloned, except for ~30 which gave either zero PCR positives in three cloning attempts (Fig. 2; black boxes) or gave positive colonies that died (Fig. 2; maroon boxes). Most clones had similar growth yields (37 °C in LB media, 16 h; 6 replicates): 94% had mean A_{600} (absorbance at 600 nm wavelength) within 2 standard deviations (s.d.) of the mean of 23 control plasmid (Co) colonies. As ~95% of the rewired networks could be maintained in *E. coli*, most added connections are well tolerated. Shuffling connections at the top of the network hierarchy could cause drastic changes, therefore the cells' tolerance is striking. For example, CRP is the most connected TF in *E. coli*, directly regulating ~400 genes⁷, yet changing regulatory inputs is possible (Fig. 2; CRP columns). Similarly, σ -factors regulate transcription globally; σ^{70} and σ^{54} (RpoD and RpoN) control ~1,000 and ~100 genes, respectively⁷ and also tolerate rewiring. Such hub genes¹⁰ could have been less resilient than less-connected genes, but the bacteria can compensate. Therefore, at least when it comes to altering regulatory inputs, the hub genes do not appear to be the Achilles' heel of the network.

GFP levels and the network structure

Each construct contains a downstream GFP ORF (Fig. 1a). Thus, GFP levels indirectly measure promoter transcription for all mutants, which can be related back to network properties (Fig. 2a). Spectrophotometer assays showed that 72% expressed GFP over 2 s.d. above mean Co (background). GFP (and A_{600}) results were also similar in minimal media with glucose, lactose or maltose as the sole carbon source, and in anaerobic conditions (Supplementary Data 1). In control RT–qPCR (reverse transcription real time quantitative PCR) assays on 84 selected clones, 70% expressed ORF transcripts >12-fold over Co (mean, 520-fold; range, 0.4 to 7,700-fold; Supplementary Fig. 2). Therefore most constructs are expressed and could potentially establish new network links. As expected,

¹EMBL/CRG Systems Biology Research Unit, Centre for Genomic Regulation (CRG), UPF, 08003 Barcelona, Spain. ²EMBL, Meyerhofstrasse 1, Heidelberg D-69117, Germany.

GFP levels vary with promoter region identity (rows, Fig. 2a). Surprisingly, there are also patterns between GFP levels and ORFs (columns, Fig. 2a). Therefore many TFs have associated expression levels that are partially promoter independent.

Analysis of variance testing confirmed that column GFP means are significantly different (one-way: F value (21 degrees of freedom, d.f.) = 8.8; P value $< 2.2 \times 10^{-16}$) and that ORFs predict GFP levels better than promoters (two-way; ORFs: F value (21 d.f.) = 9.8, P value $< 2.2 \times 10^{-16}$; promoters: F value (25 d.f.) = 3.5, P value $< 5.7 \times 10^{-8}$). ORFs could set expression because each could have a particular RNA structure, affecting translation and degradation. Alternatively, the ORF TFs could be widely active, or autoregulating through ORF binding sites. The Ecocyc database¹⁵ reports self-regulation for about two-thirds of our 22 TFs, although few ORF binding sites are currently known. Nonetheless, ORFs strongly affect expression in rewired networks.

The lowest ORFs in the wild-type hierarchy often had the lowest GFP expression (Figs 1, 2). Similarly, higher-tier factors have more interactions and significantly higher GFP (Spearman's rank correlation for GFP versus interactions: $r^2 = 0.410$; $P = 0.009$); as most network connections are positive, connecting a high-tier ORF to a low-tier promoter may increase the chance of downstream interactions indirectly activating the promoter, creating positive feedback. However, the mean GFP levels for predicted direct positive and negative feedback loops (+ and – in Fig. 2a) were not significantly different (one-sided t -test: $P = 0.393$). Thus, direct feedback loops

can behave unexpectedly *in vivo*. This itself is informative, suggesting that other levels of network control can counteract direct feedback. Also, plasmid copies increase promoter concentration and thus even weak (non-physiological) TF–promoter interactions might create unpredicted loops. Overall, the results indicate a very complex rewired network response, suggesting that dissection into small network motifs may only lead to useful insights in some cases.

Growth signatures in rewired gene networks

To explore whether acquired network connections affect bacterial growth, A_{600} timecourses were measured. The A_{600} time derivative (estimated as linear regression slope for nine sequential A readings) gives a characteristic 'growth signature', reliably distinguishing between different *E. coli* strains (C.L., manuscript in preparation). Thus, growth signatures for all 598 constructs were calculated and the sums of least-squared distances ($\sum \text{l.s.d.}$), relative to mean control Co, indicate the scale of perturbations (Fig. 2b). Most constructs have little or no effect on growth: 84% are within the 95% confidence interval of 60 Co colonies ($(0-0.4) \times 10^8 A$ units²). Therefore only 16% give distinct growth phenotypes (Fig. 2c, d). Interestingly, the corresponding genome-integrated constructs have similar but milder growth signature variations, perhaps because they are expressed 150-fold less on average (Supplementary Information).

Examining the outlier growth signatures, we noticed several patterns. For example, many constructs with *ihf* A+B ORFs have much-steeper late-growth signatures with reduced late-peaks (time, ~500 min; Fig. 2d and Supplementary Information). IHF gene products mediate the switch from exponential growth into stationary phase¹⁶ and purified IHF binds to regulatory regions in stationary phase genes¹⁶. Thus the differently regulated expression of IHF in the rewired constructs may be affecting stationary phase entry. The *ihf* A+B clones were studied further using highly-detailed GFP time-courses, as developed by the Alon group; this has been achieved for 2,000 different promoters in *E. coli*, giving an unprecedented look at *E. coli* promoter activity¹⁷. GFP fluorescence dynamics show distinct expression profiles, with GFP expression peaking during stationary phase transition, and RT-qPCR analysis of different plasmid and integrated clones reveals dose-dependence of the phenotype (Supplementary Information).

To examine ORF overexpression versus rewiring effects, we cloned 21 ORFs into arabinose-inducible pBAD202 directional TOPO vector. *rpoE* did not clone in three attempts, which may reflect its apparent toxicity in certain rewired combinations. Different induced expression levels were quantitated using RT-qPCR (Supplementary Information). ORFs *ihfA+B*, *rpoD*, *fliA*, *appY* and *rpoE* show dose dependence, with higher expression being more deleterious to growth (Supplementary Data 2). Conversely, ORFs *fis*, *lrp*, *rpoS*, *rpoH*, *arcA*, *flhDC*, *malT* and *fliA* have cases where low or medium expression alters growth more in some promoter–ORF constructs, indicating a dominance of rewiring effects over high expression. ORFs *fecI*, *hns*, *fmr*, *araC*, *glnG*, *ompR* and *csgD* have very few different growth effects in all conditions. Overall, the growth phenotypes of only 7 of the 22 ORFs tested were explained primarily by overexpression effects. Growth phenotypes are ultimately a mixture of expression levels (dosage), timing and rewiring effects.

Evolvability in rewired gene networks

As most acquired network connections affect growth minimally, the first step in evolving a new network property is easily accessed. We therefore investigated whether rewired constructs themselves provide any potential for evolution. By pooling all cloned constructs (~570, plus a 23-fold molar excess of wild-type Co) and applying selective pressures, we searched for individuals with specific fitness advantages under three conditions: (1) serial passaging of bacteria in liquid culture; (2) longevity in extended periods at 37 °C; and (3) survival after 50 °C heat shock for 1 h. Serial passaging was done in seven replica flasks, transferring 1 µl of culture mixture into 120 ml

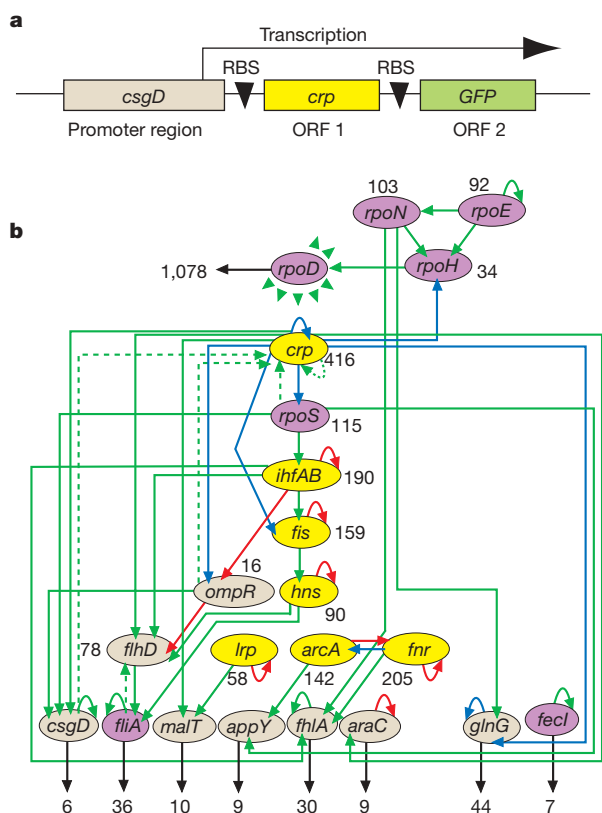


Figure 1 | Promoter–ORF network rewiring. **a**, Example of construct (*csgD*–*crpf*), with two ribosome binding sites (RBS). **b**, Network diagram of the major transcription factor and σ -factor genes used. Green, red and blue arrows denote direct activating, repressing and dual interactions, respectively, from RegulonDB^{6,7}. σ -factors, master regulators and lower-tier regulators are in purple, yellow and beige, respectively. Black numbers denote the total number of direct downstream ORF–gene interactions per node. The housekeeping σ -factor RpoD can activate all other nodes. Dotted arrows illustrate two rewired constructs (*fliA*–*flhD* and *csgD*–*crpf*); for example, CRP, RpoS, OmpR and CsgD all regulate *csgD*, thus connecting four nodes to CRP in *csgD*–*crpf*.

fresh medium, every 12–16 h. After 20 to 55 rounds, 12 network clones were repeatedly selected in independent flasks (Fig. 3a). The clones can be plotted as a ‘selectability map’ (marked ‘S’ in Fig. 2), and are associated with near-wild-type growth and low (but non-zero) GFP expression. Notably, certain *flhD* promoter–ORF combinations were enriched. *flhD* regulates flagellar genes and loss-of-function mutants increase cell division fivefold¹⁸. Flagellar genes are non-essential and cost the cell time, energy and materials. We speculate that unnaturally connected *flhD* promoters may repress flagellar biosynthesis, giving a selective advantage. Conversely, expressing FlhA flagellar σ -factor can disrupt growth (for example, *malT*–*flhA*; Fig. 2d). This correlates with flagellar biosynthesis, as 27 of the 30 largest changes in *malT*–*flhA* are upregulated flagellar or taxis genes (Supplementary Data 3). Serial passaging can select for mutations and adaptations that optimize the bacteria to their environment^{19,20}, and our results show that reconnected gene networks themselves can provide a substrate for selection.

Two further selection pressures tested the rewired networks. Stationary phase library mixtures were incubated at 37 °C, for up to 8 days, in 10 replica flasks. Alternatively, stationary cultures were heat-shocked at 42 °C (15 min) and then at 50 °C (1 h)²¹, using three rounds of heat selection, plating and harvesting. In both longevity

and heat experiments, virtually all surviving clones were *rpoS*–*ompR* (Fig. 3b, c). As other *rpoS*–promoter and *ompR*–ORF clones were never selected, it appears that both are required together. Furthermore, *rpoS*–*ompR* integrated into the bacterial chromosome is selected over wild-type in heat-shock and longevity experiments, despite much lower expression in RT-qPCR: plasmid *rpoS*–*ompR* = 650-fold over Co; integrated = 2-fold. Integrated *rpoS*–*ompR* heat selection is weaker than for plasmid (Fig. 3d, e), while longevity selection is stronger, reaching 92% after 1 week at 37 °C (Fig. 3f). By contrast, 430-fold overexpressed *ompR* ORF (in pBAD-*ompR*) is not selected over a pBAD-empty control (Fig. 3g). Therefore selection requires the rewiring combination, functioning even with low expression. While individual pressures may select for overexpression or new mutations, we have not found evidence of this. As selections were reproducible in independent tubes, and with different copy numbers, extra mutations are probably not necessary. Therefore, even in a small library space of ~600 networks, acquired connections can themselves provide specific fitness advantages.

DNA chip analysis of rewired gene networks

Affymetrix *E. coli* genome 2.0 arrays were used to get a transcriptome-wide view of rewired networks (three replicates per sample). The genes

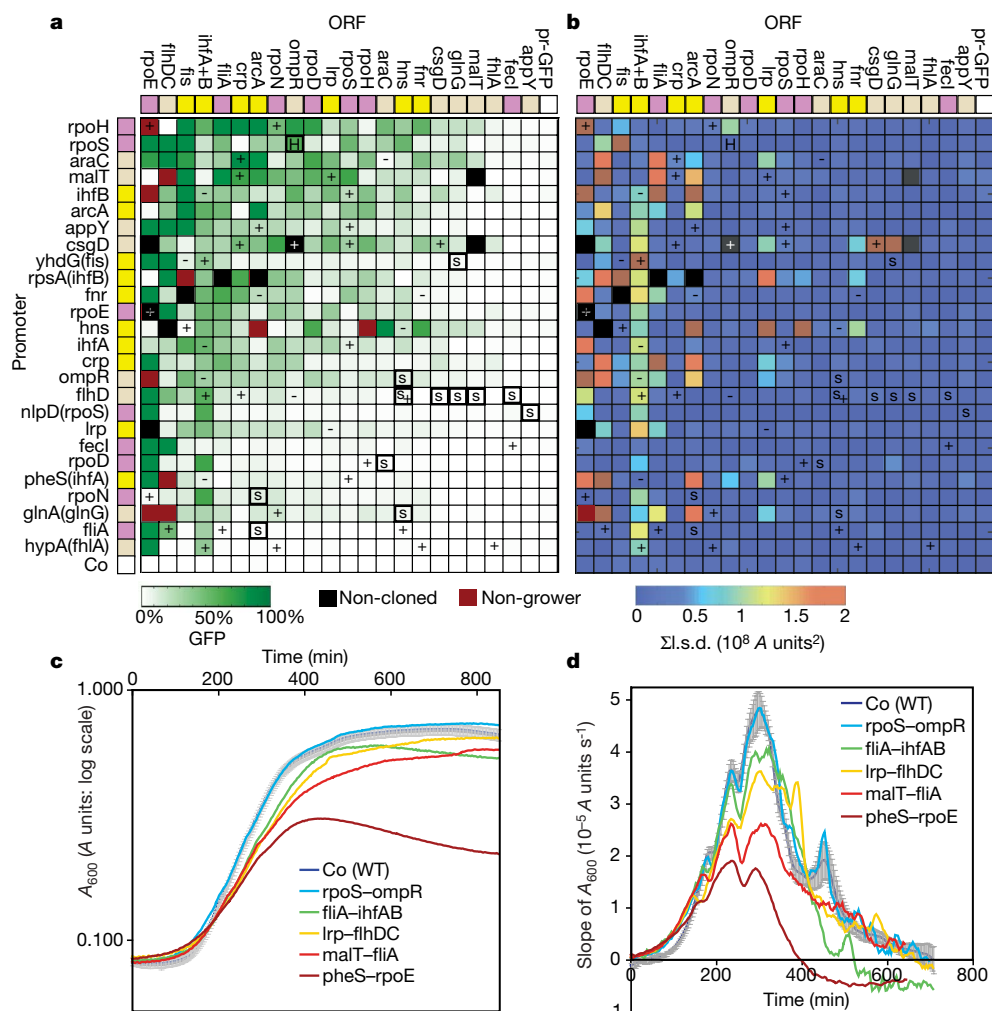


Figure 2 | GFP expression and growth signatures of promoter–ORF recombinants. σ -factors, master regulators and lower-tier regulators are in purple, yellow and beige, respectively. **a**, Green squares show mean GFP expression, ranked by columns, left-to-right, and rows, top-to-bottom (six repeats, normalized by A_{600}); non-cloned constructs are black; non-growers (maroon) vary slightly between independent colonies (panels **a** and **b**). Controls include promoter–GFP fusions (pr–GFP) and promoter-less

GFP (Co). Direct positive and negative feedback loops are marked ‘+’ or ‘–’ and selection results by ‘S’ (serial passaging) or ‘H’ (50 °C heat survival). **b**, A_{600} slopes (time-derivatives) give characteristic profiles (growth signatures), displayed by plotting the sum of least squared difference (Σ l.s.d.), relative to mean wild-type. **c**, **d**, selected growth curves (A_{600}) and signatures. Time = 0 is set at ~7 h after inoculation, removing lag phase. Error bars show 1 s.d. of 60 Co colonies.

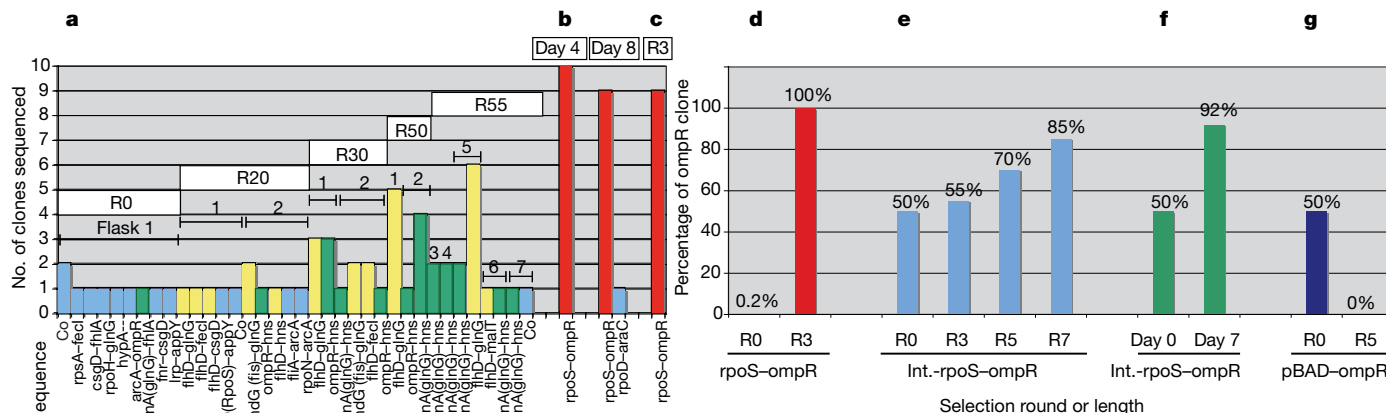


Figure 3 | Selection experiments. **a**, Serial passing of 1 μ l of culture mixture into 120 ml fresh medium, every 12–16 h. Replica flasks 1 to 7, and passage rounds R0 to R55, are indicated. Clones related to *glnA(glnG)*–*hns* (green) and *flhD–glnG* (yellow) were selected. **b**, Clones surviving stationary phase at 37 °C (day 4, day 8); *rpoS–ompR* is strongly selected (red). **c**, Clones obtained in heat survival (50 °C, 1 h) for three rounds (R3). **d**, *rpoS–ompR*

were ranked by *P* value for different expression between samples. Family-wise error rates (FWER²²) and false-discovery rates (FDR²³) measured confidence in differential expression (Table 1). Comparing *rpoS–ompR* against Co control, only 13 out of ~4,000 genes were differentially expressed with high confidence, including several up-regulated chaperone and shock genes (Table 1a; FWER < 1; <1 false positive expected). Extending the list to the 23 most significant differences yields further shock genes (FDR < 10%; 2 expected false positives). After three rounds of heat selection, 39 genes changed in

plasmid (650-fold overexpressed transcript), heat-selected over the ~570 constructs (three rounds). **e**, Integrated *rpoS–ompR* (twofold overexpressed transcript), heat-selected over integrated Co (seven rounds). **f**, Integrated *rpoS–ompR*, selected over wild-type TOP10 cells (7 days, 37 °C). **g**, *ompR* ORF in pBAD (430-fold overexpressed), is not heat-selected over pBAD vector (five rounds). **b–d**, 10 replica flasks. **e–g**, Five replica tubes, 5 PCRs per tube.

rpoS–ompR (FWER < 1), 87% being gene downregulations, including permeases (Table 1b and Supplementary Data 3). RpoS is activated in stationary phase entry, in heat stress and starvation²⁴, and positively regulates genes for acid, heat and salt tolerance^{25,26}. OmpR controls osmoregulation²⁷ and is regulated by several shock pathways to control biofilm formation^{28,29}. Furthermore, endogenous RpoS and OmpR are both positive regulators of *csg* genes, which are downstream of the *cpxA* shock signalling pathway^{30,31}. The *rpoS–ompR* survival mechanism includes chaperone and shock gene

Table 1 | DNA chip expression analysis

Rank	<i>P</i> value	FDR	FWER	+ / –	Gene	Notes
a						
1	3×10^{-13}	$10^{-7}\%$	1.1×10^{-9}	+	<i>ompR</i>	Osmotic response regulator
2	1.4×10^{-9}	$3 \times 10^{-4}\%$	5.6×10^{-6}	+	<i>nlpD</i>	Lipoprotein
3	3.1×10^{-5}	2.3%	0.13	+	<i>ycjX</i>	NTH domain
4	3.2×10^{-5}	2.3%	0.13	+	<i>ldhA</i>	D-lactate dehydrogenase
5	3.2×10^{-5}	2.3%	0.13	+	<i>dnaK</i>	*Chaperone Hsp70
6	3.4×10^{-5}	2.3%	0.14	–	<i>artM</i>	†A3T permease protein
7	5.1×10^{-5}	2.5%	0.21	+	<i>groL</i>	*GroEL, chaperone Hsp60
8	5.5×10^{-5}	2.5%	0.22	+	<i>maeB</i>	Predicted oxidoreductase
9	5.5×10^{-5}	2.5%	0.23	+	<i>dnaJ</i>	*Chaperone with DnaK; Hsp
10	7.1×10^{-5}	2.9%	0.29	+	<i>ycjF</i>	Conserved inner membrane protein
11	1.7×10^{-4}	6.2%	0.67	+	<i>clpB</i>	*Heat shock protein; Hsp
12	1.8×10^{-4}	6.2%	0.74	+	<i>htpG</i>	*Chaperone Hsp90, Hsp C 62.5
13	2.2×10^{-4}	6.7%	0.88	–	<i>artQ</i>	†A3T permease protein
14	2.5×10^{-4}	7.2%	1	+	<i>ogrK</i>	Prophage P2 OGR protein
15	2.7×10^{-4}	7.3%	1	–	<i>cspB</i>	CspB
16	3.1×10^{-4}	7.7%	1	+	<i>groS</i>	*GroES, Hsp60-binding chaperone
17	3.2×10^{-4}	7.7%	1	–	<i>yaiA</i>	ORF for hypothetical protein (hyp.)
18	3.6×10^{-4}	8.2%	1	+	<i>gntY</i>	Gluconate transport associated
19	4.0×10^{-4}	8.7%	1	+	<i>mfd</i>	*Mutation frequency decline
20	4.3×10^{-4}	8.7%	1	–	<i>cspl</i>	*Cold shock-like protein
21	4.9×10^{-4}	9.1%	1	+	<i>hmpA</i>	Dihydropteridine reductase
22	4.9×10^{-4}	9.1%	1	–	<i>bcsG</i>	*Gene involved in biofilm formation ⁴³
23	5.7×10^{-4}	9.8%	1	+	<i>hslU</i>	*Hsp hslIVU, chaperone homology
b						
1	1.1×10^{-7}	0.04%	0.0004	–	<i>gadW</i>	Regulator for acid resistance
2	2.0×10^{-7}	0.04%	0.001	–	<i>artP</i>	†A3T component
3	1.1×10^{-6}	0.1%	0.004	–	<i>artQ</i>	†A3T permease protein
4	2.2×10^{-6}	0.2%	0.009	–	<i>artM</i>	†A3T permease protein
5	6.2×10^{-6}	0.4%	0.025	–	<i>yjiO</i>	CP4-57 prophage protein (hyp.)
6	6.3×10^{-6}	0.4%	0.025	–	<i>ybcM</i>	DLP12 prophage; AraC type TF (hyp.)
7	7.4×10^{-6}	0.4%	0.030	–	<i>ygiV</i>	DNA gyrase inhibitor paralog
8	8.0×10^{-6}	0.4%	0.032	–	<i>yehZ</i>	†Osmoprotectant (permease) (hyp.)

a, List of the 23 differentially expressed genes with lowest *P* values, for *rpoS–ompR* against the control (Co). **b**, The 8 differentially expressed genes with lowest *P* values for *rpoS–ompR* (after 3 rounds of heat selection) compared against non-heat-treated *rpoS–ompR*, highlighting downregulation of arginine transport and permeases. FDR, false discovery rate; FWER, family-wise error rate; Hsp, heat shock protein; hyp., hypothetical; NTH, nucleoside triphosphate hydrolase; A3T, arginine 3rd transport system. Up- and downregulation are respectively designated by + or – in column 5. * Shock proteins. † Permease proteins.

upregulation, and permease downregulation, requiring precise expression timing and refinements after multiple rounds of heat shock.

The 'promoter-only' constructs are interesting, because high-copy promoters could titrate out factors that bind to the endogenous promoter, changing overall transcription. However, comparing the *rpoS* promoter (with GFP ORF) to Co, only three high-confidence changes were seen: *nlpD(rpoS)*, *cspB* and *ilvC* (FWER < 1). In this case, the promoter *per se* has rather little influence on the transcriptome of the cell. Unlike the relatively few changes between Co, *rpoS*, untreated *rpoS-ompR* and heat-selected *rpoS-ompR*, 359 genes were differentially expressed in *malT-flhA* versus Co (FWER < 1; Supplementary Information). This clone has a high GFP level like *rpoS-ompR* but a contrastingly altered growth signature (Fig. 2d). Therefore rewiring perturbs ~10% of genes, yet the cell remains viable. Interestingly, integrated *malT-flhA* has lower transcript expression, relative to Co (11-fold, compared with 67-fold in the plasmid), but it also has perturbed growth, albeit less pronounced (Supplementary Data 2). As >80% of constructs have near-wild-type growth characteristics, they may be much closer to the *rpoS-ompR* situation than to *malT-flhA*, with very few differentially expressed genes. In that case, the reconnected gene network, even when highly expressed, does not appear to propagate changes across the whole network.

Synthetic biology and gene networks

To understand the forces, hurdles and design principles moulding gene network evolution^{14,32–35}, we need to test our understanding by constructing synthetic model systems^{36–40}. The observations described here show that bacteria can both tolerate and exploit radical changes in their circuitry. This raises the possibility that similar experiments could be tried in other organisms, from yeast to mammals, to ascertain whether tolerance towards rewiring is a general feature of evolved biological networks. It is interesting to compare our rewiring results to those of ref. 41, when 5,280 *Saccharomyces cerevisiae* genes were overexpressed and only 15% were found to cause growth defects. The effects of rewiring (~16% growth phenotypes) include an element of dosage dependency (over-expression), but also altered timing of expression, and potentially subverting elements in more than one pathway. For *E. coli*, it is surprising that rewired clones can have such limited genome-wide transcriptional changes, indicating that bacterial networks have an in-built predisposition to dampen change. *E. coli* is a complex, tightly coordinated biological system regulated by multiple layers of molecular networks: in tampering with the transcription regulatory network alone, we learn that the static network view provides a map of poor quality to predict the result of genetic perturbations. However, some general trends are ascertainable, such as network hierarchy correlating with expression. Also, our results indicate that partition of a network into small modules (negative feedback, feed-forward, and so on) could in some cases be misleading, as the behaviour of these modules is affected to a large extent by the rest of the network in which they are embedded. The vast majority of added network connections gave no evidence of new phenotypes, even for highly connected hub genes, yet a few gave selective advantages. This pays tribute to the evolutionary potential provided to the cell by the plasticity of its genome.

METHODS SUMMARY

Cloning. The 26 promoter regions (defined as including all upstream TF binding sites annotated in Ecocyc¹⁵) were cloned with the 22 associated ORFs into pGLOW-TOPO (Invitrogen). Each construct also contained a downstream GFP ORF (with separate Shine-Dalgarno sequence). Full sequences are in Supplementary Information. For ORFs with more than one annotated promoter, both were cloned separately (for example, *rpoS* and *nlpD* promoters for *rpoS* transcription⁴²; denoted here by *nlpD(rpoS)*). *rpoD* has two promoters, and *dnaG(rpoD)* did not clone successfully. The non-expressing control plasmid (Co) contained a 66bp non-regulatory DNA sequence upstream of the promoter-less GFP ORF.

GFP measurements. Bacterial cultures (200 µl; 16 h growth) were diluted 20 µl:180 µl PBS in 96-well plates. Six independent sample readings (excitation, 485 nm; emission, 520 nm) had Co-background subtracted and were normalized for A_{600} , with a threshold to remove very low A readings (background-corrected $A_{600} < 0.03$).

Growth signatures. A quantity (0.2 µl) of 1:200-diluted overnight bacterial culture was added to 120 µl LB medium (with 100 µg ml⁻¹ ampicillin and 50 µg ml⁻¹ streptomycin) in 96-well plates. A Tecan Genios plate reader measured A_{600} (XFLUOR4 software; 37 °C; 595 nm absorbance; 3 flashes; interval 190 s; shake duration (orbital low) 130 s; 1,000 cycles, ~20 h; lids on). To avoid edge-effects, only the plates' central 60 wells were used (outer wells contained sterile medium). The assay is sensitive to volume, evaporation and lid condensation; the Tecan machine was optimal (other machines had lid effects). The slope of linear regression of the A_{600} readings, over a sliding window of nine sequential time-points, gave the growth signatures.

Integrations. About 40 representative pGLOW constructs, including Co, were integrated into the *E. coli* chromosome using *manX* locus site-directed integration (Gene Bridges Kit K006).

Selection experiments. After serial passaging, 37 °C-longevity or 50 °C-heat shock assays, samples were plated onto selective agar media and colonies were picked at random and sequenced or PCR-verified.

Full Methods and any associated references are available in the online version of the paper at www.nature.com/nature.

Received 15 December 2007; accepted 22 February 2008.

1. Blattner, F. R. *et al.* The complete genome sequence of *Escherichia coli* K-12. *Science* **277**, 1453–1474 (1997).
2. Perez-Rueda, E. & Collado-Vides, J. The repertoire of DNA-binding transcriptional regulators in *Escherichia coli* K-12. *Nucleic Acids Res.* **28**, 1838–1847 (2000).
3. Salgado, H. *et al.* RegulonDB (version 3.2): Transcriptional regulation and operon organization in *Escherichia coli* K-12. *Nucleic Acids Res.* **29**, 72–74 (2001).
4. Madan Babu, M. & Teichmann, S. A. Evolution of transcription factors and the gene regulatory network in *Escherichia coli*. *Nucleic Acids Res.* **31**, 1234–1244 (2003).
5. Shen-Orr, S. S., Milo, R., Mangan, S. & Alon, U. Network motifs in the transcriptional regulation network of *Escherichia coli*. *Nature Genet.* **31**, 64–68 (2002).
6. Martinez-Antonio, A. & Collado-Vides, J. Identifying global regulators in transcriptional regulatory networks in bacteria. *Curr. Opin. Microbiol.* **6**, 482–489 (2003).
7. Salgado, H. *et al.* RegulonDB (version 5.0): *Escherichia coli* K-12 transcriptional regulatory network, operon organization, and growth conditions. *Nucleic Acids Res.* **34**, D394–D397 (2006).
8. Barabasi, A. L. & Albert, R. Emergence of scaling in random networks. *Science* **286**, 509–512 (1999).
9. Guelzim, N., Bottani, S., Bourgine, P. & Kepes, F. Topological and causal structure of the yeast transcriptional regulatory network. *Nature Genet.* **31**, 60–63 (2002).
10. Albert, R., Jeong, H. & Barabasi, A. L. Error and attack tolerance of complex networks. *Nature* **406**, 378–382 (2000).
11. Lynch, M. & Conery, J. S. The evolutionary fate and consequences of duplicate genes. *Science* **290**, 1151–1155 (2000).
12. Hooper, S. D. & Berg, O. G. On the nature of gene innovation: Duplication patterns in microbial genomes. *Mol. Biol. Evol.* **20**, 945–954 (2003).
13. Teichmann, S. A., Park, J. & Chothia, C. Structural assignments to the *Mycoplasma genitalium* proteins show extensive gene duplications and domain rearrangements. *Proc. Natl Acad. Sci. USA* **95**, 14658–14663 (1998).
14. Teichmann, S. A. & Babu, M. M. Gene regulatory network growth by duplication. *Nature Genet.* **36**, 492–496 (2004).
15. Keseler, I. M. *et al.* EcoCyc: A comprehensive database resource for *Escherichia coli*. *Nucleic Acids Res.* **33**, D334–D337 (2005).
16. Mangan, M. W. *et al.* The integration host factor (IHF) integrates stationary-phase and virulence gene expression in *Salmonella enterica* serovar Typhimurium. *Mol. Microbiol.* **59**, 1831–1847 (2006).
17. Zaslaver, A. *et al.* A comprehensive library of fluorescent transcriptional reporters for *Escherichia coli*. *Nature Methods* **3**, 623–628 (2006).
18. Pruss, B. M. & Matsumura, P. A regulator of the flagellar regulon of *Escherichia coli*, flhD, also affects cell division. *J. Bacteriol.* **178**, 668–674 (1996).
19. Fong, S. S., Joyce, A. R. & Palsson, B. O. Parallel adaptive evolution cultures of *Escherichia coli* lead to convergent growth phenotypes with different gene expression states. *Genome Res.* **15**, 1365–1372 (2005).
20. Dekel, E. & Alon, U. Optimality and evolutionary tuning of the expression level of a protein. *Nature* **436**, 588–592 (2005).
21. Delaney, J. M., Ang, D. & Georgopoulos, C. Isolation and characterization of the *Escherichia coli* *htrD* gene, whose product is required for growth at high temperatures. *J. Bacteriol.* **174**, 1240–1247 (1992).
22. Holm, S. A simple sequentially rejective multiple test procedure. *Scand. J. Stat.* **6**, 65–70 (1979).

23. Benjamini, Y. & Hochberg, Y. Controlling the false discovery rate: A practical and powerful approach to multiple testing. *J. R. Stat. Soc. B* **57**, 289–300 (1995).
24. Loewen, P. C., Hu, B., Strutinsky, J. & Sparling, R. Regulation in the *rpoS* regulon of *Escherichia coli*. *Can. J. Microbiol.* **44**, 707–717 (1998).
25. Cheville, A. M., Arnold, K. W., Buchrieser, C., Cheng, C. M. & Kaspar, C. W. *rpoS* regulation of acid, heat, and salt tolerance in *Escherichia coli* O157:H7. *Appl. Environ. Microbiol.* **62**, 1822–1824 (1996).
26. Foster, J. W. & Moreno, M. Inducible acid tolerance mechanisms in enteric bacteria. *Novartis Found. Symp.* **221**, 55–69; discussion 70–74 (1999).
27. Pratt, L. A., Hsing, W., Gibson, K. E. & Silhavy, T. J. From acids to osmZ: Multiple factors influence synthesis of the OmpF and OmpC porins in *Escherichia coli*. *Mol. Microbiol.* **20**, 911–917 (1996).
28. Vidal, O. *et al.* Isolation of an *Escherichia coli* K-12 mutant strain able to form biofilms on inert surfaces: Involvement of a new *ompR* allele that increases curli expression. *J. Bacteriol.* **180**, 2442–2449 (1998).
29. Prigent-Combaret, C. *et al.* Complex regulatory network controls initial adhesion and biofilm formation in *Escherichia coli* via regulation of the *csgD* gene. *J. Bacteriol.* **183**, 7213–7223 (2001).
30. Cosma, C. L., Danese, P. N., Carlson, J. H., Silhavy, T. J. & Snyder, W. B. Mutational activation of the Cpx signal transduction pathway of *Escherichia coli* suppresses the toxicity conferred by certain envelope-associated stresses. *Mol. Microbiol.* **18**, 491–505 (1995).
31. Romling, U., Bian, Z., Hammar, M., Sierralta, W. D. & Normark, S. Curli fibers are highly conserved between *Salmonella typhimurium* and *Escherichia coli* with respect to operon structure and regulation. *J. Bacteriol.* **180**, 722–731 (1998).
32. Madan Babu, M., Teichmann, S. A. & Aravind, L. Evolutionary dynamics of prokaryotic transcriptional regulatory networks. *J. Mol. Biol.* **358**, 614–633 (2006).
33. Lozada-Chavez, I., Janga, S. C. & Collado-Vides, J. Bacterial regulatory networks are extremely flexible in evolution. *Nucleic Acids Res.* **34**, 3434–3445 (2006).
34. Babu, M. M., Luscombe, N. M., Aravind, L., Gerstein, M. & Teichmann, S. A. Structure and evolution of transcriptional regulatory networks. *Curr. Opin. Struct. Biol.* **14**, 283–291 (2004).
35. Poelwijk, F. J., Kiviet, D. J. & Tans, S. J. Evolutionary potential of a duplicated repressor–operator pair: Simulating pathways using mutation data. *PLoS Comput. Biol.* **2**, e58 (2006).
36. Hasty, J., McMillen, D. & Collins, J. J. Engineered gene circuits. *Nature* **420**, 224–230 (2002).
37. Elowitz, M. B. & Leibler, S. A synthetic oscillatory network of transcriptional regulators. *Nature* **403**, 335–338 (2000).
38. Gardner, T. S., Cantor, C. R. & Collins, J. J. Construction of a genetic toggle switch in *Escherichia coli*. *Nature* **403**, 339–342 (2000).
39. Isalan, M., Lemerle, C. & Serrano, L. Engineering gene networks to emulate *Drosophila* embryonic pattern formation. *PLoS Biol.* **3**, e64 (2005).
40. Isalan, M., Santori, M. I., Gonzalez, C. & Serrano, L. Localized transfection on arrays of magnetic beads coated with PCR products. *Nature Methods* **2**, 113–118 (2005).
41. Sopko, R. *et al.* Mapping pathways and phenotypes by systematic gene overexpression. *Mol. Cell* **21**, 319–330 (2006).
42. Lange, R. & Hengge-Aronis, R. The *nlpD* gene is located in an operon with *rpoS* on the *Escherichia coli* chromosome and encodes a novel lipoprotein with a potential function in cell wall formation. *Mol. Microbiol.* **13**, 733–743 (1994).
43. Solano, C. *et al.* Genetic analysis of *Salmonella enteritidis* biofilm formation: Critical role of cellulose. *Mol. Microbiol.* **43**, 793–808 (2002).

Supplementary Information is linked to the online version of the paper at www.nature.com/nature.

Acknowledgements We thank A. Martinez Arias, J. Sharpe, M. Babu, P. Bork and B. Schoenwetter for critical reading of the manuscript; P. Ribeca for RegulonDB analysis; and B. Di Ventura and S. Martinez de Pablo for cloning assistance. C.H. and E.R. were funded by European Commission FP6 Netsensor Grant 012948.

Author Contributions M.I., C.L., K.M., P.B., C.H. and M.G.-C. carried out experiments. E.R. and C.L. did computational analysis. M.I., C.L. and L.S. conceived experiments. M.I. and L.S. supervised experiments.

Author Information Microarray data are MIAME-compliant and have been deposited at ArrayExpress <http://www.ebi.ac.uk/microarray-as/aer/entry>, accession E-MEXP-732. Reprints and permissions information is available at www.nature.com/reprints. Correspondence and requests for materials should be addressed to M.I. (isalan@crg.es).

METHODS

Cloning. The 27 promoter regions and 22 ORFs were cloned from *Escherichia coli* strain Top10 (Invitrogen), using genomic PCR (DNA template extracted with a Genomic-tip 500/G (Qiagen); 1 µg per PCR). PCR conditions were typically: 97 °C, 3 min; (97 °C, 30 s; 50 °C, 30 s; 72 °C, 2 min 30 s) × 10 cycles; (97 °C, 30 s; 72 °C, 2 min 30 s) × 20 cycles. PCR products were cloned via topoisomerase then *FseI*-*PacI* cloning. Full sequences and maps are in Supplementary Information.

The promoter-less control (Co) plasmid was pGLOW-TOPO with a 66 bp DNA fragment in the TOPO cloning site: CGTCGACGTGGCGCCGCCGGATAAGGCGTTTACGTGACGGCCGCCGGGTTCTGGCTTAATTAA. This sequence was chosen empirically because it was obtained as an oligonucleotide by-product when cloning promoters into pGLOW-TOPO. The sequence contains no regulatory motifs and has no GFP-inducing activity in bacteria, as measured by fluorimetry and western blot with anti-GFP antibody.

Site-directed integration into the *E. coli* chromosome. Approximately 40 of the pGLOW constructs (representing growth phenotypes, selections and Co) were stably integrated into the *E. coli* chromosome at the *manX* locus (Gene Bridges Kit K006). The kit uses PCR to provide two 50 bp homology arms, matching the *manX* locus. Transient expression of the Red/ET recombination proteins provides a highly specific site-directed integration, which is verified by genomic PCR. The following generic primers (gel pure) amplify approximately 2.3 kb of plasmid backbone from the original pGLOW constructs (including the ampicillin resistance gene) and add *manX* homology arms: pGLOW_Amp_F, GTTGATACATGGGGAGGCAGCCCGTTCAATGCTGCCAGCCGCATTGT-CGTCGCTCAGTGGAAACGAAACTC; pGLOW_polyA_R, CGAGCATTGGAATGTAAACGCCTGCAATGACTTCATAATGCTCTTTGTCGAGCTGGTTC-TTCCGCCTCA.

Library mixtures for selections. The ~570 cloned constructs, plus 23 control (Co) samples, were inoculated from the frozen glycerol stock archive and grown in individual 200 µl wells for 16 h, as described above. The cultures were then pooled to make a library mixture. Library glycerol stocks were made by adding 4 ml of 50% glycerol to 5 ml of library culture, and storing at -80 °C.

Selection by serial passaging. 100 µl of library glycerol stock was grown in 120 ml LB medium (with 100 µg ml⁻¹ ampicillin and 50 µg ml⁻¹ streptomycin; 37 °C and orbital shaking, 300 r.p.m.). Culture samples were passaged into fresh medium every 12–16 h, in seven replica flasks; for rounds 2 and 3, 100 µl and 10 µl of culture were passaged into fresh medium, respectively; for round 4 onwards, 1 µl samples were passaged (10⁵–10⁶ c.f.u). After 20, 30, 50 and 55 rounds of passaging, samples were plated onto Petri dishes (containing 100 µg ml⁻¹ ampicillin and 50 µg ml⁻¹ streptomycin) in order to get single colonies for DNA sequencing (sequencing primers for pGLOW vector: pGLOW_TOPO_F, TGGCTAGCGTTTAACTTAAGC; pGLOW_TOPO_R, GAATTGGGACAACCTCCAGTG).

Selection by longevity in stationary phase. 1 µl of glycerol stock library mixture inoculated 2 ml LB medium (supplemented with 100 µg ml⁻¹ ampicillin and 50 µg ml⁻¹ streptomycin); 10 replica tubes; 37 °C, 300 r.p.m. After 24 h, 4 days and 8 days, 1 µl samples (diluted in 200 µl LB) were plated onto Petri dishes to get single colonies for DNA sequencing, as above.

Selection by heat shock at 50 °C. 2 ml library cultures were grown as above. 100 µl samples were then transferred to 0.2 ml PCR tubes on a PCR block, programmed to incubate at 42 °C, 15 min, 50 °C for 1 h, and then 4 °C, 5 min. 1 µl samples were immediately diluted and plated out onto Petri dishes, as above. Surviving colonies were harvested, grown to stationary phase and the entire procedure was repeated for 3 rounds. One colony was then sequenced per plate, from 10 independent selection tubes.

Affymetrix chip analysis. Sample preparation and treatment. Top10 cells containing pGLOW constructs were grown for 16 h at 37 °C (as above), diluted 1,000-fold and then grown in 5 ml (pre-warmed) LB medium for 6 h (note that cells should not be in stationary phase). 400 µl of culture was used per RNA extraction (Qiagen kit RNeasy). Absorbance measurements were taken to quantify the RNA. Aliquots were checked for RNA degradation by capillary electrophoresis. All subsequent microarray handling was carried out following Affymetrix recommendations. 15 chips (3 per sample) with MG1655 (K12) probesets (Affymetrix *E. coli* Genome 2.0 Array) were used to test the 5 bacterial populations: Co, *rpoS*—(no ORF except GFP), *rpoS*—*ompR*, *rpoS*—*ompR* after heat selection and *malT*—*fliA*. To analyse differential expression, a linear model was used through Limma software⁴⁴ and lists of probabilities of individual genes being differentially expressed were compiled. Holm family-wise error rate⁴⁵ was used to determine differential expression (FWER < 1 as cut-off: fewer than 1 false positive expected in the list of differentially expressed genes). False discovery rates⁴⁶ were used as an alternative to calculate the expected number of false positives (fewer than 1 false positive was used as a confidence cut-off to determine significant differential expression).

RT-qPCR (reverse transcription real time quantitative PCR). RNA was extracted from bacterial cultures with an RNeasy Protect Mini Kit (Qiagen). Complementary DNA was made from 500 ng total RNA, with primer p(dT)15 (Roche) and SuperScript II Reverse Transcriptase (Invitrogen). 0.2 µl cDNA, 0.3 pmol of each primer and 5 µl LightCycler 480 SYBR Green I Master mix (Roche) and a Roche Applied Science LightCycler 480 Instrument (384 wells) were used (10 µl reactions). Samples were normalized for *gnd* housekeeping gene mRNA and compared to Co expression for fold-difference calculations.

44. Smyth, G. K. Linear models and empirical Bayes methods for assessing differential expression in microarray experiments. *Stat. Appl. Genet. Mol. Biol.* **3**, article-3 (2004).
45. Holm, S. A simple sequentially rejective multiple test procedure. *Scand. J. Stat.* **6**, 65–70 (1979).
46. Benjamini, Y. & Hochberg, Y. Controlling the false discovery rate: A practical and powerful approach to multiple testing. *J. R. Stat. Soc. B* **57**, 289–300 (1995).

ARTICLES

Isolation of an active step I spliceosome and composition of its RNP core

Sergey Bessonov¹, Maria Anokhina¹, Cindy L. Will¹, Henning Urlaub² & Reinhard Lührmann¹

Formation of catalytically active RNA structures within the spliceosome requires the assistance of proteins. However, little is known about the number and nature of proteins needed to establish and maintain the spliceosome's active site. Here we affinity-purified human spliceosomal C complexes and show that they catalyse exon ligation in the absence of added factors. Comparisons of the composition of the precatalytic versus the catalytic spliceosome revealed a marked exchange of proteins during the transition from the B to the C complex, with apparent stabilization of Prp19–CDC5 complex proteins and destabilization of SF3a/b proteins. Disruption of purified C complexes led to the isolation of a salt-stable ribonucleoprotein (RNP) core that contained both splicing intermediates and U2, U5 and U6 small nuclear RNA plus predominantly U5 and human Prp19–CDC5 proteins and Prp19-related factors. Our data provide insights into the spliceosome's catalytic RNP domain and indicate a central role for the aforementioned proteins in sustaining its catalytically active structure.

Splicing of pre-messenger RNA is catalysed by the spliceosome, which consists of the U1, U2, U4/U6 and U5 snRNPs, and numerous proteins¹. During spliceosome assembly, short conserved sequences of the pre-mRNA, including the 5' and 3' splice sites and the branch point sequence (BPS) are recognized sequentially¹. Initially, the U1 and U2 snRNPs bind, forming the A complex, followed by the U4–U6.U5 tri-snRNP, generating the pre-catalytic B complex. Subsequent activation of the spliceosome entails RNP rearrangements leading to the displacement of U1 and U4 (ref. 2). The activated B* spliceosome catalyses step I of splicing, during which the branch-point adenosine attacks the 5' splice site, generating the cleaved 5' exon and intron–3'-exon lariat intermediates. The spliceosomal C complex is formed at this time and catalyses the second step of splicing, during which the intron is excised and the 5' and 3' exons are ligated to form mRNA.

A complex RNA network involving the spliceosomal small nuclear RNAs (snRNAs) and the pre-mRNA is formed during spliceosome assembly³. Initially, U1 snRNA base-pairs with the 5' splice site and U2 with the BPS. U1 is then displaced by U6, which base-pairs with the 5' splice site and also U2, and the U5 snRNA contacts the 5' exon. The resulting RNA structure, involving pre-mRNA, U2, U5 and U6, has a central role in catalysing the first step of splicing. Before the second step, additional rearrangements occur^{4,5}, but they are still not well understood.

RNA is a major component of the spliceosome's catalytic core and there is good evidence that catalysis itself is RNA based⁶. Nonetheless, establishing a catalytically active RNA network in the spliceosome requires the assistance of proteins⁷. Several proteins seem to be core components of the spliceosome. These include the following: first, Prp8, which directly contacts the 5' splice site, the BPS and the 3' splice site of the pre-mRNA⁸; second, Prp19 and a group of proteins that associate tightly with it (the 'nineteen complex' (NTC) in yeast or the Prp19–CDC5 complex in humans), which are crucial during catalytic activation^{9–13}; and third, proteins of the heteromeric SF3a and SF3b complexes, which contact the pre-mRNA at and/or upstream of the BPS, and stabilize the U2–BPS interaction^{14,15}. However, little is known about the number and nature of proteins required for maintaining a catalytically active structure in the spliceosome's core.

Purification of the B and C complexes

To identify proteins essential to the spliceosome's RNP core, we set out to isolate spliceosomes that catalyse splicing in the absence of added factors. Previously, an adenovirus-derived pre-mRNA lacking a 3' splice site and 3' exon was shown to catalyse bimolecular exon ligation (that is, step II of splicing) in nuclear extract, when offered a 3' splice-site-containing RNA *in trans*^{16,17}. To isolate catalytically active C complexes, we performed splicing *in vitro* with PM5 pre-mRNA, which contains a 60-nucleotide polypyrimidine tract but no terminal AG dinucleotide and no 3' exon (Fig. 1a). When incubated under splicing conditions with HeLa nuclear extract, PM5 underwent 5' splice site cleavage and intron lariat formation but no exon ligation (Fig. 1b), and initially B complexes and later C complexes were efficiently formed (Fig. 1c). After allowing C complexes to form on the PM5 substrate, an

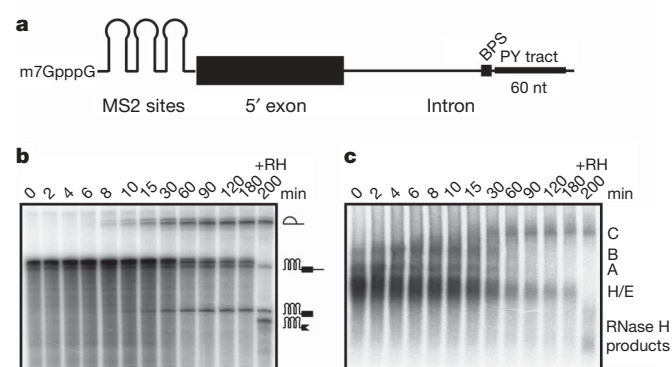


Figure 1 | Splicing of PM5 pre-mRNA lacking a 3' splice site and 3' exon. **a**, Diagram of PM5 pre-mRNA. PY, polypyrimidine tract; nt, nucleotides. **b**, **c**, Kinetics of *in vitro* splicing and splicing complex formation with PM5 pre-mRNA. Splicing was performed in HeLa nuclear extract for 0–180 min, followed by digestion with RNase H (RH) (right-hand lane). **b**, RNA was analysed by denaturing PAGE; **c**, splicing complexes were analysed on an agarose gel. The positions of the pre-mRNA, splicing intermediates and RH digestion product(s) and the H, A, B and C complexes are indicated on the right.

¹Department of Cellular Biochemistry, and ²Bioanalytical Mass Spectrometry Group, Max Planck Institute of Biophysical Chemistry, D-37077 Göttingen, Germany.

RNA with the sequence 5'-GACAG-3', where AG represents the 3' splice site, followed by a 55-nucleotide adenovirus-derived 3' exon¹⁶ (Fig. 2a) was added to the splicing reaction. To control for proper 3' splice site recognition, an identical RNA with an AG to GG mutation (5'-GACGG-3' exon), which should lead to the use of the downstream, proximal-most AG dinucleotide¹⁶, was added alternatively. Northern blotting revealed the generation of mRNA products of the expected size with both 3' splice-site-containing RNAs, showing that spliceosomes formed on PM5 can catalyse bimolecular exon ligation (Fig. 2b). No mRNA product was observed if C complexes were not allowed to form, and sequencing after RT-PCR confirmed that splicing occurred at the expected 3' splice site in each case (data not shown).

The coliphage coat protein MS2 was used to affinity purify both B and C complexes formed on the PM5 substrate; purification was performed under identical, physiological conditions. Affinity-purified B complexes contained nearly equimolar amounts of U1, U2, U4, U5 and U6 snRNA together with unspliced pre-mRNA (Fig. 3a, lanes 1 and 3). Purified C complexes, in contrast, contained nearly equimolar amounts of U2, U5 and U6 plus first-step intermediates (that is, the excised 5' exon and the intron lariat) and only small amounts of unspliced pre-mRNA (Fig. 3a, lanes 2 and 4). Thus, highly pure complexes were isolated in each case.

Purified C complexes are active

To determine whether affinity-purified C complexes are active, we performed bimolecular exon ligation assays in the presence or

absence of micrococcal nuclease (MN)-treated nuclear extract. Exon ligation was observed at an efficiency comparable to that of non-purified complexes both in the presence of MN-treated nuclear extract (Fig. 2c, lanes 1 and 2) and, more strikingly, even in its absence (Fig. 2c, lanes 3 and 4). Mutation of the 3' splice site to GG also led to the expected switch in 3' splice site use. Note that the mRNA doublet seen with both 3' substrate RNAs is due to 3' end heterogeneity and not incorrect 3' splice site use (data not shown). Bimolecular exon ligation with purified C complexes was most efficient when performed in the presence of ATP in comparison with other NTPs, and less efficient in the presence of non-hydrolysable (AMP-PNP) or slowly hydrolyzable (ATP- γ S) ATP analogues (Fig. 2d). This represents the first instance where affinity-purified, non-immobilized spliceosomal complexes on their own could be shown to possess catalytic activity, and thus indicates that our affinity-purified C complexes contain all the factors necessary for step II of splicing.

Protein dynamics of the B to C transition

Proteins present in affinity-purified C, and also B, complexes were separated by SDS-PAGE (Fig. 3b) and identified by mass spectrometry (MS) (Supplementary Tables 1 and 2). MS consistently identified about 130 proteins in B complexes, the vast majority of which had previously been found in B complexes formed on an adenovirus-derived pre-mRNA¹⁸. Affinity-purified C complexes contained about 150 proteins, about 105 of which were also consistently found in B complexes. Proteins shared by both complexes include most proteins associated with U5 and U2 snRNPs, the Prp19-CDC5 protein complex and related factors, and components of the RES (retention and splicing) complex. Several proteins are lost during the B to C transition—that is, they are found solely or predominantly in B complexes—as shown by immunoblotting (see below) and the number of peptides sequenced by MS. Although not strictly quantitative, a comparison of the number of peptides identified is a good indication of the relative amounts of a protein present in two different samples when they are directly, sequentially analysed. Proteins lost or highly underrepresented in C complexes include almost all U1 and U4

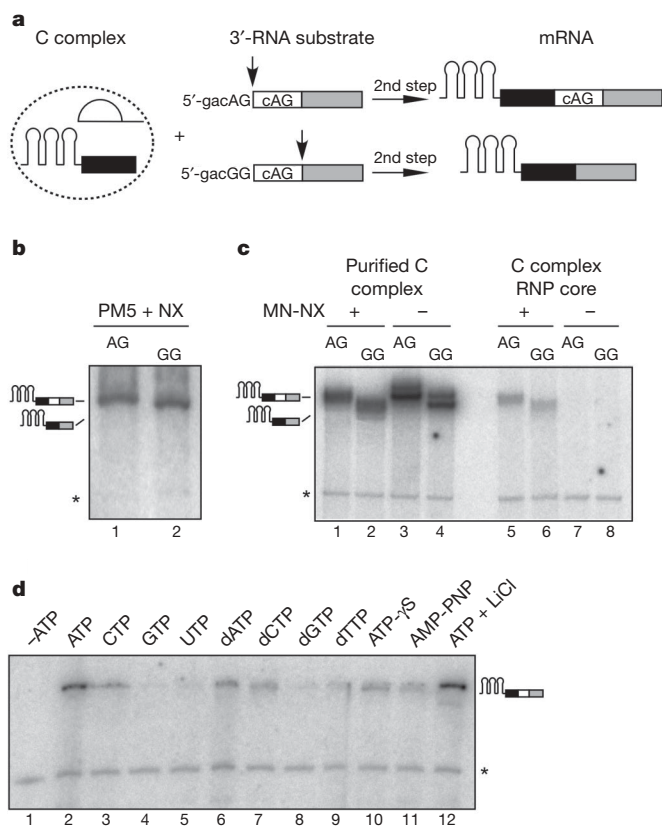


Figure 2 | Affinity-purified C complexes catalyse bimolecular exon ligation on their own. **a**, Diagram of 3' substrate RNAs and mRNA products of bimolecular exon ligation. Arrow, expected 3' splice site cleavage site. **b–d**, Bimolecular exon ligation with PM5 pre-mRNA in nuclear extract (NX) (**b**), with purified C complexes or salt-treated C-complex RNP cores with or without MN-treated NX, and AG or GG 3' RNAs (**c**), or with purified C complexes and indicated nucleotides plus AG 3' RNA (**d**). Exon ligation was monitored by northern blotting with a 3' RNA probe. Asterisk, ³²P-labelled, excised 5' exon (C complex loading control).

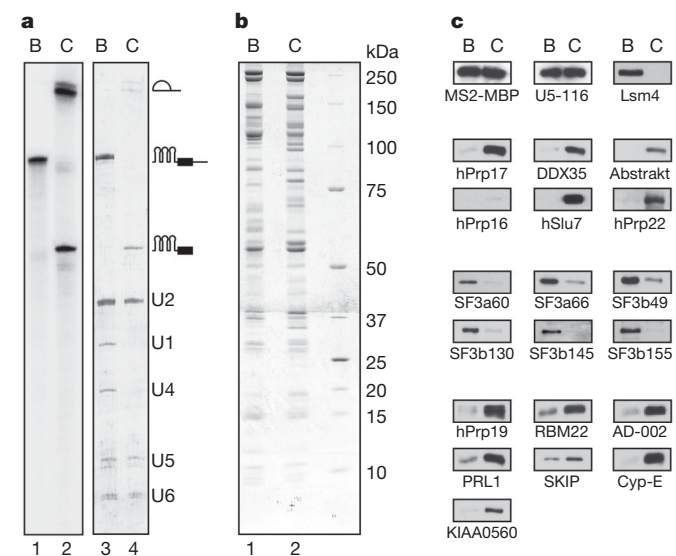


Figure 3 | Characterization of MS2 affinity-purified B and C complexes. **a**, RNA composition of MS2 affinity-purified B (lanes 1 and 3) and C (lanes 2 and 4) complexes. RNA was analysed by denaturing PAGE and detected by silver staining (lanes 1 and 2) or by autoradiography (lanes 3 and 4). RNA identities are indicated at the right. **b**, Protein composition of purified B (lane 1) and C (lane 2) complexes. Proteins were separated by SDS-PAGE and detected by staining with Coomassie blue. **c**, Protein composition of B or C complexes as revealed by immunoblotting with the indicated antibodies.

proteins, the U6 Lsm proteins, and several non-snRNP factors. Immunoprecipitation studies in yeast indicated that the Lsm proteins are destabilized during spliceosome activation, thereby allowing the 3' end of U6 to base pair with the 5' splice site¹². Our data provide direct evidence that human Lsm proteins are also destabilized or lost during the B to C transition, indicating that this important remodelling event is conserved among eukaryotes.

Several proteins were found solely or predominantly in C complexes and are thus recruited during catalytic activation or step I of splicing. These included most second-step factors, the DEAD-box helicases Abstrakt and DDX35, and the peptidyl-prolyl isomerases (PPIases) PPIL3b, PPWD1 and PPIG. Thus, one or more of these helicases or PPIases might facilitate conformational changes accompanying step II of splicing. Finally, most core components of the exon junction complex (for example, eIF4A3, Magoh and Y14) seemed to be enriched in C complexes.

To determine the absence or presence of selected proteins, we also performed immunoblotting (Fig. 3c). Antibodies against either U5–116K, a core component of B and C complexes, or the fusion protein of MS2 with maltose-binding protein (MBP) confirmed that comparable amounts of both complexes were analysed. Consistent with our MS results, Lsm4 was detected solely in B complexes, whereas the step II factors human Prp22 (hPrp22) and hSlu7, together with DDX35 and Abstrakt, were found exclusively in C complexes. Only trace amounts of hPrp16 were detected in C complexes. Because the latter catalyse exon ligation on their own, they might be stalled at a stage after hPrp16 has acted or, alternatively, the small amounts of Prp16 still present might be sufficient for step II.

More peptides were sequenced by MS for most proteins comprising the Prp19–CDC5 complex and for Prp19–CDC5-related proteins in the C versus the B complex (Supplementary Table 1). Consistent with this observation, more intense immunostaining of Prp19, RBM22, AD002, PRL1, SKIP, Cyp-E and KIAA0560 was observed with C complexes (Fig. 3c). Thus, Prp19 and related proteins seem to be enriched in C complexes, suggesting that they are more stably associated at this stage. In contrast, fewer peptides were consistently identified by MS for proteins comprising SF3a and SF3b in the C

versus the B complex (Supplementary Table 1). Immunoblotting with antibodies against various SF3a/b proteins confirmed that they are much less abundant in the C complex (Fig. 3c). Thus, SF3a/b components seem to be destabilized during the B to C transition (and are therefore lost more readily during purification). The apparent destabilization or loss of SF3a/b proteins, and stabilization of Prp19–CDC5 proteins, indicates that protein–protein and/or protein–RNA contacts involving these proteins are remodelled before or during step I of splicing.

Proteins in the spliceosome's RNP core

To determine which proteins are required for maintenance of the catalytically active RNA network in the step I spliceosome, purified C complexes were subjected to increasing concentrations of NaCl up to 1 M, followed by glycerol-gradient centrifugation. Complexes treated with 1 M salt sedimented as a single RNP peak, as determined by the distribution of ³²P-labelled RNA across the gradient (Fig. 4a). Only trace amounts of radiolabelled RNA were detected at the top of the gradient, indicating that nearly all of the excised 5' exon and lariat intron remained associated with this RNP complex. Gradient fractions 13–15 (RNP peak) contained nearly equimolar amounts of both first-step intermediates, as well as the U2, U5 and U6 snRNAs (Fig. 4b, c), suggesting that relatively homogeneous (at least at the RNA level), intact RNP particles are still present after salt treatment. In contrast, although native B and C complexes have almost identical S values (data not shown), the vast majority of B complexes treated with 1 M salt sedimented much more slowly than the salt-stable RNP cores of the C complex (Fig. 4a), indicating that the former dissociate. Thus, catalytic activation of the spliceosome seems to lead to a generally more stable core RNP conformation, suggesting that protein–RNA and protein–protein contacts in the B-complex and C-complex cores must differ.

Salt-treated C complexes had a slightly lower S value (Fig. 4e) than native complexes, which is consistent with the dissociation of a subset of proteins. We therefore analysed the protein composition of gradient fractions 13–15 containing the salt-resistant RNP complex and also gradient fractions 1–5, which should contain dissociated

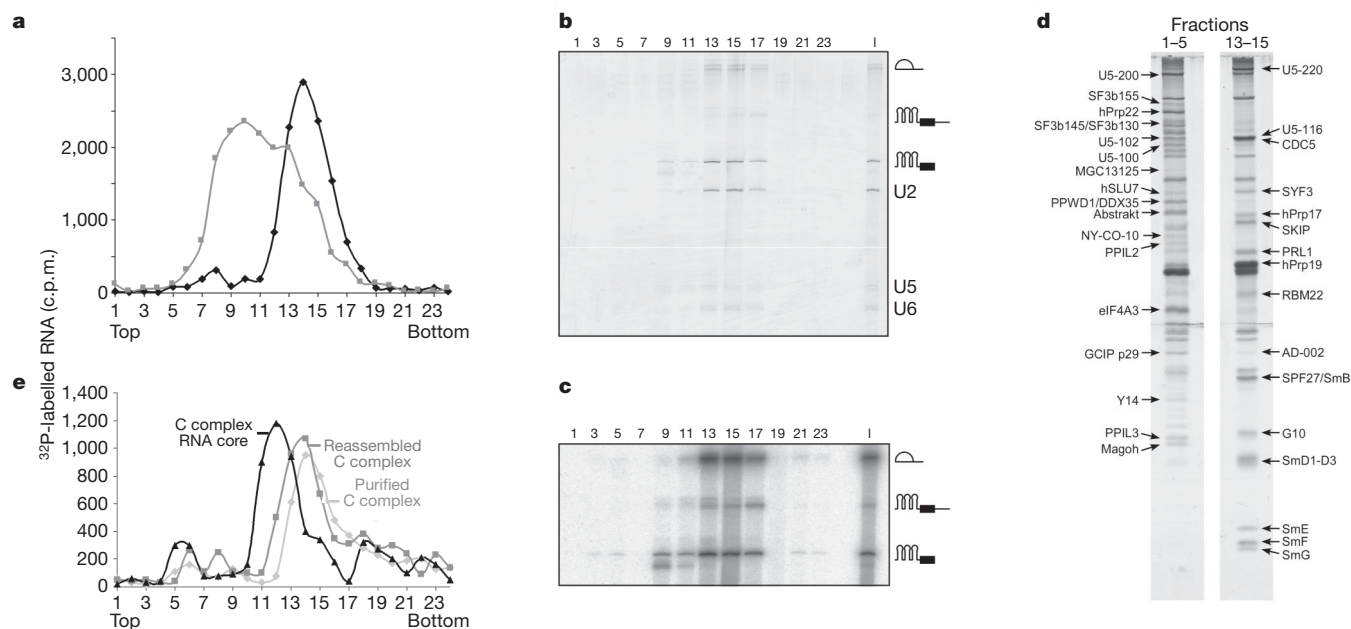


Figure 4 | U5- and Prp19–CDC5-proteins remain associated with C-complex RNP cores. **a**, Affinity-purified C complexes (black diamonds) or B complexes (grey squares) treated with 1 M NaCl and separated on glycerol gradients containing 1 M NaCl. **b**, **c**, RNA from salt-treated C complex gradient fractions, detected by silver staining (**b**) or autoradiography (**c**). I, 10% of input. **d**, Salt-treated C-complex proteins from gradient fractions 1–5 or 13–15, separated by SDS–PAGE and stained with silver. A subset of proteins exclusively or predominantly dissociated (right) or present in RNP cores (left) are indicated. **e**, Sedimentation of purified C complexes, C-complex RNP cores, and reassembled C complexes on glycerol gradients.

proteins (Fig. 4d). Proteins were separated by SDS-PAGE and analysed by MS (Supplementary Table 1). Visual comparison of the band patterns of the RNP peak with top gradient fractions reveals clear differences in their compositions. The peak contains predominantly Prp19 complex proteins and Prp19-related factors (for example, hPrp19, CDC5, hSyf3 SKIP, Prl1, RBM22, AD002 and G10) as well as the U5–220, U5–116 and U5–40K proteins, which form a highly stable heteromeric complex in higher eukaryotes¹⁹. Altogether, 37 proteins were predominantly or exclusively present in the salt-resistant RNP core complex as determined by band intensity and/or the number of peptides sequenced by MS (Supplementary Table 1), suggesting that they are tightly incorporated components of the C complex and are crucial for maintaining its catalytically active RNA network. Other proteins were found in apparently similar amounts in both fractions, whereas most, such as proteins of the exon junction complex and step II factors such as hPrp22 and hSlu7, or components of SF3a/b, were found exclusively or predominantly at the top of the gradient. These proteins therefore do not seem to be required for maintaining the RNP core of the C complex.

In contrast with C complexes isolated under physiological conditions, 1 M salt-treated C-complex cores did not support bimolecular exon ligation on their own (Fig. 2c, lanes 7 and 8). However, exon ligation was observed when the C-complex cores were supplemented with MN-digested nuclear extract, although at a lower efficiency than that observed with native C complexes (Fig. 2c, compare lanes 1 and 2 with lanes 5 and 6). Thus, the RNP core probably lacks one or more proteins required for exon ligation, but its RNA and RNP networks nonetheless remain relatively intact. C complexes incubated with MN-treated nuclear extract (reassembled C complexes) sedimented faster than salt-treated RNP cores on glycerol gradients (Fig. 4e), with an S value only slightly smaller than that of native C complexes, indicating that several proteins reassociated.

Concluding remarks

Here we have purified mammalian spliceosomes that are catalytically active on their own. This was a key step towards identifying proteins involved in stabilizing the spliceosome's catalytically active RNA network. We show that there is a large exchange of proteins during the B to C complex transition when the active site of the spliceosome is formed. Proteins comprising the heteromeric SF3a and SF3b complexes were largely underrepresented in purified C versus B complexes, suggesting that they are destabilized before or during the first catalytic step of splicing. Before the second step, the branch adenosine is probably removed from the active site of the spliceosome and replaced with the 3' splice site, which serves as the nucleophile for the second step of splicing. A recent report indicates that, in yeast, step II of splicing can proceed in the absence of U2–BPS base pairing²⁰. Thus, whereas SF3a and SF3b are essential early in the splicing reaction, they may not be required after the first catalytic step. SF3a and SF3b were for the most part absent from the salt-resistant RNP core of the C complex, raising the question of what stabilizes the association of U2 in this complex.

In contrast with SF3a/b, Prp19–CDC5 and related proteins seemed to be more stably associated in C complexes. Indeed, they, together with U5 proteins, remained associated with the pre-mRNA splicing intermediates and the U2, U5 and U6 snRNAs on treatment of purified C complexes with high salt concentrations. The presence of most human homologues of NTC proteins in the salt-stable C complex RNP core is consistent with studies in yeast demonstrating that the NTC is required for stable association of U5 and U6 with the pre-mRNA after U1 and U4 have dissociated¹². Our data additionally point to potential contributions by other Prp19-related proteins that are not part of the core Prp19–CDC5 complex, in stabilizing the catalytically active RNA structures in step I spliceosomes. The presence of hPrp8 in the salt-resistant C-complex core is also consistent with a wealth of data demonstrating that hPrp8 contacts all reactive groups of the pre-mRNA and supports the idea that it acts as a

cofactor during splicing catalysis²¹. The protein composition of the salt-stable C-complex core is highly similar to that of the human 35S U5 snRNP. This supports our previous hypothesis that the latter represents a remodelled form of U5 that is generated during spliceosome activation and is released after exon ligation as a post-spliceosomal complex²².

The ability to isolate active human C complexes and their stable RNP cores is an important step towards establishing the three-dimensional architecture of the spliceosome's RNP core. Our purified C complexes can be used to determine the structure of catalytically active spliceosomes poised for step II of splicing, either by electron microscopy or by structure probing methods. Salt-stable C-complex cores may be used in the future to identify proteins involved in catalytic step II, and also to study their interaction partners within the spliceosome. Similarly, as a result of their apparent high stability, they may ultimately be suitable for high-resolution structural studies, including X-ray crystallography.

METHODS SUMMARY

In vitro splicing. ³²P-labelled PM5 pre-mRNA was synthesized *in vitro*, and splicing was performed *in vitro* with HeLa nuclear extract²³. RNA was separated on an 8.0 M urea–10% polyacrylamide gel. Splicing complexes were analysed on agarose gels²⁴.

MS2 affinity selection and immunoblotting. MS2 affinity selection was performed as described previously¹⁸ except that an excess of DNA oligonucleotide complementary to nucleotides –6 to –18 relative to the 5' splice site was added after splicing and the reaction was incubated at 30 °C for a further 2 min (B complex) or 20 min (C complex) before glycerol-gradient centrifugation. Proteins were separated by SDS-PAGE, transferred to Hybond P membrane and immunostained with an enhanced chemiluminescence detection kit.

Mass spectrometry. Proteins were identified by liquid chromatography–tandem mass spectrometry (LC–MS/MS) after separation by SDS-PAGE as described previously¹⁸.

Bimolecular exon ligation. An excess of 3' substrate RNA was added after splicing for 180 min with PM5 substrate, and the mixture was incubated for 30 min. Alternatively, purified C complex or C-complex RNP cores were incubated for 30 min under standard splicing conditions with 3' substrate RNA. Generation of a ³²P-labelled DNA probe against the 3' substrate RNA and subsequent northern blotting were performed as described²⁵.

Isolation of C-complex RNP cores and reassembled C complexes. Purified C complexes were incubated in buffer containing 1 M NaCl and subjected to glycerol-gradient centrifugation in the presence of 1 M NaCl. For functional assays, C complexes bound to amylose beads were washed with buffer containing first 1 M NaCl, followed by 150 mM KCl (G-150). Complexes were then eluted with maltose (to generate C-complex RNP cores) or incubated with MN-treated nuclear extract and then eluted to yield reassembled C complexes. Complexes were subjected to glycerol-gradient centrifugation in the presence of G-150 buffer.

Full Methods and any associated references are available in the online version of the paper at www.nature.com/nature.

Received 11 December 2007; accepted 19 February 2008.

Published online 5 March 2008.

- Will, C. L. & Lührmann, R. in *The RNA World* (eds Gesteland, R. F., Cech, T. R. & Atkins, J. F.) 369–400 (Cold Spring Harbor Laboratory Press, Cold Spring Harbor, NY, 2006).
- Staley, J. P. & Guthrie, C. Mechanical devices of the spliceosome: motors, clocks, springs, and things. *Cell* **92**, 315–326 (1998).
- Nilsen, T. W. in *RNA Structure and Function* (eds Grundberg-Manago, M. & Simons, R. W.) 279–307 (Cold Spring Harbor Laboratory Press, Cold Spring Harbor, NY, 1998).
- Umen, J. G. & Guthrie, C. The second catalytic step of pre-mRNA splicing. *RNA* **1**, 869–885 (1995).
- Konarska, M. M., Vilarde, J. & Query, C. C. Repositioning of the reaction intermediate within the catalytic center of the spliceosome. *Mol. Cell* **21**, 543–553 (2006).
- Valadkhan, S. & Manley, J. L. Splicing-related catalysis by protein-free snRNAs. *Nature* **413**, 701–707 (2001).
- Will, C. L. & Lührmann, R. Protein functions in pre-mRNA splicing. *Curr. Opin. Cell Biol.* **9**, 320–328 (1997).
- Grainger, R. J. & Beggs, J. D. Prp8 protein: at the heart of the spliceosome. *RNA* **11**, 533–557 (2005).

9. Tarn, W. Y., Lee, K. R. & Cheng, S. C. Yeast precursor mRNA processing protein PRP19 associates with the spliceosome concomitant with or just after dissociation of U4 small nuclear RNA. *Proc. Natl Acad. Sci. USA* **90**, 10821–10825 (1993).
10. Tarn, W. Y. *et al.* Functional association of essential splicing factor(s) with PRP19 in a protein complex. *EMBO J.* **13**, 2421–2431 (1994).
11. Ajuh, P. *et al.* Functional analysis of the human CDC5L complex and identification of its components by mass spectrometry. *EMBO J.* **19**, 6569–6581 (2000).
12. Chan, S. P., Kao, D. I., Tsai, W. Y. & Cheng, S. C. The Prp19p-associated complex in spliceosome activation. *Science* **302**, 279–282 (2003).
13. Makarova, O. V. *et al.* A subset of human 35S U5 proteins, including Prp19, function prior to catalytic step 1 of splicing. *EMBO J.* **23**, 2381–2391 (2004).
14. Gozani, O., Feld, R. & Reed, R. Evidence that sequence-independent binding of highly conserved U2 snRNP proteins upstream of the branch site is required for assembly of spliceosomal complex A. *Genes Dev.* **10**, 233–243 (1996).
15. Will, C. L. *et al.* A novel U2 and U11/U12 snRNP protein that associates with the pre-mRNA branch site. *EMBO J.* **20**, 4536–4546 (2001).
16. Anderson, K. & Moore, M. J. Bimolecular exon ligation by the human spliceosome. *Science* **276**, 1712–1716 (1997).
17. Anderson, K. & Moore, M. J. Bimolecular exon ligation by the human spliceosome bypasses early 3' splice site AG recognition and requires NTP hydrolysis. *RNA* **6**, 16–25 (2000).
18. Deckert, J. *et al.* Protein composition and electron microscopy structure of affinity-purified human spliceosomal B complexes isolated under physiological conditions. *Mol. Cell. Biol.* **26**, 5528–5543 (2006).
19. Achsel, T., Ahrens, K., Brahms, H., Teigelkamp, S. & Lührmann, R. The human U5–220kD protein (hPrp8) forms a stable RNA-free complex with several U5-specific proteins, including an RNA unwindase, a homologue of ribosomal elongation factor EF-2, and a novel WD-40 protein. *Mol. Cell. Biol.* **18**, 6756–6766 (1998).
20. Smith, D. J., Query, C. C. & Konarska, M. M. Trans-splicing to spliceosomal U2 snRNA suggests disruption of branch site-U2 pairing during pre-mRNA splicing. *Mol. Cell* **26**, 883–890 (2007).
21. Collins, C. A. & Guthrie, C. The question remains: is the spliceosome a ribozyme? *Nature Struct. Biol.* **7**, 850–854 (2000).
22. Makarov, E. M. *et al.* Small nuclear ribonucleoprotein remodelling during catalytic activation of the spliceosome. *Science* **298**, 2205–2208 (2002).
23. Dignam, J. D., Lebovitz, R. M. & Roeder, R. G. Accurate transcription initiation by RNA polymerase II in a soluble extract from isolated mammalian nuclei. *Nucleic Acids Res.* **11**, 1475–1489 (1983).
24. Das, R. & Reed, R. Resolution of the mammalian E complex and the ATP-dependent spliceosomal complexes on native agarose mini-gels. *RNA* **5**, 1504–1508 (1999).
25. Hartmuth, K. *et al.* Protein composition of human prespliceosomes isolated by a tobramycin affinity-selection method. *Proc. Natl Acad. Sci. USA* **99**, 16719–16724 (2002).

Supplementary Information is linked to the online version of the paper at www.nature.com/nature.

Acknowledgements We thank T. Conrad, P. Kemkes, H. Kohansal and I. Öchsner for technical assistance; M. Raabe and U. Plessmann for their help in MS analysis; E. Makarov for raising anti-peptide antibodies; and C. Smith for providing the PYP pre-mRNA. This work was supported by grants from the Deutsche Forschungsgemeinschaft, EURASNET, the Fonds der Chemischen Industrie and the Ernst Jung Stiftung to R.L., and a Young Investigator Programme grant from EURASNET to H.U.

Author Contributions S.B., M.A., H.U. and R.L. designed experiments; S.B., M.A. and H.U. performed the experiments; S.B., M.A., C. L.W., H.U. and R.L. analysed the data; and S.B., C. L.W., H.U. and R.L. wrote the paper.

Author Information Reprints and permissions information is available at www.nature.com/reprints. Correspondence and requests for materials should be addressed to R.L. (reinhard.luehrmann@mpi-bpc.mpg.de).

METHODS

In vitro splicing and native gel analysis. MS2-binding sites were introduced at the 5' end of the PYP pre-mRNA substrate²⁶ by standard PCR techniques, and uniformly ³²P-labelled, m7G(5')ppp(5')G-capped PM5 premRNA was synthesized *in vitro* by SP6 runoff transcription. Standard *in vitro* splicing reactions contained 50% (v/v) HeLa nuclear extract prepared as described previously²³, 65 mM KCl, 3 mM MgCl₂, 2 mM ATP, 20 mM creatine phosphate and 30 nM ³²P-labelled PM5 pre-mRNA, and were incubated for 0–180 min at 30 °C. RNA was recovered and separated on an 8.0 M urea–10% polyacrylamide gel. For analysis of spliceosome assembly, 0.5 µl of heparin (5 mg ml⁻¹) was added to 20-µl aliquots of the splicing reaction at a given time, and splicing complexes were separated on a 2% native agarose gel²⁴.

MS2 affinity selection of spliceosomal B and C complexes. PM5 pre-mRNA was incubated with a 20-fold molar excess of purified MS2-MBP fusion protein¹⁸ and a 12-ml standard splicing reaction containing 10 nM (B complex) or 30 nM (C complex) ³²P-labelled pre-mRNA was incubated for 6 min (B complex) or 180 min (C complex). A 30-fold molar excess of DNA oligonucleotide complementary to nucleotides –6 to –18 relative to the 5' splice site was added and the reaction was incubated at 30 °C for a further 2 min (B complex) or 20 min (C complex). Complexes were separated on 10–30% glycerol gradients in the presence of 150 mM KCl, and 40–45S gradient fractions were subjected to affinity selection on amylose beads as described previously¹⁸. RNA was recovered from the eluted B or C complexes, analysed on a 8.0 M urea–10% polyacrylamide gel, and detected by silver staining and autoradiography. The stoichiometry of the snRNAs and pre-mRNA/splicing intermediates was determined by visual inspection of the silver-stained bands, taking into consideration the length of the individual RNAs. Protein was recovered, separated by 8%/14% step-gel SDS-PAGE and stained with Coomassie blue.

Immunoblotting. Proteins were separated by SDS-PAGE on an 8% or 12% polyacrylamide gel, transferred to Hybond P membrane and immunostained with an enhanced chemiluminescence detection kit (Pierce). Antibodies against the following proteins were used: MS2-MBP (Abcam); U5–116K (ref. 13), Lsm4 (ref. 13), hPrp19 (ref. 13), AD002 (ref. 13), KIAA0560 (ref. 13), SKIP (ref. 13), SF3a66 (ref. 15), SF3b155 (ref. 15), SF3b145 (ref. 27), SF3b130 (ref. 27), SF3b49 (ref. 27) and SF3a60 (ref. 27); RBM22 (raised against residues 179–195), hPrp22 (residues 1116–1130), hSlu7 (residues 562–577), hPrp17 (residues 92–107), hPrp16 (residues 193–207), DDX35 (residues 392–409), Abstrakt (residues 608–622), Cyp-E (residues 104–118) and Prl1 (residues 60–74).

Mass spectrometry. For MS, proteins recovered from purified B and C complexes (about 4 pmol) were separated by SDS-PAGE and stained with Coomassie blue. Entire lanes were cut into 60–70 slices and proteins were digested in-gel with trypsin and extracted as described previously¹⁸. For MS of salt-treated core complexes, proteins from the top gradient fractions or RNP peak fractions were separated by SDS-PAGE and stained with silver. For direct comparison, single bands and gel regions of the same height in both lanes of the gel were excised and the proteins therein were digested with trypsin and extracted. Peptides were analysed in an LC-coupled electrospray ionization quadrupole time-of-flight

mass spectrometer (QToF Ultima; Waters) and/or a linear ion-trap mass spectrometer (4000 QTrap; Applied Biosystems) under standard conditions. Proteins were identified by searching fragment spectra against the National Centre for Biotechnology Information non-redundant database, using Mascot as search engine. Mass accuracy was 200 p.p.m. for the parent ion (MS) and 200 milli-mass units (mmu) for the fragment ions (MS/MS) when samples were analysed by Q-ToF MS, and 1.4 Da and 400 mmu, respectively, for samples analysed on the linear ion trap. Peptides were constrained to be tryptic with a maximum of one missed cleavage site. Carbamidomethylation of cysteine residues and oxidation of methionine residues were considered as variable modifications. The highest-scoring peptide from each protein, as well as single-hit peptides, were inspected manually to eliminate any false positives in the data set. The overall numbers of sequenced peptides were counted and only fragment spectra with an ion score above 30 (Mascot) were included.

Bimolecular exon ligation. 3' substrate RNAs used in bimolecular exon ligation assays were generated by *in vitro* SP6 runoff transcription. To assay for bimolecular exon ligation in nuclear extract, 10 pmol of 3' substrate RNA were added after splicing for 180 min with 1.5 pmol of PM5 substrate (at this time point about 0.15 pmol of excised 5' exon are formed), and the reaction (50 µl) was incubated for a further 30 min. Alternatively, 0.3 pmol of either purified C complex or C-complex core RNP were incubated for 30 min under standard splicing conditions (see above) with 10 pmol of 3' substrate RNA. MN-treated nuclear extract (20% of total reaction) was added as indicated. RNA was recovered and separated on an 8.0 M urea–10% polyacrylamide gel and transferred to Hybond XL membrane. Northern blotting and the generation of a ³²P-labelled DNA probe against the 3' substrate RNA were performed as described previously²⁵.

Isolation of salt-stable C-complex RNP cores and reassembled C complexes. Purified C complexes were incubated on ice for 15 min in G buffer (20 mM Hepes pH 7.9, 1.5 mM MgCl₂) containing 1 M NaCl and then subjected to 10–30% glycerol-gradient centrifugation (150 min at 490,000g; Sorvall TH660 rotor) in the presence of 1 M NaCl. The distribution of ³²P-labelled RNA across the gradient was determined by Cherenkov counting in a scintillation counter. RNA and protein were analysed as described above. For functional assays, C complexes bound to amylose beads were washed with 20 column volumes of G buffer containing 1 M NaCl at 4 °C, followed by G buffer containing 150 mM KCl (G-150). Complexes were then either eluted with maltose (to generate C-complex RNP cores) or were first incubated at 4 °C for 30 min with MN-treated nuclear extract in G buffer containing 125 mM KCl and 0.1 mM EDTA, washed with 75 volumes of G-150 buffer, and then eluted (to yield reassembled C complexes). To compare their S values, complexes were subjected to 10–30% glycerol-gradient centrifugation (90 min at 490,000g; TH660 rotor) in the presence of G-150 buffer.

26. Wollerton, M. C., Gooding, C., Wagner, E. J., Garcia-Blanco, M. A. & Smith, C. W. Autoregulation of polypyrimidine tract binding protein by alternative splicing leading to nonsense-mediated decay. *Mol. Cell* **13**, 91–100 (2006).
27. Dybkov, O. *et al.* U2 snRNA-protein contacts in purified human 17S U2 snRNPs and in spliceosomal A and B complexes. *Mol. Cell. Biol.* **26**, 2803–2816 (2006).

A massive binary black-hole system in OJ 287 and a test of general relativity

M. J. Valtonen¹, H. J. Lehto¹, K. Nilsson¹, J. Heidt², L. O. Takalo¹, A. Sillanpää¹, C. Villforth¹, M. Kidger³, G. Poyner⁴, T. Pursimo⁵, S. Zola^{6,7}, J.-H. Wu⁸, X. Zhou⁸, K. Sadakane⁹, M. Drozd⁷, D. Koziel⁶, D. Marchev¹⁰, W. Ogloza⁷, C. Porowski⁶, M. Siwak⁶, G. Stachowski⁷, M. Winiarski⁶, V.-P. Hentunen¹¹, M. Nissinen¹¹, A. Liakos¹² & S. Dogru¹³

Tests of Einstein's general theory of relativity have mostly been carried out in weak gravitational fields where the space-time curvature effects are first-order deviations from Newton's theory¹⁻⁶. Binary pulsars⁴ provide a means of probing the strong gravitational field around a neutron star, but strong-field effects may be best tested in systems containing black holes^{7,8}. Here we report such a test in a close binary system of two candidate black holes in the quasar OJ 287. This quasar shows quasi-periodic optical outbursts at 12-year intervals, with two outburst peaks per interval^{9,10}. The latest outburst occurred in September 2007, within a day of the time predicted by the binary black-hole model and general relativity¹¹. The observations confirm the binary nature of the system and also provide evidence for the loss of orbital energy in agreement (within 10 per cent) with the emission of gravitational waves from the system¹². In the absence of gravitational wave emission the outburst would have happened 20 days later¹³.

The quasar OJ 287 has been observed optically since the late nineteenth century, but was identified as a quasar only in 1968. This quasar is of great interest because it shows a quasi-periodic pattern of prominent outbursts; these consist of 11 well-recognized outbursts and several probable outbursts, all observed before 2007¹⁴ (see the Supplementary Information for the full light curve). Because the outbursts seem to come in pairs separated by one to two years, and the pairs occur about 12 years apart, we proposed a model in which a secondary body (a black hole) pierces the accretion disk of the primary black hole and produces two impact flashes per period¹⁰. Alternative models attribute the observed behaviour to oscillations in an accretion disk¹⁵ or a jet¹⁶ of a single black hole, or to variations of the accretion rate in a disk⁹ or a wobble of a jet¹⁷ in a binary black hole system. However, these processes do not produce the sharp flashes that we consider here¹⁴. The consequences our model has for jet emission, the primary emission mode, have been calculated in several papers^{14,18}. Here we concentrate on the optical flashes associated with disk impacts. We treat them as time signals that tell us how the secondary moves around the primary in its near-keplerian orbit.

Apart from the 12-year quasi-periodicity, the most prominent bright outbursts do not repeat themselves in any easily recognizable pattern. However, the following mathematical formula gives the times of all the outburst peaks observed during the twentieth century¹⁰: take a keplerian orbit with post-newtonian corrections and assume that an outburst happens at a constant phase angle as well as

at the same phase angle plus 180°. This provides a well-defined mathematical series of outburst times. Although the series cannot be represented by a closed-form mathematical function (the same is true of the original Kepler problem), the times in the series are quickly calculable by computer. If the orbit is eccentric, there is a pair of outburst times that are close to each other relative to the orbital period.

Assuming that the constant phase angle is provided by the secondary passing through the accretion disk of the primary, the orbit can be reconstructed by using all the available information on past outbursts and straightforward astrophysics. For any general sequence of quasi-random times, there is unlikely to be a solution. There is an algorithm that converges to a solution of orbital elements if a solution exists¹³. Non-precessing orbits can be rejected immediately; no solution exists for such orbits. This is promising because, even at first order in general relativity, the major axis of the orbit must precess. Deviations of as little as a few weeks from the observed outburst times also result in insolubility. Thus, the observed sequence of outburst times is quite particular, and unlikely to arise by chance, as has been demonstrated quantitatively¹⁹.

The complete solution of the problem requires a light curve coverage of six well-defined outbursts. When the method was first applied¹⁰ there existed only four such peaks. It was not until early 2007 that there were enough data to calculate a definite orbit¹¹. The precession rate of the major axis of this orbit is 39.0° per orbit, the eccentricity of the orbit is 0.663 and the mass of the primary is 18.0×10^9 solar masses. These values are reasonable: merging binaries are expected to have eccentricities similar to this at intermediate stages of evolution²⁰, and the mass of the black hole is at the upper end of the mass range in quasars²¹ (which is encouraging, as OJ 287 is among the brightest quasars).

The first test of the orbit solution took place in September 2007, when the second peak of one of the double peaks was due to appear. The date predicted by the model was September 13 plus or minus two days. One of the sources of uncertainty in the prediction comes from the zero-point error in timing the beginning of the 1983 outburst, generally taken to be 1983.00. This figure is the fiducial time that is used in the models to compare the beginning times of different outbursts. On the basis of a light curve fit such as that shown in Fig. 1, this error is about one day. A similar error arises from the variation of orbital parameters within the range allowed by the relative timing of

¹Department of Physics and Tuorla Observatory, University of Turku, Vaisälantie 20, FI-21500 Piikkiö, Finland. ²Landessternwarte Heidelberg, Königstuhl, 69117 Heidelberg, Germany. ³Herschel Science Centre, European Space Astronomy Centre, European Space Agency, Villafraanca del Castillo Satellite Tracking Station, PO Box 78, 28691 Villanueva de la Canada, Madrid, Spain, and INSA, Paseo del Pintor Rosales 34, 28008 Madrid, Spain. ⁴British Astronomical Association Variable Star Section, 67 Ellerton Road, Kingstanding, Birmingham B44 0QE, UK. ⁵Nordic Optical Telescope, Apartado 474, E-38700 S/C de La Palma, Spain. ⁶Astronomical Observatory of the Jagiellonian University, ul. Orla 171, 30-224 Cracow, Poland. ⁷Mt. Suhora Observatory, Pedagogical University, ul. Podchorznych 2, 30-084 Cracow, Poland. ⁸National Astronomical Observatories, Chinese Academy of Sciences, 20A Datun Road, Beijing 100012, China. ⁹Astronomical Institute, Osaka-Kyoku University, Asahigaoka, Kashiwara, Osaka 582-8582, Japan. ¹⁰Department of Physics, Shoumen University, 9700 Shoumen, Bulgaria. ¹¹Warkauden Kassiopeia ry, Härkämäentie 88, 79480 Kangaslampi, Finland. ¹²Department of Astrophysics, Astronomy and Mechanics, Faculty of Physics, University of Athens, Panepistimiopolis, GR-15784 Zografos, Athens, Greece. ¹³Canakkale Onsekiz Mart University, Faculty of Physics, TR-17020 Canakkale, Turkey.

different outbursts. A third source of error is related to uncertainties in the model, in particular to the effects of accretion disk bending¹³. This effect is small for the 2007 impact, being also of the order of one day. Thus, the various sources of error contribute an uncertainty of about two days in the timing of the 2007 optical flash.

The date of September 13 is important in other respects also: if the system does not lose energy by emission of gravitational radiation, and thus the orbit does not shrink, the outburst times are delayed. In 2007 September the delay between an orbit of constant semi-major axis and an orbit shrinking by emission of gravitational radiation was 20 days; that is, the two solutions of the post-newtonian Kepler equation differed by this amount. This is a test of general relativity that was first suggested in 1997¹², and can now be performed.

The difference between the two cases would be easily resolvable in monitoring observations if there were enough observers in different parts of the world to cover the nights missed owing to unpredictable

circumstances at any one observatory. The main difficulty was the actual season; the outburst could have started at any time after September 11. Because OJ 287 undergoes conjunction with the Sun only a month before this, it is a very difficult object to observe during this season. Moreover, many telescopes do not turn close enough to the horizon to start monitoring OJ 287 in early September. Here we report results of OJ 287 monitoring between 2007 September 4 and 2007 October 20.

A total of 100 photometric observations of OJ 287 were obtained between 2007 September 4 and 2007 October 20, as shown in Fig. 2. We see that there were several outbursts from OJ 287 during this period. This is as expected, on the basis of calculations of the light curve for the 2005–2007 outburst season¹⁸. The 2005 outburst was both observed and predicted to be somewhat isolated^{22,23}, whereas the

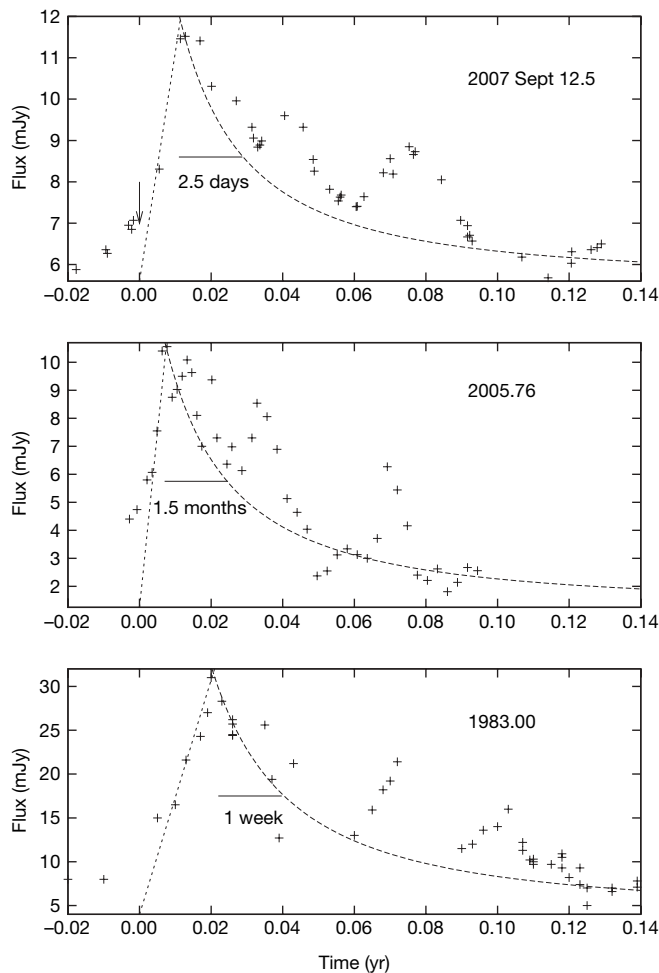


Figure 1 | Optical V-band fluxes of OJ 287 versus time in relative units. The dashed lines show the theoretical predictions¹⁰. The horizontal axis displays time in years for 1983; the zero point corresponds to 1983.00. The time given in the upper right-hand corner of each panel indicates the nominal starting time of the outburst, that is, when the dashed line crosses the time axis. For the 2007 outburst the timescale has been stretched by a factor of 2.65, and for the 2005 outburst, contracted by a factor of 7.16, so that the intrinsically different decay timescales can be shown on the same scale. The timescales are different because the speed of impact, and consequently the internal sound speed of the radiating bubble, varies with impact distance. The impact distance from the primary black hole was 13,300 AU in 2005, 4,800 AU in 1983 and 3,400 AU in 2007. The arrow in the top panel points to the inferred origin of the outburst at 12:00 UT on 2007 September 12. The next observation after this was taken at 6:00 UT on September 13, close to the predicted starting time of the outburst. In each panel, the horizontal line segment indicates the decay timescale.

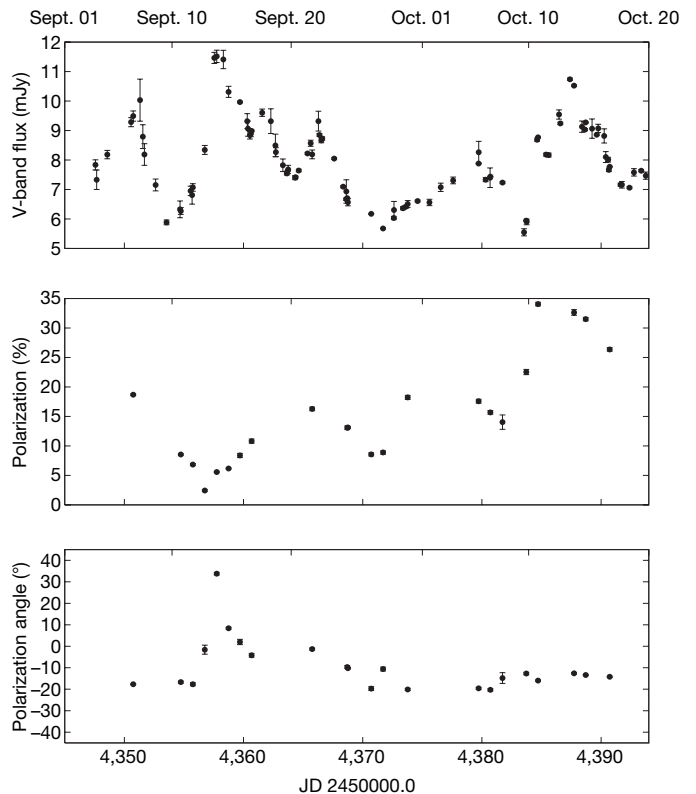


Figure 2 | Optical photometry and polarimetry of OJ 287 in September–October, 2007. The top panel shows data transformed to the V band, whereas the polarization data in the two lower panels are in the R band. The majority (93) of the 100 observations were made in the R band using 11 optical telescopes, of aperture sizes of 30–256 cm, in the Canary Islands, Europe, China and Japan. The observations were made in differential mode, that is, by obtaining charged-coupled-device images of OJ 287 and comparing the object's brightness to calibrated comparison stars in its field. The comparison sequence in ref. 26 was used, with star four as the primary reference. Star ten was used to check for offsets between different telescopes, caused, for example, by a non-standard filter band pass. In some cases offsets were found, but they were very small (<0.03 mag) and the magnitudes of OJ 287 have been corrected for this offset. The magnitudes were transformed to the V band using $V - R = 0.4$. Finally, the V-band magnitudes were converted to linear fluxes using the formula $F = 3,640 \times 10^{-0.4V}$ Jy. We also collected 21 polarimetric observations in the R band using the 2.56-m Nordic Optical Telescope in La Palma and the Calar Alto 2.2-m telescope in Spain. All data were obtained using instruments employing a half-wave plate to rotate the direction of polarization and a calcite crystal to separate the incoming light into ordinary and extraordinary beams. This effectively cancelled out any instrumental effects and the background polarization. The instrumental polarization was checked using zero-polarization stars and was found to be negligible. The polarization angle was calibrated using highly polarized stars, with published polarization values. The s.e.m. is shown by the error bars. Often it is smaller than the representative point.

2007 outburst was expected to be embedded in a series of outbursts of about equal brightness. The impact outburst we discuss here was expected to be the first outburst in the sequence, but not necessarily the brightest. For the purposes of our model it is important to identify the correct outburst in September 2007, by comparing the outbursts both with each other and with previous outbursts of the same nature.

The outburst beginning at September 12 was the brightest recorded during our period of observation. Thus, of those outbursts early in the sequence, this is the most promising one. One outburst was observed earlier, reaching its maximum brightness around September 8, and is clearly smaller than the outburst of September 12. However, maximal brightness alone is not a sufficient criterion to identify the impact outburst.

Another discriminant is the detailed light curve; the timescale of the outburst was calculated to be three days at the half-maximum, and there was a $-3/2$ -power-law decay in brightness due to adiabatic energy losses¹⁰. At the impact of the secondary on the accretion disk, a hot bubble of gas is extracted from the disk²⁴ and expands at its internal sound speed. Once the bubble has expanded to the point at which it becomes optically thin, there is a burst of radiation. The radiation fades away with further expansion of the bubble. The time of rise to the maximum flux can be very rapid near the peak, as it is related to the travel time of light through the radiating region when it becomes fully transparent. The September 12 outburst fits this description very well, whereas the other outbursts do not. Figure 1 illustrates the light curves of major 1983, 2005 and 2007 outbursts, assuming that the September 12 outburst is identified as the impact flash.

A third identifying characteristic of the impact outburst involves polarization data. The 1983 outburst is the only one for which polarization measurements have been made frequently throughout the whole outburst event, from the flux rise to its decay. In 1983 the degree of polarization dropped rapidly during the flux rise²⁵. This is also expected theoretically¹⁴. In contrast, the polarization usually rises during the outburst, as our light curve for October 10–16 demonstrates. As Fig. 2 shows, the September 12 outburst was most similar to the 1983 outburst in this respect also.

As evidence for gravitational waves in the OJ 287 binary we note that the model without gravitational waves predicts an outburst in 2007 that takes place about 20 days later than it does in the standard model. As the outburst occurred as expected, we must conclude that gravitational waves are the most probable cause of the shortening of the orbital period, and that the strength of the radiation is at the expected level with a timing accuracy of about two days out of 20; that is, the energy flux does not deviate from the value calculated using general relativity by more than 10%. In principle we could improve the prediction once future outbursts have been observed and the orbit model further improved.

However, if gravitational radiation were to follow general relativity but the second-order precession term were missing, the outburst would occur ten days earlier than was observed. Thus, the space-time curvature appears at second order as general relativity predicts. The precision of this test is two days out of 10, that is, 20%. The next major periodic outburst is expected in early January 2016, by which time there may be methods to measure the gravitational waves directly.

Received 1 December 2007; accepted 6 March 2008.

1. Misner, C. W., Thorne, K. S. & Wheeler, J. A. *Gravitation* (Freeman, San Francisco, 1973).

2. Pound, R. V. & Rebka, G. A. Gravitational redshift in nuclear resonance. *Phys. Rev. Lett.* **3**, 439–441 (1959).
3. Taylor, J. H. & Weisberg, J. M. Further experimental tests of relativistic gravity using the binary pulsar PSR1913+16. *Astrophys. J.* **345**, 434–450 (1989).
4. Hulse, R. A. The discovery of the binary pulsar. *Rev. Mod. Phys.* **66**, 699–710 (1994).
5. Walsh, D., Carswell, R. F. & Weymann, R. J. 0957 + 561 A, B: twin quasistellar objects or gravitational lens? *Nature* **279**, 381–384 (1979).
6. Ciufolini, I. & Pavlis, E. C. A confirmation of the general relativistic prediction of the Lense–Thirring effect. *Nature* **431**, 958–960 (2004).
7. Cui, W., Zhang, S. N. & Chen, W. Evidence for frame dragging around spinning black holes in X-ray binaries. *Astrophys. J.* **492**, L53–L57 (1998).
8. Bromley, B. C., Miller, W. A. & Pariev, V. I. The inner edge of the accretion disk around a supermassive black hole. *Nature* **391**, 54–56 (1998).
9. Sillanpää, A., Haara, S., Valtonen, M. J., Sundelius, B. & Byrd, G. G. OJ287 – Binary pair of supermassive black holes. *Astrophys. J.* **325**, 628–634 (1988).
10. Lehto, H. J. & Valtonen, M. J. OJ287 outburst structure and a binary black hole model. *Astrophys. J.* **460**, 207–213 (1996).
11. Valtonen, M. J. OJ287: A binary black hole system. *Rev. Mex. Astron. Astrofis. Conf. Ser.* (in the press).
12. Valtonen, M. J. & Lehto, H. J. Outbursts in OJ287: A new test for the General Theory of Relativity. *Astrophys. J.* **481**, L5–L7 (1997).
13. Valtonen, M. J. New orbit solutions for the precessing binary black hole model of OJ287. *Astrophys. J.* **659**, 1074–1081 (2007).
14. Valtonen, M. J. *et al.* Predicting the next outbursts of OJ287 in 2006–2010. *Astrophys. J.* **646**, 36–48 (2006).
15. Igumenshchev, I. V. & Abramowicz, M. A. Rotating accretion flows around black holes: convection and variability. *Mon. Not. R. Astron. Soc.* **303**, 309–320 (1999).
16. Hughes, P. A., Aller, H. D. & Aller, M. F. Extraordinary activity in the BL Lacertae object OJ287. *Astrophys. J.* **503**, 662–673 (1998).
17. Katz, J. I. A precessing disk in OJ287? *Astrophys. J.* **478**, 527–529 (1997).
18. Sundelius, B., Wahde, H., Lehto, H. J. & Valtonen, M. J. A numerical simulation of the brightness variations of OJ287. *Astrophys. J.* **484**, 180–185 (1997).
19. Pietilä, H. Possibilities and predictions of the OJ287 binary black hole model. *Astrophys. J.* **508**, 669–675 (1998).
20. Aarseth, S. J. Dancing with black holes, in *Dynamical Evolution of Dense Stellar Systems* (eds Vesperini, E., Gierz, M. & Sills, A.) (Proc. IAU Symp. 246, Cambridge Univ. Press, Cambridge, in the press); preprint at (<http://arxiv.org/abs/0710.0585>) (2007).
21. Vestergaard, M., Fan, X., Tremonti, C. A., Osmer, P. S. & Richards, G. T. Mass function of the active black holes in distant quasars from the Sloan Digital Sky Survey data release 3. *Astrophys. J.* **674**, L1–L4 (2008); preprint at (<http://arxiv.org/abs/0801.0243>) (2008).
22. Valtonen, M. J. *et al.* The 2005 November outburst in OJ287 and the binary black hole model. *Astrophys. J.* **643**, L9–L12 (2006).
23. Valtonen, M. J., Kidger, M., Lehto, H. J. & Poyner, G. The structure of the October/November 2005 outburst in OJ287 and the precessing binary black hole model. *Astron. Astrophys.* **477**, 407–412 (2008).
24. Ivanov, P. B., Igumenshchev, I. V. & Novikov, I. D. Hydrodynamics of black hole – accretion disk collision. *Astrophys. J.* **507**, 131–144 (1998).
25. Smith, P. S., Balonek, T. J., Elston, R. & Heckert, P. A. Optical and near-infrared observations of BL Lacertae objects and active quasars. *Astrophys. J. Suppl. Ser.* **64**, 459–485 (1987).
26. Fiorucci, M. & Tosti, G. VRI photometry of stars in the fields of 12 BL Lacertae objects. *Astron. Astrophys. Suppl. Ser.* **116**, 403–407 (1996).

Supplementary Information is linked to the online version of the paper at www.nature.com/nature.

Acknowledgements This work is supported by the European community (project ENIGMA), the German Science Foundation, the Japanese Ministry of Education, Culture, Sports, Science and Technology, the Chinese Academy of Sciences, the Chinese National Natural Science Foundation, the Finnish Society of Sciences and Letters, the Finnish Academy of Science and Letters, the Jenny and Antti Wihuri Foundation, the Development Association Mansikka ry, and the municipality of Varkaus.

Author Contributions M.J.V. and H.J.L. were responsible for the interpretation of the data, K.N. and J.H. organized the observational fieldwork, and the other authors contributed data points.

Author Information Reprints and permissions information is available at www.nature.com/reprints. Correspondence and requests for materials should be addressed to M.J.V. (mvaltonen2001@yahoo.com).

LETTERS

Thermalization and its mechanism for generic isolated quantum systems

Marcos Rigol^{1,2}, Vanja Dunjko^{1,2} & Maxim Olshanii²

An understanding of the temporal evolution of isolated many-body quantum systems has long been elusive. Recently, meaningful experimental studies^{1,2} of the problem have become possible, stimulating theoretical interest^{3–7}. In generic isolated systems, non-equilibrium dynamics is expected^{8,9} to result in thermalization: a relaxation to states in which the values of macroscopic quantities are stationary, universal with respect to widely differing initial conditions, and predictable using statistical mechanics. However, it is not obvious what feature of many-body quantum mechanics makes quantum thermalization possible in a sense analogous to that in which dynamical chaos makes classical thermalization possible¹⁰. For example, dynamical chaos itself cannot occur in an isolated quantum system, in which the time evolution is linear and the spectrum is discrete¹¹. Some recent studies^{4,5} even suggest that statistical mechanics may give incorrect predictions for the outcomes of relaxation in such systems. Here we demonstrate that a generic isolated quantum many-body system does relax to a state well described by the standard statistical-mechanical prescription. Moreover, we show that time evolution itself plays a merely auxiliary role in relaxation, and that thermalization instead happens at the level of individual eigenstates, as first proposed by Deutsch¹² and Srednicki¹³. A striking consequence of this eigenstate-thermalization scenario, confirmed for our system, is that knowledge of a single many-body eigenstate is sufficient to compute thermal averages—any eigenstate in the microcanonical energy window will do, because they all give the same result.

If we pierce an inflated balloon inside a vacuum chamber, very soon we find that the released air has uniformly filled the enclosure and that the air molecules have attained the Maxwell velocity distribution, the width of which depends only on the total number and energy of the air molecules. Different balloon shapes, placements, or piercing points all lead to the same spatial and velocity distributions. Classical physics explains this ‘thermodynamical universality’ as follows¹⁰: almost all particle trajectories quickly begin to look alike, even if their initial points are very different, because nonlinear equations drive them to explore the constant-energy manifold ergodically, covering it uniformly with respect to precisely the microcanonical measure. However, if the system possesses further conserved quantities that are functionally independent of the hamiltonian and each other, then time evolution is confined to a highly restricted hypersurface of the energy manifold. Hence, microcanonical predictions fail and the system does not thermalize.

In contrast, in isolated quantum systems not only is dynamical chaos absent owing to the linearity of time evolution and the discreteness of spectra¹¹, but also it is not clear under what conditions conserved quantities provide independent constraints on the relaxation dynamics. On the one hand, any operator commuting with a generic, and thus non-degenerate, hamiltonian is functionally

dependent on it¹⁴, seemingly implying that conservation of energy is the only independent constraint. On the other hand, even when operators are functionally dependent, their expectation values—considered as functionals of states—generally are not: for example, two states may have the same mean energies but different means of squared energies. For non-degenerate hamiltonians a maximal set of constants of motion with functionally independent expectation values is as large as the dimension of the Hilbert space; examples include the projectors $\hat{P}_\alpha = |\Psi_\alpha\rangle\langle\Psi_\alpha|$ to the energy eigenstates¹⁴ and the integer powers of the hamiltonian⁵.

The current numerical and analytic evidence from the study of integrable systems suggests that there exists a minimal set of independent constraints the size of which is much less than the dimension of the Hilbert space but may still be much greater than one. In previous work³ we showed that an isolated integrable one-dimensional system of lattice hard-core bosons relaxes to an equilibrium characterized not by the usual Gibbs ensemble but by a generalized Gibbs ensemble. Instead of just the energy, the Gibbs exponent contains a linear combination of conserved quantities—the occupation numbers of the eigenstates of the corresponding Jordan–Wigner fermions—the number of which is still only a tiny fraction of the dimension of the Hilbert space. Yet this ensemble works, although the usual one does not, for a wide variety of initial conditions¹⁵ as well as for a fermionic system¹⁶; it also explains a recent experimental result, the absence of thermalization in the Tonks–Girardeau gas¹. Thus, although at least some constraints other than the conservation of energy must be kept, it turns out that only a relatively limited number of additional conserved quantities with functionally independent expectation values are needed; adding further ones is redundant.

As it is not clear which sets of conserved quantities—and some are always present—constrain relaxation and which do not, it becomes even more urgent to determine whether or not generic isolated quantum systems relax to the usual thermal state. This question has received increased theoretical attention recently, because of the high levels of isolation^{1,2,17} and control^{18,19} possible in experiments with ultracold quantum gases. However, despite numerous studies of specific models, there is not yet consensus on how or even whether relaxation to the usual thermal values occurs for non-integrable systems⁷. The conventional wisdom is that it does^{8,9}, but some recent numerical results indicate otherwise, either under certain conditions⁴ or in general⁵.

To study relaxation of an isolated quantum system, we considered the time evolution of five hard-core bosons with additional weak nearest-neighbour repulsions, on a 21-site, two-dimensional lattice, initially confined to a portion of the lattice and prepared in their ground state there. Figure 1a shows the exact geometry (see also Supplementary Discussion); the relaxation dynamics begins when the confinement is lifted. Expanding the initial-state wavefunction

¹Department of Physics and Astronomy, University of Southern California, Los Angeles, California 90089, USA. ²Department of Physics, University of Massachusetts Boston, Boston, Massachusetts 02125, USA.

in the eigenstate basis of the final hamiltonian \hat{H} as $|\psi(0)\rangle = \sum_{\alpha} C_{\alpha} |\Psi_{\alpha}\rangle$, where $C_{\alpha} = \langle \Psi_{\alpha} | \psi(0) \rangle$ and the index α ranges over all the basis eigenstates $|\Psi_{\alpha}\rangle$, the many-body wavefunction evolves as $|\psi(t)\rangle = e^{-i\hat{H}t} |\psi(0)\rangle = \sum_{\alpha} C_{\alpha} e^{-iE_{\alpha}t} |\Psi_{\alpha}\rangle$, where the E_{α} are the eigenstate energies. Thus, obtaining results that are numerically exact for all times requires the full diagonalization of the 20,349-dimensional hamiltonian. The quantum-mechanical mean of any observable \hat{A} evolves as

$$\langle \hat{A}(t) \rangle \equiv \langle \psi(t) | \hat{A} | \psi(t) \rangle = \sum_{\alpha, \beta} C_{\alpha}^* C_{\beta} e^{i(E_{\alpha} - E_{\beta})t} A_{\alpha\beta} \quad (1)$$

where $A_{\alpha\beta} = \langle \Psi_{\alpha} | \hat{A} | \Psi_{\beta} \rangle$ and the asterisk denotes complex conjugation. The long-time average of $\langle \hat{A}(t) \rangle$ is then

$$\overline{\langle \hat{A} \rangle} = \sum_{\alpha} |C_{\alpha}|^2 A_{\alpha\alpha} \quad (2)$$

We note that if the system relaxes at all, it must be to this value. We find it convenient to think of equation (2) as stating the prediction of

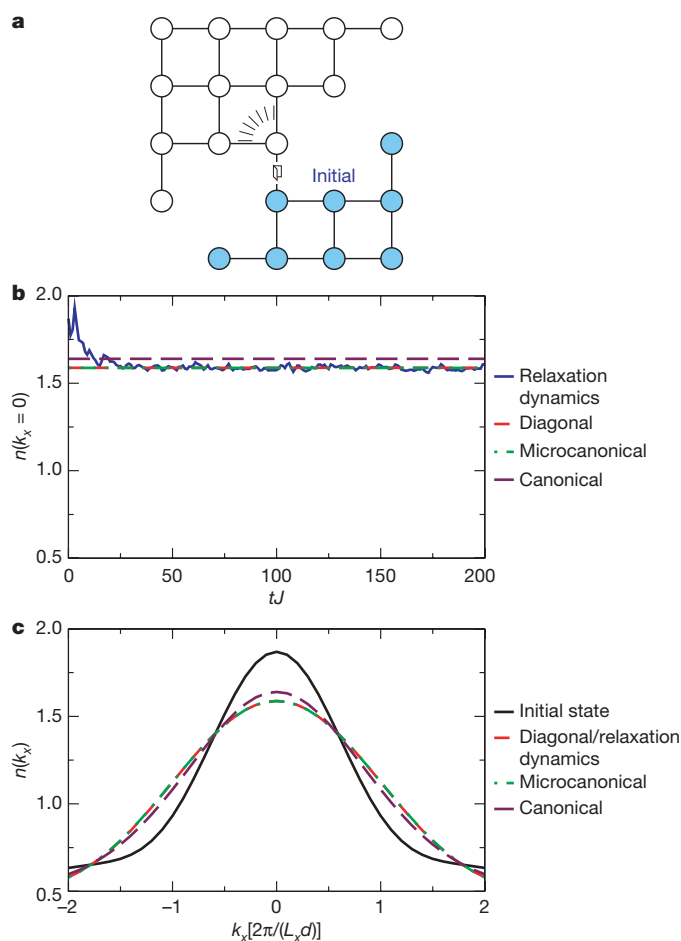


Figure 1 | Relaxation dynamics. **a**, Two-dimensional lattice on which five hard-core bosons propagate in time. The bosons are initially prepared in the ground state of the sub-lattice in the lower-right corner and released through the link indicated by the drawing of a door. **b**, The corresponding relaxation dynamics of the central component $n(k_x=0)$ of the marginal momentum distribution, compared with the predictions of the three ensembles, plotted against ‘dimensionless time’ (in our conventions J , the hopping parameter, has units of inverse time; see Supplementary Information). In the microcanonical case, we averaged over all eigenstates whose energies lie within a narrow window (see Supplementary Discussion) $[E_0 - \Delta E, E_0 + \Delta E]$, where $E_0 \equiv \langle \psi(0) | \hat{H} | \psi(0) \rangle = -5.06J$ and $\Delta E = 0.1J$. The canonical ensemble temperature is $k_B T = 1.87J$, where k_B is the Boltzmann constant, meaning that the ensemble prediction for the energy is E_0 . **c**, Full momentum distribution function in the initial state, after relaxation, and in the different ensembles. Here d is the lattice constant and $L_x = 5$ is the lattice width.

a ‘diagonal ensemble’, $|C_{\alpha}|^2$ corresponding to the weight that $|\Psi_{\alpha}\rangle$ has in the ensemble. In fact, this ensemble is precisely the generalized Gibbs ensemble introduced in ref. 3 if as integrals of motion we take all the projection operators $\hat{P}_{\alpha} = |\Psi_{\alpha}\rangle \langle \Psi_{\alpha}|$. Using these as constraints on relaxation dynamics, the theory gives the generalized Gibbs density matrix (or constrained density matrix) $\hat{\rho}_c = \exp(-\sum_{\alpha=1}^D \lambda_{\alpha} \hat{P}_{\alpha})$, where $\lambda_{\alpha} = -\ln(|C_{\alpha}|^2)$ and D is the dimension of the Hilbert space. (We note, however, that for the integrable system treated in ref. 3, the generalized Gibbs ensemble was defined using a different, minimal set of independent integrals of motion, the number of which was equal to the number of lattice sites N , which is much less than D .)

If the quantum-mechanical mean of an observable behaves thermally it should settle to the prediction of an appropriate statistical-mechanical ensemble. For our numerical experiments we chose to monitor the marginal momentum distribution along the horizontal axis $n(k_x)$ and its central component $n(k_x=0)$ (see Supplementary Information). In Fig. 1b, c we demonstrate that both relax to their microcanonical predictions. The diagonal-ensemble predictions are the same as these, but the canonical ones, although quite close, are not. This is an indication of the relevance of finite-size effects, which may be the origin of some of the apparent deviations from thermodynamics seen in the recent numerical studies of refs 4 and 5.

The statement that the diagonal and microcanonical ensembles give the same predictions for the relaxed value of \hat{A} reads

$$\sum_{\alpha} |C_{\alpha}|^2 A_{\alpha\alpha} = \langle A \rangle_{\text{microcan}}(E_0) \equiv \frac{1}{\mathcal{N}_{E_0, \Delta E}} \sum_{\alpha} A_{\alpha\alpha} \quad (3)$$

$|E_0 - E_{\alpha}| < \Delta E$

where E_0 is the mean energy of the initial state, ΔE is the half-width of an appropriately chosen energy window centred at E_0 (see Supplementary Discussion), and the normalization $\mathcal{N}_{E_0, \Delta E}$ is the number of energy eigenstates with energies in the window $[E_0 - \Delta E, E_0 + \Delta E]$. Thermodynamical universality is evident in this equality: although the left-hand side depends on the details of the initial conditions through the set of coefficients C_{α} , the right-hand side depends only on the total energy, which is the same for many different initial conditions. The following three scenarios suggest themselves as possible explanations of this universality (assuming that the initial state is sufficiently narrow in energy, as is normally the case—see Supplementary Discussion).

First, even for eigenstates close in energy, there are large eigenstate-to-eigenstate fluctuations of both the eigenstate expectation values (EEVs) $A_{\alpha\alpha}$ and the eigenstate occupation numbers (EONs) $|C_{\alpha}|^2$. However, for physically interesting initial conditions, the fluctuations in the two quantities are uncorrelated. A given initial state then performs an unbiased sampling of the distribution of the EEVs $A_{\alpha\alpha}$, resulting in equation (3).

Second, for physically interesting initial conditions, the EONs $|C_{\alpha}|^2$ almost do not fluctuate at all between eigenstates that are close in energy. Again, equation (3) immediately follows.

Third, the EEVs $A_{\alpha\alpha}$ almost do not fluctuate at all between eigenstates that are close in energy. In this case equation (3) holds without exception for all initial states that are narrow in energy (unlike in the first two scenarios, for which there may be special states that violate equation (3) despite being narrow in energy).

Deutsch and Srednicki independently proposed the third scenario, which, following Srednicki, we call the ‘eigenstate thermalization hypothesis’ (ETH)^{21,23}: the expectation value $\langle \Psi_{\alpha} | \hat{A} | \Psi_{\alpha} \rangle$ of a few-body observable \hat{A} in an energy- E_{α} eigenstate $|\Psi_{\alpha}\rangle$ of the hamiltonian of a large, interacting many-body system equals the thermal (microcanonical in our case) average $\langle A \rangle_{\text{microcan}}(E_{\alpha})$ of \hat{A} at the mean energy E_{α}

$$\langle \Psi_{\alpha} | \hat{A} | \Psi_{\alpha} \rangle = \langle A \rangle_{\text{microcan}}(E_{\alpha})$$

The ETH suggests that classical and quantum thermal states have very different natures, as depicted in Fig. 2. Although at present there

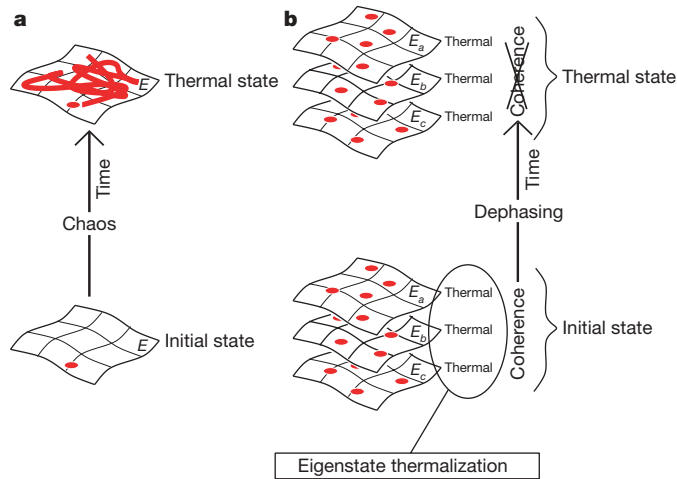


Figure 2 | Thermalization in classical versus quantum mechanics. **a**, In classical mechanics, time evolution constructs the thermal state from an initial state that generally bears no resemblance to the former. **b**, In quantum mechanics, according to the ETH, every eigenstate of the hamiltonian always implicitly contains a thermal state. The coherence between the eigenstates initially hides it, but time dynamics reveals it through dephasing.

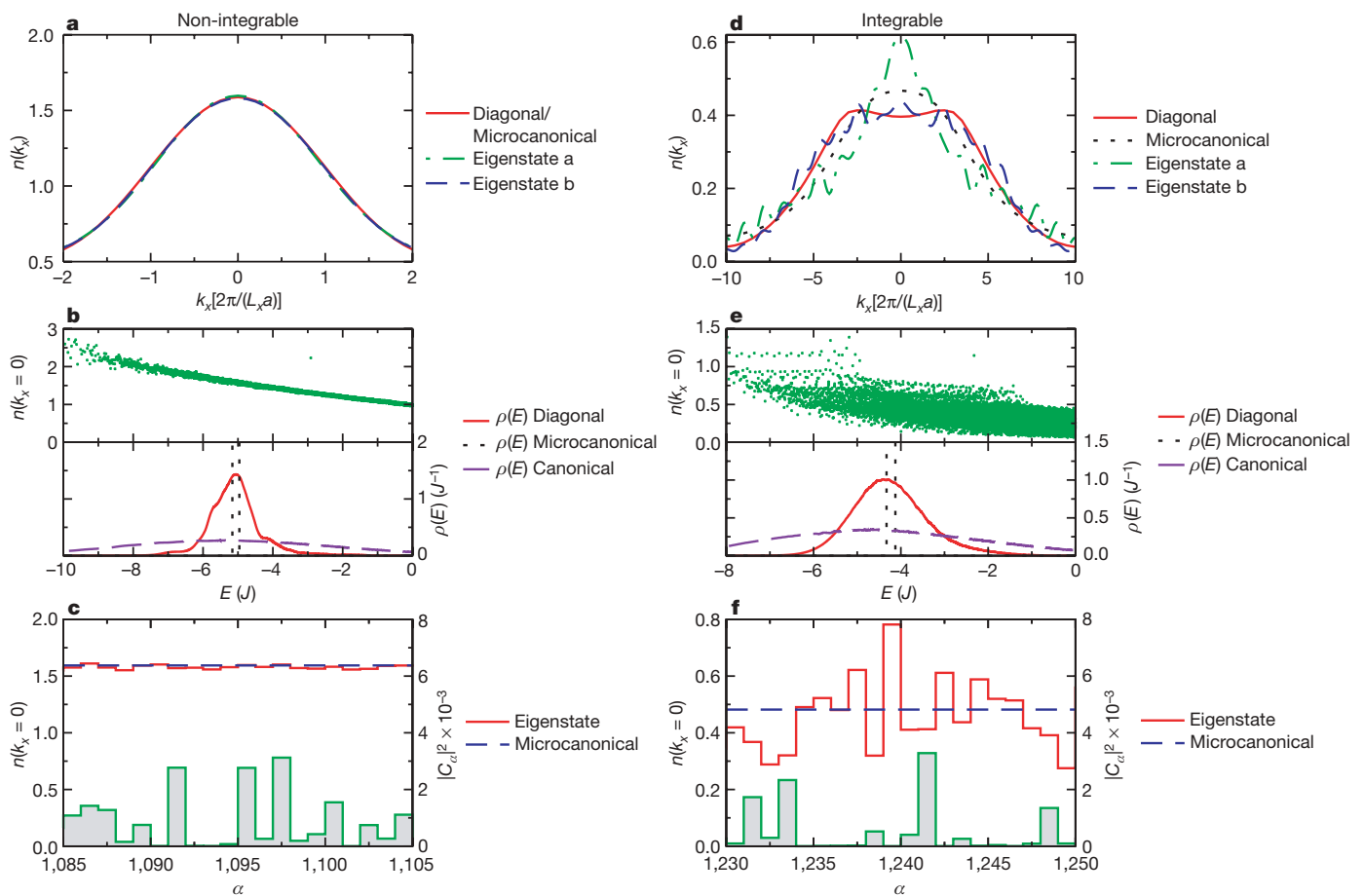


Figure 3 | Eigenstate thermalization hypothesis. **a**, In our non-integrable system, the momentum distribution $n(k_x)$ for two typical eigenstates with energies close to E_0 is identical to the microcanonical result, in accordance with the ETH. **b**, Upper panel: the EEV $n(k_x = 0)$, considered as a function of the eigenstate energy resembles a smooth curve. Lower panel: the energy distributions $\rho(E)$ (in units of J^{-1}) of the three ensembles we consider here. **c**, Detailed view of $n(k_x = 0)$ (left-hand scale) and $|C_\alpha|^2$ (right-hand scale) for 20 eigenstates around E_0 . **d**, In the integrable system, the values of $n(k_x)$ for two eigenstates, a and b, with energies close to E_0 and for the

are no general theoretical arguments supporting the ETH, some results do exist for restricted classes of systems. For instance, the ETH holds¹² in the case of an integrable hamiltonian weakly perturbed by a single matrix taken from a random gaussian ensemble. Furthermore, nuclear shell model calculations have shown that individual wavefunctions reproduce thermodynamic predictions²⁰. There are also rigorous proofs that some quantum systems, whose classical counterparts are chaotic, satisfy the ETH in the semiclassical limit^{21–24}. More generally, for low-density billiards in the semiclassical regime, the ETH follows from Berry's conjecture^{13,25}, which in turn is believed to hold in semiclassical classically chaotic systems²⁶. Finally, at the other end of the chaos–integrability spectrum, in systems solvable by Bethe ansatz, observables are smooth functions of the integrals of motion. This allows for the construction of individual energy eigenstates that reproduce thermal predictions²⁷.

In Fig. 3a–c we demonstrate that the ETH is in fact the mechanism responsible for thermal behaviour in our non-integrable system. Figure 3c additionally shows that the second scenario mentioned above does not occur, because the fluctuations in the EONs $|C_\alpha|^2$ are large. Thermal behaviour also requires that both the diagonal and the chosen thermal ensemble have sufficiently narrow energy distributions $\rho(E)$ (the product of the probability distribution and the density of states), meaning that in the energy region where the energy distributions $\rho(E)$ are appreciable, the slope of the curve of the

microcanonical and diagonal ensembles are very different from each other; that is, the ETH fails. **e**, Upper panel: the EEV $n(k_x = 0)$, considered as a function of the eigenstate energy gives a thick cloud of points rather than resembling a smooth curve. Lower panel: the energy distributions in the integrable system are similar to the non-integrable ones depicted in **b**. **f**, Correlation between $n(k_x = 0)$ and $|C_\alpha|^2$ for 20 eigenstates around E_0 . This correlation explains why in **d** the microcanonical prediction for $n(k_x)$ is larger than the diagonal one.

EEV $A_{\alpha\alpha}$ plotted against energy (here $n(k_x = 0)$ plotted against energy) does not change much; see Supplementary Discussion. As shown in Fig. 3b, this holds for the microcanonical and diagonal ensembles but not for the canonical ensemble, explaining the failure of the canonical ensemble to describe the relaxation in Fig. 1. We note that the fluctuations of the EONs $|C_\alpha|^2$ in Fig. 3b are artificially lowered by the averaging involved in the computation of the density of states (compare with Fig. 3c).

To strengthen the case for the ETH, we tested another observable. We chose it with the following consideration in mind: in our system interactions are local in space, and momentum distribution is a global, approximately spatially additive property. Thus, for the momentum distribution the ETH might arise through some simple spatial averaging mechanism. However, the ETH in fact does not depend on spatial averaging: for our final test of the ETH we chose an observable that is manifestly local in space, namely the expectation value of the occupation number of the central site of the lattice. We again found that the ETH holds (to within 3% relative standard deviation of eigenstate-to-eigenstate fluctuations).

On the other hand, Fig. 3d–f shows how the ETH fails for an isolated one-dimensional integrable system. The system consists of five hard-core bosons initially prepared in their ground state in an eight-site chain. We then link one of the ends of this chain to one of the ends of an adjoining (empty) 13-site chain to trigger relaxation dynamics. As Fig. 3e shows, $n(k_x)$ as a function of energy is a broad cloud of points, meaning that the ETH is not valid; Fig. 3f shows that the second scenario mentioned above does not occur in this system either.

Nevertheless, it might be possible for the first scenario to occur in this case, if the averages over the diagonal and the microcanonical energy distributions shown in Fig. 3e were to agree. Figure 3d shows that this does not happen. This is because, as shown in Fig. 3f, the values of $n(k_x = 0)$ for the most-occupied states in the diagonal ensemble (the largest values of the EONs $|C_\alpha|^2$) are always smaller than the microcanonical prediction, and those for the least-occupied states are always larger. Hence, the usual thermal predictions fail because the correlations between the values of $n(k_x = 0)$ and $|C_\alpha|^2$ preclude unbiased sampling of the former by the latter. These correlations have their origin in the non-trivial integrals of motion that make the system integrable and that enter the generalized Gibbs ensemble, which was introduced in ref. 3 as being appropriate for formulating the statistical mechanics of isolated integrable systems. In the non-integrable case shown in Fig. 3c, $n(k_x = 0)$ is so narrowly distributed that it does not matter whether or not it is correlated with $|C_\alpha|^2$ (we have in fact seen no correlations in the non-integrable case). Again, we note that the fluctuations of the EONs $|C_\alpha|^2$ in Fig. 3e are artificially lowered, relative to those shown in Fig. 3f, by the averaging involved in the computation of the density of states.

The thermalization mechanism outlined thus far explains why long-time averages converge to their thermal predictions. A striking

aspect of Fig. 1b, however, is that the time fluctuations are so small that after relaxation the thermal prediction works well at every instant of time. From equation (1), this might be suspected because the contribution of the off-diagonal terms is attenuated by temporal dephasing, which results from the generic incommensurability of the frequencies of the oscillating exponentials. However, this attenuation scales only as the square root of the number of dephasing terms, and is exactly compensated for by their larger number: if the number of eigenstates that have a significant overlap with the initial state is N_{states} , then the scaling of a typical C_α with N_{states} is $|C_\alpha| \sim 1/\sqrt{N_{\text{states}}}$, and the sum over off-diagonal terms in equation (1) finally does not scale down with N_{states}

$$\sum_{\substack{\alpha, \beta \\ \alpha \neq \beta}} \frac{e^{i(E_\alpha - E_\beta)t}}{N_{\text{states}}} A_{\alpha\beta} \sim \frac{\sqrt{N_{\text{states}}^2}}{N_{\text{states}}} A_{\alpha\beta, \alpha \neq \beta}^{\text{typical}} \sim A_{\alpha\beta, \alpha \neq \beta}^{\text{typical}}$$

where $A_{\alpha\beta, \alpha \neq \beta}^{\text{typical}}$ is the magnitude of a typical off-diagonal matrix element of the operator \hat{A} between energy eigenstates that have significant overlaps with the initial state. Hence, if the magnitudes of the diagonal and off-diagonal terms were comparable, their contributions would also be comparable, and time fluctuations of the average would be of the order of the average. However, this is not the case, and thus

$$A_{\alpha\beta, \alpha \neq \beta}^{\text{typical}} \ll A_{\alpha\alpha}^{\text{typical}}$$

where $A_{\alpha\alpha}^{\text{typical}}$ is the magnitude of a typical diagonal matrix element of the operator \hat{A} for an energy eigenstate that has a significant overlap with the initial state.

Figure 4a confirms this inequality for the matrix elements of the momentum distribution in our system. There is an a priori argument—admittedly dependent in part on certain hypotheses about chaos in quantum billiards—in support of this inequality in the case when the mean value of \hat{A} in an energy eigenstate is comparable to the quantum fluctuation of \hat{A} in that state²⁸.

On the other hand, the thermalization we see appears to be working a little too well: in a system as small as ours, we would expect measurement-to-measurement fluctuations to be much larger than is indicated in Fig. 1b. Indeed, as we show in Fig. 4b, the fluctuations that would actually be measured would be dominated by the quantum fluctuations of the time-dependent state. The rather large size of the quantum fluctuations relative to the thermal mean value is of course characteristic of small systems; however, the dominance of the quantum fluctuations over the temporal fluctuations of quantum expectation values is not, and is actually expected for generic systems in the thermodynamic limit²⁹.

We have demonstrated that, in contrast to the integrable case, the non-equilibrium dynamics of a generic isolated quantum system does lead to standard thermalization. We verified that this happens

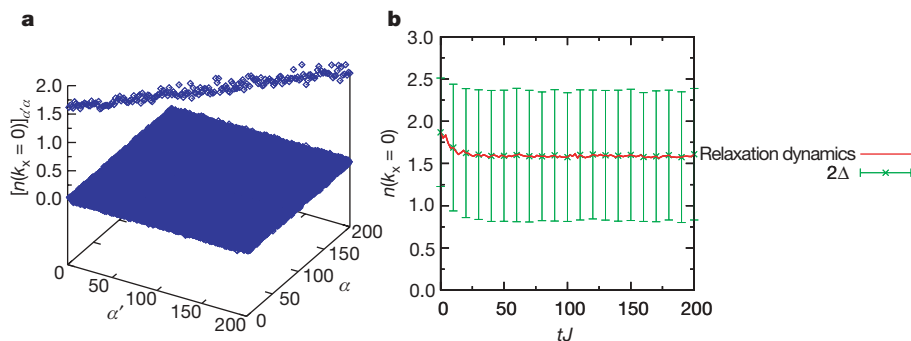


Figure 4 | Temporal versus quantum fluctuations. **a**, Matrix elements of the observable of interest $n(k_x = 0)$ as a function of state indices; the eigenstates of the hamiltonian are indexed in the order of diminishing overlap with the initial state. The dominance of the diagonal matrix elements

is apparent. **b**, The same time evolution as in Fig. 1b, with the error bars showing the quantum fluctuations $n(k_x = 0) \pm \Delta$, where $\Delta = [\langle \hat{n}^2(k_x = 0) \rangle - \langle \hat{n}(k_x = 0) \rangle^2]^{1/2}$, which are clearly much larger than the temporal fluctuations of $n(k_x = 0)$.

through the eigenstate thermalization mechanism, a scenario previously demonstrated¹² for the case of an integrable quantum hamiltonian weakly perturbed by a single matrix taken from a random gaussian ensemble, compellingly defended¹³ for the case of rarefied semiclassical quantum billiards, and conjectured by both authors to be valid in general. Our results, when combined with the others we mentioned^{12,13,20–27}, constitute strong evidence that eigenstate thermalization indeed generally underlies thermal relaxation in isolated quantum systems. Therefore, to understand the existence of universal thermal time-asymptotic states, operator expectation values in individual eigenstates should be studied. This is a problem that is linear, time independent, and conceptually far simpler than any arising in current research on nonlinear dynamics of semiclassical systems. Among the fundamental open problems of statistical mechanics that could benefit from the linear time-independent perspective are the nature of irreversibility, the existence of a Kolmogorov-Arnold-Moser-like threshold³⁰ in quantum systems and the role of conserved quantities in the approach to equilibrium. Finally, having a clear conceptual picture for the origins of thermalization may make it possible to engineer new, ‘unthermalizable’ states of matter¹², with further applications in quantum information and precision measurement.

Received 7 December 2007; accepted 13 February 2008.

- Kinoshita, T., Wenger, T. & Weiss, D. S. A quantum Newton's cradle. *Nature* **440**, 900–903 (2006).
- Hofferberth, S., Lesanovsky, I., Fischer, B., Schumm, T. & Schmiedmayer, J. Non-equilibrium coherence dynamics in one-dimensional Bose gases. *Nature* **449**, 324–327 (2007).
- Rigol, M., Dunjko, V., Yurovsky, V. & Olshanii, M. Relaxation in a completely integrable many-body quantum system: An ab initio study of the dynamics of the highly excited states of 1d lattice hard-core bosons. *Phys. Rev. Lett.* **98**, 050405 (2007).
- Kollath, C., Läuchli, A. & Altman, E. Quench dynamics and nonequilibrium phase diagram of the Bose-Hubbard model. *Phys. Rev. Lett.* **98**, 180601 (2007).
- Manmana, S. R., Wessel, S., Noack, R. M. & Muramatsu, A. Strongly correlated fermions after a quantum quench. *Phys. Rev. Lett.* **98**, 210405 (2007).
- Burkov, A. A., Lukin, M. D. & Demler, E. Decoherence dynamics in low-dimensional cold atom interferometers. *Phys. Rev. Lett.* **98**, 200404 (2007).
- Calabrese, P. & Cardy, J. Quantum quenches in extended systems. *J. Stat. Mech.* P06008 (2007).
- Sengupta, K., Powell, S. & Sachdev, S. Quench dynamics across quantum critical points. *Phys. Rev. A* **69**, 053616 (2004).
- Berges, J., Borsányi, S. & Wetterich, C. Prethermalization. *Phys. Rev. Lett.* **93**, 142002 (2004).
- Gallavotti, G. *Statistical Mechanics: A Short Treatise* (Springer, Berlin, 1999).
- Krylov, N. S. *Works on the Foundation of Statistical Physics* (Princeton Univ. Press, Princeton, 1979).
- Deutsch, J. M. Quantum statistical mechanics in a closed system. *Phys. Rev. A* **43**, 2046–2049 (1991).
- Srednicki, M. Chaos and quantum thermalization. *Phys. Rev. E* **50**, 888–901 (1994).
- Sutherland, B. *Beautiful Models* 27–30 (World Scientific, Singapore, 2004).
- Rigol, M., Muramatsu, A. & Olshanii, M. Hard-core bosons on optical superlattices: Dynamics and relaxation in the superfluid and insulating regimes. *Phys. Rev. A* **74**, 053616 (2006).
- Cazalilla, M. A. Effect of suddenly turning on interactions in the Luttinger model. *Phys. Rev. Lett.* **97**, 156403 (2006).
- Jin, D. S., Ensher, J. R., Matthews, M. R., Wieman, C. E. & Cornell, E. A. Collective excitations of a Bose-Einstein condensate in a dilute gas. *Phys. Rev. Lett.* **77**, 420–423 (1996).
- Greiner, M., Mandel, O., Esslinger, T., Hänsch, T. W. & Bloch, I. Quantum phase transition from a superfluid to a Mott insulator in a gas of ultracold atoms. *Nature* **415**, 39–44 (2002).
- Mandel, O. et al. Controlled collisions for multi-particle entanglement of optically trapped atoms. *Nature* **425**, 937–940 (2003).
- Horozi, M., Zelevinsky, V. & Brown, B. A. Chaos vs thermalization in the nuclear shell model. *Phys. Rev. Lett.* **74**, 5194–5197 (1995).
- Shnirelman, A. I. Ergodic properties of eigenfunctions. *Usp. Mat. Nauk* **29**, 181–182 (1974).
- Voros, A. *Stochastic Behavior in Classical and Quantum Hamiltonian Systems* (Springer, Berlin, 1979).
- de Verdière, Y. C. Ergodicité et fonctions propres du Laplacien. *Commun. Math. Phys.* **102**, 497–502 (1985).
- Zelditch, S. Uniform distribution of eigenfunctions on compact hyperbolic surfaces. *Duke Math. J.* **55**, 919–941 (1987).
- Heller, E. J. & Landry, B. R. Statistical properties of many particle eigenfunctions. *J. Phys. A* **40**, 9259–9274 (2007).
- Berry, M. V. Regular and irregular semiclassical wavefunctions. *J. Phys. A* **10**, 2083–2091 (1977).
- Korepin, V. E., Bogoliubov, N. M. & Izergin, A. G. *Quantum Inverse Scattering Method and Correlation Functions* 40–41 (Cambridge Univ. Press, Cambridge, 1993).
- Srednicki, M. Does quantum chaos explain quantum statistical mechanics? Preprint at (<http://arXiv.org/abs/cond-mat/9410046>) (1994).
- Srednicki, M. Thermal fluctuations in quantized chaotic systems. *J. Phys. A* **29**, L75–L79 (1996).
- José, J. V. & Saletan, E. J. *Classical Dynamics: A Contemporary Approach* 474–491 (Cambridge Univ. Press, Cambridge, 1998).

Supplementary Information is linked to the online version of the paper at www.nature.com/nature.

Acknowledgements We thank A. C. Cassidy, K. Jacobs, A. P. Young, and E. J. Heller for their comments. We acknowledge financial support from the National Science Foundation and the Office of Naval Research. We are grateful to the USC HPCC centre, where all our numerical computations were performed.

Author Information Reprints and permissions information is available at www.nature.com/reprints. Correspondence and requests for materials should be addressed to M.O. (maxim.olchanyi@umb.edu).

Electrical effects of spin density wave quantization and magnetic domain walls in chromium

Ravi K. Kumamuru^{1,†} & Yeong-Ah Soh¹

The role of magnetic domains (and the walls between domains) in determining the electrical properties of ferromagnetic materials¹ has been investigated in great detail for many years, not least because control over domains offers a means of manipulating electron spin to control charge transport in 'spintronic' devices². In contrast, much less attention has been paid to the effects of domains and domain walls on the electrical properties of antiferromagnets: antiferromagnetic domains show no net external magnetic moment, and so are difficult to manipulate or probe. Here we describe electrical measurements on chromium—a simple metal and quintessential spin density wave antiferromagnet³—that show behaviour directly related to spin density wave formation and the presence of antiferromagnetic domains. Two types of thermal hysteresis are seen in both longitudinal and Hall resistivity: the first can be explained by the quantization of spin density waves due to the finite film thickness (confirmed by X-ray diffraction measurements) and the second by domain-wall scattering of electrons^{4,5}. We also observe the striking influence of the electrical lead configuration (a mesoscopic effect) on the resistivity of macroscopic samples in the spin density wave state. Our results are potentially of practical importance, in that they reveal tunable electrical effects of film thickness and domain walls that are as large as the highest seen for ferromagnets^{6,7}.

Today, giant magnetoresistance⁸ underlies the operation of many computer hard drives, and the much-studied elemental antiferromagnet (AFM) chromium³ was incorporated as the non-ferromagnetic layer in the multilayers displaying giant magnetoresistance. Scientific interest in Cr has been renewed by the discovery of techniques to image AFM domains^{9,10} and the demonstration that Cr has a model quantum phase transition^{11,12} to an AFM spin density wave (SDW) (Fig. 1a) because of nesting of flat regions of the Fermi surface (Fig. 1b)^{3,13,14}. The SDW is characterized by the Neel temperature, T_N , at which it appears and three vectors, \mathbf{Q}' , \mathbf{Q} and \mathbf{S} , representing the nesting vector, the SDW vector and the spin orientation, all of which point along a (100)-type crystallographic axis.

We measured the resistivity ρ and Hall coefficient R_H (inversely proportional to the charge carrier density) for Cr films with thicknesses $t = 3,500$ Å, 506 Å, 430 Å and 175 Å. The resistivity drops, as for any good metal, with decreasing temperature (Fig. 1c), but displays an anomaly and also a fall in the carrier density at T_N (Fig. 1d). For all films, $T_N > 280$ K but is below the bulk $T_N = 311$ K. Film disorder, highest for the 430 Å film, smoothes the anomaly and the loss of carriers at T_N and also affects the lower-temperature R_H . Figure 1e shows the Hall conductivity σ_H calculated from ρ and R_H . Whereas σ_0 incorporates all regions of the Fermi surface equally, σ_H is much less sensitive to the flat regions because of their weighting by the inverse carrier mass¹⁵. Therefore any changes in the flat regions caused by Fermi surface nesting would appear in ρ but not as strongly

in σ_H . Figure 1e shows that σ_H remains unchanged on passing the thermal phase transition at T_N , in agreement with findings^{12,15,16} for the quantum phase transition in $\text{Cr}_{1-x}\text{V}_x$, confirming that the order affects primarily the flat regions of the Fermi surface.

Cooling and warming runs revealed two types of thermal hysteresis below T_N (Fig. 2a, b): one accompanied by a kink in the thermal derivatives of ρ and R_H , and another without such a feature. Two of the films (175 Å and 506 Å) display a kink in the thermal derivatives (Fig. 2c, d) whose position depends on the scan direction, occurring at lower temperatures during cooling than during warming. The positions of the kinks coincide with the temperatures at which the hysteresis loops in both ρ and R_H close. Remarkably, σ_H shows no kink in $d\sigma_H/dT$ and the hysteresis is small compared with the hysteresees in ρ and R_H (Fig. 3a–d). Given the insensitivity of σ_H to the flat regions of the Fermi surface¹⁵, the kinks in $d\rho/dT$ and dR_H/dT as well as the hysteresees in ρ and R_H must be due to changes in the flat parts of the Fermi surface and therefore are related to the SDW. For all four samples, ρ and R_H are larger on cooling than on warming, contradicting the simple picture in which hysteresis in the AFM order parameter alone would result in fewer carriers (larger R_H) and larger ρ on warming. The 506 Å film has two peaks: one centred at 200 K and associated with the hysteresis in the kinks, and another centred at 130 K and with an amplitude depending on which part of the sample (A or B) is contacted (Fig. 2a). Figure 2e shows the temperature (T) dependence of the ratio of the resistance in region B to that of region A measured for two pairs of leads on the same Hall bar for the 506 Å film. The normalized R_B/R_A is a T -independent constant (equal to 1) for $T > T_N$, but is T -dependent as well as hysteretic in the Neel state.

In Cr, as the film thickness is reduced, \mathbf{Q} prefers to align perpendicular to the film surface^{17–19}, and indeed, for $t < 250$ Å an SDW with \mathbf{Q} out-of-plane is predominant¹⁹. Furthermore, because of the finite t along \mathbf{Q} , only a finite number of SDW nodes (N) are allowed^{20,21}. If the film surface and its interface with the substrate impose boundary conditions on the spin structure of the film, a gradual change in the SDW wavelength (between 60 and 80 Å in bulk²²) with T is not possible. Therefore, as T is reduced, N in the film abruptly jumps up by one (Fig. 3f)^{23,24}. Because there is an energy barrier for this process, the temperature at which N changes by one is lower on cooling than on warming, leading to thermal hysteresis in N . We therefore conjectured that the kinks in the resistivity²⁴, seen for $t = 175$ Å and $t = 506$ Å, arise from jumps in N , which we verified using synchrotron X-ray diffraction from the 506 Å film.

We searched for the superstructure due to the charge density wave/strain wave (CDW/SW) associated with the SDW around the (0,0,2), (1,0,1) and (1,1,2) Bragg peaks by independently scanning h , k and l , where l is along the surface normal. From the absence of detectable superstructure along h or k above the background level, down by 10^{-6} compared with the main film Bragg peaks, and known values

¹Department of Physics and Astronomy, Dartmouth College, Hanover, New Hampshire 03755, USA. [†]Present address: Department of Material Science and Engineering, University of Illinois, Urbana-Champaign, Illinois 61801, USA.

of CDW intensities²⁵, domains with \mathbf{Q} in the plane occupy less than 8% of the film volume. In contrast, superstructure is detected at reciprocal lattice points $(h, k, l \pm 2\delta)$ for integer h and k . By tracking the incommensurability 2δ as a function of T , we determine N directly (Fig. 2f).

There are four important results. First, \mathbf{Q} is indeed quantized so that only integer numbers of CDW periods and SDW nodes are accommodated within t . Second, in various temperature windows, different perpendicular \mathbf{Q} vectors with consecutive N coexist²¹ in the probed volume. Third, the populations of domains with differing N undergo two hysteresis loops, one (H_1 in Fig. 2f) from 240 to 195 K and another (H_2) from 195 to 80 K. The two loops coincide with the two loops in the resistivity for $t = 506 \text{ \AA}$ (Fig. 2a, b), confirming that the hysteresis in resistivity is due to the hysteresis in N . Fourth, although population of a new N value happens at many temperature points either during cooling or warming, complete switching from a multi- N population to a single N happens only at 195 K during cooling (from $N = 16, 17$ to 17), and between 150 and 195 K (from $N = 17, 18$ to 17) and at 240 K (from $N = 17, 16$ to 16) during warming. The temperatures at which the jumps from $N = 16, 17$ to 17 and $N = 17, 16$ to 16 occur coincide with the temperatures at which we measure kinks in $d\rho/dT$ and dR_H/dT , demonstrating that the observed electrical effects are due to jumps in N . This corresponds to switching between $N/2 = 8$ and 8.5 SDW wavelengths confined within t .

It is important to understand not only the hysteresis itself, which the X-ray data account for, but also its sign. In particular, our electrical data for $t = 175$ and 506 \AA indicate a higher carrier density in the hysteretic regions on warming, implying that at fixed T and t , a larger N (that is, an SDW with smaller wavelength) leads to a higher

density of free carriers, and concomitantly (because SDW order reduces Fermi surface area and free carrier density) a lower SDW amplitude. This result agrees with simulations showing that the amplitude of the SDW can drop abruptly when N increases by one as t is varied²⁰.

The differences between regions A and B in the $t = 506 \text{ \AA}$ film, reflected in both the different thermal hysteresis amplitudes (Fig. 2a) and the T -dependent resistance ratio (Fig. 2e), are a manifestation of new mesoscopic behaviour: spatial fluctuations of the order parameter affect the transport in the Neel state, despite the averaging effects expected for our high-quality thin films of 1-mm lateral dimensions. Indeed, because R_B/R_A is temperature-dependent throughout the Neel state, the two regions have different order parameter configurations at all $T < T_N$. The temperature window where the thermal hystereses in A and B are different (peaks centred at 130 K in Fig. 2a) coincides with H_2 in Fig. 2e and f, pointing to the same mechanism, namely the difference in the distribution of \mathbf{Q} with $N = 17, 18$ in region A and B as we cycle T . Because N affects the strength of the order parameter, different distributions of N in regions A and B as a function of T can give rise to different thermal hysteresis amplitudes and a T -dependent and hysteretic R_B/R_A . We surmise from this picture and from Fig. 2a that region B has a larger volume fraction that switches from $N = 17$ to 18 when $N = 18$ appears below 80 K on cooling, leading to a larger thermal hysteresis in the population of N between 80 and 195 K. This will give rise to a larger reduction of resistance in region B than region A (after factoring out the sample geometry) and a reduced ratio R_B/R_A for $80 < T < 195 \text{ K}$ on warming.

Although the \mathbf{Q} domain statistics can explain the hysteresis effects, they cannot explain why the normalized R_B/R_A deviates from 1 when

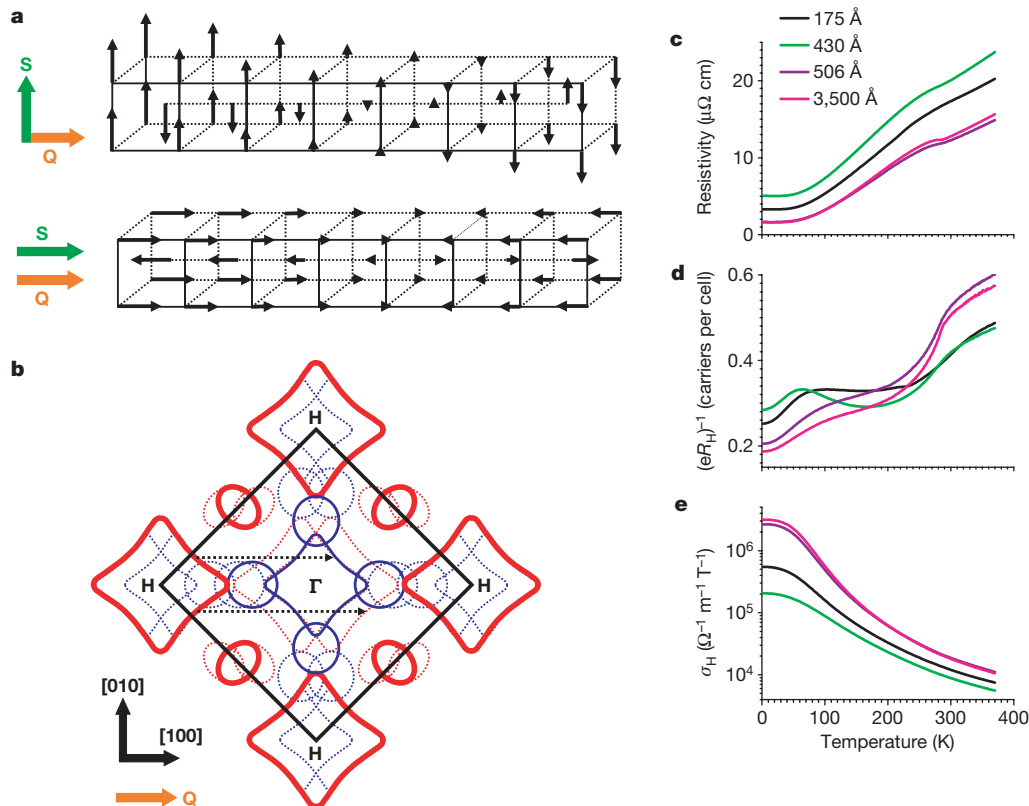
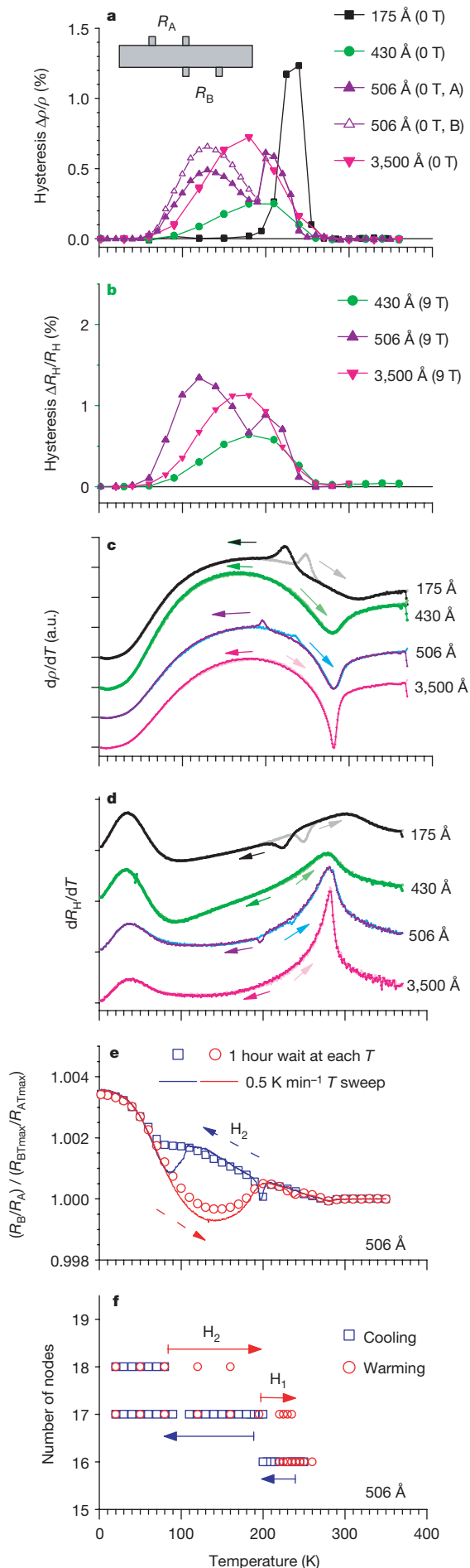


Figure 1 | Antiferromagnetic spin density wave due to Fermi surface nesting in chromium and its influence on the transport coefficients. **a**, Schematic diagram of transverse ($\mathbf{Q} \perp \mathbf{S}$) and longitudinal ($\mathbf{Q} \parallel \mathbf{S}$) SDW in Cr. **b**, Schematic diagram of Cr Fermi surface nesting in the k_x - k_y plane. The electron octahedron (solid blue lines) is smaller than the hole octahedra (solid red lines), owing to which two nesting vectors $(1 - \delta)$ and $(1 + \delta)$ are formed³ (dashed lines with arrowheads). The dotted lines show the Fermi

surface shifted by the two nesting vectors. **c**, **d**, **e**, Resistivity (magnetic field $H = 0$ tesla), inverse Hall coefficient ($H = 1$ tesla) and Hall conductivity ($H = 1$ tesla) of the four Cr films. For both X-ray and transport experiments, we used the conventional unit cell with lattice constant $a = 2.88 \text{ \AA}$, which contains two Cr atoms. We believe that the upturn in the inverse Hall coefficient at low temperature for the 430 \AA film comes from disorder³¹.



the system displays a single value of N (which is the case for most temperatures between 250 K and 80 K during cooling), or why the normalized R_B/R_A is usually greater than 1 on warming in H_2 , instead of smaller than 1 as expected for a higher volume fraction of $N = 18$ domains in B. Possible explanations include defects invisible to X-rays, spatial fluctuations of the order parameter even for a single N , and contact resistance between the metal bonding wire and partially gapped Cr. Because the order parameter can jump abruptly on simply adding one Cr monolayer, film roughness can induce spatial fluctuations thereof²⁰. Also, the contacts do have an effect: the T -dependence of R_B/R_A changes after bonding new contacts using the same pairs of leads. This is not a measurement error because, when the contacts are left intact, the T -dependence of R_B/R_A is reproducible over many temperature cycles.

It is natural to ask why the quantization effect is stronger for $t = 175$ Å (Fig. 2a, c, d) than for $t = 506$ Å and why there is no kink in the thermal derivatives of the resistivity for $t = 430$ Å. From comparison of the CDW wavelength to t , we estimate that in the 175 Å film N will need to change from 6 to 7 on cooling, in contrast to the 506 Å film, where we measure a change from 16 to 17 (ref. 26). The larger relative change in N , corresponding to a SDW wavelength change which is roughly a factor of two larger for $t = 175$ Å, can account for the similarly larger effect in the sharp component of the electrical hysteresis for the 175 Å film. We attribute the absence of a kink in the resistivity data for $t = 430$ Å to the rougher film surface (6.7 Å r.m.s. versus 2.6 Å over $0.5 \mu\text{m}^2$ for $t = 175, 506$ Å) and smaller grain sizes, which limits the lateral size over which the SDW can have a well-defined N . Although we suspect that a large fraction of the sample has Q out of plane, the Q domains will be small and there will be distributions of different N values (determined by local film thickness) in different parts of the sample, which change smoothly without a sharp switching in N as T is varied.

SDW quantization accounts for the behaviour of the three thinnest samples but not that of $t = 3,500$ Å, because t is too large for the boundary conditions to impose quantization of the SDW. To explain a gradually evolving hysteresis in ρ and R_H covering almost the entire AFM phase, from T_N to 50 K (Fig. 2a, b), we invoke AFM domains, which evolve with temperature⁹ into history-dependent configurations. At first sight, the anisotropic resistance of the electronically tetragonal Q domains is then all that is needed to understand the hysteresis, whose 1% magnitude, a measure of the difference between two multidomain configurations, is well below the 8% maximum resistance anisotropy reported²⁷ for single- Q bulk crystals. Resistivity is always smaller on warming than on cooling, which could arise if there were a preference—dictated by strain—for

Figure 2 | Thermal hysteresis below T_N in the transport coefficients, thermal derivatives, and X-ray measurement of the charge density wave. **a**, Hysteresis in resistivity ($\Delta\rho/\rho = (\rho_{\text{cooling}} - \rho_{\text{heating}})/(\rho_{\text{cooling}} + \rho_{\text{heating}})/2$) in the four films. These are significantly larger than the fractional change of 10^{-5} observed in noise measurements³⁰. **b**, Hysteresis in R_H plotted for three films. **c**, **d**, Derivatives of resistivity ($H = 9$ tesla) and Hall coefficient ($H = 9$ tesla) during cooling and warming. Two of the films, 175 Å and 506 Å, show a hysteretic kink in both the resistivity and the Hall coefficient. The temperature range for hysteresis is 25 K for the 175 Å film and 38 K for the 506 Å film. **e**, Ratio of the resistance in region B to that of region A after factoring out the sample geometry (by normalization to R_B/R_A in the paramagnetic state at $T = 350$ K). It is a constant above T_N , but T -dependent and hysteretic below T_N . **f**, Number of nodes N , which is given by $2\delta t/a$, in the 506 Å film measured by X-ray scattering during cooling and warming. In the cooling cycle, N is 16 at 250 K, and stays constant until it reaches 200 K when 17 nodes start to be populated. The switching to 17 nodes is complete at 195 K. As the sample is cooled further, 18 nodes coexist with 17 nodes below 80 K. In the warming cycle, the coexistence of 17 and 18 nodes persists up to 160 K, and is followed by a single value of 17 nodes at 195 K. Coexistence of 17 and 16 nodes is observed between 220 and 235 K, and is followed by a switch to 16 nodes at 240 K. The temperatures at which N switches from 16 to 17 during cooling (195 K) and from 17 to 16 during warming (240 K) coincide with the kinks in the resistivities in **c** and **d**.

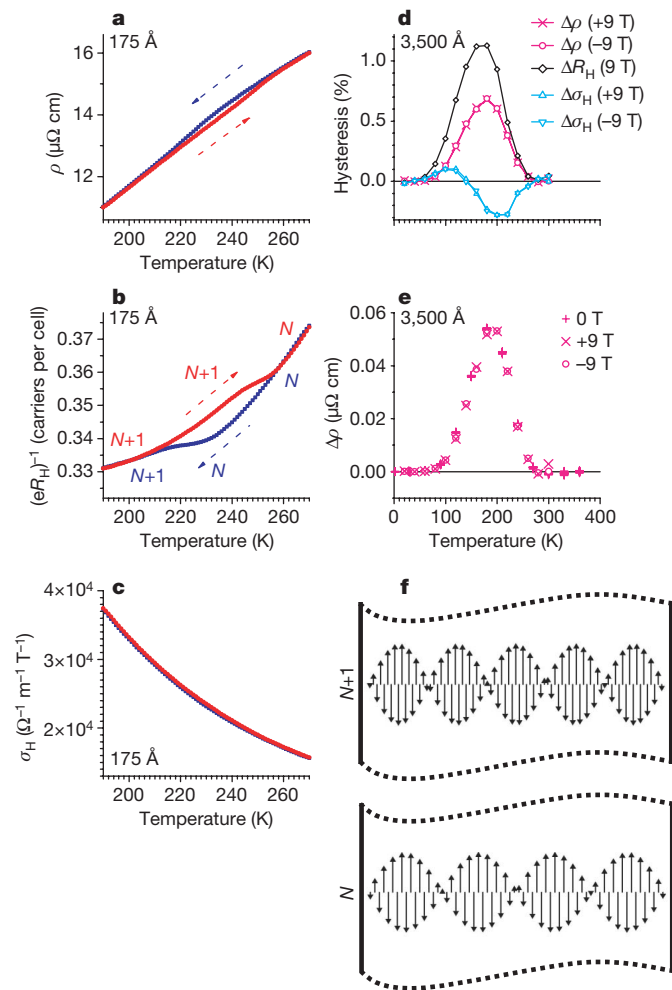


Figure 3 | Thermal hysteresis of transport coefficients observed in the thinnest and thickest films, and schematic diagram of quantization of SDW. **a, b,** Resistivity ($H = 2$ tesla) and inverse Hall coefficient ($H = 2$ tesla) of the 175 Å film show a clear hysteresis due to an abrupt change in N in the SDW. The direction of scan and N are shown in **b**. **c,** Values of σ_H ($H = 2$ tesla) show much smaller hysteresis. **d,** Hysteresis in resistivity and Hall coefficient in the 3,500 Å film. Hysteresis in σ_H is non-zero. **e,** Hysteresis in the resistivity measured at 0 and ± 9 tesla for the 3,500 Å film. **f,** Schematic diagram of the change in the number of SDW nodes. The vertical boundaries indicate the film surfaces, which impose boundary conditions on the CDW such as a node (as shown in the diagram) or an antinode.

\mathbf{Q} to rotate out of the plane when cooling the sample, as domains with $\mathbf{Q} \parallel \mathbf{J}$ have a higher intradomain resistance than domains with $\mathbf{Q} \perp \mathbf{J}$; \mathbf{J} is the current density. However, in this case, the hysteresis amplitude would be field-dependent because the transverse magnetoresistance $\Delta\rho/\rho = [\rho(H) - \rho(H=0)]/\rho(H=0)$ (magnetic field \mathbf{H} perpendicular to \mathbf{J} , which is our measurement configuration) depends strongly on the orientation of \mathbf{Q} relative to \mathbf{J} and \mathbf{H} (ref. 28). Within experimental error, the thermal hysteresis is field-independent up to the highest fields measured (9 tesla, Fig. 3e), and it is therefore highly improbable that intradomain resistance anisotropy is the primary cause of the hysteresis.

Following the example of bulk chromium⁴, the most obvious cause must then be the resistance due to interfaces between the domains. As \mathbf{Q} rotates by 90° at the domain walls (\mathbf{Q} domains), the electronic structure rotates by 90° as well (Fig. 4a, b), so that an electron at the ungapped corners of the octahedra or in one of the ellipsoids, with a k vector perpendicular to \mathbf{Q} in one domain, will see a rotated Fermi surface in the neighbouring domain that no longer has a state at the same k and energy (Fig. 4b). Domain walls will therefore scatter electrons strongly if the mean free path, which we estimate²⁹ from

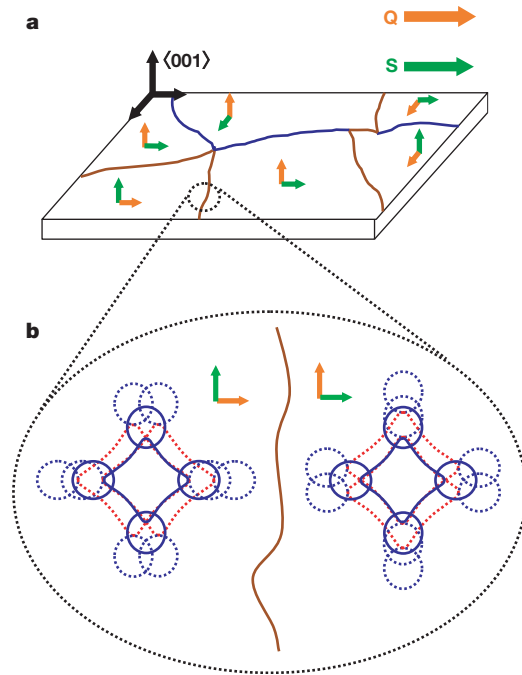


Figure 4 | Domain wall scattering due to Fermi surface mismatch.

a, Schematic diagram of a film with a few of the possible antiferromagnetic domains. \mathbf{Q} domain walls are shown in dark brown and \mathbf{S} domain walls are shown in dark blue. **b,** Schematic diagram depicting the mismatch of electron Fermi surfaces on the two sides of a \mathbf{Q} domain wall.

our data and the reported Fermi surface area of the electron ellipsoids³ to vary from 10 nm at ambient to 100 nm at 2 K, is larger than the domain wall width.

Domains will grow on cooling, leaving fewer domain walls as scatterers on reheating; the lack of thermal hysteresis below 50 K arises from freezing of domains. The domain wall picture can explain the thermal hysteresis for our thickest film as well as the lack of the effect in the thinnest film below 200 K, for which we suspect \mathbf{Q} to be single-valued and perpendicular to the film throughout the sample. The domain walls affect R_H as well as ρ , in agreement with the bulk Cr results⁴. What is entirely new, beyond our simple demonstration of the domain wall physics using the absence of a field effect on the thermal hysteresis, is our discovery that by varying t we can tune between behaviour dominated by domain walls for thick films and the quantized density wave regime for thin films. Open questions concern how R_H depends on N and domain configuration, how to model the electronic structure of walls including those between domains with different N , and how electrons scatter from the walls. We speculate that the walls are more metallic than the interiors, as magnetic order (and the associated Fermi surface gapping) is frustrated by the presence of two different directions or values of \mathbf{Q} .

METHODS SUMMARY

We grew chromium films using magnetron sputtering on MgO (001) substrates at 200°C with an initial seed layer grown at 650°C and a post-deposition annealing at $600\text{--}700^\circ\text{C}$. X-ray diffraction measurements show that the films are single-crystal and epitaxial with the in-plane axes rotated by 45° with respect to the MgO crystal axes. The 430 Å film has the largest mosaicity with a full width at half maximum of 1.26° compared with 0.62° for $t = 175$ Å and 0.27° for $t = 506$ Å. Hall bars were made by photolithography and etching with the long axis of the Hall bar along Cr (100), and directly wire-bonded with aluminium wires to the sample holder. The Hall bars are 1 mm wide and distance between voltage pads are 1 mm (typically) or 0.5 mm. The resistivity ρ at low temperature measures the disorder in the films. The residual resistivity ratios $\text{RRR} = R(300\text{ K})/R(4.2\text{ K})$ of our films are 8.0, 7.4, 4.0 and 5.2, respectively, in the order of decreasing thickness. These are two orders of magnitude smaller than the best values observed in bulk chromium²⁸, because of the higher residual resistivity arising from quenched disorder, but compare well with other thin

films grown by molecular beam epitaxy³⁰. We conducted all electrical measurements in a Quantum Design PPMS system with a 9-T superconducting magnet. Magnetic field was kept constant throughout each cooling and warming cycle in all the hysteresis measurements. We eliminated thermal cycling errors in hysteresis measurements by allowing adequate time for temperature to settle down at each point. The CDW measurements on the 506 Å film were done at beamlines 4-ID-D and 33-BM at Argonne National Laboratory using 8-keV X-rays. Slits defined the incident X-ray beam dimensions as 300 µm × 100 µm at 4-ID-D and 500 µm × 500 µm at 33-BM.

Full Methods and any associated references are available in the online version of the paper at www.nature.com/nature.

Received 14 November 2007; accepted 29 January 2008.

- Marrows, C. H. Spin-polarised currents and magnetic domain walls. *Adv. Phys.* **54**, 585–713 (2005).
- Zutic, I., Fabian, J. & Das Sarma, S. Spintronics: Fundamentals and applications. *Rev. Mod. Phys.* **76**, 323–410 (2004).
- Fawcett, E. Spin-density-wave antiferromagnetism in chromium. *Rev. Mod. Phys.* **60**, 209–283 (1988).
- Jaramillo, R. *et al.* Microscopic and macroscopic signatures of antiferromagnetic domain walls. *Phys. Rev. Lett.* **98**, 117206 (2007).
- Shpyrko, O. G. *et al.* Direct measurement of antiferromagnetic domain fluctuations. *Nature* **447**, 68–71 (2007).
- Marrows, C. H. & Dalton, B. C. Spin mixing and spin-current asymmetry measured by domain wall magnetoresistance. *Phys. Rev. Lett.* **92**, 097206 (2004).
- Ebels, U. *et al.* Spin accumulation and domain wall magnetoresistance in 35 nm Co wires. *Phys. Rev. Lett.* **84**, 983–986 (2000).
- Baibich, M. N. *et al.* Giant magnetoresistance of (001)Fe/(001)Cr magnetic superlattices. *Phys. Rev. Lett.* **61**, 2472–2475 (1988).
- Evans, P. G. *et al.* X-ray microdiffraction images of antiferromagnetic domain evolution in chromium. *Science* **295**, 1042–1045 (2002).
- Bode, M. *et al.* Atomic spin structure of antiferromagnetic domain walls. *Nature Mater.* **5**, 477–481 (2006).
- Yeh, A. *et al.* Quantum phase transition in a common metal. *Nature* **419**, 459–462 (2002).
- Lee, M., Husmann, A., Rosenbaum, T. F. & Aeppli, G. High resolution study of magnetic ordering at absolute zero. *Phys. Rev. Lett.* **92**, 187201 (2004).
- Lomer, W. M. Electronic structure of chromium group metals. *Proc. Phys. Soc. Lond.* **80**, 489–496 (1962).
- Rotenberg, E. *et al.* Electron states and the spin density wave phase diagram in Cr(110) films. *N. J. Phys.* doi:10.1088/1367-2630/7/1/114 (2005).
- Norman, M. R., Si, Q. M., Bazaliy, Y. B. & Ramazashvili, R. Hall effect in nested antiferromagnets near the quantum critical point. *Phys. Rev. Lett.* **90**, 116601 (2003).
- Bazaliy, Y. B., Ramazashvili, R., Si, Q. & Norman, M. R. Magnetotransport near a quantum critical point in a simple metal. *Phys. Rev. B* **69**, 144423 (2004).
- Takeda, M. *et al.* Spin density wave in epitaxial Cr(001)/Sn and Cr(001)/Au multilayers with nonmagnetic spacer layers. *J. Phys. Soc. Jpn.* **69**, 1590–1593 (2000).
- Sonntag, P. *et al.* Magnetic phase diagram for spin-density waves in thin epitaxial Cr(001) films. *J. Magn. Magn. Mater.* **183**, 5–18 (1998).
- Bodeker, P. *et al.* Reorientation of spin density waves in Cr(001) films induced by Fe(001) cap layers. *Phys. Rev. Lett.* **81**, 914–917 (1998).
- Shi, Z. P. & Fishman, R. S. Interplay between spin density wave and proximity magnetic layers. *Phys. Rev. Lett.* **78**, 1351–1354 (1997).
- Niklasson, A. M. N., Johansson, B. & Nordstrom, L. Spin density waves in thin chromium films. *Phys. Rev. Lett.* **82**, 4544–4547 (1999).
- Werner, S. A., Arrott, A. & Kendrick, H. Temperature and magnetic-field dependence of antiferromagnetism in pure chromium. *Phys. Rev.* **155**, 528–539 (1967).
- Mibu, K. *et al.* Discrete change of spin-density-wave modulation in Cr(100)/Sn multilayers as a function of Cr layer thickness. *Phys. Rev. Lett.* **89**, 287202 (2002).
- Fullerton, E. E. *et al.* Hysteretic spin-density-wave ordering in confined geometries. *Phys. Rev. Lett.* **91**, 237201 (2003).
- Hill, J. P., Helgesen, G. & Gibbs, D. X-ray scattering study of charge and spin-density-waves in chromium. *Phys. Rev. B* **51**, 10336–10344 (1995).
- Fishman, R. S. & Shi, Z. P. Collinear spin-density-wave ordering in Fe Cr multilayers and wedges. *Phys. Rev. B* **59**, 13849–13860 (1999).
- Muir, W. B. & Stromols, J. O. Electrical resistance of single-crystal single-domain chromium from 77 to 325 degrees K. *Phys. Rev. B* **4**, 988–991 (1971).
- Arko, A. J., Marcus, J. A. & Reed, W. A. High-field galvanomagnetic effects in antiferromagnetic chromium. *Phys. Rev.* **1**, 671–683 (1968).
- Ziman, J. M. *Electrons and Phonons*. (Oxford Univ. Press, Oxford, 1960).
- Michel, R. P. *et al.* Electrical-noise measurements on chromium films. *Phys. Rev. B* **44**, 7413–7425 (1991).
- Furuya, Y. Temperature and magnetic-field dependence of Hall-coefficient on antiferromagnetic chromium. *J. Phys. Soc. Jpn.* **40**, 490–497 (1976).

Acknowledgements We thank the Burke foundation for their generous support of the project, J. Karapetrova, Z. Islam and J. Lang at Argonne National Laboratory and M. Vaudin at NIST for assisting the X-ray measurements, and the Rockefeller Foundation for the Bellagio Residency where this manuscript was completed.

Author Information Reprints and permissions information is available at www.nature.com/reprints. Correspondence and requests for materials should be addressed to Y.-A.S. (yeong-ah.soh@dartmouth.edu).

METHODS

Sample fabrication and a few measurement details are described in the Methods Summary. Additional details of the experiments are as follows.

Current was applied in the form of a 7-Hz square wave to eliminate thermal voltages. Hall coefficient was measured using $+H$ and $-H$ values to eliminate any coupling to the longitudinal resistivity due to misaligned bonding wires. Temperature error due to cycling was found to be about 0.05% at a sweep rate of 0.5 K min^{-1} over the range of 350 K. Therefore, for hysteresis measurements in Fig. 2a, b and e, and Fig. 3d and e, discrete measurements were made with a 1-h delay at each point. The 1-h delay was added after the measured sample holder temperature reached the desired value, to allow the sample to reach equilibrium with its environment. This was found to be sufficient to eliminate temperature cycling errors. All measurements were made in a vacuum of about 10^{-2} torr.

Mean free path was calculated using the equation²⁹ $\sigma = e^2 A \Sigma / (12\pi^3 \hbar)$ where Σ is the Fermi surface area and A is the mean free path. Only the electron ellipsoids were considered for this calculation. Total Fermi surface of the electron ellipsoids^{3,32} is taken to be 1.32 Au^2 .

32. Laurent, D. G., Callaway, J., Fry, J. L. & Brener, N. E. Band-structure, Fermi-surface, Compton profile, and optical conductivity of paramagnetic chromium. *Phys. Rev. B* **23**, 4977–4987 (1981).

LETTERS

Changing boreal methane sources and constant biomass burning during the last termination

Hubertus Fischer¹, Melanie Behrens¹, Michael Bock¹, Ulrike Richter¹, Jochen Schmitt¹, Laetitia Loulergue², Jerome Chappellaz², Renato Spahni³, Thomas Blunier^{3†}, Markus Leuenberger³ & Thomas F. Stocker³

Past atmospheric methane concentrations show strong fluctuations in parallel to rapid glacial climate changes in the Northern Hemisphere^{1,2} superimposed on a glacial–interglacial doubling of methane concentrations^{3–5}. The processes driving the observed fluctuations remain uncertain but can be constrained using methane isotopic information from ice cores^{6,7}. Here we present an ice core record of carbon isotopic ratios in methane over the entire last glacial–interglacial transition. Our data show that the carbon in atmospheric methane was isotopically much heavier in cold climate periods. With the help of a box model constrained by the present data and previously published results^{6,8}, we are able to estimate the magnitude of past individual methane emission sources and the atmospheric lifetime of methane. We find that methane emissions due to biomass burning were about 45 Tg methane per year, and that these remained roughly constant throughout the glacial termination. The atmospheric lifetime of methane is reduced during cold climate periods. We also show that boreal wetlands are an important source of methane during warm events, but their methane emissions are essentially shut down during cold climate conditions.

The atmospheric concentration of CH₄, the second most important anthropogenic greenhouse gas, is determined by a balance between natural and anthropogenic CH₄ sources and sinks that is still debated. Photochemically induced oxidation in the troposphere and stratosphere, and uptake by methanotrophic bacteria in aerated soils, represent the most important sinks^{9,10}. The dominating natural CH₄ sources comprise tropical and boreal wetlands, ruminants, and biomass burning^{10,11}. These sources all differ in their carbon and hydrogen isotopic signature. In addition, a release of CH₄ from marine gas hydrates^{12,13} and emissions from plants under aerobic conditions are currently debated^{14,15}. Most probably all those sources and sinks were subject to palaeoclimatic changes, as reflected by CH₄ being as low as 360 parts per billion (10⁹) by volume (p.p.b.v.) during the Last Glacial Maximum (LGM), compared with up to 725 p.p.b.v. in the preindustrial Holocene epoch^{3,16,17}. Throughout the glacial period and during the last transition, CH₄ changed by up to 200 p.p.b.v. (refs 3, 18) in parallel with rapid climate changes. Using the interhemispheric CH₄ gradient in ice cores, an increase of high-latitude CH₄ sources in the Northern Hemisphere was derived for warm periods^{3,17}. However, a more detailed quantitative source attribution is still missing.

Such quantitative constraint on the sources can be derived from methane isotopic measurements on ice cores^{6,7}, making use of the different isotopic signatures of the CH₄ sources and the different isotopic fractionation factors for the individual removal processes (Supplementary Table 1). In Fig. 1 typical isotopic signatures for

different CH₄ sources are summarized, spanning a wide range of $\delta^{13}\text{CH}_4$ and $\delta\text{D}(\text{CH}_4)$. This shows that $\delta^{13}\text{CH}_4$ strongly constrains the amount of CH₄ released by biomass burning, because pyrogenic CH₄ is the only natural source strongly enriched in ¹³C. The fractionation caused by the sinks is illustrated by the offset of the isotopic signature in atmospheric CH₄ and the calculated emission averages. This fractionation is very pronounced (~200‰) for $\delta\text{D}(\text{CH}_4)$ but rather small (5–7‰) for $\delta^{13}\text{CH}_4$.

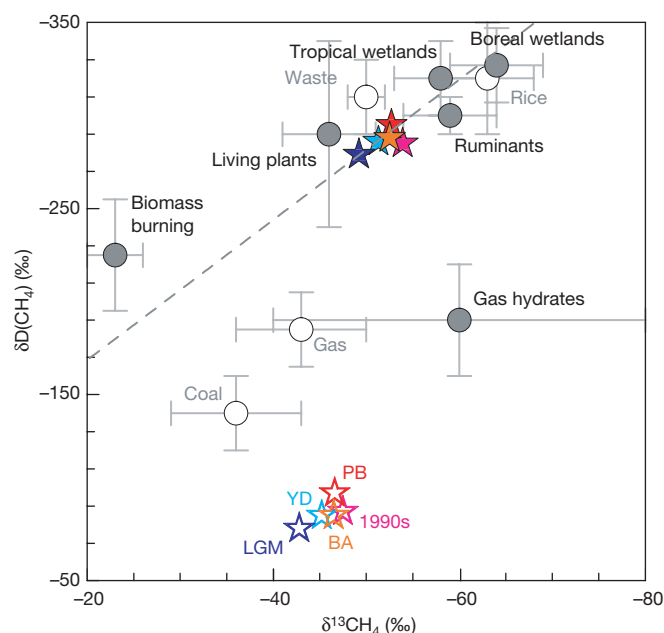


Figure 1 | Typical carbon and hydrogen isotopic signatures of different CH₄ sources used in the Monte Carlo model. Data are from refs 10 and 11 and references therein. Mainly anthropogenic sources are indicated by open circles, mainly natural sources by dark grey dots. The error bars indicate the spread of reported values¹⁰. No δD values for plant emissions are available so far. We used a value of -290‰ , which does not influence our model outcome. Open stars indicate the modelled average atmospheric $\delta^{13}\text{CH}_4$ and $\delta\text{D}(\text{CH}_4)$ for the 1990s, preboreal Holocene (PB), Younger Dryas (YD), Bølling/Allerød (BA) and LGM. Filled stars represent best-guess model estimates for average $\delta^{13}\text{CH}_4$ and $\delta\text{D}(\text{CH}_4)$ emitted, where we limited atmospheric lifetimes to values larger than 5 yr. The dashed line represents a linear fit through these isotopic emission averages. $\delta\text{D} = [(D/H)_{\text{sample}} / (D/H)_{\text{standard}}] - 1$ in ‰, where standard is standard mean ocean water (SMOW); $\delta^{13}\text{C} = [(^{13}\text{C}/^{12}\text{C})_{\text{sample}} / (^{13}\text{C}/^{12}\text{C})_{\text{standard}}] - 1$ in ‰, where standard is VPDB

¹Alfred Wegener Institute for Polar and Marine Research, Columbusstrasse, 27568 Bremerhaven, Germany. ²Laboratoire de Glaciologie et Geophysique de l'Environnement, CNRS-UJF, 54 rue Molière, 38400 Grenoble, France. ³Climate and Environmental Physics, Physics Institute, University of Bern, Sidlerstrasse 5, 3012 Bern, Switzerland. †Present address: Centre for Ice and Climate, Niels Bohr Institute, University of Copenhagen, Juliane Maries Vej 30, 2100 Copenhagen OE, Denmark.

Using high-precision gas chromatography isotope ratio mass spectrometry (see Supplementary Information) we have been able to derive a high-resolution $\delta^{13}\text{CH}_4$ ice-core record over the last glacial–interglacial transition. We carried out carbon isotopic analyses on 34 samples from the EPICA (European Project for Ice Coring in Antarctica) ice core from Dronning Maud Land (EDML)⁸. With its present accumulation rate of 6.4 cm water equivalent per year and an age distribution (width at half maximum) in the air bubbles of 60 yr, this core is especially suited to derive higher-resolution records over the last glacial cycle.

In Fig. 2 our $\delta^{13}\text{CH}_4$ record is plotted together with the CH_4 concentrations from the EDML and the Greenland GRIP ice core^{3,8}. Clearly, the most conspicuous features of our $\delta^{13}\text{CH}_4$ data are the high isotopic values of around -42.8‰ during the LGM followed by a 3.5‰ decrease to about -46.3‰ during the preboreal Holocene. The preboreal value is about 0.8‰ more enriched than values from the Law Dome ice core (Antarctica)¹⁹ for the time interval 1–2 kyr before present (BP) when CH_4 was about 40 p.p.b.v. lower¹⁷. At the same time the interhemispheric CH_4 gradient¹⁷ and, thus, the boreal methane source strength was comparable. This implies a relatively higher contribution of isotopically light boreal CH_4 emissions to the

total CH_4 budget in the late preindustrial Holocene compared with the preboreal Holocene. Alternatively, the lower $\delta^{13}\text{CH}_4$ values could be affected by increased rice cultivation and/or livestock in the late Holocene. Whether a significant anthropogenic influence on CH_4 had already started by 5000 yr BP as recently hypothesized²⁰ cannot be answered at this point.

Our $\delta^{13}\text{CH}_4$ record shows also significant variations in parallel with the rapid CH_4 changes during the Bølling/Allerød–Younger Dryas oscillation, with $\delta^{13}\text{CH}_4$ values during the Bølling/Allerød similar to the preboreal Holocene (about -46.3‰) but with slightly lower CH_4 concentrations. During the Younger Dryas, $\delta^{13}\text{CH}_4$ increased to around -45‰ . Our data do not support $\delta^{13}\text{CH}_4$ values during the Younger Dryas/preboreal transition measured on outcropping ice on the west Greenland margin⁷, which generally show isotopically lighter $\delta^{13}\text{CH}_4$ values before than after the end of the Younger Dryas. In view of the much higher scatter of those data and the potential of isotopic artefacts occurring in this warm outcropping ice, we think that our high-precision ice-core data reflect more closely the isotopic changes in atmospheric methane.

In principle, changes in the source as well as in the fractionation of the sinks may contribute to the observed changes. The latter effect is small because a global glacial–interglacial temperature increase of 5°C would decrease the carbon isotope fractionation by only $0.2\text{--}0.3\text{‰}$ ^{21–23} and also changes in lifetime have a negligible effect on $\delta^{13}\text{CH}_4$. Accordingly, the $\delta^{13}\text{CH}_4$ values indicate mainly a shift to isotopically heavier sources during cold climate periods. Thus, either an isotopically enriched CH_4 source (such as biomass burning) increased, or a depleted source (such as wetlands) decreased. Considering the 50% reduction of atmospheric CH_4 concentrations and the lack of an interhemispheric gradient in the LGM, a reduction of boreal wetland emissions is more likely. To constrain the emission by individual sources, we used a simple model of the CH_4 cycle with two tropospheric and two stratospheric boxes driven by prescribed emission fluxes for time intervals of relatively constant CH_4 : the preboreal Holocene, Younger Dryas, Bølling/Allerød and LGM (see Supplementary Information). The model has been validated for recent conditions and reflects CH_4 observations very well. For the last deglaciation our $\delta^{13}\text{CH}_4$ data from EDML, together with $\delta\text{D}(\text{CH}_4)$ data from Greenland⁶ and CH_4 concentrations from both polar regions^{3,8,16}, provide four constraints for the model. However, with six natural sources and three sink processes, the solution of the model is still underdetermined. To find possible solutions we used a Monte Carlo approach (see Supplementary Information). For many of the sources, the resulting probability distributions are not discriminating, owing to a considerable overlap in the isotopic signatures. However, robust quantitative constraints can be derived for the atmospheric lifetime, biomass burning and boreal wetland emissions.

In our initial estimate, which is constrained only by ice-core observations (see Supplementary Information), the atmospheric lifetime decreased from the recent value of a little more than 8 yr to around 5.6 yr in the preboreal Holocene and Bølling/Allerød, in good agreement with estimates of preindustrial runs using a three-dimensional model of chemistry and transport²⁴. In the Younger Dryas our most likely result indicates a strong lifetime decrease to 4.4 yr and to 3.7 yr in the LGM (Fig. 3a). Although a lifetime decrease is expected from the much lower atmospheric CH_4 concentration and reduced emissions of volatile organic carbon species during the LGM^{25,26}, this decrease of more than 50% relative to present is much stronger than predicted by current estimates from a three-dimensional chemistry model²⁶. However, as also shown in Fig. 3, lifetimes similar to those model estimates also fulfil our data constraints, but are less likely. Such longer lifetimes require a reduction in tropical wetland emissions to explain the lower CH_4 concentrations during the LGM. In summary, data as well as models indicate a shorter CH_4 lifetime during past climate periods in the range of 3–7 yr.

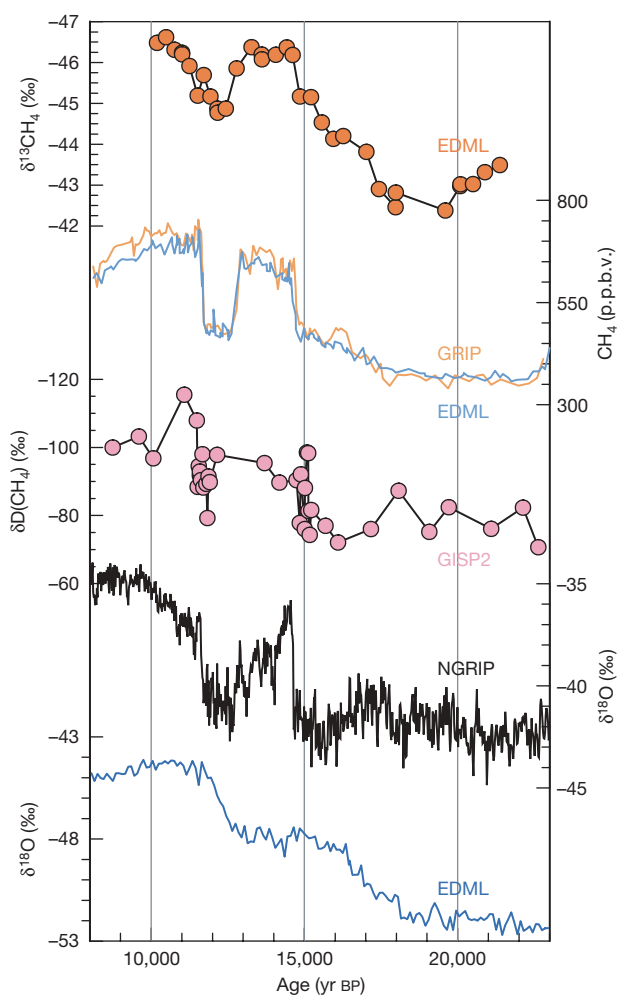


Figure 2 | Glacial/interglacial changes in methane and climate. Carbon isotopic signature of methane (scale reversed) in the EDML ice core together with Greenland (GRIP) and EDML methane concentrations^{3,8}, $\delta\text{D}(\text{CH}_4)$ in the GISP2 ice core⁶ (scale reversed) and the temperature proxy $\delta^{18}\text{O}$ from EDML⁸ and NGRIP¹. All data sets are given on the GICC05 age scale after CH_4 synchronization⁸, except for GISP2 $\delta\text{D}(\text{CH}_4)$ data given on their individual methane synchronized age scale⁶. Values of $\delta^{13}\text{CH}_4$ were corrected for gravitational enrichment in the firn column (see Supplementary Information) and are referenced against VPDB.

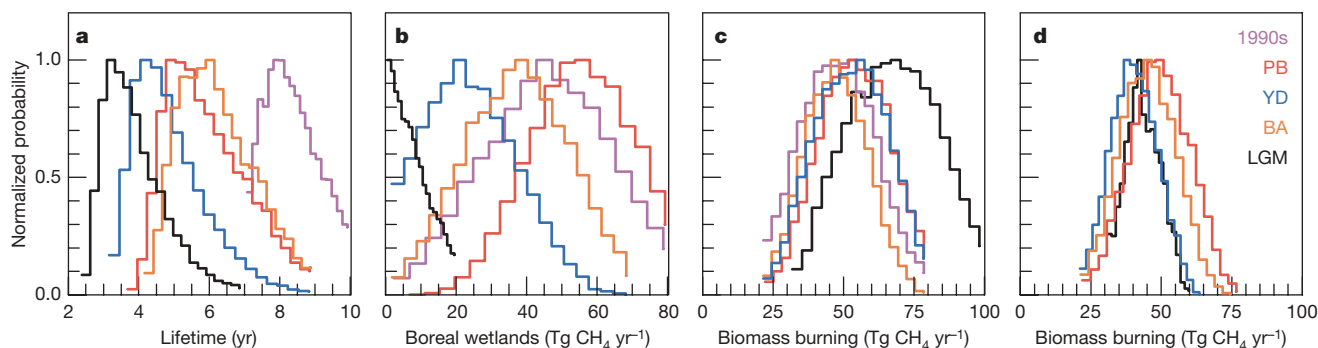


Figure 3 | Methane box model results. Normalized probability functions (NPF) for (a) atmospheric lifetime, (b) boreal wetland and (c) biomass burning emissions for the 1990s (pink), preboreal Holocene (PB, red), Younger Dryas (YD, blue), Bølling/Allerød (BA, orange) and the LGM (black) as derived in our data-constrained Monte Carlo box model. d, The

The higher atmospheric δCH_4 together with the lack of an inter-hemispheric CH_4 gradient requires the boreal wetland source in our model to be essentially shut down during the LGM, in line with the extreme cold and vastly expanded continental ice sheets in the high-latitude Northern Hemisphere. Part of the carbon isotope variation observed over the transition may also stem from a shift in the wetland substrate from C4 to C3 plants, following different photosynthetic pathways. However, such a shift cannot explain the size of the observed $\delta^{13}\text{CH}_4$ change or the changes in the interhemispheric gradient. A reduction of boreal wetlands connected to a reduced inter-hemispheric CH_4 gradient and more enriched $\delta^{13}\text{CH}_4$ is also supported for the Younger Dryas. In contrast, the $\delta^{13}\text{CH}_4$ values derived from outcropping ice on the west Greenland margin⁷ show isotopically lighter $\delta^{13}\text{CH}_4$ values during the Younger Dryas, which are difficult to reconcile with the interhemispheric gradient indicating a decrease in boreal CH_4 emissions.

Furthermore, quantitative constraints are derived from our $\delta^{13}\text{CH}_4$ data for pyrogenic CH_4 emissions. In our initial estimate (allowing for short atmospheric lifetimes) our model suggests somewhat higher biomass burning emissions during the LGM, where significant changes in vegetation cover and aridity occurred^{27,28}. When we additionally constrain atmospheric lifetimes in Fig. 3d to longer than 5 yr in line with chemistry models, our best-guess estimate for biomass burning emissions remains close to about $45 \text{ Tg CH}_4 \text{ yr}^{-1}$ throughout the transition, with slightly lower biomass burning during cold periods. Evidence for temporally constant biomass burning emissions is also provided by global vegetation modelling²⁹, but the modelled biomass burning CH_4 emission is 50% lower than our Monte Carlo estimate.

Secondary trends in $\delta^{13}\text{CH}_4$ occurred during the LGM and preboreal Holocene. For instance $\delta^{13}\text{CH}_4$ decreased slowly during the preboreal Holocene, when temperatures in Greenland and the CH_4 concentration gradient slightly increased. This may be attributed to expanding boreal sources, for example related to increased thermokarst emissions at that time³⁰. During the late glacial (22,000–20,000 yr BP), $\delta^{13}\text{CH}_4$ slowly increased by about 1‰ while CH_4 remained constant. A change in the carbon isotopic signature of the biomass fuelling wildfires by 3‰, caused by of a shift from C3- to C4-dominated grasslands, could largely explain this secondary trend in $\delta^{13}\text{CH}_4$ despite constant biomass burning emissions. Alternatively, it may represent a slow reduction of wetland emissions compensating a synchronous increase in biomass burning emission.

The result of our steady-state modelling is indicated by the average signatures of CH_4 emissions for past conditions in Fig. 1. These best-guess average emissions lie on a line roughly through the wetland isotopic signature, illustrating the changing influence of boreal wetland emissions on the isotopic CH_4 budget. This clearly shows that a CH_4 contribution from deuterium-enriched marine gas hydrates is

not supported by the observed isotope changes. However, quantification of a short CH_4 outburst from marine hydrates will require more high-resolution isotope data around rapid climate warmings together with time-resolved isotope modelling of the atmospheric CH_4 cycle and diffusion effects in the firn column. In summary, our new carbon isotopic constraint is able to determine the change in average CH_4 emissions from boreal wetlands and biomass burning very well, showing that the latter source was surprisingly stable over a wide range of climate conditions. This provides an important test for vegetation models and together with revised atmospheric chemistry models will improve our understanding of the oxidative capacity of the atmosphere in the past.

METHODS

We performed $\delta^{13}\text{CH}_4$ measurements on 150–200 g of ice using a purge and trap extraction coupled to a gas chromatography isotope ratio mass spectrometer. We separated CH_4 from other gases using gas chromatography and quantified isotopic ratios on CO_2 after quantitative combustion of CH_4 . Absolute standardization is achieved in every run using (i) a pure CO_2 standard (ii) a pure CH_4 standard admitted to the gas chromatography helium stream and (iii) 10 ml (STP) of a synthetic air standard admitted into the extraction vessel. All $\delta^{13}\text{CH}_4$ values are referenced against Vienna Pee Dee belemnite (VPDB) and corrected for gravitational enrichment. Replicate samples from the EDML ice core have been measured on five depth intervals showing a mean standard deviation of $\pm 0.09\text{‰}$ with somewhat larger uncertainties for glacial samples with low CH_4 concentration. This is also in line with the reproducibility of the air standards. In summary, we estimate the reproducibility of our measurements to be better than 0.15‰.

Potential source emissions were determined in steady state using a box model of the atmospheric CH_4 cycle. The atmosphere is divided into northern and southern tropospheric and stratospheric boxes with prescribed air mass exchange. Methane emissions into the northern and southern troposphere are prescribed with fixed isotopic signatures (refs 10, 11 and references therein; Supplementary Table 1). The model takes into account oxidation in the troposphere and stratosphere and uptake by aerated soils¹⁰. To constrain CH_4 emissions in the past the model was run in a Monte Carlo mode, where emissions of each individual source and the lifetime were randomly picked within reasonable limits and compared with the data constraints.

For more details on the analyses and model used, see Supplementary Information.

Received 18 June 2007; accepted 5 February 2008.

1. North Greenland Ice Core Project members. High resolution climate record of the northern hemisphere reaching into the last interglacial period. *Nature* **431**, 147–151 (2004).
2. Johnsen, S. J. *et al.* Irregular glacial interstadials recorded in a new Greenland ice core. *Nature* **359**, 311–313 (1992).
3. Dällenbach, A. *et al.* Changes in the atmospheric CH_4 gradient between Greenland and Antarctica during the last glacial and the transition to the Holocene. *Geophys. Res. Lett.* **27**, 1005–1008 (2000).
4. Spahni, R. *et al.* Atmospheric methane and nitrous oxide of the late Pleistocene from Antarctic ice cores. *Science* **310**, 1317–1321 (2005).

5. Petit, J. R. *et al.* Climate and atmospheric history of the past 420,000 years from the Vostok ice core, Antarctica. *Nature* **399**, 429–436 (1999).
6. Sowers, T. Late Quaternary atmospheric CH₄ isotope record suggests marine clathrates are stable. *Science* **311**, 838–840 (2006).
7. Schaefer, H. *et al.* Ice record of $\delta^{13}\text{C}$ for atmospheric CH₄ across the Younger Dryas–Preboreal transition. *Science* **313**, 1109–1112 (2006).
8. EPICA community members One-to-one coupling of glacial climate variability in Greenland and Antarctica. *Nature* **444**, 195–198 (2006).
9. Khalil, M. A. K., Shearer, M. J. & Rasmussen, R. A. in *Atmospheric Methane: Sources, Sinks, and Role in Global Change* (ed. Khalil, M. A. K.) 168–179 (Springer, Berlin, 1993).
10. Quay, P., Stutsman, J., Wilbur, D., Dlugokencky, E. & Brown, T. The isotopic composition of atmospheric methane. *Glob. Biogeochem. Cycles* **13**, 445–461 (1999).
11. Whiticar, M. J. in *Atmospheric Methane: Sources, Sinks, and Role in Global Change* (ed. Khalil, M. A. K.) 138–167 (Springer, Berlin, 1993).
12. Kennett, J. P., Cannariato, K. G., Hendy, I. L. & Behl, R. J. Carbon isotopic evidence for methane hydrate instability during Quaternary interstadials. *Science* **288**, 128–133 (2000).
13. Brook, E. J., Harder, S., Severinghaus, J., Steig, E. J. & Sucher, C. M. On the origin and timing of rapid changes in atmospheric methane during the last glacial period. *Glob. Biogeochem. Cycles* **14**, 559–572 (2000).
14. Keppler, F., Hamilton, J. T. G., Braß, M. & Röckmann, T. Methane emissions from terrestrial plants under aerobic conditions. *Nature* **439**, 187–191 (2006).
15. Dueck, T. A. *et al.* No evidence for substantial aerobic methane emission by terrestrial plants: a ¹⁴C-labelling approach. *New Phytol.* doi:10.1111/j.1469-8137.2007.02103.x (2007).
16. Chappellaz, J. *et al.* Synchronous changes in atmospheric CH₄ and Greenland climate between 40 and 8 kyr BP. *Nature* **366**, 443–445 (1993).
17. Chappellaz, J. *et al.* Changes in the atmospheric CH₄ gradient between Greenland and Antarctica during the Holocene. *J. Geophys. Res.* **102**, 15987–15997 (1997).
18. Flückiger, J. *et al.* N₂O and CH₄ variations during the last glacial epoch: Insight into global processes. *Glob. Biogeochem. Cycles* **18**, doi:10.1029/2003GB002122 (2004).
19. Ferretti, D. F. *et al.* Unexpected changes to the global methane budget over the past 2000 years. *Science* **309**, 1714–1717 (2005).
20. Ruddiman, W. F. The anthropogenic greenhouse era began thousands of years ago. *Clim. Change* **61**, 261–293 (2003).
21. Cantrell, C. A. *et al.* Carbon kinetic isotope effect in the oxidation of methane by the hydroxyl radical. *J. Geophys. Res.* **95**, 22455–22462 (1990).
22. Tyler, S. C., Crill, P. M. & Brailsford, G. W. ¹³C/¹²C fractionation of methane during oxidation in a temperate forested soil. *Geochim. Cosmochim. Acta* **58**, 1625–1633 (1994).
23. Saueressig, G., Bergamaschi, P., Crowley, J. N., Fischer, H. & Harris, G. W. Carbon kinetic isotope effect in the reaction of CH₄ with Cl atoms. *Geophys. Res. Lett.* **22**, 1225–1228 (1995).
24. Lelieveld, J., Crutzen, P. & Dentener, F. J. Changing concentration, lifetime and climate forcing of atmospheric methane. *Tellus* **50B**, 128–150 (1998).
25. Kaplan, J. O., Folberth, G. & Hauglustaine, D. A. Role of methane and biogenic volatile organic compound sources in late glacial and Holocene fluctuations of atmospheric methane concentrations. *Glob. Biogeochem. Cycles* **20**, doi:10.1029/2005GB002590 (2006).
26. Valdes, P. J., Beerling, D. J. & Johnson, C. E. The ice age methane budget. *Geophys. Res. Lett.* **32**, doi:10.1029/2004GL021004 (2005).
27. Mahowald, N. *et al.* Dust sources and deposition during the last glacial maximum and current climate: A comparison of model results with paleodata from ice cores and marine sediments. *J. Geophys. Res.* **104**, 15895–15916 (1999).
28. Kaplan, J. O. Wetlands at the Last Glacial Maximum: Distribution and methane emissions. *Geophys. Res. Lett.* **29**, doi:10.1029/2001GL013366 (2002).
29. Thonicke, K., Prentice, I. C. & Hewitt, C. Modeling glacial-interglacial changes in global forest fire regimes and trace gas emissions. *Glob. Biogeochem. Cycles* **19**, doi:10.1029/2004GB002278 (2005).
30. Walter, K. M., Edwards, M. E., Grosse, G., Zimov, S. A. & Chapin, F. S. III. Thermokarst lakes as a source of atmospheric CH₄ during the last deglaciation. *Science* **318**, 633–636 (2007).

Supplementary Information is linked to the online version of the paper at www.nature.com/nature.

Acknowledgements This work is a contribution to EPICA, a joint European Science Foundation/European Commission scientific programme, funded by the EU and by national contributions from Belgium, Denmark, France, Germany, Italy, the Netherlands, Norway, Sweden, Switzerland and the United Kingdom. The main logistical support was provided by IPEV and PNRA (at Dome C) and AWI (at Dronning Maud Land). This is EPICA publication no. 190. We thank I. Levin for providing reference air samples and for comments on the manuscript. We thank the logistics team (led by C. Drücker), the drilling team (led by F. Wilhelms) and all helpers in the field at EDML for making the science possible. Financial support for this study has been provided in part by the German Secretary of Education and Research program GEOTECHNOLOGIEN and Deutsche Forschungsgemeinschaft.

Author Information Reprints and permissions information is available at www.nature.com/reprints. Correspondence and requests for materials should be addressed to H.F. (hubertus.fischer@awi.de).

LETTERS

Sophisticated particle-feeding in a large Early Cambrian crustacean

Thomas H. P. Harvey¹ & Nicholas J. Butterfield¹

Most Cambrian arthropods employed simple feeding mechanisms requiring only low degrees of appendage differentiation^{1–3}. In contrast, post-Cambrian crustaceans exhibit a wide diversity of feeding specializations and possess a vast ecological repertoire. Crustaceans are evident in the Cambrian fossil record, but have hitherto been known exclusively from small individuals with limited appendage differentiation⁴. Here we describe a sophisticated feeding apparatus from an Early Cambrian arthropod that had a body length of several centimetres. Details of the mouthparts resolve this taxon as a probable crown-group (pan)crustacean, while its feeding style, which allowed it to generate and handle fine food particles, significantly expands the known ecological capabilities of Cambrian arthropods. This Early Cambrian record predates the major expansions of large-bodied, particle-handling crustaceans by at least one hundred million years^{5,6}, emphasizing the importance of ecological context in driving adaptive radiations.

Abundant organic-walled fossils were extracted from a 2-cm-thick subsurface shale unit of the late Early Cambrian (515–510 Myr ago) Mount Cap Formation, Northwest Territories, Canada (Bele drill-core O-35; depth 1,351 m)⁷. The authigenicity of the HF-isolated fossils is demonstrated by their orange-brown colour, near-two-dimensionality, occurrence within petrographic thin sections, and the presence of associated diagenetic pyrite.

The most commonly recovered fossils are cuticle fragments ($n = 3,425$), which are recognized as arthropodan on the basis of characteristic spines and setae. The assemblage includes at least 35 distinct spine/seta morphologies, a diversity typical of extant crustaceans but well beyond that reported from aquatic chelicerates, living or extinct. Most of these fossils have close morphological counterparts among extant crustaceans and are likely to have served comparably diverse mechanical, chemosensory and mechanosensory roles⁸. Most significantly, recurrent associations of the various spines and setae—for example, of robust serrated, hooked, clubbed and saw-toothed morphologies (for example, Fig. 1a–d), as well as more delicate plumose and pappose arrangements, such as coplanar filter plates (Fig. 1e–g)—are identified as armatures derived from highly specialized appendages with clear adaptations for scraping and filtering fine particulate food. Pronounced functional localization within appendages is implied by the many highly modified setal morphologies, the discreteness of the various associations, and the regionalization of particular armature-types within larger, less fragmentary specimens (Fig. 1a–c) (see also Supplementary Fig. 1).

The Mount Cap assemblage also includes a number of discretely shaped cuticular elements, of which two categories are particularly notable. The first ($n = 79$) consists of double-walled ovoid to triangular structures bearing a distinctive marginal spination of repeated short spines alternating with single longer ones (Fig. 2a–c). With no plane of bilateral symmetry, these are likely to have been paired in life, and the consistent marginal position of the spine rows

implies a relatively flattened profile. Among arthropod body parts, these fossils exhibit broad similarities to various tail or exopod flaps⁹, and to the terminal articles of walking appendages¹⁰. However, the closest comparison is with the maxillary lobes of various malacostracan and cirripede crustaceans^{10,11}, which also have conspicuously straight spine rows and precisely developed patterns of alternating spine lengths—features presumably related to their role in grasping and tearing food particles.

The second category of discrete elements ($n = 63$) is represented by single-walled, fusiform structures with distinctively fringed margins (Fig. 2d–h). The area enclosed by the fringe bears parallel lineations, approximately 2 μm wide, aligned perpendicular to the long axis. The lineations are composed of imbricating palmate cuticular scales which progressively lengthen towards one of the margins to form the fringing setae, and shorten medially until they merge into a low-relief region (Fig. 2f–h). Among extant arthropods, this style of ornamentation is unique to the molar surfaces of mandibles—the grinding elements of the perioral appendages of ‘mandibulates’ (crustaceans, hexapods and myriapods)¹²; particularly close comparisons with the Mount Cap mandibles may be found among branchiopod crustaceans (Fig. 2i–k).

The presence of triturating molar surfaces alone would demonstrate an Early Cambrian occurrence of mandibulate-type appendage tagmosis (in the sense of ref. 13), as would the extensive fields of specialized setae and the integrated setal associations discussed above. We note, however, that none of these specializations is functional in isolation: each represents a separate step in the process of generating and transporting fine particles to the mouth. Additionally, the relative sizes of the various non-molar Mount Cap elements corroborate their identification as mouthparts rather than other body organs. As such, there is a compelling case for reassembling most, if not all, of these co-occurring elements as a single complex feeding apparatus with probable adaptations for benthic ‘grazing’—the latter based on the prominence of robust serrate setal forms¹⁴, including highly modified saw-toothed setae (Fig. 1d and Supplementary Fig. 1d; compare ref. 10). Food particles would initially have been scraped from surfaces using appendage parts adorned with saw-toothed, serrate and hooked setae (Fig. 1b, d and Supplementary Fig. 1d, l, n), further processed by filter plates (Fig. 1e–g and Supplementary Fig. 1c) and more delicate setal associations (Fig. 1c and Supplementary Fig. 1j, m), and finally triturated by the mandibular molar surfaces (Fig. 2d–h) before being passed on to the oesophagus via the long molar-fringing setae (Fig. 2f).

Reassembled, the Mount Cap feeding apparatus is fundamentally more sophisticated than that of any other documented Cambrian arthropod, most of which processed food and passed it towards the mouth using a homonomous series of spiny gnathobases bordering a food groove^{2,15}—a feeding style retained by post-Cambrian trilobites and aquatic chelicerates. Various stem-group euarthropods, and

¹Department of Earth Sciences, University of Cambridge, Downing Street, Cambridge, CB2 3EQ, UK.

perhaps some of the ‘great appendage arthropods’, used an even simpler mechanism in which an anterior pair of raptorial appendages acquired food and passed it back to the mouth^{2,15,16}. Among Orsten-type faunas, which include a diversity of small (<2 mm) arthropods preserved via three-dimensional diagenetic phosphatization, the Late Cambrian *Rehbachella* exhibits the most functionally derived particle-handling mechanism, bearing a well-differentiated mandible and a modest diversity of setae⁹. Even here, however, there are no Mount Cap-style molar surfaces, coplanar filter plates, or monotypic fields of highly modified setae. Moreover, any variation in non-mandibular armature that the Orsten taxa do express occurs along gradients of size rather than among regions of differentiated morphology, in striking contrast to the Mount Cap apparatus.

The degree of feeding appendage differentiation exhibited by the Mount Cap crustacean carries implications for its phylogenetic position, because increasing feeding complexity is considered to reflect increasing phylogenetic distance along the lineage leading to crown-group crustaceans¹⁶. The Mount Cap crustacean is fundamentally more differentiated than any of the phosphatocopines, the most derived stem-group forms identified thus far¹⁶, from which its more crownward position can be inferred. Placement within the crown group, however, can only be established unambiguously by identifying a synapomorphy diagnostic of an extant subset of the clade¹⁷.

Treating crown group ‘Crustacea’ as equivalent to crown-group Pancrustacea/Tetraconata (that is, crustaceans plus hexapods^{18–20}), we argue that the style of molar surface ornamentation described here is such a character. Among pancrustaceans, a discrete, planar, ovoid/crescentic region of molar ornamentation bearing rows of distally divided scales that shorten unilaterally and become confluent is widely distributed within (and restricted to) a subclade of the crown group containing malacostracans, branchiopods and hexapods to the exclusion of ostracods and branchiurans (resolved by two independent molecular phylogenies^{19,20}). This scenario of character evolution is sensitive to the internal phylogeny of pancrustaceans, but not to the relationship of myriapods to other ‘mandibulates’ (which may or may not form a clade¹⁸): the comparable ovoid region of molar ornamentation developed in some diplopod millipedes is likely to be derived among myriapods¹² and therefore evolved convergently, on land, later in the Palaeozoic.

Unambiguously identified crustaceans are rare in the Cambrian fossil record, despite earlier views to the contrary. Superficially crustacean-like members of the Middle Cambrian Burgess Shale fauna²¹, for example, are no longer considered as occupying even stem-group positions²², and details of soft-part anatomy suggest positions for phosphatocopines and bradoriids among stem-group crustaceans and stem-group euarthropods, respectively¹⁶, thus

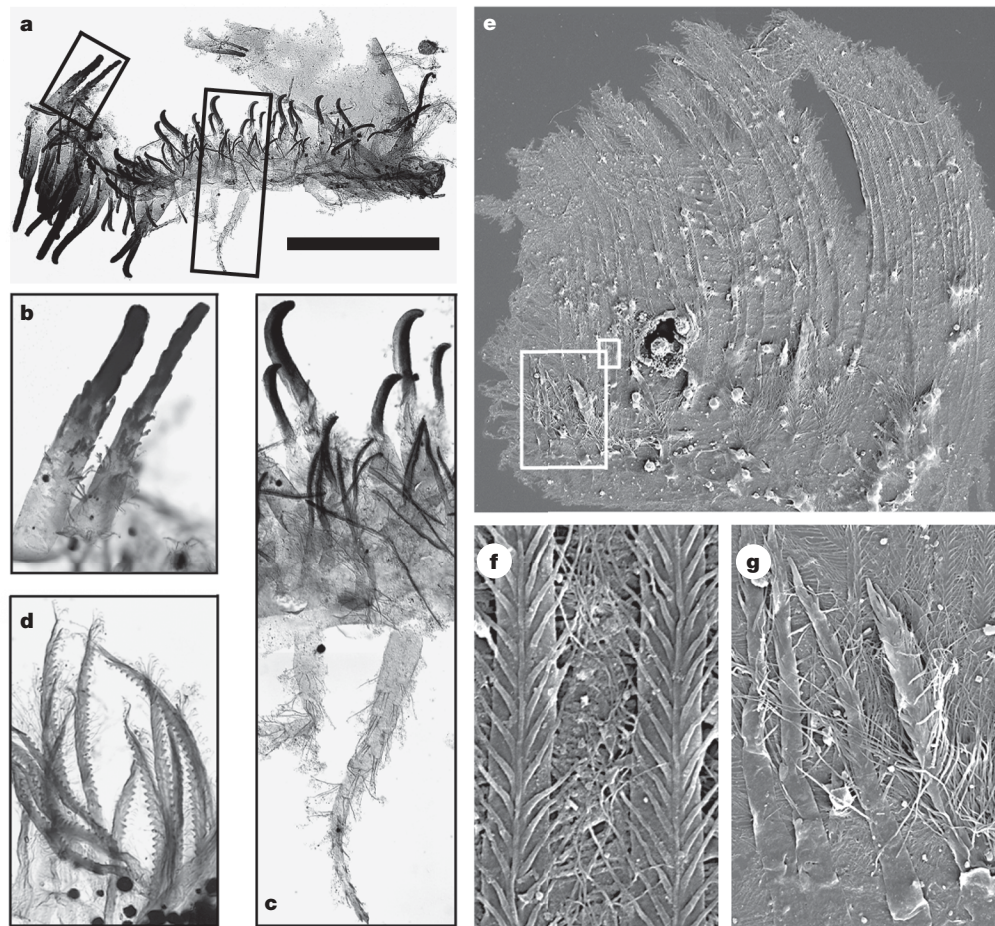


Figure 1 | Fossil arthropod setae and setal armatures from the Early Cambrian Mount Cap Formation. Specimens are stored at the Geological Survey of Canada (GSC); see Supplementary Information for additional details. **a–c**, Portion of an appendage that is functionally differentiated into regions of contrasting setal armature (GSC 34928). **a**, Overview; **b**, detail of robust, biserially serrate setae; **c**, detail of an association of robust hooked setae, slender biserially serrate setae, and thin-walled papposerrate setae with branching setules. Boxes in **a** locate areas magnified in **b** and **c**. **d**, Detail from a monotypic group of 150 saw-toothed setae which bifurcate distally

and have delicate setules inserted along their length (GSC 34929). **e–g**, Filter plate, consisting of a coplanar series of spinulated plumose setae, with setules forming a regular, submicrometre mesh (detail in **f**), paralleled by a row of biserially serrate spatulate setae with long setules attached proximally (detail in **g**) (GSC 34930). Boxes in **e** locate areas magnified in **f** and **g**. **a–d** are light micrographs in which images of different focal planes have been montaged to achieve even focus; **e–g** are scanning electron micrographs of gold-coated specimens. Scale bars: **a**, 215 µm; **b**, **c**, 65 µm; **d**, 30 µm; **e**, 90 µm; **f**, 6 µm; **g**, 25 µm.

removing support for a Cambrian record of ostracods²³. Putative crustaceans from the Early Cambrian Chengjiang fauna^{24,25} have yet to reveal convincing diagnostic synapomorphies¹⁶. The purported mandibles of *Pectocaris*, for example, have not been observed to bear gnathal edges²⁵, leaving no compelling evidence for either crustacean affinity or mandibulate-style feeding; this fossil otherwise most closely resembles demonstrably stem-group euarthropods²². Apart from the Mount Cap fossils, only Orsten-type biotas preserve unambiguously identified crustaceans^{4,26}. Putative crown-group representatives are largely restricted to the Late Cambrian⁴, though a single Early Cambrian example, *Yicaris*, has recently been reported²⁶. In contrast to the Mount Cap taxon, however, it is not clear that *Yicaris* fulfils the crown-group membership criterion¹⁷ requiring expression of a synapomorphy shared with a subset of extant crustaceans. The pivotal character proposed by ref. 26 as uniting *Yicaris* with 'entomostracans' is that of multiple, prominent basipod endites on post-mandibular appendages. However, such endites are also known from the post-maxillary appendages of an early malacostracan²⁷, suggesting that the condition in *Yicaris* is also consistent with a stem-group placement, at least in the context of the Malacostraca versus Entomostraca scheme of ref. 26.

The distinction of the Mount Cap taxon relative to other Cambrian crustaceans lies not only in its greater functional sophistication, but also in its much greater size. Using regressions of body length versus molar surface length in extant crustacean taxa, we estimate the body length of the fossil to have been in the range of 5 cm, and certainly of macroscopic dimensions (see Supplementary Figs 2 and 3). This size context sheds light on the ecological

capabilities of Cambrian arthropods. In contrast to the poorly selective feeding apparatuses of macroscopic trilobites and Chengjiang/Burgess Shale arthropods, the Mount Cap crustacean combined large size with precise and selective particle handling, a strategy that we suggest requires substantially greater mechanical sophistication and appendage differentiation in macroscopic than in microscopic animals, due in part to their operation in much higher Reynolds number environments. The resulting morphological toolkit would have carried enormous adaptive potential for new feeding styles such as planktic herbivory⁷, for which the early Cambrian radiation of ornamented phytoplankton provides strong proxy evidence²⁸.

Differential taphonomy plays an important role in our reading of early crustacean evolution. The absence from Orsten assemblages of taxa bearing Mount Cap-type characters probably reflects the 2 mm body size limit inherent to Orsten taphonomy: a sample dominated by underdeveloped larvae and miniaturized, potentially secondarily simplified, adults⁴ clearly under-represents both contemporaneous disparity and functional sophistication. By contrast, Burgess Shale/Chengjiang-type arthropods often attain macroscopic dimensions, but generally fail to express equivalent fine-scale detail of mouthparts (though most, if not all, exhibit low degrees of appendage tagmosis^{16,22} and so are likely to lack comparable mouthparts in any event). The preservation of the Mount Cap fossils appears to be unique in providing submicrometre resolution of the feeding anatomy of centimetre-sized Cambrian arthropods, revealing a previously unseen dimension to early crustacean evolution.

The long-term success of crustaceans has been attributed to their propensity to localize functionality between body regions and

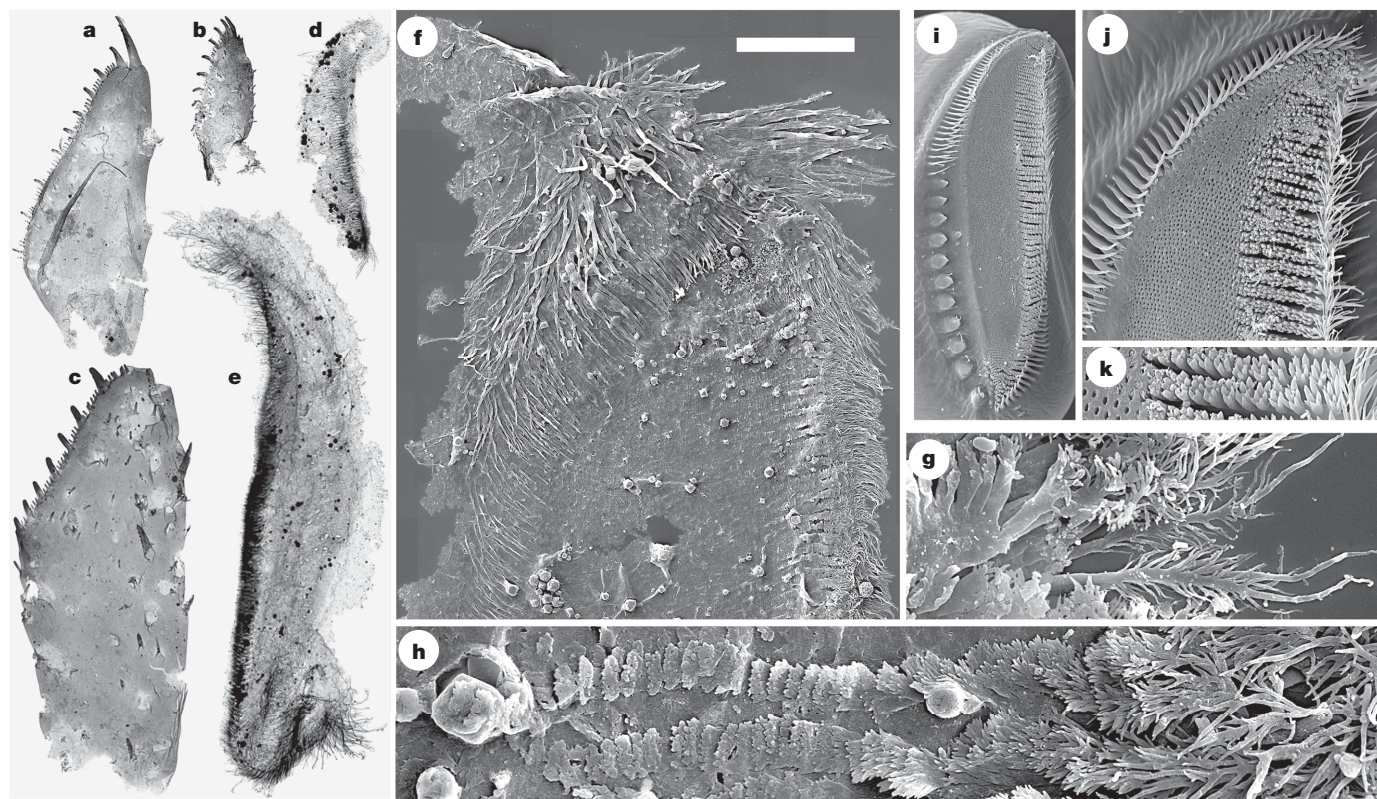


Figure 2 | Mount Cap cuticular elements with discrete bounding shapes (a–h), and mandibular molar surfaces of a modern branchiopod crustacean (i–k). Mount Cap specimens are stored at the GSC; see Supplementary Information for additional details. **a–c**, Double-walled structures bearing straight, marginal spine rows with precisely developed spine length alternation (GSC 34931–34933). **d–h**, Single-walled structures identified as mandibular molar surfaces. **d, e**, Light micrographs to show size variation (GSC 34934–34935). **f–h**, Scanning electron micrographs to show the fine-scale ornamentation, including details of the imbricating palmate cuticular

scales which lengthen to form the pappose setal fringe of one of the molar margins (**g**, right hand side), and shorten to merge with the low-relief molar region (**h**, left hand side) (GSC 34936–34938). Note the crystals of diagenetic pyrite. See Supplementary Fig. 2 for additional specimens. **i–k**, Scanning electron micrographs of the mandibular molar surface of a modern anostracan branchiopod crustacean, *Branchinella lyrifera*, exhibiting a closely comparable ornamentation; images courtesy of S. Richter. For imaging methods, see Fig. 1. Scale bars: **a–c**, 200 μ m; **d, e**, 110 μ m; **f**, 50 μ m; **g**, 6 μ m; **h**, 8 μ m; **i**, 110 μ m; **j**, 40 μ m; **k**, 15 μ m.

appendages^{2,13,29}. The Mount Cap crustacean reveals that extensive, mandibulate-type mouthpart differentiation originated by at least the latter part of the Early Cambrian, while comparison with the contemporaneous Orsten arthropods suggests that this development was driven by the feeding efficiency requirements of larger-bodied taxa. Even so, there is a conspicuous interval of time separating these early innovations from the later Palaeozoic–Mesozoic rise of crustaceans to ecological dominance^{5,6}. The spectacular radiations of large-bodied, particle-handling malacostracans, first during the Devonian and Carboniferous, and later (in the form of decapods) during the Jurassic and Cretaceous, postdate the Cambrian by 100 and 300 million years, respectively⁵—intervals too long to be attributed to taphonomic bias alone. Like the Phanerozoic history of brachiopods and bivalves³⁰, the replacement of a Cambrian/Palaeozoic fauna of messy-feeding arthropods by the altogether more sophisticated habits of ‘Modern’ crustaceans can be viewed in terms of competitive exclusion, incumbency replacement, shifts in the physical environment, or simply the long-term success of a more adaptable technology operating in an increasingly demanding biosphere. The emerging crustacean record emphasizes the central importance of ecology in driving macroevolutionary trends.

Received 15 October 2007; accepted 16 January 2008.

Published online 12 March 2008.

- Boxshall, G. A. The evolution of arthropod limbs. *Biol. Rev.* **79**, 253–300 (2004).
- Budd, G. E. in *The Ecology of the Cambrian Radiation* (eds Zhuravlev, A. Yu. & Riding, R.) 404–427 (Columbia Univ. Press, New York, 2001).
- Hughes, N. C. Trilobite tagmosis and body patterning from morphological and developmental perspectives. *Integr. Comp. Biol.* **43**, 185–206 (2003).
- Maas, A. et al. The ‘Orsten’ – more than a Cambrian Konservat-Lagerstätte yielding exceptional preservation. *Palaeoworld* **15**, 266–282 (2006).
- Sepkoski, J. J. Jr. Crustacean biodiversity through the marine fossil record. *Contrib. Zool.* **69**, 213–221 (2000).
- Briggs, D. E. G. & Clarkson, E. N. K. in *Major Evolutionary Radiations* (eds Taylor, P. D. & Larwood, G. P.) 165–186 (Systematics Association Special Volume No. 42, Clarendon Press, Oxford, 1990).
- Butterfield, N. J. Burgess Shale-type fossils from a Lower Cambrian shallow-shelf sequence in northwestern Canada. *Nature* **369**, 477–479 (1994).
- Garm, A. Mechanical functions of setae from the mouth apparatus of seven species of decapod crustaceans. *J. Morphol.* **260**, 85–100 (2004).
- Waloszek, D. The Upper Cambrian *Rehbachella* and the phylogeny of Branchiopoda and Crustacea. *Fossils Strata* **32**, 1–202 (1993).
- Fryer, G. The feeding mechanism of some atyid prawns of the genus *Caridina*. *Trans. R. Soc. Edinb.* **64**, 217–244 (1960).
- Garm, A. & Høeg, J. T. Functional mouthpart morphology of the squat lobster *Munida sarsi*, with comparison to other anomurans. *Mar. Biol.* **137**, 123–138 (2000).
- Edgecombe, G. D., Richter, S. & Wilson, G. D. F. The mandibular gnathal edges: homologous structures throughout Mandibulata? *Afr. Invertebr.* **44**, 115–135 (2003).
- Cisne, J. L. Evolution of the world fauna of aquatic free-living arthropods. *Evol. Int. J. Org. Evolution* **28**, 337–366 (1974).
- Coelho, V. R., Williams, A. B. & Rodrigues, S. de A. Trophic strategies and functional morphology of feeding appendages, with emphasis on setae, of *Upogebia omissa* and *Pomatogebia operculata* (Decapoda: Thalassinidea: Upogebiidae). *Zool. J. Linn. Soc.* **130**, 567–602 (2000).
- Bousfield, E. L. A contribution to the natural classification of Lower and Middle Cambrian arthropods: food-gathering and feeding mechanisms. *Amphipacificia* **2**, 3–34 (1995).
- Waloszek, D., Maas, A., Chen, J. & Stein, M. Evolution of cephalic feeding structures and the phylogeny of Arthropoda. *Palaeogeogr. Palaeoclimatol. Palaeoecol.* **254**, 273–287 (2007).
- Budd, G. E. & Jensen, S. A critical reappraisal of the fossil record of the bilaterian phyla. *Biol. Rev.* **75**, 253–295 (2000).
- Richter, S. The Tetraconata concept: hexapod–crustacean relationships and the phylogeny of Crustacea. *Org. Divers. Evol.* **2**, 217–237 (2002).
- Regier, J. C., Shultz, J. W. & Kambic, R. E. Pancrustacean phylogeny: hexapods are terrestrial crustaceans and maxillopods are not monophyletic. *Proc. R. Soc. Lond. B* **272**, 395–401 (2005).
- Mallatt, J. & Giribet, G. Further use of nearly complete 28S and 18S rRNA genes to classify Ecdysozoa: 37 more arthropods and a kinorhynch. *Mol. Phylogenet. Evol.* **40**, 772–794 (2006).
- Briggs, D. E. G. in *Crustacean Phylogeny* Vol. 1 of *Crustacean Issues* (ed. Schram, F. R.) 1–22 (Balkema, Rotterdam, 1983).
- Budd, G. E. A palaeontological solution to the arthropod head problem. *Nature* **417**, 271–275 (2002).
- Hou, X., Siveter, D. J., Williams, M., Waloszek, D. & Bergström, J. Appendages of the arthropod *Kunmingella* from the early Cambrian of China: its bearing on the systematic position of the Bradiriida and the fossil record of the Ostracoda. *Phil. Trans. R. Soc. Lond. Ser. B* **351**, 1131–1145 (1996).
- Chen, J.-Y., Vannier, J. & Huang, D.-Y. The origin of crustaceans: new evidence from the Early Cambrian of China. *Proc. R. Soc. Lond. B* **268**, 2181–2187 (2001).
- Hou, X.-G., Bergström, J. & Xu, G.-H. The Lower Cambrian crustacean *Pectocaris* from the Chengjiang biota, Yunnan, China. *J. Paleontol.* **78**, 700–708 (2004).
- Zhang, X.-G., Siveter, D. J., Waloszek, D. & Maas, A. An epipodite-bearing crown-group crustacean from the Lower Cambrian. *Nature* **449**, 595–598 (2007).
- Briggs, D. E. G., Sutton, M. D., Siveter, D. J. & Siveter, D. J. A new phyllocarid (Crustacea: Malacostraca) from the Silurian fossil-Lagerstätte of Herefordshire, UK. *Proc. R. Soc. Lond. B* **271**, 131–138 (2004).
- Butterfield, N. J. Macroevolution and macroecology through deep time. *Palaeontology* **50**, 41–55 (2007).
- Bambach, R. K. in *Phanerozoic Diversity Patterns* (ed. Valentine, J. W.) 191–253 (Princeton Univ. Press, Princeton, New Jersey, 1985).
- Sepkoski, J. J. Jr. in *Evolutionary Paleobiology* (eds Jablonski, D., Erwin, D. H. & Lipps, J. H.) 211–255 (Univ. Chicago Press, Chicago, 1996).

Supplementary Information is linked to the online version of the paper at www.nature.com/nature.

Acknowledgements We thank S. Richter for providing the images used in Fig. 2i–k. This work is supported by the Department of Earth Sciences, University of Cambridge, and a NERC studentship (to T.H.P.H.).

Author Information Reprints and permissions information is available at www.nature.com/reprints. Correspondence and requests for materials should be addressed to T.H.P.H. (thar04@esc.cam.ac.uk).

LETTERS

The complete genome of an individual by massively parallel DNA sequencing

David A. Wheeler^{1*}, Maithreyan Srinivasan^{2*}, Michael Egholm^{2*}, Yufeng Shen^{1*}, Lei Chen¹, Amy McGuire³, Wen He², Yi-Ju Chen², Vinod Makhijani², G. Thomas Roth², Xavier Gomes², Karrie Tartaro^{2†}, Faheem Niazi², Cynthia L. Turcotte², Gerard P. Irzyk², James R. Lupski^{4,5,6}, Craig Chinault⁴, Xing-zhi Song¹, Yue Liu¹, Ye Yuan¹, Lynne Nazareth¹, Xiang Qin¹, Donna M. Muzny¹, Marcel Margulies², George M. Weinstock^{1,4}, Richard A. Gibbs^{1,4} & Jonathan M. Rothberg^{2†}

The association of genetic variation with disease and drug response, and improvements in nucleic acid technologies, have given great optimism for the impact of 'genomic medicine'. However, the formidable size of the diploid human genome¹, approximately 6 gigabases, has prevented the routine application of sequencing methods to deciphering complete individual human genomes. To realize the full potential of genomics for human health, this limitation must be overcome. Here we report the DNA sequence of a diploid genome of a single individual, James D. Watson, sequenced to 7.4-fold redundancy in two months using massively parallel sequencing in picolitre-size reaction vessels. This sequence was completed in two months at approximately one-hundredth of the cost of traditional capillary electrophoresis methods. Comparison of the sequence to the reference genome led to the identification of 3.3 million single nucleotide polymorphisms, of which 10,654 cause amino-acid substitution within the coding sequence. In addition, we accurately identified small-scale (2–40,000 base pair (bp)) insertion and deletion polymorphism as well as copy number variation resulting in the large-scale gain and loss of chromosomal segments ranging from 26,000 to 1.5 million base pairs. Overall, these results agree well with recent results of sequencing of a single individual² by traditional methods. However, in addition to being faster and significantly less expensive, this sequencing technology avoids the arbitrary loss of genomic sequences inherent in random shotgun sequencing by bacterial cloning because it amplifies DNA in a cell-free system. As a result, we further demonstrate the acquisition of novel human sequence, including novel genes not previously identified by traditional genomic sequencing. This is the first genome sequenced by next-generation technologies. Therefore it is a pilot for the future challenges of 'personalized genome sequencing'.

To catalogue the genomic diversity within a single individual, a total of 106.5 million high-quality reads were generated by 454-sequencing³, representing approximately 24.5 billion DNA bases. Reads that aligned to the genome were further filtered using stringent criteria to ensure the accuracy of mapping, resulting in 93.2 million reads aligned to reference genome sequence. The reference genome sequence was thus covered to an average depth of 7.4-fold (Fig. 1a). The alignments between the uniquely mapped reads and the reference genome were used to catalogue genetic variation in the

subject's DNA, including single nucleotide polymorphisms (SNPs), small insertions and deletions (indels), and copy number variation (CNV).

The 454 base-calling software provides error estimates (Q values) for each base. We developed a three-step filtering process using the patterns of error and associated Q values from the 454 base-calling software to improve the accuracy of SNP discovery. An initial 14 million variant positions were filtered to 3.32 million putative SNPs (Table 1).

Comparison of these putative SNPs in the subject's genome with those in the dbSNP (dbSNP: <http://www.ncbi.nlm.nih.gov/projects/SNP/>) revealed 2.72 million in common ('known SNPs'). Approximately 99% of SNPs in dbSNP are bi-allelic. At only 10,425 positions did the subject's variant not match the variant found in dbSNP. Although some of these could represent a third allele in the population, or an error in the dbSNP polymorphism record, we conservatively estimated the false discovery rate in the known SNPs to be approximately 0.38% based on the mismatches with dbSNP.

The remaining 0.61 million SNPs were at positions not previously identified as polymorphic in dbSNP ('novel SNPs'). The known SNPs were divided almost equally between homozygous (50.2%) and heterozygous (49.8%) SNPs, whereas within the novel SNPs heterozygotes predominate (83.3%) compared with homozygotes (16.7%). Because most common alleles in human populations are already captured in dbSNP, novel variants are expected to be rare, and therefore much more likely to be found as heterozygotes.

We assessed the accuracy of the known SNPs derived from DNA sequencing by comparison with the experimental genotyping of the subject's DNA using an Affymetrix 500K microarray. Compared with a haploid reference sequence, there are four possible outcomes of SNP array genotyping: homozygous for the reference allele; homozygous for the variant (non-reference) allele; heterozygous; and assay failure. Table 2 shows the results for 494,713 markers that were successfully genotyped. The subject's DNA sequence exhibited only the reference allele at 99.4% of the markers homozygous for the reference and at 95.1% of markers homozygous for the variant. Genotyping identified 135,413 heterozygous markers of which 75.8% exhibited two alleles in the 454-reads. The lower sensitivity of detection of heterozygotes is predicted by a Poisson process of sampling DNA fragments modelled on a diploid genome (Methods). Consistent

¹Human Genome Sequencing Center, Baylor College of Medicine, One Baylor Plaza, Houston, Texas 77030, USA. ²454 Life Sciences, Roche Diagnostics, 20 Commercial Street, Bradford, Connecticut 06405, USA. ³Center for Ethics and Health Policy, Baylor College of Medicine, One Baylor Plaza, Houston Texas 77030, USA. ⁴Department of Molecular and Human Genetics, Baylor College of Medicine, One Baylor Plaza, Houston Texas 77030, USA. ⁵Department of Pediatrics, Baylor College of Medicine, One Baylor Plaza, Houston Texas 77030, USA. ⁶Texas Children's Hospital, Texas Medical Center, Houston, Texas 77030, USA. [†]Present addresses: Molecular Imaging Systems, Carestream Health, Inc., 4 Science Park, New Haven, Connecticut 06511, USA (K.T.); Rothberg Institute for Childhood Diseases, 530 Whitfield Street, Guilford, Connecticut 06437, USA (J.M.R.).

*These authors contributed equally to this work.

with this model, the coverage was lower at the 24.2% of heterozygous positions where DNA sequencing represented only one of the correct alleles (Fig. 1b and Supplementary Table 2). The Poisson model further shows that 13-fold average coverage would be required to detect 99% of all heterozygous SNPs (Supplementary Fig. 4).

The DNA sequencing genotypes disagree with the SNP array genotyping in 4,948 cases, or 1.0% of the time; another 3,499 markers (0.30%) had no coverage, consistent with the genome-wide redundancy of the sequence. Assuming the sensitivity and specificity of the markers on the microarray is representative of those found throughout the human genome, we estimate the total number of SNPs in the subject's genome to be approximately 3.7 million (see 'Sensitivity and specificity of SNP discovery' in Supplementary Information).

We identified 222,718 indels ranging from 2 to 38,896 bp, with 113,539 in common with indels in dbSNP; 85,418 indels are found as homozygotes, and 137,300 were heterozygotes. Insertions account

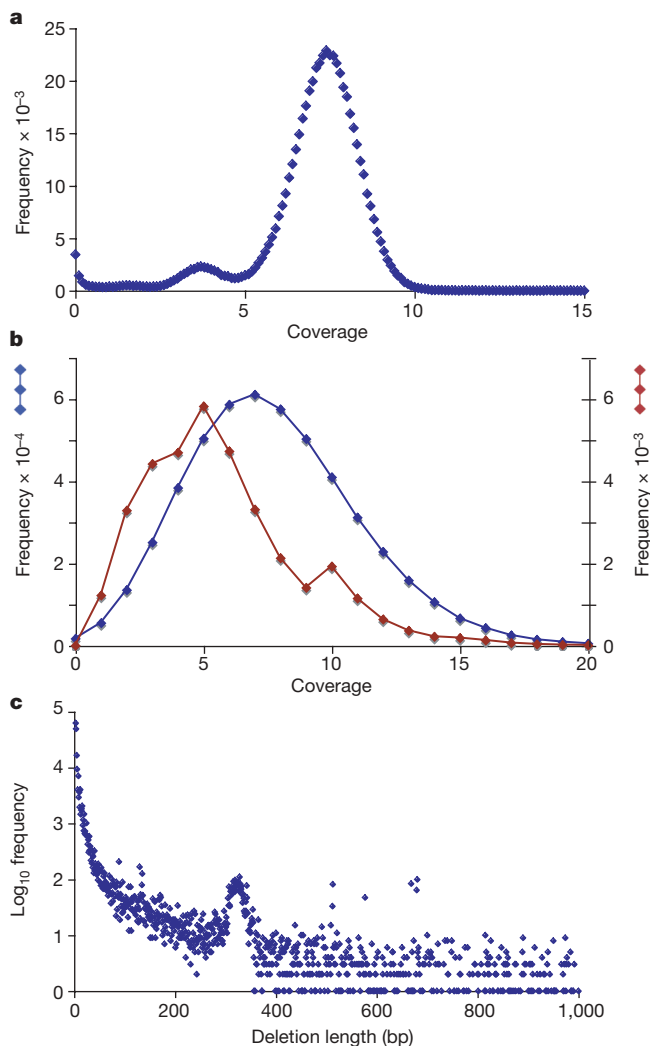


Figure 1 | 454-Sequencing of individual genome generated even coverage enabling genome-wide detection of variation. **a**, Distribution of sequence coverage of reference genome by 454-reads is random. Coverage, calculated in consecutive 5-kb windows, exhibited a Poisson distribution with a mean of 7.4-fold across all chromosomes except the X. Shoulder at 3.7X represents coverage of the X chromosome. **b**, Coverage is a key factor in detection of both alleles at heterozygous positions. For 31,709 markers heterozygous by microarray, but which exhibited only a single allele by DNA sequencing, the coverage was lower (red line, mean 5.7X) than the overall coverage for all SNPs (blue line, mean 7.8X). **c**, Size distribution of deletions. Deletions were readily observed in alignments of 454-reads to the reference genome. Note the peak in the size range at 300–350 bases owing to polymorphic *Alu* transposon insertion sites.

Table 1 | Single nucleotide variation in 454 reads

Subject	Filter*	Total variation	Known†	Novel
Watson	Raw	14,829,087	3,283,273	11,545,814
	1	4,427,488	2,815,322	1,612,166
	2	3,971,513	2,752,991	1,218,522
	3	3,322,093	2,715,296	606,797
Venter‡	4	3,470,669	2,822,902	647,767

* Filters: raw, all base substitution from cross_match alignments; 1, $S_v > 28$ (see Methods); 2, filter 1 plus ratio of variant to total coverage > 0.2 ; 3, filter 2 plus eliminate SNPs close to homopolymer runs > 5 bp; 4, (Venter) Phred (ref. 20) $Q > 15$, ratio of variant to total coverage > 0.2 .

† Variants found in build 126 of dbSNP (<http://www.ncbi.nlm.nih.gov/SNP/>).

‡ SNPs found in genome of Venter: see ref. 2 and supplementary material therein.

for 65,677 events, and deletions 157,041. A portion of the deletion size distribution from 2 to 1000 bp is shown in Fig. 1c. The distribution of deletions shows the relative enrichment for events in the range 300–350 bases in length, as expected from the known polymorphism of *Alu* SINE elements^{4,5}. The size range over which insertions are detected is limited by the length of the reads; in the analysis of our 250 base-pair 454-sequencing reads, the largest observed was 208 bp.

A total of 345 indels were observed to overlap coding sequence and had the potential to alter protein function. We designed primers to amplify and validate by Sanger sequencing 111 of these events with a size range of 3–50 bases. A total of 78 indels were successfully validated of which 66 were observed to be in length multiples of 3, ranging from 3 to 33 bp, and hence not expected to cause protein translation frame shifts. Sixty-five of these indels were found as heterozygotes. Surprisingly, a 4-bp deletion in exon 11 of *SGEF* was found to be homozygous; however, this gene is highly conserved in vertebrate species from rhesus macaque to stickleback, and all manifest the same 4-bp deletion in their genome (Supplementary Fig. 5). Furthermore, two other independent human messenger RNAs (mRNAs) harbour the deletion as well, suggesting the subject's allele was the wild type and that the reference harbours a rare insertion.

CNVs are local gains or losses of regions in the genome owing to duplication or deletion that can be associated with genetic disease⁶ and which should be detectable by variation in the average DNA sequence coverage of the region. A comparative genomic hybridization (CGH) microarray analysis of the subject's DNA revealed 23 apparent CNV regions ranging in size from 26 kb to 1.6 Mb: 9 with DNA gains and 14 with a loss. The sequence coverage data exhibited a gain or loss congruent with the CGH result at 18 of the 23 regions (Supplementary Table 4). Regions of CNV are polymorphic in populations, segregating as alleles with varying frequency^{7,8}. Consequently, the interpretation of a CGH microarray depends on the reference genome with which the subject is compared. This difference in reference standard is unavoidable when comparing CGH with DNA sequencing results using National Center for Biotechnology Information (NCBI) build 36 as the reference, which is not based on a single individual and for which no physical DNA sample exists. We experimentally demonstrated variation in CGH results by repeating the CGH array using a second reference genome and two different array platforms, demonstrating the effect the reference DNA has on the outcome of a CGH experiment (Supplementary Table 4).

An individual region of homozygous loss was characterized further using CGH results and DNA sequencing (Supplementary Fig. 6c). Sequence alignment of the subject's reads spanning the breakpoint of

Table 2 | Microarray validation of 454 SNPs

Affymetrix genotype*	Affymetrix SNP array	454 Sequence†	Agreement (%)
Homo ref.	254,753	253,348	99.4
Homo var.	104,547	99,387	95.1
Hetero	135,413	102,702	75.8

* Homo ref., homozygous for reference allele; homo var., homozygous for the variant allele; hetero, heterozygous.

† The genotype based on the alleles observed in 454 reads at each position of an Affymetrix marker.

a homozygous deletion region reveals a 2-bp addition at the breakpoint junction, suggesting non-homologous end joining⁶ was the mechanism involved in generating the deletion, and demonstrating the feasibility of using 454 sequence reads for identifying CNV breakpoints (Supplementary Fig. 6c). Several other CNV regions were flanked by repeats and segmental duplications, and likely occur by non-allelic homologous recombination, as was reported recently for the CNV loss at 22q13.1 (ref. 9) (see CNV 23 in Supplementary Table 4).

None of the CNV regions we defined are currently known to be involved in a recognizable phenotype; however, either trait or disease susceptibility correlations could occur in the future¹⁰. Thirty-four genes are predicted to be affected by these gains and losses, including two separate olfactory receptor groups, several genes with possible roles in cancers of the prostate, breast and colon, a gene from the HLA-D locus, and two proteins thought to be involved in RNA editing (Supplementary Table 4).

Among the 3.3 million SNPs found in the subject's genome were 8,996 non-synonymous changes in known SNPs and 1,573 in novel SNPs. We compared the non-synonymous known SNPs with the Human Gene Mutation Database (HGMD), the largest current compendium of human disease alleles¹¹. Thirty-two alleles exactly matched mutations reported in the HGMD whereas an additional 310 of these were in HGMD genes but were either alleles or amino-acid positions not previously characterized as disease-causing. In 12 cases the specific alterations and loci consisted of genes where homozygous recessive alleles can give rise to disease or other recognizable phenotype (Table 3); and 20 cases are reported to be associations with increased disease risk (Supplementary Table 5).

Ten of the 12 alleles in Table 3 are thought to be highly penetrant, Mendelian recessive disease-causing alleles. Seven of ten were heterozygous in the subject's genome sequence; the other three only exhibited one allele but have an average sequence coverage less than fivefold. Because the subject does not have these three diseases, and we expect not to recover the second allele for 24% of heterozygous positions, it is likely that he is not homozygous for these disease allele positions. We note that there are not yet any systematic studies of the population frequencies of these alleles. Nevertheless, the subject is a carrier for ten highly penetrant genetic disease loci found in the HGMD data set consisting of 900 genes. It has been estimated there are fewer than ten lethal equivalents in each person^{12–14}. Because we have drawn ten from an HGMD subset of the genome, we would predict the subject harbours a much greater number of deleterious Mendelian mutant alleles than is commonly estimated.

In addition, a sampling of 3,898 of the non-synonymous SNPs were tested for their possible functional impact on the protein

sequence using the software Polyphen¹⁵. Polyphen classified 7.3% as 'probably damaging', suggesting these changes will be of functional consequence to the protein. The remainder were classified as either 'possibly damaging' (13%) or 'benign' (74%).

The genome sequence of another individual (C. Venter) was recently reported². That study reported a 7.5-fold genome coverage using Sanger reads. The Venter genome harboured approximately 2.8 million known SNPs and about 0.74 million novel SNPs, in close agreement with the results from 454-reads of the Watson genome at a similar fold coverage. The two individuals shared 1.68 million of the SNPs, of which 5,230 were non-synonymous, accounting for 58% of the subject's non-synonymous SNPs. Watson and Venter are each distinguished from the reference by 3,766 and 3,882 non-synonymous SNPs, respectively, and therefore are different from each other by 7,648 protein coding changes. This is the most comprehensive comparison of the non-synonymous difference between two diploid genomes yet undertaken.

The subject's data also contained 1.5 million reads of novel sequence that did not map to build-36, corresponding to about 1.4% of the total sequence data. Approximately 65% of the unmapped sequences matched to known human repeats enriched for satellite DNA and other repeat elements characteristic of heterochromatin (Supplementary Fig. 7). The novel reads were assembled into approximately 170,000 contigs spanning 48 Mb. After removing contigs with fewer than 100 bp of contiguous unique sequence, 110,000 contigs spanning 29 Mb remained, which is close to the 25 Mb of euchromatic sequence predicted to be absent from the reference genome¹. These non-repeat contigs closely match to 33 human complementary DNA (cDNA) sequences from a variety of tissues and predicted functions (Supplementary Table 6) having no known map location on the human reference genome (see Methods). To assess further the gene-coding potential of these novel DNA sequences, we compared conceptual translations of the contigs greater than 1,000 bp (1,279 in all) with the GenBank non-redundant (NR) protein database. This search yielded 60 significant, but not identical, matches to 49 different proteins in humans and other vertebrates (Supplementary Table 7). The annotations of several of these transcripts are consistent with transcription factor or signalling molecules. Therefore it is possible this diploid genome sequence will contribute important new genes to the human genome.

The sequencing method used in this study has many advantages over traditional capillary sequencing. It is inherently scalable, which means that sequencing costs in the miniature continue to decrease and throughput increases as the density of the sequencing reactions on the chip increases, and read lengths get longer³. In this study we sequenced the genome of Dr Watson for less than US\$1 million,

Table 3 | SNPs matching HGMD mutations causing disease or other phenotypes

HGMD accession	Chromosome	Coordinate	HUGO symbol	Gene name	Cytogenetic	Phenotype	Zygosity
CM003589	1	97937679	DPYD	Dihydropyrimidine dehydrogenase	1q22	Dihydropyrimidine dehydrogenase deficiency	Heterozygous
CM950484	1	157441978	FY	Duffy blood-group antigen	1q	Duffy blood group antigen, absence	Homozygous*
CM942034	4	619702	PDE6B	Phosphodiesterase 6B, cGMP-specific, rod, beta	4p16.3	Retinitis pigmentosa 40	Heterozygous
CM021718	9	36208221	GNE	UDP-N-acetylglucosamine 2-epimerase	9p	Myopathy, distal, with rimmed vacuoles	Heterozygous
CM980633	10	50348375	ERCC6	Excision repair cross-complementing rodent repair deficiency, complementation group 6 protein (CSB)	10q	Cockayne syndrome	Homozygous†
CM050716	11	76531431	MYO7A	Myosin VIIA	11q13.5	Usher syndrome 1b	Homozygous†
CM950928	12	46812979	PFKM	Phosphofructokinase, muscle	12q13.3	Glycogen storage disease 7	Homozygous*
CM032029	14	20859880	RPGRIP1	Retinitis pigmentosa GTPase regulator interacting protein 1	14q11	Cone-rod dystrophy	Heterozygous
CM984025	19	18047618	IL12RB1	Interleukin-12 receptor, beta 1	19p13.1	Mycobacterial infection	Heterozygous
CM024138	19	41014441	NPHS1	Nephrosis-1, congenital, Finnish type	19q	Congenital nephrotic syndrome, Finnish type	Heterozygous
CM910052	22	49410905	ARSA	Arylsulphatase A	22q	Metachromatic leukodystrophy	Heterozygous

* Coverage at these SNP positions is less than 5. However, both produce benign phenotypes.

† Coverage at these SNP positions is greater than 5. Both would produce severe phenotypes if they were truly homozygous.

Box 1 |**Protection of human subjects**

Is institutional review board approval required for this project?

Considerations. Approval by an institutional review board (IRB) is required for all research involving human subjects. Federal regulation defines research as 'a systematic investigation, including research, development, testing and evaluation, designed to develop or contribute to generalizable knowledge.' A human subject is defined according to the regulations as 'a living individual about whom an investigator ... conducting research obtains (1) data through intervention or interaction with the individual, or (2) identifiable private information.' (45 CFR 46.102). Baylor College of Medicine, Houston, Texas, requires that all proposed activities at the college be reviewed to determine if they meet the regulatory definitions for research involving human subjects (Baylor College of Medicine, IRB Procedures, November 2006). The research team and the Baylor College of Medicine IRB agreed that the activities associated with this project constitute research involving human subjects. IRB review helps to ensure ethical research conduct and appropriate subject protection. It also sets an important standard for future research in the field of personalized genomics.

Management. The research protocol was written in consultation with an ethicist and reviewed by the Baylor College of Medicine IRB. The research participant's identity was not revealed to the IRB, to ensure objectivity. Although the practical management of many of the ethical issues depended on the unique expertise of the research participant, this did not affect review or approval of the research protocol.

Returning research results to research participants

Should the research participant be able to receive information about their individual genome sequence?

Considerations. Dr Watson requested that he receive information about all data generated from this research project. Generally, patients have a right to receive medical information, but this right does not typically extend to individual research results. Concerns include validity of genetic tests not performed in a Clinical Laboratory Improvement Amendments (CLIA)-approved laboratory, the unknown clinical significance of much of the generated data, and protecting subjects from potentially harmful information, such as information about genetic risk of uncertain penetrance. These considerations have to be weighed against the ethical principles of respect for autonomy and the right to receive relevant information about oneself, as well as the principle of reciprocity, which suggests a right to receive information in exchange for research participation.

Management. The research team felt that because of Dr Watson's unique expertise he would be able to understand adequately the significance and limitations of these data. Therefore, out of respect for his autonomous decision to receive the information, Dr Watson was given his entire genome sequence on a miniature hard drive. Genetic counselling was provided to help with interpretation and to ensure adequate understanding of the information given and the limitations of its clinical significance. It remains controversial whether other research participants who do not share Dr Watson's expertise ought to be informed of individual results of genetic research. Certainly for many, whole-genome data will be meaningless. A more analysed form of the data may therefore be required.

Should the research participant be able to request that certain information be redacted before individual and/or public disclosure?

Considerations. Although patients generally have a right to receive certain medical information, they can waive that right and request that information be withheld from them. The right not to know of a genetic risk is legally sanctioned but remains ethically controversial. Even if this right is recognized, however, decisions about redactions must be made *a priori* to preserve the right not to know a particular finding. In the context of whole-genome sequencing research, because genomic information is stable over time but our understanding of the clinical significance of that information continues to grow at a very fast pace, we cannot anticipate future findings that may reveal genetic risk information that the participant may not have wanted to know. We also cannot entirely eliminate the risk that inferences could be made about the missing information from downstream and/or upstream data.

Management. Because Dr Watson is knowledgeable about and familiar enough with the current literature in genetics to assess research findings and to make an informed decision about what risk information he does and does not want to receive, his right to redact information was respected. Decisions about redactions were made *a priori* and the problems associated with future findings, as well as general concerns about receiving specific genetic information, were discussed with a genetic counsellor. Dr Watson requested that all gene information about apolipoprotein E be redacted, citing concerns about the association that has been shown with Alzheimer's disease. These data were redacted and were not analysed by the research team. Again, this approach is not generalizable and may not be appropriate for other research participants.

Data release and data flow

Should the participant's genome sequence be publicly released?

Considerations. There is great scientific interest in accessing and studying the data generated from this project. To maximize scientific and clinical use, public data release is strongly encouraged in genomic research. Dr Watson is personally committed to a policy of open access to DNA data. However, because DNA is a unique identifier, there are privacy risks associated with data sharing. Because this project was publicly announced and Dr Watson was individually identified, there was concern about his privacy interests and the potential harm that could result from the misuse of his genetic information.

Management. An individual can waive their right to privacy and share personal information with others. Dr Watson decided to share his personal genome by releasing it into a publicly accessible scientific database. The privacy risks associated with public data broadcast were explained.

What, if any, obligations are owed to third-party relatives?

Considerations. Because genetic information is familial by nature, Dr Watson's participation in this research raised concerns about what obligations, if any, were owed to his close biological relatives. Dr Watson's autonomy-based rights had to be weighed against the rights and welfare of his biological relatives. There are three research-related activities that raise concerns about obligations to third-party relatives: consent for research participation; returning research-related results; and data release.

1. Third-party relatives are not typically considered research participants and their consent is not generally required for research participation. The participant's autonomous decision to participate in research typically outweighs any objections raised by third-party relatives.

2. In the clinical context, the physician's duty to warn biological relatives of genetic risk remains controversial. In the research context, because the data are not validated in an approved laboratory, the obligation to warn at-risk relatives is even more tenuous. As in the clinic, all research participants should be informed of the risks to relatives and encouraged to discuss research results with them. In this project, genetic counselling was offered for family members, free of charge.

3. There are privacy risks associated with the public release of genomic data for the individual research participant. There are also risks, though of a more uncertain nature, of public release for close biological relatives, especially when the participant is clearly identified and the release of his data is publicized. What obligation, if any, does an investigator have to protect third-party relatives from these privacy risks?

Management. Risks to relatives were disclosed and thoroughly discussed with the research participant. He was strongly encouraged to discuss these issues with biological relatives and to make a family decision about research participation and data release. The issue of whether investigators should publicly release Dr Watson's data without familial consent was avoided by presenting the edited genome sequence to Dr Watson who then released it himself directly into publicly accessible databases. This did not alleviate any moral obligation Dr Watson may have to protect his biological relatives from the uncertain privacy risks associated with public data release. It is also unlikely that future research participants will be able to facilitate their own data release, making the question of obligations to third-party relatives a policy priority.

whereas the genome of Venter by Sanger sequence reportedly cost approximately US\$100 million. Although not used in this study, this sequencing technology allows the production of mate-paired reads. The use of mate-pair reads will enable assessment of a wider range of indels and other structural rearrangements, and facilitate the incorporation of new sequence into the reference genome¹⁶. The principal weakness of the method is that it currently does not allow efficient detection of single-base indels in homopolymers. Future developments in chemistry and software will improve the ability to identify single-base indels.

A key aim of personal genome sequencing is to identify genome sequences that may be associated with disease, or are predictive of response to medication. The need to make genotype–phenotype correlations before having predictive value is at the heart of both the excitement and the dilemma of the new era of genomic medicine¹⁷. Thus the ability to sequence individuals readily using high-throughput, scalable, low-cost, completely *in vitro* technology, as demonstrated here, is an important milestone in our ability to connect ‘personalized genomes’ to ‘personalized medicine’ and enable these critical correlations to be made.

METHODS SUMMARY

Mapping and alignment to the genome. DNA sequencing on the Genome Sequencer FLX instrument (454, Inc.) is described in detail in Methods. Reads, averaging approximately 250 bases, were mapped on to the human reference genome, NCBI build 36, by sequence alignment using Basic Local Alignment Search Tool (BLAST)-like alignment tool (BLAT). Reads were removed from subsequent analysis that failed to meet minimum criteria (see Methods). Reads that passed the alignment quality criteria were realigned to local reference genome fragments using Cross_match software; the refined alignments were parsed for sequence variation between the subject and the reference. An error model was developed to separate sequencing error from true genomic variation, and the location and type of each putative true variant was tabulated (see Methods).

Assembly of non-matching reads. One and a half million reads that failed to find a match in the reference genome sequence (‘no-hit’ reads) and another 2.2 million reads with low-quality alignments to the reference were pooled for sequence assembly. All reads were trimmed to remove the last 50 bases in which most of the sequencing error lies. Reads less than 50 bases after trimming were discarded. The assembly of the remaining 2.6 million trimmed reads followed the standard ATLAS-WGS procedure^{18,19}.

Laboratory analysis of genomic DNA. A DNA sample from the subject was labelled and annealed to the Affymetrix 500K GeneChip array to provide independent laboratory analysis of the subject’s SNPs and conformation of the DNA sequencing coverage. To compare local fluctuation in DNA sequencing coverage with copy number variation in the subject’s genome, three additional DNA samples were labelled and mixed each in a 1:1 ratio with separately labelled control DNAs. The mixtures were annealed to each of two Agilent 244K array CGH chips and one Nimblegen HD2 chip.

Full Methods and any associated references are available in the online version of the paper at www.nature.com/nature.

Received 3 December 2007; accepted 4 March 2008.

1. The International Human Genome Sequencing Consortium. Finishing the euchromatic sequence of the human genome. *Nature* **431**, 931–945 (2004).
2. Levy, S. *et al.* The diploid genome sequence of a single individual. *PLoS Biol.* **5**, e254–e286 (2007).

3. Margulies, M. *et al.* Genome sequencing in microfabricated high-density picolitre reactors. *Nature* **437**, 376–380 (2005).
4. Bennett, E. A., Coleman, L. E., Tsui, C., Pittard, W. S. & Devine, S. E. Natural genetic variation caused by transposable elements in humans. *Genetics* **168**, 933–951 (2004).
5. The Chimpanzee Sequencing and Analysis Consortium. Initial sequence of the chimpanzee genome and comparison with the human genome. *Nature* **437**, 69–87 (2005).
6. Lupski, J. R. & Stankiewicz, P. Genomic disorders: molecular mechanisms for rearrangements and conveyed phenotypes. *PLoS Genetics* **1**, 627–633 (2005).
7. Weber, J. L. *et al.* Human diallelic insertion/deletion polymorphisms. *Am. J. Hum. Genet.* **71**, 854–862 (2002).
8. Redon, R. *et al.* Global variation in copy number in the human genome. *Nature* **444**, 444–454 (2006).
9. Kidd, J. M., Newman, T. L., Tuzun, E., Kaul, R. & Eichler, E. E. Population stratification of a common APOBEC gene deletion polymorphism. *PLOS Genetics* **3**, 584–592 (2007).
10. Lupski, J. R. Structural variation in the human genome. *N. Engl. J. Med.* **356**, 1169–1171 (2007).
11. Stenson, P. D. *et al.* Human Gene Mutation Database (HGMD): 2003 update. *Hum. Mutat.* **21**, 577–581 (2003).
12. Halligan, D. L. & Keightley, P. D. How many lethal alleles? *Trends Genet.* **19**, 57–59 (2003).
13. Bittles, A. H. & Neel, J. V. The costs of human inbreeding and their implications for variations at the DNA level. *Nature Genet.* **8**, 117–121 (1994).
14. Vogel, F. & Motulsky, A. G. *Human Genetics: Problems and Approaches* 2nd edn 487–502 (Springer-Verlag, New York, 1986).
15. Ramensky, V., Bork, P. & Sunyaev, S. Human non-synonymous SNPs: server and survey. *Nucleic Acids Res.* **30**, 3894–3900 (2002).
16. Korbel, J. O. *et al.* Paired-end mapping reveals extensive structural variation in the human genome. *Science* **318**, 420–426 (2007).
17. McGuire, A. L., Caulfield, T. & Cho, M. K. Research ethics and the challenge of whole genome sequencing. *Nature Rev. Genet.* **9**, 152–156 (2008).
18. Havlak, P. *et al.* The Atlas genome assembly system. *Genome Res.* **14**, 721–732 (2004).
19. Richards, S. *et al.* Comparative genome sequencing of *Drosophila pseudoobscura*: chromosomal, gene, and cis-element evolution. *Genome Res.* **15**, 1–18 (2005).
20. Ewing, B. & Green, P. Base-calling of automated sequencer traces using phred. II. Error probabilities. *Genome Res.* **8**, 186–194 (1998).

Supplementary Information is linked to the online version of the paper at www.nature.com/nature.

Acknowledgements We thank J. D. Watson for his participation, encouragement and engagement. We thank J. Belmont for discussion of HGMD data. We also thank the following individuals for their technical support: S. Attiya, M. Braverman, J. Brunelle, C. Celone, Z. Chen, A. Sanchez, W. Song, and personnel from 454 Sequencing Center and R&D.

Author Information The CEL files for the Affymetrix 500K Genome array and GPR files for the Agilent_1 and Agilent_2 CGH arrays are deposited in Gene Expression Omnibus under series accession number GSE10668. All SNPs and insertion/deletions from 454-reads are deposited in dbSNP under handle bcmhgsc_jdw; contigs from the assembly of 454-reads not matching the reference genome are deposited in Genbank under accession number ABKV01000000. All 454-reads are deposited in the Trace Archive of the National Center for Biotechnology Information under Center_name = ‘CSHL’ and Center_project = ‘Project JIM’. Reprints and permissions information is available at www.nature.com/reprints. This paper is distributed under the terms of the Creative Commons Attribution-Non-Commercial-Share Alike licence, and is freely available to all readers at www.nature.com/nature. The authors declare competing financial interests: details accompany the paper at www.nature.com/nature. M.E., W.E., Y.-J.C., V.M., G.T.R., X.G., F.N., C.L.T., G.P.I. and M.M. are current employees of 454 Life Sciences, which is owned by Roche Diagnostics, receive a salary for their work and are eligible for bonuses administered by 454 Life Sciences and Roche Diagnostics. Correspondence and requests for materials should be addressed to J.M.R. (jonathan.rothberg@gmail.com) or R.A.G. (agibbs@bcm.tmc.edu).

METHODS

DNA sequencing. Genomic DNA was purified from white blood cells from Dr Watson by using the Flexigene DNA kit (Qiagen). Five micrograms of DNA were sheared by nebulization and fractionated on agarose gel to isolate 450–550 base fragments. These were used to construct a single-stranded library that was used as template for single-molecule PCR on 28- μ m diameter beads in emulsions³. The amplified template beads were recovered after emulsion breaking and selective enrichment. Sequencing primer was annealed to the template and the beads were incubated with *Bst* DNA polymerase, apyrase and single-stranded binding protein. A slurry of the template beads, enzyme beads (required for signal transduction) and packing beads (for *Bst* DNA polymerase retention) was loaded into the wells of a 70 mm \times 75 mm picotiter plate. The picotiter plate was inserted in the flow cell and subjected to pyro-sequencing on the Genome Sequencer FLX instrument (454, Inc.).

The Genome Sequencer FLX flows 100 cycles of four solutions containing either dTTP, α SdATP, dCTP and dGTP reagents, in that order, over the cell. For each dNTP flow, a single 38-s image was captured by a CCD (charge-coupled device) camera on the sequencer. The images were processed in real time to identify template-containing wells and to compute associated signal intensities. The images were further processed for chemical and optical cross-talk, phase errors and read quality before base calling was performed for each template bead.

Mapping 454-reads to reference genome. We generated sequence with 234 runs on Genome Sequencer FLX instruments (454 Inc.), which produced over 105 million bases per run. Reads were aligned to the human reference genome, NCBI build 36 (<http://hgdownload.cse.ucsc.edu/goldenPath/hg18/bigZips/>), using BLAT. All but 1.5 million reads found one or more match locations in the reference genome. The best match in the genome was used as the location for the reads with multiple matches. Poor-quality alignments were defined as those reads aligning over less than 90% of their length, or with more than four substitutions or insertions/deletions with respect to the reference, or reads that matched two locations with nearly equal match score. Ninety-three million reads comprising 7.4-fold coverage (Fig. 1a, see also Supplementary Fig. 2) passed the filtering criteria and were realigned to local genome segments (41 kb each) using Cross_match software. The limitation of a 41-kb genomic fragment placed an upper limit on the sizes of indels that could be detected.

Filtering criteria for SNPs. Mismatch base positions found among the 454-reads were scored using a scaling of the associated error probabilities (Q , see 'Scoring system for mismatch base positions' in Supplementary Information). The variant score, S_v , was the sum of scaled 454 Q values. Only variant positions with scores $S_v \geq 28$ were considered. In addition, the ratio of variant bases to total coverage was required to be not less than 0.2.

Known SNPs were associated with homopolymer runs of more than 5 bp less than 3% of the time, whereas novel SNPs were associated 33% of the time. Therefore novel variants were removed if they were associated with a homopolymer run of more than 5 bp within 13 bases of the SNP; a novel variant was also removed if it was associated with a 5-bp homopolymer run and $S_v \leq 54$ (see 'Filtering, criteria for SNPs' in Supplementary Information).

Genotyping with sequence data. The sensitivity of detecting heterozygous SNPs by whole-genome shotgun sequencing is limited by the depth-coverage. If the average depth-coverage is C , the coverage k for each base of the genome approximately follows the Poisson distribution²¹:

$$f(k|C) = \frac{C^k \bullet e^{-C}}{k!}$$

For each heterozygous SNP site of the diploid genome, covered by K reads, the number of reads i representing one of the two alleles follows the binomial distribution:

$$f(i|K, 0.5) = \frac{K!}{i!(K-i)!} \bullet 0.5^K$$

Given that a heterozygous SNP call required observation of at least two reads from both alleles at the SNP site, the sensitivity of detecting heterozygous SNPs was computed based on the two statistical distributions described above (Supplementary Fig. 4).

Filtering criteria for insertions and deletions. Indels were often associated with short tandem repeats sequences, which caused ambiguity in sequence alignments. Among separately aligned reads, indels in close proximity to one another may represent the same event. Based on our analysis of the spacing between indels, a given deletion or insertion is grouped with the previous one if: (1) the two events are the same type (insertion or deletion); (2) the ratio of the smaller to the larger is greater than or equal to 0.8; (3) the distance between the start coordinates is less than 15 bp for indels larger than 6 bp, or seven times the indel size for indels less than or equal to 6 bp. Furthermore, we required valid indels to be supported by at least two reads and have a ratio of variant to reference greater than 0.25. Errors in measurement of homopolymer length were a source of systematic error for indels one base in length, so they were ignored for this study.

Analysis of 'no-hit' reads. A total of 169,643 contigs were assembled with a total size of 48 Mb and an N50 size (the size at which 50% of the genome is contained within contiguous sequences of this size or greater) of 296 bp. Human repeats in the contigs were masked using RepeatMasker, and contigs containing fewer than 100 contiguous bases of unique sequence were set aside. The remaining 110,353 contigs spanned 29 Mb, with an N50 size of 267 bp; 1,294 contigs were longer than 1,000 bp, and the longest was 10,724 bp.

We used Mega BLAST (<http://www.ncbi.nlm.nih.gov/blast/megablast.shtml>) with the 'expect' parameter set to 10^{-30} to compare these contigs to a human mRNA sequence database of over 40,000 sequences (<http://hgdownload.cse.ucsc.edu/goldenPath/hg18/bigZips/mrna.fa.gz>). Significant matches were found to 417 mRNA sequences, which had no map coordinates on build 36. We selected from this set 104 mRNA that matched 886 contigs with greater than 96% identity, and which were covered across more than 40% of the mRNA length. The contigs matching these mRNA sequences ranged in size from 296 to 5121 bp. The 104 mRNA sequences were compared with the reference genome using BLAT to confirm they did not have a matching gene on the reference genome. Forty-four were eliminated by this test; 27 had a partial hit, but the genomic match and the contig match did not overlap on the mRNA sequence; 33 of the mRNA sequences had no hit.

Comparative genome hybridization. For the Agilent 244K array, the Human Genome CGH 244K Array (Agilent Technologies, Inc.) contains 238,459 formatted 60-base oligonucleotides, representing a compiled view of the human genome at an average resolution of 9 kb. DNA digestion, labelling and hybridization were performed according to the manufacturer's instructions, with minor modifications. Two separate experiments differed in the reference DNA used for comparison: 'Agilent_1' used a standard reference caucasian male (Kleberg Cytogenetics Laboratory, Baylor College of Medicine); 'Agilent_2' used a caucasian male, NA10851, Coriell Institute for Medical Research. For the Nimblegen HD2 array, we tested a second sample of experimental DNA co-annealed with reference DNA, Coriell Institute for Medical Research number NA10851, to a NimbleChip HD2 Array (NimbleGen Systems, Inc.) in collaboration with NimbleGen Systems. The HD2 array has 2.1 million oligonucleotides, each between 50 and 75 bases, with a reported resolution of about 5 kb. Log₂ ratios were analysed for variation in copy number using NimbleGen SignalMap software.

Affymetrix Gene Chip 500. Duplicate genomic DNA samples from lymphocytes, 250 ng each, were annealed to the Affymetrix 250K NspI and 250K Styl arrays according to the manufacturer's protocol (see 'Affymetrix Gene Chip 500' in Supplementary Information for further details).

21. Lander, E. S. & Waterman, M. S. Genomic mapping by fingerprinting random clones: a mathematical analysis. *Genomics* 2, 231–239 (1988).

Chromatin dynamics during epigenetic reprogramming in the mouse germ line

Petra Hajkova¹, Katia Ancelin^{1*†}, Tanja Waldmann^{2*}, Nicolas Lacoste³, Ulrike C. Lange¹, Francesca Cesari¹, Caroline Lee¹, Genevieve Almouzni³, Robert Schneider² & M. Azim Surani¹

A unique feature of the germ cell lineage is the generation of totipotency. A critical event in this context is DNA demethylation and the erasure of parental imprints in mouse primordial germ cells (PGCs) on embryonic day 11.5 (E11.5) after they enter into the developing gonads^{1,2}. Little is yet known about the mechanism involved, except that it is apparently an active process. We have examined the associated changes in the chromatin to gain further insights into this reprogramming event. Here we show that the chromatin changes occur in two steps. The first changes in nascent PGCs at E8.5 establish a distinctive chromatin signature that is reminiscent of pluripotency. Next, when PGCs are residing in the gonads, major changes occur in nuclear architecture accompanied by an extensive erasure of several histone modifications and exchange of histone variants. Furthermore, the histone chaperones HIRA and NAP-1 (NAP111), which are implicated in histone exchange, accumulate in PGC nuclei undergoing reprogramming. We therefore suggest that the mechanism of histone replacement is critical for these chromatin rearrangements to occur. The marked chromatin changes are intimately linked with genome-wide DNA demethylation. On the basis of the timing of the observed events, we propose that if DNA demethylation entails a DNA repair-based mechanism, the evident histone replacement would represent a repair-induced response event rather than being a prerequisite.

The specification of about 40 primordial germ cells (PGCs) from *Blimp1* (also known as *Prdm1*)-expressing PGCs precursors is accompanied by expression of *stella* (*Dppa3*) on E7.25 (refs 3 and 4). After their subsequent migration into the developing gonads, PGCs exhibit a marked genome-wide DNA demethylation between E11.5 and E12.5, including erasure of genomic imprints, which is supposedly an active process^{1,2} (Supplementary Fig. 1). The mechanism of this DNA demethylation process is unknown, but we reasoned that it might be linked with changes in chromatin and histone modifications. However, with only 2,000 PGCs per gonad, investigation of this fundamental event is technically difficult, especially because PGCs are also temporally asynchronous and difficult to culture *in vitro*.

We first investigated the status of the chromatin in nascent PGCs at E8.5 (100 PGCs per embryo; Supplementary Fig. 1) and found distinctive changes in chromatin (Supplementary Fig. 2). These changes included loss of dimethylation of lysine 9 of histone H3 (H3K9me2) despite the presence of G9a (also known as EHMT2, a histone methyltransferase), which is responsible for this modification. PGC specification is also unaffected in *G9a*^{-/-} embryos (ref. 5, and K.A. and P.H., unpublished). The erasure of H3K9me2 in nascent PGCs could be due to competition with H3K9ac or to down-regulation of GLP (EHMT1) from the G9a–GLP complex⁶. Early

PGCs also show enhancement of trimethylation of lysine 27 of histone H3 (H3K27me3) concomitantly with EZH2, a polycomb group enzyme. In addition, there is enrichment of methylation of lysine 4 of histone H3 (H3K4me2 and H3K4me3) and of many histone acetylation marks, especially H3K9ac (Supplementary Fig. 2), as well as symmetrical methylation of arginine 3 on histones H4 and H2A (H4/H2AR3me2s) attributed to the BLIMP1–PRMT5 complex⁵.

Notably, this germ cell chromatin signature is established specifically in PGCs (not detected in the contemporary somatic cells) before their entry into the gonads, and is associated with the expression of pluripotency-specific genes: *Sox2*, *Oct4* (*Pou5f1*), *Nanog* and *stella*⁷. This chromatin state is also potentially crucial for the derivation of pluripotent embryonic germ cells from PGCs between E8.5 and E11.5. It is against this background that subsequent events follow when PGCs enter into the developing gonads at E10.5.

The first sign of chromatin changes in gonadal PGCs at E11.5 is a rapid loss of linker histone H1 (Fig. 1a), accompanied by ‘loosening’ of the chromatin (as revealed by the loss of detectable chromocentres, identified by intensively stained DAPI foci) and by the significant enlargement of nuclei (Fig. 1b, c). Notably, HP1s (α , β and γ), ATRX and M33 (also known as CBX2), which are normally associated with constitutive and facultative heterochromatin, also redistribute or disappear (Supplementary Fig. 3a, b and data not shown). There is also concomitant loss of H3K9me3 and H3K27me3, which represent marks of constitutive and facultative heterochromatin, respectively (Fig. 2a, b and Supplementary Figs 4–7), as well as loss of the repressive H4/H2AR3me2s⁵. Although removal of these repressive histone modifications could make the chromatin more ‘permissive’ for DNA demethylation, they may underlie more profound changes in nuclear structure. Indeed, we also found that modifications associated with the transcriptionally active chromatin, such as H3K9ac, are also lost (Supplementary Fig. 7 and data not shown). Notably, nuclear histones are still accessible to antibodies, as revealed by the persistence of the H3 signal in PGCs (Supplementary Fig. 6).

Whereas the erasure of differential DNA demethylation of imprinted genes in E11.5 PGCs^{1,2} persists until new imprints are imposed later during gametogenesis⁸, the chromatin decondensation and restructuring are transient, with most PGCs regaining the typical appearance of bright 4,6-diamidino-2-phenylindole (DAPI)-stained chromocentres around E12.5 (Fig. 1b). Concomitantly, the H3K9me3 marks reappear and the proteins associated with pericentromeric heterochromatin relocate forming a pattern resembling that seen in the surrounding somatic cells (Fig. 2 and Supplementary Fig. 3). Other chromatin changes also revert to the original state, although with diverse kinetics. For example, there is rapid reappearance of linker histone H1, but that of H3K27me3 is slower. Notably,

¹Wellcome Trust/Cancer Research UK Gurdon Institute of Cancer and Developmental Biology, University of Cambridge, Tennis Court Road, Cambridge, CB2 1QN, UK. ²Max-Planck-Institute of Immunobiology, Stuebeweg 51, 79108 Freiburg, Germany. ³CNRS/Institute Curie, 26 rue d'Ulm, 75248 Paris cedex 05, France. [†]Present address: LBMC/UMR 5665, Ecole Normale Supérieure de Lyon, 46 allée d'Italie, 69364 LYON Cedex 07, France.

*These authors contributed equally to this work.

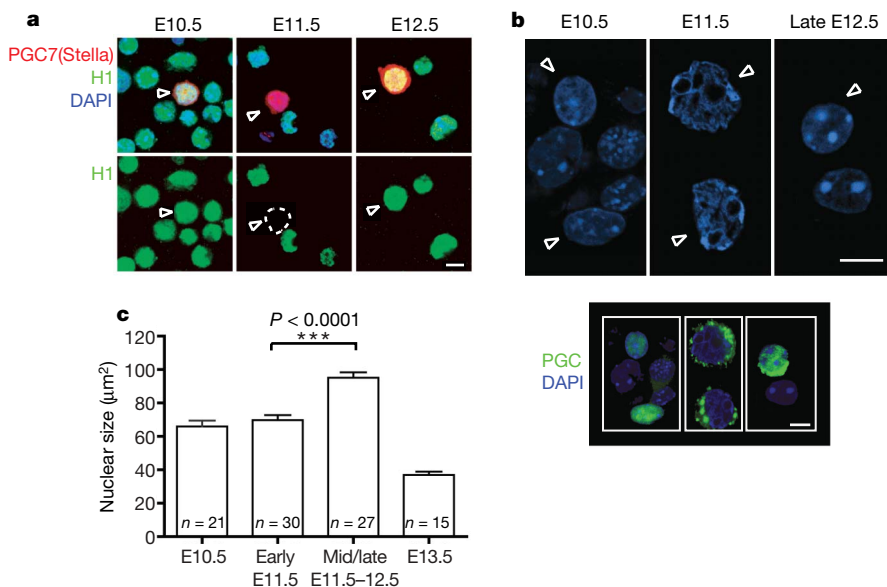


Figure 1 | After the entry of PGCs into the gonads, germ cell chromatin undergoes rapid conformational changes. a, Disappearance of linker histone H1 in PGCs at E11.5. PGC7/Stella (red) was used as a germ-cell-specific marker. PGCs are depicted by arrowheads. **b**, Increase in the nuclear size and disappearance of chromocentres in PGCs at E11.5, as observed by DAPI staining of a cell suspension from genital ridges. PGCs are depicted by arrowheads. The lower panel shows identification of PGCs by staining with a germ-cell-specific marker (SSEA1, stage specific embryonic antigen 1, or OCT4). Scale bars, 10 μm . **c**, Measurement of the nuclear size on the cryosections from E10.5–E13.5 genital ridges shows a transient change in the size of germ cell nuclei. The increase is highly statistically significant (*t*-test). The measured PGC nuclei were identified on the cryosections using OCT4 stainings (data not shown). The error bars represent standard deviations; *n* indicates the number of replicates.

some histone modifications are lost altogether, including H3K9ac and H4/H2AR3me2s (Supplementary Fig. 7). Hence, alongside permanent changes in DNA methylation, there are also persistent changes in chromatin modifications. The reprogramming process thus exerts the erasure of epigenetic memory at multiple and distinct levels. Importantly, none of these changes are seen in the surrounding somatic cells.

Three possible scenarios may explain the extensive loss of histone modifications in PGCs. First, site-specific de-modification enzymes, such as demethylases and deacetylases, could remove histone tail modifications. Second, the amino-terminal tails of histones may be clipped off. Third, the existing histones could be replaced by new histones carrying different combinations of histone tail modifications⁹. Both of the latter would involve histone replacement. The

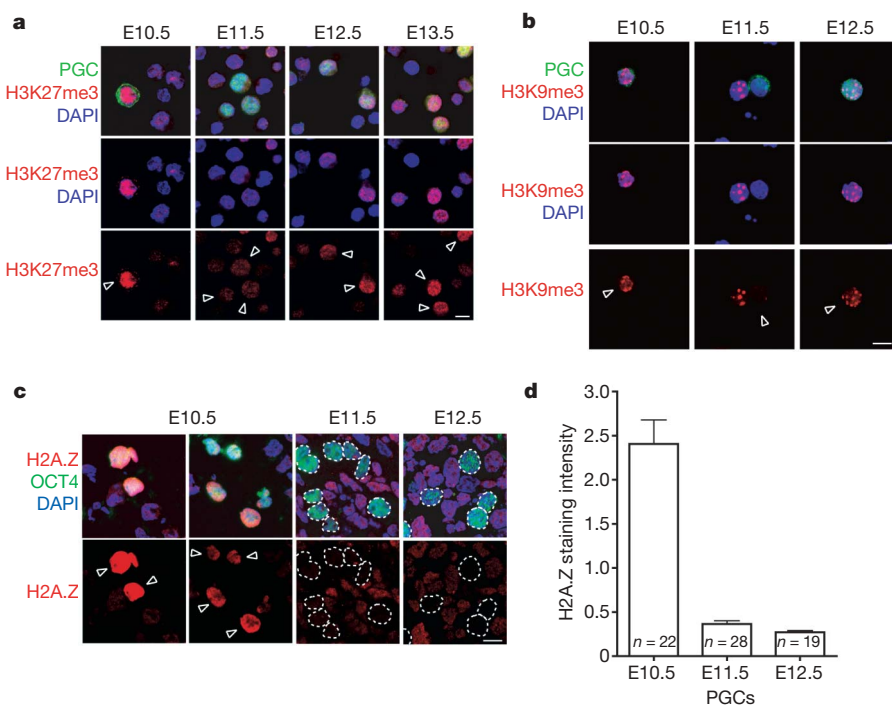


Figure 2 | Chromatin changes observed in PGCs at E11.5. a, The presence of H3K27me3 in PGCs. At E10.5, nuclei of PGCs contain high levels of H3K27me3 as part of their germline chromatin signature (for details, see text). This chromatin mark is lost in PGCs at E11.5 and re-gained between E12.5 and E13.5. Notably, the loss of H3K27me3 occurs despite the continuous presence of EZH2 responsible for this modification in PGCs (data not shown). **b**, Loss of H3K9me3 in PGCs at E11.5. Stainings were performed on single-cell suspensions from genital ridges between E10.5 and E13.5. The shown epigenetic changes are detectable in 70–90% of PGCs depending on the developmental stage of the embryo. Germ cells were stained in green using the germ-cell-specific markers SSEA1 or OCT4, and are depicted by arrowheads. Scale bar, 10 μm . **c**, The immunofluorescence

stainings of cryosections of embryonic gonads (as described in Methods). OCT4-positive germ cells (depicted by arrowheads) are stained in green. Note high levels of H2A.Z in early postmigratory PGCs at E10.5 and the disappearance of the H2A.Z staining in later developmental stages (E11.5 and E12.5), while the signal in surrounding somatic cells remains relatively constant. Scale bar, 10 μm . **d**, Quantification of the H2A.Z signal in germ cells. To normalize between different samples, the intensity of H2A.Z staining was calculated as the mean pixel intensity in every PGC divided by the mean pixel intensity in surrounding somatic cells. The *y*-axis values thus represent the intensity of H2A.Z staining in PGCs in comparison with that in surrounding somatic cells. The error bars represent standard deviations; *n* indicates the number of replicates.

concomitant disappearance of numerous histone modifications is suggestive of histone replacement. Furthermore, although the rapid loss of H4/H2AR3me2s³ could be due to PADI4 enzymatic activity by means of citrullination^{10,11}, this enzyme acts predominantly on mono-methylated arginines and is inhibited by arginine dimethylation¹⁰. In all investigations we were unable to detect PADI4 expression in our single-cell complementary DNAs PGC libraries or a significant increase in citrullination of H4R3 (data not shown). This prompted us to investigate histone replacement during this reprogramming event.

Histone variants H2A.Z and H3.3 (refs 12 and 13), as opposed to the canonical histones (H2A, H2B, H3.1, H3.2 and H4), are synthesized in a cell-cycle-independent manner and can be incorporated into the chromatin outside the S phase. We reasoned that a 'large scale' histone replacement would cause a shift in the contribution of certain histone variants in germ-cell chromatin. Indeed, we detected significant levels of H2A.Z in early E10.5 PGCs; most of the signal is lost by E11.5–E12.5, whereas the levels remain relatively constant in the neighbouring somatic cells (Fig. 2c, d and Supplementary Fig. 8). Considering that the doubling time of PGCs is about 16 h⁷, active displacement of this histone variant is more likely than dilution through replication and cell division.

The lack of suitable antibodies for H3.3 precludes similar studies on this histone variant. Biochemical approaches to separate the histone variants (for example, by AUT gels)¹⁴ also proved to be technically unfeasible owing to the limited number and asynchronous nature of PGCs.

However, we discovered an alternative approach: fluorescence-activated cell sorting (FACS) purification of PGCs from *Oct4*–GFP transgenic mice¹ revealed a change in green fluorescent protein (GFP) intensity at E11.5. Under appropriate conditions we could

detect two major populations of E11.5 PGCs, those with lower (population A) and higher (population B) GFP signal; however, the GFP signal of E10.5 and E12.5 PGCs appeared homogeneous (Fig. 3a). The two populations of E11.5 PGCs also differed in their side-scatter values (SSCs), suggesting changes in their intracellular physical properties (data not shown). Notably, population B is highly transient and only detectable during a 3–4 h period.

We found distinct chromatin differences between populations A and B of E11.5 PGCs: population A stains for linker histone H1 and H2A.Z, whereas population B is devoid of both. This confirms that population B is at a more advanced stage (Fig. 3b). Interestingly, the loss of linker histone H1 precedes the loss of nucleosomal histone H2A.Z (Fig. 3b). Furthermore, the loss of H2A.Z in population B correlates with the loss of other modifications, such as H3K9ac, H3K9me3 and H3K27me3, as well as H2A/H4R3me2s⁵. Notably, the modifications on histone H3 are lost before the disappearance of H2A.Z.

Two additional observations support our findings. First, PGCs of both A and B populations are in the G2 phase of the cell cycle (Supplementary Fig. 9), suggesting that the loss of histone modifications is not linked to replication-coupled dilution. Second, before the disappearance of H1 and H2A.Z, we transiently detected the signal for these histones, as well as for macroH2A and H4K5ac in the cytoplasm of some PGCs of population B (Supplementary Figs 10 and 11). This suggests that at least some of the nucleosomal histones may be transferred to the cytoplasm, possibly for degradation.

Histone chaperones could have a critical role during mobilization of histones, and their apparent eviction and replacement in PGCs. Whereas a chromatin assembly factor 1 (CAF-1) complex can deposit the canonical histone H3.1 onto chromatin during DNA replication, the complex containing histone chaperone HIRA can deposit the

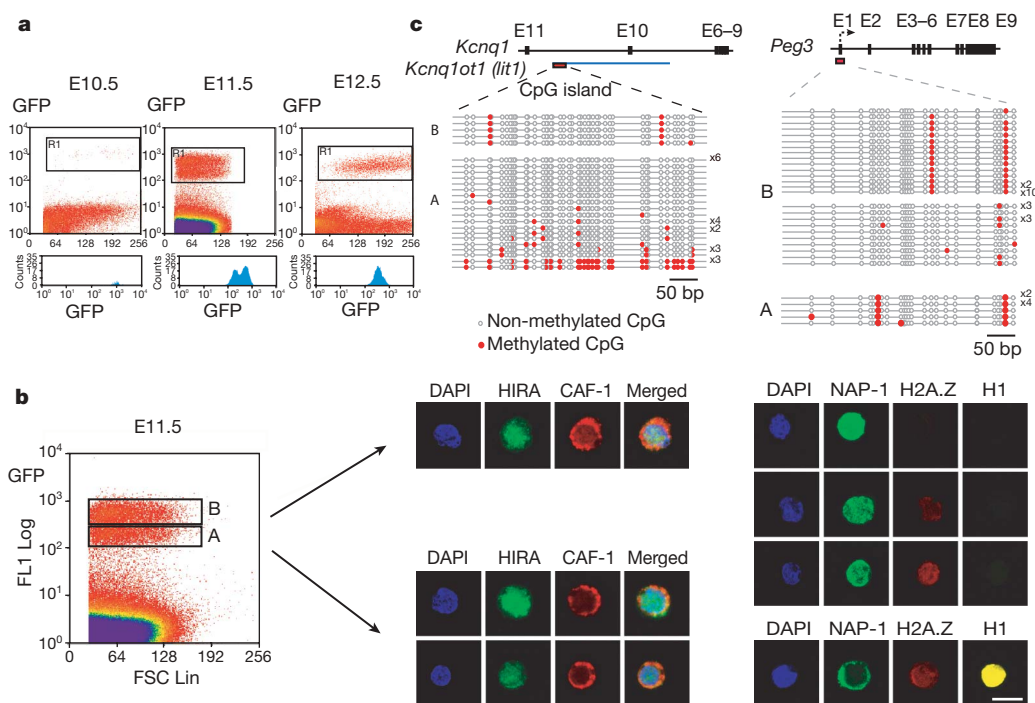


Figure 3 | Separation and analysis of PGCs undergoing distinct phases of the reprogramming process. **a**, Transient appearance of two populations of GFP-expressing PGCs at E11.5. The x and y axis represent the FSC (forward scatter) and GFP intensity values, respectively. The lower panels show the profiles of the GFP (germ-cell specific) signal. Note the appearance of two distinct peaks at E11.5. **b**, Separation and analysis of the chromatin configuration of the two populations of PGCs, denoted A and B, at E11.5. Population B is more advanced and shows loss of histone H1 and H2A.Z. Top images, population A; bottom images, population B. Note the cytoplasmic localization of CAF-1 in these populations and the

relocalization of NAP-1 from the cytoplasm to the nucleus in population B (for details see the text). Cells shown here are representative of the populations. Between 50 and 100 PGCs were examined for each population. Scale bar, 10 μ m. **c**, Analysis of DNA methylation of *Peg3* and *lit1* (*Kcnq1ot1*) DMRs in distinct populations of E11.5 PGCs using bisulphite genomic sequencing. Each line represents an independent clone. Open and closed circles represent non-methylated and methylated CpGs, respectively. The numbers represent the number of sequenced clones with identical methylation profile.

non-replicative H3.3 histone variant¹⁵. It is notable, therefore, that the largest subunit of CAF-1, p150, is predominantly cytoplasmic, whereas HIRA is enriched in the nucleus in PGCs in both A and B populations (Fig. 3b and Supplementary Fig. 12a). This unusual localization of p150 suggests that the process at work is unlikely to involve the CAF-1 complex.

Next we examined the histone chaperone with affinity for H1, H2A and H2B—nucleosome assembly protein 1 (NAP-1)^{16–19}. By forming complexes with H2A–H2B dimers, NAP-1 enhances the release of H3 and H4 during transcription¹⁷. Moreover, NAP-1 is also capable of extracting linker histones from chromatin of HeLa cells, which results in extended chromatin fibres¹⁶. Indeed, we detected much higher levels of NAP-1 in PGCs compared to the signal in neighbouring somatic cells where the protein was predominantly in the cytoplasm (Supplementary Fig. 12b). Furthermore, the disappearance of H1 from PGCs coincides with the relocalization of NAP-1 from the cytoplasm to the nucleus (compare populations A and B), suggesting its role in the removal of H1 in PGCs (Fig. 3b). Because NAP-1 can also interact with H2A.Z as well as direct nucleosomal disassembly *in vitro*^{17–19}, it is likely that NAP-1 has a significant role in the reprogramming process. Indeed, a recent study in fission yeast shows that NAP-1 may also be involved in nucleosomal disassembly *in vivo*²⁰. Together with our study, these are the first indications of the potential role of NAP-1 in chromatin disassembly processes *in vivo*.

We previously showed that PGCs undergo genome-wide DNA demethylation that included imprinted loci around E11.5 (ref. 1). In light of this work, we investigated the kinetics of DNA demethylation of *Peg3* and *lit1* (also known as *Kcnq1ot1*) loci as representatives

of imprinted genes. Bisulphite analysis under optimal conditions^{1,21,22} repeatedly detected only the demethylated *Peg3* and *lit1* alleles in PGCs of the B population, whereas PGCs in population A revealed some methylated alleles of *lit1* but none from the *Peg3* locus (Fig. 3e). Surprisingly and unexpectedly, bisulphite analysis of population A proved technically challenging, requiring a larger number of cells. Furthermore, the PCR products often showed signs of clonality, suggesting that only a limited number of amplifiable DNA molecules are present in the PGCs in population A. Additional analysis of global levels of 5-methylcytosine (5mC) revealed variable DNA methylation within population A, whereas population B seemed to be devoid of 5mC (Supplementary Fig. 13). Taken together, DNA demethylation occurs in population A and is followed by chromatin remodelling in population B.

Our study provides novel insights regarding the erasure of epigenetic modifications, which is pivotal for genomic reprogramming generally. Two possible models could account for the marked temporal and spatial relationship between DNA demethylation and chromatin changes. First, the ‘accessibility model’ predicts that decondensation of chromatin may precede DNA demethylation to allow a putative DNA demethylase to access DNA (Fig. 4a). Alternatively, DNA demethylation may occur by means of the DNA repair pathway, as exemplified by the methylcytosine-specific DNA glycosylases in plants^{23–25}. Although no similar enzymes have yet been identified in mammals, it is possible that DNA demethylation here may also be connected with DNA repair²⁶. Because it has been shown that DNA repair may be intimately connected with the structural chromatin changes and histone replacement^{27,28} (as recently demonstrated for nucleotide excision repair and double-strand-break repair processes^{29,30}), DNA-repair-driven demethylation could directly induce chromatin changes and histone replacement (Fig. 4 ‘repair model’). Our evidence suggests that the loss of DNA methylation occurs before histone replacement, which supports the repair model. Notably, our evidence also shows that the erasure of epigenetic memory in PGCs occurs not only at the level of DNA methylation, but also at the level of chromatin. This overall erasure of epigenetic information in PGCs may be crucial for resetting the genome for the eventual acquisition of totipotency.

METHODS SUMMARY

PGCs were isolated by FACS sorting of GFP-positive cells from OCT4–GFP transgenic mice. Immunofluorescence staining of PGCs and neighbouring somatic cells was carried out on trypsinized single-cell suspensions that were fixed and processed for confocal microscopy. Alternatively, the urogenital ridges were cryosectioned and prepared for staining and confocal microscopy. The FACS-sorted PGCs (populations A and B) were also prepared for 5mC staining using monoclonal 5mC antibody as described in the Methods. DNA methylation analysis of *Peg3* and *lit1* imprinted genes was carried out by bisulphite sequencing¹. All the antibodies used in this study have previously been used in other studies and verified to generate authentic signals. Further details are provided in the Methods.

Full Methods and any associated references are available in the online version of the paper at www.nature.com/nature.

Received 27 July 2007; accepted 17 January 2008.

Published online 19 March 2008.

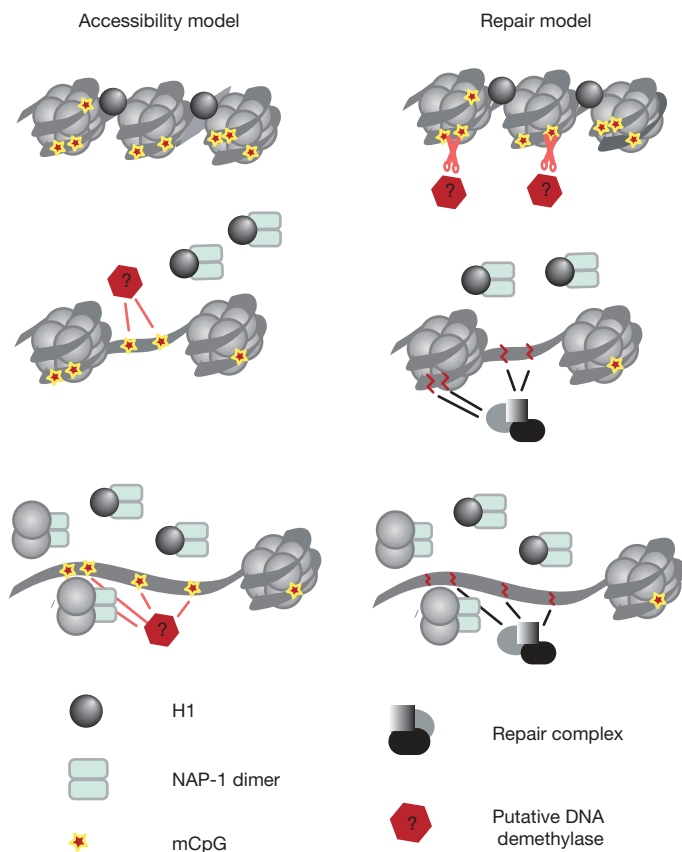


Figure 4 | Possible connections between chromatin changes and the DNA demethylation process. Changes in chromatin structure may be seen as prerequisite for the DNA demethylation process (accessibility model, left). Alternatively, DNA demethylation in PGCs can occur by means of the DNA repair pathway (right) as described in plants^{23,24,25}. The resulting DNA damage and repair could potentially induce chromatin remodelling, which would occur as a consequence of DNA demethylation (for details see the text).

- Hajkova, P. *et al.* Epigenetic reprogramming in mouse primordial germ cells. *Mech. Dev.* 117, 15–23 (2002).
- Lee, J. *et al.* Erasing genomic imprinting memory in mouse clone embryos produced from day 11.5 primordial germ cells. *Development* 129, 5697–5706 (2002).
- Saitou, M. *et al.* Specification of germ cell fate in mice. *Phil. Trans. R. Soc. Lond. B* 358, 1363–1370 (2003).
- Ohinata, Y. *et al.* Blimp1 is a critical determinant of the germ cell lineage in mice. *Nature* 436, 207–213 (2005).
- Ancelin, K. *et al.* Blimp1 associates with Prmt5 and directs histone arginine methylation in mouse germ cells. *Nature Cell Biol.* 8, 623–630 (2006).
- Seki, Y. *et al.* Cellular dynamics associated with the genome-wide epigenetic reprogramming in migrating primordial germ cells in mice. *Development* 134, 2627–2638 (2007).

7. Surani, M. A. *et al.* Mechanism of mouse germ cell specification: a genetic program regulating epigenetic reprogramming. *Cold Spring Harb. Symp. Quant. Biol.* **69**, 1–9 (2004).
8. Allegrucci, C., Thurston, A., Lucas, E. & Young, L. Epigenetics and the germline. *Reproduction* **129**, 137–149 (2005).
9. Bannister, A. J., Schneider, R. & Kouzarides, T. Histone methylation: dynamic or static? *Cell* **109**, 801–806 (2002).
10. Cuthbert, G. L. *et al.* Histone deimination antagonizes arginine methylation. *Cell* **118**, 545–553 (2004).
11. Wang, Y. *et al.* Human PAD4 regulates histone arginine methylation levels via demethyliminination. *Science* **306**, 279–283 (2004).
12. Henikoff, S., Furuyama, T. & Ahmad, K. Histone variants, nucleosome assembly and epigenetic inheritance. *Trends Genet.* **20**, 320–326 (2004).
13. Kaufman, P. D. & Almouzni, G. in *DNA Replication and Human Disease* (ed. DePamphilis, M. L.) 121–40 (Cold Spring Harbor Laboratory Press, Cold Spring Harbor, New York, 2006).
14. Zweidler, A. Resolution of histones by polyacrylamide gel electrophoresis in presence of nonionic detergents. *Methods Cell Biol.* **17**, 223–233 (1978).
15. Tagami, H., Ray-Gallet, D., Almouzni, G. & Nakatani, Y. Histone H3.1 and H3.3 complexes mediate nucleosome assembly pathways dependent or independent of DNA synthesis. *Cell* **116**, 51–61 (2004).
16. Kepert, J. F., Mazurkiewicz, J., Heuvelman, G. L., Toth, K. F. & Rippe, K. NAP1 modulates binding of linker histone H1 to chromatin and induces an extended chromatin fiber conformation. *J. Biol. Chem.* **280**, 34063–34072 (2005).
17. Levchenko, V. & Jackson, V. Histone release during transcription: NAP1 forms a complex with H2A and H2B and facilitates a topologically dependent release of H3 and H4 from the nucleosome. *Biochemistry* **43**, 2359–2372 (2004).
18. Park, Y. J., Chodaparambil, J. V., Bao, Y., McBryant, S. J. & Luger, K. Nucleosome assembly protein 1 exchanges histone H2A–H2B dimers and assists nucleosome sliding. *J. Biol. Chem.* **280**, 1817–1825 (2005).
19. Lorch, Y., Maier-Davis, B. & Kornberg, R. D. Chromatin remodeling by nucleosome disassembly *in vitro*. *Proc. Natl Acad. Sci. USA* **103**, 3090–3093 (2006).
20. Walfridsson, J., Khorosjutina, O., Matikainen, P., Gustafsson, C. M. & Ekwall, K. A genome-wide role for CHD remodelling factors and Nap1 in nucleosome disassembly. *EMBO J.* **26**, 2868–2879 (2007).
21. Durcova-Hills, G. *et al.* Influence of sex chromosome constitution on the genomic imprinting of germ cells. *Proc. Natl Acad. Sci. USA* **103**, 11184–11188 (2006).
22. Paulsen, M. *et al.* Sequence conservation and variability of imprinting in the Beckwith–Wiedemann syndrome gene cluster in human and mouse. *Hum. Mol. Genet.* **9**, 1829–1841 (2000).
23. Choi, Y. *et al.* DEMETER, a DNA glycosylase domain protein, is required for endosperm gene imprinting and seed viability in *Arabidopsis*. *Cell* **110**, 33–42 (2002).
24. Gehring, M. *et al.* DEMETER DNA glycosylase establishes MEDEA polycomb gene self-imprinting by allele-specific demethylation. *Cell* **124**, 495–506 (2006).
25. Gong, Z. *et al.* ROS1, a repressor of transcriptional gene silencing in *Arabidopsis*, encodes a DNA glycosylase/lyase. *Cell* **111**, 803–814 (2002).
26. Morgan, H. D., Santos, F., Green, K., Dean, W. & Reik, W. Epigenetic reprogramming in mammals. *Hum. Mol. Genet.* **14**, R47–R58 (2005).
27. Green, C. M. & Almouzni, G. When repair meets chromatin. First in series on chromatin dynamics. *EMBO Rep.* **3**, 28–33 (2002).
28. Nilsen, H., Lindahl, T. & Verreault, A. DNA base excision repair of uracil residues in reconstituted nucleosome core particles. *EMBO J.* **21**, 5943–5952 (2002).
29. Polo, S. E., Roche, D. & Almouzni, G. New histone incorporation marks sites of UV repair in human cells. *Cell* **127**, 481–493 (2006).
30. Linger, J. & Tyler, J. K. The yeast histone chaperone chromatin assembly factor 1 protects against double-strand DNA-damaging agents. *Genetics* **171**, 1513–1522 (2005).

Supplementary Information is linked to the online version of the paper at www.nature.com/nature.

Acknowledgements The authors thank N. Miller for technical assistance and expertise with FACS sorting and S. Jackson for stimulating discussions and critical reading of the manuscript. Additionally, we thank D. Tremethick, P. Adams and T. Jenuwein for sharing their antibodies. K.A. was a recipient of a Marie Curie and a Newton Trust fellowships, F.C. was a holder of a Marie Curie Fellowship and U.C.L. was supported by a Wellcome Trust PhD studentship. This work was funded by grants from the Wellcome Trust to M.A.S.

Author Contributions P.H. designed and performed the experiments and analysed the data. K.A. performed the analysis of chromatin in early PGCs. T.W., N.L., G.A. and R.S. were involved in the histone variant studies. U.C.L., F.C. and C.L. helped to prepare the samples for cryosectioning and FACS sorting. G.A. and R.S. contributed to experimental design. M.A.S. was involved in the experimental design and, together with P.H., wrote the paper.

Author Information One of the authors, F.C., was temporarily on the staff at *Nature* while the manuscript was being reviewed, but was not in any way involved in this process. Reprints and permissions information is available at www.nature.com/reprints. Correspondence and requests for materials should be addressed to M.A.S. (as10021@mole.bio.cam.ac.uk).

METHODS

Embryo collection and PGC preparation. PGCs were isolated from outbred MF1 mice. Noon of the day of the vaginal plug was designated as E0.5. For the FACS sorting, the dissected urogenital ridges from embryos carrying the *Oct4-GFP* transgene were trypsinized and treated with hyaluronidase before the FACS sorting using the MoFlo (Cytomation Bioinstruments). The purity of PGCs was examined independently using OCT4 staining, and was always in excess of 98%.

Immunofluorescence staining. The urogenital ridges of the relevant developmental stages were trypsinized and the single-cell suspension settled on the poly-L-lysine (Sigma-Aldrich)-treated slides. The cells were briefly washed with $1 \times$ PBS and fixed in 4% PFA in PBS for 15 min at room temperature (22 °C). The cells were permeabilized for 30 min using PBS, 1% BSA, 0.1% Triton TX-100. The antibody staining was carried out in the same buffer at 4 °C overnight (16–18 h). The slides were subsequently washed three times in PBS, 1% BSA, 0.1% Triton TX-100 (5 min each wash), were incubated with Alexa-dye-conjugated secondary antibodies (Molecular Probes) for 1 h at room temperature in the dark, washed once for 5 min in PBS, 1% BSA, 0.1% Triton TX-100 and twice for 5 min in PBS. The slides were then mounted in Vectashield with DAPI (Vector Laboratories) and imaged using a BioRad Radiance 2100 confocal microscope. The quantification of nuclear size and staining intensity was performed on cryosections (see below) using Velocity software.

For cryosections, the dissected urogenital ridges (E12.5 and E13.5) or trunks of embryos (E10.5 and E11.5) were fixed in 4% PFA (or in 2% PFA for H2A.Z stainings) for 4 h at 4 °C, washed three times for 10 min in PBS and incubated in 15% sucrose (in PBS) overnight at 4 °C. The material was then mounted in OCT matrix (Cell Path) and stored at -80 °C until cryo-sectioning. The cryosections were post-fixed with 4% PFA in PBS for 5 min, washed three times for 5 min in PBS, permeabilized, and processed further as above.

5-Methylcytosine staining. The FACS-sorted cells of populations A and B as well as the somatic cells of the genital ridges were allowed to attach to the poly-L-lysine (Sigma-Aldrich)-treated slides for 15 min at room temperature. After the fixation with 4% PFA in PBS for 10 min, the cells were washed three times for 5 min in PBS and permeabilized in PBS, 1% BSA, 0.5% TX-100 for 30 min. The slides were then washed with PBS and treated with 4 M HCl for 20 or 30 min (PGCs or somatic cells, respectively) at 37 °C. After extensive PBS washes, the slides were blocked in PBS, 1% BSA, 0.1% TX-100 for 30 min and hybridized in the same buffer with 5mC antibody at 4 °C overnight. The slides were

subsequently washed three times in PBS, 1% BSA, 0.1% Triton TX-100 (5 min each wash) and incubated with Alexa-dye-conjugated secondary antibodies (Molecular Probes) for 1 h at room temperature in the dark, washed once for 5 min in PBS, 1% BSA, 0.1% Triton TX-100 and twice for 5 min in PBS, followed by RNaseA treatment (1 mg ml^{-1} for 30 min) and propidium iodide staining (0.25 mg ml^{-1} for 10 min). The slides were then mounted in Vectashield (Vector laboratories) and imaged as above.

Antibodies. The following antibodies were used: H2A.Z (gift of D. Tremethick), 1:200 (the specificity of the antibody was tested on the AUT gels; data not shown); H1 (Abcam), 1:200; ATRX (Santa Cruz Biotechnologies), 1:50; H3K9me2 (Upstate), 1:400; H3K9me3 and H3K9me27 (gift of T. Jenuwein), 1:500; H3K9ac (Abcam), 1:300; NAP-1 (Abcam), 1:200; H3K4me2 and H3K4me3 (Abcam), 1:500; HIRA (gift of P. Adams), combination of monoclonal antibodies; CAF-1 (anti-p150; gift of G. Almouzni), 1:100; and 5mC antibody (gift of A. Nivelau), 1:50.

Bisulphite sequencing. The FACS-sorted PGCs were embedded in SeaPlaque LMP agarose and processed as described previously. Nested PCR approach was used for the PCR amplification of *Peg3* and *lit1* DMR regions as in ref. 1. For *Peg3*, the primers used were: F1, TTTTATGATTTTGTGGGGTTTAAATA; R1, AATCCCTATCACCTAAATAACATCCCTACA; F2, TTGATAATAGTAG-TTTGATTGGTAGGGTGT; R2, ATCTACAACCTTATCAATTACCCTTAAAAA. The PCR conditions were as follows: first PCR (primers F1, R1): 95 °C for 5 min, 95 °C for 1 min, 58 °C for 75 s, 72 °C for 60 s (35 cycles), followed by 72 °C for 10 min and kept at 4 °C. Second PCR (primers F2, R2): 95 °C for 5 min, 95 °C for 1 min, 58 °C for 75 s, 72 °C for 60 s (35 cycles), followed by 72 °C for 10 min and kept at 4 °C. For *lit1*, the primers used were: F1, TATTATTTTGGTGTGGTT-ATATCGGGTTA; R1, ATTTTCTTCAACACCCTTCTTTCCCT; F2, GGG-TTATAAAGTTTAGGGGTTTTAGATT; R2, AAACCTTTCTATCAACTT-AATCCCAAC. The PCR conditions were as follows: first PCR (primers F1, R1): 95 °C for 5 min, 95 °C for 1 min, 57 °C for 75 s, 72 °C for 60 s (35 cycles), followed by 72 °C for 10 min and kept at 4 °C. Second PCR (primers F2, R2): 95 °C for 5 min, 95 °C for 1 min, 57 °C for 75 s, 72 °C for 60 s (35 cycles), followed by 72 °C for 10 min and kept at 4 °C.

The PCR products were gel purified, cloned into a T/A cloning vector (pGEM Easy System I, Promega) and transformed into Top10 ultracompetent *Escherichia coli* (Invitrogen). The inserts were verified using colony PCR and sequenced using an external sequencing service.

LETTERS

Integration of growth and specification in chick wing digit-patterning

Matthew Towers^{1†}, Ruth Mahood¹, Yili Yin¹ & Cheryll Tickle^{1†}

In the classical model of chick wing digit-patterning¹, the polarizing region—a group of cells at the posterior margin of the early bud—produces a morphogen gradient, now known to be based on Sonic hedgehog (Shh)^{2,3}, that progressively specifies anteroposterior positional identities in the posterior digit-forming region⁴. Here we add an integral growth component to this model by showing that Shh-dependent proliferation of prospective digit progenitor cells is essential for specifying the complete pattern of digits across the anteroposterior axis. Inhibiting Shh signalling in early wing buds reduced anteroposterior expansion, and posterior digits were lost because all prospective digit precursors formed anterior structures. Inhibiting proliferation also irreversibly reduced anteroposterior expansion, but instead anterior digits were lost because all prospective digit precursors formed posterior structures. When proliferation recovered in such wings, *Shh* transcription was maintained for longer than normal, suggesting that duration of *Shh* expression is controlled by a mechanism that measures proliferation. Rescue experiments confirmed that Shh-dependent proliferation controls digit number during a discrete time-window in which Shh-dependent specification normally occurs. Our findings that Shh signalling has dual functions that can be temporally uncoupled have implications for understanding congenital and evolutionary digit reductions.

Early work suggested that growth might play an integral part in the classical model of chick wing anteroposterior (thumb to little finger) patterning. In this model, the polarizing region, in addition to producing a morphogen which acts as a classical specification gradient^{1,5} (Fig. 1a), also produces a growth signal that coordinately controls the size of the potential digit-forming field (Fig. 1b)^{6–8}. The specification gradient is now known to be based on Shh signalling^{2,3} but the existence of a growth signal remains speculative. Recently it has been shown that the three most posterior digits in the mouse are progressively derived from *Shh*-expressing cells, leading to the suggestion that growth rather than a morphogen gradient may specify the pattern of these digits⁹. This progressive growth mechanism is unlikely to contribute to chick wing digit-patterning (Fig. 1c), because, in addition to confirming earlier work that digit progenitor populations in the posterior part of early buds contribute to each digit¹⁰, we also showed that only digit 4 is derived from *Shh*-expressing cells (Fig. 1d, e).

To test whether Shh has a role in growth control during chick wing digit-patterning, we treated embryos at early bud stages Hamburger Hamilton stage 20 (HH20) with cyclopamine, an inhibitor of Shh signalling. As reported¹¹, cyclopamine treatment leads to either fusion of digits 3 and 4, or loss of digit 4 (Fig. 2d–f, top panel; normal pattern, Fig. 2c, top panel). In the classical morphogen model, when Shh signalling is reduced, digits 2 and 3 would come from posterior cells, whereas more anterior cells would not form digits at all (Fig. 2a); if growth is integral, however, the size of the digital field would be

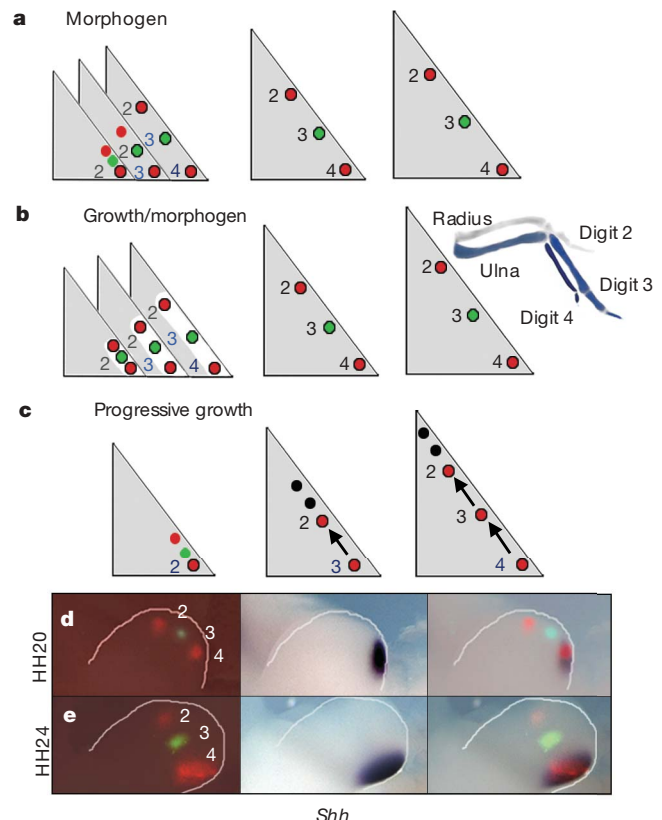


Figure 1 | Models of chick wing digit-patterning. **a–c**, Predicted fates of cells in early bud (red/green dots). **a**, Morphogen gradient model^{1,5}. Shh gradient sequentially specifies progressively more posterior fates⁴ across bud (red/green spots; black circle indicates specification). Shh concentration specifying each element is shown by coloured digit numbers and indicated on skeleton (high, dark blue; low, grey). Digit fate irreversibly determined (black numbers). **b**, Growth/morphogen gradient model. Entire digital field (white box) initially specified as digit 2, then anteroposterior expansion enlarges digital field, allowing Shh gradient to specify additional digits with progressively posterior fates. **c**, Progressive-growth model. All digit progenitors specified by time of exposure to a constant level of Shh signalling (dark-blue digit numbers) in the polarizing region⁹ (arrows show cell displacement away from the polarizing region). Note that cells that are most anterior (red/green spots) do not give rise to digits (black spots). Model reminiscent of classical progress-zone model of proximodistal patterning²⁸. **d–e**, Fate-mapping digit progenitors in the posterior part of the chick wing bud over 24 h; HH20 (**d**), HH24 (**e**). Cell populations stay separate; *Shh*-expressing cells only give rise to digit 4.

¹Division of Cell and Developmental Biology, WTB/MSI Complex, University of Dundee, Dow Street, Dundee DD1 5EH, UK. [†]Present address: Department of Biology and Biochemistry, University of Bath, Claverton Down Road, Bath BA2 7AY, UK.

reduced and just give rise to digits 2 and 3 (Fig. 2b). Fate-mapping individual cyclopamine-treated wing buds over 48 h showed reduced separation of digit progenitors across the anteroposterior axis in wings in which digit 4 was ultimately lost (Fig. 2d–f, bottom; control, Fig. 2c, bottom). Furthermore, the entire potential digital field contributed to digits 2 and 3, thus showing that growth is an essential component of the morphogen model (Fig. 1b).

In other systems, genes encoding cell-cycle regulators that promote the G1–S phase transition are direct targets of Shh signalling¹². In early chick wing buds (HH20/21), *N-myc* is expressed in posterodistal (posterior tip) mesenchyme in the prospective digital field and 24 h later (HH24), around the entire distal margin (Fig. 2g). *CyclinD1* is diffusely expressed throughout early buds, later becoming predominantly localized to posterodistal mesenchyme (Fig. 2h), and *CyclinD2* is expressed in the polarizing region of early buds, later extending distally (Fig. 2i). After exposure to cyclopamine (20 h), *N-myc* (8/8) and *CyclinD1* expression were unaffected (10/10) (Fig. 2j, k), but *CyclinD2* expression was undetectable (11/14) (Fig. 2l). Although TUNEL and BrdU labelling showed no obvious changes in apoptosis/proliferation (data not shown), at 20 h, fluorescence-activated cell sorting (FACS) of posterior halves of cyclopamine-treated buds

showed reduced S-phase cell numbers (Supplementary Fig. 1), consistent with Shh signalling controlling mesenchymal proliferation in the early bud. To investigate this further, we implanted Shh beads anteriorly in HH20 buds, which, unlike cyclopamine treatment, affects full digit pattern². At 12 h, *N-myc* expression increased around the bead (5/6 cases), whereas at 16 h *CyclinD1* expression increased distally (9/9) (Fig. 2m, n, top). At 18 h, FACS of anterior halves of Shh-treated buds confirmed increased S-phase cell numbers (Supplementary Fig. 1). Ectopic *CyclinD2* expression was undetectable (10/10) within 24 h (Fig. 2o, top) but present at 44 h (4/4; data not shown). It has been proposed that a mesenchymally derived maintenance factor for the apical ectodermal ridge controls growth by relaying signals from the posterior of the bud¹³, but Shh still induced expression of both *N-myc* (5/7) and *CyclinD1* (6/6) after removal of the anterior ridge (Fig. 2m, n, bottom; *CyclinD2* was unaffected, Fig. 2o, bottom). Furthermore, in wing buds of the polydactylous chicken *talpid*³ mutant, in which Gli3-processing, a transcriptional effector of Shh signalling, is defective¹⁴, *CyclinD1* and *CyclinD2* are ectopically expressed distally (Fig. 2q, r; *N-myc*, Fig. 2p). These data suggest that Shh, independently of ridge signalling, overcomes Gli3-mediated repression of expression of G1–S regulators in the digital field.

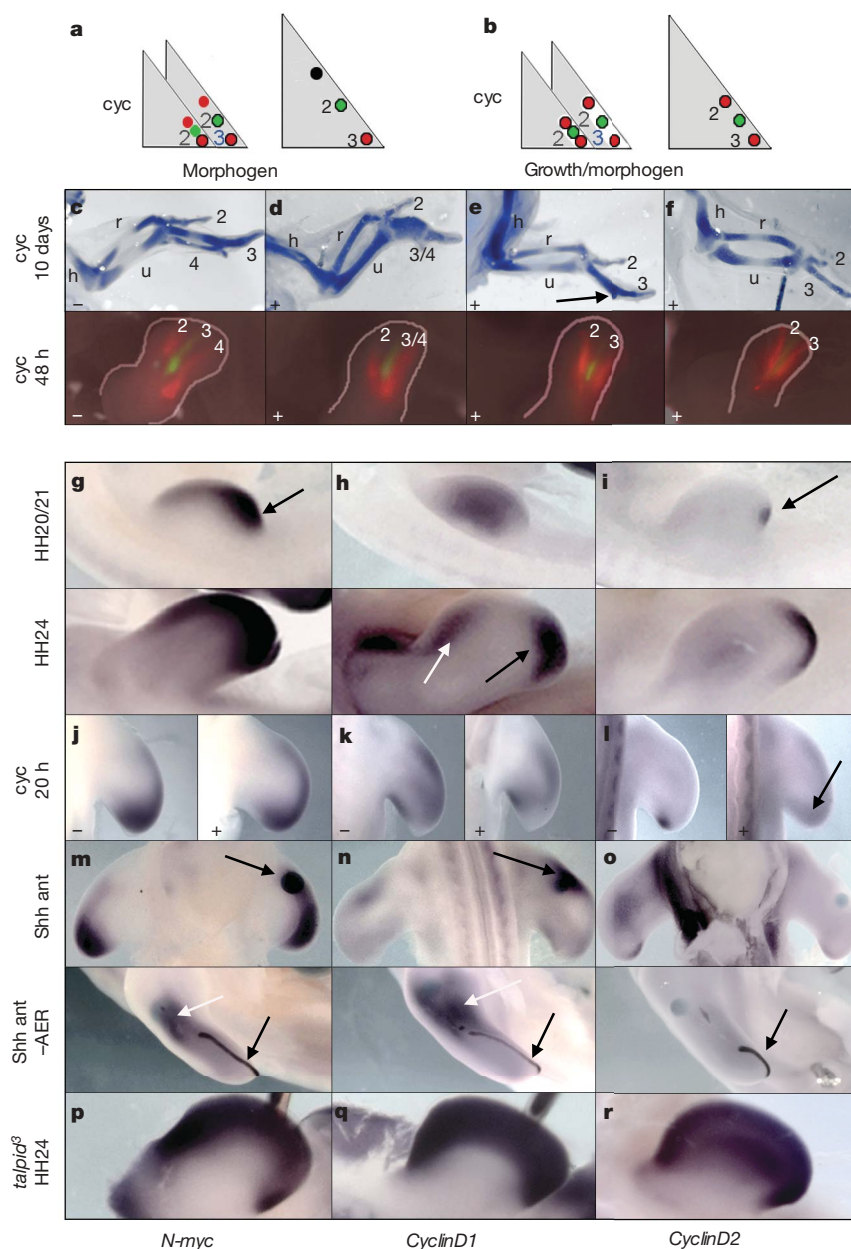


Figure 2 | Inhibiting Shh causes loss of posterior elements. h, Humerus; r, radius; u, ulna.

a, b, Potential effects of cyclopamine (cyc) on fate-maps of digit progenitors. Morphogen model (**a**), two groups of cells specified by decreased Shh signalling as digits 2 and 3 (red/green spots outlined with black-specified cells), anterior-most group fails to receive Shh and contribute to digit development (black spot). Growth/morphogen model (**b**) entire digital field specified by Shh as digits 2 and 3. **c–f**, Skeletons (top) and earlier fate-maps (48 h, bottom) after systemic cyclopamine treatment at HH20. Control skeleton and fate-map (**c**), labelled cells expand into handplate and separate; cyclopamine-treated skeletons and fate-maps (**d–f**); distal expansion of all progenitor groups occurs, progressive restriction in separation correlates with digit 4 loss. Note digit 4 tip emanating from digit 3 (arrow, **e**). **g–r**, Cell-cycle gene regulation in wing buds. **g–i**, Normal wing buds. Top panels: HH20/21. *N-myc* (**g**) throughout bud with high levels posteriorly (arrow), *CyclinD1* throughout bud (**h**), *CyclinD2* in the polarizing region (arrow, **i**). Bottom panels: HH24. *N-myc* throughout distal bud (**g**), *CyclinD1* predominantly posterodistally (black arrow, **h**; anterior expression, white arrow), *CyclinD2* within and distal to the polarizing region (**i**). **j–l**, Systemic 20 h cyclopamine treatment (right panels, +), controls (left panels, –). *N-myc* (**j**) and *CyclinD1* (**k**) unaffected, *CyclinD2* lost (**l**, right arrow). **m–o**, Top panels: anterior Shh beads in right bud. Ectopic *N-myc* (arrow, **m**) within 12 h, *CyclinD1* above endogenous levels within 16 h (arrow, **n**), *CyclinD2* not induced within 24 h (**o**). Bottom panels: anterior Shh bead in bud with anterior ridge removed (posterior ridge; black arrow, **m**). Ectopic *N-myc* (white arrow, **m**) and *CyclinD1* (white arrow, **n**), but no *CyclinD2* within 24 h (**o**). **p–r**, HH24 *talpid*³ buds. *N-myc* (**p**), *CyclinD1* (**q**), *CyclinD2* (**r**) throughout distal bud.

To test directly the role of proliferation in wing digit-patterning, we inhibited growth by either overexpressing the cyclin-dependent kinase inhibitor, *p21^{cip1}*, or applying the deacetylase inhibitor trichostatin A (TSA), which induces *p21^{cip1}* transcription¹⁵ (Supplementary Fig. 2). With both *p21^{cip1}* and TSA treatments, inhibiting growth rather than Shh signalling also led to a reduction in digit number; however, in contrast, anterior instead of posterior elements were lost: radius and digits 2 and 3 after treatment at early stages (HH20/21) and digit 2 at HH22 (Fig. 3a–e, top; Supplementary Fig. 3 and Supplementary Table 1). Treatment after HH23 had no effects on pattern, although all elements were smaller (Supplementary Fig. 3 and Supplementary Table 1). Characterizing the effects of *p21^{cip1}* and TSA treatments of HH20/21 buds in more detail showed that anteroposterior expansion was reduced, caused by a combination of cell-cycle arrest and ensuing apoptosis, the relative contributions of which were difficult to determine precisely (Supplementary Figs 2 and 4). FACS and BrdU labelling of TSA-treated wings revealed a 12–18 h G2/M arrest and reduced S-phase cell numbers (S-phase progression was unaffected) accompanied by decreased cell-cycle gene expression (Supplementary Figs 1, 2 and 4). After this arrest, staining with Nile blue at 18–24 h (data not shown) and TUNEL labelling showed increased apoptosis throughout distal regions (Supplementary Fig. 4). Interestingly, specific G2–M inhibitors—colchicine and vinblastine—produced identical digit-patterning defects to TSA (data not shown; see also refs 16, 17). Earlier studies of aphidicolin-treated (G1–S inhibitor) chick wings reported ectopic digits and occasional loss of anterior elements¹⁸, thus showing that this latter defect is not caused by interference of a specific cell-cycle transition.

To understand the basis of loss of anterior elements, we fate-mapped digit progenitor cells in growth-arrested HH20/21 wing buds. If growth controls size of the digit-forming field, all prospective digit progenitors would contribute to digit 4 (Fig. 3f). In contrast, the morphogen gradient model predicts that only the most posterior cells would form digit 4 (Fig. 3g). Analysis of TSA-treated buds clearly supports the former prediction. At 48 h, although no appreciable anteroposterior expansion occurred (Fig. 3b–e, bottom, 3h, $n = 24$), and even when it was decreased by non-specific apoptosis, each labelled group of digit progenitor cells remained equally viable and contributed to distal development (Fig. 3e, bottom). In contrast, in control buds ($n = 16$), in which significant anteroposterior expansion occurred, each labelled cell population widened and expanded distally to give separate streams (Fig. 3a, bottom, h). These results show that posterior specification can be uncoupled from, and occur without, anteroposterior growth (Fig. 3f). However, growth normally plays an integral role in digit patterning (Fig. 1b) by expanding the size of the digital field that can initially only accommodate one digit.

Normal wings developed when bud widths were reduced by 500–600 μm (one-third) at 48 h (Fig. 3b, h). However, for each further reduction of about 200 μm , an individual element of anteroposterior pattern was lost (Fig. 3c–e, h) indicating that a growth threshold of net cell proliferation/apoptosis is required for formation of each element. In contrast, proximodistal (shoulder to finger-tip) pattern was unaffected by reducing mesenchymal cell number and growth, and specification of this axis remained coupled (Fig. 3b–e).

To visualize posterior specification of the unexpanded digital field, we examined *Ptc1* expression (read-out of Shh signalling) in two

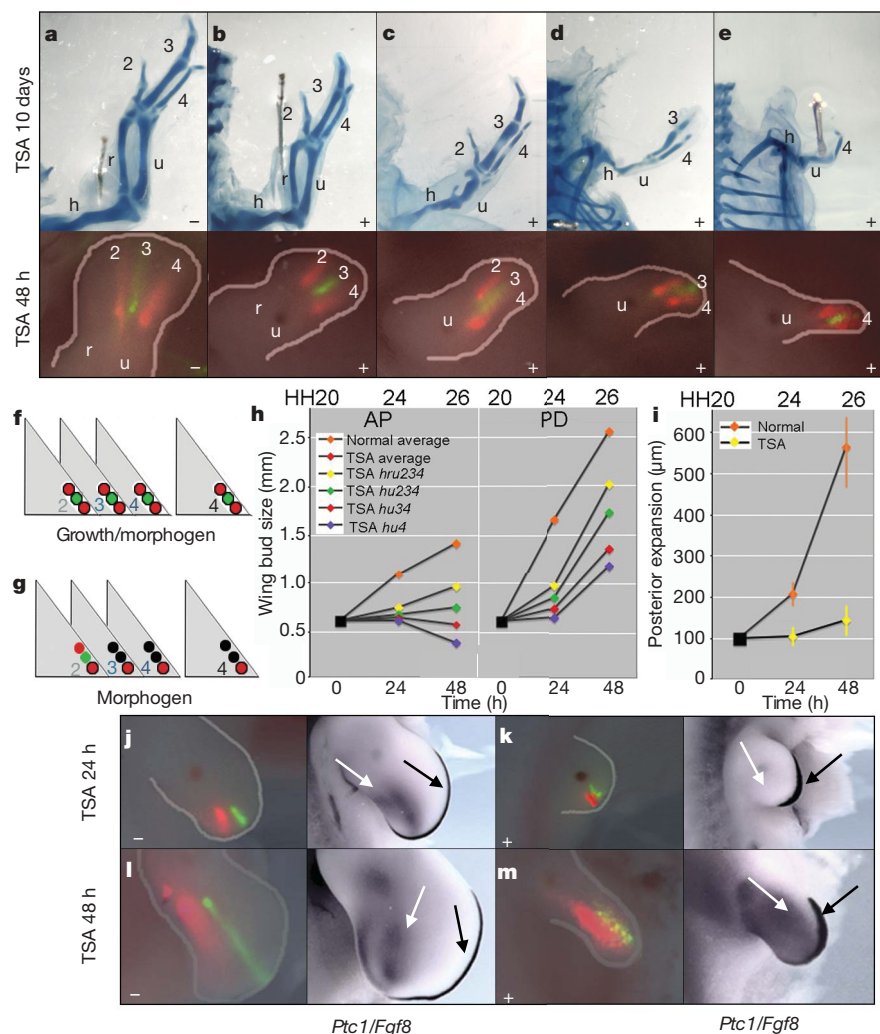


Figure 3 | Inhibiting anteroposterior expansion causes loss of anterior elements. a–e, Skeletons (top) and earlier fate-maps (48 h bottom) after TSA bead treatment at HH20/21. Control DMSO bead-treated (–) skeleton and earlier fate-map (a), cells expand into handplate and separate. TSA bead-treated (+) skeletons and fate-maps (b–e), distal expansion of all progenitor groups always occurs, anterior structures progressively fail to form as width decreases. f–g, Predicted fate-maps after growth inhibition. Growth/morphogen model (f), digit progenitors fail to expand but progressively specified (red/green spots outlined with black) and equally contribute to digit 4; morphogen model (g), only most posterior cells specified (red spot outlined with black), anterior cells do not give rise to digits (black); f is correct (see e). h, Anteroposterior/proximodistal measurements of DMSO bead control and TSA bead-treated buds at 24 h and 48 h. i, Posterior expansion between two groups of cells reduced in TSA bead-treated buds compared to DMSO-bead treated at 24 h and 48 h. Bars indicate highest and lowest values for each experiment. j–m, Left: examples of fate-mapped buds (see i) and, right, *Ptc1* in mesenchyme (white arrows), *Fgf8* in ridge (black arrows). Twenty-four hours, *Fgf8*/*Ptc1* in DMSO bead-treated bud (j, right), *Fgf8* expressed, *Ptc1* absent in TSA bead-treated bud (k, right). Forty-eight hours, *Fgf8*/*Ptc1* in DMSO (l, right) and TSA bead-treated bud (m, right).

groups of labelled cells. Groups separated widely in control wings, showing that the posterior of the bud expands approximately twofold over 24 h ($n = 7$) and five- to sixfold over 48 h ($n = 8$) (compare Fig. 3i with Fig. 3h and left panels in Fig. 3j, l) while often merging in TSA-treated buds over 24 h ($n = 7$) and 48 h ($n = 11$) (Fig. 3i, and left panels in Fig. 3k, m). *Ptc1* was expressed in both groups of labelled cells in TSA-treated wings at 48 h (white arrow, Fig. 3m, right), but only in the more posterior group in controls (white arrow, Fig. 3l, right). Unexpectedly, Shh signalling appeared to be interrupted in TSA-treated buds because *Ptc1* expression was undetectable at 24 h (white arrow, Fig. 3k, right; control, Fig. 3j, right). Several other targets of Shh signalling, including *Gremlin* and *Fgf4*, behaved similarly to *Ptc1*, whereas *dHAND* and *Tbx3* were relatively unaffected (Supplementary Fig. 5).

Because the dynamics of Shh signalling appeared to be altered, we investigated the full profile of *Shh* transcription in TSA-treated wings. During normal wing development, *Shh* transcripts are detectable at high levels for 36–40 h (Fig. 4a and Supplementary Fig. 6; $n > 5$ for each time point). However, depending on length of exposure to TSA between HH20 and HH23, high-level *Shh* transcription was lost for 6–21 h (Fig. 4b–e and Supplementary Fig. 6). Surprisingly, once returned, *Shh* expression was prolonged by a similar duration at later stages (Fig. 4b–e and Supplementary Fig. 6), explaining why narrowed buds are posteriorized, unlike

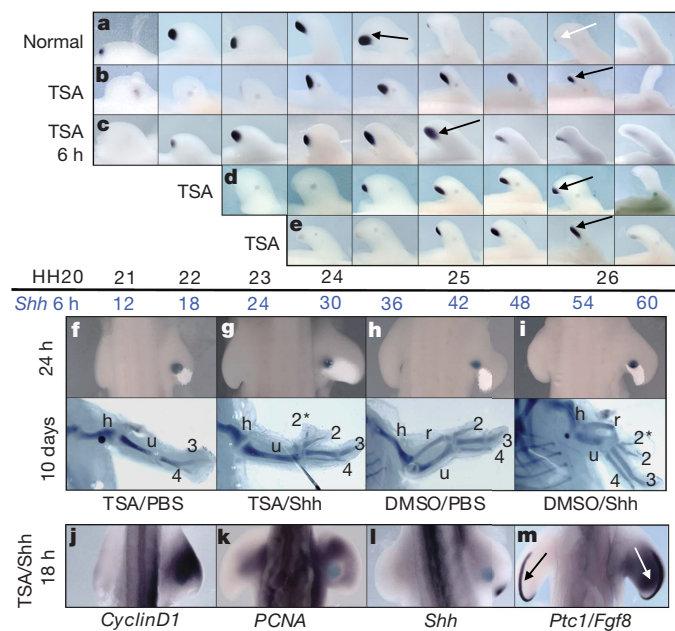


Figure 4 | *Shh* expression after growth arrest and Shh-mediated rescue of digit patterning. **a–e**, Time course of *Shh* expression during wing development initiating at HH18 (ref. 2). Normal untreated buds (**a**), high-level *Shh* expression until HH24/25 (black arrow, 36 h; very low expression until 54 h, white arrow). TSA bead-treated HH20/21, HH20/21 (6 h treatment), HH22 and HH23 buds (**b–e**), *Shh* expression lost but then high-level expression extended by approximately same duration (arrows). **f–m**, Shh-rescue experiments; systemic TSA-treated embryos (control DMSO), Shh bead (control PBS) in right bud. Shh beads (24 h) increased expansion in the posterior of TSA-treated buds (18 h) (**g**, compared with controls, **f**, **h**, **i**). Bottom: skeletons in rescue experiments. Loss of radius/digit 2 in TSA-treated embryo (**f**, compared with normal pattern, **h**); Shh beads rescued digit development in TSA-treated embryos, giving an extra digit 2* anteriorly; note missing radius (**g**, bottom, compared with controls, **f**, **h**, **i**, bottom). Shh beads can also induce an extra digit 2* anteriorly in DMSO-treated buds (**i**, bottom). **j–m**, Gene expression in rescue experiments. Loss of *CyclinD1* (**j**), *PCNA* (**k**), *Shh* (**l**) and *Ptc1* in left-hand buds 12 h after TSA treatment, but rescued by Shh beads (18 h) in right-hand buds (*Ptc1*, white arrow; *Fgf8*, black arrow, **m**).

cyclopamine-treated buds where further posterior specification is not possible. Interestingly, the G2/M inhibitor colchicine failed to inhibit *Shh* expression, but like TSA prolonged *Shh* expression (data not shown), suggesting that duration of *Shh* transcription is controlled by cell proliferation. This intrinsic timer contrasts with the proposed extrinsic timer regulated by anteroposterior growth separating *Shh*- and *Gremlin*-expressing cells¹⁹. Furthermore, *Shh* and *Gremlin* expression domains remain closely associated in severely narrowed TSA-treated buds (Supplementary Fig. 7).

Our results suggest that Shh controls both proliferation and specification of digit progenitors. Therefore, we tested whether applying Shh to growth-arrested buds could rescue digit pattern. We implanted Shh beads posteriorly to right buds at HH20–HH21, and added TSA systemically after 6 h. After 24 h, combined TSA/Shh treatment promoted expansion of posterodistal labelled cells (Fig. 4g, top; controls, Fig. 4f, h, i, top) and after 18 h FACS showed increased S-phase cell numbers (Supplementary Fig. 1), indicating that Shh regulates G2/M²⁰ as well as G1–S progression. At 18 h, *CyclinD1* (4/5), *Proliferating Cell Nuclear Antigen* (4/4), *Shh* (4/4) and *Ptc1* (6/6) (Fig. 4j–m) expression was rescued and ultimately a complete set of digits developed, sometimes with an additional digit 2 (Fig. 4g, bottom; controls, Fig. 4f, h, i, bottom; Supplementary Table 2). Thus, Shh signalling overrides TSA-induced cell-cycle arrest, and anteroposterior specification and growth occur together.

We have shown that Shh fulfils a dual role in chick wing digit-patterning, integrating proliferation with specification through the control of cell-cycle regulators. Thus we extend the classical morphogen-based model (Fig. 1b and Supplementary Fig. 8)^{6–8}. An elegant feature of the model is that a wide range of different wing patterns can

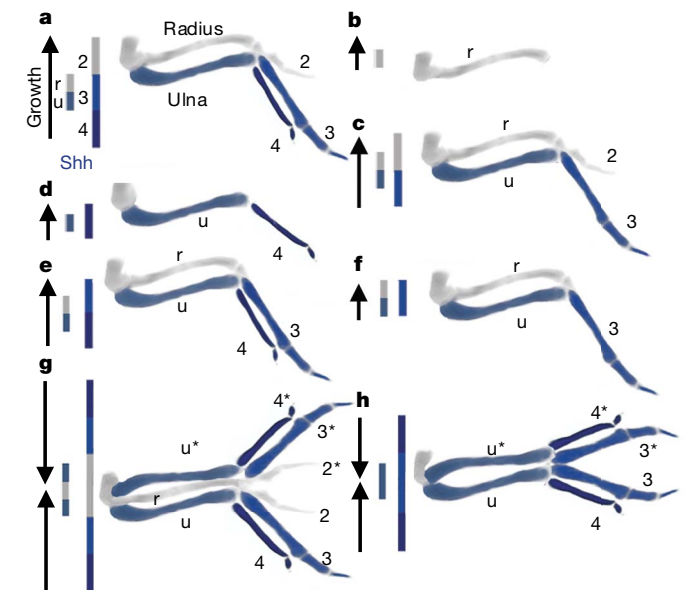


Figure 5 | Shh-dependent modulation of digit pattern. **a–h**, Shh-dependent anteroposterior growth irreversibly controls digit number during fixed time (vertical line), and Shh signalling modulates digit identity independently (grey, low Shh, specifies anterior radius/digit 2; deep blue, high Shh, specifies posterior ulna/digit 4). Normal chick wing (**a**; ru234). Mutants lacking Shh function, such as the chick *oligozeugodactyly* mutant³ (**b**; r), no digits specified owing to truncated outgrowth. Decreased Shh signalling after cyclopamine exposure (**c**; ru23). TSA-treated wing bud at HH20/21 (**d**; u4). TSA-treated wing bud at HH22 (**e**; ru34); note specification of forearm elements is unaffected as they are already irreversibly determined²⁸. Possible mechanism by which posterior and anterior digits can be lost together (**f**; ru3). Classical polarizing region grafting experiments to the anterior margin showed that increased growth accompanies mirror-image digit duplications (**g**; uu*4322*3*4*)^{1,29}. The same operation as in (**g**) but X-irradiation inhibits growth⁷; failure of anteroposterior expansion to accommodate the positional values results in missing anterior elements (**h**; uu*433*4*).

be generated by altering timing of the labile specification phase relative to the fixed irreversible growth phase (Fig. 5a–h). In normal development, Shh signalling integrates growth and specification in concert, and three digits form in the typical anteroposterior pattern (Fig. 5a). Inhibiting Shh signalling causes a simultaneous decrease in both growth and specification, leading to loss of posterior structures (Fig. 5b, c). In contrast, inhibiting growth also leads to loss of structures but Shh-dependent specification still continues and anterior structures are lost (Fig. 5d, e). If Shh signalling is attenuated after growth inhibition, then both anterior and posterior structures will be lost (Fig. 5f). Growth also contributes to digit patterns induced by anterior grafts of the polarizing region, as suggested in early experiments in which wings with polarizing region grafts were irradiated and anterior digits were lost (Fig. 5g, h and ref. 7).

Applying this growth/morphogen model of anteroposterior patterning can give insights into congenital and evolutionary limb reductions. Strikingly, anterior limb elements are lost after embryonic exposure to valproate in humans²¹, a clinically used deacetylase inhibitor structurally unrelated to TSA²², and in Feingold's patients²³ lacking functional *N-myc* (Fig. 5d, e, and Supplementary Fig. 8). Intriguingly, loss of anterior and posterior digits together in lizards such as *Hemiergis* is associated with decreased cell proliferation and shortened duration of *Shh* transcription²⁴ (Fig. 5f). Our observations also suggest that Shh only specifies digit identities in proliferative cells; thus cell fate could be irreversibly determined by a cellular memory mechanism²⁵ linked to cell-cycle progression. In a wider context, growth-dependent pattern specification could reflect a general developmental strategy that may be used in other systems patterned by Shh, as well as those patterned by other morphogens.

METHODS SUMMARY

Whole-mount RNA *in situ* hybridization. This was performed as previously described²⁶.

Bead implantations. AG1-X2 beads were soaked in $1 \mu\text{g} \mu\text{l}^{-1}$ TSA and implanted into wing buds. Shh ($10 \mu\text{g} \mu\text{l}^{-1}$) bead implantations were as described²⁷.

Whole-embryo treatments. TSA ($20 \mu\text{l}$, $0.05 \mu\text{g} \mu\text{l}^{-1}$) was directly added to the embryo. Cyclopamine was applied as described¹¹.

Cell-cycle analyses. For FACS, wing buds were trypsinized for 30 min. Cell suspensions were washed twice in PBS and fixed in 70% ethanol overnight, then washed twice and resuspended in PBS containing 0.1% Triton X-100, $50 \mu\text{g} \text{ml}^{-1}$ of propidium iodide and $50 \mu\text{g} \text{ml}^{-1}$ of RNase A before being analysed by FACS. BrdU and TUNEL labelling on cryosectioned wing buds ($7 \mu\text{m}$) were performed with Roche kits.

Posterior wing bud fate-mapping assay. Spots ($25 \mu\text{m}$) of either DiI or DiO were microinjected into the posterior of buds. After 24 or 48 h, images of cell traces were captured, and, when necessary, eggs re-incubated for cartilage staining.

Electroporation. Two microlitres of $3 \mu\text{g} \mu\text{l}^{-1}$ of pcDNA3.1-*p21* (human *p21^{cip1}*) or control pcDNA3.1-*p21BamHI* were microinjected into posterior areas of buds before being electroporated at 40 V for $2 \times 50 \text{ ms}$ with $2 \times 200 \text{ ms}$ intervals.

Posterior wing bud expansion assays. One $50 \mu\text{m}$ spot of DiI was microinjected into the posterior of buds, and images were captured 24 h later. In *p21^{cip1}* over-expression experiments, $1 \mu\text{l}$ of $3 \mu\text{g} \mu\text{l}^{-1}$ of vector DNA was mixed with $1 \mu\text{l}$ of $3 \mu\text{g} \mu\text{l}^{-1}$ of pCAGGS-RFP then microinjected into a $50 \mu\text{m}$ area of the posterior region of the bud (see above), and images were captured after 24 h.

Alcian blue skeletal preparations. Embryos were fixed in 100% ethanol for two days, then transferred to 0.1% alcian blue in 80% ethanol/20% acetic acid for one day, before being cleared in 1% KOH.

Wing bud measurements. All measurements made with Openlab software (Improvision).

Full Methods and any associated references are available in the online version of the paper at www.nature.com/nature.

Received 13 November 2007; accepted 15 January 2008.

Published online 19 March 2008.

1. Tickle, C., Summerbell, D. & Wolpert, L. Positional signalling and specification of digits in chick limb morphogenesis. *Nature* **254**, 199–202 (1975).

2. Riddle, R. D., Johnson, R. L., Laufer, E. & Tabin, C. Sonic hedgehog mediates the polarizing activity of the ZPA. *Cell* **75**, 1401–1416 (1993).
3. Ros, M. A. *et al.* The chick oligozeugodactyly (ozd) mutant lacks sonic hedgehog function in the limb. *Development* **130**, 527–537 (2003).
4. Yang, Y. *et al.* Relationship between dose, distance and time in Sonic Hedgehog-mediated regulation of anteroposterior polarity in the chick limb. *Development* **124**, 4393–4404 (1997).
5. Wolpert, L. Positional information and the spatial pattern of cellular formation. *J. Theor. Biol.* **25**, 1–47 (1969).
6. Cooke, J. & Summerbell, D. Cell cycle and experimental pattern duplication in the chick wing during embryonic development. *Nature* **287**, 697–701 (1980).
7. Smith, J. C. & Wolpert, L. Pattern formation along the anteroposterior axis of the chick wing: the increase in width following a polarizing region graft and the effect of X-irradiation. *J. Embryol. Exp. Morphol.* **63**, 127–144 (1981).
8. Summerbell, D. The control of growth and the development of pattern across the anteroposterior axis of the chick limb bud. *J. Embryol. Exp. Morphol.* **63**, 161–180 (1981).
9. Harfe, B. D. *et al.* Evidence for an expansion-based temporal Shh gradient in specifying vertebrate digit identities. *Cell* **118**, 517–528 (2004).
10. Vargesson, N. *et al.* Cell fate in the chick limb bud and relationship to gene expression. *Development* **124**, 1909–1918 (1997).
11. Scherz, P. J., McGlinn, E., Nissim, S. & Tabin, C. J. Extended exposure to Sonic hedgehog is required for patterning the posterior digits of the vertebrate limb. *Dev. Biol.* **308**, 343–354 (2007).
12. Roy, S. & Ingham, P. W. Hedgehogs tryst with the cell cycle. *J. Cell Sci.* **115**, 4393–4397 (2002).
13. Zwillig, E. & Hansborough, L. Interactions between limb bud ectoderm and mesoderm in the chick embryo. III. Experiments with polydactylous limbs. *J. Exp. Zool.* **132**, 219–239 (1956).
14. Davey, M. G. *et al.* The chicken *talpid3* gene encodes a novel protein essential for Hedgehog signaling. *Genes Dev.* **20**, 1365–1377 (2006).
15. Ocker, M. & Schneider-Stock, R. Histone deacetylase inhibitors: signalling towards p21(*cip1*/waf1). *Int. J. Biochem. Cell Biol.* **39**, 1367–1374 (2007).
16. Alberch, P. & Gale, E. A. Size dependence during the development of the amphibian foot. Colchicine-induced digital loss and reduction. *J. Embryol. Exp. Morphol.* **76**, 177–197 (1983).
17. Gabriel, M. L. The effect of local applications of colchicine on Leghorn and polydactylous chick embryos. *J. Exp. Zool.* **101**, 339–350 (1946).
18. Ohsugi, K., Gardiner, D. M. & Bryant, S. V. Cell cycle length affects gene expression and pattern formation in limbs. *Dev. Biol.* **189**, 13–21 (1997).
19. Scherz, P. J., Harfe, B. D., McMahon, A. P. & Tabin, C. J. The limb bud Shh-Fgf feedback loop is terminated by expansion of former ZPA cells. *Science* **305**, 396–399 (2004).
20. Barnes, E. A., Kong, M., Ollendorff, V. & Donoghue, D. J. Patched1 interacts with cyclin B1 to regulate cell cycle progression. *EMBO J.* **20**, 2214–2223 (2001).
21. Sharony, R. *et al.* Preaxial ray reduction defects as part of valproic acid embryofetopathy. *Prenat. Diagn.* **13**, 909–918 (1993).
22. Phiel, C. J. *et al.* Histone deacetylase is a direct target of valproic acid, a potent anticonvulsant, mood stabilizer, and teratogen. *J. Biol. Chem.* **276**, 36734–36741 (2001).
23. Alessandri, J. L. *et al.* Syndrome de Feingold. *Arch. Pédiatr.* **7**, 637–640 (2000).
24. Shapiro, M. D., Hanken, J. & Rosenthal, N. Developmental basis of evolutionary digit loss in the Australian lizard *Hemiergis*. *J. Exp. Zool.* **297B**, 48–56 (2003).
25. Smith, J. C. Evidence for a positional memory in the development of the chick wing bud. *J. Embryol. Exp. Morphol.* **52**, 105–113 (1979).
26. Nieto, A., Patel, K. & Wilkinson, D. G. in *Methods in Cell Biology* (ed. Bronner Fraser, M.) 219–235 (Academic, San Diego, 1996).
27. Drossopoulou, G. *et al.* A model for anteroposterior patterning of the vertebrate limb based on sequential long- and short-range Shh signalling and Bmp signalling. *Development* **127**, 1337–1348 (2000).
28. Summerbell, D., Lewis, J. H. & Wolpert, L. Positional information in chick limb morphogenesis. *Nature* **244**, 492–496 (1973).
29. Saunders, J. W. & Gasseling, M. T. in *Mesenchymal-Epithelial Interactions* (eds Fleischmeyer, R. & Billingham, R. E.) 78–97 (Williams and Wilkins, Baltimore, 1968).

Supplementary Information is linked to the online version of the paper at www.nature.com/nature.

Acknowledgements We thank: The Medical Research Council (C.T., M.T.) and the Royal Society (C.T., R.M. and Y.Y.) for funding; ARK Genomics (Edinburgh), the Biotechnology and Biological Science Research Council and the University of Manchester Institute of Science and Technology for EST clones; K. Ball for the *p21^{cip1}* vector; D. Burt for *talpid3* embryos; J. Richman for Shh protein; R. Clarke for FACS. M.T. thanks A. Münsterberg for support.

Author Information Reprints and permissions information is available at www.nature.com/reprints. Correspondence and requests for materials should be addressed to C.T. (cat24@bath.ac.uk).

METHODS

Whole-mount RNA *in situ* hybridization. This technique was performed as previously described²⁶. Details of probes used are available on request. All images were captured with a ProgRes C14 camera (Jenoptik) in conjunction with Openlab software (Improvision). In *Gremlin/Shh* double *in situ*, *Shh* was developed first with NBT/BCIP detection of digoxigenin-labelled riboprobe (purple) and then *Gremlin* developed with INT/BCIP detection of fluorescein-labelled riboprobe (orange).

Bead implantations. In all experiments, fertilized chicken White Leghorn eggs were incubated at 38 °C, windowed and staged according to Hamburger and Hamilton³⁰. TSA (Sigma) was dissolved in DMSO (Sigma) to make a concentration of 1 µg µl⁻¹. Higher concentrations frequently caused loss of entire wings; lower concentrations rarely led to patterning defects. AG1-X2 beads (Bio-rad) were soaked in TSA for 30 min, washed twice in DMEM (Gibco) and then implanted into wing buds using fine tungsten needles. DMSO beads were used as controls and washed identically. *Shh* (10 µg µl⁻¹) and PBS bead implantations were performed as previously described²⁷. In ectodermal ridge-removal experiments, fine tungsten needles were used to tease the anterior ridge away carefully from the wing bud before beads were implanted into the underlying mesenchyme; successful ridge removal was determined by analyses of *Fgf8* expression.

Whole-embryo treatment with TSA and cyclopamine. Vitelline membranes were carefully removed from around the wing bud region, and 20 µl of TSA dissolved in DMSO (0.05 µg µl⁻¹) was directly added to the embryo through a Gilson pipette. Higher concentrations often caused lethality and lower concentrations rarely caused patterning defects. The same amount of DMSO (minus TSA) was applied as a control. Cyclopamine (Sigma) dissolved in control carrier (45% 2-hydropropyl-β-cyclodextrin in PBS, Sigma) was applied as previously described¹¹ with 5 µl applied at 0 h and again at 12 h.

Cell-cycle analyses. For FACS, wing buds were carefully dissected with fine tweezers in ice-cold PBS, pooled from separate experiments (between two and four) and trypsinized (0.5%, Gibco) for 30 min before being disaggregated into a single-cell suspension. Cells were washed twice in PBS and fixed in 70% ethanol overnight. Cells were then washed twice in PBS (containing 1% bovine serum albumin) and re-suspended in PBS containing 0.1% Triton X-100, 50 µg ml⁻¹ propidium iodide and 50 µg ml⁻¹ RNase A (Sigma). After incubation at room temperature for 20 min, cells were analysed for cell-cycle distribution with a FACS Calibur flow cytometer and Cell Quest software (Becton Dickinson). Pulse-width analysis was used to exclude cell doublets and aggregates from the analysis. Cells with a DNA content between 2N and 4N were designated as being in the G1, S or G2/M phase of the cell cycle. The number of cells in each phase of the cell cycle was expressed as a percentage of the total number of cells present. For FACS of BrdU-labelled cells, 50 µg of BrdU was added systemically *in ovo* after removal of vitelline membranes, and embryos re-incubated for 1 h. Single cells were prepared as above before being stained for BrdU incorporation with the Roche BrdU labelling kit. Intensity of labelling was measured with a FACS Calibur flow cytometer and Cell Quest software (Becton Dickinson). S-phase cells incorporating BrdU showed a typical horseshoe pattern reflecting intensity of staining through different stages of S-phase and remaining cells were designated as G1 or G2/M phase based on level of autofluorescence. BrdU and TUNEL labelling on cryosectioned wing buds (7 µm) were performed using Roche kits. Wing buds were fixed overnight in 4% PFA, washed in PBS and infiltrated in PBS (containing 7.5% gelatin/15% sucrose) overnight at 38 °C. Wing buds were orientated in plastic moulds, allowed to set at 4 °C, snap-frozen

in isopentane, stored at -80 °C overnight and then sectioned with a Leica CM1900 cryostat.

Posterior wing bud fate-mapping assay. Spots (25 µm) of either DiI (1,1'-dioctadecyl-3,3',3'-tetramethylindolyl-carbocyanine) or DiO (3,3'-dioctadecyloxycarbocyanine perchlorate) (Molecular Probes) were microinjected into the sub-apical posterior region of wing buds¹⁰ with a fine glass needle attached to a PiospritzerII (General Valve Corporation). Two red (DiI) spots were injected 300 µm apart with yellow (DiO) midway between. In experiments involving treatments, TSA/DMSO beads were then implanted, or cyclopamine (or control conjugant 45% 2-hydropropyl-β-cyclodextrin) applied systemically. Embryos were fixed in 4% PFA after 24 or 48 h. Cell traces were visualized later with the GFP or Texas red filters of a Leica Fluorescence Dissection Microscope, and images captured with a ProgRes C14 camera (Jenoptik). Images of some embryos were captured *in ovo*, and the eggs re-incubated until a later stage for cartilage staining of subsequent wing skeletons.

Electroporation. Two microlitres of 3 µg µl⁻¹ pcDNA3.1-*p21* (human *p21*^{cip1}) or pcDNA3.1-*p21BamHI* (empty vector control) were mixed with 2 µl of 3 µg µl⁻¹ pCAGGS-RFP (RFP) and a small amount of Fast green dye to stain tissue and aid consistency of injection. Approximately 0.1 µl was microinjected into posterior areas of wing buds in the area within and immediately adjacent to the polarizing region by a fine glass needle attached to a PiospritzerII (General Valve Corporation). Wing buds were electroporated at 40 V for 2 × 50 ms with 2 × 200 ms intervals by a CUY21 electroporator (Bex Co., Ltd). Electrodes were used with the cathode placed under the bud and the anode over the trunk.

Posterior wing bud expansion assays. One 50 µm spot of DiI was microinjected into a region subjacent to the posterior margin in equivalent positions for all cases by a fine glass needle attached to a PiospritzerII (General Valve Corporation). In rescue experiments, *Shh* beads (10 µg µl⁻¹) or control PBS beads were implanted into the posterior of wing buds in the presence or absence of 20 µl of TSA dissolved in DMSO (0.05 µg µl⁻¹) applied to the wing region with a Gilson pipette. Embryos were processed 24 h later as described above, and some were fixed in 4% PFA and used for *in situ* analyses. In *p21*^{cip} overexpression experiments, 1 µl of 3 µg µl⁻¹ of vector DNA (see above) was mixed with 1 µl of 3 µg µl⁻¹ of pCAGGS-RFP (RFP) and Fast green dye, then microinjected into a 50 µm area of the posterior region of the wing bud (aided by Fast green staining of tissue); 24 h after electroporation (see above), the extent of expansion of labelled groups of cells was assessed by RFP fluorescence with the Texas red filter of a Leica Fluorescence Dissection Microscope, and the images captured with a ProgRes C14 camera (Jenoptik).

Alcian blue skeletal preparations. Embryos were fixed in 100% ethanol for two days, then transferred to 0.1% alcian blue (BDH) in 80% ethanol/20% acetic acid for one day, before being cleared in 1% KOH and then stored in 100% glycerol (preparations were photographed in 80% glycerol). All images were captured with a ProgRes C14 camera (Jenoptik) in conjunction with Openlab software (Improvision). Digit identities were classified according to length and number of phalanges.

Wing bud measurements. All measurements were taken with a ProgRes C14 camera (Jenoptik) in conjunction with the measure command of the Openlab software (Improvision). Anteroposterior lengths were measured in a straight line across the bud from either end of the ectodermal ridge; proximodistal lengths were measured from the base to the tip of the bud.

30. Hamburger, V. & Hamilton, H. L. A series of normal stages in the development of the chick embryo. *J. Morphol.* **88**, 49–92 (1951).

NAD synthase NMNAT acts as a chaperone to protect against neurodegeneration

R. Grace Zhai^{1,2,3*}, Fan Zhang^{1*}, P. Robin Hiesinger^{2,†}, Yu Cao³, Claire M. Haueter² & Hugo J. Bellen^{2,3,4}

Neurodegeneration can be triggered by genetic or environmental factors. Although the precise cause is often unknown, many neurodegenerative diseases share common features such as protein aggregation and age dependence. Recent studies in *Drosophila* have uncovered protective effects of NAD synthase nicotinamide mononucleotide adenylyltransferase (NMNAT) against activity-induced neurodegeneration and injury-induced axonal degeneration^{1,2}. Here we show that NMNAT overexpression can also protect against spinocerebellar ataxia 1 (SCA1)-induced neurodegeneration, suggesting a general neuroprotective function of NMNAT. It protects against neurodegeneration partly through a proteasome-mediated pathway in a manner similar to heat-shock protein 70 (Hsp70). NMNAT displays chaperone function both in biochemical assays and cultured cells, and it shares significant structural similarity with known chaperones. Furthermore, it is upregulated in the brain upon overexpression of poly-glutamine expanded protein and recruited with the chaperone Hsp70 into protein aggregates. Our results implicate NMNAT as a stress-response protein that acts as a chaperone for neuronal maintenance and protection. Our studies provide an entry point for understanding how normal neurons maintain activity, and offer clues for the common mechanisms underlying different neurodegenerative conditions.

Injury-induced axonal degeneration is dramatically delayed in wallerian degeneration slow (*Wld^S*) mice, a mutant strain that overexpresses a chimaeric protein containing the NAD synthase NMNAT^{3,4}. The *Wld^S* chimaeric protein offers neuroprotection against axonal degeneration^{2,5–7} as well as a variety of neurodegenerative conditions^{8–11}. *Wld^S* protein contains the amino (N)-terminal 70-amino-acid fragment of ubiquitination factor E4B (Ube4b), a unique 18-amino-acid linking region translated from the 5' untranslated region (UTR) of *Nmnat1*, and the entire coding sequence of *Nmnat1*^{4,12}. Conflicting results exist in mammalian systems as to whether *Nmnat1* exerts protective effects^{13–15} and whether NAD is required^{4,14,15}. *Drosophila* contains only one NMNAT gene, whose overexpression delays axonal degeneration². This study and our finding that NMNAT functions as a maintenance factor to protect against activity-induced neurodegeneration¹ suggest that NMNAT alone can protect against multiple neurodegenerative insults. Our recent finding that enzymatically inactive NMNAT retains neuroprotective capabilities also exposed a hitherto unknown molecular function¹.

To test if NMNAT is a general factor required for neuronal maintenance and protection, we first examined the effects of NMNAT overexpression in a *Drosophila* model for SCA1. Overexpression of wild-type NMNAT or enzyme-inactive NMNAT (NMNAT-WR)¹ suppresses the degenerative phenotypes induced by overexpression of *Drosophila* ataxin-1 (dAtx-1). It also offers moderate protection against the severe phenotypes caused by overexpression of

human ataxin-1 with an expanded (82) poly-glutamine tract (hAtx-1[82Q])¹⁶ (Fig. 1). These findings, and the observations that NMNAT protects from axonal injury², from photoreceptor injury caused by intense light, and that its loss causes massive neurodegeneration¹, indicate that NMNAT is a versatile neuroprotective agent.

To define the mechanisms of NMNAT function, we turned to a mammalian cell-culture-based assay to evaluate the effect of NMNAT on hAtx-1[82Q] aggregation. When transfected into Cos7

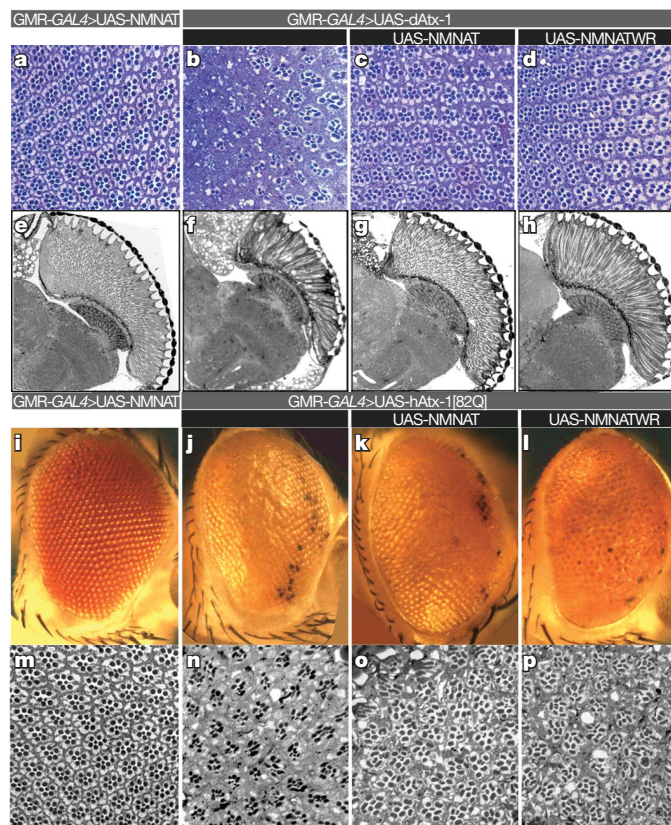


Figure 1 | NMNAT suppresses toxicity induced by ataxin-1. **a–h**, Ommatidial morphology of cross section (**a–d**) and horizontal section (**e–h**) of 15-day-old control fly (**a, e**), and flies overexpressing dAtx-1 (**b–d, f–h**). Overexpression of wild-type NMNAT (**c, g**) or enzyme-inactive NMNAT-WR (**d, h**) restores the rhabdomere degeneration phenotype. **i–p**, Eye exterior morphology and ommatidial morphology of two-day-old control fly (**i, m**), and flies overexpressing hAtx-1[82Q] (**j–l, n–p**). Overexpression of hAtx-1[82Q] leads to rough eye (**j**) and reduced rhabdomere size (**n**) phenotypes that are partly suppressed by co-expression of NMNAT (**k, o**) or NMNAT-WR (**l, p**).

¹Department of Molecular and Cellular Pharmacology, Miller School of Medicine, University of Miami, Miami, Florida 33136, USA. ²Howard Hughes Medical Institute, Baylor College of Medicine, ³Department of Molecular and Human Genetics, Baylor College of Medicine, ⁴Program in Developmental Biology, Baylor College of Medicine, Houston, Texas 77030, USA. [†]Present address: Department of Physiology and Green Center Division for Systems Biology, University of Texas Southwestern Medical Center at Dallas, Dallas, Texas 75390, USA.

*These authors contributed equally to this work.

cells, hAtx-1[82Q] forms numerous and often large protein aggregates in both nucleus and cytoplasm¹⁷ (Fig. 2a, b), which are similar to the pathological aggregates found in the neurons of *SCA1* mice or *SCA1* patients¹⁷. hAtx-1[82Q] appears to be distributed diffusely and/or in aggregated forms in cells (Supplementary Fig. 1A–F). When NMNAT and hAtx-1[82Q] are co-expressed in cells, the percentage of cells with hAtx-1[82Q] aggregates is reduced and more cells contain diffuse hAtx-1[82Q] (Supplementary Fig. 1I). The fluorescence intensity of total hAtx-1[82Q] and its aggregates is significantly reduced (Fig. 2d). This reduction mimics the effect of Hsp70¹⁷ (Fig. 2d), a chaperone known to suppress the pathology associated with hAtx-1[82Q] expression in *SCA1* mice¹⁸. This similarity between NMNAT and Hsp70 for aggregate formation was further supported when we analysed the solubility of the hAtx-1[82Q] protein by detergent fractionation and high-speed centrifugation. Co-expression of NMNAT or Hsp70 reduced the level in the detergent-insoluble fraction (Fig. 2e, g), arguing that NMNAT, like Hsp70, participates in aggregate reduction. To test whether NMNAT promotes protein degradation through the proteasome-mediated pathway¹⁷, we impaired the pathway with an inhibitor (MG-132) and evaluated its impact on the protein level of hAtx-1[82Q]. As shown in Fig. 2d, treatment with MG132 increased the total level of hAtx-1[82Q] and aggregates in all cells, including the cells that are co-transfected with NMNAT or Hsp70. Similarly, the level of detergent-insoluble hAtx-1[82Q] is increased in all cells (Fig. 2e, lanes 4–6 compared with lanes 1–3), suggesting that the proteasome is important in controlling aggregate formation. However, the insoluble hAtx-1[82Q] in Hsp70 or NMNAT co-transfected cells is lower than in vector-transfected cells (Fig. 2e, g). This suggests that NMNAT and Hsp70 act only partly through the proteasome to reduce aggregate levels, and that both Hsp70 and NMNAT might also function independently from the proteasome-mediated pathway. Human ataxin-1 without poly-Q expansion (hAtx-1[2Q]) also forms aggregates when expressed in these cells (Supplementary Fig. 1H). This is not surprising, as it has been shown that ataxin proteins without the poly-glutamine expansion also induce neurodegeneration when overexpressed¹⁶, and overexpression of *Drosophila* ataxin-1 with no poly-glutamine domain induces neurodegeneration (Fig. 1b, f). Importantly, NMNAT is also able to reduce the level of aggregation and the detergent-insoluble fraction of hAtx-1[2Q] (Fig. 2f, h and Supplementary Fig. 1J). These observations suggest that NMNAT reduces the aggregation and promotes the

degradation of ataxin proteins, partly through the proteasome-mediated pathway.

We next examined the *in vivo* response of NMNAT and Hsp70 upon the induction of aggregation of hAtx-1[82Q]. Endogenous NMNAT is located primarily in the cell bodies of most central nervous system neurons¹, including those of the optic lobes (Fig. 3a). When hAtx-1[82Q] is overexpressed using the pan-neuronal driver *nervana-GAL4*¹⁹, numerous hAtx-1[82Q] aggregates form in the cell bodies (Fig. 3b, l), similar to cultured cells (Fig. 2). However, unlike in cultured cells, we do not observe diffuse hAtx-1[82Q] localization. Interestingly, endogenous NMNAT is induced and recruited into these aggregates (compare Fig. 3a, b, f, g). This upregulation and recruitment is very similar to the Hsp70 response when hAtx-1[82Q] is overexpressed (Fig. 3p, q), and expression of dAtx-1 or hAtx-1[82Q] increases the protein level of endogenous NMNAT (Supplementary Fig. 2) and Hsp70.

When NMNAT is overexpressed with *nervana-GAL4*, the protein is not only present in cell bodies, but also in axons (Fig. 3c, h, w). This is consistent with its protective effects in axonal degeneration when overexpressed². To test the effects of hAtx-1[82Q] on the localization of overexpressed NMNAT, we overexpressed both proteins together. NMNAT is recruited into the hAtx-1[82Q] aggregates (see also Fig. 3d, i, n, x) and so is the enzymatically inactive NMNAT-WR (Fig. 3e, j, o, y). The recruitment of NMNAT into hAtx-1[82Q]-induced aggregates is specific, because green fluorescent protein (GFP) is not incorporated into the aggregates when co-expressed (Supplementary Fig. 3). The addition of NMNAT into hAtx-1[82Q] aggregates likely reduces the toxicity associated with hAtx-1[82Q] because the total level of hAtx-1[82Q] is reduced when co-expressing NMNAT or NMNAT-WR (Supplementary Fig. 3E). Taken together, our studies suggest that, in cultured cells, NMNAT functions with the proteasome to reduce the level of aggregation; in the fly brain, NMNAT is recruited into the hAtx-1[82Q] aggregates to reduce the neuronal toxicity induced by hAtx-1[82Q].

In wild-type brains, the level of Hsp70 was below our detection limit (Fig. 3p). However, when hAtx-1[82Q] is overexpressed, Hsp70 expression is strongly induced (compare Fig. 3p, q) and it co-localizes with endogenous NMNAT and hAtx-1[82Q] aggregates (Fig. 3b, q, v). When overexpressed, both enzymatically active and inactive forms of NMNAT are recruited with Hsp70 into hAtx-1[82Q] aggregates (Fig. 3i, j, s, t). These data indicate that NMNAT is upregulated and

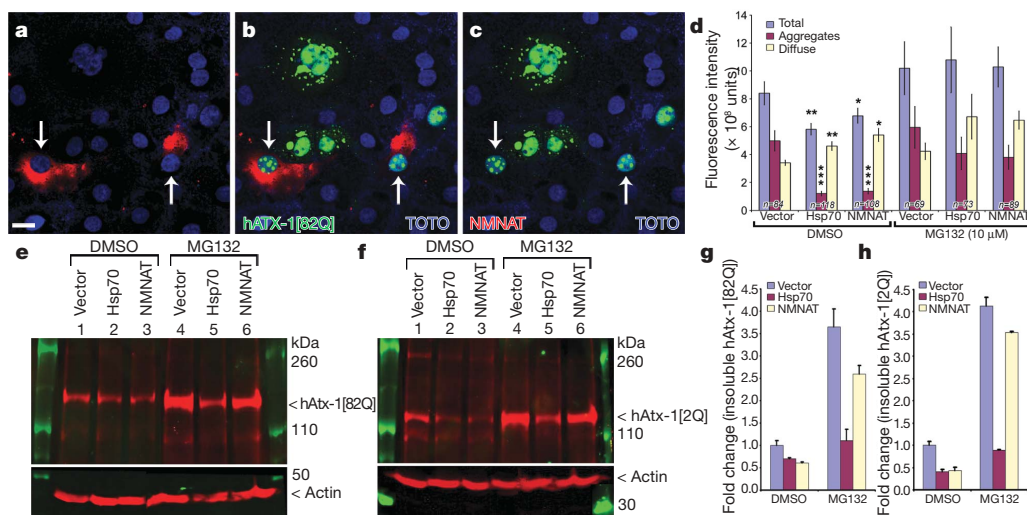


Figure 2 | NMNAT acts as a chaperone in cultured cells. a–c, Cos7 cells are co-transfected with hAtx-1[82Q]-GFP (green) and NMNAT (red). TOTO3 staining (blue) marks nuclei. Scale bar in a for a–c, 20 μ m. d, Quantification of GFP fluorescence. Aggregates are defined as objects at least 0.4 μ m² and 3,600 intensity units. Error bars, s.e.m. * P < 0.05, ** P < 0.01, *** P < 0.005 (analysis of variance post-hoc test). e–h, Western analysis (e, f) and

quantification (g, h) of detergent-insoluble fractions of cells transfected with hAtx-1[82Q]-GFP (e) or hAtx-1[2Q]-GFP (f) and vector, NMNAT or Hsp70, and treated with either DMSO or 10 μ M MG132. The level of insoluble hAtx-1[82Q] (g) or hAtx-1[2Q] (h) in the DMSO-treated cells is equal to 1 (fold). Error bars, s.e.m.; n = 4.

recruited into the hAtx-1[82Q] aggregates in a manner similar to Hsp70, drawing yet another parallel between the function of these two proteins.

Next, we assayed whether NMNAT has chaperone activity. To measure the *in vivo* chaperone activity of NMNAT, we used the assay in which refolding of heat-denatured luciferase is monitored as a measure for chaperone activity²⁰. In this assay, heat denaturation, combined with the protein-synthesis inhibitor cycloheximide, renders the endogenous levels of molecular chaperones insufficient to recover luciferase activity fully (Fig. 4a). When we transfect NMNAT as well as its adenylyltransferase-inactive forms (NMNAT-WR and -H30), they all protect luciferase from unfolding during heat shock (red bars in Fig. 4b) and enhance refolding after heat shock (yellow bars in Fig. 4b). In this assay, the chaperone activities of all forms of NMNAT are similar to that of mammalian Hsp70 or *Drosophila* Hsp83, the homologue of mammalian Hsp90²¹. These data indicate that NMNAT protects proteins from unfolding and promotes refolding, either by acting as a chaperone or by regulating the activity of other chaperones.

To distinguish between these possibilities, we used an *in vitro* biochemical assay to measure chaperone activity. This assay measures the chaperone's ability to reduce thermally or chemically induced aggregation of a model protein substrate such as citrate synthase or insulin²² (Fig. 4c). As shown in Fig. 4e, Hsp70 efficiently reduces thermally induced aggregation of citrate synthase at 43 °C in

the absence of ATP, in a concentration-dependent manner, confirming that it acts as a chaperone²³. Lysozyme, which has no known chaperone activity, does not effectively suppress thermally induced aggregation of citrate synthase (Fig. 4d). Incubation of citrate synthase with increasing amounts of NMNAT results in a concomitant decrease in citrate synthase aggregation (Fig. 4f). The chaperone activity is quantified by the relative aggregation rate (Fig. 4g), and by the percentage of aggregation reduction at the saturation point (Fig. 4h). The reduction in light scattering (absorbance at 360 nm) is not due to a loss of substrate proteins by degradation, as the levels of citrate synthase remain the same with or without added chaperones (Supplementary Fig. 4). Similar results were obtained with insulin as a model substrate (Fig. 4i), where aggregation of insulin is induced by adding the reducing agent DTT. As in the hAtx-1[82Q] aggregation experiments, enzymatically inactive NMNAT-WR and another inactive NMNAT, NMNAT-H30,¹ are both able to suppress protein aggregation effectively (Fig. 4g, h). This further suggests that the chaperone activity of NMNAT is independent of its NAD synthesis activity. Both wild-type and enzymatically inactive NMNAT efficiently inhibit aggregation in a similar manner to Hsp70, unlike bovine serum albumin (BSA) or lysozyme (Fig. 4i). Note that the human homologue hsNMNAT3 displays chaperone activity similar to the *Drosophila* proteins (Fig. 4b, g, h, i), suggesting that the NMNAT homologues function similarly¹.

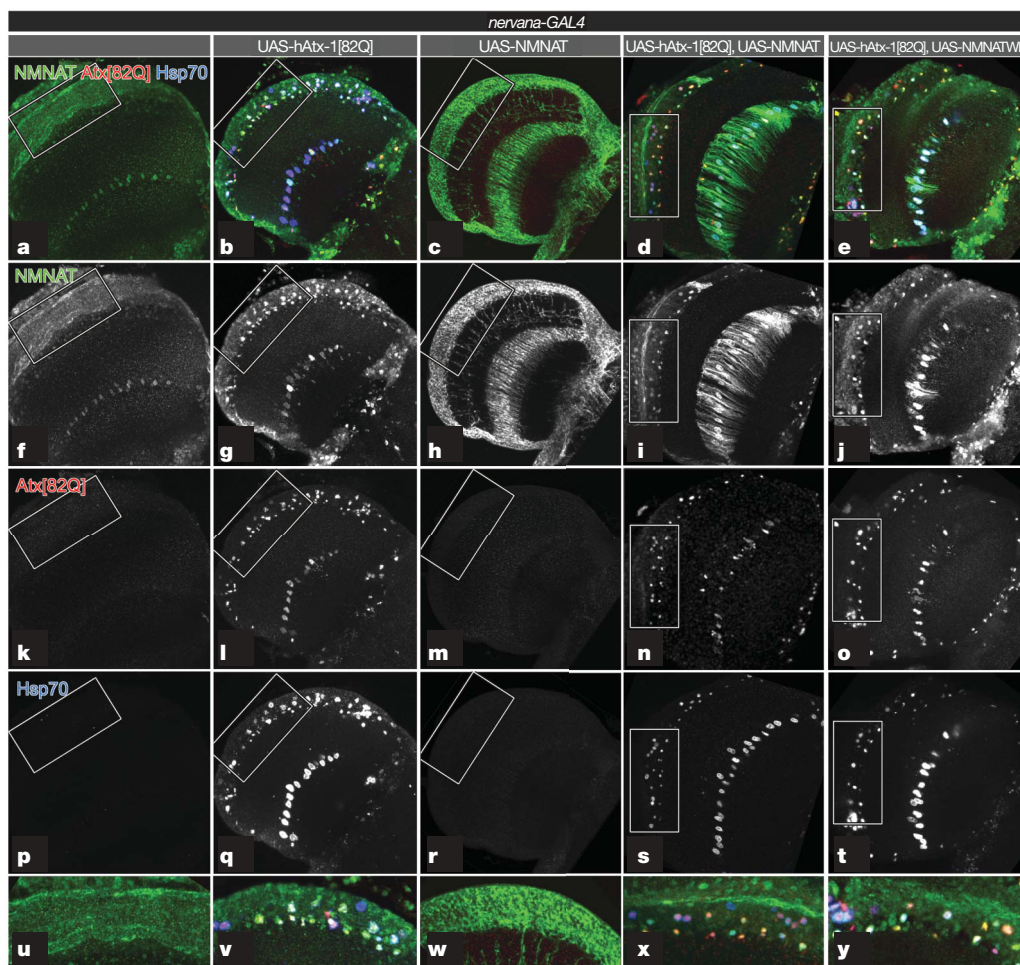


Figure 3 | Endogenous and overexpressed NMNAT proteins are recruited with Hsp70 into the hAtx-1[82Q] aggregates. a–e, Seven-day-old adult fly brains were stained for NMNAT (green; f–j), hAtx-1[82Q] (red; k–o) and Hsp70 (blue; p–t). Higher magnifications of boxed areas are shown in u–y. Endogenous NMNAT is primarily nuclear (f). hAtx-1[82Q] forms nuclear aggregates (l). Endogenous NMNAT is upregulated and recruited to

the aggregates (g). NMNAT is distributed to the cytoplasm when singly overexpressed (h), but is recruited to ataxin aggregates when co-expressed with hAtx-1[82Q] (i, n). Enzymatically inactive NMNAT-WR is also recruited into ataxin aggregates when co-overexpressed with hAtx-1[82Q] (j, o). Hsp70 is upregulated and recruited into the aggregates (q, s, t).

If NMNAT has chaperone activity independent of its NAD synthesis ability, there may be a specific domain associated with this function. We therefore created three truncated proteins: NMNAT- Δ C, deleting the carboxy (C)-terminal domain including the ATP binding motif; NMNAT- Δ N, deleting the N-terminal catalytic motif; and NMNAT- Δ CN, deleting both N and C termini (Supplementary Fig. 5A). The N-terminal catalytic motif is not essential for the chaperone activity (Supplementary Fig. 5C); however, the C-terminal domain containing the ATP-binding domain is required, as neither NMNAT- Δ C nor NMNAT- Δ CN have chaperone activity (Supplementary Fig. 5B, D). These data provide additional evidence that NMNAT's chaperone and NAD synthesis activities can be dissociated.

To explore further the structural nature of the chaperone function, we searched for primary sequence similarity between NMNAT and known chaperones, but did not find any sequence homology. However, a DALI search²⁴ using the structural coordinates of NMNAT1 (Protein Data Bank identity code 1KKU) and NMNAT3 (identity code 1NUR)²⁵ against the entire Protein Data Bank revealed

that both NMNAT1 and NMNAT3 share similarity with chaperone universal stress protein A (UspA; identity code 1JMV)²⁶, with a Z score of 5.1, and Hsp100 (identity code 1JBK)²⁷, with a Z score of 2.8. A structural superposition of NMNAT1 and UspA showed 13% sequence identity and a root mean squared deviation of 3.0 Å over the entire length of the protein. Hence, NMNAT proteins display structural similarities with known chaperones.

The induction and recruitment of NMNAT upon hAtx-1[82Q] aggregate formation suggest that NMNAT is also a stress-response protein similar to heat-shock proteins. The redistribution of over-expressed NMNAT and co-localization with Hsp70 at intracellular aggregates suggest that NMNAT may act in concert or in parallel with Hsp70. Our data also indicate that NMNAT and Hsp70 act independently, as we observe additive effects when mixing the two proteins in our *in vitro* assay (Supplementary Fig. 6). The chaperone function of NMNAT is likely linked to the proteasome-mediated pathway, as NMNAT is able to reduce the aggregation and promote the degradation of misfolded proteins. The chaperone activity offers an explanation for the broad protective activity of NMNAT in different

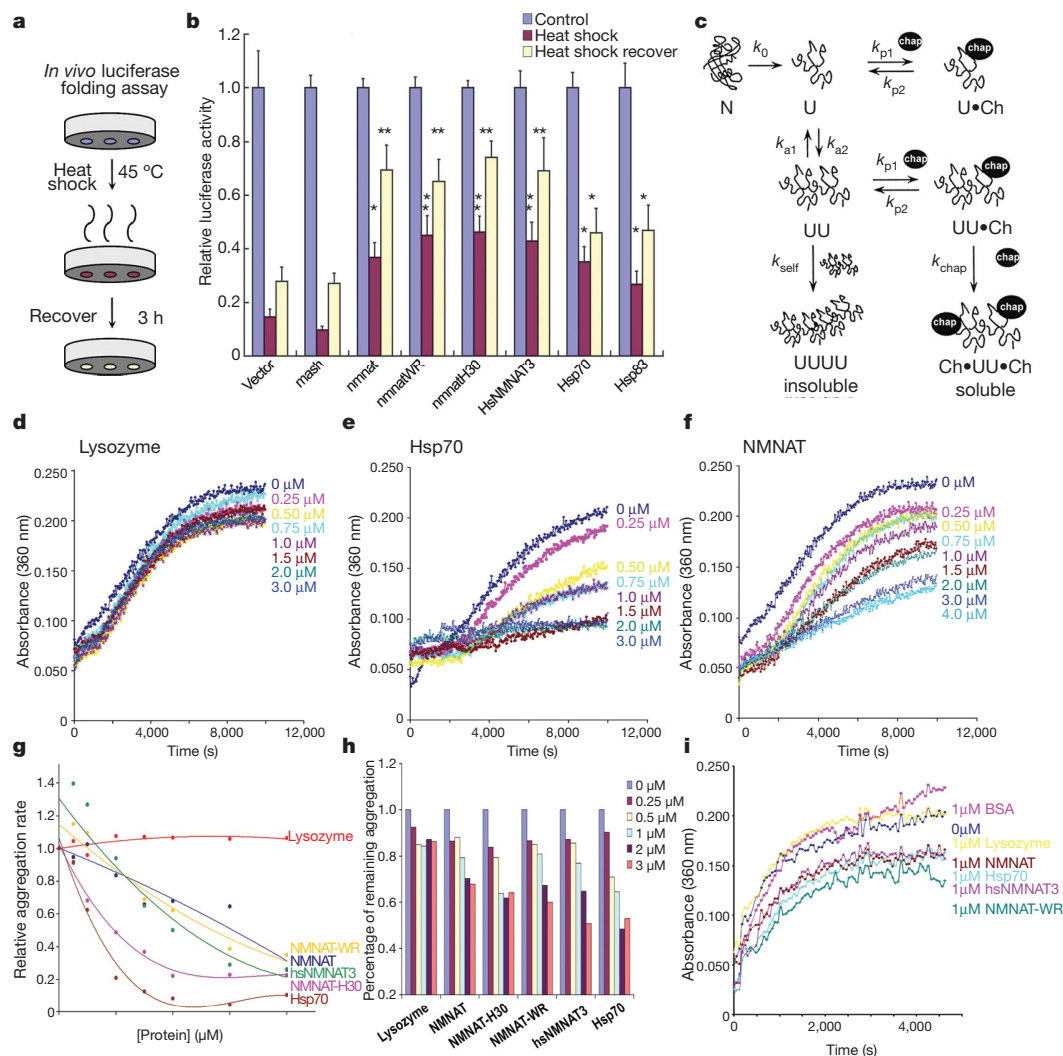


Figure 4 | *In vivo* and *in vitro* chaperone activity assays. **a**, **b**, Luciferase activity was measured without heat shock as controls (blue columns), after 15 min heat shock at 45 °C (red columns) or after 3 h recovery at room temperature (yellow columns). The luciferase activities relative to the controls are displayed. Error bars, s.e.m. **P* < 0.05, ***P* < 0.01; (analysis of variance post-hoc test); *n* = 4, triplicate sampling. **c**, Protein aggregation and its inhibition by chaperones. **d**–**h**, Aggregation of citrate synthase²² is

prevented by addition of Hsp70 (**e**, **g**), NMNAT (**f**, **g**) or human hsNMNAT3 (**g**) but not by lysozyme (**d**). **g**, The relative aggregation rate is calculated by the change in absorbance per minute and the aggregation rate of CS alone is set to 1. (**h**) The percentage of remaining aggregation is calculated at the saturation point (8000 s). **i**, Insulin aggregation is inhibited by Hsp70, NMNAT, NMNAT-WR or hsNMNAT3 but not BSA or lysozyme.

neurodegenerative conditions. Interestingly, a recent study on the protein–protein interaction network for human inherited ataxias has put NMNAT within the interactome of human ataxin-1²⁸.

In summary, our work in *Drosophila* indicates that NMNAT functions as a chaperone independently of its enzymatic activity. Several studies on wallerian degeneration have suggested that the NAD synthesis activity of NMNAT is required for protection of axon degeneration^{14,29}. This difference might be partly due to the distinct mechanisms underlying the injury-induced degeneration and other types of neurodegeneration. Further characterization of the role of NMNAT in different degenerative processes will help reveal the mechanisms of neurodegeneration.

METHODS SUMMARY

The ataxin-1 aggregation assay was performed as described¹⁷ with modifications. Retina sections and transmission electron microscopy were performed as described¹. Western blot analysis was performed with infrared-dye-conjugated secondary antibodies and imaged on an Odyssey® system (LI-COR Biosciences). The luciferase folding assay was performed as described^{21,30}. Confocal microscopy was performed with a Zeiss LSM 510 confocal Axiovert 200M microscope. Fluorescence analysis was performed with MetaMorph 5.07 (Molecular Devices/Universal Imaging Corp.), Amira 3.0 (TGS, Inc.) and Adobe Photoshop 7.0. The aggregation measurements were performed as described²². We searched three-dimensional structures on DALI sever²⁴ (<http://www.ebi.ac.uk/dali/>); the structure superposition was done with PyMol structure analysis software.

Full Methods and any associated references are available in the online version of the paper at www.nature.com/nature.

Received 14 November 2007; accepted 16 January 2008.

Published online 16 March 2008.

- Zhai, R. G. *et al.* *Drosophila* NMNAT maintains neural integrity independent of its NAD synthesis activity. *PLoS Biol.* **4**, e416 (2006).
- MacDonald, J. M. *et al.* The *Drosophila* cell corpse engulfment receptor draper mediates glial clearance of severed axons. *Neuron* **50**, 869–881 (2006).
- Gillingwater, T. H. & Ribchester, R. R. Compartmental neurodegeneration and synaptic plasticity in the Wld^S mutant mouse. *J. Physiol. (Lond.)* **534**, 627–639 (2001).
- Mack, T. G. *et al.* Wallerian degeneration of injured axons and synapses is delayed by a *Ube4b/Nmnat* chimeric gene. *Nature Neurosci.* **4**, 1199–1206 (2001).
- Ribchester, R. R. *et al.* Persistence of neuromuscular junctions after axotomy in mice with slow Wallerian degeneration (C57BL/Wld^S). *Eur. J. Neurosci.* **7**, 1641–1650 (1995).
- Hoopfer, E. D. *et al.* Wlds protection distinguishes axon degeneration following injury from naturally occurring developmental pruning. *Neuron* **50**, 883–895 (2006).
- Ludwin, S. K. & Bisby, M. A. Delayed wallerian degeneration in the central nervous system of Ola mice: an ultrastructural study. *J. Neurol. Sci.* **109**, 140–147 (1992).
- Gillingwater, T. H., Haley, J. E., Ribchester, R. R. & Horsburgh, K. Neuroprotection after transient global cerebral ischemia in Wld^S mutant mice. *J. Cereb. Blood Flow Metab.* **24**, 62–66 (2004).
- Ferri, A., Sanes, J. R., Coleman, M. P., Cunningham, J. M. & Kato, A. C. Inhibiting axon degeneration and synapse loss attenuates apoptosis and disease progression in a mouse model of motoneuron disease. *Curr. Biol.* **13**, 669–673 (2003).
- Samsam, M. *et al.* The Wld^S mutation delays robust loss of motor and sensory axons in a genetic model for myelin-related axonopathy. *J. Neurosci.* **23**, 2833–2839 (2003).
- Sajadi, A., Schneider, B. L. & Aebischer, P. Wld^S-mediated protection of dopaminergic fibers in an animal model of Parkinson disease. *Curr. Biol.* **14**, 326–330 (2004).
- Conforti, L. *et al.* A *Ufd2/D4Cole1e* chimeric protein and overexpression of *Rbp7* in the slow Wallerian degeneration (*Wld^S*) mouse. *Proc. Natl Acad. Sci. USA* **97**, 11377–11382 (2000).
- Conforti, L. *et al.* NAD⁺ and axon degeneration revisited: *Nmnat1* cannot substitute for Wld^S to delay Wallerian degeneration. *Cell Death Differ.* **14**, 116–127 (2007).
- Araki, T., Sasaki, Y. & Milbrandt, J. Increased nuclear NAD biosynthesis and SIRT1 activation prevent axonal degeneration. *Science* **305**, 1010–1013 (2004).
- Wang, J. *et al.* A local mechanism mediates NAD-dependent protection of axon degeneration. *J. Cell Biol.* **170**, 349–355 (2005).
- Tsuda, H. *et al.* The AXH domain of ataxin-1 mediates neurodegeneration through its interaction with Gfi-1/Senseless proteins. *Cell* **122**, 633–644 (2005).
- Cummings, C. J. *et al.* Chaperone suppression of aggregation and altered subcellular proteasome localization imply protein misfolding in SCA1. *Nature Genet.* **19**, 148–154 (1998).
- Cummings, C. J. *et al.* Over-expression of inducible HSP70 chaperone suppresses neuropathology and improves motor function in SCA1 mice. *Hum. Mol. Genet.* **10**, 1511–1518 (2001).
- Sun, B., Xu, P. & Salvaterra, P. M. Dynamic visualization of nervous system in live *Drosophila*. *Proc. Natl Acad. Sci. USA* **96**, 10438–10443 (1999).
- Parsell, D. A., Kowal, A. S., Singer, M. A. & Lindquist, S. Protein disaggregation mediated by heat-shock protein Hsp104. *Nature* **372**, 475–478 (1994).
- Rutherford, S. L. & Lindquist, S. Hsp90 as a capacitor for morphological evolution. *Nature* **396**, 336–342 (1998).
- Chang, Z. *et al.* *Mycobacterium tuberculosis* 16-kDa antigen (Hsp16.3) functions as an oligomeric structure *in vitro* to suppress thermal aggregation. *J. Biol. Chem.* **271**, 7218–7223 (1996).
- Kubo, Y. *et al.* Two distinct mechanisms operate in the reactivation of heat-denatured proteins by the mitochondrial Hsp70/Mdj1p/Yge1p chaperone system. *J. Mol. Biol.* **286**, 447–464 (1999).
- Holm, L. & Sander, C. New structure–novel fold? *Structure* **5**, 165–171 (1997).
- Zhang, X. *et al.* Structural characterization of a human cytosolic NMN/NaMN adenyllyltransferase and implication in human NAD biosynthesis. *J. Biol. Chem.* **278**, 13503–13511 (2003).
- Sousa, M. C. & McKay, D. B. Structure of the universal stress protein of *Haemophilus influenzae*. *Structure* **9**, 1135–1141 (2001).
- Li, J. & Sha, B. Crystal structure of the *E. coli* Hsp100 ClpB N-terminal domain. *Structure* **11**, 323–328 (2003).
- Lim, J. *et al.* A protein–protein interaction network for human inherited ataxias and disorders of Purkinje cell degeneration. *Cell* **125**, 801–814 (2006).
- Jia, H. *et al.* Identification of a critical site in Wld(s): essential for *Nmnat* enzyme activity and axon-protective function. *Neurosci. Lett.* **413**, 46–51 (2007).
- Michels, A. A. *et al.* Hsp70 and Hsp40 chaperone activities in the cytoplasm and the nucleus of mammalian cells. *J. Biol. Chem.* **272**, 33283–33289 (1997).

Supplementary Information is linked to the online version of the paper at www.nature.com/nature.

Acknowledgements We thank H. Zoghbi and R. Morimoto for reagents. We thank H. Zoghbi, H. Gilbert, H.-C. Lu, X. Zhou, P. Tsoulfas and A. Malhotra for technical suggestions and discussions. We also thank G. McNamara and the Analytical Imaging Core Facility at the University of Miami for imaging assistance. Some confocal imaging was supported by the BCM Mental Retardation and Developmental Disabilities Research Center. R.G.Z., P.R.H., C.M.H. were supported by the HHMI. H.J.B. is an HHMI investigator. R.G.Z. and F.Z. are also supported by the PhRMA Foundation and the Florida Department of Health, James and Esther King Biomedical Research Program.

Author Contributions R.G.Z. and H.J.B. conceived the experiments. R.G.Z., P.R.H., Y.C. and C.M.H. performed the genetic and *in vivo* experiments. R.G.Z. and F.Z. performed the *in vitro* experiments. R.G.Z. and H.J.B. wrote the manuscript.

Author Information Reprints and permissions information is available at www.nature.com/reprints. Correspondence and requests for materials should be addressed to R.G.Z. (gzhai@med.miami.edu) or H.B. (hbellen@bcm.edu).

METHODS

Retina sections and transmission electron microscopy. Flies of different ages were dissected and fixed at 4 °C in 2% paraformaldehyde, 2% glutaraldehyde, 0.1 M sodium cacodylate, 0.005% CaCl_2 (pH 7.2) and post-fixed in 2% OsO_4 . Thick sections (200 nm) of retina were stained with 1% toluidine blue O, 1% sodium tetraborate (Electron Microscopy Sciences). Thin sections (50 nm) were stained with 4% uranyl acetate and 2.5% lead nitrate. Morphological features were scored double-blind by several observers.

Ataxin-1 aggregation assay in cultured cells. The ataxin-1 aggregation assay was performed as described¹⁷ with the following modifications. Briefly, Cos7 cells were doubly transfected with either pEGFP-*hAtx-1[82Q]* and pCMV-*nmnat* or pEGFP-*hAtx-1[82Q]* and pCMV-*hsp70* using Lipofectamine (Invitrogen). After 48 h, cells were fixed and immunolabelled for NMNAT or Hsp70. Cell nuclei were labelled with TOTO3 (Molecular Probes).

Confocal image acquisition and quantification. Confocal microscopy was performed with a Zeiss LSM 510 confocal Axiovert 200M microscope equipped with Lasos HeNe 633, HeNe 543, argon ion 488 and Coherent UV Enterprise 351/364 nm laser lines and four identical photomultiplier tubes for blue, green, orange and near infrared fluorescence. Fluorescence analysis was performed with MetaMorph 5.07 (Molecular Devices/Universal Imaging Corp.), Amira 3.0 (TGS, Inc.) and Adobe Photoshop 7.0.

Protein fractionation and western blot analysis. To separate proteins into soluble or insoluble extracts, proteins from cultured Cos7 cells were extracted with RIPA buffer (50 mM Tris (pH 8), 150 mM NaCl, 1 mM EDTA, 1% NP40, 0.5% sodium deoxycholate, 0.1% SDS, 1 mM PMSF) and Complete protease inhibitor cocktail (Roche). The detergent-soluble fraction was defined as the supernatant of the cell lysates after centrifugation at 120,000g for 15 min. After removal of the supernatant, the pellets were washed with RIPA buffer and then suspended in 8 M urea, 4% SDS, 0.125 M Tris (pH 6.8), 12 mM EDTA and 3% β -mercaptoethanol. Western blot analysis was performed with infrared dye conjugated secondary antibodies, IR700 and IR800 (LI-COR Biosciences); blots were imaged and processed on an Odyssey® Infrared Imaging system.

In vivo luciferase folding assay. The luciferase folding assay was performed as described^{21,30}. Briefly, *Drosophila* S2 cells were triply transfected with pAC-*actin-GAL4*, pUAST-*luciferase* and one of the following plasmids: pUAST vector, pUAST-*Mash1*, pUAST-*nmnat*, pUAST-*nmnat-WR*, pUAST-*nmnat-H30A*, pUAST-*hsAT3*, pUAST-*hsp70* or pUAST-*hsp83*. At 24 h after transfection, the protein synthesis inhibitor cycloheximide was added and cells were subjected to a 15 min heat shock in an air incubator at 45 °C (which induced efficient unfolding of luciferase without killing the cells) and then allowed to recover at room temperature. Luciferase activity was measured with the Luciferase Assay System (Promega).

Aggregation measurements. Aggregation measurements were done as described²². Briefly, substrate proteins citrate synthase (Sigma) or insulin (Sigma) were mixed with either BSA (Sigma), egg white lysozyme (Sigma) or affinity-purified recombinant NMNAT, NMNAT-WR, NMNAT-H30, hsNMNAT3 or Hsp70 proteins in HEPES (pH 7.4) buffer. The aggregation of denatured citrate synthase was induced by incubation at 43 °C. The aggregation of insulin was induced by adding reducing agent DTT. Aggregation was monitored by measuring the apparent absorption at 360 nm, because of the Rayleigh scattering of citrate synthase or insulin homo-aggregates versus time. We used a FluoStar Optima plate reader (BMG Labtech) for measurements. The relative chaperone activity of NMNAT was calculated as the scattering of citrate synthase aggregates with time versus NMNAT concentration.

Immunocytochemistry of fly brains. Adult brains were fixed in PBS with 3.5% formaldehyde for 15 min and washed in PBS with 0.4% Triton X-100. We used the following antibody dilutions: NMNAT 1:1000; ataxin (gift from Huda Zoghbi, and from NeuroMabs Facility): 1:700; and secondary antibodies conjugated to Cy3, Cy5 or Alexa 488 (Jackson ImmunoResearch; Molecular Probes) were used at 1:250. All antibodies were incubated at 4 °C overnight in the presence of 5% normal goat serum.

Three-dimensional structure alignment. The search for similar protein structure was done on DALI server²⁴ (<http://www.ebi.ac.uk/dali/>). The three-dimensional structure superposition was done with PyMol structure analysis software.

LETTERS

Retinotopic order in the absence of axon competition

Nathan J. Gosse¹, Linda M. Nevin² & Herwig Baier^{1,2}

The retinotectal projection has long been studied experimentally and theoretically, as a model for the formation of topographic brain maps^{1–3}. Neighbouring retinal ganglion cells (RGCs) project their axons to neighbouring positions in the optic tectum, thus re-establishing a continuous neural representation of visual space. Mapping along this axis requires chemorepellent signalling from tectal cells, expressing ephrin-A ligands, to retinal growth cones, expressing EphA receptors⁴. High concentrations of ephrin A, increasing from anterior to posterior, prevent temporal axons from invading the posterior tectum. However, the force that drives nasal axons to extend past the anterior tectum and terminate in posterior regions remains to be identified. We tested whether axon–axon interactions, such as competition, are required for posterior tectum innervation. By transplanting blastomeres from a wild-type (WT) zebrafish into a *lakritz* (*lak*) mutant, which lacks all RGCs⁵, we created chimaeras with eyes that contained single RGCs. These solitary RGCs often extended axons into the tectum, where they branched to form a terminal arbor. Here we show that the distal tips of these arbors were positioned at retinotopically appropriate positions, ruling out an essential role for competition in innervation of the ephrin-A-rich posterior tectum. However, solitary arbors were larger and more complex than under normal, crowded conditions, owing to a lack of pruning of proximal branches during refinement of the retinotectal projection. We conclude that dense innervation is not required for targeting of retinal axons within the zebrafish tectum but serves to restrict arbor size and shape.

Axons originating in the temporal retina form connections with the anterior (rostral) part of the tectum, whereas nasally located RGCs project to posterior (caudal) tectum (Fig. 1a). Although a single gradient of repulsive ephrin A (Fig. 1b) is sufficient to explain the projection of temporal axons to anterior tectum, the preference of nasal axons for posterior tectum, where ephrin A molecules are most highly concentrated, has remained unexplained. Nasal axons carry fewer EphA receptors and are less sensitive to ephrin A^{6,7}, but they still avoid high concentrations of ephrin A *in vitro*⁸. Our current understanding of retinotectal mapping therefore relies on a postulated second gradient of activity. In principle, such a gradient could either be presented by the target, independently of axonal input, or be produced by interactions between axons.

To distinguish between these possibilities it is useful to consider the case of a single axon terminating in the tectum in the absence of all other axons (Fig. 1c, d). If the map is formed by one-to-one matching of retinal and tectal markers (chemoaffinity)^{9,10}, then the projection of this solitary axon should be indistinguishable from that of an axon originating from the same retinal position under normal, crowded conditions (Fig. 1c). If, alternatively, interactions between RGC axons are responsible for the production of a second, posterior-directing activity, then retinotopy should be altered when no other axons are present (Fig. 1d shows one possible outcome). Recent studies have proposed that individual axons determine their spatial

order by comparing their own ephrin-A/EphA signalling levels with that of their neighbours or with that of all other axons^{11–14}. These models have been very successful in explaining the plasticity of the map in response to surgical and genetic manipulations^{3,15}, although pure chemoaffinity theories have also accomplished this¹⁶. Competition for a limiting supply of target-derived factors (such as neurotrophins) has been proposed as a cellular mechanism for spreading retinal input over the available tectal territory^{12,15,17}. If competition is the force driving nasal axons into repellent territory, then in the absence of other axons, a single nasal axon should always terminate preferentially in the anterior tectum (Fig. 1d).

We have now tested this prediction by creating mosaic zebrafish eyes with only one RGC. Cells were transplanted at the blastula stage from WT donors into *lak* mutant host embryos (Fig. 2a). *lak* mutants

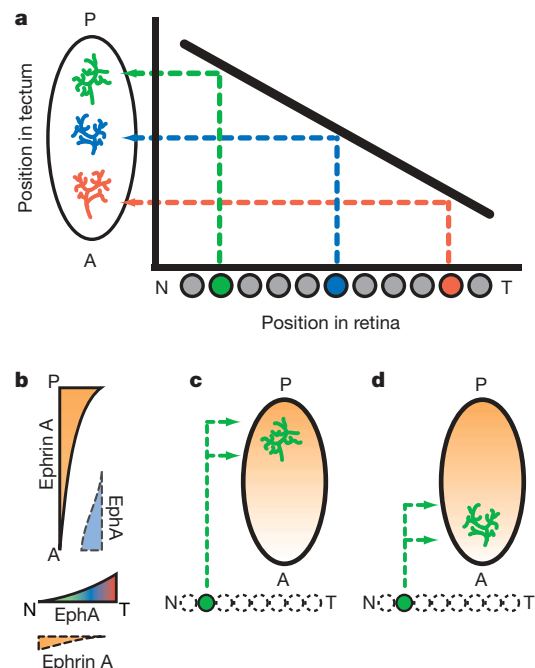


Figure 1 | Two potential mechanisms for formation of the retinotectal map. **a**, Graphical representation of the normal retinotectal mapping function. Increasingly nasal (N) RGCs project to increasingly posterior (P) regions of the optic tectum. A, anterior; T, temporal. **b**, Gradients of tectal ephrin-A ligands and retinal EphA receptors repel axons from the posterior tectum. Additionally, retina and tectum express countergradients of ephrin A and EphA, respectively. **c**, **d**, Hypothetical maps formed by solitary axons. If chemoaffinity (**c**) between axons and targets guides retinotectal mapping, then solitary nasal axons retain projections to posterior tectum. If axon–axon competition (**d**) drives nasal axons to posterior tectum, then solitary axons should terminate in the anterior tectum, where ephrin-A signalling is lowest.

¹Program in Developmental Biology, and ²Program in Neuroscience, University of California, San Francisco, Department of Physiology, 1550 Fourth Street, San Francisco, California 94158-2324, USA.

fail to develop any RGCs as a result of disruption of the proneural transcription factor *Ath5* (*Atoh7*)⁵. WT cells in the mutant environment may undergo the full RGC differentiation programme^{18,19}. The *lak* mutant has no known defects outside the retina, and *ath5* mRNA is only found in the retina. To reveal single RGCs and their axons, WT donor embryos carried the *Brn3c:mGFP* transgene, which is expressed in roughly half of RGCs projecting to the tectum²⁰. We then selected for analysis those chimaeras in which single green fluorescent protein (GFP)-labelled axons were resolvable in the tectum.

In chimaeras consisting of a WT host that had received cells from a WT donor ($WT^{Brn3c:mGFP} \rightarrow WT$; $n = 30$ axons), donor-derived, GFP-labelled RGCs showed stereotyped retinotectal projections (Fig. 2b). Their axons exited from the retina, crossed the midline and innervated the contralateral optic tectum, forming a branched terminal arbor. In *lak* hosts ($WT^{Brn3c:mGFP} \rightarrow lak$; $n = 19$ axons),

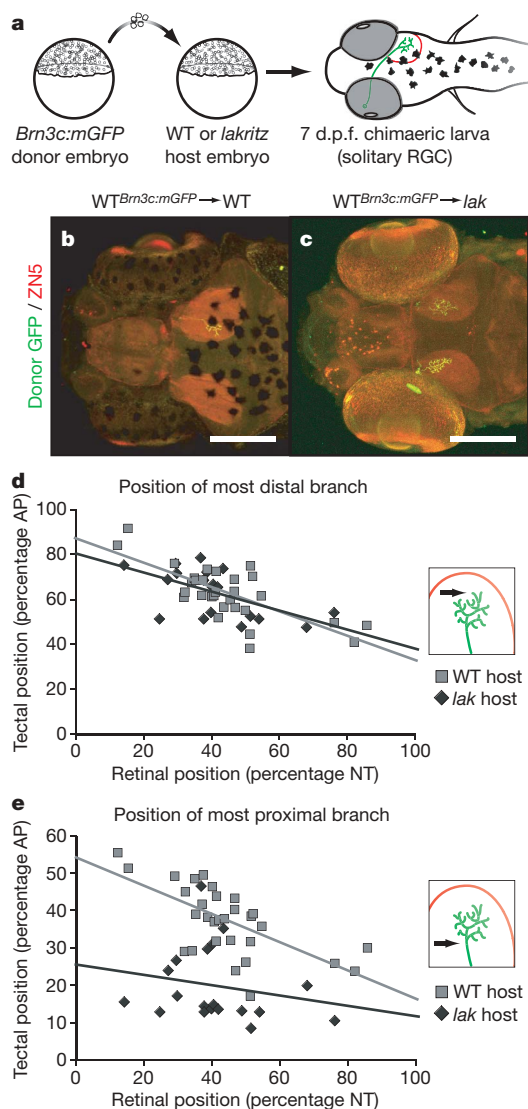


Figure 2 | Retinotectal mapping functions in the presence or absence of axon-axon interactions. **a**, Cell transplantation from WT into *lak* mutants generates chimaeras with single RGC axons. **b, c**, Chimaeric larvae at 7 d.p.f. with GFP-labelled RGC axon arbors (green) and tectal neuropil (red, stained with zn-5). Scale bar, 200 μ m. **b**, $WT^{Brn3c:mGFP} \rightarrow WT$ chimaera with single labelled arbor. **c**, $WT^{Brn3c:mGFP} \rightarrow lak$ chimaera, with single arbor on the left tectum and two fainter arbors on the right tectum. **d, e**, Retinotectal mapping functions for chimaeras at 7 d.p.f.; 0–100% anteroposterior (AP) is 180 μ m. The most distal extension of RGC arbors is not different between WT and *lak* hosts (**d**). The most proximal branchpoint is shifted anteriorly in *lak* hosts (**e**).

solitary axons remained capable of the multiple pathfinding steps required for innervation of the contralateral tectum (Fig. 2c). Many of these axons projected well beyond the anterior tectum. A minority of solitary RGCs showed pathfinding errors within the retina that were not seen under normal conditions, when their cell body was in a peripheral region, at a distance from the optic fissure (Supplementary Video 1). Our results clearly show that RGC–RGC interactions are not absolutely required for innervation of the posterior tectum.

To analyse possible changes in retinotopy, we compiled summary mapping functions at 7 days after fertilization (d.p.f.) for single axons that had developed under either crowded or solitary conditions. We therefore determined the locations of the RGC soma along the nasal–temporal axis in the retina and its axonal arbor in the tectum (see Supplementary Fig. 2 for an example of such an analysis). In WT zebrafish, axons enter the tectum at its anterior pole, extend only in a posterior direction, and do not overshoot their target. Because single terminal arbors in larval zebrafish cover about 5–10% of the tectal surface^{21–23}, we derived two separate mapping functions for each experimental condition: one for the most distal branch, the other for the most proximal branch of each arbor.

As predicted by earlier axon-tracing studies in zebrafish^{21,24}, crowded axons formed a continuous map. Both distal and proximal branch positions conformed to roughly linear and parallel mapping functions (Fig. 2d, e). A very similar relationship was seen for the distal branches in solitary axons (Fig. 2d). In fact, slope and absolute values of the mapping function were indistinguishable from the crowded condition (*F*-test, $P = 0.630$), suggesting that posterior targeting of RGC axons occurred in the absence of axon–axon interactions.

However, a strong difference was seen for the proximal branches (Fig. 2e; *F*-test, $P < 0.00001$). Although retinotopic order was retained, the slope of the mapping function was shallower, indicating that solitary axons formed (or maintained) branches more anteriorly than crowded axons and that this shift was more pronounced for the nasal axons than for temporal axons.

We examined whether the observed anterior shift in proximal branching could be caused by altered retinal or tectal positional cues. The expression of *epha4b*, a marker for temporal retina, was unchanged in the *lak* mutant retina (Fig. 3a, b). Furthermore, the mRNA gradient of *efna5b*, the gene encoding ephrin A5b, was maintained in the mutant tectum (Fig. 3c, d). Together, these findings suggest that the nasal–temporal axis of the retina is normally patterned in *lak* mutants and that tectal guidance cues are unaffected by the absence of retinal innervation.

Although molecular patterning appears normal in *lak* mutants, it was possible that retinal input might be necessary for tectal cell differentiation. By imaging individual tectal cells labelled with membrane-bound GFP (see Methods), we found morphologically normal neuronal and glial-like cells in the *lak* mutant tectum (Fig. 3c–h). Additionally, a quantitative survey revealed no difference between WT and *lak* in relative abundance of five distinct morphological cell types (Supplementary Fig. 3).

To verify that our transplantations did not disrupt NT patterning of the retina and that solitary RGCs adopt appropriate positional fates, we analysed *efna5b* expression as a specific marker for nasal RGCs (Fig. 3k, l; see Methods for details). In the $WT^{Brn3c:mGFP} \rightarrow WT$ retina, graded *efna5b* expression persisted (Fig. 3m). In $WT^{Brn3c:mGFP} \rightarrow lak$ chimaeras, small numbers of donor-derived RGCs visibly expressed *efna5b* in nasal locations but not in the temporal retina ($n = 6$; Fig. 3n), which is consistent with previous findings that retinal positional identity is specified before, and independently of, RGC genesis^{18,25,26}.

Finally, we ruled out a delay of tectal innervation in $WT^{Brn3c:mGFP} \rightarrow lak$ chimaeras by imaging chimaeras at 80 h after fertilization, an early stage of RGC tectal innervation. RGC axons, tipped with growth cones, were seen in the tecta of both WT and *lak*

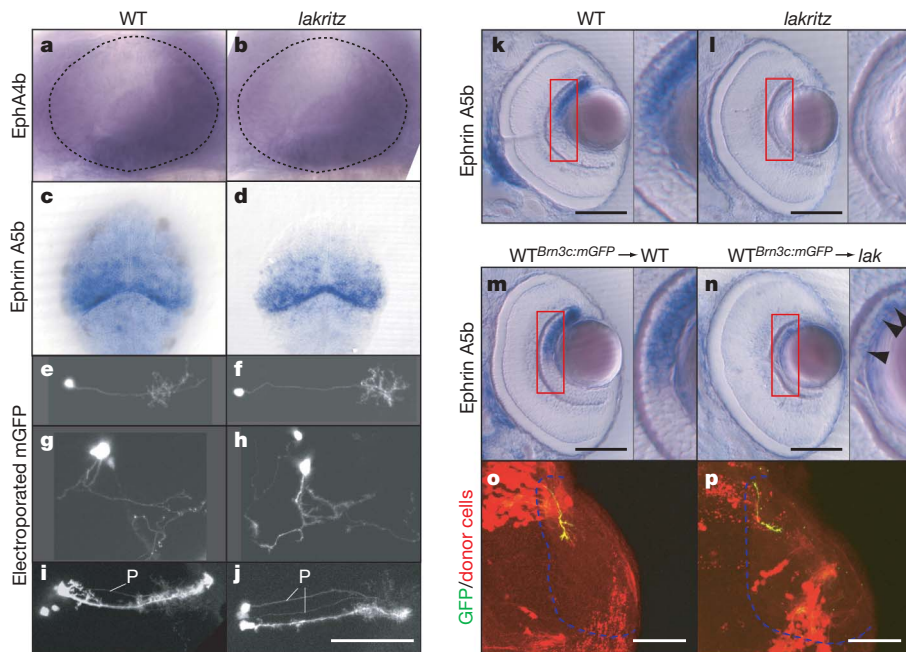


Figure 3 | Evidence for normal patterning of retina and tectum in *lak* mutants. **a, b**, Temporal retinal *epha4b* expression in WT (**a**) and *lak* (**b**) at 28 h after fertilization. Optic fissure is at lower left. **c, d**, Tectal expression of *efna5b* is unchanged between WT (**c**) and *lak* (**d**). **e–j**, Tectal cellular composition in WT (**e, g, i**) and *lak* (**f, h, j**). Scale bar, 100 μm . ‘Palm cells’ (**e, f**), ‘vine cells’ (**g, h**), and ‘giant kelp cells’ (radial glia, **i, j**; also present here, ‘palm cells’ labelled P) are present in normal numbers. **k–n**, *efna5b* expression in larvae at 80 h after fertilization. Insets show magnifications of the red boxes. Scale bar, 100 μm . *efna5b* is present in nasal RGCs in WT (**k**), but completely absent in *lak* (**l**). Expression is unaffected in WT hosts (**m**). Donor-derived nasal RGCs express *efna5b* (**n**, arrowheads) in *lak* hosts. **o, p**, A single GFP-labelled axon extends into the tectum of WT (**o**) and *lak* (**p**) host at 80 h after fertilization. Scale bar, 50 μm .

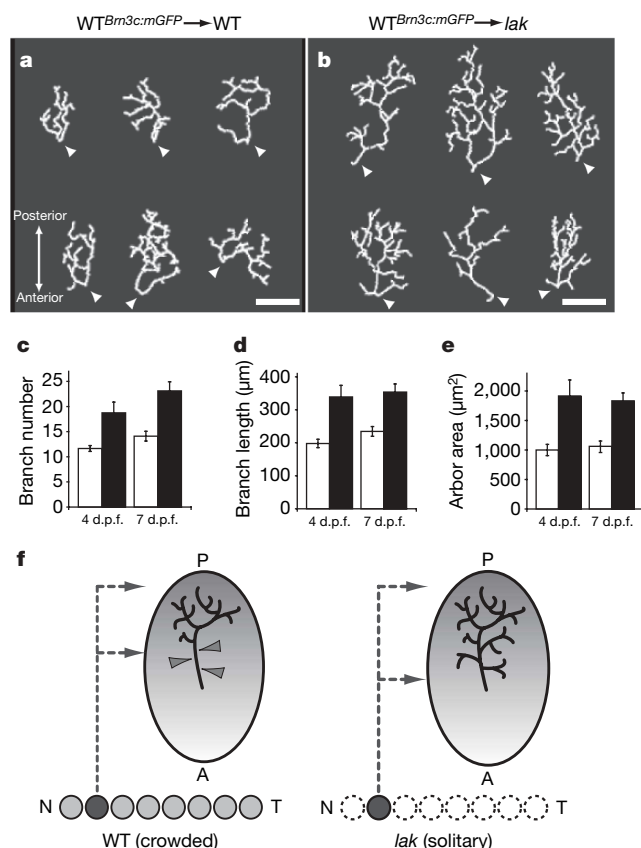


Figure 4 | Axon competition restricts axon arbor size and complexity. **a, b**, Examples of RGC axon arbors at 7 d.p.f. in WT (**a**) and *lak* (**b**) hosts. Arrowheads indicate positions of the most proximal branch. Scale bar, 50 μm . **c–e**, At both 4 and 7 d.p.f., arbors have a greater number of branches (**c**), total branch length (**d**) and area (**e**) in *lak* hosts (filled columns) than in WT hosts (open columns). Results are shown as means \pm s.e.m. For all 4 d.p.f., $P < 0.01$ (two-tailed t -test, $n = 17$ WT, $n = 8$ *lak*). For all 7 d.p.f., $P < 0.01$ (two-tailed t -test, $n = 19$ WT, $n = 19$ *lak*). **f**, Summary interpretation. RGC axons project retinotopically, but are elongated, in the absence of axon–axon interactions. Proximal branches are normally pruned (triangle tips) by competition with other axons, but persist in solitary arbors (right).

hosts (Fig. 3o, p). The axon arbor phenotype is therefore unlikely to be a consequence of developmental differences of the tectum in $WT^{Bm3c:mGFP} \rightarrow lak$ chimaeras, but rather is attributable to the difference in the density of RGC axons.

We predicted from the mapping functions of solitary axons (see Fig. 2d, e) that their arbors would be larger than those under crowded conditions. Indeed, morphometric analysis of arbor shapes revealed that solitary arbors covered a larger territory and had an increased number and length of branches (Fig. 4a, b). This increase in arbor size and complexity was already evident at 4 d.p.f. and became more pronounced by 7 d.p.f., through the net addition of branches (Fig. 4c–e). These findings suggest that axonal arbors are normally restricted in their initial size by the presence of other axons. This is consistent with the view that competition for target territory refines the map by suppressing or eliminating branches in retinotopically inappropriate territory². Solitary axons in zebrafish showed a positional bias: excessive branching occurred largely on the proximal side of the arbor (Fig. 4f).

Our results indicate that, at least under our experimental conditions, RGC axon–axon interactions, including competition, are not required for retinotopic targeting along the anterior–posterior axis. Although this does not rule out the possibility that competition can profoundly influence the map in a densely innervated tectum^{2,3,13}, our findings support a mapping mechanism that requires a second tectum-derived gradient, balancing the repellent signal provided by ephrin A molecules. This gradient, whether provided by the growth-promoting effect of ephrin A on nasal axons²⁷, by reverse chemo-repellent signalling from tectally expressed EphA to retinal axons²⁸ or by a different mechanism^{29,30}, is sufficient to guide axons to the posterior tectum. Within the termination zone, axon–axon interactions then sculpt the axonal arbor and restrict branching along the length of the axon.

METHODS SUMMARY

Generation of chimaeras. About 5,000 blastomere transplantations were performed, with the use of WT donor embryos carrying the *Bm3c:mGFP* transgene and WT or *lak* host embryos. Chimaeric embryos with donor-derived clones in the neural retina were selected at 30–36 h after fertilization, then raised for subsequent analysis of RGC axon mapping and arbor morphology.

Immunostaining, imaging and quantification. Larvae with small numbers of RGC axons were selected at appropriate time points and imaged live, or fixed and immunostained for GFP and monoclonal antibody zn-5 (Zebrafish International Resource Center). RGC soma position was calculated as the

percentage of distance from the nasal pole of the retina along the nasal–temporal axis. Tectal positions were measured as the percentage of the distance between the anterior and posterior poles of the tectum. Individual axon arbors were imaged at 4 or 7 d.p.f. and analysed with Object-Image, blind to host genotype, as described previously²³.

In situ hybridization. Whole-mount *in situ* hybridization was performed as described previously¹⁸.

Single cell electroporation. Small numbers of tectal cells were transfected with GFP in live larvae at 4 or 5 d.p.f. and imaged at 6 or 7 d.p.f.

Full Methods and any associated references are available in the online version of the paper at www.nature.com/nature.

Received 22 August 2007; accepted 4 February 2008.

Published online 26 March 2008.

1. Goodhill, G. J. Contributions of theoretical modeling to the understanding of neural map development. *Neuron* **56**, 301–311 (2007).
2. Ruthazer, E. S. & Cline, H. T. Insights into activity-dependent map formation from the retinotectal system: a middle-of-the-brain perspective. *J. Neurobiol.* **59**, 134–146 (2004).
3. Lemke, G. & Reber, M. Retinotectal mapping: new insights from molecular genetics. *Annu. Rev. Cell Dev. Biol.* **21**, 551–580 (2005).
4. Flanagan, J. G. Neural map specification by gradients. *Curr. Opin. Neurobiol.* **16**, 59–66 (2006).
5. Kay, J. N., Finger-Baier, K. C., Roeser, T., Staub, W. & Baier, H. Retinal ganglion cell genesis requires *laktitz*, a zebrafish *atonal* homolog. *Neuron* **30**, 725–736 (2001).
6. Hornberger, M. R. *et al.* Modulation of EphA receptor function by coexpressed ephrinA ligands on retinal ganglion cell axons. *Neuron* **22**, 731–742 (1999).
7. Carvalho, R. F. *et al.* Silencing of EphA3 through a *cis* interaction with ephrinA5. *Nature Neurosci.* **9**, 322–330 (2006).
8. Monschau, B. *et al.* Shared and distinct functions of RAGS and ELF-1 in guiding retinal axons. *EMBO J.* **16**, 1258–1267 (1997).
9. Sperry, R. W. Chemoaffinity in the orderly growth of nerve fiber patterns and connections. *Proc. Natl Acad. Sci. USA* **50**, 703–710 (1963).
10. Gierer, A. Model for the retino-tectal projection. *Proc. R. Soc. Lond. B* **218**, 77–93 (1983).
11. Honda, H. Competition between retinal ganglion axons for targets under the servomechanism model explains abnormal retinocollicular projection of Eph receptor-overexpressing or ephrin-lacking mice. *J. Neurosci.* **23**, 10368–10377 (2003).
12. Yates, P. A., Holub, A. D., McLaughlin, T., Sejnowski, T. J. & O'Leary, D. D. Computational modeling of retinotopic map development to define contributions of EphA–ephrinA gradients, axon–axon interactions, and patterned activity. *J. Neurobiol.* **59**, 95–113 (2004).
13. Reber, M., Burrola, P. & Lemke, G. A relative signalling model for the formation of a topographic neural map. *Nature* **431**, 847–853 (2004).
14. Tsigankov, D. N. & Koulakov, A. A. A unifying model for activity-dependent and activity-independent mechanisms predicts complete structure of topographic maps in ephrin-A deficient mice. *J. Comput. Neurosci.* **21**, 101–114 (2006).
15. Goodhill, G. J. & Xu, J. The development of retinotectal maps: a review of models based on molecular gradients. *Network* **16**, 5–34 (2005).
16. Willshaw, D. Analysis of mouse EphA knockins and knockouts suggests that retinal axons programme target cells to form ordered retinotopic maps. *Development* **133**, 2705–2717 (2006).
17. Fraser, S. E. & Perkel, D. H. Competitive and positional cues in the patterning of nerve connections. *J. Neurobiol.* **21**, 51–72 (1990).
18. Kay, J. N., Link, B. A. & Baier, H. Staggered cell-intrinsic timing of *ath5* expression underlies the wave of ganglion cell neurogenesis in the zebrafish retina. *Development* **132**, 2573–2585 (2005).
19. Poggi, L., Vitorino, M., Masai, I. & Harris, W. A. Influences on neural lineage and mode of division in the zebrafish retina *in vivo*. *J. Cell Biol.* **171**, 991–999 (2005).
20. Xiao, T., Roeser, T., Staub, W. & Baier, H. A GFP-based genetic screen reveals mutations that disrupt the architecture of the zebrafish retinotectal projection. *Development* **132**, 2955–2967 (2005).
21. Stuermer, C. A. Retinotopic organization of the developing retinotectal projection in the zebrafish embryo. *J. Neurosci.* **8**, 4513–4530 (1988).
22. Hua, J. Y., Smear, M. C., Baier, H. & Smith, S. J. Regulation of axon growth *in vivo* by activity-based competition. *Nature* **434**, 1022–1026 (2005).
23. Smear, M. C. *et al.* Vesicular glutamate transport at a central synapse limits the acuity of visual perception in zebrafish. *Neuron* **53**, 65–77 (2007).
24. Baier, H. *et al.* Genetic dissection of the retinotectal projection. *Development* **123**, 415–425 (1996).
25. Brennan, C. *et al.* Two Eph receptor tyrosine kinase ligands control axon growth and may be involved in the creation of the retinotectal map in the zebrafish. *Development* **124**, 655–664 (1997).
26. Picker, A. *et al.* Requirement for the zebrafish mid-hindbrain boundary in midbrain polarisation, mapping and confinement of the retinotectal projection. *Development* **126**, 2967–2978 (1999).
27. Hansen, M. J., Dallal, G. E. & Flanagan, J. G. Retinal axon response to ephrin-As shows a graded, concentration-dependent transition from growth promotion to inhibition. *Neuron* **42**, 717–730 (2004).
28. Rashid, T. *et al.* Opposing gradients of ephrin-As and EphA7 in the superior colliculus are essential for topographic mapping in the mammalian visual system. *Neuron* **47**, 57–69 (2005).
29. von Boxberg, Y., Deiss, S. & Schwarz, U. Guidance and topographic stabilization of nasal chick retinal axons on target-derived components *in vitro*. *Neuron* **10**, 345–357 (1993).
30. Ichijo, H. & Bonhoeffer, F. Differential withdrawal of retinal axons induced by a secreted factor. *J. Neurosci.* **18**, 5008–5018 (1998).

Supplementary Information is linked to the online version of the paper at www.nature.com/nature.

Acknowledgements We thank T. Xiao, A. Picker, U. Drescher, K. Haas and H. Cline for reagents and advice, and J. Pinkston-Gosse and members of the Baier laboratory for review of the manuscript. This work was supported by the National Institutes of Health (H.B. and N.J.G.) and a March of Dimes Research Grant (H.B.).

Author Contributions N.J.G., L.M.N. and H.B. devised experiments. N.J.G. performed all transplantation experiments and quantified images. L.M.N. conducted single-cell labelling studies in the tectum. N.J.G. and H.B. wrote the manuscript.

Author Information Reprints and permissions information is available at www.nature.com/reprints. Correspondence and requests for materials should be addressed to H.B. (herwig.baier@ucsf.edu).

METHODS

Generation of chimaeras. WT donor embryos carrying the *Brn3c:mGFP* transgene²⁰ were injected with a solution of 1–4% tetramethylrhodamine-conjugated dextran and 1–4% biotin-conjugated dextran (Invitrogen). Host embryos were collected from heterozygous *lak* carrier incrosses, or heterozygous male carriers mated to homozygous *lak* mutant females. Donor and host embryos were dechorionated enzymatically by incubation for 5–8 min in a solution of 0.5 mg ml⁻¹ pronase (Sigma) in water. Chimaeric embryos with rhodamine-positive clones in the neural retina were selected at 30–36 h after fertilization, and raised in 0.2 mM phenylthiocarbamide to inhibit melanin synthesis.

Smaller donor-derived clones, which are more likely to give rise to single RGCs, were found in locations biased towards the central retina, probably as a result of the proliferation of cells in the post-embryonic peripheral retina.

Immunohistochemistry. Larvae carrying fewer than four RGC axons were selected at 3, 4 or 7 d.p.f. and stained for GFP and zn-5 as described previously²⁰, with the following modifications: larvae at 80 h after fertilization and 7 d.p.f. were permeabilized in 1 mg ml⁻¹ collagenase in PBS for 1.5 and 2.5–3.0 h, respectively. Anti-GFP and zn-5 antibodies were used at 1:2,000 and 1:400 dilutions, and donor-derived cells in larvae at 80 h after fertilization and 7 d.p.f. were identified by reaction with Alexa-fluor-conjugated avidin (Invitrogen).

Imaging and quantification. Larvae at 4 d.p.f. were anaesthetized and immobilized in 1% low-melting-point agarose. Whole-mount stained 7 d.p.f. larvae were mounted in ~90% glycerol. Dorsal confocal stacks were collected with a Bio-Rad MRC 1024 or Zeiss LSM Pascal microscope.

Custom-designed macros in Object-Image (available at <http://simon.bio.uva.nl/Object-Image/1-Introduction.html>) were used for image analysis. Mapping functions were obtained blind to host genotype and retinal cell body position.

RGC soma position (percentage NT) was calculated as the percentage of distance from the nasal pole of the retina along the nasotemporal axis (Supplementary Fig. 2a–c):

$$\text{Percentage NT} = 100 \times [(\text{NT}_{\text{max}} - \text{NT}_{\text{DV}})/2 + \text{NT}_{\text{cell}}]/\text{NT}_{\text{max}}$$

where NT_{max} is the maximum distance from nasal to temporal locations in the ganglion cell layer, NT_{DV} is the distance from nasal to temporal poles at the dorsal–ventral position of the cell, and NT_{cell} is the distance from the nasal pole to the cell body. (All distances were measured as curved lines along the inner plexiform layer, as revealed with zn-5 reactivity.)

Tectal positions were measured as the percentage of the distance between the anterior and posterior poles of the tectum, demarcated by extent of zn-5 label (Supplementary Fig. 2d–f).

Summary retinotectal mapping functions were assembled for 7 d.p.f. larvae with 30 RGCs in 27 WT^{*Brn3c:mGFP*}→WT chimaera eyes, and 19 RGCs in 18 WT^{*Brn3c:mGFP*}→*lak* chimaera eyes.

Individual axon arbors were imaged at 4 or 7 d.p.f. and analysed with Object-Image, blind to host genotype, as described previously²³. Axon arbor stick-figures were exported directly from morphometric analysis and prepared with Adobe Photoshop.

In situ hybridization. Digoxigenin-labelled *epha4b* antisense probes were synthesized *in vitro* as published²⁶. Whole-mount *in situ* hybridization was performed as described previously¹⁸. For sections, larvae were mounted in gelatin/albumin and 25-μm slices were cut with a Leica vibratome. Stained embryos were imaged with a SPOT charge-coupled device camera mounted on a Leica dissecting microscope or Zeiss compound microscope with differential interference contrast optics, and prepared with Adobe Photoshop.

Single-cell electroporation and morphological analysis. Small numbers of neurons were labelled in live larvae by using a method adapted from ref. 31. Tectal cells were transfected with either *α-tubulin:GFP*, *eFlx:GFP* or mixed *α-tubulin:gal4;UAS:GFP* plasmids at a DNA concentration of 1.5 μg μl⁻¹. WT and *lak* mutant larvae were electroporated at 4 or 5 d.p.f. and imaged as above at 6 or 7 d.p.f.

In ‘palm cells’, cell bodies are located near the tectal midline, neurites in the tectal neuropil. In ‘vine cells’, cell bodies are located in the tectum, arbors extend to more ventral brain structures. In glial-like ‘giant kelp cells’, cell bodies are directly apposed to the tectal midline; endfeet are at the dorsal surface of the brain, superficial to RGC input layers.

31. Haas, K., Sin, W. C., Javaherian, A., Li, Z. & Cline, H. T. Single-cell electroporation for gene transfer *in vivo*. *Neuron* **29**, 583–591 (2001).

LETTERS

LNA-mediated microRNA silencing in non-human primates

Joacim Elmén^{1*}, Morten Lindow^{1*}, Sylvia Schütz², Matthew Lawrence³, Andreas Petri¹, Susanna Obad¹, Marie Lindholm¹, Maj Hedtjärn¹, Henrik Frydenlund Hansen¹, Urs Berger⁴, Steven Gullans³, Phil Kearney¹, Peter Sarnow², Ellen Marie Straarup¹ & Sakari Kauppinen^{1,5}

microRNAs (miRNAs) are small regulatory RNAs that are important in development and disease^{1–3} and therefore represent a potential new class of targets for therapeutic intervention⁴. Despite recent progress in silencing of miRNAs in rodents^{5,6}, the development of effective and safe approaches for sequence-specific antagonism of miRNAs *in vivo* remains a significant scientific and therapeutic challenge. Moreover, there are no reports of miRNA antagonism in primates. Here we show that the simple systemic delivery of a unconjugated, PBS-formulated locked-nucleic-acid-modified oligonucleotide (LNA-antimiR) effectively antagonizes the liver-expressed miR-122 in non-human primates. Acute administration by intravenous injections of 3 or 10 mg kg^{−1} LNA-antimiR to African green monkeys resulted in uptake of the LNA-antimiR in the cytoplasm of primate hepatocytes and formation of stable heteroduplexes between the LNA-antimiR and miR-122. This was accompanied by depletion of mature miR-122 and dose-dependent lowering of plasma cholesterol. Efficient silencing of miR-122 was achieved in primates by three doses of 10 mg kg^{−1} LNA-antimiR, leading to a long-lasting and reversible decrease in total plasma cholesterol without any evidence for LNA-associated toxicities or histopathological changes in the study animals. Our findings demonstrate the utility of systemically administered LNA-antimiRs in exploring miRNA function in rodents and primates, and support the potential of these compounds as a new class of therapeutics for disease-associated miRNAs.

miRNAs are small endogenous non-coding RNAs that post-transcriptionally repress the expression of protein-coding genes by base-pairing with the 3' untranslated regions (UTRs) of the target messenger RNAs^{1,2,7}. Emerging evidence suggests that animal miRNAs are important in the control of many biological processes^{1–3,8}. In addition, miRNAs have been implicated in viral infections, cardiovascular disease and neurological and muscular disorders, as well as in the onset and progression of cancers^{9–19}. miR-122 is a liver-expressed miRNA implicated in cholesterol and lipid metabolism^{5,6} and in hepatitis C virus (HCV) replication^{14,20}, underscoring miR-122 as a potential therapeutic target for the treatment of hypercholesterolemia and hepatitis C infection. To develop an efficient approach for miR-122 targeting *in vivo*, we first evaluated the potency of different LNA-modified DNA oligonucleotides (LNA-antimiRs) in cultured Huh-7 cells with the use of a luciferase reporter assay for miR-122. Our screen implied that inhibition of miR-122 function was affinity dependent and identified a high-affinity LNA-antimiR (more than 50% LNA, melting temperature 80 °C), which

mediated efficient derepression of the luciferase reporter at 5 nM concentration (Supplementary Fig. 1a). This oligonucleotide showed improved potency compared with a 2'-O-methyl oligonucleotide and two LNA-antimiRs of lower affinity in inhibiting HCV replication in Huh-7 cells harbouring the HCV-N replicon NNeo/C-5B (Supplementary Fig. 2). Moreover, when adapted to silencing of three additional miRNAs in HeLa cells, our LNA-antimiR design showed high potency for all targeted miRNAs (Supplementary Fig. 1b).

Next, we examined whether combining the high-affinity LNA-antimiR with phosphorothioate modifications could enable the delivery and silencing of miR-122 *in vivo* without additional conjugation chemistries. As shown in Fig. 1a, uptake of unconjugated LNA-antimiR in the murine liver was achieved by three intraperitoneal injections of saline-formulated LNA-antimiR with a complete phosphorothioate backbone. This coincided with the detection of a shifted band on the northern blot (Fig. 1a), indicating that the mature miR-122 is sequestered in a heteroduplex with LNA-antimiR. However, this mechanism of action does not necessarily apply to other types of miRNA antagonist. LNA-mediated silencing of miR-122 function led to a threefold derepression of the direct miR-122 target mRNA, *Aldoa*, which encodes aldolase A (ref. 6) (Fig. 1b). Single intraperitoneal injections at doses ranging from 1 to 200 mg kg^{−1} LNA-antimiR resulted in dose-dependent and sustained decrease in total plasma cholesterol with a median effective dose (ED₅₀) of 10 mg kg^{−1} (Fig. 1c). Moreover, intraperitoneally delivered LNA-antimiR at doses ranging from three injections of 1–25 mg kg^{−1} showed markedly improved efficiency in antagonizing miR-122 in comparison with mice that were treated with either cholesterol-conjugated antagomir-122 (refs 6, 21) or a phosphorothiolated LNA-antimiR with only 30% LNA and lower affinity²² (melting temperature 70 °C) using the same dosing regimen (Supplementary Fig. 3). This is consistent with a previous report in mice in which efficient miR-122 silencing by antagomir-122 required much higher doses: from three doses of 40 mg kg^{−1} to three doses of 80 mg kg^{−1} (ref. 21), whereas our findings show that LNA enables the design of highly substituted LNA-antimiR oligonucleotides that can mediate potent miR-122 antagonism *in vivo* at a considerably lower dose.

To validate this conclusion, we antagonized miR-122 in a diet-induced obesity mouse model by using two weekly intraperitoneal doses of 5 mg kg^{−1} LNA-antimiR for six weeks, which resulted in the efficient sequestration of mature miR-122 and a sustained decrease in total cholesterol by 30% without any elevations in hepatotoxicity markers in the serum or in lipid accumulation in the liver (Fig. 1d,

¹Santaris Pharma, Bøge Allé 3, DK-2970 Hørsholm, Denmark. ²Department of Microbiology and Immunology, 299 Campus Drive, Stanford University School of Medicine, Stanford, California 94305, USA. ³RxGen Inc, 100 Deepwood Drive, Hamden, Connecticut 06517, USA. ⁴UB-in situ, PO Box 463, Natick, Massachusetts 01760, USA. ⁵Wilhelm Johannsen Centre for Functional Genome Research, Department of Cellular and Molecular Medicine, University of Copenhagen, Blegdamsvej 3, DK-2200 Copenhagen N, Denmark.

*These authors contributed equally to this work.

e, and Supplementary Fig. 4). In contrast, treatment with either saline or LNA mismatch control did not affect the cholesterol levels, concurring with detection of the mature miR-122 by northern blots in both groups (Fig. 1d, e). The marked derepression of the miR-122 targets, *Aldoa* (Fig. 1f) and *Bckdk22* (data not shown), in LNA-antimiR-treated mice, but not in LNA-mismatch-treated mice, implies that antagonism of miR-122 *in vivo* by LNA-antimiR is specific. Consistent with this notion, clustering of the liver gene expression data revealed that all the LNA-antimiR-treated animals ($n = 5$ per group) had highly similar expression profiles as shown by a uniform cluster on the same main dendrogram branch, which was divergent from the saline and LNA mismatch control groups (Fig. 1g). Antagonism or ectopic expression of a miRNA has previously been shown to result in an increase or decrease in mRNAs, which show enrichment of miRNA seed matches in the 3' UTRs^{6,7,22,23}. Indeed, correlation of the presence of miR-122 seed matches with expression changes confirmed that messages with seed matches to miR-122 tended to be derepressed in the LNA antimiR-treated animals compared with those in control mice (Fig. 1h; Kolmogorov–Smirnov test, $P = 2.4 \times 10^{-14}$ for 8-mer seed). This demonstrates that the liver mRNA changes in the LNA-antimiR-treated mice are due mainly to the silencing of miR-122.

To examine whether our LNA-antimiR approach could be used for miR-122 antagonism in non-human primates, we undertook an efficacy study in African green monkeys (*Chlorocebus aethiops*). Systemic administration of PBS-formulated LNA-antimiR in drug-naïve female African green monkeys by three intravenous injections of doses ranging from 1 to 10 mg kg⁻¹ ($n = 5$ per group) resulted in a

dose-dependent and sustained decrease in total plasma cholesterol in primates (Fig. 2a and Supplementary Information), which is consistent with the cholesterol lowering observed in miR-122-antagonized mice. Animals that received the high-dose LNA-antimiR (three doses of 10 mg kg⁻¹) showed a maximum decrease in cholesterol of 40% at 23 days after treatment ($P = 0.001$), whereas the middle-dose group (three doses of 3 mg kg⁻¹ LNA-antimiR) showed a 20% lowering of cholesterol ($P = 0.02$) at the same time point (Fig. 2a). Despite the observed fluctuations in total cholesterol levels over time, the effect on cholesterol lowering was clearly dose dependent, as shown by the cholesterol trend plots of each treatment group normalized to control monkeys (Fig. 2b). Northern blot analyses of RNA samples extracted from LNA-antimiR-treated monkey liver biopsies, performed 24 h after the last dose, confirmed miR-122 silencing as demonstrated by dose-dependent accumulation of the shifted LNA-antimiR•miR-122 heteroduplex and the depletion of mature miR-122 compared with PBS-treated control monkey samples (Fig. 2c). In addition, *in situ* hybridization in frozen monkey-liver biopsies showed accumulation of the LNA-antimiR in the liver sections of treated monkeys but not in PBS controls (Fig. 2d–g), whereas high-resolution *in situ* hybridization showed that the LNA-antimiR was localized primarily in the cytoplasm of primate hepatocytes (Fig. 2h).

LNA-mediated antagonism of miR-122 in primates was effective and long-lasting, as shown by a decrease in total plasma cholesterol for seven weeks ($P < 0.05$, two-sided *t*-test) in the LNA-antimiR high-dose group and for five weeks ($P < 0.05$) in the middle-dose group (Fig. 2b and Supplementary Information). The cholesterol

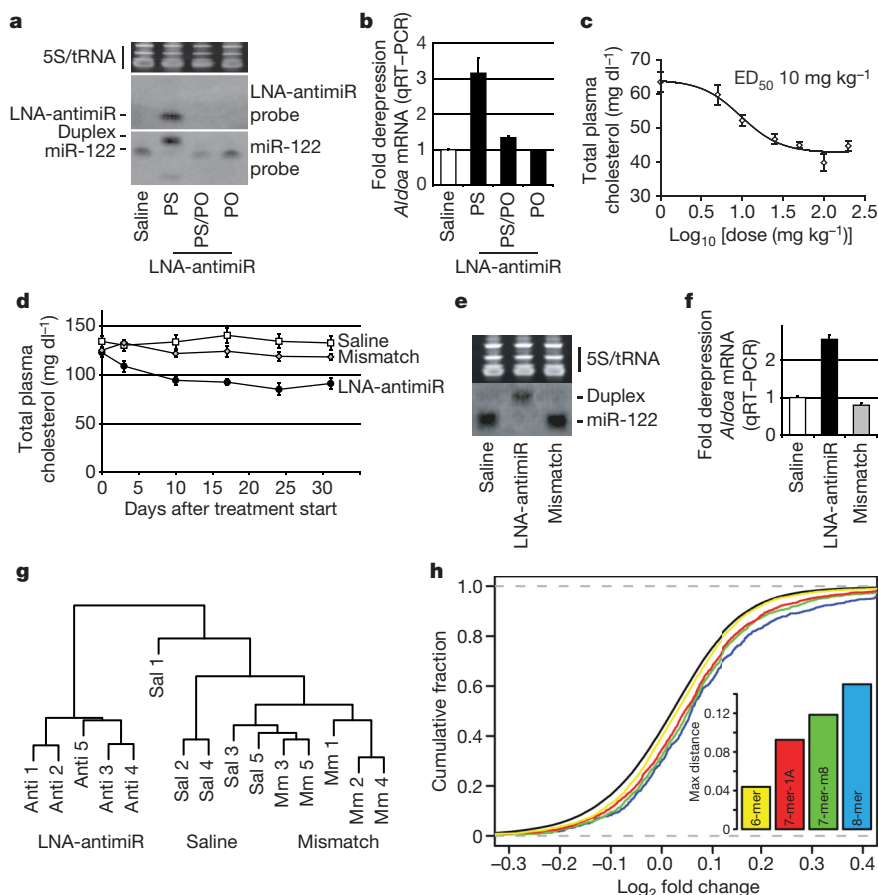


Figure 1 | Silencing of miR-122 function in normal and hypercholesterolaemic mice by LNA-antimiR. **a**, Northern blot of liver RNA from mice treated with LNA-antimiR with a complete phosphorothioate backbone (PS), a mixed phosphorothioate/phosphodiester backbone (PS/PO) or an unmodified phosphodiester (PO) backbone. The northern blot was probed for LNA-antimiR and re-probed for miR-122. **b**, Derepression of the direct miR-122 target *Aldoa* (same samples as in **a**, normalized to glyceraldehyde-3-phosphate dehydrogenase; means and s.e.m., $n = 5$). **c**, Total plasma cholesterol in mice after treatment with single intraperitoneal doses of LNA-antimiR ranging from 1 to 200 mg kg⁻¹ (means \pm s.e.m., $n = 5$ except for 1 mg kg⁻¹ LNA-antimiR ($n = 4$)). **d**, Total plasma cholesterol levels in hypercholesterolaemic mice treated with saline, LNA-antimiR or LNA mismatch control, respectively, at a dose of 5 mg kg⁻¹ intraperitoneally twice weekly over a six-week period (means \pm s.e.m., $n = 10$ except for saline ($n = 9$)). **e**, miR-122 northern blot (same mice as in **d**). **f**, Quantification of *Aldoa* mRNA (same samples as in **e**; means and s.e.m., $n = 10$ except for saline ($n = 9$)). **g**, Unsupervised clustering of liver mRNA expression profiles (same mice as in **d**). **h**, Expression changes of liver mRNAs in LNA-antimiR-treated mice relative to controls. mRNAs are grouped by the presence or absence of different types of canonical miR-122 seed matches in the 3' UTR. Separation from mRNAs without seed matches (maximum distance from the black trace) is shown in the inset; this was significant for all types of site ($P = 1.4 \times 10^{-6}$, $P = 2.2 \times 10^{-13}$, $P < 10^{-15}$ and $P = 2.4 \times 10^{-14}$ (Kolmogorov–Smirnov test) for 6-mer, 7-mer-1A (6-mer site with an A across from nucleotide position 1 of miR-122), 7-mer-m8 (an exact match to nucleotide positions 2–8 of miR-122) and 8-mer sites, respectively).

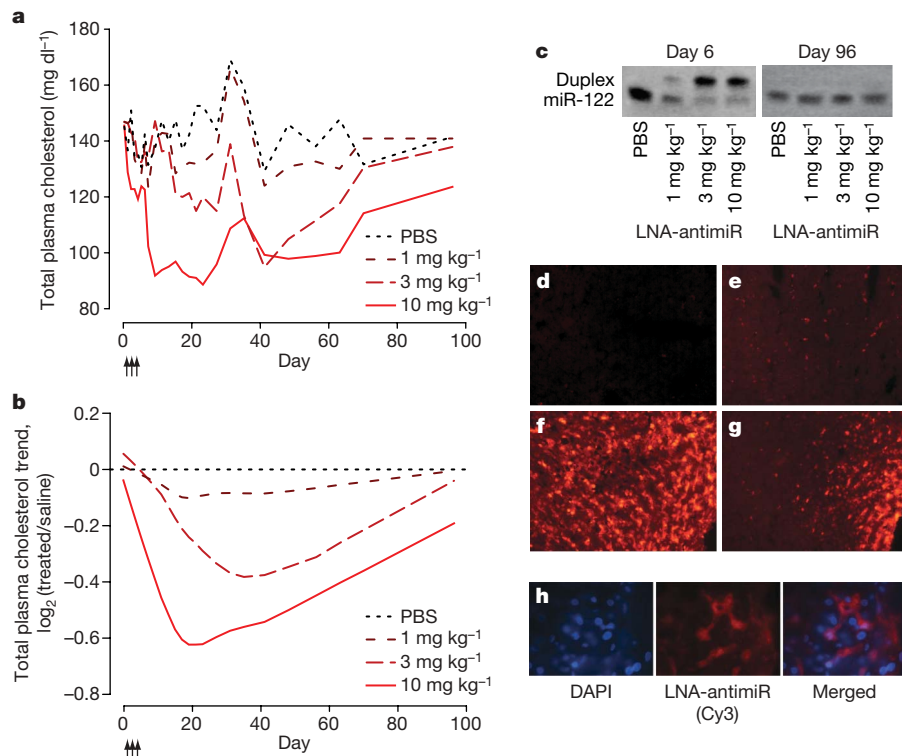


Figure 2 | Silencing of miR-122 in non-human primates by LNA-antimiR. **a**, Total plasma cholesterol levels in African green monkeys treated with LNA-antimiR or PBS by three i.v. injections over five days (arrows) ($n = 5$ per group). **b**, Trend plots of the cholesterol data in **a**, normalized to the PBS control group, Lowess-smoothed and \log_2 -transformed. **c**, Northern blot analysis of monkey liver RNA samples from liver biopsies performed on day 6 and 96. **d–g**, *In situ* detection of LNA-antimiR in liver biopsies on day 6 (same animals as in **c**): **d**, PBS; **e**, 1 mg kg^{-1} LNA-antimiR; **f**, 3 mg kg^{-1} LNA-antimiR; **g**, 10 mg kg^{-1} LNA-antimiR. **h**, Cytoplasmic localization of LNA-antimiR in hepatocytes (day 6, 10 mg kg^{-1} LNA-antimiR).

levels gradually returned towards baseline over a period of three months after treatment with LNA-antimiR, which is consistent with normalization of mature miR-122 levels and clearance of the LNA-antimiR compound from the liver as detected by northern blots and *in situ* hybridization, respectively, in a second set of monkey liver biopsies performed 96 days after initiation of LNA-antimiR treatment (Fig. 2c, and data not shown). Decreases in both high-density lipoprotein (HDL) and its major apolipoprotein, ApoA-I, as well as in low-density lipoprotein (LDL) and its principal apolipoprotein, ApoB, were detected in LNA-antimiR-treated monkeys (Supplementary Information), which concur with previous findings in miR-122-antagonized mice⁵. Although differences in the ApoA-I/ApoB ratios between the high-dose LNA-antimiR-treated and control animals (Supplementary Information) did not achieve statistical significance ($P > 0.05$, two-sided t -test on each day), the ratio seemed to be slightly lower in the high-dose group, suggesting a more pronounced effect on ApoA-I and HDL.

We observed no acute or subchronic toxicities in the LNA-antimiR-treated primates as shown by the clinical chemistries, which remained within normal limits for all measurements throughout the study in the treatment groups (Supplementary Information), with the exception of transient, liver-biopsy-associated spikes in creatine phosphokinase, aspartate aminotransferase (AST), alanine aminotransferase (ALT) and bilirubin. There were no changes in blood coagulation profiles associated with treatment with LNA-antimiR (Fig. 3a and Supplementary Information). Moreover, histopathology investigations of the liver biopsies revealed no treatment-correlated abnormalities in the LNA-antimiR-treated primates (Fig. 3b–e and Supplementary Information). To dissociate the effects of any liver-biopsy-associated toxicities in the safety evaluation of LNA-antimiR treatment, two additional non-biopsy groups ($n = 5$) treated either with the high dose of LNA-antimiR (three doses of 10 mg kg^{-1}) or PBS, respectively, were included in the primate study. We did not observe any hepatotoxicity or renal toxicity in these animals as demonstrated by the absence of increases in the levels of the plasma transaminases ALT and AST or of bilirubin, creatine phosphokinase or creatinine after treatment with three doses of 10 mg kg^{-1} LNA-antimiR in comparison with PBS controls (Fig. 3a

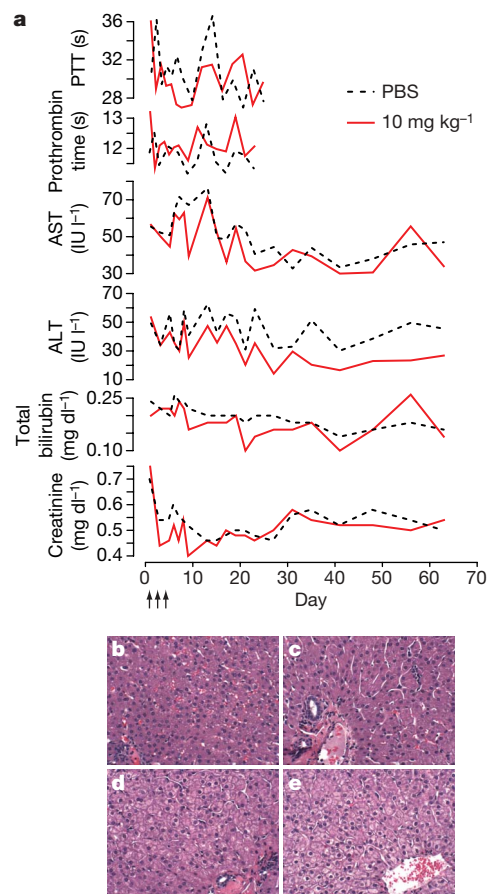


Figure 3 | LNA-mediated miR-122 silencing is safe in non-human primates. **a**, Partial thromboplastin time (PTT), prothrombin time, AST, ALT, total bilirubin and creatinine levels assessed in African green monkeys after treatment with PBS or three doses of 10 mg kg^{-1} LNA-antimiR. **b–e**, Photomicrographs of haematoxylin/eosin-stained sections from liver biopsies on day 6: **b**, PBS; **c**, 1 mg kg^{-1} LNA-antimiR; **d**, 3 mg kg^{-1} LNA-antimiR; **e**, 10 mg kg^{-1} LNA-antimiR.

and Supplementary Information). All study animals tolerated both the LNA-antimiR compound and sample collection procedures well, and all were in good health for at least ten months after treatment with LNA-antimiR.

Taken together, our results demonstrate potent antagonism of miR-122 by a simple delivery of a unconjugated high-affinity LNA-antimiR oligonucleotide in mice and non-human primates. The therapeutic value of antagonizing miR-122 was inferred in two species, in which treatment of hypercholesterolaemic mice with two weekly intraperitoneal injections of 5 mg kg^{-1} LNA-antimiR and treatment of African green monkeys with three intravenous injections of 3 or 10 mg kg^{-1} LNA-antimiR resulted in an effective and long-lasting decrease in plasma cholesterol without any evidence for LNA-associated toxicities. Although additional studies will be needed to optimize the dosing regimen and to assess the biodistribution and safety of LNA-antimiR compounds after long-term treatment, our findings highlight the utility of LNA-mediated silencing in studying miRNA function in rodents and primates as well as in the future development of miRNA-based therapeutics.

METHODS SUMMARY

The LNA-modified oligonucleotides were synthesized as unconjugated LNA/DNA mixers with a complete phosphorothioate backbone. The 2'-O-methyl oligonucleotides for HCV replication assays and the antagomir-122 were synthesized as described^{6,14}. Saline-formulated compounds were administered into normal and hypercholesterolaemic C57BL/6J mice by intraperitoneal injections, and blood samples were collected for measurements of cholesterol and serum transaminases. Liver samples were prepared for RNA extraction, miRNA quantification and liver histopathology. Microarray expression profiling of mouse liver RNAs was performed in accordance with standard Affymetrix protocols and the data were submitted to the ArrayExpress database. For data analysis, standard Bioconductor²⁴ packages were used. Transcript 3' UTRs were searched for the presence of miR-122 seed matches²⁵ by using in-house Perl scripts. mRNA quantification was conducted with standard TaqMan assays (Applied Biosystems). Thirty female drug-naïve young adult African green monkeys were assigned to six groups ($n = 5$ per group) and dosed once daily on days 1, 3 and 5 by intravenous infusions over about 10 min at a rate of $24 \text{ ml kg}^{-1} \text{ h}^{-1}$. Four treatment groups received PBS or 1, 3 or 10 mg kg^{-1} PBS-formulated LNA-antimiR, all of which received liver biopsies, whereas two groups received PBS or 10 mg kg^{-1} PBS-formulated LNA-antimiR without liver biopsies. Blood samples were collected for clinical chemistry and haematology measurements. Total cholesterol was determined enzymatically in microtitre plates. Lipoprotein cholesterol distributions were determined by fast protein liquid chromatography and the apolipoprotein levels by enzyme-linked immunosorbent assay. *In situ* detection of LNA-antimiR was performed on frozen liver sections of LNA-antimiR-treated and control monkeys by using a FAM-labelled LNA probe and horseradish peroxidase (HRP)-conjugated polyclonal rabbit anti-fluorescein isothiocyanate antibodies (Dako) combined with Cyanine 3-Plus tyramide (Perkin-Elmer). Northern blot analyses of liver RNAs were performed with a 5' FAM-labelled LNA-modified miR-122 probe and an anti-fluorescein-HRP antibody (NEF710; Perkin-Elmer) combined with the enhanced chemiluminescence advanced kit for detection (GE Healthcare Life Sciences).

Full Methods and any associated references are available in the online version of the paper at www.nature.com/nature.

Received 6 December 2007; accepted 1 February 2008.

Published online 26 March 2008; corrected 17 April 2008 (details online).

1. Ambros, V. The functions of animal microRNAs. *Nature* **431**, 350–355 (2004).
2. Bartel, D. P. MicroRNAs: genomics, biogenesis, mechanism, and function. *Cell* **116**, 281–297 (2004).
3. Kloosterman, W. P. & Plasterk, R. H. The diverse functions of microRNAs in animal development and disease. *Dev. Cell* **11**, 441–450 (2006).
4. Soifer, H. S., Rossi, J. J. & Sætrom, P. MicroRNAs in disease and potential therapeutic applications. *Mol. Ther.* **12**, 2070–2079 (2007).

5. Esau, C. *et al.* miR-122 regulation of lipid metabolism revealed by *in vivo* antisense targeting. *Cell Metab.* **3**, 87–98 (2006).
6. Krutzfeldt, J. *et al.* Silencing of microRNAs *in vivo* with 'antagomirs'. *Nature* **438**, 685–689 (2005).
7. Grimson, A. *et al.* MicroRNA targeting specificity in mammals: determinants beyond seed pairing. *Mol. Cell* **27**, 91–105 (2007).
8. Alvarez-Garcia, I. & Miska, E. A. MicroRNA functions in animal development and human disease. *Development* **132**, 4653–4662 (2005).
9. Abelson, J. F. *et al.* Sequence variants in SLITRK1 are associated with Tourette's syndrome. *Science* **310**, 317–320 (2005).
10. Calin, G. A. & Croce, C. M. MicroRNA signatures in human cancers. *Nature Rev. Cancer* **6**, 857–866 (2006).
11. Eisenberg, I. *et al.* Distinctive patterns of microRNA expression in primary muscular disorders. *Proc. Natl Acad. Sci. USA* **104**, 17016–17021 (2007).
12. Esquela-Kerscher, A. & Slack, F. J. Oncomirs—microRNAs with a role in cancer. *Nature Rev. Cancer* **6**, 259–269 (2006).
13. He, L. *et al.* A microRNA polycistron as a potential human oncogene. *Nature* **435**, 828–833 (2005).
14. Jopling, C. L., Yi, M., Lancaster, A. M., Lemon, S. M. & Sarnow, P. Modulation of hepatitis C virus RNA abundance by a liver-specific microRNA. *Science* **309**, 1577–1581 (2005).
15. Lu, J. *et al.* MicroRNA expression profiles classify human cancers. *Nature* **435**, 834–838 (2005).
16. Pedersen, I. M. *et al.* Interferon modulation of cellular microRNAs as an antiviral mechanism. *Nature* **449**, 919–922 (2007).
17. Triboulet, R. *et al.* Suppression of microRNA-silencing pathway by HIV-1 during virus replication. *Science* **315**, 1579–1582 (2007).
18. van Rooij, E. *et al.* Control of stress-dependent cardiac growth and gene expression by a microRNA. *Science* **316**, 575–579 (2007).
19. Yang, B. *et al.* The muscle-specific microRNA miR-1 regulates cardiac arrhythmogenic potential by targeting GJA1 and KCNJ2. *Nature Med.* **13**, 486–491 (2007).
20. Randall, G. *et al.* Cellular cofactors affecting hepatitis C virus infection and replication. *Proc. Natl Acad. Sci. USA* **104**, 12884–12889 (2007).
21. Krutzfeldt, J. *et al.* Specificity, duplex degradation and subcellular localization of antagomirs. *Nucleic Acids Res.* **35**, 2885–2892 (2007).
22. Elmen, J. *et al.* Antagonism of microRNA-122 in mice by systemically administered LNA-antimiR leads to up-regulation of a large set of predicted target mRNAs in the liver. *Nucleic Acids Res.* doi:10.1093/nar/gkm1113 (2007).
23. Lim, L. P. *et al.* Microarray analysis shows that some microRNAs downregulate large numbers of target mRNAs. *Nature* **433**, 769–773 (2005).
24. Gentleman, R. C. *et al.* Bioconductor: open software development for computational biology and bioinformatics. *Genome Biol.* **5**, R80.1–R80.16 (2004).
25. Lewis, B. P., Burge, C. B. & Bartel, D. P. Conserved seed pairing, often flanked by adenosines, indicates that thousands of human genes are microRNA targets. *Cell* **120**, 15–20 (2005).

Supplementary Information is linked to the online version of the paper at www.nature.com/nature.

Acknowledgements All primate studies were performed at the St Kitts Biomedical Research Foundation, St Kitts, West Indies. We thank A. Konge, A. Koustrup, B. Nordbo, H. W. Høvring, J. J. Jørgensen, K. R. Nielsen, L. Bang, H. Brostrøm, O. Olsen, R. Sølberg, U. Steinmeier, J. Staruk, C. Kent, E. Nisbett, M. Struharik and R. Valles for technical assistance. This study was supported by grants from the Danish National Advanced Technology Foundation, the Danish Medical Research Council and the Lundbeck Foundation (to S.K.) and by grants from the National Institutes of Health (to P.S.). The Wilhelm Johannsen Centre for Functional Genome Research was established by the Danish National Research Foundation.

Author Contributions J.E. and M. Lindow contributed equally to this study. J.E., M. Lindow, M. Lawrence, U.B., S.O., M.H., A.P., S.S. and E.M.S. performed experiments and contributed data. H.F.H. performed the synthesis of all oligonucleotides. J.E., M. Lindow, M. Lawrence, M. Lindholm, H.F.H., P.K., S.G., P.S., E.M.S. and S.K. designed experiments and discussed the data. S.K. supervised the study and wrote the paper together with J.E. and M. Lindow.

Author Information The microarray data have been submitted to the ArrayExpress database under accession number E-MEXP-1406. Reprints and permissions information is available at www.nature.com/reprints. The authors declare competing financial interests: details accompany the full-text HTML version of the paper at www.nature.com/nature. Correspondence and requests for materials should be addressed to S.K. (sk@santaris.com).

METHODS

Oligonucleotides. Unconjugated LNA-modified DNA oligonucleotides were synthesized with a complete phosphorothioate backbone, except for uptake studies where additional LNA oligonucleotides with a 50% phosphorothioate or a phosphodiester backbone were used. The sequence of the high-affinity LNA-antimiR was 5'-CcAttGTcaCaCtCC-3', the LNA mismatch oligonucleotide used in mouse studies was 5'-CcAttCTcaCaCtGC-3', and the LNA control used in the HCV replication assays was 5'-CcAttCTgaCcCtAC-3' (LNA in capitals, DNA in lower case, capital C denotes LNA methylcytosine). The 2'-O-methyl oligonucleotides for HCV replication assays and the antagomir-122 were synthesized as described^{6,14}.

In vivo experiments. C57BL/6J female mice were administered once on alternate days over a five-day period with saline or saline-formulated LNA-antimiR, antagomir-122 or LNA mismatch control, allowing the mice to receive an injection volume of 10 ml kg⁻¹ with daily intraperitoneal doses ranging from 1 to 25 mg kg⁻¹. The mice were killed 48 h after treatment. Before killing, retro-orbital sinus blood was collected in EDTA-coated tubes followed by isolation of the plasma fraction and measurement of total cholesterol with ABX Pentra Cholesterol CP (Horiba ABX Diagnostics). In the mouse dose-response study, single intraperitoneal injections ranging from 1 to 200 mg kg⁻¹ LNA-antimiR were administered and plasma cholesterol was measured six days after treatment. Diet-induced obesity mouse model was generated by feeding C57BL/6J female mice on a high-fat diet (D12492; Research Diets) for 13 weeks. Hypercholesterolaemic mice were treated with two weekly intraperitoneal doses of 5 mg kg⁻¹ LNA-antimiR or LNA control for six weeks. Serum ALT and AST levels were determined with enzymatic assays (Horiba ABX Diagnostics).

Thirty female drug-naïve young adult African green monkeys were assigned to six treatment groups ($n = 5$ per group) and dosed once daily on days 1, 3 and 5 by intravenous infusion over about 10 min at a rate of 24 ml kg⁻¹ h⁻¹ by means of a catheter inserted into the saphenous vein. Four groups, all of which received liver biopsies, were treated with PBS or 1, 3 or 10 mg kg⁻¹ PBS-formulated LNA-antimiR, and two other groups received PBS or 10 mg kg⁻¹ PBS-formulated LNA-antimiR without liver biopsies. The animals were sedated with ketamine (7.5 mg kg⁻¹) and xylazine (1.5 mg kg⁻¹) before and during dosing and at biopsy and phlebotomy time points. Percutaneous liver biopsies were performed 1 and 90 days after treatment to obtain two core biopsies from the right and left lobes. Half of each biopsy was immediately immersed in RNAlater (Qiagen), and the remaining biopsy was divided into samples for fixation in paraformaldehyde for haematoxylin/eosin staining and into cryopreservation for *in situ* analysis. Blood samples were obtained for the biopsied animals before and 24 h after treatment by means of superficial venipuncture, and additional blood samples were collected for all treatment groups throughout the study. Samplings were performed before feeding after a period of 12 h without access to food, to minimize dietary effects on cholesterol measurements.

Primate haematology, clinical chemistry and plasma lipid measurements and lipoprotein analysis. Haematology measurements were made by optical and mechanical methods and an automated cell counter; clinical chemistries were measured with a Hitachi 747 analysis system (Antech Diagnostics). Total plasma cholesterol was determined enzymatically in microtitre plates. Lipoprotein cholesterol distributions were determined by fast protein liquid chromatography

and apolipoproteins with an enzyme-linked immunosorbent assay by M. Wilson.

In situ hybridization. Detection of LNA-antimiR was performed on 10- μ m primate liver cryosections. Slides were thawed, fixed in 4% paraformaldehyde for 10 min at room temperature (25 °C) and treated with acetic anhydride/triethanolamine followed by rinsing in PBS. Slides were pre-hybridized at 48 °C for 30 min in 50% formamide, 5 \times SSC (standard saline citrate), 500 μ g ml⁻¹ yeast transfer RNA, 1 \times Denhardt's solution. LNA-antimiR was detected with a complementary FAM-labelled LNA probe hybridized to liver sections for 30 min at 48 °C followed by three 10-min post-hybridization washes in 0.1 \times SSC at 52 °C. After exposure for 10 min to 3% H₂O₂, slides were preincubated for 15 min with TN buffer (0.1 M Tris-HCl pH 7.5, 0.15 M NaCl) containing 1% blocking reagent (TNB buffer, TSA kit; Perkin-Elmer) and subsequently with polyclonal rabbit anti-fluorescein isothiocyanate antibodies conjugated to HRP (diluted 1:500 in TNB; Dako) for 30 min. Slides were rinsed with TN buffer containing 0.3% Triton X-100, and incubated with Cyanine 3-Plus tyramide (diluted 1:100 in amplification buffer; Perkin-Elmer). The slides were rinsed and mounted in Vectashield containing DAPI (Vector Laboratories) and analysed on a Leica epifluorescence microscope equipped with a charge-coupled device camera (Leica Microsystems) and NIS-Elements software.

Microarray expression profiling and miR-122 target site analysis. Liver RNAs from hypercholesterolaemic mice were labelled and hybridized to Affymetrix Mouse Genome 430 2.0 arrays in accordance with the manufacturer's instructions. The *expresso* function from the *affy*-package was used for low-level data analysis with *rma*-based background correction, quantile normalization and summarizing probe sets by Bioconductor's²⁴ implementation of the Li and Wong summary method. Expression profiles were subjected to hierarchical clustering with euclidean distance measure and Ward's agglomeration method. The array data were submitted to the ArrayExpress database. Affymetrix probe sets were mapped to Ensembl genes and transcripts by using Ensembl-Biomart. Transcript 3' UTRs were searched for miR-122 seed matches²⁵ with the use of in-house Perl scripts. When genes had alternative 3' UTRs, only the longest sequence was used.

Northern blot analysis and real-time RT-PCR. Trizol-extracted liver RNAs (10–15 μ g per sample) were subjected to electrophoresis in 15% denaturing Novex TBE-urea polyacrylamide gels (Invitrogen), transferred to Zeta Probe plus membrane (Bio-Rad) and hybridized overnight with 5' FAM-labelled LNA-modified miR-122 probe in ULTRAhyb-Oligo (Ambion) at 45 °C. The membranes were washed twice for 30 min in Low Stringency wash solution no. 1 (Ambion) at 45 °C, rinsed twice in PBST and blocked in ECL advanced blocking solution (GE Healthcare Life Sciences) for 1 h at room temperature, and then rinsed twice in PBST. An anti-fluorescein-HRP antibody (NEF710, diluted 1:1,000 in blocking solution; Perkin-Elmer) was incubated with the membrane for 1 h at room temperature, followed by rinsing twice in PBST, washing for 15 min and then three washes (5 min each) in PBST at 25 °C. The ECL advanced kit (GE Healthcare Life Sciences) was used for detection employing the VersaDoc imaging system (Bio-Rad). mRNA quantification was performed with TaqMan assays and a 7500 real-time PCR instrument (Applied Biosystems).

CORRIGENDUM

doi:10.1038/nature06871

A photosynthetic alveolate closely related to apicomplexan parasites

Robert B. Moore, Miroslav Oborník, Jan Janouškovec, Tomáš Chrudimský, Marie Vancová, David H. Green, Simon W. Wright, Noel W. Davies, Christopher J. S. Bolch, Kirsten Heimann, Jan Šlapeta, Ove Hoegh-Guldberg, John M. Logsdon Jr & Dee A. Carter

Nature 451, 959–963 (2008)

In Fig. 2c of this Article, the GenBank accession number DQ174732 was incorrectly cited. The correct accession number is DQ174731 (*Chromera velia*).

ERRATUM

doi:10.1038/nature06872

Hax1-mediated processing of HtrA2 by Parl allows survival of lymphocytes and neurons

Jyh-Rong Chao, Evan Parganas, Kelli Boyd, Cheol Yi Hong, Joseph T. Opferman & James N. Ihle

Nature 452, 98–102 (2008)

In Fig. 1a of this Letter, the light blue line was incorrectly labelled as *Hax1/Bak* DKO, $n = 13$. The light blue line should be labelled *Hax1/Bax* DKO, $n = 13$.

ERRATUM

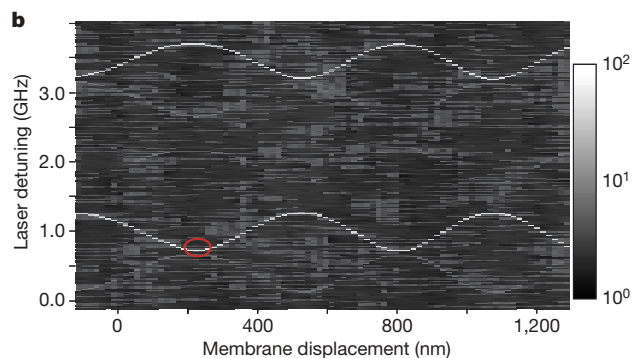
doi:10.1038/nature06898

Strong dispersive coupling of a high-finesse cavity to a micromechanical membrane

J. D. Thompson, B. M. Zwickl, A. M. Jayich, Florian Marquardt, S. M. Girvin & J. G. E. Harris

Nature 452, 72–72 (2008)

In the print and HTML versions of this Letter, Fig. 2b was printed incorrectly. The PDF version published online is correct. The corrected Fig. 2b is shown below.



CORRIGENDUM

doi:10.1038/nature06871

A photosynthetic alveolate closely related to apicomplexan parasites

Robert B. Moore, Miroslav Oborník, Jan Janouškovec, Tomáš Chrudimský, Marie Vancová, David H. Green, Simon W. Wright, Noel W. Davies, Christopher J. S. Bolch, Kirsten Heimann, Jan Šlapeta, Ove Hoegh-Guldberg, John M. Logsdon Jr & Dee A. Carter

Nature 451, 959–963 (2008)

In Fig. 2c of this Article, the GenBank accession number DQ174732 was incorrectly cited. The correct accession number is DQ174731 (*Chromera velia*).

ERRATUM

doi:10.1038/nature06872

Hax1-mediated processing of HtrA2 by Parl allows survival of lymphocytes and neurons

Jyh-Rong Chao, Evan Parganas, Kelli Boyd, Cheol Yi Hong, Joseph T. Opferman & James N. Ihle

Nature 452, 98–102 (2008)

In Fig. 1a of this Letter, the light blue line was incorrectly labelled as *Hax1/Bak* DKO, $n = 13$. The light blue line should be labelled *Hax1/Bax* DKO, $n = 13$.

ERRATUM

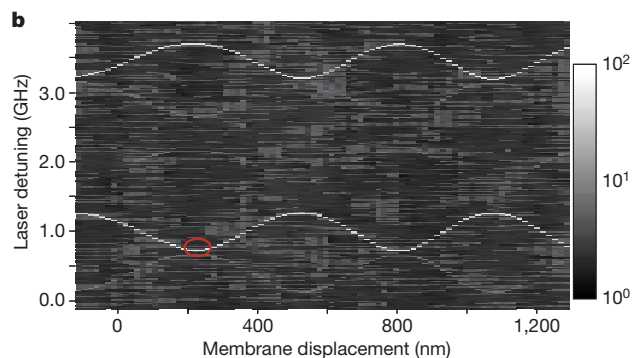
doi:10.1038/nature06898

Strong dispersive coupling of a high-finesse cavity to a micromechanical membrane

J. D. Thompson, B. M. Zwickl, A. M. Jayich, Florian Marquardt, S. M. Girvin & J. G. E. Harris

Nature 452, 72–72 (2008)

In the print and HTML versions of this Letter, Fig. 2b was printed incorrectly. The PDF version published online is correct. The corrected Fig. 2b is shown below.



CORRIGENDUM

doi:10.1038/nature06871

A photosynthetic alveolate closely related to apicomplexan parasites

Robert B. Moore, Miroslav Oborník, Jan Janouškovec, Tomáš Chrudimský, Marie Vancová, David H. Green, Simon W. Wright, Noel W. Davies, Christopher J. S. Bolch, Kirsten Heimann, Jan Šlapeta, Ove Hoegh-Guldberg, John M. Logsdon Jr & Dee A. Carter

Nature 451, 959–963 (2008)

In Fig. 2c of this Article, the GenBank accession number DQ174732 was incorrectly cited. The correct accession number is DQ174731 (*Chromera velia*).

ERRATUM

doi:10.1038/nature06872

Hax1-mediated processing of HtrA2 by Parl allows survival of lymphocytes and neurons

Jyh-Rong Chao, Evan Parganas, Kelli Boyd, Cheol Yi Hong, Joseph T. Opferman & James N. Ihle

Nature 452, 98–102 (2008)

In Fig. 1a of this Letter, the light blue line was incorrectly labelled as *Hax1/Bak* DKO, $n = 13$. The light blue line should be labelled *Hax1/Bax* DKO, $n = 13$.

ERRATUM

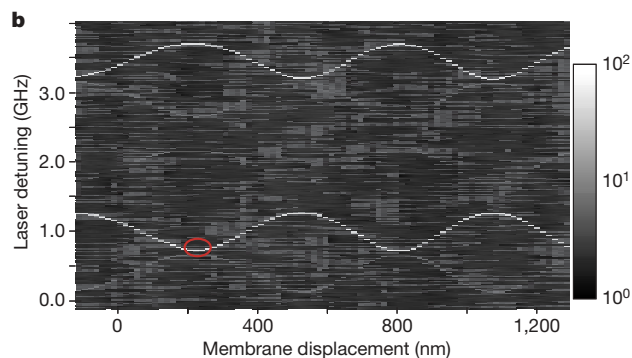
doi:10.1038/nature06898

Strong dispersive coupling of a high-finesse cavity to a micromechanical membrane

J. D. Thompson, B. M. Zwickl, A. M. Jayich, Florian Marquardt, S. M. Girvin & J. G. E. Harris

Nature 452, 72–72 (2008)

In the print and HTML versions of this Letter, Fig. 2b was printed incorrectly. The PDF version published online is correct. The corrected Fig. 2b is shown below.



Could it be a small world after all?

Sophisticated technologies can now explore nano-scale forces and interactions. But most biologists are staying on the sidelines, waiting to see if these technologies can really help them. Nathan Blow reports.

For years, biophysicists have been characterizing the small forces associated with cells and molecules using a variety of techniques born in the worlds of physics, chemistry and even materials science. They are pushing their instruments further in the attempt to measure molecular forces in the sub-piconewton range, and some biologists, at least, are becoming more interested in finding out the extent to which these forces have a role in biological processes.

"The more that the biological community thinks about the role of forces, the more likely it will be that these measurements are made," says Daniel Fletcher, a bioengineer at the University of California, Berkeley. But he adds that it is a real "chicken and egg" situation: how can you convince yourself that forces are important if you do not measure them, but if they are not important, why measure them?

"We need other biologists to use these techniques," says Carlos Bustamante, a biophysicist at the University of California, Berkeley. Bustamante has been developing and using 'optical traps' (which hold and manipulate molecules by means of small forces) for more than a decade as part of his work investigating the effects of very small forces on biomolecules. He thinks that if more biologists started to use these tools, the technology would move further, faster. There is consensus on one thing: techniques and instrumentation will have to become more robust and user-friendly if any wider adoption of these methods is going to take place.

One emerging trend that might pique the interest of biologists hesitant to explore the nanoscale world is the integration of different technologies. Whether it is combining Foerster resonance energy transfer (FRET) with optical traps or carbon nanotubes with atomic force microscopy (AFM) or even AFM with confocal microscopy, different tools are being integrated in an attempt to maximize our understanding of highly complex molecular interactions, while potentially providing novel insights into the world of the single molecule.

Microscopy by force

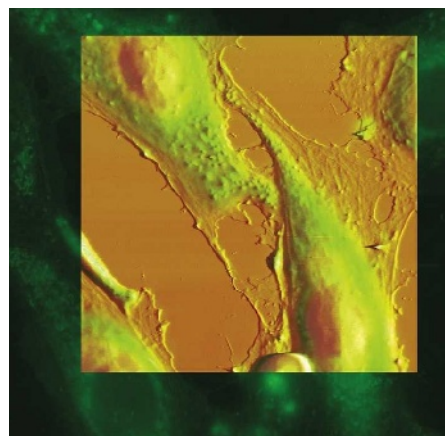
AFM, which was developed more than 20 years ago, has a resolution of a fraction of a nanometre — 1,000 times better than the optical diffraction limit. This resolution is achieved by scanning a sample with a cantilevered tip and measuring deflection of the cantilever with a laser to give topological information such as height, length and shape. Different in principle from optical microscopy, AFM's 'touch scanning' approach can image a surface and measure its associated forces at the same time.

AFM was first used in materials science and physics to examine surface properties of semiconductors for process-control applications. And although the interest of biophysicists in applying AFM to study cell surfaces and interactions between single molecules has resulted in advances in the technology, including new modes of scanning in liquids and with live cells, AFM is still a baby in the biology world. "It is relatively young in its development, but I see more and more cell biologists starting to explore the potential of AFM and similar methods to investigate the role and influence of mechanical properties," says Sebastian Tille, senior life sciences product marketing manager at Veeco Instruments in Woodbury, New York.

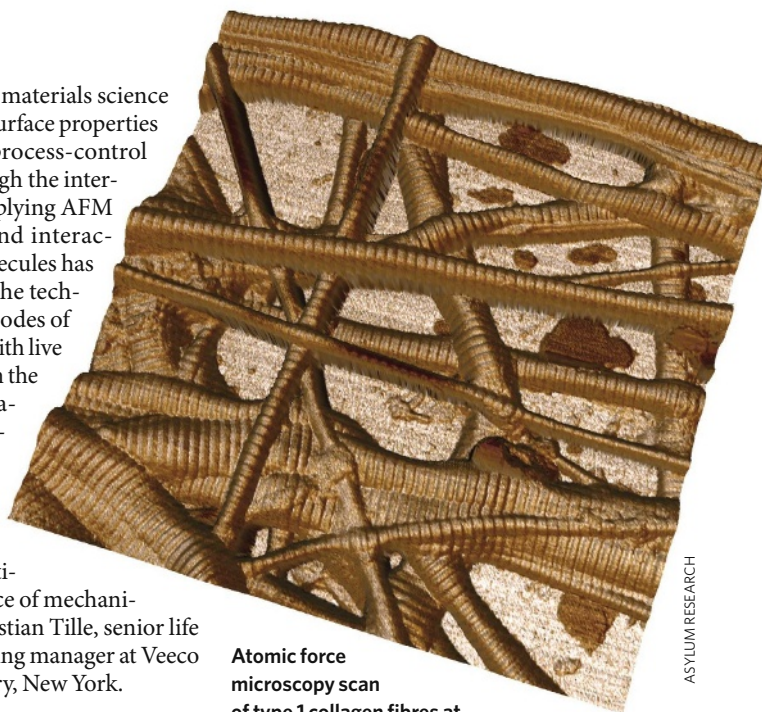
Hooke's law

The basis of AFM lies in Hooke's law of elasticity — a simple equation expressing the force generated within a spring when compressed in terms of a 'spring constant' and the length of the spring. Developers have been toying with this relationship for years in their efforts to improve the springs (or cantilevers) used in AFM.

"Cantilevers are essentially springs, typically 50–200 micrometres in length," says Roger Proksch, president of AFM specialists Asylum Research in Santa Barbara, California, "and when they are manufactured, there is a degree of uncertainty in their dimension." As the spring constant depends on these dimensions, this uncertainty can lead to measurement



Fluorescence image of live cells overlaid on an atomic force microscopy topographic image of the same cells.



Atomic force microscopy scan of type 1 collagen fibres at a resolution of 5 micrometres.

errors. Proksch says this makes spring calibration a crucial procedure for AFM users. In fact, last year he found more than ten new papers in the literature describing new methods of spring calibration or modifications to old methods.

What is needed is a way of getting an independent measure of the stiffness of the cantilever. "People are still trying to solve this problem in a better way, and getting this into a commercial instrument would be an important step forward," Proksch says.

Advances in the technology behind cantilevers have also enabled the use of AFM to measure forces in liquid samples. Tille notes the use of cantilevers in a 'tapping mode', where the cantilever oscillates across the sample while amplitude is monitored to keep the cantilever at a steady level compared with the surface. This has also helped AFM move towards different biological applications, he says. "It is a much more gentle method of exploring soft matter such as cells and single molecules," he says, compared with the 'contact mode' in which the tip is directly moved across the surface.

Future cantilever developments might also help to solve another issue facing AFM: speed. Imaging cells with AFM can be slow, taking up to 5 minutes or more to form the image. Developers say that speeding up this experience might entice more biologists to use AFM.

Proksch says that if the size of the current cantilevers can be reduced, the result would be faster motion and scan times. He provides

ASYLUM RESEARCH

VEECO INSTRUMENTS



Asylum Research's MFP-3D AFM system can be combined with different microscopy modes.

a simple analogy: imagine twanging a ruler hanging off the end of a desk, it vibrates at a certain frequency. Now if the ruler were shrunk by a factor of 1,000, the frequency of vibration would dramatically increase. "Today a cantilever in fluid has a resonance frequency of 5–50 kilohertz, we would like to see cantilevers that go from 500 kHz to 5 MHz," he says, noting that a smaller cantilever is something he expects to see in the very near future.

Length or, in the case of AFM, the distance from the cantilever tip to the surface, is the other part of Hooke's law and an issue that developers have worked hard on, notably by using piezoelectric materials to move AFM tips. "Piezo's are great: turn a knob, change the potential by a volt and you can move an ångström," says Proksch, who also notes that implementing the idea was no small feat. When the potential across the piezoelectric material is changed it will move an ångström as desired, but then in the next few minutes, or even seconds, it will move another ångström — a phenomenon known as creep. Researchers have attacked this problem and a related problem — hysteresis — in a number of ways, with some AFM developers, including Asylum, deciding to place sensors around the piezoelectric material to measure the creep directly. Fletcher says that with these sensors providing feedback as the tip moves over the surface, this form of drift has been largely eliminated — although his group has had to work through drift issues of its own (see 'When one cantilever is not enough').

Many of the advances that AFM developers are working on now involve moving the technology into the hands of biologists. Both Veeco and Asylum have started to combine optical and force microscopes in a single system. Tille notes that Veeco's BioScope II is compatible with advanced light microscopy modalities when the AFM is placed on the top of an inverted microscope.

"With registration between the optical image and the AFM tip, the user can select regions of interest to correlate fluorescence signals in cells with high-resolution topography," Tille says. In addition to Asylum and Veeco, other companies such as Park Systems in Santa Clara, California, and Novascan Technologies in Ames, Iowa, are exploring combining various optical microscopy techniques with AFM.

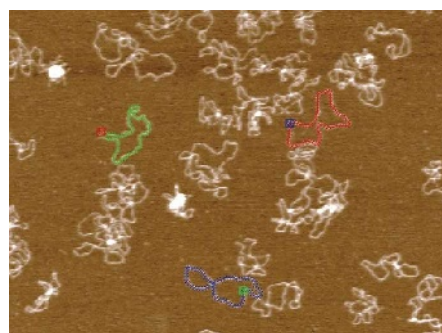
Feeling single-molecule interactions

"I think one of the most important advantages of AFM is that you can measure a structure's dynamics and function at the same time," says Peter Hinterdorfer, a biophysicist at the Institute for Biophysics at Johannes Kepler University in Linz, Austria.

Hinterdorfer's group has been exploring the molecular recognition of ligands and receptors by combining AFM with antibodies to simultaneously obtain cell topography and recognition images in a method the group calls TREC. "This is basically a counterpart to immunofluorescence in which we try to localize receptors," explains Hinterdorfer. The AFM tip is functionalized by attaching antibodies and then is brought into contact with the cell membrane. The binding between ligand and receptor can be measured, while obtaining topographical information at the same time.

Hinterdorfer is quick to point out that the advantage of AFM for TREC, compared with other optical techniques, is its higher lateral resolution, which can be combined with the ability to obtain mechanical parameters of the cell surface. Although his group developed TREC several years ago, most of the work has been done with either model systems with membrane preparations or fixed cells. "For single cells there is a lot more to do, because at the moment we are used to TREC on fixed cells, but we are working on live cells as well," says Hinterdorfer, adding that as high-speed AFM is improved, he expects to see more work following physiological processes in living cells using methods such as TREC.

Whereas Hinterdorfer and others use AFM to measure interactions between individual molecules, other groups are trying to visualize such interactions. Some groups are investigating carbon nanotubes as sensors. "Our interest in carbon nanotubes for biological applications is mainly as optical



AFM software offers the ability to outline the contours of individual molecules.

diagnostics," says Michael Strano, a chemical engineer at the Massachusetts Institute of Technology in Cambridge. "Carbon nanotubes can tell you about the chemical environment of a very small region of space," he says, and they have optical properties that make them unique for sensor applications (see 'Shrinking down gas chromatography').

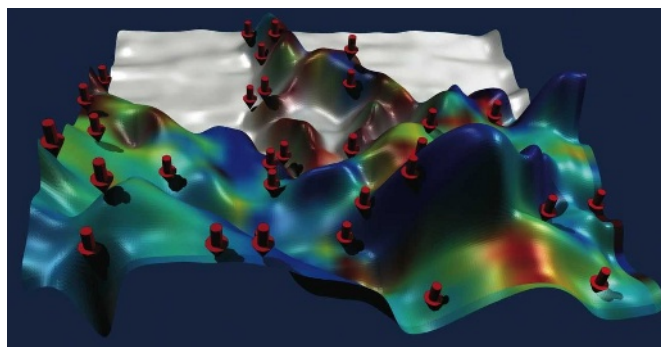
Carbon nanotubes can emit light in the near infrared, which eliminates issues of background fluorescence as this is a part of the spectrum in which very few biological systems autofluoresce. In addition, unlike dyes, or even quantum dots, which can photobleach over time, carbon nanotubes are extremely photostable, allowing measurement of fluorescence changes to obtain molecular-level information.

Strano and his group have spent a lot of time working out how to get carbon nanotubes into living cells and to understand how and why, once inside, they move around. Using single-particle tracking methods, they recently showed that the nanotubes can either diffuse around the cell in a confined pattern or be actively transported. "We are systematically studying these complex behaviours," says Strano, "it is going to take some effort to sort out and ultimately learn to control them."

Strano's team and others are interested in the application of carbon nanotubes as optical sensors to detect single-molecule binding events. "Our lab has recently demonstrated that we can detect biologically important molecules binding to nanotubes at the single-molecule level in real time," says Strano. The one-dimensional electronic property of carbon nanotubes means high electron density at a very narrow region of energy. One result of this property is that when

a carbon nanotube absorbs a particular photon, the absorbance has a very sharp maximum. This allows a single carbon nanotube to be visualized with spectroscopy, and also gives researchers the opportunity to see if a nanotube responds to a biomolecule in a single-molecule association event.

"We have few tools to study analyte fluxes at very low concentration levels," notes Strano. His idea is to use carbon nanotubes as local amplifiers of a single interaction



Interaction map of the surface of a HeLa cell using functionalized AFM.

event, because the event disproportionately affects the nanotube properties and the nanotube has such a large optical cross-section. Other groups are exploring different technologies to detect single-molecule interactions.

Taekjip Ha is a physicist from the University of Illinois at Urbana-Champaign who has been developing fluorescence resonance energy transfer (FRET) approaches for studying single-molecule interactions. "It took several years to convince ourselves that this technique was going to be very useful to obtain biophysical and biological measurements," says Ha.

Although some studies using single-molecule FRET have been done in living cells, the vast majority of experiments have been *in vitro*. "This is due to technical limitations," says Ha, "the probes are not bright enough for robust measurements in living cells." But he does think that the use of quantum dots could enable the more widespread use of single-molecule FRET in living cells — with one small change. "It is currently difficult to do a single-molecule

FRET experiment using quantum dots because those made commercially are too big."

A quantum dot plus its coating, which is needed to solubilize the dot and conjugate to a biomolecule, can easily be more than 20 nanometres in diameter — much larger than the 10 nanometres maximum separation required for a FRET experiment. Ha thinks that single-molecule FRET in living cells will have to wait until the next generation of quantum dots. He thinks this is only a matter of time, as he sees no reason why quantum dots cannot be made smaller.

Setting the trap

"The area of single-molecule manipulation goes back to 1991," recalls Bustamante. "At that time we did an experiment using gravity and the weight of little beads to extend the DNA." Bustamante and others soon turned their attention from beads and gravity to a more sophisticated technique called 'optical tweezers', developed by Stephen Chu, currently at University of California, Berkeley, and Arthur Ashkin,

now retired from Bell Labs and Lucent Technologies. This technique can trap and manipulate molecules with diameters of nanometres.

Optical tweezers make use of a focused laser beam to trap and hold dielectric objects. Developed in the late 1980s and used extensively in the 1990s, researchers only recently started to see a need for even higher-resolution optical tweezer systems. "I think during that earlier time our objective was to be able to follow and extend molecular motors, see molecules unfold and measure the mechanical properties of nucleic acids," says Bustamante, "and you could do quite a bit of research without going into extremely high resolution." But today, Bustamante thinks the biology has actually pulled biophysicists towards studying things at a smaller scale — requiring more stability, less drift, more spatial resolution and improved temporal resolution from optical tweezers.

For high-resolution optical tweezers to work, the key issue of drift had to be overcome. One approach, developed by Steven Block's group

WHEN ONE CANTILEVER IS NOT ENOUGH

"I did my doctoral work building force and optical microscopy systems," says Daniel Fletcher, a bioengineer at the University of California, Berkeley. "I was an instrument developer and did not really get to use them, as the main goal was always to develop a new contrast mechanism or achieve the best resolution." But all that changed when Fletcher started his postdoc training and saw cells crawling.

"I realized that although we could build these fancy instruments that control forces down to the piconewton level or below, we had no clue how to assemble complex molecular systems that do what the crawling cells could do." This led Fletcher to study the dynamic actin networks of crawling cells using atomic force microscopy (AFM) and optical traps.

The biochemistry of the actin system has been studied for more than 20 years and actin networks can be grown *in vitro*, which provides the opportunity to directly probe how network assembly is

involved in force generation and shape-changes in cells. "What we have been trying to do with both AFM and optical traps is to create a controlled resistance to the growth of these networks and study their behaviour," he says. One approach that Fletcher's group uses is to grow actin networks on the ends of its AFM cantilever and then monitor how the networks adapt to different loads and how those forces influence the architecture of the structures generated.

Using AFM in this manner provided a challenge, requiring Fletcher to use his instrument-development skills. "One of the things that AFM is not good at doing is measuring sustained displacement over long time periods, because the surface can drift relative to the cantilever,"

says Fletcher.

Cantilevers are not directly connected to the surface being scanned — they are held by a fluid cell, held by a mount, which is connected to a moving stage that is connected through an even longer path to the surface. The distance between cantilever and surface helps to make crucial calculations of the extent of deflection of the cantilever by the surface. Fletcher explains that because of this large mechanical path from the surface to the cantilever, which can alter the reference position of the cantilever relative to the surface due to thermal drift, the forces measured over time can change even if the sample does not. At short time scales this might not be an issue, but for his team, trying to measure actin growth continuously on the microscope tip over hours, drift of this sort can potentially influence the data collected.

Fletcher decided that one approach to correcting for this drift would be a dual cantilever

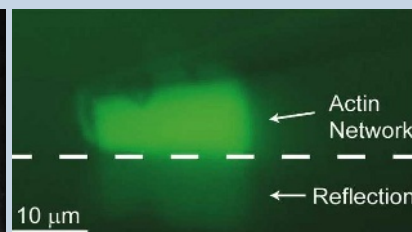
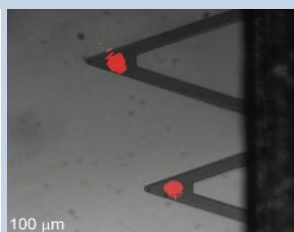
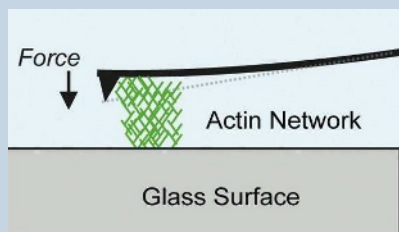
AFM system. Having two adjacent cantilevers allows one cantilever to always be in contact with the surface while the second measures the growth of the actin networks. Fletcher says that by always having one cantilever on the surface, they can now detect movement or drift directly and use feedback to correct the cantilever's position.

Fletcher continues to develop new approaches to making force measurements. His team recently developed an epi-fluorescence 'side-view' AFM device (most commercial systems come with the AFM system mounted on top of a microscope) to visualize growing actin networks between the cantilever and the surface. "Where people interested in single-, or even multimolecule, biophysics can continue to make contributions is in developing better tools that help to overcome the limitations of existing technologies and reveal new behaviour of biological systems."

N.B.



Daniel Fletcher studies actin networks using atomic force microscopy.



Side-view AFM (left) and the two-cantilever approach (centre) for studying actin-network growth.

D. FLETCHER, S. PAREKH & O. CHAUDHURI, UNIV. CALIFORNIA, BERKELEY

at Stanford University, California, is to attach a molecule to two beads and use two optical tweezers, neither of which is physically attached to the lab environment, to hold the molecule. Bustamante's group recently added another element to this approach — the use of a single laser beam that splits into the two optical tweezers, to control for variation in laser light by providing feedback on both traps (J. R. Moffitt *et al. Proc. Natl Acad. Sci. USA* **103**, 9006–9011; 2006).

Companies are eyeing the area of optical tweezers seriously. Carl Zeiss in Jena, Germany now offers the Palm Micro Tweezers that use either a red or near infrared laser that can be split into two independent traps. Arryx, in Chicago, Illinois, has taken a different approach for its optical-tweezer technology, called BioRyx 200, which is a holographic optical trap created from a spatial light modulator and allows the control of up to 200 objects simultaneously.

Ha is starting to combine optical tweezers with single-molecule FRET to study the enzymes involved in transcription and translation.



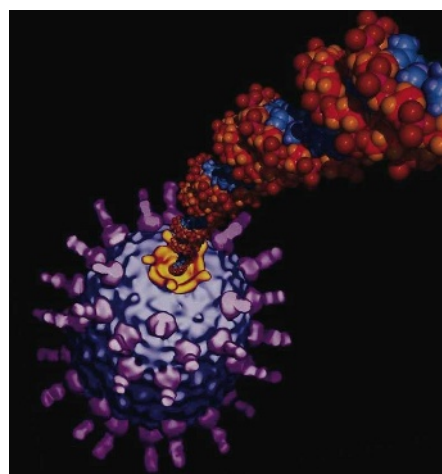
Carlos Bustamante would like to see a wider adoption of techniques to study single molecules.

He thinks that the combination of these techniques is necessary as single-molecule research moves towards studying more complex properties of enzymes and proteins. "It is now possible to measure the fundamental reaction steps of the enzymes using optical traps to obtain single base pair resolution," says Ha, but he adds that using FRET allows conformational changes of the enzymes themselves to be monitored at the same time. This combination allowed Ha's team to directly measure via fluorescence conformational changes as a function of applied force to dissect the landscape of the Holliday junction — a mobile junction between four strands of DNA (S. T. Hohng *et al. Science* **318**, 279–283; 2007).

Added colour

Ha is moving into three-colour FRET with optical traps to get more information from each experiment. Whereas two-colour FRET can measure one distance, multiple-colour FRET will provide additional distance information from each experiment. Ha is using three-colour FRET (one donor and two acceptors) to study the diffusion of protein on single-stranded DNA and the enzymatic activity of the ribosome.

Bustamante is also excited about the possibility of using FRET with optical tweezers. "The bottom line is that it will allow you to follow a particular biological process in a multi-dimensional fashion," he says. His lab has built a prototype optical trap, called 'minitweezers', that will incorporate fluorescence. With this, the team hopes to bring together the whole optical table into an instrument the size of two



Schematic representation of a molecule attached to a bead within an optical trap.

coffee cans, Bustamante says.

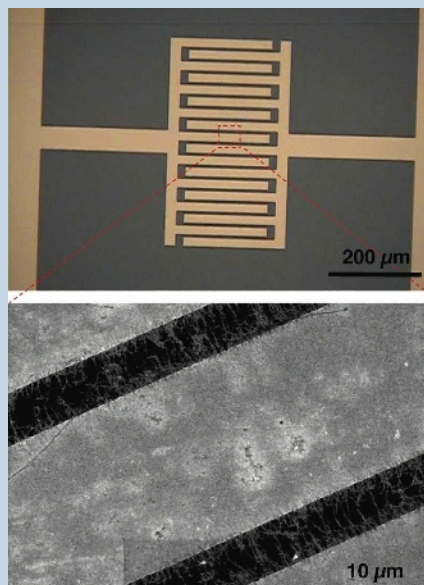
Measurements of force and interaction at the single-molecule level are being reported with increased frequency. And there is interest from the wider biological community: at the 2007 meeting of the American Society for Cell Biology there was a session focused on the analysis of mechanical forces. "It was pretty amazing to see a ballroom of more than a thousand people listening to talks on the significance of mechanical properties of cells," Tille says. And with developers actively trying to engage biologists while continuing to advance the power of these technologies, one has to wonder how many more will be listening next year.

Nathan Blow is technology editor for *Nature* and *Nature Methods*.

SHRINKING DOWN GAS CHROMATOGRAPHY

Imagine looking down at your watch to check the time, while the same watch performs chromatography to determine the chemical composition of the air around you. Although unlikely to be in the shops any time soon, recent advances in carbon nanotube technology and surface chemistry could make very small gas-chromatography devices a future reality.

Michael Strano's group at the Massachusetts Institute of Technology in Cambridge has been developing a highly sensitive, miniaturized gas-chromatography instrument based on carbon nanotubes. Sensitivity was key for this device, Strano wanted to be able to detect analytes in the part-per-trillion range — an amount so small it can be difficult to grasp at first. "This is like opening a small vial in a crowded high-school gymnasium,"



Micro-GC nanotube sensor array (above); close up of a nanotube with array (below).

explains Strano, "even if you open the vial and shut it quickly, you

have actually released hundreds of parts per trillion of this mixture everywhere."

For the backbone of its new gas-chromatography instrument, Strano's group created single-walled nanotube, chemi-resistor arrays in which the nanotubes were aligned between electrodes.

Changes in the electrical resistance can be analysed as a desired molecule binds the nanotube. To tune the binding of the analyte to the arrays the group also had to develop a new chemistry (C. Y. Lee and M. S. Strano *J. Am. Chem. Soc.* **130**, 1766–1773;

2008). "You can use mean basicity to target whether your molecules

will bind very strongly, in between, or not at all," explains Strano. Then using a microelectromechanical systems device it should be possible to have precise control over which molecules bind to the array.

As a proof-of-principle, Strano's group created a very simple device by etching a chromatography column on a chip. Using a 100-micrometre trench the team showed that mixtures can be separated and, using a fast detector, it is possible to transduce each peak as it comes out.

Strano group's demonstrated parts-per-trillion detection on its device, confirming the potential of this approach to miniaturized, on-chip gas chromatography. And for Strano, seeing an actual physical device working at that level was extremely rewarding. "We are engineers, so we try to make devices that work."

N.B.

event, because the event disproportionately affects the nanotube properties and the nanotube has such a large optical cross-section. Other groups are exploring different technologies to detect single-molecule interactions.

Taekjip Ha is a physicist from the University of Illinois at Urbana-Champaign who has been developing fluorescence resonance energy transfer (FRET) approaches for studying single-molecule interactions. "It took several years to convince ourselves that this technique was going to be very useful to obtain biophysical and biological measurements," says Ha.

Although some studies using single-molecule FRET have been done in living cells, the vast majority of experiments have been *in vitro*. "This is due to technical limitations," says Ha, "the probes are not bright enough for robust measurements in living cells." But he does think that the use of quantum dots could enable the more widespread use of single-molecule FRET in living cells — with one small change. "It is currently difficult to do a single-molecule

FRET experiment using quantum dots because those made commercially are too big."

A quantum dot plus its coating, which is needed to solubilize the dot and conjugate to a biomolecule, can easily be more than 20 nanometres in diameter — much larger than the 10 nanometres maximum separation required for a FRET experiment. Ha thinks that single-molecule FRET in living cells will have to wait until the next generation of quantum dots. He thinks this is only a matter of time, as he sees no reason why quantum dots cannot be made smaller.

Setting the trap

"The area of single-molecule manipulation goes back to 1991," recalls Bustamante. "At that time we did an experiment using gravity and the weight of little beads to extend the DNA." Bustamante and others soon turned their attention from beads and gravity to a more sophisticated technique called 'optical tweezers', developed by Stephen Chu, currently at University of California, Berkeley, and Arthur Ashkin,

now retired from Bell Labs and Lucent Technologies. This technique can trap and manipulate molecules with diameters of nanometres.

Optical tweezers make use of a focused laser beam to trap and hold dielectric objects. Developed in the late 1980s and used extensively in the 1990s, researchers only recently started to see a need for even higher-resolution optical tweezer systems. "I think during that earlier time our objective was to be able to follow and extend molecular motors, see molecules unfold and measure the mechanical properties of nucleic acids," says Bustamante, "and you could do quite a bit of research without going into extremely high resolution." But today, Bustamante thinks the biology has actually pulled biophysicists towards studying things at a smaller scale — requiring more stability, less drift, more spatial resolution and improved temporal resolution from optical tweezers.

For high-resolution optical tweezers to work, the key issue of drift had to be overcome. One approach, developed by Steven Block's group

WHEN ONE CANTILEVER IS NOT ENOUGH

"I did my doctoral work building force and optical microscopy systems," says Daniel Fletcher, a bioengineer at the University of California, Berkeley. "I was an instrument developer and did not really get to use them, as the main goal was always to develop a new contrast mechanism or achieve the best resolution." But all that changed when Fletcher started his postdoc training and saw cells crawling.

"I realized that although we could build these fancy instruments that control forces down to the piconewton level or below, we had no clue how to assemble complex molecular systems that do what the crawling cells could do." This led Fletcher to study the dynamic actin networks of crawling cells using atomic force microscopy (AFM) and optical traps.

The biochemistry of the actin system has been studied for more than 20 years and actin networks can be grown *in vitro*, which provides the opportunity to directly probe how network assembly is

involved in force generation and shape-changes in cells. "What we have been trying to do with both AFM and optical traps is to create a controlled resistance to the growth of these networks and study their behaviour," he says. One approach that Fletcher's group uses is to grow actin networks on the ends of its AFM cantilever and then monitor how the networks adapt to different loads and how those forces influence the architecture of the structures generated.

Using AFM in this manner provided a challenge, requiring Fletcher to use his instrument-development skills. "One of the things that AFM is not good at doing is measuring sustained displacement over long time periods, because the surface can drift relative to the cantilever,"

says Fletcher.

Cantilevers are not directly connected to the surface being scanned — they are held by a fluid cell, held by a mount, which is connected to a moving stage that is connected through an even longer path to the surface. The distance between cantilever and surface helps to make crucial calculations of the extent of deflection of the cantilever by the surface. Fletcher explains that because of this large mechanical path from the surface to the cantilever, which can alter the reference position of the cantilever relative to the surface due to thermal drift, the forces measured over time can change even if the sample does not. At short time scales this might not be an issue, but for his team, trying to measure actin growth continuously on the microscope tip over hours, drift of this sort can potentially influence the data collected.

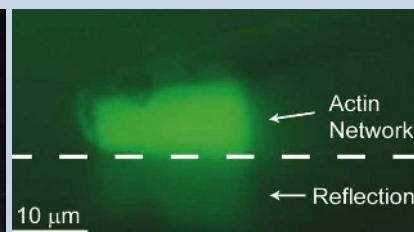
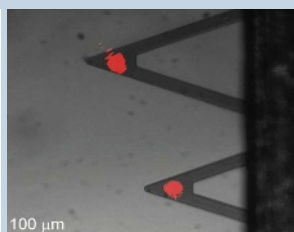
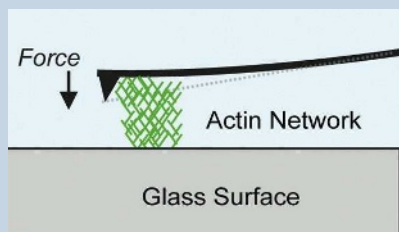
Fletcher decided that one approach to correcting for this drift would be a dual cantilever

AFM system. Having two adjacent cantilevers allows one cantilever to always be in contact with the surface while the second measures the growth of the actin networks. Fletcher says that by always having one cantilever on the surface, they can now detect movement or drift directly and use feedback to correct the cantilever's position.

Fletcher continues to develop new approaches to making force measurements. His team recently developed an epi-fluorescence 'side-view' AFM device (most commercial systems come with the AFM system mounted on top of a microscope) to visualize growing actin networks between the cantilever and the surface. "Where people interested in single-, or even multimolecule, biophysics can continue to make contributions is in developing better tools that help to overcome the limitations of existing technologies and reveal new behaviour of biological systems." N.B.



Daniel Fletcher studies actin networks using atomic force microscopy.



Side-view AFM (left) and the two-cantilever approach (centre) for studying actin-network growth.

at Stanford University, California, is to attach a molecule to two beads and use two optical tweezers, neither of which is physically attached to the lab environment, to hold the molecule. Bustamante's group recently added another element to this approach — the use of a single laser beam that splits into the two optical tweezers, to control for variation in laser light by providing feedback on both traps (J. R. Moffitt *et al. Proc. Natl Acad. Sci. USA* **103**, 9006–9011; 2006).

Companies are eyeing the area of optical tweezers seriously. Carl Zeiss in Jena, Germany now offers the Palm Micro Tweezers that use either a red or near infrared laser that can be split into two independent traps. Arryx, in Chicago, Illinois, has taken a different approach for its optical-tweezer technology, called BioRyx 200, which is a holographic optical trap created from a spatial light modulator and allows the control of up to 200 objects simultaneously.

Ha is starting to combine optical tweezers with single-molecule FRET to study the enzymes involved in transcription and translation.



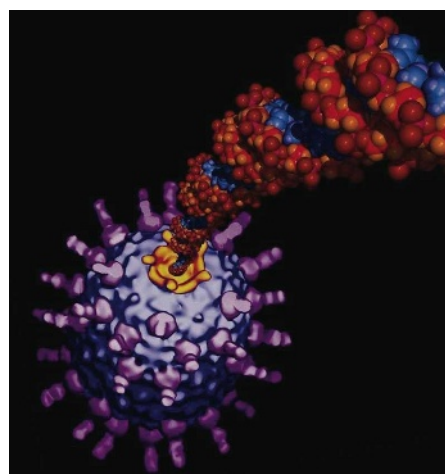
Carlos Bustamante would like to see a wider adoption of techniques to study single molecules.

He thinks that the combination of these techniques is necessary as single-molecule research moves towards studying more complex properties of enzymes and proteins. "It is now possible to measure the fundamental reaction steps of the enzymes using optical traps to obtain single base pair resolution," says Ha, but he adds that using FRET allows conformational changes of the enzymes themselves to be monitored at the same time. This combination allowed Ha's team to directly measure via fluorescence conformational changes as a function of applied force to dissect the landscape of the Holliday junction — a mobile junction between four strands of DNA (S. T. Hohng *et al. Science* **318**, 279–283; 2007).

Added colour

Ha is moving into three-colour FRET with optical traps to get more information from each experiment. Whereas two-colour FRET can measure one distance, multiple-colour FRET will provide additional distance information from each experiment. Ha is using three-colour FRET (one donor and two acceptors) to study the diffusion of protein on single-stranded DNA and the enzymatic activity of the ribosome.

Bustamante is also excited about the possibility of using FRET with optical tweezers. "The bottom line is that it will allow you to follow a particular biological process in a multi-dimensional fashion," he says. His lab has built a prototype optical trap, called 'minitweezers', that will incorporate fluorescence. With this, the team hopes to bring together the whole optical table into an instrument the size of two



Schematic representation of a molecule attached to a bead within an optical trap.

coffee cans, Bustamante says.

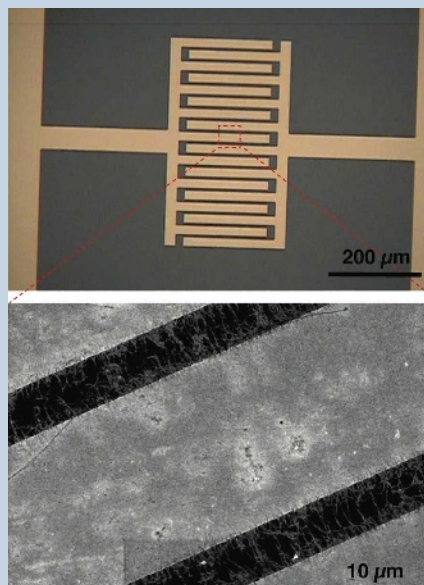
Measurements of force and interaction at the single-molecule level are being reported with increased frequency. And there is interest from the wider biological community: at the 2007 meeting of the American Society for Cell Biology there was a session focused on the analysis of mechanical forces. "It was pretty amazing to see a ballroom of more than a thousand people listening to talks on the significance of mechanical properties of cells," Tille says. And with developers actively trying to engage biologists while continuing to advance the power of these technologies, one has to wonder how many more will be listening next year.

Nathan Blow is technology editor for *Nature* and *Nature Methods*.

SHRINKING DOWN GAS CHROMATOGRAPHY

Imagine looking down at your watch to check the time, while the same watch performs chromatography to determine the chemical composition of the air around you. Although unlikely to be in the shops any time soon, recent advances in carbon nanotube technology and surface chemistry could make very small gas-chromatography devices a future reality.

Michael Strano's group at the Massachusetts Institute of Technology in Cambridge has been developing a highly sensitive, miniaturized gas-chromatography instrument based on carbon nanotubes. Sensitivity was key for this device, Strano wanted to be able to detect analytes in the part-per-trillion range — an amount so small it can be difficult to grasp at first. "This is like opening a small vial in a crowded high-school gymnasium,"



Micro-GC nanotube sensor array (above); close up of a nanotube with array (below).

explains Strano, "even if you open the vial and shut it quickly, you

have actually released hundreds of parts per trillion of this mixture everywhere."

For the backbone of its new gas-chromatography instrument, Strano's group created single-walled nanotube, chemi-resistor arrays in which the nanotubes were aligned between electrodes.

Changes in the electrical resistance can be analysed as a desired molecule binds the nanotube. To tune the binding of the analyte to the arrays the group also had to develop a new chemistry (C. Y. Lee and M. S. Strano *J. Am. Chem. Soc.* **130**, 1766–1773;

2008). "You can use mean basicity to target whether your molecules

will bind very strongly, in between, or not at all," explains Strano. Then using a microelectromechanical systems device it should be possible to have precise control over which molecules bind to the array.

As a proof-of-principle, Strano's group created a very simple device by etching a chromatography column on a chip. Using a 100-micrometre trench the team showed that mixtures can be separated and, using a fast detector, it is possible to transduce each peak as it comes out.

Strano group's demonstrated parts-per-trillion detection on its device, confirming the potential of this approach to miniaturized, on-chip gas chromatography. And for Strano, seeing an actual physical device working at that level was extremely rewarding. "We are engineers, so we try to make devices that work."

N.B.

COMPANY	PRODUCTS/ACTIVITY	LOCATION	URL
Atomic force microscopy instruments and accessories			
Agilent Technologies	Atomic force microscopy (AFM) instruments, along with other instrumentation for genomics and proteomics research	Santa Clara, California	www.agilent.com
Asylum Research	MFP-3D family of AFM instruments for biological and material-sciences applications; integrated optical and force microscopy systems	Santa Barbara, California	www.asylumresearch.com
Impact Analytical	Provider of contract AFM services to researchers	Midland, Michigan	www.impactanalytical.com
Nanonics Imaging	Combination SEM and AFM in one instrument; AFM probes and accessories; low-temperature AFM and Raman spectroscopy AFM instrumentation	Jerusalem Israel	www.nanonics.co.il
Nanoscience Instruments	AFM systems, probes and accessories; Nanosurf AFM systems; vibration isolation tables	Phoenix, Arizona	www.nanoscience.com
Novascan Technologies	AFM instruments, tips and probes with particles, microspheres and beads	Ames, Iowa	www.novascan.com
nPoint	Manufactures precision motion and control devices for nanoscale research and manufacturing applications	Madison, Wisconsin	www.npoint.com
Omicron NanoTechnology	AFM instruments and accessories	Taunusstein, Germany	www.omicron-instruments.com
Park Systems	AFM instruments for biological, semiconductor and polymer-science applications	Santa Clara, California	www.parkafm.com
Physik Instrumente	Piezoelectric materials, nanopositioning and scanning stages, and micropositioning products	Palmbach, Germany	www.physikinstrumente.com
PolyInsight	AFM services provider for surface analysis	Akron, Ohio	www.polyinsight.com
SP Magic	AFM controllers for accurate imaging and data acquisition; cantilevers	Marciana, Italy	www.spmagic.com
Veeco Instruments	AFM and SFM instruments, controllers, accessories and applications; automated AFM; AFM with integrated optical microscopy	Woodbury, New York	www.veeco.com
Optical traps/tweezers and accessories			
Arryx	BioRxy 200 holographic optical trap; software and accessories for optical traps	Chicago, Illinois	www.arryx.com
Elliot Scientific	Standard and custom-designed optical-tweezer systems	Hertfordshire, UK	www.elliotscientific.com
Lightspeed Technologies	Complete optical-tweezer systems, accessories for tweezer applications	Campbell, California	www.light-speed-tech.com
PALM/Carl Zeiss	Optical tweezers and dissection systems	Jena, Germany	www.zeiss.com
Cell imaging and sorting			
Cytanome	High-speed optical cell sorting	Boston, Massachusetts	www.cytanome.com
Dako USA	Automated cellular imaging, fluorescent-activated cell-sorting instruments and kits	Carpinteria, California	www.dakousa.com
Hamamatsu	Imaging systems	Hamamatsu City, Japan	www.hamamatsu.com
Improvision	Three-dimensional imaging software	Coventry, UK	www.improvision.com
Leica Microsystems	Light microscopes, stereomicroscopes and confocal microscopes; software for use in image analysis	Wetzlar, Germany	www.leica-microsystems.com
Intracellular Imaging	Digital fluorescence imaging and photometry systems	Cincinnati, Ohio	www.intracellular.com
Mauna Kea Technologies	Miniaturized fluorescence confocal microscopy system for <i>in vivo</i> intratissue imaging	Paris, France	www.maunakeatech.com
Micro Video Instruments	Microscopes and accessories	Avon, Massachusetts	www.mvi-inc.com
MMI Molecular Machines and Industries	Equipment for micromanipulation and microdissection	Heidelberg, Germany	www.molecular-machines.com
Nanoptek	Digital tunnelling microscopes	Concord, Massachusetts	www.nanoptek.com
Nikon	Imaging solutions, microscopes, objectives, digital cameras, imaging software and analysis tools	Melville, New York	www.nikoninstruments.com
Olympus America	Microscopes and imaging systems; digital imaging; <i>in vivo</i> imaging solutions	Center Valley, Pennsylvania	www.olympusamerica.com
Omega Optical	Optical filters and coatings for imaging; custom filters	Brattleboro, Vermont	www.omegafilters.com
Optronics	Digital cameras for microscopes; image-analysis software	Goleta, California	www.optronics.com
Princeton Instruments	Equipment for imaging and spectroscopy	Trenton, New Jersey	www.princetoninstruments.com
Semrock	Optical filters for microscopy applications	Rochester, New York	www.semrock.com

COMPANY	PRODUCTS/ACTIVITY	LOCATION	URL
General			
Applied Biophysics	Automated instruments for cell monitoring and electric cell-substrate impedance sensing	Troy, New York	www.biophysics.com
Alexis Biochemicals	Suppliers of reagents for molecular- and cell-biology research	Lausanne, Switzerland	www.alexis-corp.com
Andor Technology	Microscopy, chemiluminescent kits, single molecule detection, cameras and imaging solutions for FRET experiments, and total internal reflectance microscopy systems	Belfast, Northern Ireland	www.andor.com
Beckman Coulter	Automated tools for genomics and proteomics research	Fullerton, California	www.beckmancoulter.com
BioFlow Technology	Bioreactor systems for the culturing of cells in a three-dimensional environment	Novi, Michigan	www.bioflowtech.com
Biomol	Services for chemical synthesis, cell culture and antibody production	Hamburg, Germany	www.biomol.de
Bio-Rad	Products, instruments and software for life-sciences research	Hercules, California	www.bio-rad.com
BMG Labtechnologies	Microplate and array readers and handling systems	Offenburg, Germany	www.bmglabtech.com
Brinkmann Instruments	Laboratory instrument supplier; consumables	Westbury, New York	www.brinkmann.com
Cambrex	Products for molecular- and cell-biology research	East Rutherford, New Jersey	www.cambrex.com
EMD Biosciences	Calbiochem, Novabiochem and Novagen product lines	San Diego, California	www.emdbiosciences.com
Enzo Life Sciences	Consumables and reagents for molecular biology, gene-expression and genomic analysis	New York	www.enzo.com
Eppendorf	Consumables for molecular biology; instrumentation	Hamburg, Germany	www.eppendorf.com
EUGENEX Biotechnologies	Development of test cell lines	Taegerwilen, Switzerland	www.eugenex.com
Geneservice	Genomic and proteomic resources including DNA samples, cDNA and genomic libraries; contract services including DNA sequencing, microarray analysis and SNP genotyping	Cambridge, UK	www.geneservice.co.uk
Gilson	Pipettes, automated liquid-handling, liquid chromatography systems and software	Middleton, Wisconsin	www.gilson.com
Hamilton Company	Automated liquid-handling stations	Reno, Nevada	www.hamiltoncompany.com
Harvard Apparatus	Instruments and equipment for electrophysiology and cell biology	Holliston, Massachusetts	www.harvardapparatus.com
Horiba Jobin Yvon	Spectroscopy systems and accessories including Raman, atomic emission and UV spectroscopy	Edison, New Jersey	www.jobinyvon.com
Integra Biosciences	Equipment for sterilization, liquid handling, cell culture and sample storage	Baar, Switzerland	www.integra-biosciences.com
Invitrogen	Kits and reagents for molecular-biology research; fluorescent probes for FRET experiments	Carlsbad, California	www.invitrogen.com
Irvine Scientific	Defined media for cell-culture applications; custom media services	Santa Ana, California	www.irvinesci.com
Merck	Chemicals, kits and reagents for molecular- and cell-biology-related research	Darmstadt, Germany	www.merck.de
Molecular Devices	Liquid-handling and microplate-processing equipment; imaging instruments	Sunnyvale, California	www.moleculardevices.com
MP Biomedicals	Reagents and chemicals for research	Aurora, Ohio	www.mpbio.com
Nalge Nunc International	Labware	Rochester, New York	www.nalgenunc.com
New England Biolabs	Molecular-biology-related reagents, kits and enzymes	Ipswich, Massachusetts	www.neb.com
Opticell	Automated cell-culture devices	Westerville, Ohio	www.opticell.com
Perkin Elmer Life Sciences	Instruments, reagents and kits for life-sciences research	Waltham, Massachusetts	las.perkinelmer.com
Pierce Chemical	Protein assays, purification, western blotting	Rockford, Illinois	www.piercenet.com
Premier Biosoft	Software for life-sciences research	Palo Alto, California	www.premierbiosoft.com
Roche Diagnostics	Reagents and kits for molecular biology; genomics instrumentations and software	Lewes, UK	www.roche-applied-science.com
SeqWright	Contract services in genomics including next-generation DNA sequencing, microarray analysis, and qPCR	Houston, Texas	www.seqwright.com
Stratagene	Tools and reagents for molecular biology, genomics and proteomics research	La Jolla, California	www.stratagene.com
Takara Bio	Reagents, kits and consumables for molecular biology	Shiga, Japan	www.takara-bio.com
Tocris Cookson	Chemicals for life-science research; contract research services	Avonmouth, UK	www.tocris.com
Wako USA	Speciality chemicals supplier; clinical diagnostic reagents	Richmond, Virginia	www.wakousa.com
USB	Chemicals and reagents for molecular biology	Cleveland, Ohio	www.usweb.com

● see advertisement

naturejobs

**JOBS OF
THE WEEK**

It starts with a panic attack in the middle of the night. You realize that spending your days pipetting — or collecting soil samples or mixing solutions or sorting through reams of data related to the collision of atomic particles — might not be for you. Perhaps the slow pace of your research irks you; perhaps you are more fascinated by the 'bigger picture'. Perhaps, you realize while in that strange place between sleep and wakefulness, a more 'unconventional' science career is in order.

Shobita Parthasarathy recounted how she went about pursuing a 'big-picture' career at a graduate conference on careers in science and technology in Washington DC on 5 April. She considered a career in research, but decided to do a PhD in science and technology studies at Cornell University in Ithaca, New York. It is a niche field, focusing on analysis of the social and political aspects of research and innovation. She went on to become an assistant professor of public policy at the University of Michigan, where she also co-directs the university's certificate programme in science, technology and society.

There is an incredible and ever-expanding range of opportunities open to intelligent people with a desire to branch out beyond the traditional disciplines. But how can a fledgling science specialist find these various career niches, large and small?

We hope that Naturejobs is a valuable source of information and insight for those looking for their first science job, contemplating career changes or just monitoring career trends. And to develop that role we would like your input: What sort of career insights are you looking for? What stories do you find informative and enjoyable? Let us know by filling out a brief readership survey that will help reshape our section: it's available at <http://tinyurl.com/6c6hmy>. As an incentive, two randomly selected respondents will receive online gift certificates.

We will continue to provide scientist job-seekers and others with analysis, advice and stories of career rebirth. Maybe we will even help some of you sleep a bit easier.

Gene Russo is editor of Naturejobs.

CONTACTS

Editor: Gene Russo

European Head Office, London
The Macmillan Building,
4 Crinan Street, London N1 9XW, UK
Tel: +44 (0) 20 7843 4961
Fax: +44 (0) 20 7843 4996
e-mail: naturejobs@nature.com

European Sales Manager:
Andy Douglas (4975)
e-mail: a.douglas@nature.com
Business Development Manager:
Amelie Pequignot (4974)
e-mail: a.pequignot@nature.com
Natureevents:

Claudia Paulsen Young (+44 (0) 20 7014 4015)
e-mail: c.paulsenyoung@nature.com
France/Switzerland/Belgium:
Muriel Lestringuez (4994)
Southwest UK/RoW: Nils Moeller (4953)

Scandinavia/Spain/Portugal/Italy:
Evelina Rubio-Hakansson (4973)
Northeast UK/Ireland:
Matthew Ward (+44 (0) 20 7014 4059)
North Germany/The Netherlands:
Reya Silao (4970)
South Germany/Austria:
Hildi Rowland (+44 (0) 20 7014 4084)

Advertising Production Manager:
Stephen Russell
To send materials use London address above.
Tel: +44 (0) 20 7843 4816
Fax: +44 (0) 20 7843 4996
e-mail: naturejobs@nature.com
Naturejobs web development: Tom Hancock
Naturejobs online production: Dennis Chu

US Head Office, New York
75 Varick Street, 9th Floor,
New York, NY 10013-1917
Tel: +1 800 989 7718

Fax: +1 800 989 7103
e-mail: naturejobs@natureny.com

US Sales Manager: Peter Bless

India
Vikas Chawla (+91 1242881057)
e-mail: v.chawla@nature.com

Japan Head Office, Tokyo
Chiyoda Building, 2-37 Ichigayatamachi,
Shinjuku-ku, Tokyo 162-0843
Tel: +81 3 3267 8751
Fax: +81 3 3267 8746

Asia-Pacific Sales Manager:
Ayako Watanabe (+81 3 3267 8765)
e-mail: a.watanabe@natureasia.com
Business Development Manager, Greater China/Singapore:
Gloria To (+852 2811 7191)
e-mail: g.to@natureasia.com

Aerial view of Research Triangle Park member GlaxoSmithKline.

BEYOND THE TRIANGLE

RESEARCH TRIANGLE PARK

Anthony Atala wasn't planning to move. When recruiters at Wake Forest University in Winston-Salem, North Carolina, contacted him in 2002, Atala was establishing a centre for tissue engineering and cell therapies at Harvard Medical School in Boston, Massachusetts. Wake Forest and Piedmont Triad Research Park, the university's affiliate in the same city, were looking to establish their own centre.

"I had no intention of leaving Boston," says Atala. But he listened to the recruitment pitch and visited the site. A few statistics piqued his interest: North Carolina had just risen to the coveted number three spot on the list of top biotechnology states. It was also among the top states for biotechnology investment and for small-business research grants from the National Institutes of Health. The numbers appealed to Atala, who considers industry collaboration to be a key component of his research.

Back in Boston, Atala was struggling to recruit senior scientists. "It was easy to recruit the young scientist who is going to come and lease an apartment five blocks down," says Atala. But even with larger salaries, senior scientists looking to own their own homes may have to live an hour and a half away. North Carolina housing is cheaper, and although the locals love to complain about the traffic, the clogged highways of Massachusetts and California are far worse. In January 2004, Atala decided to move to Winston-Salem.

Although best known in technology circles for its venerable Research Triangle Park (RTP), North Carolina has several other parks. When the RTP turns 50 next year, nearby Centennial Campus in Raleigh will turn 25 (see 'Life in a technopolis'). The University of North Carolina (UNC) in Chapel Hill will next year start construction on a new research park to be called Carolina North. And in Kannapolis, once a mill town, some former textile workers will be busy taking biotechnology courses to prepare for the completion of the North Carolina Research Campus.

Many states have begun to turn to research parks

As North Carolina's Research Triangle Park nears its fiftieth birthday, **Heidi Ledford** investigates how research parks across the state are coping with mounting pressure from outside competition.

to drive economic development. The competition is heating up and park administrators in North Carolina are bracing themselves for the challenge.

Striving to compete

The RTP is considered to be one of the best technology parks in the world. But while it jostles with parks in Maryland and New Jersey for the number three ranking in life sciences (that California and Massachusetts will remain ranked first and second is a foregone conclusion; the real race is for third place), research parks in China and India are also closing in. "If we're going to compete on a global scale, we're going to have to create larger networks," says Rick Weddle, chief executive of the Research Triangle Foundation of North Carolina, which manages the RTP.

One strategy is uniting the North Carolina parks under a single brand to maximize the region's appeal to a wide range of companies. Each park has its own strengths. A large company looking to establish a major office in North Carolina would probably turn to the 2,800-hectare RTP. Atala himself says that he was not interested in the RTP; he wanted Piedmont's tight relationship between industry and academia.

Other companies may want to leave academia's shadow. Don Gabriel, a professor at the UNC and a co-founder of its spin-off Invitro, which develops pharmaceutical assays, says he might have chosen the RTP even if the UNC's Carolina North were up and running. "We were trying to make the statement that we are an independent company," says Gabriel.

And then there are the topical specialties: the North Carolina Research Campus plans to focus on nutrition. That attracted BioMarker Group, a company that makes diabetes tests, from Winston-Salem. Meanwhile, the strength of North Carolina State University's engineering department lured Michael Creed, co-founder of McKim & Creed, an engineering consultancy firm, to Centennial Campus.

Last month, park directors from around the state had preliminary discussions on working together under

the North Carolina brand. Weddle says that he sees the RTP playing the role of sales portal, as companies interested in North Carolina usually contact the RTP first. The RTP Foundation could then help companies choose their best location — even if that location is not within the RTP. Weddle claims competition within the state is limited. “Rather, we’ll be competing on a global scale with other locations that have similar technology footprints,” he says.

“We’d all like to bask in the glory of the RTP,” says Mark Crowell, the UNC’s associate vice-chancellor for economic development and technology transfer. “And frankly, the RTP is going to run out of land at some point.”

Shifting focus

The RTP has also tried to diversify to make itself more resilient to economic change. Despite a lull in the information-technology sector around 2000, the past few years have been lucrative. The park has recruited 18 new firms since 2004, creating more than 6,300 new jobs.

In some cases, diversification has meant recruiting from those not traditionally associated with research parks. Among the RTP’s biggest deals in the past three years were large parcels of land sold to the financial-sector companies Credit Suisse and Fidelity. “It has enabled us to move way, way up the food chain in terms of average salaries,” says Weddle, who adds that the financial firms, with their large data banks and private software development, are not far removed from the park’s traditional focus on information technology.

Over the past decade, the park has also tripled the number of companies with 250 or fewer employees. Small firms are a focal point for growth, says Weddle. For Joseph Izatt, a biomedical engineer at Duke University in Durham, North Carolina, who co-founded a biological-imaging spin-off called Bioptigen, moving the business to an RTP incubator was an obvious choice. The location is close to companies such as GlaxoSmithKline that could become collaborative partners. “It’s kind of a no-brainer to go to the park,” says Izatt. “It makes us feel



Anthony Atala (left) left Harvard for North Carolina. The Research Triangle Park (above) aims to attract more scientists to the state.

like a real, grown-up company.” Nurturing start-ups is particularly important in North Carolina given the paucity of local venture-capital firms. “We have less than ten funds,” says Robert Taber, director of science and technology at Duke University. “It’s an order of magnitude difference from Boston and California.” One reason, says Taber, may be that the RTP has not produced a major, homegrown biotech success. “People don’t realize the impacts of the Genentechs and the Biogens and the Genzymes,” says Taber, referring to large biotech firms in California and Massachusetts.

Atala does not regret his decision to move. The Wake Forest Institute for Regenerative Medicine now has about 150 employees. Space constraints would have made such speedy expansion impossible in Boston, he says. And early worries that losing the Harvard affiliation might make recruiting harder were unfounded. “It turned out that I had the opposite problem,” says Atala. “All these people wanted to come, and I ended up having to make the tough decisions.” ■

Heidi Ledford writes for Nature from Cambridge, Massachusetts.

WFUBMC/RESEARCH TRIANGLE PARK



LIFE IN A TECHNOPOLIS

It’s a warm spring afternoon, and ‘Hungry Hank’ Roberts, proprietor of Hungry Hank’s Hotdogs, has set up his cart in North Carolina State University’s Centennial Campus in Raleigh. It looks out of place: hotdog stands belong on city corners, not in research parks.

Yet Hungry Hank (pictured) has a steady stream of customers from around the campus. As his patrons linger to socialize, it becomes clear why the property managers invited Hank. A chatty hotdog vendor and a sunny day create the perfect blend for social networking.

It is part of the campus’s aim to create a ‘technopolis’ where researchers can live, work and play. That model is growing in popularity, according to a 2007 report from the

Association of University Research Parks, and Centennial Campus’s emphasis on lifestyle helped earn it the association’s 2007 ‘Outstanding Research Science Park’ award. The state government has supported a ‘Millennium



Centennial Campus: somewhere to live, work and play.

Campuses’ initiative to create similar parks across the state.

Still, much of the campus’s 445-hectare area has not been developed. Although the buildings are nearly at full capacity, the campus has only 1,900 corporate and government employees, far short of the 12,500 it hopes to have when construction is complete. Over the years, the campus has cultivated a mix of large and small companies, government offices and university buildings. And down the road, a new park called Centennial Biomedical Campus is currently under construction. The biomedical park plans to open 150,000 square metres of working space over the next 25 years.

Of the three major universities

in the ‘research triangle’ — Duke University in Durham, the University of North Carolina at Chapel Hill and North Carolina State University — the last has its feet planted most firmly in the applied sciences. Companies at Centennial Campus reflect the university’s strengths in materials science, agriculture and engineering. Centennial partnership developer Amy Lubas jokingly refers to the site of its future golf course — now a vast smear of red clay soil — as the park’s “turf-management project”, then quickly turns serious. “No really,” she says. “North Carolina State University does have one of the top turf-management programmes in the country.”

H.L.

H. LEDFORD

MOVERS

Gregory Crawford, dean, College of Science,
University of Notre Dame, Notre Dame, Indiana



2006–present: Dean of engineering and professor of physics, Brown University, Providence, Rhode Island

2006–present: Co-founder/scientific adviser, Corum Medical, Providence, Rhode Island

2001–06: Associate professor of engineering and physics, Brown University, Providence, Rhode Island

Gregory Crawford says he owes his career success to two words: “What if?” Framing basic research questions in this manner has helped him find ways to turn ideas into tangible solutions and products. As the new dean of the College of Science at the University of Notre Dame in Indiana, Crawford plans to use this strategy to emphasize the value of interdisciplinary projects with real-world applications.

On receiving his undergraduate degree in physics and mathematics from Kent State University in Ohio, Crawford had been set to study nuclear physics. But rather than spend time putting a project in place, he took advantage of an offer to begin graduate research immediately at Kent State’s famed Liquid Crystal Institute. This put him at the forefront of a revolution in liquid-crystal displays.

Crawford’s PhD adviser, Bill Doane, then the director of the Liquid Crystal Institute, credits Crawford’s ambition and drive. As a PhD student, Doane says, Crawford helped solve some basic problems in liquid-crystal physics — for example, the measurement of a fundamental constant that relates to certain properties of liquid-crystal displays, such as how fast the material becomes aligned in a particular direction.

After a sabbatical at the Xerox Palo Alto Research Center in California, Crawford’s drive took on entrepreneurial zeal. “It pushed my creativity,” says Crawford, adding that, in today’s competitive research climate, working in a high-tech industry before joining academia offers valuable perspective.

In his next position as professor of physics and engineering at Brown University in Providence, Rhode Island, Crawford taught a class on entrepreneurship. While searching for research ideas for that class, he made contacts at the medical school. This resulted in a collaboration that yielded an optical device that uses liquid-crystal technology to measure haemoglobin concentrations in the blood non-invasively. Crawford calls it one of his greatest career accomplishments so far, on account of its promising applications. He has subsequently co-founded two biomedical companies — Corum Medical and Myomics.

“In many ways, my push into the life sciences and biomedical technology elevated me as a researcher and broadened my scope,” says Crawford. That background, he says, was pivotal in his recruitment to Notre Dame. There, he plans to continue to “think big”. He will start by applying his ‘what if’ questions to complex problems such as those of global health and infectious-disease research, which he says Notre Dame is well positioned to tackle.

Virginia Gewin

BRICKS & MORTAR

Nucleus of growth at Louisville

The University of Louisville in Kentucky last month unveiled a \$300-million plan to construct five life-sciences buildings. Project leaders aim to generate \$2.3 billion and 8,700 jobs over 20 years. The initiative, NUCLEUS, will include space to incubate biotech companies and provide services in technology transfer, business development and intellectual property.

“There was no space, no economic incentives to incubate and develop start-ups,” says president James Ramsey. “We weren’t doing much in the way of research. We didn’t have much infrastructure in place. We didn’t have life-science seed funds. We didn’t have venture funds to invest in start-up companies.” The city, state and university all realized they needed to make changes for the area’s historically manufacturing-based economy to be competitive, he says.

The first step was a 1997 state programme called ‘Bucks for Brains’. The state matched donors to create endowed chairs. So far, it has raised \$198 million and helped the university to triple the number of endowed chairs to 126. That has increased the university’s competitiveness for federal research dollars. The Bucks for Brains scholars have brought in more than \$144 million in additional federal funding. In 2007, the university had

the nation’s biggest 10-year increase in US National Institutes of Health (NIH) funding.

That programme helped set the stage for the new life-science park, says Manuel Martinez-Maldonado, vice-president of research. He says the NUCLEUS project will help with the next step: attracting companies to the area and spinning off start-ups from the university’s research. He hopes the university will compete for clinical trials and attract related services, such as contract-research organizations.

To that end, the NIH awarded the university \$22 million in 2005 to build the Center for Predictive Medicine, one of 13 national biosafety level-3 labs that will develop vaccines to protect against bioterrorism and emerging diseases. The lab will open by the end of this year. It should help the university to carve out research niches in areas such as *in vivo* imaging of host-virus interactions, Martinez-Maldonado says.

NUCLEUS will offer services to help researchers at all stages of drug and technology development, says Vickie Yates Brown, chief executive and president of the new organization. It will allow the university to take research “from the mind to the marketplace” she adds.

Paul Smaglik

POSTDOC JOURNAL

Passion and obsession

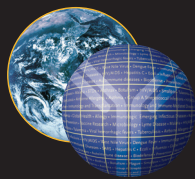
Lately I’ve been struggling to maintain balance in life. And on a recent Sunday, I almost teetered off the edge. At midnight I was still working through a long list of tomato seeds to be sown for this summer’s experiments.

Between organizing new projects for my next career move and preparing pancakes for my daughters while my wife treats her dental patients, I am stretched thin. Meanwhile, my free moments are consumed by doing or thinking about research — and as I’m a mentor as well, not necessarily my own.

From the outside, one might say I’m obsessed, but I prefer a more positive spin. I have passion. My friends have seen it when I talk about my excitement for growing giant pumpkins, and my parents claim it started with a fascination with frogs. Nowadays, the movement of pollen from one flower to another excites me; I visualize their chromosomes doing a molecular dance.

Having crossed paths with many scientific minds, I think I can spot those with passion rather than obsession. The passionate ones exude joy, and insist on sharing that joy with others. It’s passion that keeps the sparks flying, the ideas flowing, and my eyes open past midnight on Sundays. But I did get to bed before one o’clock. Had I stayed up any longer, there’s a chance that obsession might have stolen away my joy.

Zachary Lippman is a postdoctoral fellow at the Hebrew University of Jerusalem’s faculty of agriculture.



Help Us Help Millions

Tenure Track/Tenure Investigator Positions in Systems Immunology and Infectious Disease Modeling

The National Institute of Allergy and Infectious Diseases (NIAID), Division of Intramural Research (DIR) is seeking several outstanding individuals for its new Program in Systems Immunology and Infectious Disease Modeling (PSIIM).

Modern technology allows the analysis of immune responses and host-pathogen interactions at multiple levels - from intracellular signaling networks, to individual cell behavior, to the functioning of a tissue, organ, and even the whole organism. The challenge is not only to collect the large amounts of data, but also to organize it in a manner that enhances our understanding of how the immune system operates or how pathogens affect their hosts. To do this, it is necessary to develop detailed quantitative models that can be used to predict the behavior of a complex biological system. These models can help explain the mechanisms underlying physiological and pathological responses to infection or vaccination, which can then be employed to design better therapies or vaccines.

Achieving these goals requires an interdisciplinary effort and for this reason the PSIIM is organized as an integrated team of scientists and support staff. Within the PSIIM, there will be groups with expertise in the areas of computational biology, bioinformatics, proteomics, genomics, cell biology, immunology, and infectious diseases. These teams will have access to the latest technology for gene expression profiling, high content screening of RNAi libraries for the discovery of pathway components, imaging tools, genomic and proteomic analysis, cores for the genetic manipulation of animals, and a substantial computer infrastructure. They will also have access to BSL3 facilities for working with infectious agents of high priority for human health and biodefense. Although the PSIIM has been established within NIAID and has an immune / infectious disease focus, it is also expected to play a major role in fostering the growth of systems biology efforts throughout the NIH and involving diverse biomedical areas.

Current teams in the PSIIM include Immunology, Computational Biology – Modeling and Simulation, and Molecular / Cell Biology – High-throughput screening. The PSIIM is now recruiting for tenure track or tenure level team leader appointments in the following areas:

Bioinformatics / Biostatistics: the incumbent will lead a group focused on developing and implementing computational tools and statistical methods for the analysis of genomic and proteomic data. The ideal candidate will have a strong background in statistics, mathematics, programming, and modeling biological systems as well as a strong interest in collaboration with biologists for the elucidation of biological mechanisms. The group will include expertise in software development (C++, Java, Perl, SQL etc.), knowledge of bioinformatic tools, databases and algorithms, and experience with heterogeneous computer environments (UNIX, Windows, Mac).

Proteomics: the incumbent will lead a group involved in the development and application of new methods for the determination of protein number, binding affinities, post-translational modification, and

other qualitative and quantitative aspects of protein expression and behavior that are necessary for computer modeling and simulation. Tools such as mass spectrometry and microfluidic-based multiplexed binding assays are expected to be key elements in the efforts of this group. A strong background in protein biochemistry and the relevant instrumentation needed for high-throughput, high-sensitivity analysis is required.

Genomics: the incumbent will be responsible for developing novel approaches to the systems-wide analysis of such issues as transcription factor and epigenetic control of gene expression, the effects of allelic polymorphism on gene expression and function, quantitative measurement of gene expression, and the role of non-coding regions and transcripts such as miRNAs in regulating gene/gene product expression patterns. Knowledge of modern methods in high-throughput analysis of gene transcription, transcription factor binding site identification, analysis of epigenetic modifications, and analysis of gene regulatory circuits is required; bioinformatics experience is desirable.

These positions and the research activities they conduct are fully funded by the intramural research program of NIAID. Each team leader is expected to build a working group consisting of postdoctoral fellows, students, technicians, and staff scientists. The team leaders will work with the Program Director to help set the goals for the PSIIM and to determine how best to reach these goals as an integrated group. To ensure appropriate career trajectories for those joining the PSIIM team effort, the NIH has modified its tenure policies to take specific account of contributions made in such a team science setting. Applicants should be seeking a difficult challenge in which creativity, technical expertise, and a strong desire to achieve in a team setting will be critical for success.

Interested candidates may contact Dr. Ronald Germain, Program Director, PSIIM, DIR, NIAID at (301) 496-1904 or email (rgermain@niaid.nih.gov) for additional information about these positions.

To apply, submit your curriculum vitae, bibliography, and a detailed statement of how your expertise can contribute to the success of the PSIIM program, to Wanda Jackson at NIAID.DIR.Search@niaid.nih.gov. In addition, three letters of reference must be sent directly from your three referees to Dr. Robert Hohman, Chair, NIAID Search Committee, c/o Wanda Jackson at NIAID.DIR.Search@niaid.nih.gov or 10 Center Drive, MSC 1356, Building 10, Room 4A22, Bethesda, Maryland 20892-1356. Email is preferred. Completed applications MUST be received by **Friday, May 23rd**. Please refer to ad #019 for bioinformatics/biostatistics, #020 for proteomics, and #021 for genomics on all correspondence. Information regarding the DIR laboratories is available at: <http://www3.niaid.nih.gov/about/organization/dir/default.htm> and information on working at NIAID is available on our website at: <http://healthresearch.niaid.nih.gov>

For more information about the NIAID systems biology program, please visit <http://www.nih.gov/catalyst/2006/06.09.01/page1.html>



Department of Health and Human Services
National Institutes of Health
National Institute of Allergy and Infectious Diseases
Proud to be Equal Opportunity Employers



OPPORTUNITIES @ NIH THE NATIONAL INSTITUTES OF HEALTH



**National Institute of Mental Health
Scientific Director
Division of Intramural Research Programs**



The National Institute of Mental Health, a major research component of the National Institutes of Health (NIH) and the Department of Health and Human Services (DHHS), is seeking exceptional candidates for the position of Scientific Director, Division of Intramural Research Programs (DIRP). The Scientific Director, DIRP will lead and manage a vibrant basic, behavioral and clinical research program with a budget of approximately \$160 million and a staff of over 1,000, including 53 independent principal investigators and over 300 pre/post doctoral and visiting fellows (<http://intramural.nimh.nih.gov>).

Assisted by a Board of Scientific Counselors, an external advisory group that undertakes rigorous reviews of the NIMH intramural research programs, the Scientific Director will be responsible for developing and implementing an overall vision for the DIRP that is consistent with the mission and strategic objectives of the NIMH. This effort would encompass the recruitment of new faculty, the expansion of the Division and its programs into several new, state-of-the-art research facilities on the NIH's Bethesda, Maryland campus, and the management of scientific resources at the NIMH DIRP, including an extensive network of core service facilities, such as an fMRI Facility, a Transgenic Mouse Facility, and a Scientific and Statistical Computing Core, to name a few. It will also include working with other neuroscience Scientific Directors at NIH to develop trans-NIH initiatives.

Applicants must have a Ph.D., M.D., or equivalent degree in the biomedical sciences, with broad senior-level research experience and experience in direct administration of a research program. Applicants should be known and respected within their profession, both nationally and internationally, as distinguished individuals of outstanding scientific competence. Salary is commensurate with experience and accomplishments. Support and resources are also available to allow the Scientific Director to lead his/her own research laboratory. Experience with NIH administrative policies, procedures, and operations is highly desirable but not essential.

Interested candidates should send a letter of interest, including a brief description of research and administrative experience, and a curriculum vitae and bibliography to: **Chair, NIMH Scientific Director Search Committee at NIMHsearch@mail.nih.gov or at 6001 Executive Blvd, Room 8235, MSC 9669 Bethesda, MD 20892-9669 (for express or courier delivery use Rockville, MD 20852).** Review of applications will begin on **May 5, 2008**, but applications will continue to be accepted and considered until the position is filled. For questions contact **Dr. Thomas Insel, Director, NIMH at tinsel@mail.nih.gov.**

The NIH encourages the application and nomination of qualified women, minorities, and individuals with disabilities.
HHS and NIH are Equal Opportunity Employers.



PROGRAM DIRECTOR, RETINAL DISEASES PROGRAM

The National Eye Institute (NEI), National Institutes of Health (NIH) in Bethesda, Maryland, is seeking exceptional candidates for the position of Health Scientist Administrator in the Division of Extramural Research. The Division coordinates all aspects of the NEI extramural research grants and contracts program. The position advertised is for a Program Director in the Retinal Diseases Program. The Program supports clinical and laboratory research on diabetic retinopathy, sickle cell retinopathy, and other vascular abnormalities of the retina; inflammatory diseases of the retina; retinoblastoma; retinitis pigmentosa and other inherited retinal degenerations; macular degeneration; and retinal detachment and vitreal disorders. Future directions for this program are expected to employ promising new technologies and collaborations with new disciplines, such as bioengineering, which hold great promise for understanding retinal diseases.

The incumbent will direct and oversee the administration of a research grant portfolio in the field of retinal diseases. This includes developing, managing, administering, and evaluating a comprehensive program of grants; advising NEI senior staff regarding both the scientific and administrative matters affecting the retinal diseases research portfolio; representing NEI in broader NIH extramural matters; coordinating program planning and evaluation activities; and providing reports and statistics related to the Retinal Diseases Program.

This is a career Federal position. The salary range is \$69,764 – \$127,442 per annum, commensurate with qualifications and professional experience. A full benefits package is available, which includes retirement, Thrift Savings Plan participation, health, life, and long-term care insurance.

Applications will be accepted through 05/23/2008. The complete vacancy announcement, along with mandatory qualifications and application procedures, can be obtained via the USAJOBS website at <http://www.usajobs.com>. Please refer to announcement number **NEI-08-240055-DE**. For questions, please contact **Ms. Thomascene White at (301) 435-5713 or whitet1@od.nih.gov.** **Applications and supporting documentation must be received by close of business, 05/23/2008.**



Center for Cancer Research

DIRECTOR, CANCER STEM CELL and DEVELOPMENTAL BIOLOGY PROGRAM

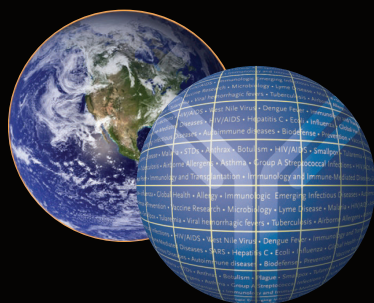
Application Deadline: May 30, 2008

The National Cancer Institute (NCI) is seeking an outstanding scientist to serve as the first *Director of the Cancer Stem Cell and Developmental Biology Program* in the Center for Cancer Research (CCR). This is an exciting opportunity to establish a nationally recognized program in stem cell and developmental biology research. The Director will lead a collaborative community of investigators who are committed to advancing this field with the goal of fostering novel therapeutic approaches that target cancer stem cells. The program will be supported by a wide array of intellectual and technological resources, including dedicated, high quality technology cores relevant to stem cell biology, such as imaging/visualization (both in vitro and in vivo), in vitro stem cell assays, transgenic models, genetics, gene/drug delivery, FACS, proteomic analysis (including high-throughput mass spectrometry), and human genetics/bioinformatics. In addition, the cancer stem cell and developmental biology initiative will be supported with stable financial resources and a training program in cancer stem cell and developmental biology for talented post-doctoral fellows.

The National Cancer Institute is part of the National Institutes of Health (NIH) in the Department of Health and Human Services (DHHS), a federal government agency. The Center for Cancer Research is the largest component of the intramural biomedical research effort at NIH. The research environment is collaborative and highly conducive to advancing translational research, emphasizing multidisciplinary and interdisciplinary team science. For more information go to: <http://ccr.cancer.gov/default.asp>.

Applicants must have a Ph.D., M.D., or M.D. /Ph.D. degrees and a documented history of research success. Currently tenured faculty or faculty eligible for tenure at NIH, with a demonstrated commitment to stem cell biology, are encouraged to apply. Salary will be commensurate with experience and accomplishments. Applications should include: A letter indicating the position of interest including a statement of research interests; a career synopsis; and a current *curriculum vitae* and complete bibliography.

Applications must be postmarked or received by email at hooperl@mail.nih.gov by **May 30, 2008**. Send applications to: Douglas Lowy, M.D., Chair, Cancer Stem Cell and Developmental Biology Program Search Committee, c/o Laura Hooper, Executive Secretary, Center for Cancer Research, 31 Center Drive, 31/3A11, MSC 2440, Bethesda, MD. 20892-2440.



NIAID

**DEPARTMENT OF HEALTH AND HUMAN SERVICES
NATIONAL INSTITUTES OF HEALTH
NATIONAL INSTITUTE OF ALLERGY AND INFECTIOUS DISEASES
Division of Intramural Research / Laboratory of Host Diseases**

Hematopoietic Stem Cells: Transplant and Gene Therapy

The Genetic Immunotherapy Section (GIS) of NIAID, NIH is recruiting up to three Postdoctoral Fellows for laboratory studies of the biology and immunology of human hematopoietic stem cell transplantation and gene therapy. Areas of study include gene transfer vector development including lentivectors, biology of gene transfer into hematopoietic stem cells, mechanisms of stem cell engraftment, immunology of graft versus host disease, and mechanisms of immune tolerance relating to transplant and gene therapy. The GIS has an active clinical research program in these areas developing therapies for inherited immune deficiencies, providing opportunity for candidates to work in an environment where bench research has a strong translational component.

Extensive experience in molecular biology is required. Previous training in one of the areas of study noted above is highly desirable. Willingness to work with murine models is required. Salary is based on relevant experience and education.

Candidates should send by email their curriculum vitae together with a statement describing relevant training and interest plus full contact information for three to five individuals who may be contacted to provide letters of reference (include email subject heading: Fellowship recruit GIS LHD):

Harry L. Malech, MD, Laboratory of Host Diseases,
Genetic Immunotherapy Section, NIAID/NIH
Building 10, Room 5-3750, MSC1456
10 Center Drive, Bethesda, MD 20892-1456
Email: hmalech@nih.gov

For further information, please visit:
<http://www3.niaid.nih.gov/labs/aboutlabs/lhd/geneticImmunotherapySection/malech.htm>



THE NATIONAL INSTITUTES OF HEALTH
NIH
OPPORTUNITIES @ NIH

NW129519R

THE NIH IS DEDICATED TO BUILDING A DIVERSE COMMUNITY IN ITS TRAINING AND EMPLOYMENT PROGRAMS

GREAT SCIENTISTS NEED GREAT LABORATORIES.

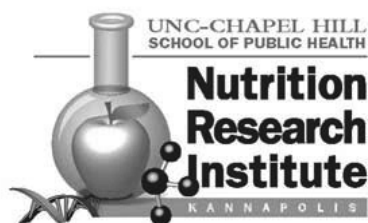
Opening 2008!

The **Nutrition Research Institute** and the Department of Nutrition in the School of Public Health at the University of North Carolina at Chapel Hill are jointly recruiting tenured or tenure-track positions to be located on the North Carolina Research Campus in Kannapolis.

The NRI is positioned to become the world leader in each of its focus areas: brain development, cancer, obesity and eating disorders. Cutting edge equipment available nowhere else in the world, coupled with breakthrough scientific methods in genetics and metabolomics, will make possible a vision of individualized nutrition never before realized.

We offer a brand-new, high-tech facility focusing on nutrigenomics and metabolomics as they apply to human nutrition, hard money research support, excellent start-up packages, new labs and office space, capacity to conduct human and mouse research, state-of-the-art instrumentation and equipment in metabolomics and nutrigenomics, and an outstanding intellectual environment on campus with programs from 7 universities.

For more information about the NRI, visit www.uncnri.org.



We strongly encourage applications from women, minorities, and individuals with disabilities. The University of North Carolina at Chapel Hill is an Equal Opportunity Employer.

WE'VE GOT BOTH.

NW129752R

Endowed Chair at Duke University in Experimental Condensed Matter Physics

The Department of Physics at Duke University invites applications and nominations for an Endowed Chair in Experimental Condensed Matter Physics, including Biological Physics, at the tenured Full Professor level to begin on or after January 2009. We are looking for candidates who have a primary interest in the fundamental physics of hard or soft condensed matter systems and demonstrated excellence in research and teaching. The successful candidate is expected to lead a world class program and will benefit from potential overlap with current university thrusts in nanoscience, imaging, and/or optics and photonics.

Applications should include a complete curriculum vitae and publication list, and a statement of research and teaching.

Application should be made via
<https://academicjobsonline.org>

Additional material may be sent to: Prof. Robert Behringer, Chair of the Search Committee, c/o Florin Damian, Department of Physics, Duke University Box 90305, Durham, NC 27708-0305.

The search committee will begin evaluation of applicants on June 1, 2008. Duke University is an Equal Opportunity/Affirmative Action Employer; we particularly encourage applications from women and minorities.

NW129428R

**Read *Naturejobs*
regularly.**

**For better career
prospects.**



naturejobs

Professor of Global Environmental Health

Duke University's Nicholas School of the Environment and Earth Sciences and the Duke Global Health Institute (DGHI) have an opening for a tenured associate or full professor of global environmental health. The Nicholas School, with an interdisciplinary faculty of 75, offers professional (Master of Environmental Management) and graduate (M.S. and Ph.D.) degrees and directs Duke's undergraduate environmental programs. DGHI undertakes and coordinates global health educational, research, and policy related programs involving many disciplines throughout the university, including the medical center.

The candidate must have a M.D. or a Ph.D. in a relevant field, which we interpret broadly. Relevant subjects include, but are not limited to, epidemiology, toxicology, public policy, and public health, as well as environmental issues as they relate to health outcomes – for example, the relationship between climate change and disease vector distribution. Knowledge of qualitative and quantitative methods integral to population-based science and human health/ecosystem health interconnections are preferred. Broad understanding of the global environmental health field and experience undertaking environmental health research in a developing country setting are essential.

The successful applicant is expected to lead the multi-disciplinary Global Environmental Health signature research initiative at DGHI (<http://globalhealth.duke.edu/>). He/she should have a nationally recognized, externally funded research program and relevant experience with the administrative components of research programs, and will be expected to contribute to relevant teaching programs. There are numerous opportunities for interdisciplinary collaboration within the Nicholas School and DGHI, as well as with multiple other academic units across the university. Consideration of applications begins June 1, 2008 and continues until the position is filled.

Send letter of interest, curriculum vitae, a one to two page summary of research and teaching plans, relevant papers and publications, and three references to Chair, Global Environmental Health Search Committee, Nicholas School of the Environment, Box 90328, Duke University, Durham, NC 27708-0328.

Duke University is an Equal Opportunity/Affirmative Action Employer.

NW130286R



The M.U.R.D.O.C.K. Study

A major initiative of the Duke Translational Medicine Institute, the Measurement to Understand Reclassification of Disease of Cabarrus/Kannapolis (M.U.R.D.O.C.K.) Study serves as a foundation for the research getting underway at the North Carolina Research Campus in Kannapolis, North Carolina. Through a generous gift from Mr. David H. Murdock, owner of Dole Foods, Inc., the study brings together the multidisciplinary expertise of clinicians, scientists, bioinformaticists, healthcare providers, and many others from Duke University, the local communities, and other universities in a highly collaborative campus environment to participate in this unprecedented research opportunity.

In the study's first horizon, molecular and imaging data will be generated and analyzed to reclassify diseases—such as cardiovascular disease, hepatitis C, osteoarthritis, and obesity—using the state-of-the-art Core Laboratory and world-class technologies being placed at the North Carolina Research Campus. The unique, integrative data set that emerges will both require and facilitate the development of novel informatics methodologies.

In addition to a high-performance computing environment, researchers will have access to a wide variety of resources and expertise for genomics, proteomics, metabolomics, imaging, microscopy, analytical chemistry, and clinical chemistry. Researchers involved with the M.U.R.D.O.C.K. Study and the North Carolina Research Campus thus will be able to validate newly generated hypotheses using an array of technologies and populations. In addition, these data will enable translation back into pathway analysis for fundamental understanding of the mechanisms of health and disease. The analytical results of the M.U.R.D.O.C.K. Study will be translated into clinical trials for future prospective studies in the North Carolina region and beyond so that, ultimately, disease treatments will be tailored to improve health outcomes and transform the next generation of medical practice.

Opportunities for collaboration and employment are being explored.
For more information, please contact murdock-study@duke.edu.

Re-Writing the Textbook of Medicine



147 West Avenue
 Kannapolis, North Carolina 28081
 704.250.5850
www.dtmi.duke.edu

 **Duke Translational Medicine Institute**

NW129866R

2009 Grant Programs for Physician-Scientists

The Burroughs Wellcome Fund is an independent private foundation dedicated to advancing the biomedical sciences by supporting research and other scientific and educational activities.

**BURROUGHS
 WELLCOME
 FUND** 

919.991.5100
www.bwfund.org

2009 Clinical Scientist Awards in Translational Research

Deadline: October 1, 2008
 \$750,000 over five years for established physician-scientists

Candidate must have an M.D. or M.D.-Ph.D. degree, hold an appointment or joint appointment in a subspecialty of clinical medicine, and hold a current license to practice medicine in the U.S. or Canada. Candidates must be academic investigators at the assistant professor or early associate professor level, holding a tenure-track or equivalent position at the time of application and present evidence of having established an independent research career.

2009 Career Awards for Medical Scientists

Deadline: October 1, 2008
 \$700,000 over five years for postdoctoral-faculty bridging support

Candidates should have a clinical degree. Proposals must be in the area of basic biomedical, disease oriented, translational, or molecular, genetic, or pharmacological epidemiology research. Proposals in reproductive science are encouraged. Health services research or large-scale clinical trials are ineligible. Candidates must have at least two years of research experience and be in a mentored position at the time of application. Candidates who have tenure-track faculty positions are ineligible.

For full guidelines and eligibility, visit www.bwfund.org.

NC STATE UNIVERSITY

Fruit & Vegetable Science Institute

NC Research Campus • Kannapolis, NC



The North Carolina State University Fruit and Vegetable Science Institute is part of an integrated effort across the North Carolina Research Campus to adapt emerging technologies for plant improvement and human health benefits. The Institute, which will be staffed by the N.C. State University College of Agriculture and Life Sciences, will develop a new generation of fruits and vegetables with superior nutritional and horticultural characteristics. Researchers will use the most advanced scientific tools to provide new insights into cellular processes, then translate these breakthroughs through genomics and plant breeding into plants with desired traits. The Institute offers an exciting opportunity to complement and expand the N.C. State University mission to benefit the social and economic well being of the people of North Carolina, the nation and the world.

The Institute will play a key role in the larger vision of David Murdock for the North Carolina Research Campus. Much of the work of faculty from other universities will focus on nutrition, determining optimal nutritional characteristics for various fruits and vegetables. College of Agriculture and Life Sciences faculty will work with this information to develop plants that meet nutritional requirements and will determine

how best to produce those plants commercially. Plant breeding will be a pivotal part of the effort. N.C. State University already has active breeding programs for blueberries, strawberries, brambles and sweet potatoes. In addition, the Institute will develop a breeding program for leafy vegetables such as lettuce.

The N.C. Research Campus offers state-of-the art facilities to determine protein structures that mediate growth, resistance and nutrient production, and for molecular imaging of cellular function. In addition, an agricultural research station is being constructed as part of the campus. The station will include more than 45,000 square feet of greenhouses and 100 acres of fields devoted to agricultural experiments.

The faculty positions N.C. State University is filling on the N.C. Research Campus are 12-month, 100% research, tenure-track positions. While located at the N.C. State Fruit and Vegetable Science Institute, the scientists who fill these positions will be part of a world-class team tenured with any of the College of Agriculture and Life Sciences departments to include Plant Biology, Genetics, Horticultural Science, Food Science, Plant Pathology and others.

Available Positions (Search Phase Completed)

- ▶ Leafy Vegetable Breeder - Assistant/Associate Professor
- ▶ Strawberry Breeder - Assistant/Associate Professor
- ▶ Applied Molecular Geneticist for Fruit and Vegetable Cultivar Development - Assistant/Associate Professor
- ▶ Postharvest Physiologist - Assistant/Associate/Full Professor

Hiring the Following Positions at All Levels (July 1, 2008 through June 30, 2009)

- | | |
|---------------------------|--|
| ▶ Quantitative Geneticist | ▶ Genomics, Systems Biologist |
| ▶ (2) Phytochemists | ▶ Plant Molecular Biologist, Pathway Engineering |
| ▶ Metabolomics Scientist | ▶ Plant Biochemist |

Superior Agriculture
for a Healthier Future

COLLEGE OF
AGRICULTURE & LIFE SCIENCES
ACADEMICS • RESEARCH • EXTENSION

704.250.5400 • fvsi_info@ncsu.edu • www.ncsu.edu/fvsi/

NW128944R

GROUNDBREAKING OPPORTUNITIES

at The David H. Murdock Research Institute



The David H. Murdock Research Institute (DHMRI) was established as a public charity to support groundbreaking research at the North Carolina Research Campus. Destined to be the catalyst of major scientific discoveries in health and nutrition, the DHMRI will offer capabilities ranging from next-generation DNA sequencing to cutting-edge confocal imaging and the world's first actively-shielded 950 MHz NMR. The DHMRI will be the first of its kind, housing this unique collection of state-of-the-art instrumentation in one central location.



With construction of the Core Laboratory building nearing completion, we are looking to hire full-time directors and technical staff for the Genomics, Metabolomics, Proteomics and Integrated Microscopy core laboratories. We will also be hiring directors and staff members to join the Information Technology and Bioinformatics teams.

Career opportunities available at www.DHMRI.org

DHM | RI

David H. Murdock Research Institute

109 WEST AVENUE, KANNAPOLIS, NORTH CAROLINA 28081

704 | 250 | 2600

www.DHMRI.org

NW130352A



Not paid what you're worth? Big irritant.

Tactics to improve your salary.

naturejobs

North Carolina values science—and scientists agree it's one of the best places in the world to work and live. It's home to world-class research institutions including: Duke; Wake Forest; the University of North Carolina-Chapel Hill, North Carolina State University and the 14 other UNC-system universities; RTI International; the Hamner Institutes for Health Sciences; the National Institute of Environmental Health Sciences; and the Environmental Protection Agency. There's nowhere else in the world like North Carolina.

Biotechnology Works in North Carolina...

...wouldn't you like to?

- The North Carolina Biotechnology Center supports life science education, research, and commercialization statewide with:
 - Grant and loan programs
 - Intellectual-exchange programs
 - Centers of Innovation in marine biotechnology, natural biotechnology and integrative medicine, nanobiotechnology, and advanced medical technologies
- 2007 Nobel Laureate Dr. Oliver Smithies of UNC-Chapel Hill is one of 52 outstanding scientists recruited to the state so far with \$9.6 million in Biotechnology Center grants. He is the seventh scientist with strong North Carolina ties to win the Nobel Prize for chemistry, physiology or medicine since 1988
- About 150 bioscience patents are granted each year to our university and corporate scientists
- The Biotechnology Center encourages start-up companies with: low-interest loan programs; one-on-one consultations; networking events; and venture capital referrals
- North Carolina has 450 bioscience companies employing 55,000 people earning an average of \$70,000
- These bioscience companies include: 260 R&D companies; 93 contract research and testing companies; 97 production and manufacturing companies
- Opportunities also abound here at major bioscience companies, including GlaxoSmithKline, BASF, Bayer, Biogen Idec, Cardinal Health, Merck, Novartis, Novo Nordisk, Novozymes, Syngenta, Talecris and Wyeth



2007 Nobel Laureate Dr. Oliver Smithies
Recruited in 1987 with Biotechnology
Center Faculty Recruitment Grant;
Excellence Professor,
University of North Carolina-Chapel Hill



**North Carolina
Biotechnology Center**

15 T.W. Alexander Drive | P.O. Box 13547 | Research Triangle Park, N.C. 27709-3547
With regional offices in **Asheville** | **Charlotte** | **Greenville** | **Wilmington** | **Winston-Salem**

www.ncbiotech.org

After the snow

Who will save the servants?

C. N. Simms

Maybe it's the background noise of my husband's resonant snoring that conjures up the images of falling snow hitting the ground with dull, forceful regularity. It feels apt that I wake in a cold sweat, given the subject of my sepia-tinted dreams.

My husband stirs. "The same dream again?" he asks from his prone position, his weary concern tempered with impatience as I cross to the window. He cedes to the pillow without waiting for a reply and, as always, my faint hopes are scattered by the hurricane winds whipping half-seen objects silently down the desolate street.

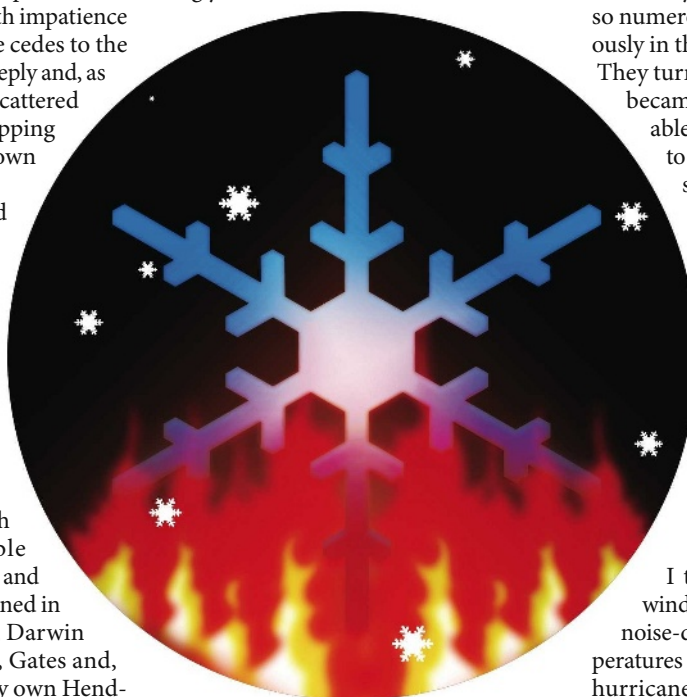
It wasn't the ones you'd expect. It wasn't the sheep or the crops. It wasn't even the humans we managed to grow once the ethical barriers had crumbled to the tide of discovery. It was the first ones, the bacteria. It's all so far in the past now that most people think that the bacteria have always been here.

Acclaim and blame lie with Saint Craig Venter, double Nobel laureate, entrepreneur and genetic pioneer. He's mentioned in the same breath as Gandhi, Darwin and Einstein. With Trump, Gates and, more recently, with our very own Henderson. Back then they were having trouble with global warming, but amid spiralling population growth and struggles to keep hold of financial reins as a global recession bucked bankers out of buildings, they could do nothing about climate change.

Fortunately that wasn't the end, because geneticists managed to manufacture a bacterium's genome by sticking together small segments of DNA. It seems so staid considering that in a few hours I'll be using a Henderson localized DNA-adjusting kit to choose the perfume I'll emit from my pores today, but back then it was phenomenal stuff. Despite all our advances, Henderson will never be canonized. The church fell not long after Venter's time and now all we have are thousands of apocalypse-chasing groups, a mish-mash of old, dead religions. There's little comfort to be found there.

The simple bacterium mimicked was *Mycoplasma genitalium*. The smallest known free-living natural bacterium. And the copied genome was to become

the first genuine artificially created life. Not exactly intelligent, but alive and capable of reproducing. How did they do it? At the researchers' behest, corporations made hundreds of specific sections of DNA, each one just a few hundred bases long. Enzymes stitched the overlapping fragment ends together, creating a carbon copy of the genome of the bacterium. Two long years later, after labs had twice been



burned to the ground by protesters, they finally managed to get the created genome to take root inside a bacterial cell.

The main problem had been that the DNA was inert. The ultrasterile techniques delayed finding the cause, but eventually the researchers made an error. You can always count on human error. The stray segment of DNA that found its way into a pipette was enough to kick-start the cell into action. All they had to do from then on was attach a few bases of DNA from something that had lived and the artificial genomes would come to life. Why, we don't know, but we still need that spark.

The door to creation was not so much opened, as blown to shards. Soon we could create larger and larger genomes, but work always continued on those bacteria. Researchers pared genomes down to the barest of essentials. Then they added in a few carefully selected genes. First they tried to make bacteria that could produce carbon-based fuels. It didn't work. Not

effectively. So they tried genes that enabled bacteria to take in greenhouse-gas molecules such as carbon dioxide, using the carbon to make new cell walls for further division and releasing oxygen molecules into the atmosphere.

And there it was, the solution to part of the global-warming problem. It started on a small scale, but eventually the bacteria were everywhere. In some places they were so numerous that fires started spontaneously in their oxygen-rich surroundings. They turned back the clock for us. They became a part of life, doing innumerable crucial tasks. I even had some to keep our apartment on the right side of carbon neutral. We let the bacteria do our job for us, and they did it well.

Atmospheric carbon levels dropped, the ice caps stopped melting, the seas stemmed their inevitable rise and the wildlife in the seven world-wide protected zones began to reproduce again. It was too late for the corals and most of the fish, but we have new fish now. We did have new fish.

"We should have known," I tell the bleak early-morning winds, their strength disguised by the noise-dampening glass. Increased temperatures mean that most mornings bring hurricanes nowadays. He's fallen asleep again, I think, he won't hear me. He hardly ever listens even when he's awake.

"Alice," he says, shading his eyes to see the silhouette of my body, highlighted by the reflection of street lights in the fierce eddies and swirls of the air behind the window. "It's four. It's not snowing. It will never snow. Now come back to bed."

We took every precaution to stop the bacteria from mutating. But that meant that when they started to die, they couldn't adapt. We still don't know what's killing them. And now the world is worse than it's ever been.

"Maybe we won't be able to do it. Maybe we'll have to do what they failed to do back then and cut emissions."

"It still won't snow."

"You know what I mean."

"Honey, you'll be back in the lab in a few hours. Save the world then."

C. N. Simms is a jack-of-all-trades whose former careers span corporate and social divides. He has no current plans to create a genome.

JACEY